STUDIES OF FLUIDIC SYSTEMS FOR ENVIRONMENTAL APPLICATIONS

A Thesis Submitted for the Degree of
Philosophiae Doctor
of the University of Wales

by

Darrell A. Egarr MEng AMIMechE

Cardiff School of Engineering
University of Wales, Cardiff

August 2005

UMI Number: U585046

UMI

Dissertation Publishing

ProQuest

DECLARATION

This work has not been accepted in substance for any degree and is not being concurrently submitted in candidature for any degree

Signed .... (Candidate)

Date ... 29/08/05

STATEMENT 1
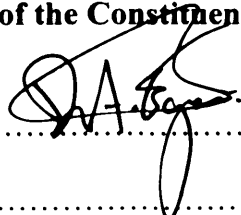
This thesis is the results of my own investigations, except where otherwise stated.

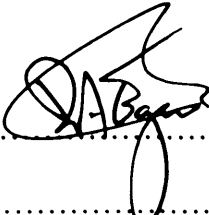Other sources are acknowledged by footnotes giving explicit references. A bibliography is appended.

Signed .... (Candidate)

Date ... 29/08/05

STATEMENT 2

I hereby give consent for my thesis, if accepted, to be available for photocopying and for inter-library loans **after expiry of a bar on access approved by the University of Wales on the special recommendation of the Constituent Institution/University College concerned.**

Signed .... (Candidate)

Date ... 29/08/05

Abstract

A Hydrodynamic Vortex Separator (HDVS) is a form of Combined Sewer Overflow (CSO) used for solid-liquid separation. HDVSs are also used at sewage treatment works for the separation of grits that are transported through the sewer network. The residence time of the fluid that passes through these devices is increased by the rotational nature of the flow and hence, the time that gravity has to act on particulates is also increased. This feature of the fluid dynamics means that a HDVS may also be used as a contact vessel for disinfection of wastewater during a CSO event. To date the physics of these systems is not completely understood in terms of particulate separation.

To achieve a greater understanding of the HDVS an initial sensitivity study using Computational Fluid Dynamics (CFD) was carried out looking at factors that may influence the efficiency and to gain an insight into variables that should be accounted for during experimentation and test rig design. Following this sensitivity study a 0.75m diameter HDVS was studied under laboratory conditions where it was found that a parameter described as the particle surface load controls the efficiency of the HDVS and not the particle settling velocity as previously thought. A model was developed to describe the retention efficiency and was also applied to scaling. However, more work is required to achieve a greater understanding of the application of the retention efficiency model to larger separators.

Experimental trials on a 3.4m diameter HDVS were undertaken and from this it was found that the most suitable residence time distribution model for a HDVS is the axial dispersion model. Attempts to use CFD to model the separation efficiency of such systems have to date failed. However, validations of the residence time characteristics are reasonable. This has allowed CFD to be used to study the application of residence time to disinfection where it has been shown that an existing disinfection model may be developed to describe the disinfection performance of a HDVS. Scaling laws have also been developed using CFD for the residence time and CFD has consequently given an insight into the fluid dynamics within the HDVS.

Acknowledgements

Nomenclature

Symbol	Quantity	Units
A	Area	m^2
A	Parameter of the logistic function	
a	Constant	
B	Constant	
B	Parameter of the logistic function	
b	Constant	
C	Concentration	kg/m^3 (cfu/ml)
C	Parameter of the logistic function	
C_D	Drag coefficient	
C_u	Convection term	kg/ms^3
$C_{1\epsilon}$	Constant	
$C_{2\epsilon}$	Constant	
$C_{3\epsilon}$	Constant	
C_μ	Parameter for calculating turbulent viscosity	
D	Dispersion coefficient	m^2/s
D	Parameter of the logistic function	
D_b	Binary diffusivity	m^2/s
D_f	Dispersive fraction	
D_{HDVS}	HDVS diameter	m (ft)
$D_{L,ij}$	Turbulent diffusion term	kg/ms^3
$D_{T,ij}$	Turbulent diffusion term	kg/ms^3
D_t	Turbulent diffusivity	m^2/s
d	Diameter	m
d	Dispersion number	
E	Empirical constant	
E	Exit-Age distribution	s^{-1}
e	Coefficient of restitution	
F	Force	N
F	Response to a step input	
F_{ij}	Production by system rotation term	kg/ms^3
f	Pump frequency	Hz
G_b	Generation of turbulent kinetic energy due to buoyancy	kg/ms^3
G_k	Generation of turbulent kinetic energy due to mean velocity gradients	kg/ms^3
G_{ij}	Buoyancy production term	kg/ms^3
g	Acceleration due to gravity	m/s^2
H	Head	m
h	Height	m

Symbol	Description	Units
h_l	Head loss	m
I	Internal-Age distribution	s^{-1}
j	Lethal number of reactions	
K	Apparent kinetic rate constant	s^{-1}
K	Constant	
$K_{geometry}$	Geometry constant	
k	Head loss coefficient	
k	Decay rate	s^{-1}
k	Kinetic rate constant	$m^3/kg.s$ (litres/min.mg)
k	Turbulent kinetic energy per unit mass	m^2/s^2
k^*	First order residual decay rate	s^{-1}
L_r	Length ratio for geometric similarity	
M	Total mass	kg
m	Constant	
m	Mass	kg
m_d	Particle surface load	kg/m^2
$\dot{m}$	Mass flowrate	kg/s
N	Number of CSTRs	
N	Number of micro-organisms	
n	Coefficient of dilution	
n	Number of measurements / variants / sample size	
P_{ij}	Stress production term	kg/ms^3
p	Pressure	N/m^2
Q	Flowrate	m^3/s (litres/second)
Q	Number of phases	
q	Flowrate	m^3/s (litres/second)
Re	Reynolds number	
R_t^2	Coefficient of determination	
r	Radial position	m
S	Strength of vortex	m^2/s
s	Standard deviation of a small sample	
s	Standard deviation of a large sample	
Sc_t	Turbulent Schmidt number	
S_φ	Source term	kg/m^3s
T	ADZ residence time	s
t	Statistic t	
t	Time	s
t	Mean residence time	s
Δt	Sampling time	s
U	Mean velocity at inlet	m/s

Symbol	Description	Units
U_r	Rise velocity / Surface loading rate	m^3/m^2s (litres/m^2s)
U^*	Friction velocity (Non dimensionalised)	
U_τ	Friction velocity	m/s
u	Velocity	m/s
V_e	ADZ volume	m^3
$\dot{V}$	Volume flowrate	m^3/s
X	Constant	
X	Upstream concentration	kg/m^3
x	Sample mean	
Y	Constant	
Y_M	Contribution of the fluctuating dilation in compressible turbulent to the overall dissipation rate	kg/ms^3
y_p	Distance from the wall to point 'P'	m
y^*	Displacement boundary layer thickness (Non dimensionalised)	
y^+	Local Reynolds number	
Z	Constant	
z	Height	m
α	Under relaxation factor	
α	Volume fraction	
β	Empirically derived constant	
δ	Nearest integer value of $\theta/\Delta t$	
ε	Turbulent dissipation rate	m^2/s^3
ε_{ij}	Dissipation term	kg/ms^3
Γ	Diffusion coefficient	kg/ms
φ	Arbitrary variable	
φ	Scalar quantity	
φ_{ij}	Pressure strain term	kg/ms^3
η	Efficiency	%
K	Constant	
κ	Von-Karmon's constant	
N	Number of time constants	
μ	Absolute viscosity	kg/ms
μ_T	Turbulent/Eddy viscosity	kg/ms
μ_L	Laminar viscosity	kg/ms
θ	Transport time delay	s
ρ	Density	kg/m^3
σ^2	Variance of the residence time distribution	s^2
σ_k	Turbulent Prandtl number of turbulent kinetic energy	
σ_ε	Turbulent Prandtl number of turbulent dissipation rate	
T	Time constant	s

τ	Shear stress	N/m^2
τ	Theoretical residence time	s
$\overset{.}{\tau}$	Residence time in one CSTR	s
υ	Kinematic viscosity	m^2/s
ω	Angular velocity	rad/s
ξ	Dummy time variable of integration	s
ψ	Sphericity	
ς	Normally distributed random number	

Subscripts

B	Buoyancy
D	Drag
d	Diffusion
f	Fluid
g	Gravity
h	Hydrodynamic
i,j,k	i, j, k direction
i	Sampling interval
in	Instantaneous
m	Model
n	Normal
P	Point 'P'
p	Particle
p	Prototype
q	qth phase
t	Tangential
t	Time
x,y,z	x, y, z direction
w	Wall
θ	Normalised
0	Initial value

Acronyms

ADE	Advection Dispersion Equation
ADM	Axial Dispersion Model
ADZ	Aggregated Dead Zone
APWA	American Public Works Association
CFU	Colony Forming Unit
CPU	Computer Processing Unit
CSO	Combined Sewer Overflow
CSTR	Continuously Stirred Tank Reactor
DPM	Discrete Phase Model
DRW	Discrete Random Walk
EMF	Electromotive Force
EPA	Environment Protection Agency
EQS	Environmental Quality Standards
HDVS	Hydrodynamic Vortex Separator
HVAC	Heating, Ventilation and Air Conditioning
LES	Large Eddy Simulation
LDA	Laser Doppler Anemometry
MRT	Mean Residence Time
NV	Normalised Variance
PAA	Peracetic Acid
PET	Polyester
PISO	Pressure-Implicit with Splitting of Operators
PIV	Particle Image Velocimetry
PRESTO!	Pressure Staggering Option
RMS	Root Mean Square
RSM	Reynolds Stress Model
RTD	Residence Time Distribution
SCUFA	Self-Contained Underwater Fluorescence Apparatus
SG	Specific Gravity
SIMPLE	Semi-Implicit Method for Pressure-Linked Equations
SIMPLEC	SIMPLE-Consistent
THM	Trihalomethanes
TISM	Tanks In Series Model
UDF	User Defined Function
UDS	User Defined Scalar
UV	Ultra Violet
VOF	Volume Of Fluid

Contents

Appendices 354

1 Introduction

1.1 Background

The oldest and most traditional forms of urban drainage in developed Europe are combined sewers, whereby storm and surface water, as well as foul wastes, are transported to sewage treatment works in the same pipeline. The first problem associated with this system is that during, or after, a storm where the quantity of water being passed through the system exceeds the design limit, Combined Sewer Overflows (CSOs) are required, which may pass polluting water and organic material into a receiving water course, such as a river.

One type of CSO is the 'Storage Chamber' which is essentially a large tank used to 'store' water until the storm load subsides. An inherent problem with storage chambers however is that sedimentation takes place, dictating a maintenance commitment (Stovin and Saul, 2000). A second type of CSO is the 'high side weir'. This is a large rectangular channel with an invert at the bottom for channelling the fluid and solids during dry weather (Burt *et al.*, 2002).

An alternative to combined sewers, adopted in countries such as America and Australia, is the provision of a 'sanitary sewer' which carries domestic sewage and industrial wastes and alternative means for treating surface water, for example grass swales. These are grass-lined channels for conveying runoff from roads and impervious areas. Grass swales also settle out suspended particulates due to lower velocities and the grass which acts as a filter (Roach and Beecham, 2004). An obvious problem associated with these is the removal of particulates that will accumulate over time.

A second problem with combined sewers is that a large quantity of grit can be transported to sewage treatment works which requires removal at the preliminary stage of treatment, necessary to avoid damage to machinery such as pumps and valves and accumulation in downstream process chambers (Gardner and Deamer, 1996). A method of grit removal at a sewage treatment works is the use of a Hydrodynamic Vortex Separator (HDVS) and which may also be used as a CSO (Andoh and Saul, 2003). Collected solids within the HDVS can be removed either by a continuous or periodic base flow. The concept of the HDVS was first investigated by Smisson in the 1960's who aimed to "develop a device which could constrain the flow entering to follow a long path through the unit. This would then lengthen the time that gravity, aided by other forces due to the rotary motion induced by the kinetic energy of

the flow, would have to act on the wastewater" (Andoh and Smisson, 1993). Thus, in contrast to the hydrocyclone, where the separation of particles is due to the flow itself being centrifugal (Svarovsky, 1984), in the HDVS the separation of particles is due to the rotary nature of the flow that increases the residence time of the particle and hence the time that gravity has to act. Another difference between the HDVS and the hydrocyclone is that the HDVS must operate in the vertical position, whereas hydrocyclones may be inclined or even inverted in the case of small cyclones (Svarovsky, 1984).

For the HDVS, the fluid residence time is a key parameter which will have a major contribution to the effectiveness of a chemical contactor process. The residence time will determine the strength and quantity of reagents required to aid processes such as the coagulation and flocculation of colloidal particles or disinfectant that is required if a HDVS is to be used to disinfect the spill during an overflow event.

1.2   Hydrodynamic Vortex Separators (HDVSs)

In this work, three HDVSs are studied, all of which are marketed by Hydro International Plc. The main focus is on the Grit King$^{\circledR}$. However, during the course of the study, two other HDVSs have been investigated; the Eff-Pac^{TM} Clarifier and the Storm King$^{\circledR}$.

The Eff-Pac^{TM} Clarifier was intended for industrial applications. The design of the Eff-Pac^{TM} Clarifier that would be supplied is dependent on the customer's requirements and hence, may be similar to one of the other HDVSs being studied in this work (Grit King$^{\circledR}$ and Storm King$^{\circledR}$). However, the Eff-Pac^{TM} Clarifier that is studied here is significantly different to the other two HDVSs and is shown in Figure 1-1.

All the HDVSs are similar in that they consist of a tangential inlet marked 'A' in Figure 1-1 and a cone 'B' and dip plate 'C'. Each also has a benching skirt indicated in Figure 1-1 by 'K'. The Eff-Pac^{TM} Clarifier differs to the Grit King$^{\circledR}$ and Storm King$^{\circledR}$ in that the cone is supported on three legs and does not have a deflector plate.

A Inlet
B Cone
C Dip Plate
D Baffle Plate
E Weir
F Spill Way
G Overflow
H Underflow
I Vessel Wall
J Sludge Hopper
K Benching skirt
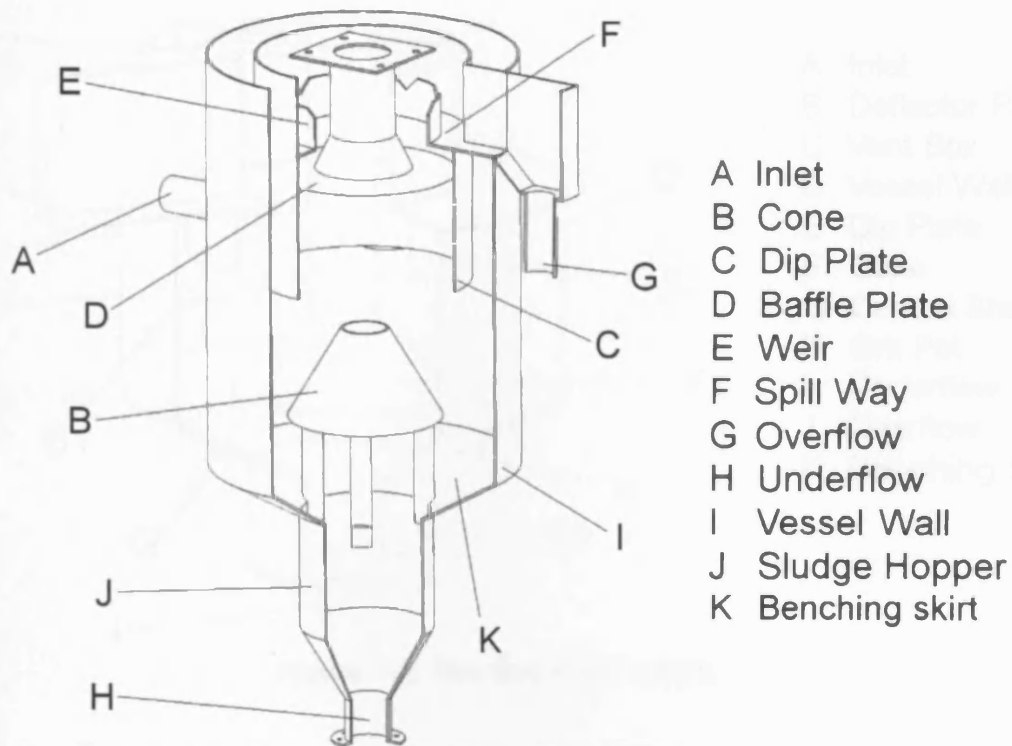
Figure 1-1. The Eff-Pac™ Clarifier HDVS.

The Eff-Pac™ Clarifier may operate with a continuous base flow (also known as an underflow or throughflow) component where fluid leaves the HDVS through the underflow marked 'H' in Figure 1-1. Thus, the flow enters the HDVS through the tangential inlet and flows between the dip plate and the vessel wall, 'I'. The fluid tends to take a downward path and either leaves through the underflow, 'H' or passes up through the centre of the HDVS between the dip plate and the baffle plate, 'D', over the weir 'E' and through the overflow 'G'.

The Grit King® shown in Figure 1-2 is usually installed at sewage treatment works and its primary purpose is for removing grit from the incoming fluid. This HDVS is therefore only concerned with the separation of particulates with a specific gravity greater than the fluid. Separated solids are removed either by the base flow component or by the use of a submersible pump, typically on an intermittent 'batch' basis over a period of approximately five minutes every thirty (Hydro International Plc, 2003, Private Communication). The Grit King® is therefore considered in this study operating without a base flow component.
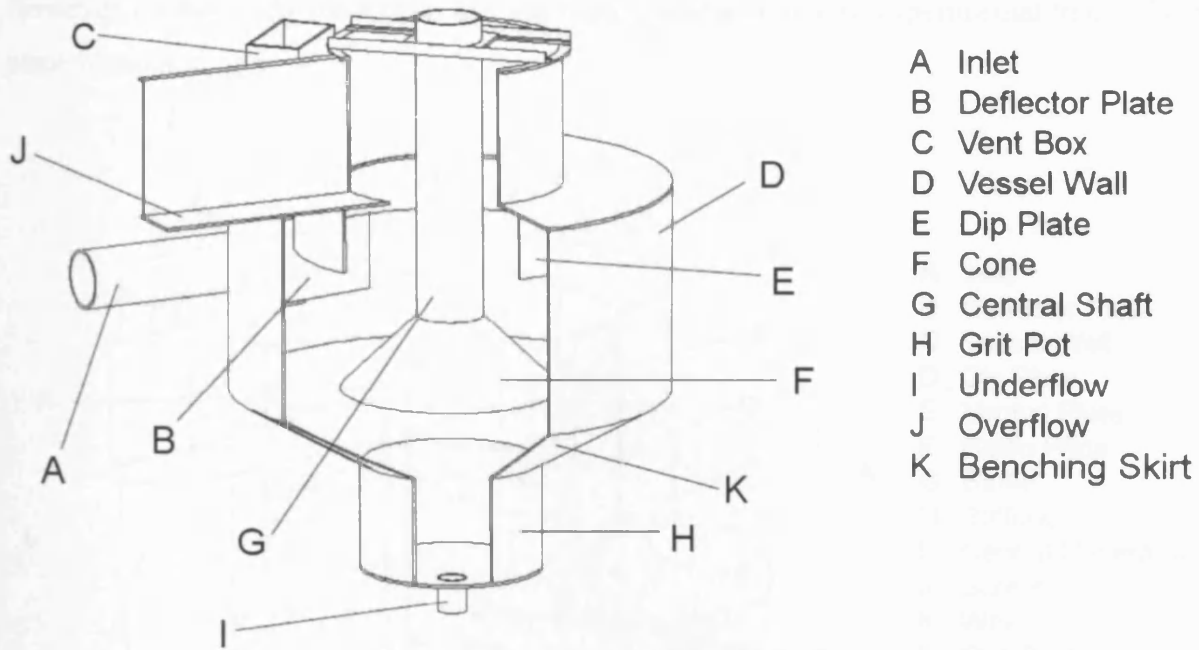
Figure 1-2. The Grit King® HDVS.

A Inlet
B Deflector Plate
C Vent Box
D Vessel Wall
E Dip Plate
F Cone
G Central Shaft
H Grit Pot
I Underflow
J Overflow
K Benching Skirt

The Grit King® has a cone 'F' marked in Figure 1-2 which is suspended from a central shaft 'G'. This central shaft allows a pipe and/or a submersible pump to be dropped into the grit pot 'H' to remove separated solids when the installation is not able to include the facility for an underflow component. Although the underflow in Figure 1-2 is central, tangential underflows can be used as an alternative. When the Grit King® fills air may become trapped between the vessel wall 'D' and the dip plate 'E', which would effectively reduce the volume of the fluid that the HDVS could hold. The vent box 'C' therefore allows this air to escape. Thus, the fluid enters through the tangential inlet 'A' and is directed by the deflector plate 'B' around the outside of the separator. As the fluid reaches the bottom of the cone, particles may become trapped under the cone in the grit pot. The fluid then passes up through the centre of the HDVS between the central shaft and the dip plate prior to discharging through the overflow 'J'.

Figure 1-3 shows the third HDVS, known as the Storm King®. This HDVS is typically installed as a CSO device and therefore operates with a continuous base flow component which allows fluid and separated solids to pass through the sewer network. Floatable materials inevitably present in a sewer network may become trapped on the screen 'J'. This HDVS would therefore have a self priming siphon attached to the overflow 'L' that produces a backwash to wash floatable material trapped on the screen into the central underflow 'I'.

However, in this study the siphon has not been considered, due to experimental trials taking place without it.

A Inlet
B Deflector Plate
C Vessel Wall
D Dip Plate
E Venturi Plate
F Baffle Plate
G Baffle
H Stiffener
I Central Underflow
J Screen
K Weir
L Overflow
M Cone
N Helix
O Underflow
P Benching Skirt
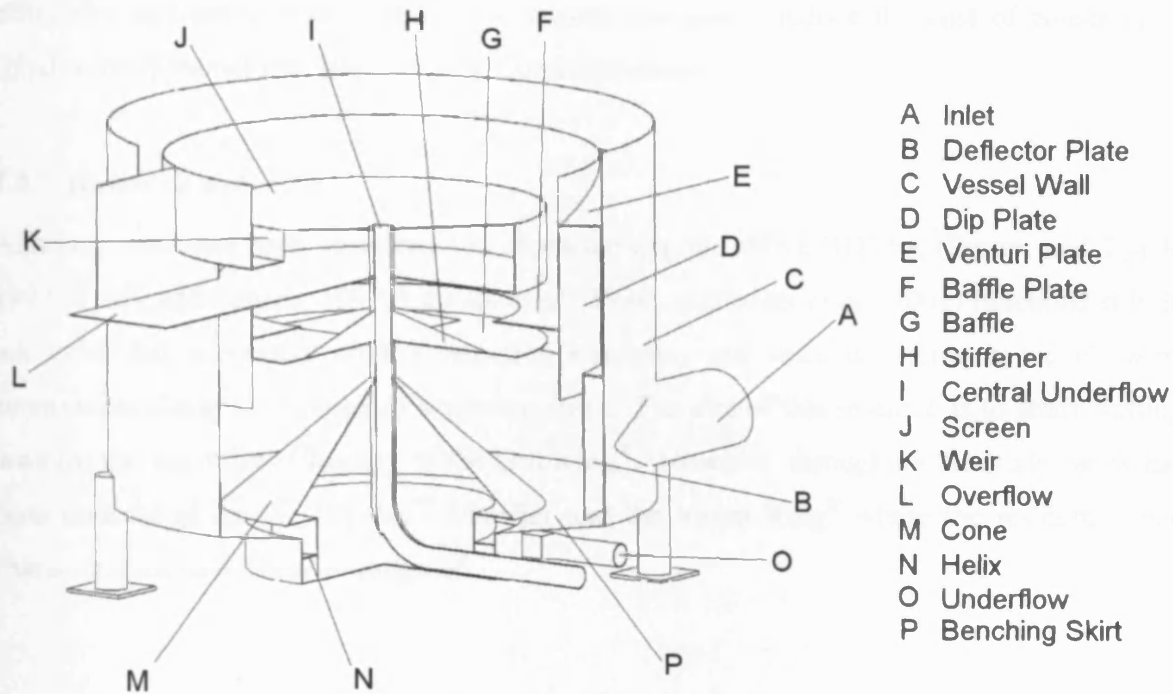
Figure 1-3. The Storm King® HDVS.

On entry to the Storm King® the fluid strikes a deflector plate marked 'B' in Figure 1-3. Like the Eff-Pac™ Clarifier and the Grit King®, the Storm King® has several internal components. Dissimilar to the Eff-Pac™ Clarifier and the Grit King® a helix, 'N', below the cone 'M' entrains fluid and separated solids into a tangential underflow 'O'. Whilst the fluid is within the Storm King® it may swirl between the vessel wall, 'C' and the dip plate, 'D', to which a downward motion to the fluid is applied by a Venturi plate, 'E' and which also guides the fluid under the overflow. Prior to the fluid passing over the overflow it must pass between a baffle, 'G', which is attached to the central underflow and which is supported by stiffeners 'H' and a second baffle attached to the dip plate, 'F'. From here the fluid passes over the weir, 'K' and through the screen onto the overflow, where it discharges.

Differences in the design of each separator are partly owing to the way in which each is constructed. For example, a Storm King® which is used as a CSO will be constructed mainly from concrete. Hence, the cone will be solid except for the central underflow. The major factor that accounts for the difference in the design of each HDVS however is the evolution of the product over the years. For example the configuration of the cone in the Eff-Pac™

Clarifier has been shown to enhance re-entrainment of particulates from the sludge hopper which is undesirable (Hydro International Plc, 2005, Private Communication). Other parts of separators such as baffles etc have been shown to only contribute slightly to the retention efficiency and are therefore omitted on current designs to reduce the cost of construction (Hydro International Plc, 2005, Private Communication).

1.3   Research aim

Although work has been undertaken in characterising the above HDVSs, (Fenner and Tyack, 1997; Tyack and Fenner, 1997; Luyckx *et al.*, 1998; Alkhaddar *et al.*, 2001) functions still do not exist that accurately predict retention efficiency and residence time, hence allowing economical sizing for a range of separator sizes. The aim of this research is to attain scaling laws for the retention efficiency of the Grit King$^{®}$. However, throughout the study, work has been undertaken on the Eff-Pac$^{™}$ Clarifier and the Storm King$^{®}$ where the residence time characteristics have been investigated.

2 Theory

2.1 Particle mechanics

2.1.1 Terminal velocity in a Newtonian fluid

Researchers have related the efficiency of CSOs to the settling velocity of the particles (Frederick and Markland, 1967; Halliwell and Saul, 1980; Luyckx *et al.*, 1998). Hence, the calculation of the terminal settling velocity is of importance.

A Newtonian fluid is distinguished from a Non-Newtonian fluid in that a Non-Newtonian fluid has a viscosity that is "dependent upon the rate in which the fluid is sheared. Thus, the use of a single viscosity is not appropriate" (Brown and Heywood, 1991). Water is a Newtonian fluid (Fox and McDonald, 1998). Non-Newtonian fluids include blood, milk and gelatine (Massey, 1984).

The rate at which a particle descends in a semi-infinite expanse of fluid is dependent upon the gravitational force acting on the particle and the frictional drag which "consists of viscous and inertial components" (Brown and Heywood, 1991).

Newton's second law of motion, when applied to a sphere, gives

$$F_g - (F_B + F_D) = m\frac{du_p}{dt} \tag{2-1}$$

Where: F_D = Drag force, N F_B = Buoyancy force, N

  F_g = Gravitational force, N m = Mass of sphere, kg

  u_p = Velocity of sphere, m/s t = Time, s

The terminal settling velocity of a spherical particle occurs when

$$F_D + F_B = F_g \tag{2-2}$$

When the spherical particle has reached the terminal settling velocity, the drag coefficient can be shown to be given by

$$C_D = \frac{4dg\left(\rho_p - \rho_f\right)}{3u_{pt}^2 \rho_f} \qquad (2\text{-}3)$$

Where: C_D = Drag coefficient d = Particle diameter, m

     g = Acceleration due to gravity, m/s^2 ρ_p = Particle density, kg/m^3

     ρ_f = Fluid density, kg/m^3 u_{pt} = Terminal velocity of sphere, m/s

Rearranging Equation 2-3 to make the terminal velocity the subject gives

$$u_{pt} = \sqrt{\frac{4dg(\rho_p - \rho_f)}{3C_D \rho_f}} \qquad (2\text{-}4)$$

The particle Reynolds number for a sphere is given by Equation 2-5 and the relation between the drag coefficient of a sphere and particle Reynolds number is shown in Figure 2-1.

$$\mathrm{Re}_p = \frac{du_{pt}\rho_f}{\mu} \qquad (2\text{-}5)$$

Where: Re_p = Particle Reynolds number μ = Absolute viscosity, kg/ms
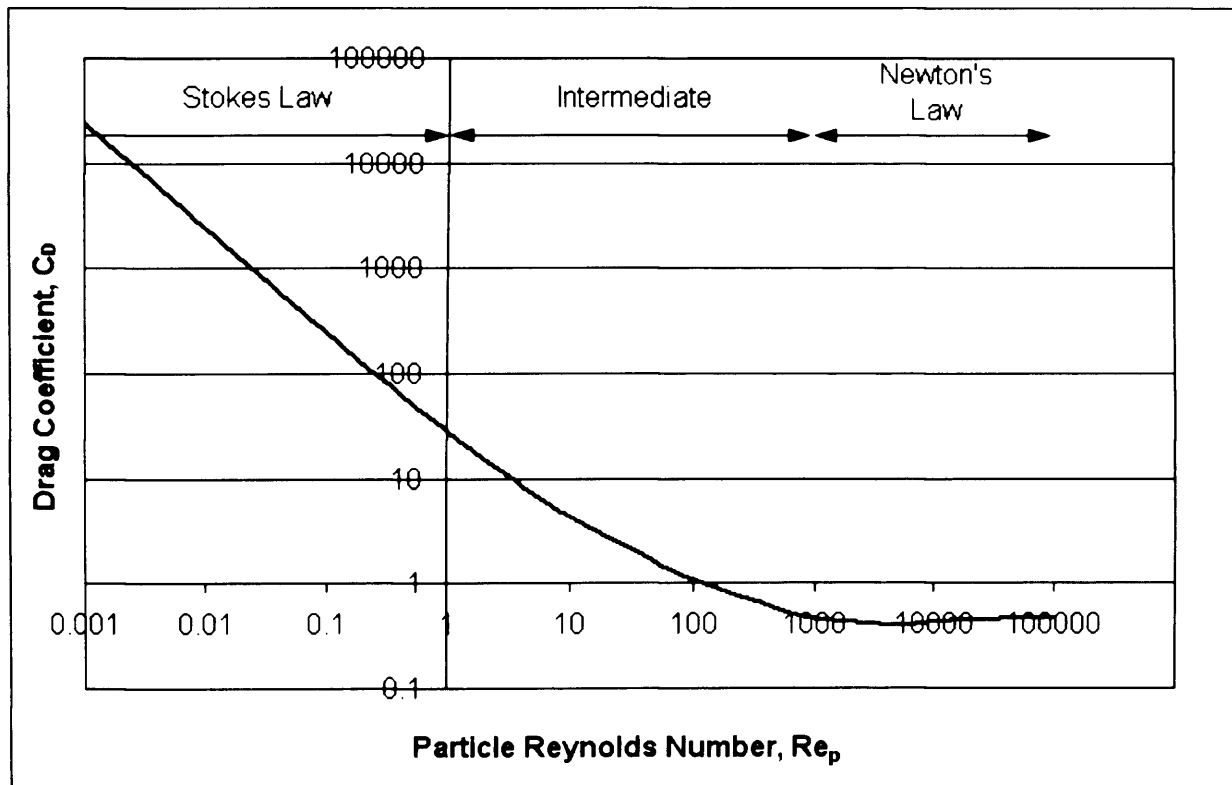
Figure 2-1. Relation between particle Reynolds number and drag coefficient for spherical particles descending at the terminal velocity in a Newtonian fluid. Adapted from Brown and Heywood (1991).

From Figure 2-1, it can be seen that three regimes exist. These are summarised in Table 2-1.

Table 2-1. Drag regimes and Reynolds number ranges. Adapted from Brown and Heywood (1991).

Regime	Reynolds number range
Stokes Law	$Re_p \leq 1$
Intermediate	$1 < Re_p \leq 1000$
Newton's Law	$1000 < Re_p \leq 2 \times 10^5$

Turton and Levenspiel (1986) fitted a single equation to the curve shown in Figure 2-1 given by

$$C_D = \frac{24}{Re_p(1 + 0.173\,Re_p^{0.657})} + \frac{0.413}{1 + 16300\,Re_p^{-1.09}} \qquad (2\text{-}6)$$

Equation 2-6 was fitted for Reynolds numbers up to 2×10^5.

Given that only the properties of a spherical particle are known i.e. diameter and density, as well as the fluid properties i.e. density and viscosity, two unknowns exist in Equation 2-4 which are the drag coefficient and the terminal velocity. The drag coefficient, Equation 2-6, is computed using the particle Reynolds number, Equation 2-5, which also requires knowledge of the terminal velocity of the particle. Hence an iterative approach is required. This involves taking an estimate for the particle Reynolds number to calculate the drag coefficient which is then used to make a first estimate of the terminal velocity in Equation 2-4. The estimated terminal velocity is used to recalculate the particle Reynolds number and so on until a satisfactory accuracy of the terminal velocity has been calculated. A simple program for this can be written in a spreadsheet package such as MS-Excel[®].

2.1.2 Shape factor

Most real particles are not spherical and the shape of the particle influences the drag. "Sphericity is defined as the surface area of a sphere with the same volume as the particle divided by the surface area of the particle" (Brown and Heywood, 1991) which is given by

$$\psi = \frac{4\pi\left(\dfrac{3V}{4\pi}\right)^{\frac{2}{3}}}{A_p}$$

(2-7)

Where: ψ = Sphericity $\qquad$ A_p = Surface area of particle, m^2

$\qquad$ V = Volume of sphere with same volume as the particle, m^3

Determining the surface area of an irregular shaped particle is extremely complex and a simplification is to approximate the particle shape to a regularly shaped particle whose surface area is simple to evaluate for which examples are given in Table 2-2.

Table 2-2. Sphericity of regularly shaped particles.

Shape	Sphericity (ψ)
Sphere	1.0
Octahedron	0.847
Cube	0.806
Prism (length of side, a)	
a.a.2a	0.767
a.2a.2a	0.761
a.2a.3a	0.725
Cylinders (Height, h, and radius, r)	
h=r/15	0.254
h=r/10	0.323
h=r/3	0.594
h=r	0.827
h=3r	0.860
h=10r	0.691
h=20r	0.580

For non spherical particles, a relationship for the drag coefficient is given by (Haider and Levenspiel, 1989)

$$C_D = \frac{24}{Re_p}\left(1 + b_1 Re_p^{b_2}\right) + \frac{b_3 Re_p}{b_4 + Re_p}$$

(2-8)

Where:

$b_1 = \exp\left(2.328 - 6.4581\psi + 2.4486\psi^2\right)$ (2-9)

$b_2 = 0.0964 + 0.5565\psi$ (2-10)

$b_3 = \exp\left(4.905 - 13.8944\psi + 18.4222\psi^2 - 10.2599\psi^3\right)$ (2-11)

$b_4 = \exp\left(1.4681 + 12.2584\psi - 20.7322\psi^2 + 15.8855\psi^3\right)$ (2-12)

2.1.3 Time to establish terminal velocity

To determine the settling velocity of a particle, researchers have used settling columns of various forms (Pisano, 1996). For a particle released in the fluid from rest, a period of time will elapse before the force of gravity and the drag forces are balanced and the terminal settling velocity has been attained. Hence, sufficient distance in the settling column should be provided for the terminal settling velocity to be achieved. An estimate for the time taken to achieve the terminal settling velocity can be computed from Equation 2-13 which is derived by Mironer (1979).

$$u_p = \frac{e^N - 1}{e^N + 1} u_{p\infty} \tag{2-13}$$

Where

$$N = \frac{t}{T} \tag{2-14}$$

$$T = \frac{m_p + m_h}{C_D \rho_f u_{p\infty} A} \tag{2-15}$$

Where: A = Projected area of particle, m^2 N = Number of time constants

T = Time constant, s m_p = Mass of spherical particle, kg

u_p = Velocity of sphere, m/s

m_h = Hydrodynamic mass of spherical particle, kg

Thus, the velocity of the sphere may be calculated after N time constants as a percentage of the terminal velocity. The derivation of Equation 2-13 assumes that the drag coefficient is constant over the acceleration of the particle. This according to Mironer (1979) is reasonable except at the start of the particle's motion, where the flow is low Reynolds number.

An estimate of the distance required for the particle to attain the terminal settling velocity can therefore be made by integrating the velocity-time curve defined by Equation 2-13.

2.1.4 Wall effects

"The interaction of the fluid displaced by a falling particle with the wall of the container slows down the descent of the particle" (Brown and Heywood, 1991). Fidleris and Whitmore (1961) based on experimental results, present a series of curves that allow the terminal

velocity for the bounded condition to be calculated from the unbounded condition. This is shown in Figure 2-2.

Reynolds Number, $Re_d = \dfrac{d\,U_\infty\,\rho_f}{\mu_f}$
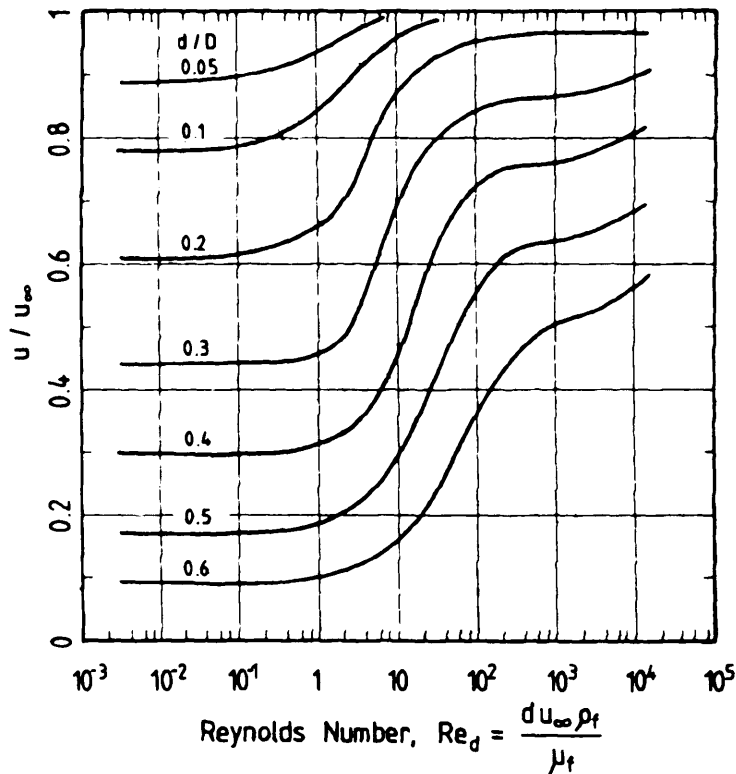
Figure 2-2. The effect of the particle-column diameter ratio on the relationship between the terminal velocity and particle Reynolds number. Adapted from Fidleris and Whitmore (1961), source Brown and Heywood (1991).

2.1.5 Coefficient of restitution

When a particle strikes a wall there will be a loss in the momentum of the particle. The coefficient of restitution defines the amount of momentum retained by a particle after a collision with a wall. The 'normal coefficient of restitution' defines the amount of momentum that is retained by the particle in the normal direction to the wall. Similarly, the 'tangential coefficient of restitution' defines the amount of momentum retained by the particle in the direction tangential to the wall. This property will also be related to the material of the particle. For instance a rubber ball when dropped will bounce back to a height not far from where it was dropped whereas a rock will have a very small bounce.

The normal coefficient of restitution is given by

$$e_n = \frac{u_{2,n}}{u_{1,n}}$$

(2-16)

Where: e_n = Normal coefficient of restitution

$u_{1,n}$ = Velocity normal to wall before collision, m/s

$u_{2,n}$ = Velocity normal to wall after collision, m/s

The tangential coefficient of restitution is given by

$$e_t = \frac{u_{2,t}}{u_{1,t}}$$

(2-17)

Where: e_t = Tangential coefficient of restitution

$u_{1,t}$ = Velocity tangential to wall before collision, m/s

$u_{2,t}$ = Velocity tangential to wall after collision, m/s

2.2 Residence time

2.2.1 Overview

The flow characteristic of any system will lie somewhere between plug flow (pure advection with no dispersion) and completely mixed. In a complete plug flow operating condition, the response to a pulse injection is such that all elements being tracked leave the device at the same residence time, indicated in Figure 2-3 'A'. In a completely mixed or Continuously Stirred Tank Reactor (CSTR), the elements of fluid being tracked will leave the device over a range of residence times, shown in Figure 2-3 'B'. Between these two limits, both advection and dispersion processes occur, producing typical Residence Time Distributions (RTDs), Figure 2-3 'C'. Levenspiel (1962) discusses this in detail.

A. Plug Flow

C | Width=0
t

B. Completely Mixed

C
t

C. Arbitrary Flow

C
t
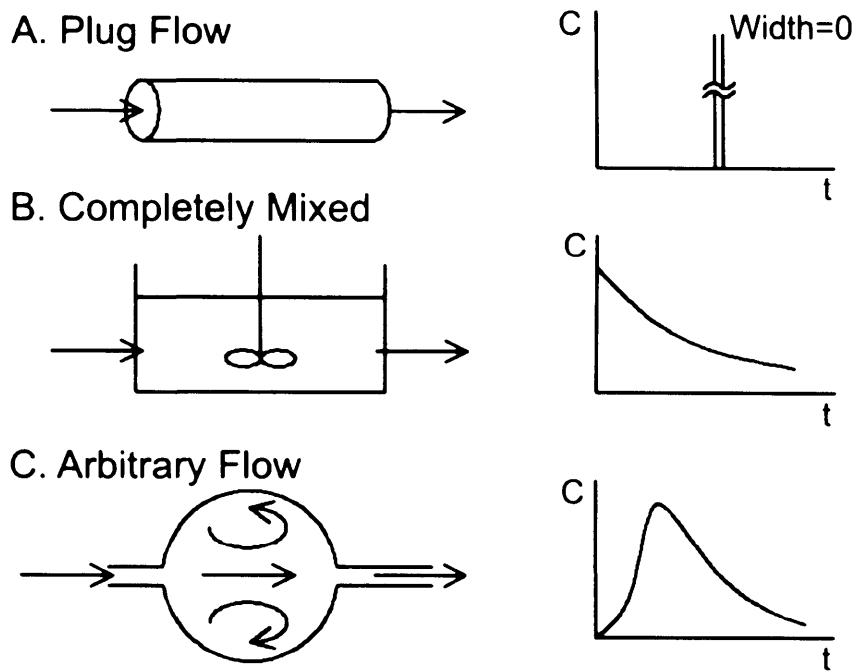
Figure 2-3. Concentration vs. time plots in response to different types of flow. Adapted from Levenspiel (1962).

2.2.2   Residence time theory

The theoretical mean residence time of a system is given by (Levenspiel, 1962)

$$\tau = \frac{V}{Q}$$

(2-18)

Where: τ = Theoretical mean residence time, s V = Fluid volume, m^3
        Q = Flowrate, m^3/s

The normalised mean residence time is then given by (Levenspiel, 1962)

$$t_\theta = \frac{t}{\tau}$$

(2-19)

Where: t_θ = Normalised mean residence time $\bar{t}$ = Mean residence time, s

If the normalised mean residence time is equal to 1 at the downstream sampling position, then it may be assumed that the fluid is passing through the system in the theoretical residence time, τ. If the normalised mean residence time is less than 1 then short circuiting may be occurring and when greater than 1, the device may be described as holding the fluid for an extended period of time, compared with τ. The normalised mean residence time does not give any detail on the shape of the distribution which, for example, may have a normalised value of 1 but which may be skewed towards the origin indicating that short circuiting is

taking place through part of the system and that other regions hold the fluid for an extended period.

To study the residence time characteristic, a number of inputs of tracer may be applied to a system. The first is a pulse input to produce a plot known as a 'C' curve which is a function of the concentration of tracer in the exit stream with time. This can be used to produce an 'E' curve known as an Exit-Age distribution function where 'E dt' is the fraction of material in the exit stream with an age between 't' and '$t + dt$' and is given by (Levenspiel, 1962)

$$E = \frac{C}{\int_0^\infty C.dt} = \frac{C.Q}{M}$$ (2-20)

Where: E = Exit-Age distribution, s^{-1} C = Concentration at time t, kg/m^3
       M = Total mass of tracer, kg

In practice a perfect pulse input cannot be achieved and researchers are known to make the assumption that a perfect pulse input has been introduced (Alkhaddar *et al.*, 1999; Tyack and Fenner, 1998a).

A second method is a step input to produce a plot known as an 'F' curve. At time t a point on the 'F' curve is given by C/C_0 where C is the concentration in the outflow at time t and C_0 is the concentration in the inlet stream i.e. the 'F' curve is a function of the fraction of tracer concentration in the exit stream with time.

The 'E' and 'F' curve are related by (Teefy and Singer, 1990)

$$E = \frac{dF}{dt}$$ (2-21)

$$F = \int E dt$$ (2-22)

Where: F = 'F' distribution

Hence, from Equation 2-21, the slope on each segment of the 'F' curve is a point in the 'E' curve. From Equation 2-22, the cumulative area under the 'E' curve at any time is a point on the 'F' curve.

A third way to determine the residence time characteristics is to fill the system with tracer and drain to determine the Internal Age distribution, known as an 'I' curve, where 'I dt ' is defined in the same way as 'E dt '. This may be derived from the 'F' curve by

$$I = 1 - F \qquad\qquad (2\text{-}23)$$

Where: I = Internal Age distribution, s^{-1}

The mean residence time is calculated from the first moment about the origin (Levenspiel, 1962).

$$t = \frac{\int_0^{\tau} C t \, dt}{\int_0^{\tau} C . dt} \qquad\qquad (2\text{-}24)$$

The second moment about the mean defines the variance of the distribution, which is a measure of the spread of the distribution, given by (Levenspiel, 1962)

$$\sigma^2 = \frac{\int_0^{\tau} \left(t - t \right)^2 C \, dt}{\int_0^{\tau} C \, dt} \qquad\qquad (2\text{-}25)$$

Where: σ^2 = Variance of the distribution, s^2

Characterisation of the RTD using Equation 2-24 and 2-25 shall be referred to as the 'method of moments' as used by Higgins (2000).

Both Equations 2-24 and 2-25 rely on sampling until the tracer concentration is equal to zero, otherwise, error will be introduced. In many situations the long 'tails' on observed distributions make it difficult to calculate a meaningful value of the variance (Fischer *et al.*, 1979). To overcome this problem an RTD model may be fitted to the data to estimate the variance.

2.2.3 Fitting an RTD model

If an upstream and downstream temporal concentration distribution has been recorded, mass balancing the data is required prior to fitting an RTD model, because RTD models assume the tracer to be conserved. Mass balancing is achieved by multiplying the downstream data with

a factor determined from the upstream tracer mass divided by the measured downstream tracer mass (Guymer, 2002). The mass balance correction factor does not change the shape of the RTD and hence the mean residence time and variance are also unaffected. This is possibly best explained in that the mass balance correction factor simply cancels from the numerator and denominator when calculating the mean and variance from the first moment about the origin and second moment about the mean respectively i.e. Equations 2-24 and 2-25.

When fitting a model to the data, an optimisation technique by Guymer (2002) may be used to fine tune the parameters in the RTD model. In the case of the Axial Dispersion Model (ADM) (see Section 2.2.4.1), the mean residence time and the normalised variance, for the Tanks In Series Model (TISM) (see Section 2.2.4.2), the number of tanks and the mean residence time, for the Aggregated Dead Zone (ADZ) model (see Section 2.2.4.3), the ADZ residence time and the transport time delay and for the Advection Dispersion Equation (ADE) (see Section 2.2.4.4), the travel time and dispersion coefficient.

The assessment of the fit of the RTD model is by the R_t^2 value given by (Young *et al.*, 1980)

$$R_t^2 = 1 - \frac{\sum_{t=1}^{n}(c_t - p_t)^2}{\sum_{t=1}^{n}c_t^2}$$ (2-26)

Where: c_t = Measured data p_t = Predicted data n = Number of measurements

R_t^2 = Coefficient of determination

"A value for R_t^2 of unity indicates an exact fit whereas a value less than zero implies the prediction fails to describe any part of the measured data" (Guymer, 2002). The optimisation technique employs a 2×2 matrix of the two coefficients that are to be optimised and the range between the constants that give the highest R_t^2 value are reduced until a satisfactory accuracy has been achieved for each. This is demonstrated in Figure 2-4.
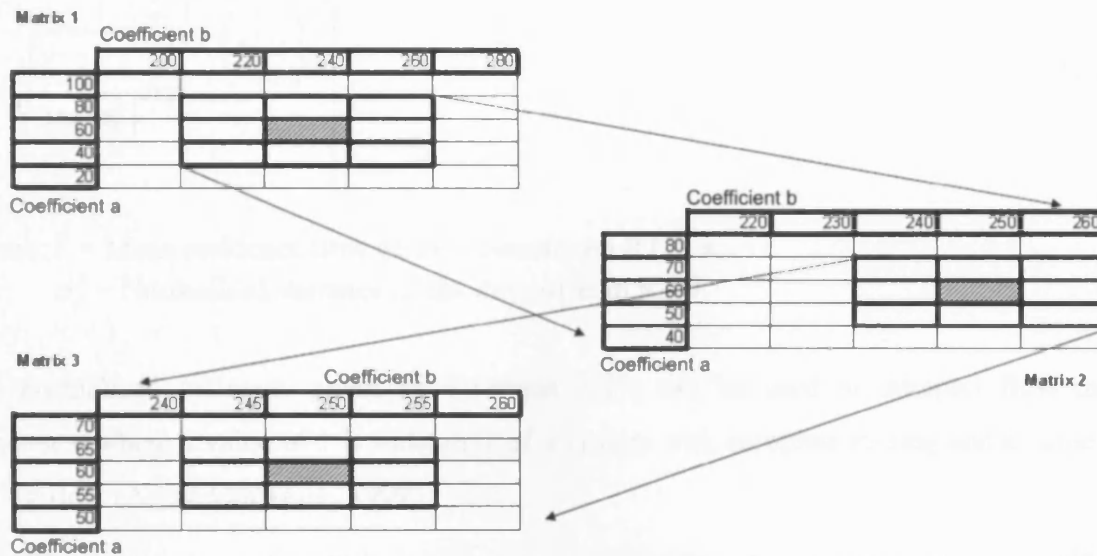
Figure 2-4. A schematic of the optimisation procedure. Adapted from Guymer (2002).

There are numerous RTD models that may be fitted to observed RTDs. Four of these are described in the subsequent sections.

2.2.4 RTD models

2.2.4.1 Axial Dispersion Model (ADM)

The axial dispersion model, first formulated by Langmuir (1908) is given by Equation 2-27 for a non reacting tracer. The model is usually referred to as though it describes the passage of fluid in a pipe or channel.

$$\frac{\partial C}{\partial t} + u \frac{\partial C}{\partial z} - D \frac{\partial^2 C}{\partial z^2} = 0 \tag{2-27}$$

Where: C = Concentration, kg/m^3 u = Mean velocity, m/s
       t = Time, s z = Position along the pipe, m
       D =Dispersion coefficient, m^2/s

The first term is included so that transient inputs may be used. The second term describes convective flow in the axial direction and the third term adds a diffusive mechanism which causes convective flux to be augmented by a diffusive flux (Nauman and Buffham, 1983). For disinfection contactors, "closed-closed" boundary conditions are considered acceptable, where no mixing occurs at the inlet or outlet (Teefy and Singer, 1990). With these boundary conditions, the exact solution to the ADM can only be written as an infinite series (Nauman and Buffham, 1983). According to Haas *et al.* (1997), based on work by Aris and Amundson (1957), an approximation to the exact solution is given by (Nauman and Buffham, 1983)

$$E = \sqrt{\frac{t}{2\pi t^3 \sigma_\theta^2}} \exp\left[-\frac{\left(t-t\right)^2}{2t t \sigma_\theta^2} \right]$$

(2-28)

Where: t = Mean residence time of the downstream RTD, s

σ_θ^2 = Normalised variance of the downstream RTD

The normalised variance, given by Equation 2-29, can be used to interpret flow model responses, where a value of 1 is indicative of a system with complete mixing and a value of 0 is plug flow (Alkhaddar *et al.*, 1999).

$$\sigma_\theta^2 = \frac{\sigma^2}{t^2}$$

(2-29)

Where: σ^2 = Variance of the downstream RTD, s^2

The RTD curve generated by the ADM does not take into account the inlet distribution of the tracer i.e. determines the response to an instantaneous 'slug' injection. This may inhibit the accuracy of the model if knowledge of the upstream distribution is unknown. Provided that a trace for the upstream distribution is recorded, the travel time of the observed profile downstream is therefore the difference between the mean time of passage of the upstream and downstream distributions.

2.2.4.2   Tanks In Series Model (TISM)

The tanks in series model (Levenspiel, 1962) assumes that a series of CSTRs of equal volume, are connected in series and the Exit-Age distribution function is given in Higgins (2000).

$$E = \frac{N^N t^{N-1}}{t^N (N-1)!} \exp\left(\frac{-Nt}{t} \right)$$

(2-30)

Where: N = Number of CSTRs t = Mean residence time of the downstream RTD, s

If the number of tanks is found to be 1, then this correlates to a system with a completely mixed flow regime. As the number of tanks approach infinity, the mixing characteristics approach plug flow. The normalised variance may be approximated to the number of tanks by

$$\sigma_\theta^2 = \frac{1}{N}$$

(2-31)

This is valid when the number of tanks exceeds 3 such that the variance of the TISM and the ADM are identical to 3 decimal places. The TISM tends to have a higher peak than the ADM and this discrepancy decreases as the number of tanks increases i.e. as the mixing characteristics approach plug flow. Like the ADM, the RTD curve generated by the TISM model takes no account of the inlet distribution of the tracer.

2.2.4.3 Aggregated Dead Zone (ADZ) model

The ADZ model has been developed for modelling the transport of dissolved material mainly in a stream or river. Comparison between experimental data and ADZ predictions are given by Young and Wallis (1986) for tracer experiments that were carried out predominantly on the River Conder, UK. Wallis *et al.* (1989) have used the ADZ model for modelling longitudinal dispersion in an open channel within a laboratory, to determine a methodology for developing a model for simulating the passage of pollutants in rivers. A further application of the ADZ model is by Guymer *et al.* (1996) for predicting the passage of a pollutant through a surcharged benched manhole.

The term 'dead zone' is used "as a bulk parameter that not only describes the effect of the segregated regions of flow, but also other dispersive catalysts such as eddies, viscous sub layers and velocity profile" (Guymer, 2002).

The derivation of the ADZ model is given by Young and Wallis (1986).

In all practical applications, the monitoring of the concentration at a sampling point is during discrete time intervals and the discrete form of the ADZ model is given by

$$C_i = -aC_{i-1} + bX_{i-\delta}$$

(2-32)

Where: C = Downstream concentration, kg/m³ X = Upstream concentration, kg/m³
       i = Sampling interval

       δ = Nearest integer value of $\dfrac{\theta}{\Delta t}$

Where: Δt = Sampling time, s θ = Transport time delay, s

The ADZ residence time, T, is given by

$$T = \frac{V_c}{Q} = -\frac{\Delta t}{\ln(-a)}$$ (2-33)

Where: V_c = ADZ volume, m^3

Thus, a is given by

$$a = -\exp\left(\frac{-\Delta t}{T}\right)$$ (2-34)

and b is given by

$$b = 1 + a$$ (2-35)

The relationship between the exact solution to the ADZ model and Equation 2-32 only applies when the tracer is conserved, $\theta / \Delta t$ is an integer value and $X(t - \theta)$ is constant over the sampling interval. Since in practise the latter two are rarely satisfied precisely, solutions of Equation 2-32 are approximations to the exact solution (Wallis *et al.*, 1989).

The dispersive fraction, defined by Equation 2-36, is the proportion of the reach that is responsible for dispersion of the tracer (Guymer, 2002).

$$D_f = \frac{T}{\bar{t}}$$ (2-36)

Where: D_f = Dispersive Fraction

The travel time, $\bar{t}$, is the time difference between the mean residence time of the upstream and downstream distribution, given by

$$\bar{t} = \bar{t}_2 - \bar{t}_1$$ (2-37)

Where: $\bar{t}_1$ = Mean residence time of upstream distribution, s

$\bar{t}_2$ = Mean residence time of downstream distribution, s

The time delay, θ, is given by the delay between the first arrival of tracer upstream and first arrival downstream, thus:

$$\theta = \theta_2 - \theta_1 \qquad (2\text{-}38)$$

Where: θ_1 = First arrival of tracer upstream, s

   θ_2 = First arrival of tracer downstream, s

The ADZ residence time is also given by (Guymer, 2002)

$$T = t - \theta \qquad (2\text{-}39)$$

Figure 2-5 illustrates the ADZ parameters.
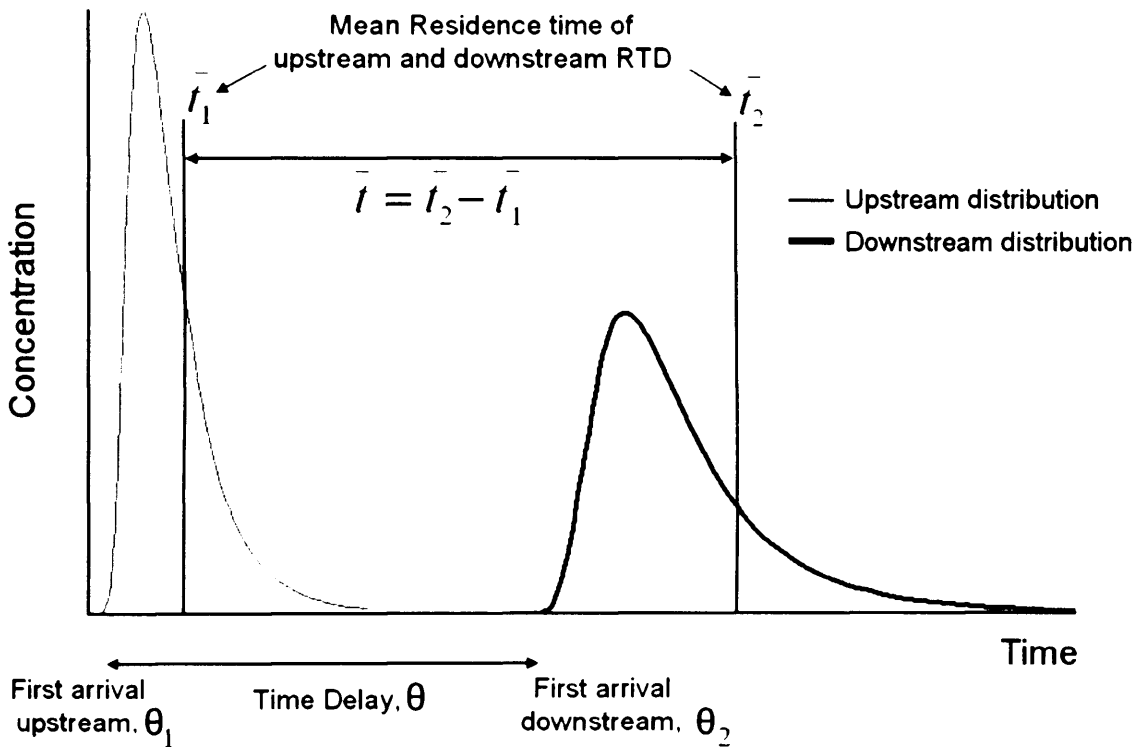
Figure 2-5. ADZ summary. Adapted from Guymer (2002).

To define a and b in Equation 2-32, only the ADZ residence time and the transport time delay are required.

2.2.4.4   Advection-Dispersion Equation (ADE)

The ADE is derived from Equation 2-40 where the response to an instantaneous 'slug' injection is given in Rutherford (1994)

$$C = \frac{M}{A\sqrt{4\pi Dt}}\exp\left[-\frac{(x-ut)^2}{4Dt}\right]$$ (2-40)

Where: A = Cross-sectional area of channel, m^2

x = Distance between site 1 and 2, m (Site 1 is upstream of site 2)

Equation 2-40 is a solution to Equation 2-27 and may be used to route a temporal concentration distribution by treating each point on the upstream concentration distribution as an instantaneous slug injection. The resulting profiles are then summed to give a predicted downstream profile. The routing procedure uses the 'frozen cloud assumption' to transform the concentration versus time profile at site 1 into a concentration versus distance profile. This is routed to give a concentration versus distance profile at site 2 which is then transformed to a concentration versus time profile. This is summarised by Equation 2-41. Further details can be found in Fischer *et al.* (1979) and Rutherford (1994).

$$C(x_2,t) = \int_{\tau=-\infty}^{\infty} \frac{C(x_1,\xi)u}{\sqrt{4\pi D\left(t_2-t_1\right)}}\exp\left[-\frac{u^2\left(t_2-t_1-t+\xi\right)^2}{4D\left(t_2-t_1\right)}\right]d\xi$$ (2-41)

Where: $C(x_1,\xi)$ = Observed concentration as a function of time at site 1 located at x_1, kg/m^3

$C(x_2,t)$ = Predicted concentration as a function of time at site 2 located at x_2, kg/m^3

ξ = Dummy time variable of integration, s

t_1 and t_2 = Mean time of passage at site 1 and 2 respectively where

$$t_2 = t_1 + \frac{x_2-x_1}{u}$$ (2-42)

The frozen cloud assumption is that the dispersing cloud changes its shape only slightly during the time taken to pass site 1 (Fischer *et al.*, 1979). For the response to a 'slug' injection and for a small dispersion coefficient, the ADE predicts a temporal concentration profile similar to Equation 2-40. As the dispersion coefficient increases, the temporal concentration distribution predicted by Equation 2-40 becomes more skewed and the ADE deviates, predicting a profile that is in contrast predominantly Gaussian. Hence, when fitting the ADE to skewed profiles, a reasonable fit may not be achieved.

2.3 Flow modelling

The Computational Fluid Dynamic (CFD) package FLUENT was used for all simulations described in this work.

2.3.1 Grid generation

FLUENT uses a control-volume technique to obtain a converged solution. This consists of using each cell in the mesh as a control-volume and integrating the governing equations over each cell to produce equations for the 'unknowns'. Thus, the first stage in producing the model is to create the geometry of the HDVS and to apply a mesh. The grid[1] generation was carried out in GAMBIT during the pre-processing stage.

2.3.1.1 Meshing

When meshing a 2D model, the type of cell that may be employed is a triangular or quadrilateral cell. When meshing a 3D model, the types of cell that could be employed are tetrahedral, hexahedral, prism/wedge and pyramid.

Different meshing schemes are available for either faces or volumes. Details of these are available in Fluent Inc. (2002). The type of cells used will depend upon the set-up time, the computational expense in terms of the number of cells that will be generated and numerical diffusion. These points are discussed in more detail below.

Set-up time

The construction of grids incorporating quadrilateral or hexahedral cells can be very time consuming and sometimes impossible. However, for a simple geometry there may not be any time saved by using triangular or tetrahedral cells.

Computational expense

For a complex geometry or when the range of length scales of the flow is large, then a mesh constructed from triangular/tetrahedral cells can be created with fewer cells than a mesh comprising of quadrilateral/hexahedral cells. This is because a tetrahedral mesh allows cells to be clustered whereas hexahedral grids force cells to be placed where they are not needed

---

[1] The 'mesh' is the same as the 'grid' and these two words are used interchangeably throughout.

(Fluent Inc., 2003). One advantage of quadrilateral/hexahedral however is that they permit a much larger aspect ratio than triangular/tetrahedral cells. This is because a large aspect ratio in a triangular/tetrahedral cell will affect the skewness of the cell, which is undesirable, as it will affect the accuracy and convergence of the iterations.

Numerical diffusion

Numerical diffusion is a consequence of representing the fluid flow in discrete form. It arises from truncation errors, but can be reduced in a number of ways. The first is to use the second order discretization scheme used in FLUENT. This is when the accuracy of the solution is increased by calculation of the second order terms. One problem with this is that sometimes the solution is unable to converge. A second solution is to refine the mesh, as the amount of numerical diffusion is inversely related to the resolution of the mesh. A third solution is to have the flow aligned with the mesh i.e. the use of quadrilateral or hexahedral cells.

2.3.1.2   Mesh quality

The quality of the mesh/grid depends upon the cell shape, the aspect ratio, the smoothness and the node density and clustering. These are discussed individually below.

Cell shape

The shape of a cell has a significant effect on the accuracy of the solution. A cell's shape is characterised by its aspect ratio and also its skewness. These are defined as:

- Aspect ratio – a measure of the stretching of the cell.
- Skewness – the difference between the cell's shape and the shape of an equilateral volume.

In general, the aspect ratio should not exceed 5:1. Quadrilateral cells should have vertices close to 90° and triangular cells should have vertices close to 60° and have all angles less than 90° (Fluent Inc., 2003).

Smoothness

Large truncation errors occur when there are rapid changes in volume between adjacent cells. A truncation error is the difference between the partial derivatives in the governing equations and their discrete approximations (Fluent Inc., 2003).

Node density and clustering

The accuracy of the solution increases as the grid resolution increases up to the point of grid independency. However, with this the Computer Processing Unit (CPU) and memory requirements increase in order to provide the solution and post-process the results. More economical use of grid points can be made by refining the grid to be finer in certain areas than in others.

When modelling turbulent flow, a few considerations have to be made. One of these is to have a few cells inside the boundary layer so that any separation can be seen. Another is that turbulent flow is more susceptible to grid dependency than laminar flow. This is due to the interaction of the mean flow and turbulence.

2.3.2 Turbulent or laminar flow?

The transition from laminar to turbulent flow in a circular pipe occurs at Reynolds numbers in the range of 2000 to 4000 (Massey, 1984). Reynolds number is defined as

$$Re = \frac{\rho_f dU}{\mu} \tag{2-43}$$

Where: Re = Reynolds number $\qquad$ ρ_f = Fluid density, kg/m^3
$\qquad$ d = Pipe diameter, m $\qquad$ U = Average velocity, m/s
$\qquad$ μ = Absolute viscosity, kg/ms

To assess whether the flow is turbulent in the inlet pipe the Reynolds number is calculated. In all simulations using CFD the inlet pipe Reynolds number is greater than 4000 and therefore considered to be turbulent. However, this does not mean to say that turbulence continues within the HDVS body. Laminar conditions are known to be maintained at higher than the transitional Reynolds number for flow in a curved channel and cyclone conditions accentuate this effect (Bradley, 1965). However, turbulent conditions are assumed to exist within the HDVS due to the random fluctuations observed on the free surface and to ensure that a turbulent velocity profile was predicted at the inlet to the HDVS, turbulent models were chosen to solve the Navier-Stokes equations throughout the entire domain.

In all models, the turbulence intensity at the inlet was specified as being 5%. The turbulence intensity is defined as the ratio of the magnitude of the Root Mean Square (RMS) velocity fluctuations to the reference velocity (Fluent Inc., 2003) and the reference velocity is taken as

the inlet velocity. A value of 5% was considered appropriate based on development of the turbulence within the inlet pipe.

2.3.3 Turbulence models

Consider an elemental volume of fluid

$$V = \partial x_i \partial x_j \partial x_k \qquad (2\text{-}44)$$

The continuity equation for an incompressible fluid in the x direction is then given by

$$\frac{\rho \partial (u_i)}{\partial x_i} = 0 \qquad (2\text{-}45)$$

The left hand term considers the net flow of mass in and out of the elemental volume in the x component.

The momentum equation is known as the Navier-Stokes equation due to independent derivation by the two nineteenth-century researchers (Douglas *et al.*, 2001). For a Newtonian incompressible fluid, the Navier-Stokes momentum equation in rectangular coordinates in the x direction is given by

$$\rho \frac{Du_i}{Dt} = F_i - \frac{\partial p}{\partial x_i} + \mu \nabla^2 u_i \qquad (2\text{-}46)$$

Similar expressions apply to the y and z direction where

$$\frac{D\vec{U}}{Dt} = u_i \frac{\partial \vec{U}}{\partial x_i} + u_j \frac{\partial \vec{U}}{\partial x_j} + u_k \frac{\partial \vec{U}}{\partial x_k} + \frac{\partial \vec{U}}{\partial t} \qquad (2\text{-}47)$$

$$\nabla^2 = \frac{\partial^2}{\partial x_i^2} + \frac{\partial^2}{\partial x_j^2} + \frac{\partial^2}{\partial x_k^2} \qquad (2\text{-}48)$$

The left hand term of Equation 2-46 is the rate of change of momentum per unit volume. The first term on the right hand side of Equation 2-46, F_i, is the body force per unit volume. The remainder of the right hand side represents the surface force per unit volume (pressure force represented by the term in p and the viscous force represented by the term with μ) (Franzini and Finnemore, 1997).

A complete time dependent solution of Equation 2-46 in turbulent flows in complex geometries cannot be achieved due to the limitation of computer processing (Fluent Inc., 2003). Equation 2-46 may be simplified to reduce processing requirements. Reynolds averaging results in a time averaged form of Equation 2-46. Shames (1992) comments that it is "more significant from a physical standpoint to reach relations for mean time averages since it is these averages which are readily observed". Another method to reduce processing requirements of Equation 2-46 is 'filtering'.

2.3.3.1 Large Eddy Simulation (LES) / Filtering

LES computes large eddies in a time-dependent simulation. This approach requires filtering of eddies that are smaller than the filter, the filter generally taken as the size of the mesh. Filtering results in the creation of additional terms that must be modelled to achieve closure. (Closure meaning that there are enough equations to solve all the unknowns). However, the LES model is still in its infancy (Fluent Inc., 2003) and also requires large computer resources. Fluent Inc. (2003) therefore recommends the use of Reynolds averaged turbulence models.

2.3.3.2 Reynolds (Ensemble) averaging

In Reynolds averaging the velocity components are decomposed into the mean and fluctuating components i.e.

$$u_{in} = \bar{u} + u'$$ (2-49)

Where: u_{in} = Instantaneous velocity, m/s u = Time averaged velocity, m/s
     u' = Fluctuating velocity, m/s

The same also applies to the pressure and other scalar quantities i.e.

$$\varphi = \bar{\varphi} + \varphi'$$ (2-50)

Where: φ denotes a scalar such as pressure.

Substituting expressions of the form of Equations 2-49 and 2-50 for the flow variables into Equation 2-46 yields the ensemble-averaged momentum equation for the x direction

$$\rho \frac{Du_i}{Dt} = F_i - \frac{\partial p}{\partial x_i} + \mu \nabla^2 u_i - \rho \left(\frac{\partial \overline{(u'_i)^2}}{\partial x_i} + \frac{\partial \overline{(u'_i u'_j)}}{\partial x_j} + \frac{\partial \overline{(u'_i u'_k)}}{\partial x_k} \right)$$ (2-51)

Similar expressions apply to the y and z direction.

The terms $-\rho \overline{u'^2_i}$, $-\rho \overline{u'_i u'_j}$ and $-\rho \overline{u'_i u'_k}$ are known as the Reynolds stresses. These must be modelled in order to close Equation 2-51. To approximately model the Reynolds stresses the Boussinesq hypothesis (Hinze, 1975) may be employed to relate the Reynolds stresses to the mean velocity gradients. The disadvantage of the Boussinesq hypothesis is that it assumes the turbulent viscosity, μ_t, to be isotropic, which is not always the case. The Boussinesq hypothesis is used in the k-ε turbulence models.

2.3.3.3   Standard k-ε model

The standard k-ε model (Launder and Spalding, 1972) is a two-equation model in which the solution of two separate transport equations allow the turbulent velocity and length scales to be independently determined (Fluent Inc., 2003).

The standard k-ε model is valid for low turbulent flows due to the assumption in its derivation that the flow is fully turbulent and that the effect of molecular viscosity is negligible i.e. the model assumes the velocity fluctuations to be isotropic.

The two transport equations are:

$$\frac{\partial}{\partial t}(\rho k) + \frac{\partial}{\partial x_i}(\rho k u_i) = \frac{\partial}{\partial x_j}\left[\left(\mu + \frac{\mu_T}{\sigma_k}\right)\frac{\partial k}{\partial x_j}\right] + G_k + G_b - \rho \varepsilon - Y_M$$ (2-52)

$$\frac{\partial}{\partial t}(\rho \varepsilon) + \frac{\partial}{\partial x_i}(\rho \varepsilon u_i) = \frac{\partial}{\partial x_j}\left[\left(\mu + \frac{\mu_T}{\sigma_\varepsilon}\right)\frac{\partial \varepsilon}{\partial x_j}\right] + C_{1\varepsilon}\frac{\varepsilon}{k}(G_k + C_{3\varepsilon}G_b) - C_{2\varepsilon}\rho\frac{\varepsilon^2}{k}$$ (2-53)

Where: ρ =Fluid density, kg/m^3 k = Turbulent kinetic energy, m^2/s^2

μ_T = Turbulent/eddy viscosity, kg/ms ε = Turbulent dissipation rate, m^2/s^3

σ_k = 1.0 = Turbulent Prandtl number for turbulent kinetic energy

σ_ε = 1.3 = Turbulent Prandtl number for turbulent dissipation rate

G_k = Generation of turbulent kinetic energy due to the mean velocity gradients, kg/ms^3

G_h = Generation of turbulence kinetic energy due to buoyancy, kg/ms^3

Y_M = Represents the contribution of the fluctuating dilatation in compressible turbulence to the overall dissipation rate, kg/ms^3

$C_{1\epsilon}$ = 1.44 $C_{2\epsilon}$ = 1.92 $C_{3\epsilon}$ = Constant

The Turbulent/eddy viscosity is given by

$$\mu_T = \rho C'_\mu \frac{k^2}{\epsilon}$$

(2-54)

Where: C_μ =0.09

$C_{1\epsilon}$, $C_{2\epsilon}$, C_μ, σ_k and σ_ϵ are constants derived empirically.

The generation of turbulent kinetic energy, G_k, due to mean velocity gradients is given by

$$G_k = -\rho \overline{u'_i u'_j} \frac{\partial u_j}{\partial x_i}$$

(2-55)

However, Equation 2-55 must be evaluated according to the Boussinesq hypothesis such that

$$G_k = \mu_T S^2$$

(2-56)

Where S is the modulus of the mean rate-of-strain tensor given by

$$S \equiv \sqrt{2S_{ij}S_{ij}}$$

(2-57)

The degree to which the dissipation rate is affected through buoyancy is determined through $C_{3\epsilon}$. It will be assumed that there is a zero temperature gradient throughout the HDVS and buoyancy effects can therefore be neglected.

Calculation of Y_M is only applicable at high Mach number flows, not present in a hydrodynamic vortex separator.

Details on the generation of turbulent kinetic energy due to buoyancy, G_h and calculation of $C_{3\epsilon}$ and Y_M can be found in Fluent Inc. (2003).

2.3.3.4   RNG k-ε model

The RNG k-ε model (Yakhot and Orszag, 1986; Choudhury, 1993) has been derived using a statistical technique called Renormalization Group Theory. The model is very similar to the standard k-ε model but with the following modifications:

- An additional term in the ε equation which improves the accuracy for rapidly strained flow

- Includes an analytically-derived differential formula which considers the viscosity that accounts for low Reynolds number effects

- The effect of swirl on turbulence is included which gives greater accuracy for swirling flows

- Includes an analytical formula for turbulent Prandtl numbers whereas the standard k-ε model relies upon constant values, inputted by the user

In the RNG k-ε model C_μ has been derived using RNG theory and is equal to 0.0845, which is close to the empirically derived value of 0.09 used in the standard k-ε model.

Details on the transport equations for RNG k-ε model are given in Fluent Inc. (2003).

2.3.3.5   Realizable k-ε model

Although not used in this work, it is worth noting that the realizable k-ε model proposed by Shih *et al.* (1995) was intended to address deficiencies of traditional k-ε models. This includes sensitising C_μ to the mean flow and turbulence as the notion of C_μ being variable is suggested by Reynolds (1987) and is also well substantiated by experimental evidence (Fluent Inc., 2003). A new equation for modelling dissipation is also introduced which addresses the difficulty of modelling axisymmetric jets.

2.3.3.6   Reynolds Stress Model (RSM)

The Reynolds Stress Model (Launder *et al.*, 1975; Gibson and Launder, 1978; Launder, 1989a) is the most sophisticated of the turbulence models and abandons the theory that the turbulence is isotropic. The RSM "closes the Reynolds-averaged Navier-Stokes equations by solving transport equations for the Reynolds stresses, together with an equation for the dissipation rate" (Fluent Inc., 2003). The result of this is that for 2D flows an extra five

equations are solved and for 3D flow, an extra seven. "Since the RSM accounts for the effects of streamline curvature, swirl, rotation and rapid changes in strain rate in a more rigorous manner than one-equation and two-equation models, it has greater potential to give accurate predictions for complex flows" (Fluent Inc., 2003).

The transport equation for the Reynolds stresses, $\rho u'_i u'_j$ is

$$\underbrace{\frac{\partial}{\partial t}\left(\rho u'_i u'_j\right)}_{\text{Local Time Derivative}} + \underbrace{\frac{\partial}{\partial x_k}\left(\rho u_k u'_i u'_j\right)}_{C_{ij}\,=\text{Convection}} = \underbrace{-\frac{\partial}{\partial x_k}\left[\rho\overline{u'_i u'_j u'_k} + \overline{p(\delta_{kj}u'_i + \delta_{ik}u'_j)}\right]}_{D_{T,ij}\,=\text{Turbulent Diffusion}}$$

$$+ \underbrace{\frac{\partial}{\partial x_k}\left[\mu\frac{\partial}{\partial x_k}\left(\overline{u'_i u'_j}\right)\right]}_{D_{L,ij}\,=\text{Molecular Diffusion}} - \underbrace{\rho\left(\overline{u'_i u'_k}\frac{\partial u_j}{\partial x_k} + \overline{u'_j u'_k}\frac{\partial u_i}{\partial x_k}\right)}_{P_{ij}\,=\text{Stress Production}} - \underbrace{\rho\beta\left(g_i\overline{u'_j\theta} + g_j\overline{u'_i\theta}\right)}_{G_{ij}\,=\text{Buoyancy Production}}$$

$$+ \underbrace{\overline{p\left(\frac{\partial u'_i}{\partial x_j} + \frac{\partial u'_j}{\partial x_i}\right)}}_{\varphi_{ij}\,=\text{Pressure Strain}} - \underbrace{2\mu\overline{\frac{\partial u'_i}{\partial x_k}\frac{\partial u'_j}{\partial x_k}}}_{\varepsilon_{ij}\,=\text{Dissipation}} - \underbrace{2\rho\Omega_k\left(\overline{u'_j u'_m}\varepsilon_{ikm} + \overline{u'_i u'_m}\varepsilon_{jkm}\right)}_{F_{ij}\,=\text{Production by System Rotation}}$$

(2-58)

Of the various terms in Equation 2-58, C_{ij}, $D_{L,ij}$, P_{ij} and F_{ij} do not require any modelling. $D_{T,ij}$, G_{ij}, φ_{ij} and ε_{ij} do require modelling in order to close the equation.

The turbulent diffusive transport, $D_{T,ij}$, can be modelled according to a generalised gradient-diffusion model of Daly and Harlow (1970). To reduce numerical instabilities however, FLUENT uses a simplified form by Lien and Leschziner (1994) which uses a scalar turbulent diffusivity.

The pressure strain, φ_{ij}, is modelled by default using a linear pressure strain model according to the proposals of Gibson and Launder (1978), Fu *et al.* (1987) and Launder (1989a and 1989b). Unless otherwise stated, the linear pressure strain model is implemented when using the RSM. When the linear pressure strain model is applied to near wall flows where enhanced wall treatment is being used modifications to the linear pressure strain model are made according to suggestions by Launder and Shima (1989).

There is the option to abandon the linear pressure strain model and use a quadratic pressure strain model proposed by Speziale *et al.* (1991). This according to Fluent Inc. (2003) has been demonstrated to give better performance in a range of basic shear flows.

In a flow where the temperature gradient is zero, the effect of buoyancy can be neglected.

Details on the modelling of the dissipation rate and further details on the turbulent diffusive transport and pressure strain can be found in Fluent Inc. (2003).

2.3.3.7 Near-wall modelling

The presence of a wall will affect the velocity due to the no-slip boundary condition, which also affects the turbulence. The RSM and k-ε models are valid primarily in the regions far from the walls and special treatment must therefore be given close to the wall.

Numerous experiments have shown that generally three subdivisions in the near wall region exist (Fluent Inc., 2003). This is shown in Figure 2-6 with experimental data indicated by Δ and O. The inner most layer is known as the viscous sublayer where the flow is laminar and the effect of molecular viscosity is dominant. In the outer region is a fully turbulent region and connecting the two is an interim region called the buffer layer where the effect of molecular viscosity and turbulence are equally important (Fluent Inc., 2003).
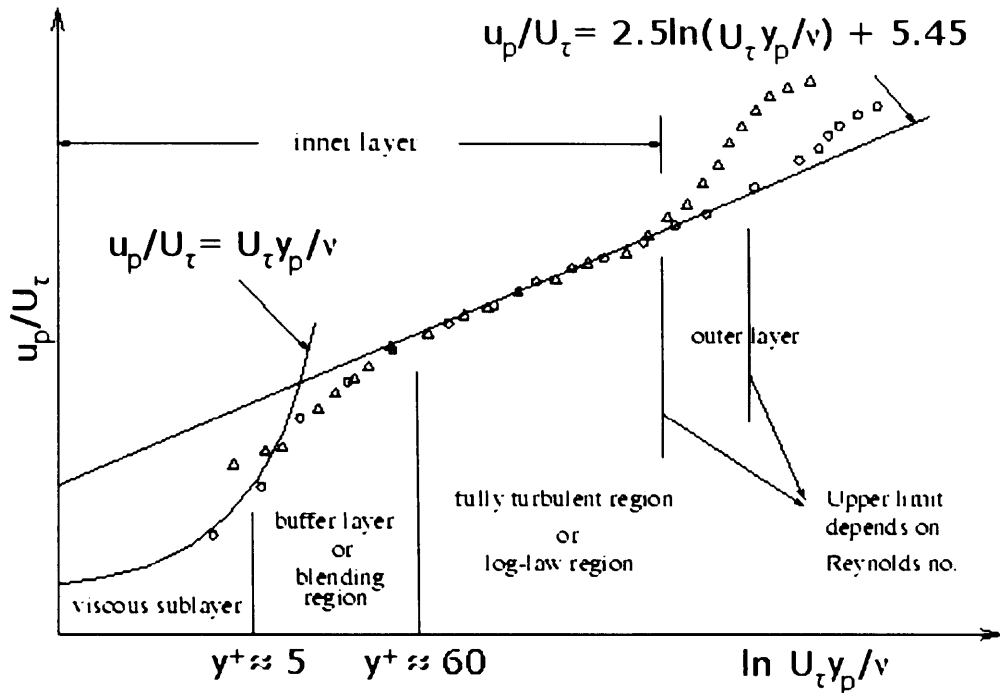
Figure 2-6. Subdivisions of the near wall region. Adapted from Fluent Inc. (2003).

There are two approaches to modelling the near wall region. The first is where semi-empirical wall functions are applied which bridge the viscosity affected inner region with the fully turbulent outer region. This means that the y^+ value in the model should be of the order of 30 to 60. The second approach is where the "turbulence models are modified to enable the viscosity-affected region to be resolved with a mesh all the way to the wall, including the viscous sublayer" (Fluent Inc., 2003). This approach will be referred to as 'near-wall modelling'. For near-wall modelling to be effective, the y^+ value should be less than 10 and may even have to be approximately 1 depending on the near wall model being used. This means that near wall modelling is computationally more expensive in that a greater number of cells must be placed close to the wall, as demonstrated in Figure 2-7. For this reason, standard wall functions have been used throughout the modelling described.
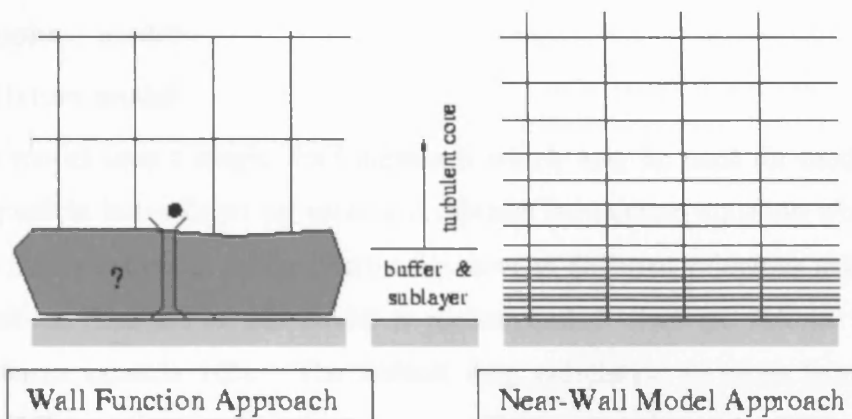
Figure 2-7. Two modelling approaches to wall treatment (Fluent Inc., 2003).

The standard wall functions are based on the proposals of Launder and Spalding (1974).

The friction velocity in non-dimensional form, U^*, is given by

$$U^* = \frac{u_P}{U_\tau} = \frac{1}{\kappa} \ln\left(Ey^*\right) \tag{2-59}$$

Where: u_P = Mean fluid velocity at point 'P', m/s U_τ = Friction velocity, m/s
   κ = von Karman's constant (=0.42) E = Empirical constant (=9.793)
   y^* = Displacement boundary layer thickness

Where

$$U^* = \frac{u_P C_\mu^{1/4} k_P^{1/2}}{\tau_w / \rho} \tag{2-60}$$

Where: τ_w = Wall shear stress, N/m^2 k_P = Turbulent kinetic energy at point 'P'

The local Reynolds number, y^+, is given by

$$y^+ = \frac{U_\tau y_P}{\upsilon} \tag{2-61}$$

Where: y_P = Distance from point 'P' to the wall, m υ = Kinematic viscosity, m^2/s

The displacement boundary layer thickness in non-dimensional form is given by

$$y^* = \frac{\rho C_\mu^{1/4} k_P^{1/2} y_P}{\mu} \tag{2-62}$$

Details on the enhanced wall treatment can be found in Fluent Inc. (2003).

2.3.4 Multiphase models

2.3.4.1 Mixture model

The mixture model uses a single fluid approach which may be used for modelling bubbly, droplet and particle laden flows by solving a mixture momentum equation which allows the phases to be interpenetrating. Each phase may move at different velocities using the concept of slip velocities. The use of this model is recommended when the volume fraction of the secondary phases exceeds 10%. The default drag correlation is taken from Schiller and Naumann (1935).

2.3.4.2 Eulerian model

The Eulerian model may be used for modelling bubbly, droplet and particle laden flows. A momentum equation is solved for each phase, making this model the most computationally expensive of all the multiphase models. The use of this model is recommended when the volume fraction of the secondary phases exceeds 10%. A range of drag correlation functions are available with the Eulerian model such as Schiller and Naumann (1935), Morsi and Alexander (1972) and Wen and Yu (1966).

2.3.4.3 The Discrete Phase Model (DPM)

The Discrete Phase Model may be used for modelling bubbly, droplet and particle laden flows. The trajectories of a second 'discrete phase' are computed in a Lagrangian frame of reference. This model assumes that the volume fraction of the second phase does not exceed 10% and that particle-particle interactions do not exist.

Equations of motion

The trajectory of a particle is determined by integrating the force balance on the particle, which is given by (Fluent Inc., 2003)

$$\frac{du_p}{dt} = F_D(u - u_p) + \frac{g_x(\rho_p - \rho_f)}{\rho_p} \tag{2-63}$$

Where: t = Time, s u = Fluid velocity, m/s

$F_D(u - u_p)$ in Equation 2-63 is the drag force per unit particle mass with units of m/s^2 where

$$F_D = \frac{18\mu}{\rho_p d_p^2} \frac{C_D \, \text{Re}}{24}$$ (2-64)

Where: Re = Relative Reynolds number

The relative Reynolds number is given by

$$\text{Re} = \frac{\rho_f d_p \, | u_p - u |}{\mu}$$ (2-65)

For spherical particles, the drag coefficient, C_D, is taken from Morsi and Alexander (1972) and is given by

$$C_D = a_1 + \frac{a_2}{\text{Re}} + \frac{a_3}{\text{Re}^2}$$ (2-66)

a_1, a_2 and a_3 are constant at a range of particle Reynolds number for a smooth spherical sphere given by Morsi and Alexander (1972).

For non spherical particles, the drag coefficient is taken from Haider and Levenspiel (1989), Equation 2-8.

Length scale

The length scale controls the time step used to integrate the equations of motion for a particle (Fluent Inc., 2003) and the time step is given by

$$\Delta t = \frac{L}{u_p + u}$$ (2-67)

Where: Δt = Time step, s L = Length scale, m

The length scale is the distance the particle travels before the equations of motion are solved again.

Coupling between the discrete and continuous phases

When the particle trajectory is computed, the momentum gained or lost by the particle is recorded within the CFD software. The option to include the effect of the discrete phase (particles) on the continuous phase (water) is available and achieved by solving the particle trajectory equations and continuous phase equations alternately until the solution of both phases stop changing. Fluent Inc. (2003) gives details on the equation used for momentum

transfer. The momentum transfer is then applied as a momentum sink in the continuous phase momentum balance (Fluent Inc., 2003).

Stochastic particle tracking

Stochastic particle tracking is used to represent the turbulent dispersion of particles. In FLUENT the Discrete Random Walk (DRW) model is used where "the interaction of a particle with a succession of discrete stylised fluid phase turbulent eddies is simulated" (Fluent Inc., 2003).

The particle trajectory is computed using the instantaneous value of the fluctuating velocity, which is given by

$$u_{in} = u + u'$$
(2-49)

The velocity fluctuations that exist during the lifetime of the eddy are given by

$$u' = \zeta \sqrt{\overline{u'^2}}$$
(2-68)

Where: ζ = Normally distributed random number

The right hand side of Equation 2-68, neglecting ζ, is the RMS of the velocity fluctuations.

The k-ε turbulence models assume that the flow is isotropic. Since the kinetic energy of turbulence is known, then the RMS velocity fluctuations can be obtained from Equation 2-69.

$$\sqrt{\overline{u'^2}} = \sqrt{\overline{v'^2}} = \sqrt{\overline{w'^2}} = \sqrt{\frac{2k}{3}}$$
(2-69)

For the RSM the flow is not assumed to be isotropic, so the fluctuating velocities are given by

$$u' = \zeta \sqrt{\overline{u'^2}}$$
(2-70)

$$v' = \zeta \sqrt{\overline{v'^2}}$$
(2-71)

$$w' = \zeta \sqrt{\overline{w'^2}}$$
(2-72)

"The particle is assumed to interact with the fluid phase eddy over the smaller of the eddy lifetime and the eddy crossing time. When this time is reached, a new value of the instantaneous velocity is obtained by applying a new value of ζ" (Fluent Inc., 2003). Details on the calculation of the eddy lifetime and the eddy crossing time can be found in Fluent Inc. (2003).

2.3.4.4 Volume Of Fluid (VOF) model

The volume of fluid model assumes that two or more phases are not interpenetrating i.e. immiscible fluids. In the case of water and air, if the volume fraction of water is α_w, then three conditions are possible in a control volume:

$\alpha_w = 0$ The control volume is full of air

$\alpha_w = 1$ The control volume is full of water

$0 < \alpha_w < 1$ The cell contains the interface between water and air

The summation of the volume fraction of each phase in each control volume is equal to unity. Thus

$$\sum_{q=1}^{Q} \alpha_q = 1$$

(2-73)

Where: α_q = Volume fraction of the qth phase Q = Number of phases

Momentum Equation

A single momentum equation is solved throughout the entire grid and the resulting velocity field is shared by all the phases. Properties, such as density, viscosity etc, are determined by taking the average of the property in the control volume. Thus, the density is given by

$$\rho = \sum_{q=1}^{Q} \alpha_q \rho_q$$

(2-74)

The momentum equation is therefore dependent upon the volume fractions of each phase through the properties of ρ and μ (Fluent Inc., 2003). The result of this shared field approximation is that when there is a large velocity difference between the two phases, large errors can occur.

Interpolation near the surface

To determine the shape of the interface, FLUENT may apply one of four schemes. Both the 'Geometric Reconstruction Scheme' and the 'Donor-Acceptor Scheme' apply a special treatment to cells that lie near the interface of two phases, whereas the 'Euler Explicit' and the 'Implicit' schemes treat all cells in the same manner.

The Geometric Reconstruction Scheme is based on the work of Youngs (1982) and is the most accurate method of representing the interface between two phases in FLUENT. The interface is represented using a piecewise-linear approach which assumes that the interface between two fluids may be represented as a linear slope within each cell.

The Donor-Acceptor Scheme (Hirt and Nichols, 1981) may only be applied to quadrilateral/hexahedral cells. This scheme identifies one cell as being a 'donor' of fluid and a neighbour cell is being an 'acceptor'. The amount of fluid that is convected from one cell to the other is limited by the amount of fluid in the donor cell and the free volume in the acceptor cell. With this scheme, the interface orientation is either horizontal or vertical and hence, the scheme is therefore less accurate than the Geometric Reconstruction Scheme. The interface orientation is determined based on its motion as well as the volume fraction gradient of the phase.

The Euler explicit approach uses FLUENT's finite difference-interpolation schemes applied to the volume fraction values computed in the previous time step.

The implicit scheme requires the volume fraction values at the current time step, hence, "a standard scalar transport equation is solved iteratively for each of the secondary-phase volume fractions at each time step" (Fluent Inc., 2003).

2.3.5 The solver

A coupled and segregated solver is available. The default is the 'Segregated Solver' so called as it solves the momentum and continuity equations sequentially. This solver has traditionally been used for incompressible to mildly compressible flows and is therefore used throughout the modelling presented. An overview of the segregated solver is shown in Figure 2-8.
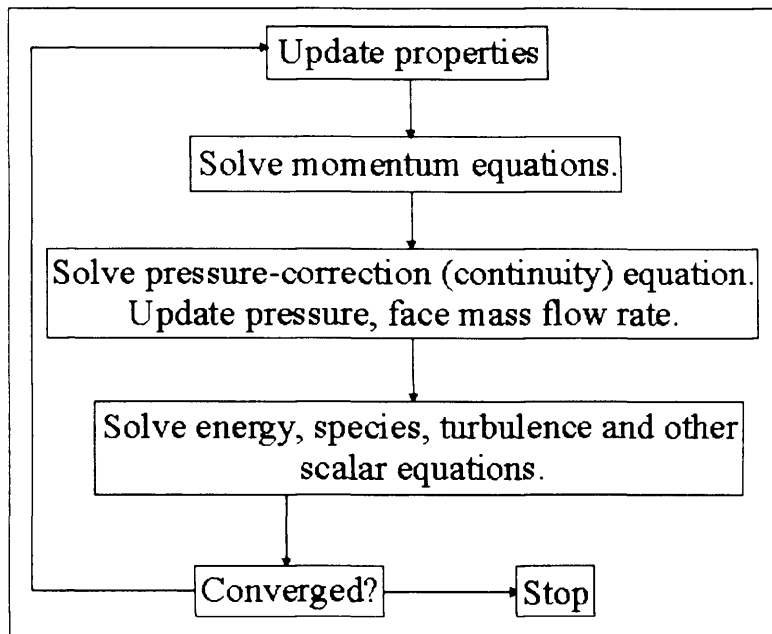
Figure 2-8. An overview of the segregated solution method.
Adapted from Fluent Inc. (2003).

2.3.6 Solution controls

2.3.6.1 Pressure-velocity coupling

Pressure-velocity coupling is relevant only to the segregated solver. This is because the momentum and continuity equations are solved sequentially and in this procedure, the continuity equation is used as an equation for pressure. However, for incompressible flows, the pressure is not directly related to density and an algorithm is used to introduce pressure into the continuity equation. FLUENT offers three pressure-velocity coupling algorithms. The default is the SIMPLE (Semi-Implicit Method for Pressure-Linked Equations) algorithm (Patankar, 1980). The SIMPLEC algorithm (Vandoormaal and Raithby, 1984) will benefit convergence only if it is limited by the pressure-velocity coupling. Otherwise SIMPLE and SIMPLEC will give similar convergence rates. The third algorithm is PISO (Pressure-Implicit with Splitting of Operators). This algorithm belongs to the SIMPLE family of algorithms but is recommended for transient calculations and also transient and steady-state calculation on highly skewed meshes. Further details can be found in Fluent Inc. (2003).

2.3.6.2 Pressure interpolation schemes

The default pressure interpolation scheme, which will be referred to as the 'standard pressure interpolation scheme', is valid provided that pressure variations between cell centres are smooth. Such a situation where cells must be packed to adequately solve the pressure

variation is strongly swirling flows. The 'standard pressure interpolation scheme' assumes that the pressure gradient at the wall is zero. This is valid for boundary layers but not in the presence of body forces or curvature. FLUENT offers four additional pressure interpolation schemes. (Linear, second-order, body-force weighted and PRESTO!) The PRESTO! (PREssure STaggering Option) scheme is recommended for highly swirling flows and flows in strongly curved domains. Further details can be found in Fluent Inc. (2003).

2.3.6.3   Discretization

Discretization describes the scheme that is being used to calculate the field variables. The 'First-order Upwind' discretization scheme calculates first order terms only. This is acceptable when the flow is aligned with the grid, but when the flow crosses the grid lines, numerical diffusion occurs. Hence, the 'Second-order upwind' provides a more accurate solution by calculating the second order terms. This increases the accuracy of tetrahedral grids which the flow can never be aligned with.

2.3.6.4   Under-relaxation

Under-relaxation changes the amount by which the computed value, φ, changes after each iteration. It is sometimes necessary to change the under-relaxation factors, otherwise the solution will oscillate (become unstable) and/or diverge.

In the simplest form "the new value of the variable within a cell depends upon the old value, the computed change in the variable and the under-relaxation factor as follows" (Fluent Inc., 2003)

$$\varphi = \varphi_{old} + \alpha \Delta \varphi \qquad\qquad (2\text{-}75)$$

Where: φ = New value of variable φ_{old} = Old value of variable
          α = Under-relaxation factor

The iterative approach to computing a solution requires that some form of judging convergence must be considered. Throughout modelling, this has generally been judged based on the change of the residuals and also monitoring the static pressure.

2.3.7 User Defined Functions (UDFs)

UDFs allow the CFD user to create a sub routine written in the 'C' programming language which can be used to customise and also increase the capabilities of the simulation software. For example, custom material properties may be defined using a UDF such as a temperature dependent density. An example of increasing the capabilities of the software to a very specific problem is by using a UDF to access the computed variables to perform post processing calculations e.g. computing the power extracted by a turbine (Egarr *et al.*, 2004; Egarr *et al.*, 2005). Appendix A contains the UDFs used during modelling in this work.

2.4 Statistical analysis

2.4.1 Propagation of uncertainties

In many situations, a quantity is determined by combining two or more measured values. For example, the terminal settling velocity of a sphere is determined by combining the time taken for the sphere to descend a predetermined distance. Errors will be introduced for example in the precision of the stop clock and also the rule used to define the distance. Error will also be introduced by the person timing in that there will be an error in the actual distance that the particle covers while the stop clock is running. Methods of analysing the propagation of error are described by Taylor (1982).

2.4.2 Standard deviation

Situations often arise where, for example, the mean of a population is required, whether it be the mean age of the UK population, or the mean particle size in a large population of particles. Under these circumstances it is not possible to account for every individual in the population and estimates have to be made based on a sample of the population. The standard deviation is a measure of how widely values are dispersed from the mean. For a large sample, n greater than 30, the standard deviation is given in Alder and Roessler (1975)

$$s = \sqrt{\frac{\sum_{i=1}^{n}\left(X_i - \overline{X}\right)^2}{n}}$$

(2-76)

Where: s = Standard deviation of a large sample
n = Number of variants, X_1, X_2, X_3 etc

When the sample is small, n less than 30, a better approximation is given in Alder and Roessler (1975)

$$s = \sqrt{\frac{n}{n-1}}\, s = \sqrt{\frac{\sum_{i=1}^{n}\left(X_i - \bar{X}\right)^2}{n-1}} \tag{2-77}$$

Where: s = Standard deviation of a small sample

2.4.3   Confidence interval

When a sample of a population has to be used to derive for example the mean, it is often preferable to find an interval estimate which is "constructed in such a way that we have a certain confidence that the interval contains the unknown parameter" (Chatfield, 1997) e.g. particle diameter.

Since the population mean is unknown, then the population standard deviation is also likely to be unknown. In this case, the sample standard deviation, s, is used to estimate the population standard deviation and the 100(1- α) per cent confidence interval for the population mean is given by

$$\bar{x} \pm t_{\frac{\alpha}{2},n-1} \frac{s}{\sqrt{n}} \tag{2-78}$$

Where: $\bar{x}$ = Sample mean n = Sample size

The statistic t follows a distribution called the t-distribution which is symmetric with a mean zero (Chatfield, 1997). As the number of degrees of freedom, $n-1$, approach infinity, the t-distribution approaches the normalised distribution and provided the sample size is 30 or more, the standard normal distribution is a good approximation to the t-distribution (Miller *et al.*, 1990). NIST/SEMATECH e-Handbook, 2005, tabulates upper critical values of Student's t-distribution up to 100 degrees of freedom.

3 Literature review

3.1 Development of the Hydrodynamic Vortex Separator (HDVS)

The concept of hydrodynamic separation of solids in sewers was first observed by Smisson and who consequently pursued research of the separation of sewage in circular tanks in the 1950's and 1960's (Smisson, 1967). The aim of Smisson's research was to "develop a device which could constrain the flow entering to follow a long path through the unit. This would then lengthen the time that gravity, aided by other forces due to the rotary motion induced by the kinetic energy of the flow, would have to act on the wastewater" (Andoh and Smisson, 1993). The first full scale vortex units were constructed in Bristol, United Kingdom (Andoh and Smisson, 1993).

In the 1970's Smisson continued his research in America with an American Public Works Association (APWA), which resulted in the development of the United States Environment Protection Agency (US EPA) "Swirl Concentrator" for the removal of settleable solids from CSOs (Andoh and Smisson, 1993). For this work, Smisson received an "APWA award of merit in recognition of the excellence of his work, ingenuity, resourcefulness and grasp of hydraulic engineering principles" (Andoh and Smisson, 1993).

Continued research in the United Kingdom by Hydro International Plc has led to the development of a range of HDVSs which include the Storm King®, Grit King® and Eff-Pac™ Clarifier Separators.

3.2 Flow patterns within the HDVS

The mean flow pattern within a HDVS is a "downward helical flow in the outer region and an upward helical flow near the central region" with a shear zone separating the two in the form of a "zero velocity surface cylindrical around the vessel" (Andoh and Smisson, 1993). With the two differing helical flows, there is a "non-uniform axial flow profile with downwards flow along the walls and upward flow along the axis" (Andoh and Smisson, 1993). It is also reported that, due to the presence of internal components such as a central cone, baffle plate and dip plate "highly stabilised flow patterns" exist in the separator (Andoh and Smisson, 1993).

Tyack and Fenner (1999) modelled a 1.6m diameter Grit King[®] using FIDAP, a finite element CFD program, using the RNG k-ε turbulence model (see Section 2.3.3.4) with 56 824 elements. Comparison of experimental 3 component velocity measurements were of the same order as those predicted in the CFD models. One of the conclusions to their work was that CFD can be used to obtain data that is difficult to collect experimentally (Tyack and Fenner, 1999). From their models, they determined that "the flow pattern is helical with secondary recirculation patterns. The general flow is downward on the outside of the separator body and upwards towards the outlet at the centre of the device" (Tyack and Fenner, 1999). This is in agreement with Andoh and Smisson (1993). Tyack and Fenner (1999) also found that "there is an asymmetrical flow pattern within the device due to the high velocities at the inlet causing skewing of the flow around the central shaft and cone". The presence of a zone separating the upward and downward flow patterns was also detected and "the position of the shear zone appears to vary around the separator and may not be located directly under the dip plate as previously thought" (Tyack and Fenner, 1999).

Figure 3-1 shows a plot of tracer concentration at the base flow, overflow and the total outflow against time for a tracer test on a Grit King[®] with an inflow rate of 35.6 litres per second.
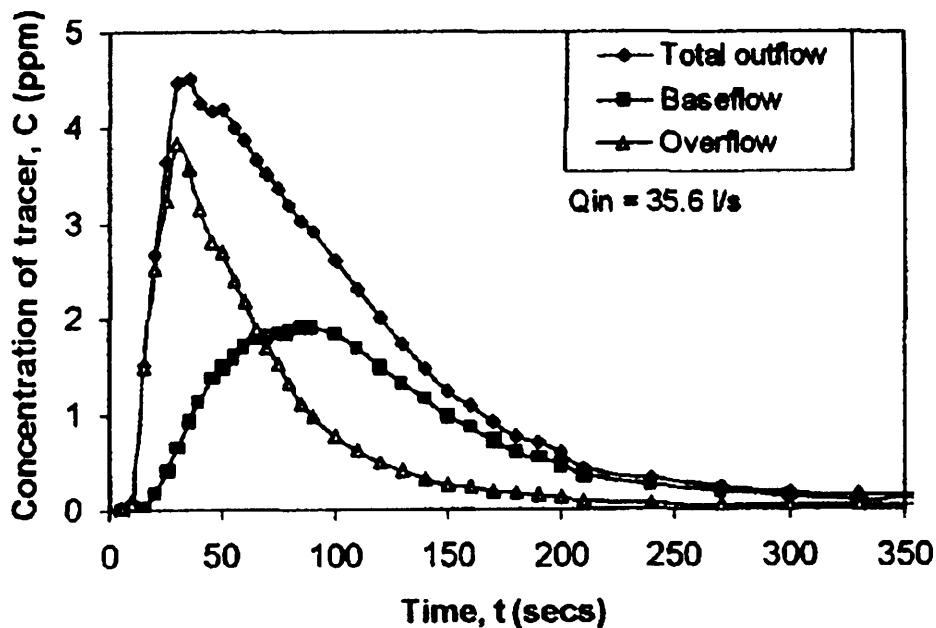

Figure 3-1. Residence time distributions from a Grit King[®] (Tyack and Fenner, 1998a).

A proposed flow regime deduced from the experimental 3-component velocity measurements and the RTD plots of Figure 3-1 is shown in Figure 3-2 and the justification for this regime is:

"The fluid enters the separator and is swept around the separator between the dip plate and the outside wall, where there is a considerable amount of mixing due to the turbulent nature of the flow. Some of this flow is immediately swept up and out of the overflow creating an immediate tracer response, as illustrated in Figure 3-1. A proportion of the flow passes into the region between the shear zone and the central shaft and except for a region close to the central shaft and cone the flow passes up and out of the overflow, which accounts for the extended tail on the RTD. A downward flow immediately next to the shaft and cone has been detected in velocity measurements" (Tyack and Fenner, 1998a).
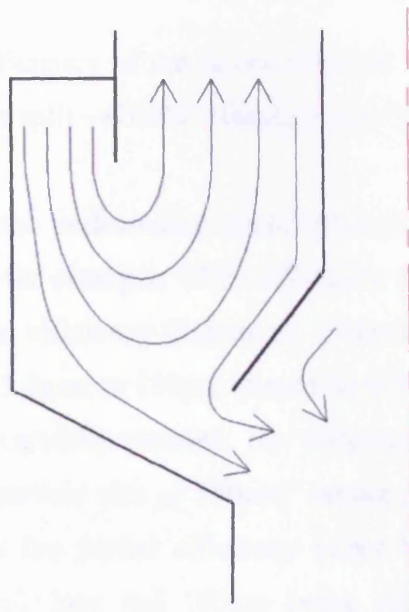
Figure 3-2. Flow proposed by Tyack and Fenner (1998a).
Adapted from Tyack and Fenner (1998a).

Tyack and Fenner (1998a) have also suggested that the delayed response in the RTD for the base flow is due to the longer path that the fluid must take to reach the base flow and the lower velocities in the centre of the separator.

3.3   Retention efficiency

3.3.1   Defining the retention efficiency

Assessment of the efficiency of a HDVS when carried out using a substance such as sand may be defined in a number of ways, all be it, "logic notwithstanding" (Gardner and Deamer, 1996).

Total efficiency: "The fraction of mass of the grit in the influent liquor which is retained by the device" (Gardner and Deamer, 1996).

Partial efficiency: "The fraction of that grit in the influent liquor which is between two defined sizes (e.g. 150μm and 300μm) and which is retained by the device" (Gardner and Deamer, 1996).

Grade efficiency: "The fraction of that grit in a single size in the influent liquor which is retained by the device" (Gardner and Deamer, 1996).

Reduced efficiency: "The efficiency of the device after the linear scale 0→100% has been mapped to the linear scale flow split →100%" (Gardner and Deamer, 1996).

It should also be noted that if the performance specification is loosely worded, then it is easy to misinterpret the definition, for example, "95% efficiency of all particles down to 150μm" can mean either that the partial efficiency (5.0mm to 150μm) or the grade efficiency (i.e. for single size) for all sizes from 5.0mm to 150μm should be 95% (Gardner and Deamer, 1996). Even if the specification is carefully worded, the efficiency can still be ambiguous, for example, "95% efficient at a particle size of 150μm" cannot in practice be measured directly but must be approximated by the partial efficiency either between 212μm and 150μm or between 150μm and 105μm (212μm and 105μm being the nearest available sieve sizes) (Gardner and Deamer, 1996). This clearly demonstrates the complexity and ambiguity of some of the definitions used to define the efficiency of a separation device.

3.3.2   Presentation of retention efficiency

Presenting the retention efficiency (partial or grade) plotted against a dimensionless group can be a useful means of presentation if all retention efficiency curves fall onto roughly a single curve. This allows a function to be fitted to the single curve which then allows the prediction of retention efficiency for all particles on which experimental testing was carried out.

Frederick and Markland (1967) studying a stilling pond which is a form of CSO treatment chamber, related the efficiency to the dimensionless group $u_{p\infty}C_D^{0.5}/U$ for particulates of a uniform size and settling velocity, where $u_{p\infty}$ is the settling velocity of the particle, C_D the

drag coefficient and U the mean velocity at the inlet. This dimensionless group can be computed directly in conjunction with Equation 2-4 when the particle properties are known.

Halliwell and Saul (1980) also studying CSO chambers, related the efficiency to the dimensionless group $u_{p\infty}/U$ for beads of a known settling velocity. Hedges (1994) found that using this dimensionless group, retention efficiency characteristics of a prototype separator and two scale models (1:10 and 1:20) were identical for plastic and nylon beads of a known settling velocity, suggesting that for steady state conditions, retention efficiencies determined in a laboratory can be used to determine the performance of a full scale HDVS. Application of $u_{p\infty}/U$ requires either knowledge of the particle settling velocity from settling velocity data or knowledge of the particle properties such that the particle settling velocity may be computed. This dimensionless group was applied to efficiency curves for a high side weir overflow by Burt *et al.* (2002) who report that $u_{p\infty}C_D^{0.5}/U$ is preferable when different particle size classes are being considered though reasons for this are not given.

A slight twist to the dimensionless group $u_{p\infty}/U$ is $u_{p\infty}/U_r$ which is known as the Hazen number and is given in Luyckx *et al.* (2004).

Where: $U_r = \dfrac{Q}{A}$ = Rise velocity or surface loading rate, m/s or m^3/m^{2}s

Where: Q = Overflow discharge flowrate, m^3/s

A = Horizontal area of the chamber, m^2

The Hazen number has more relevance to a HDVS where a $u_{p\infty}/U_r$ value of 1 can be imagined to be the point at which the settling velocity of the particle is balanced against the rise velocity of the fluid in the HDVS. In practice, this is not the case due to the fluid mechanics within the vortex separator.

3.3.3 Modelling HDVS efficiency

Luyckx *et al.* (2002) derived a single semi-empirical formula for predicting the efficiency of a range of CSO devices including a high side weir, vortex separator, hydrodynamic separator and a swirl separator. During experimental testing, Bakelite was used whose characteristics

show that the settling velocity for one grade could be almost ±1cm/s. The generalised efficiency relationship Luyckx *et al.* (2002) proposed is

$$\eta = 1 - \left(1 - \frac{q}{Q}\right)\exp\left[-1.5K_{geometry}.Ha.f(\text{Re})\right]$$ (3-1)

Where: η = Efficiency, % q =Throughflow/base flow, m³/s
   Q =Inflow, m³/s $K_{geometry}$ =Geometry constant
   Ha = Hazen number   Re = Reynolds number

This was derived from a more general expression of

$$\eta = 1 - \left(1 - \frac{q}{Q}\right).\exp\left[-K.f_1\left(\frac{u_p}{U}\right).f_2\left(\frac{h}{D}\right).f_3\left(\frac{D}{d}\right).f_4(\text{Re})\right]$$ (3-2)

Where: h =Height of overflow crest, m K = Constant
   D =Diameter of the body of the overflow chamber, m

In Equation 3-1 the Hazen number was found to be the dominating parameter. Thus, the surface loading rate is said to be controlling the efficiency for a particle with a known settling velocity.

Luyckx *et al.* (1998) studied the retention efficiency of a Storm King®. Four different size ranges of Bakelite were used for four different flow splits. There was found to be no influence from the inlet conditions described by the Froude number (Luyckx *et al.*, 1998). Expressing the efficiency as a percentage of the mass of particulate collected at the base flow compared with the total mass put into the system an efficiency formula for the HDVS was given by

$$\eta = 1 - \left(1 - \frac{q}{Q}\right)\exp\left(-112.6\frac{u_{p\infty}}{U}\right)$$ (3-3)

This function demonstrated that the efficiency was only dependent on the flow ratio q/Q and the ratio $u_{p\infty}/U$ (Luyckx *et al.*, 1998). One limitation in the derivation of Equation 3-3 was that only particulates of a single density were considered. Another limitation is that Equation 3-3 does not consider scaling effects.

Fenner and Tyack (1997) derived a hybrid scaling protocol which incorporated Froude and Hazen scaling for predicting retention efficiencies. The formula was validated against

observed retention efficiencies from a 0.3m and 1.6m diameter Grit King®. The 0.3m diameter unit had a tangential overflow whereas the 1.6m diameter unit (studied in Chapter 10) had an overflow that was central. Apart from these differences, the two separators were geometrically similar. The proposed retention efficiency scaling law is given by

$$Q_{\text{prototype}} = Q_{\text{model}} \left[\left(\eta_m L_r^2 \right) + \left(1 - \eta_m \right) L_r^{2.5} + \frac{d}{3} \left(1 - \eta_m \right) L_r^{2.5} \right] \tag{3-4}$$

Where: Q =Flowrate, m³/s

    η_m = Model efficiency (%)/100 at corresponding Q_m flow

    L_r = Length ratio for geometric similarity

    d = Average particle diameter, mm

Clearly from Equation 3-4, the scaling law is dependent on knowledge of the efficiency of a scaled unit. The performance of a unit with a tangential overflow compared to one with a central overflow is not reported, which may limit the suitability of Equation 3-4 for geometrically scaled units. A limitation of the study was that only particles of a single density were considered.

3.3.4 Predicting the retention efficiency using CFD

There are two approaches to the assessment of the efficiency of a HDVS using CFD. The first is through the use of a multiphase model as used by Okamoto *et al.* (2002) for studying a Storm King® where "device efficiency is determined from a knowledge of outlet concentrations compared to those at the inlet" (Faram and Harwood, 2003) and "deposition and accumulation effects can be represented" (Faram and Harwood, 2003). The second approach is through the use of Lagrangian particle tracking where "discrete, non interacting particles of defined size and density are released into the flow domain" (Faram and Harwood, 2003) and "particles that leave through an underflow, if present, or that remain in the system after a defined time, or that enter a defined 'sediment collection region' are deemed to have been 'trapped' and those that leave through an overflow are deemed to have 'escaped'" (Faram and Harwood, 2003). Faram and Harwood (2003) have shown that collection efficiency is also a function of time in that particles collected in the grit pot can be re-entrained into the flow.

Within the 'Lagrangian tracking routine' also known as the 'Discrete Phase Model' (DPM), there are quite a large number of variables and boundary conditions that can affect the

predicted efficiencies. Thus, in order to compute accurate particle tracks, a validation should be carried out to investigate the influence of these variables and boundary conditions. Stovin and Saul (1998) have investigated a number of the variables when tracking particles in storage chambers. As the application is different to a HDVS, not all the validation work that was carried out applies to modelling a vortex separator. It was found that when using the 'Stochastic turbulence model' (see Section 2.3.4.3), that 50 simulations were required before a "deviation of ±2.5% from the population mean, at a confidence level of 99%" (Stovin and Saul, 1998) was obtainable. With respect to the 'step length factor', they found that "neither halving nor doubling the step length factor had any significant effect on the resulting efficiency prediction" (Stovin and Saul, 1998). The step length factor is roughly equivalent to the number of time steps required to traverse the current continuous phase control volume (Fluent Inc., 2003) and controls the frequency with which the equations of motion for the particle are updated.

3.4 Settling velocity characterisation

Pollutants in wastewater may be of the form of floatable material, solids in suspension, colloidal solids and matter in solution (Andoh and Smisson, 1996). Suspended solids can range from sub micron to hundreds of millimetres and Table 3-1 summarises the time taken for spherical particles to settle through a distance of approximately 0.3m of water under gravity assuming Stokes Law (Andoh and Smisson, 1996).

Table 3-1. Effects of decreasing size of spheres on settling velocity. Adapted from Andoh and Smisson (1996).

Particle diameter, / mm	Order of size	Time required to settle (SG = 2.65)	Time required to settle (SG = 1.20)
10	Gravel	0.4 seconds	1.2 seconds
1	Coarse Sand	3.0 seconds	9 seconds
0.1	Fine Sand	34 seconds	5 minutes
0.01	Silt	56 minutes	8 hours
0.001	Bacteria	4 days	32 days
0.0001	Colloidal	1 year	9 years
0.00001	Colloidal	> 50 years	> 50 years
0.000001	Colloidal	> 50 years	> 50 years

Clearly Table 3-1 shows that particles down to silt and fine sand tend to settle within practical time scales. A Specific Gravity (SG) of 2.65 represents a grit/sand like material and organic materials tend to have a specific gravity in the range 1.02 to 1.20 (Andoh and Smisson, 1996). Given the variable nature of the material present in wastewater, there have been a number of methods developed in order to characterise the settling velocity of particulates in wastewater from a particular catchment. These include X-ray radiation, ultrasound and radioactive tracers (Williams *et al.,* 1990) all of which are generally expensive and complicated (Zhu *et al.,* 2000). More practical methods are described in Sections 3.4.1.1 to 3.4.1.3.

3.4.1 Determination of settling velocity

3.4.1.1 Settling column methods

Figure 3-3 shows a stationary settling column having side withdrawals along the column length. Typical dimensions for the settling column are 1.5 to 2m in length and a diameter of 0.15 to 0.20m. Two to four sampling ports (6 to 15mm diameter) equally spaced is typical. Prior to the start of the test, various methods have been used to mix the sample, the most successful being slotted plunger plates attached to a hand rod (Pisano, 1996).
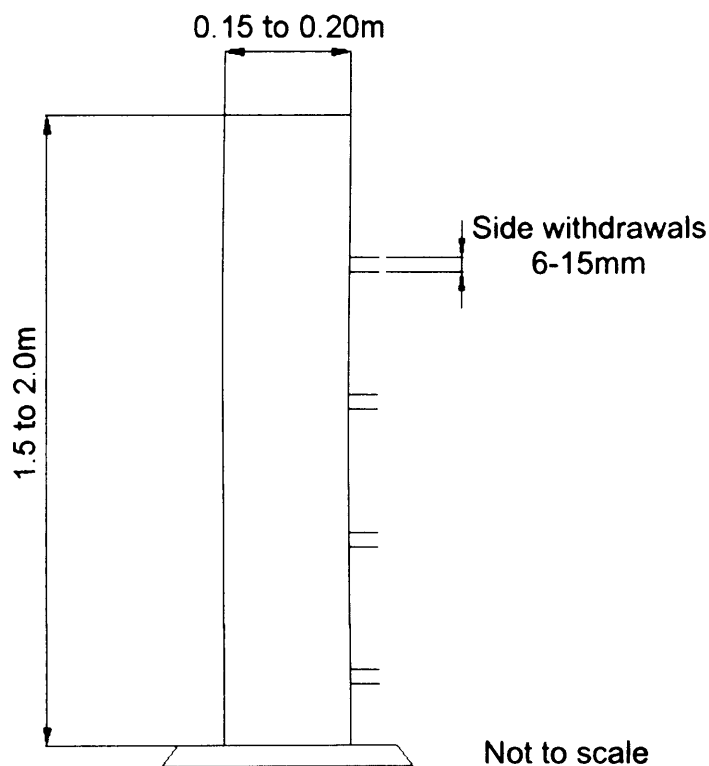

Figure 3-3. Settling column with side withdrawals. Adapted from Pisano (1996).

A variation of this method involves mixing the column contents prior to the settling velocity test. This involves rotating the column about its axis in order to adequately mix the contents, quickly stop the rotation and begin the test. Figure 3-4 shows an example (Connick and Pisano, 1981)[2] where the column could be rotated by mechanical means about the axial and longitudinal directions and included flow stators inside the column to assist the mixing. This particular column was 1.83m in length and 0.28m in diameter and included nine push rod style sampling intakes, 10mm in diameter, 0.15m apart placed on alternate sides of the column. Each push rod was designed to take a sample from the centre of the column and then be withdrawn to create a flush seal. The column was found to be difficult to use as it was prone to structural failure, leaking seals and the mixing appeared to entrain air as well as shear larger organic and flocculant materials (Pisano, 1996).
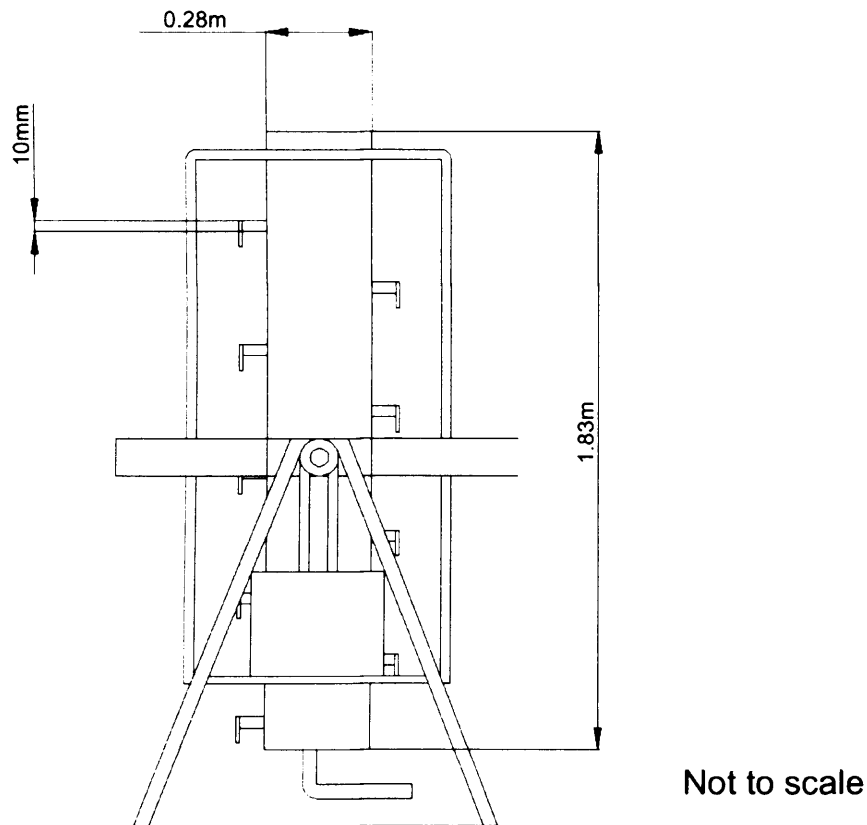

Figure 3-4. Settling column with side withdrawals and which can be rotated by mechanical means. Adapted from Pisano (1996).

Another variation is to place the column in a collar and yoke at its centre point and to flip the column to mix the contents. This, although inexpensive to construct, meant that the column is usually limited to a length of 1.2m with no more that 3 sampling points (Pisano, 1996).

---

[2] A literature search was unable to locate the paper to this reference.

For effective sampling with these systems, solids should have a settling velocity between 1 and 10cm/s, as faster moving particles will fall before the first sample is taken. (Samples are typically taken at 30 second intervals). Taking a large number of samples will reduce the height of the water surface in the column and this must be considered when determining the settling velocity. A longer column helps to solve some of these problems, but increases the head and taking small volume samples becomes harder (Pisano, 1996).

A settling column developed at UFT in Germany reported by Michelbach and Wöhrle (1993) which will be referred to as the 'UFT Settling Column', Figure 3-5, was designed for collecting solids with settling velocities in the range 0.01 to 23.3cm/s. Solids are suspended in a feeding mechanism in approximately 75ml of water. The feeding mechanism slides over the Perspex cylinder which allows settleable solids to descend through the settling column which is 0.7m in length. Floatable material is thus captured in the feeding mechanism.
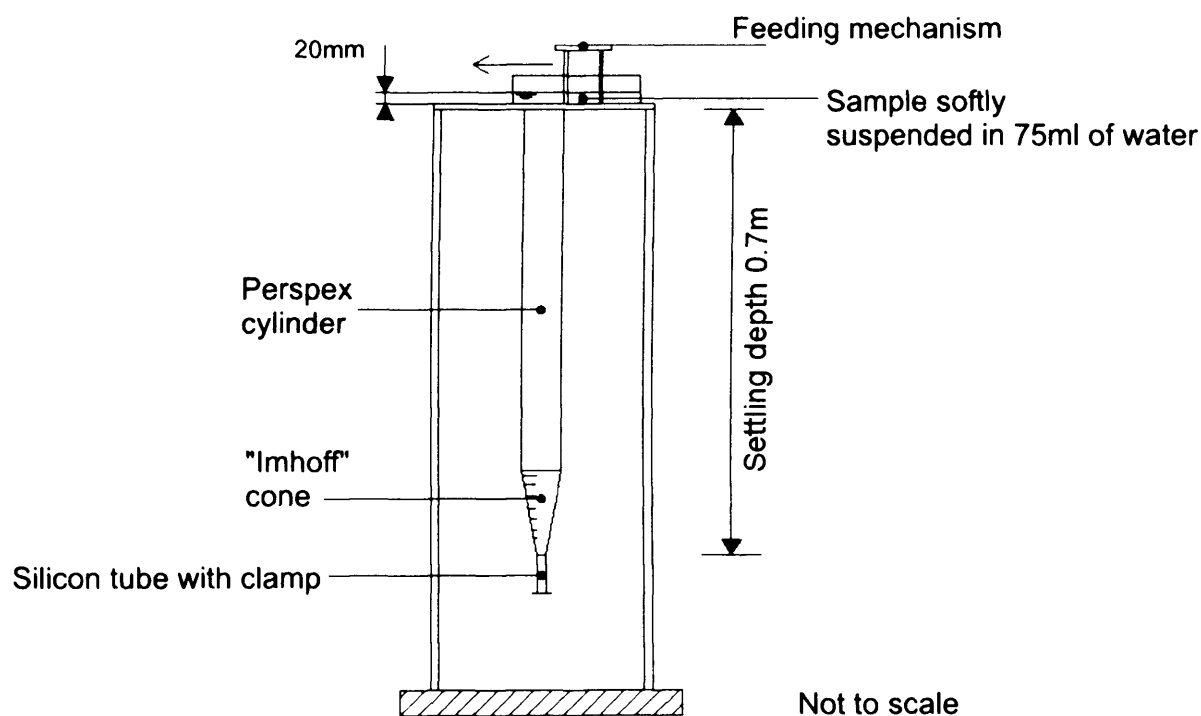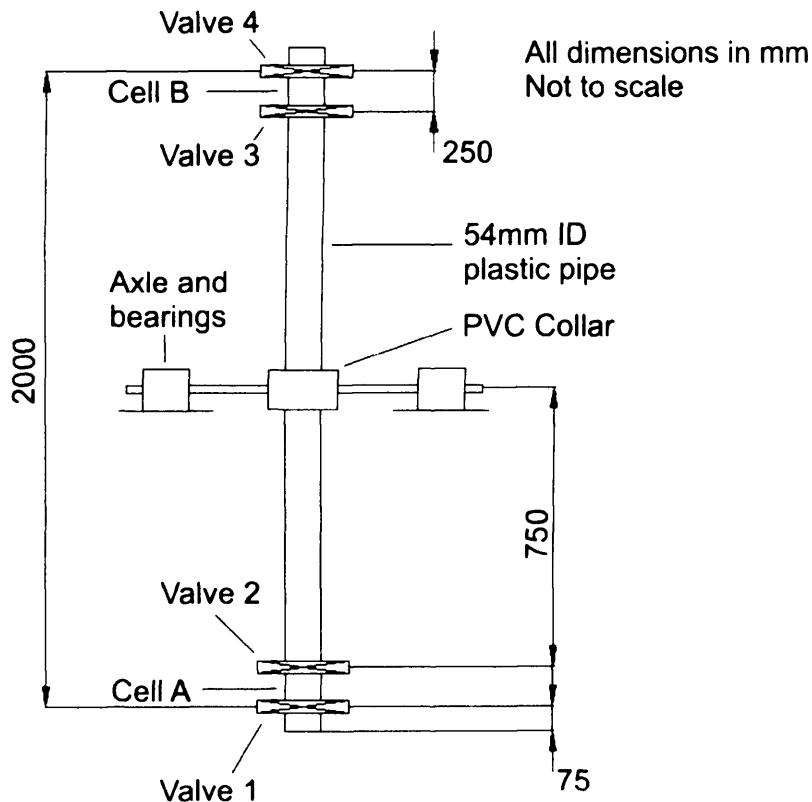

Figure 3-5. The UFT settling column. Adapted from Michelbach and Wöhrle (1993).

The development of a method for characterising the settling velocity distribution of crude and storm sewage is described by Tyack *et al.* (1996). The length of the column was partly based

on work reported by Owen (1970)[3] where it was concluded that for solids concentration below 4mg/litre, the distance for flocculating particles to acquire their terminal velocity is 1.5 to 2m. For discrete particles, the terminal velocity is reached in a very short time span, often a fraction of a second (Michell, 1970). With these factors considered, the central settlement length of the column was 1.5m as a longer length would make the column harder to fit into a laboratory. The diameter of the column was chosen based on observations of settling velocity of synthetic media and crude sewage in column diameters of 34, 54 and 64mm in diameter. A settling velocity profile was observed in the smallest diameter column and the influence of the walls decreased as the column diameter increased. A 54mm diameter column was considered acceptable. The settling column is shown in Figure 3-6. Sewage liquor is the choice of liquid phase over say tap water or distilled water, as the aim is to represent the settlement conditions of primary sewage. Using tap water would alter the density and viscosity, hence the settling velocity. Tap water would also require degassing and for hindered settling to occur, the particles need to settle through a suspension of solids.

Figure 3-6. Settling column described by Tyack et al. (1996).
Adapted from Tyack et al. (1996).

---

[3] A literature search was unable to locate the report to this reference.

A method to determine the settling velocity distribution using the settling column in Figure 3-6 is described by Tyack *et al.* (1996). The apparatus used requires a 5 litre sample of sewage, compared with other methods where a 1 litre sample is used (Tyack *et al.*, 1996). Due to the variability in sewage, the larger sample means that a more representative sample is used in the test (Tyack *et al.*, 1996). The larger sample also means that very fine slow settling fractions are detectable on a precision balance (Tyack *et al.*, 1996). Removing the fractions from an end cell that is then refilled means that no adjustment has to be made for loss of settlement length. The apparatus is inexpensive to construct and the results can be obtained within 36 hours of the sample being taken (Tyack *et al.*, 1992). The disadvantage of using valves is that when they are opened/closed, turbulence is created, that can result in the transfer of particles into the cells.

3.4.1.2   Conductance method

Although this method utilises a settling column, the technique relies on the conductivity of a slurry. This method is reported by Vergouw *et al.* (1997) and Uribe-Salas *et al.* (1992). The conductivity is dependent on the solids content and this property is therefore used to detect changes as the solids settle. In the case where the solids are non-conducting, as the front descends, the conductance increases, Figure 3-7. The change in conductance with time can be used to determine the settling velocity.
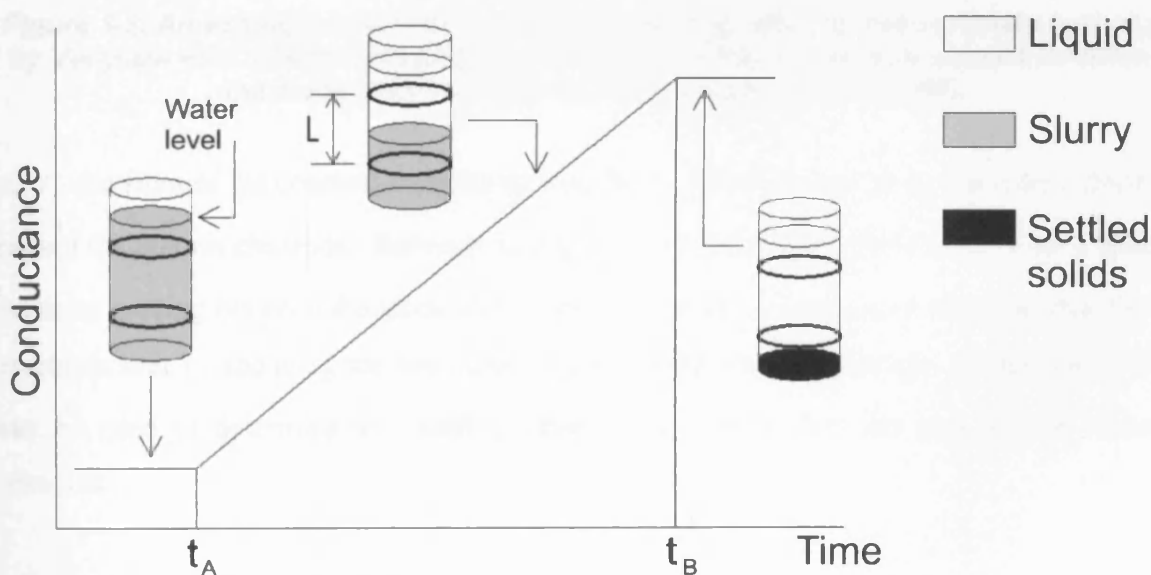

Figure 3-7. Principle of the conductance method for determining the settling velocity of a slurry. Adapted from Vergouw et al. (1997).

At t_A in Figure 3-7, the front starts to pass the top electrode on the settling column. At t_B, the front passes the bottom electrode. Knowing t_A, t_B and the distance between the electrodes, L, the average settling velocity is given by:

$$u_p = \frac{L}{t_B - t_A}$$ (3-5)

In the case where multiple fronts exist, the technique can be used to determine the settling velocity of each front. Figure 3-8 shows an example where two size classes of silica were used, both with the same density.
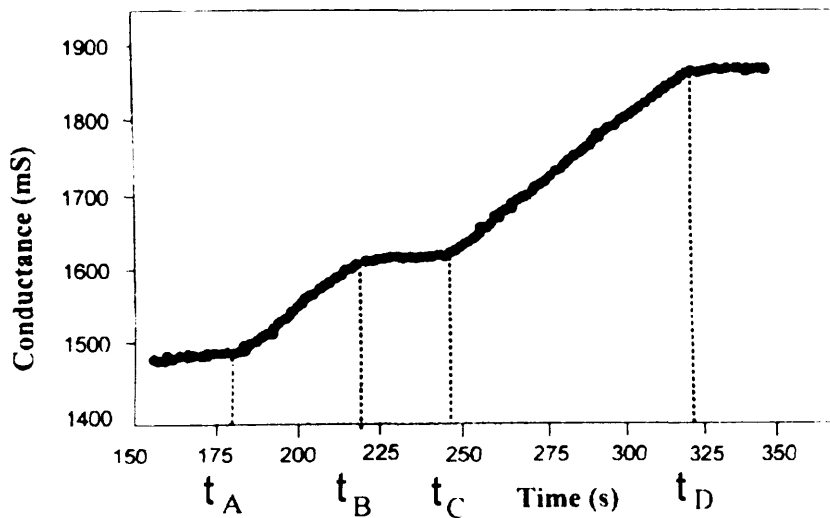

Figure 3-8. An example where the automated settling velocity measurement technique by Vergouw et al. (1997) measures the settling velocity of two size classes of silica in the same sample. Adapted from Vergouw et al. (1997).

At t_A the front of the coarsest particles passes the top electrode and at t_B the coarse front has passed the bottom electrode. Between t_B and t_C there is a period where there is not a front of particles passing between the electrodes. The onset of the fine grade of silica passing the top electrode is at t_C and at t_D the fine silica has passed the bottom electrode. Hence, the method can be used to determine the settling velocity of a slurry that has two distinct sizes of particles.

3.4.1.3 Light intensity method

This technique has been developed by Zhu *et al.* (2000). Again, the method utilises a settling column, but the method relies on detecting the intensity of light that passes through a slurry.

Where the slurry concentration is high, the intensity of the light is low and vice versa. The greatest variation in the intensity of light is at the solid-liquid interface, Figure 3-9 and by taking a series of images as the slurry settles, the interface may be tracked and the settling velocity determined.
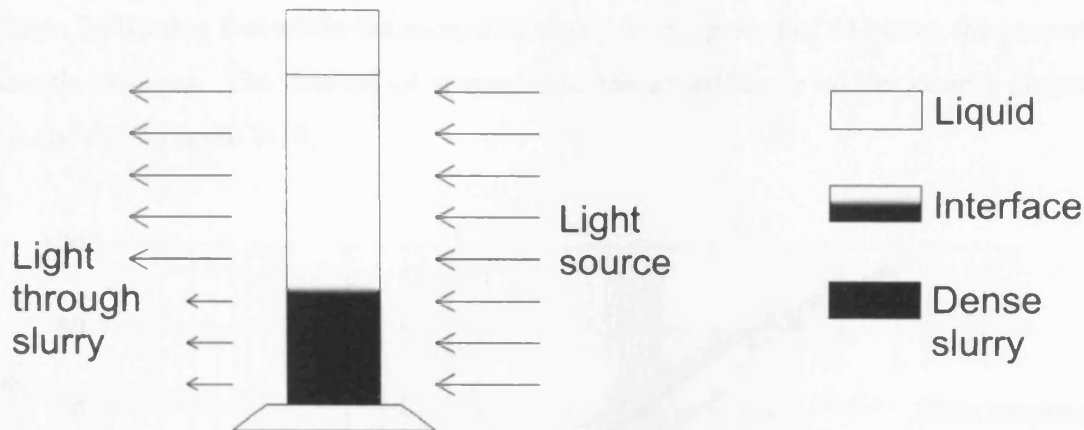

Figure 3-9. Principle of the light-intensity, solid-liquid interface tracking method. Adapted from Zhu et al. (2000).

The location of the solid-liquid interface is determined using image processing software that utilises a technique currently unavailable in commercial image processing software packages (Zhu *et al.*, 2000).

3.4.2   Comparison of settling velocity techniques

Aiguier *et al.* (1996) have compared settling velocity characterisation techniques reported by Tyack *et al.* (1996) and Michelbach and Wöhrle (1993).

It was found that in the technique by Michelbach and Wöhrle (1993) the sample used in the test does not represent the full distribution of particles in the sample, but only those that settle in 2 hours in an Imhoff Cone and with a settling velocity greater than 0.01cm/s. Hence, the settling velocities measured are always greater than those measured using the technique by Tyack *et al.* (1996) where the entire sample is used.

Three aspects of the methods were also studied by Aiguier *et al.* (1996); storage, volume of suspended solids in the column and the nature of the water.

3.4.2.1   Storage

A sample was collected, split into smaller samples and these were refrigerated, frozen, or stored at room temperature. A test was carried out on one of the samples on the day of collection. It was found from a test carried out on the following day on a sample that was refrigerated, frozen and stored at room temperature gave different results to the test on day of collection, indicating that while the sample is stored over a period of 24 hours, the property of the sample changes. The method of storage also has an influence on the sample properties. This is shown in Figure 3-10.
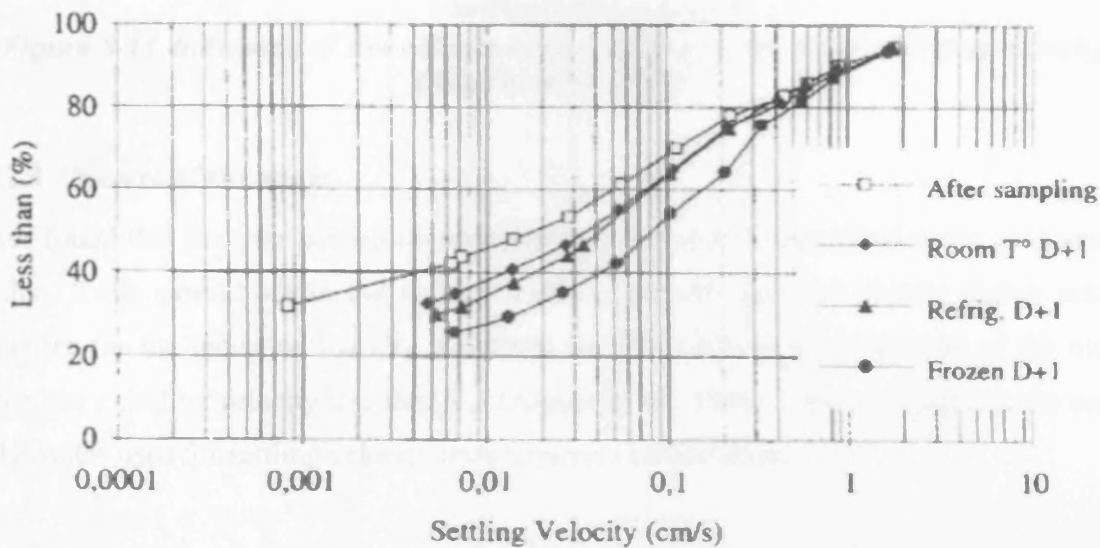

Figure 3-10. Influence of storage on settling velocity (Aiguier et al., 1996).

3.4.2.2   Volume of suspended solids in the column

Three tests were carried out with a suspended solids volume of 3, 6 and 10ml using the UFT settling column (Michelbach and Wöhrle, 1993). Figure 3-11 shows that the higher the concentration of particles, the higher the settling velocity. However, Aiguier *et al.* (1996) report that further tests were required in order to confirm this result. This does nevertheless highlight that the concentration of particles in the sample is a factor that influences the settling velocity and one would expect that a representative concentration be required in the sample in order to obtain an accurate reflection of the settling velocity of particles in the system that is being studied.
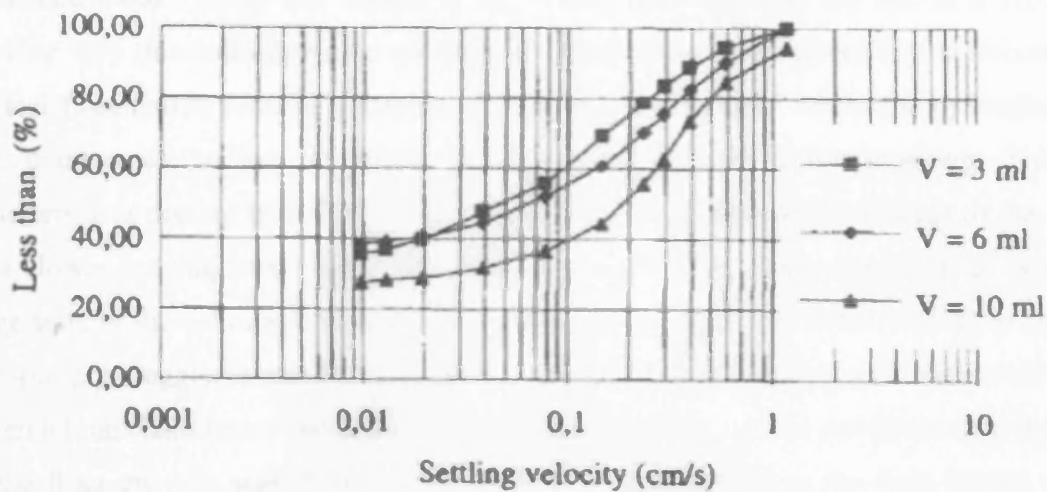
Figure 3-11. Influence of the volume of suspended solids on the settling velocity (Aiguier et al., 1996).

3.4.2.3 Nature of the water

It was found that the tests carried out in drinking water and demineralised water gave similar results. Tests carried out in the residue from the Imhoff cone had slightly higher settling velocities for the indicator V_{90} (V_x is defined such that X% is the proportion of the matter which has a settling velocity less than V_x) (Aiguier *et al.*, 1996). This indicates that the nature of the water used for settling velocity tests requires consideration.

3.5 Residence time

3.5.1 Application of residence time

Guymer *et al.* (2002) have investigated the residence time distribution in storage tanks of varying length and report that the results give "an insight into the hydraulic processes affecting soluble pollutants as they pass through a storage tank and thus may help to improve the design and operation of storage tanks".

The residence time of a system will also influence the effectiveness of chemical contacting processes such as disinfection and coagulation and flocculation. Boner *et al.* (1993) report a study in Columbus, Georgia, of a comparison between a HDVS and a conventional mixed basin preceded by a sedimentation basin used for disinfection of the fluid from a CSO. It was found that the HDVS was three times more effective at disinfection and up to ten times more effective in removing total suspended solids and other pollutants.

Andoh and Cook (1995) and Andoh *et al.* (1996) have reported the use of a HDVS in removing very fine colloids by the addition of chemicals to aid coagulation and flocculation. An ideal flocculation process is known as 'tapering flocculation' where the hydraulic shear forces decrease as the flow progresses, to reduce the possibility of floc break-up. This flow characteristic is present in a HDVS due to a faster rotating flow on the outside of the device and a slower moving inner zone (Andoh and Cook, 1995). For coagulation to occur the charge state of the colloids is altered by a coagulation aid and allows the colloids to coalesce and form larger agglomerates by flocculation. Flocculation is aided by a flocculant aid which is often a long chain heavy molecular weight polyelectrolyte. As the residence time increases and the flocs grow in size, their settling velocity also increases, so the flocs have a greater chance of being removed from the effluent.

3.5.2 Residence time studies on HDVSs

Tyack and Fenner (1998a) carried out residence time trials on a 1.6m diameter Grit King[®] operating without a base flow component. Table 3-2 shows the reported mean residence time, theoretical mean residence time and dispersion number. The normalised variance is also included which has been derived from the reported variance and mean residence time.

Table 3-2. Residence time data for a 1.6m diameter Grit King[®] operating without a base flow component. Adapted from Tyack and Fenner (1998a).

Flowrate, / litres per second	Mean residence time, / s	Theoretical mean residence time, (V=1.75m³), / s	Dispersion number, *d*	Normalised variance
10.67	147	164	0.32	0.44
15.51	107	113	0.24	0.38
20.22	78	87	0.15	0.25
24.85	75	70	0.35	0.47
29.76	68	59	0.28	0.41
35.33	47	50	0.34	0.47
39.93	43	44	0.27	0.39
45.65	43	38	0.67	0.64
51.81	34	34	0.20	0.32
55.20	34	32	0.20	0.32
60.20	30	29	0.22	0.34

The dispersion number, *d*, was derived using

$$\frac{\sigma^2}{\bar{t}^2} = 2d - 2d^2 \left(1 - e^{\frac{-1}{d}} \right)$$

(3-6)

Table 3-2 shows that at all flowrates the mean residence time is approximately the same as the theoretical mean residence time. Thus, it is inferred from the mean residence time and dispersion number/normalised variance in Table 3-2, "that all the inflow passes through the entire device in the expected time, but there may be a zone that is holding the flow over an extended period (causing the long tail). This slack zone then creates some short circuiting in the rest of the separator which causes the peak in the residence time distribution" (Tyack and Fenner, 1998a). Further analysis of the data in Table 3-2 is given in Section 10.4.

Residence time characterisation of a 0.75m diameter Eff-Pac™ Clarifier, shown in Figure 3-12, has been carried out by Higgins *et al.* (1998) using a pulse injection of lithium chloride at flowrates between 0.25 and 8 litres per second operating without a base flow component. It was found that for flowrates greater than 1.5 litres per second, the difference between the theoretical and experimental mean residence times were quite small indicating that the fluid passes through the separator in the expected residence time.
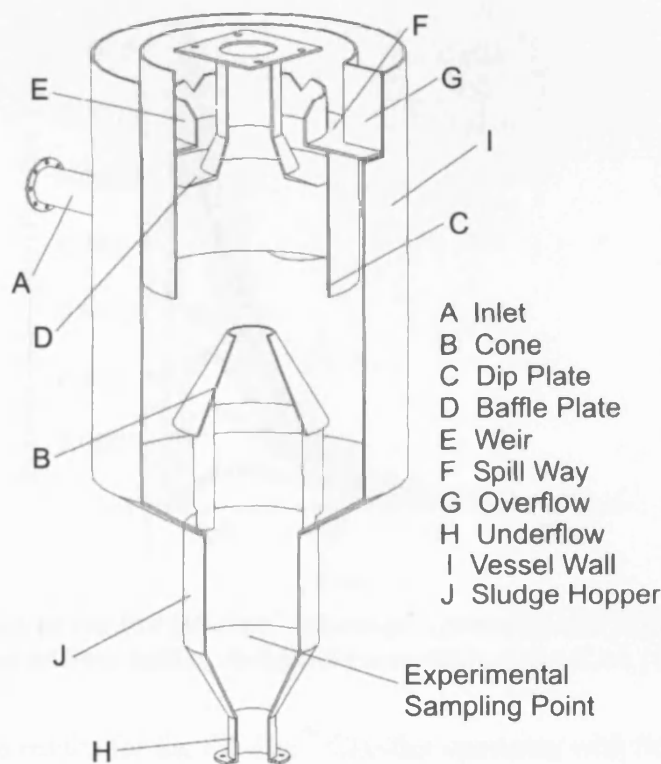

A Inlet
B Cone
C Dip Plate
D Baffle Plate
E Weir
F Spill Way
G Overflow
H Underflow
I Vessel Wall
J Sludge Hopper

Experimental
Sampling Point

Figure 3-12. 0.75m diameter Eff-Pac™ Clarifier.

At flowrates less than 1.5 litres per second the differences between experimental and theoretical mean residence times were greatest. "Under these conditions the sludge hopper is considered to behave as a stagnant region, where a significant portion of the tracer is held" (Higgins *et al.*, 1998).

The same HDVS has also been studied operating with a flow split of 10, 20, 30 and 40% for which RTD curves are given in Figure 3-13. It was found that the device had a "plug flow mixing characteristic with a degree of non-ideal flow behaviour" (Alkhaddar *et al.*, 1999). This is due to the significant peak of the curves and the long tailing effect where tracer concentration was being measured at 5 to 6 times the predicted theoretical mean residence time. It was initially thought that the base flow RTD curve would peak before the underflow RTD curve (Alkhaddar *et al.*, 1999). In the results presented here this was not the case. However, Alkhaddar *et al.* (1999) found that for a sampling point in the underflow at a slightly different position, the base flow RTD curve did in fact peak before the overflow and this highlights the importance of the sample location and poorly mixed conditions of the tracer.
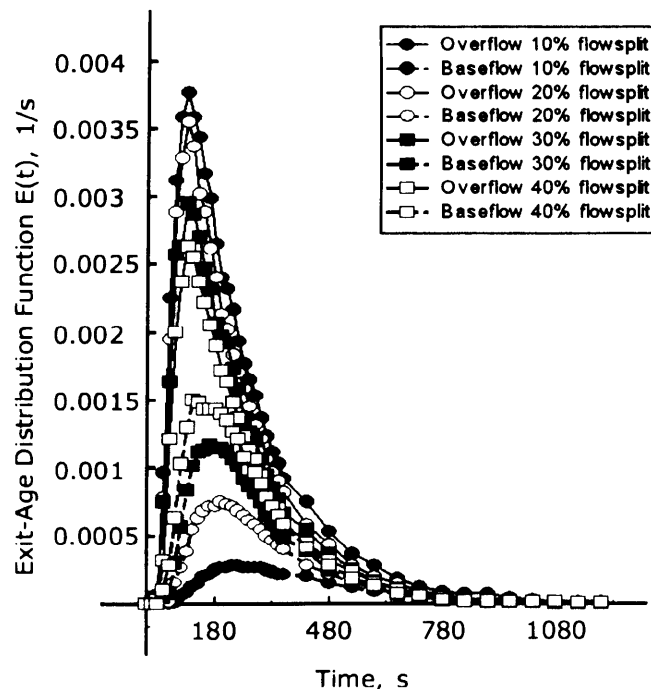

Figure 3-13. RTD curves for the Eff-Pac™ Clarifier operating at 2 litres per second over a range of flow splits. Adapted from Alkhaddar et al. (1999).

Further analysis of the results for the Eff-Pac™ Clarifier operating with flow splits between 10 and 40% are given in Chapter 8.

Alkhaddar *et al.* (2001) have developed a 'combined mathematical' model for predicting the residence time distribution of the Eff-Pac™ Clarifier operating without a base flow component. The approach to this model was through an extension of the TISM as the shape of the residence time curve could not be represented accurately by either the TISM or ADM alone (Alkhaddar *et al.*, 2001). However, an optimisation technique to acquire a good fit of an RTD model was not attempted (Higgins, 2000). The model proposed by Alkhaddar *et al.* (2001) was developed by assuming that the HDVS being modelled could be described by three CSTRs, connected in series all having ideal CSTR behaviour. It was also assumed that one of these tanks can exchange with a slow mixing zone, represented by a fourth tank and that the inlet and outlet could be connected by a bypass with an adjustable flowrate, hence allowing short-circuiting. The configuration of this combined model can be seen in Figure 3-14.
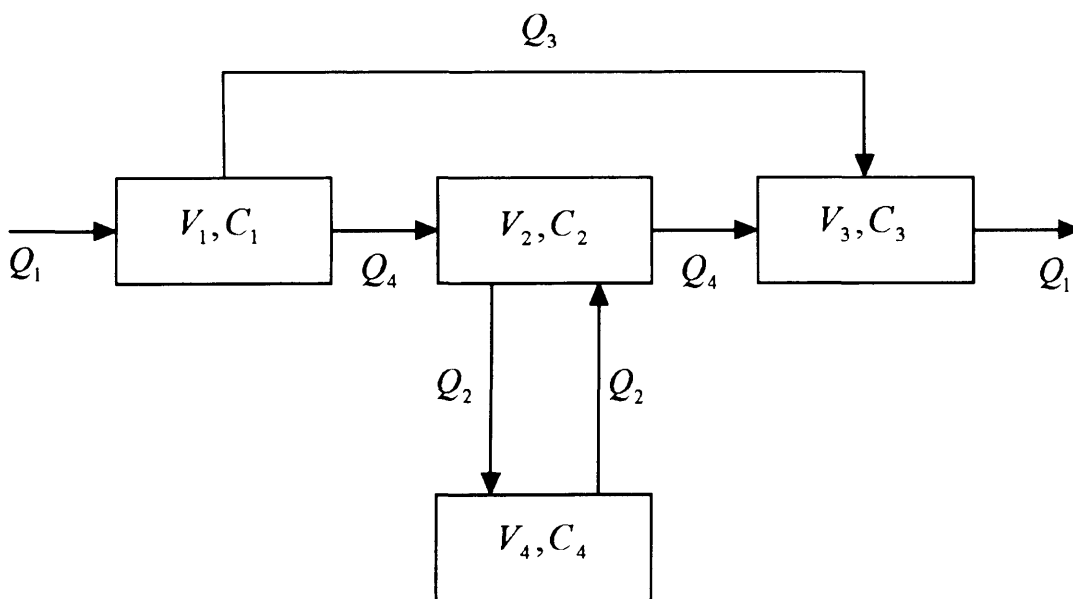
Figure 3-14. Configuration of the combined mathematical model.
Adapted from Alkhaddar et al. (2001).

The successful application of this model requires boundary conditions to be set. Alkhaddar *et al.* (2001) have found that with an increasing inlet flowrate, by-passing increases and the slow mixing volume decreases. Thus the boundary conditions selected must be based on knowledge of experimental results. Figure 3-15 shows a successful application of the model to a 375mm diameter HDVS operating at an inlet flowrate of 15 litres per minute.
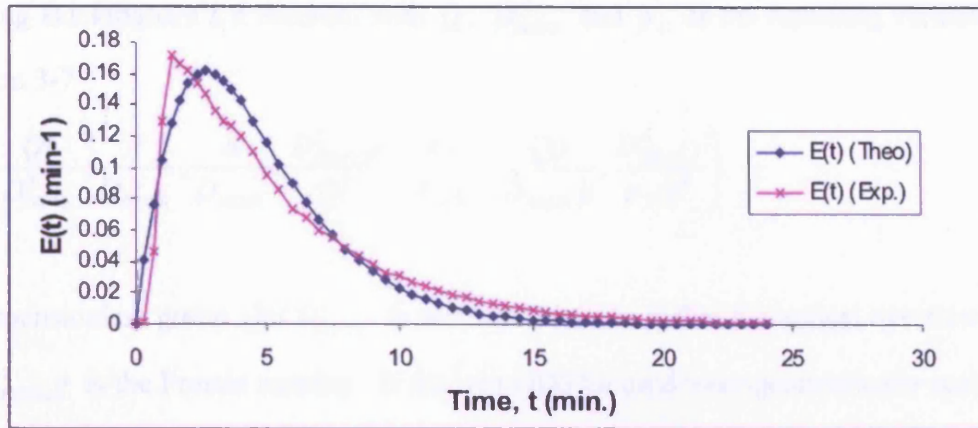
Figure 3-15. Comparison of the combined mathematical model with experimental data for a 375mm diameter HDVS at an inlet flowrate of 15 litres per minute (Alkhaddar et al., 2001).

Tyack and Fenner (1997) carried out RTD trials on two Grit Kings®, one 0.3m in diameter which will be referred to as the 'model' and another 1.6m in diameter, which will be referred to as the 'prototype'. A scaling protocol by Tyack and Fenner (1997) was derived to predict the residence time in the following manner;

Considering Buckingham's π theorem, the relevant parameters were chosen by considering the characteristics of the residence time, the separator, the fluid flow and the liquid. Table 3-3 shows the parameters related to each of these characteristics.

Table 3-3. The relevant parameters related to each characteristic.

Characteristic	Relevant Parameters
Residence time	t D_{HDVS} h
Separator	D_{HDVS} d h τ
Fluid flow	Q g h_L τ
Liquid	ρ_f μ

Where: t = Residence time, s D_{HDVS} =Diameter of separator body, m

h =Height of separator body, m d =Inlet pipe diameter, m

Q =Flowrate, m³/s g =Acceleration due to gravity, m/s²

h_L =Head loss across separator, m ρ_f =Density of fluid, kg/m³

μ =Absolute viscosity of fluid, kg/ms

τ =Shear stress between separator and fluid, N/m²

Applying Buckingham's π theorem with Q, D_{HDVS} and ρ_f as the repeating variables yields

Equation 3-7

$$t = f\left(\frac{Qt}{D_{HDVS}^3}, \frac{d}{D_{HDVS}}, \frac{h}{D_{HDVS}}, \frac{D_{HDVS}^5 g}{Q^2}, \frac{h_L}{D_{HDVS}}, \frac{Q\rho}{D_{HDVS}\mu}, \frac{D_{HDVS}^4 \tau}{\rho_f Q^2} \right)$$

(3-7)

The dimensionless group Qt / D_{HDVS}^3 is the ratio of the actual to theoretical overflow rate and

$Q^2 / D_{HDVS}^5 g$ is the Froude number. If the two HDVSs used were geometrically scaled and if

t is set as $\bar{t}$, the mean residence time, then

$$\frac{Q_m \bar{t}_m}{D_m^3} = \frac{Q_p \bar{t}_p}{D_p^3}$$

(3-8)

and

$$\frac{Q_m}{Q_p} = \left(\frac{D_m}{D_p} \right)^{\frac{5}{2}}$$

(3-9)

Where suffix m denotes the model HDVS and suffix p denotes the prototype HDVS. If the

ratio for geometric similarity, L_r is defined as

$$L_r = \frac{D_p}{D_m}$$

(3-10)

Then rearranging Equation 3-8 to make $\bar{t}_p$ the subject and substituting Equation 3-9 gives the

scaling protocol

$$\bar{t}_p = L_r^{0.5} \, \bar{t}_m$$

(3-11)

Tyack and Fenner (1997) found that the theoretical and actual mean residence time coincide
only when the 'active' volume of flow is considered, shown in Figure 3-16, which is "the
volume between the outside wall of the separator body and the vertical line located at the
position of the dip plate" (Tyack and Fenner, 1997). (This is discussed in Section 10.4).
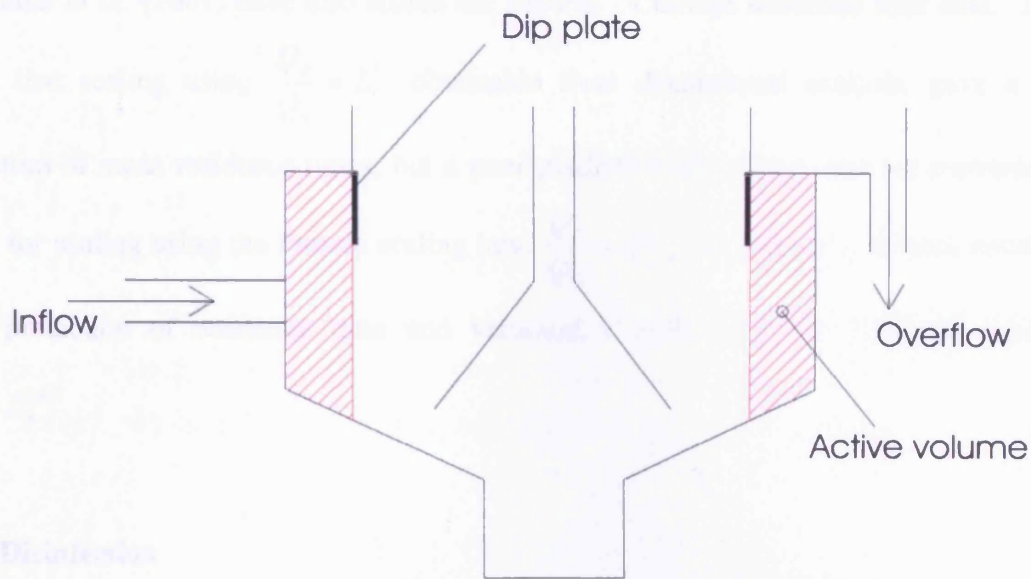
Dip plate

Inflow

Overflow

Active volume

**Figure 3-16. A schematic of the 'active' volume.
Adapted from Tyack and Fenner (1997).**

Figure 3-17 shows mean residence times after scaling the 0.3m diameter model tests up to the 1.6m diameter prototype tests using the scaling protocol Equation 3-11 and the Froude number to scale the flowrate. As can be seen, "the fit of the scaled model data to the prototype is very good" (Tyack and Fenner, 1997).
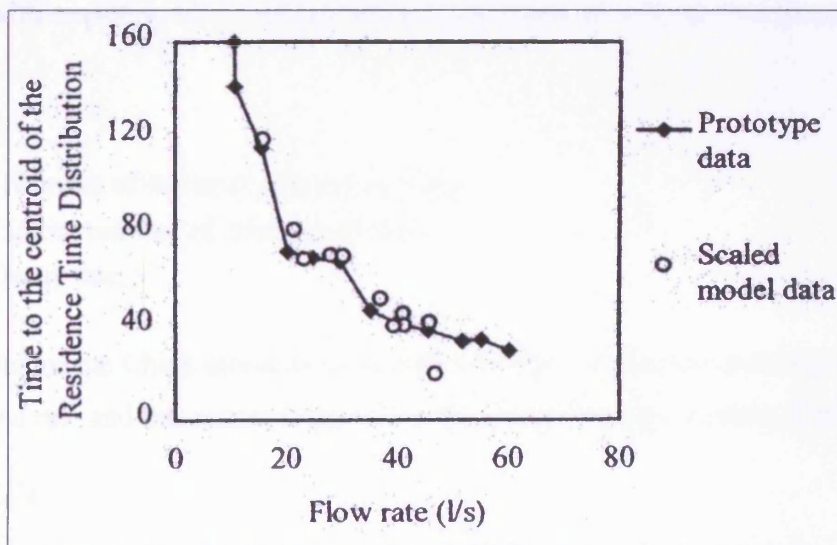
**Figure 3-17. The result of scaling the residence time data using the scaling protocol
and scaling the flowrate using the Froude number (Tyack and Fenner, 1997).**

Alkhaddar *et al.* (2001) have also scaled the Eff-Pac™ Clarifier residence time data. It was found that scaling using $\dfrac{Q_p}{Q_m} = L_r^3$, obtainable from dimensional analysis, gave a good prediction of mean residence times, but a poor prediction of variance and the converse was found for scaling using the Froude scaling law, $\dfrac{Q_p}{Q_m} = L_r^{2.5}$. To achieve a balance between a good prediction of residence time and variance, a scale factor of 2.85 was used i.e.

$$\frac{Q_p}{Q_m} = L_r^{2.85}.$$

3.6 Disinfection

3.6.1 Disinfection models

Since the early 1900's, a number of rate equations have been proposed to describe the inactivation of micro-organisms. The first of these given by Chick (1908) describes the death of micro-organism as first order with respect to time i.e.

$$\frac{\partial N}{\partial t} = -kN \tag{3-12}$$

Where: N = Number of micro-organisms

Integrating with respect to time and replacing at the limits $N = N_0$ at $t = 0$ gives

$$\frac{N_t}{N_0} = e^{-kt} \tag{3-13}$$

Where: N_t = Number of micro-organisms at time t

N_0 = Initial number of micro-organisms

k = Decay rate, s^{-1}

A development of the Chick model is to include the effect of the concentration of disinfectant on the survival rate and this model is known as the Chick-Watson equation (Chick, 1908)

$$\ln \frac{N_t}{N_0} = -kC^n t \tag{3-14}$$

Where: C = Disinfectant concentration, kg/m^3 n = Coefficient of dilution

k = Rate constant, $m^3/kg.s$

This model assumes that the concentration of disinfectant remains constant with time i.e. there is no disinfectant demand. This equation would most likely be applicable therefore if disinfectant was used in excess. However, with economic objectives, the aim is to achieve the required reduction in micro-organisms with the minimum practical quantity of disinfectant. The assumption that disinfectant concentrations remain constant is therefore not realistic. Much of the batch inactivation data that has been reported for various organisms contain shoulders or a tailing off or a combination of both of these. This behaviour has been attributed to "homogenous clumping, unequal resistance to disinfectant by various organisms in the culture and initial resistance of individual organisms" (Severin *et al.*, 1984). An equation by Hom (1972) was developed as an extension of Equation 3-14 and is given by

$$\ln \frac{N_t}{N_0} = -kC^n t^m$$

(3-15)

Where: m = Empirical constant

A later equation by Severin *et al.* (1984) was in the form of a series event kinetic model, given by

$$\frac{N_t}{N_0} = e^{-kCt} \sum_{i=0}^{j-1} \frac{(kCt)^i}{i!}$$

(3-16)

Where: j = Integer representing the lethal number of reactions per organism
k = Mixed second order reaction rate, m³/kg.s

In this model, the term kC may be replaced by the apparent kinetic rate constant K. This kinetic model assumes disinfection to be occurring "with uniformly distributed and unchanging chemical concentrations" and "the inactivation of single organisms can be viewed as undergoing a series of damaging reactions or events. Damage is considered to occur in integer time steps" (Severin *et al.*, 1984).

Haas and Joffe (1994) modified the Hom model to produce a kinetic rate equation that takes account of the disinfectant decay:

$$\ln \frac{N_t}{N_0} = -\left(\frac{m}{nk^*}\right)^m k(C_0)^n \left[1 - \exp\left(-\frac{nk^* t}{m}\right)\right]^m$$

(3-17)

Where: k^* = First order residual decay rate, s⁻¹
C_0 = Initial disinfectant concentration, kg/m³

3.6.2 Methods of disinfecting wastewater

3.6.2.1 Ultra Violet (UV) light

One method for disinfecting wastewater is through the use of Ultra Violet (UV) lamps. This has been used at the Columbus water works, Georgia. The effectiveness of UV is dependent on the lamp intensity, contact time and pre-treatment quality which affects the light transmittance and has an associated high power requirement. The performance is relatively independent to the temperature of the water and pH (Hydro Int. Plc, 2002) and does not produce any problematic by products (Averill *et al.*, 1997). UV systems fit as modules into existing channels with minimal modifications required (Reed, 1998). Thus, treated water is discharged from a HDVS into a channel which incorporates a UV module for treating the wastewater. The UV light intensity may be affected by the age of the lamps and fouling of the sleeve that covers the lamps (Hydro Int. Plc, 2002).

3.6.2.2 Chemical disinfection

Chlorine has been widely used as the primary disinfectant for potable water treatment for over 100 years (Li, 2004). However, "free chlorine also reacts with contaminants such as NH_4^+, NO_2^-, H_2S, Fe^{++}, Mn^{++} and organic compounds. Due to the chlorine demand created by these compounds, chlorine tends to be applied until the demand is met and free chlorine appears" (Pretorius and Pretorius, 1999). Hence, the process wastes a certain quantity of chlorine. The reaction of free chlorine with certain organic compounds present in wastewater leads to the formation of trihalomethanes (THMs) which have associated health risks. This is a particular concern when treated sewage effluent is reused as drinking water (Pretorius and Pretorius, 1999).

Pretorius and Pretorius (1999) report that chloramines have "a reduction in the formation of THMs" and "greater disinfectant stability resulting in a reduction in disinfectant demand". A disadvantage of chloramines is that they have a "relatively long lifetime, compared with free chlorine, after discharge to the receiving environment, possibly with toxicity problems" (Pretorius and Pretorius, 1999). Chloramines are produced by the reaction of free chlorine with ammonia which produces monochloramine (NH_2Cl), dichloramine ($NHCl_2$) and trichloramine (NCl_3) and the quantity of each that is produced depends on the proportion of chlorine and ammonia present, the reaction time, temperature and pH (Li, 2004). Ward *et al.* (1984) found that the disinfectant strength of the three species vary, with monochloramine

being less effective than dichloramine. The effectiveness of chlorine or chloramines as a disinfectant is dependent on the "initial concentration of micro-organisms, disinfectant concentration, contact time, temperature and pH" (Pretorius and Pretorius, 1999).

A third chemical that may be used for disinfecting wastewater is peracetic acid (PAA). This is formed by reacting acetic acid with hydrogen peroxide. When PAA breaks down, its products are acetic acid, hydrogen peroxide and eventually, O_2 and H_2O. The overall risk to organic integrity may therefore be minimal compared to chlorine related disinfectants which do not break down as readily (Hydro Int. Plc, 2002). It has been found by Sanchez-Ruiz *et al.* (1995) that the pH significantly influences the inactivation of micro-organisms, where alkaline conditions achieve a lower inactivation than neutral or acidic conditions. The optimum dose for treating raw sewage with PAA reported by Sanchez-Ruiz *et al.* (1995) "seems to be 20mg/litre with a contact time of about 10 minutes", with higher doses and contact times having little effect on the efficiency of PAA.

Storm water that has received chemical treatment and which is discharged from a CSO may eventually be received by a natural water course. The fluid will therefore require the chemical disinfectant to be neutralised to acceptable levels prior to being spilled into a river to avoid pollution of the water course. Guidelines on acceptable levels or Environmental Quality Standards (EQS) in England and Wales, UK, are available from the Environment Agency (Environment Agency, 2004, Private Communication).

3.6.3 Disinfection of a continuous flow system

Pretorius and Pretorius (1999) carried out batch inactivation studies using monochloramine as a disinfectant on "secondary treated effluent from a typical biological nutrient removal wastewater treatment plant, treating mainly domestic sewage" (Pretorius and Pretorius, 1999). This should give a more realistic indication of the effectiveness of monochloramine compared with using pure culture bacteria and distilled water. The batch inactivation studies were carried out in sterile sample bottles at a pH6, 7 and 8, at 25±1°C, using a monochloramine concentration in the range of 1 to 5mg/litre. The required pH was acquired using a concentrated phosphate buffer solution. Once the required pH and temperature had been achieved, a sample was taken to acquire the original faecal coliform count. Monochloramine was then added to the test water to acquire the desired concentration and the pH measured to

ensure that it was at the required level. The solution was continuously stirred and samples taken at predetermined contact times. The samples were then neutralised using sterilised thiosulfate solution. The surviving faecal coliform count was then taken, whilst also considering the dilution of the neutralising thiosulfate solution.

Having carried out the batch inactivation studies, kinetic rate Equations 3-14 to 3-17 were fitted to the data. It was found that the kinetic rate equation by Severin *et al.* (1984), Equation 3-16, generally gave the best fit, with j equal to 2. It was also found that Equation 3-16 gave values for the apparent kinetic rate constant that increased with an increase in the monochloramine concentration and increased with decreasing pH, as would be expected from a study by Ward *et al.* (1984). By plotting the concentration of the monochloramine against the apparent kinetic rate constant, at each pH and using a linear fit through each set of data, it was found that for a pH6, the kinetic rate constant was approximately 0.56 litres/min.mg, at pH7 0.31 litres/min.mg and at pH8 0.27 litres/min.mg.

To verify that the results from the batch inactivation studies were applicable to a continuous flow system, disinfection was carried out using two bench scale chlorine contact tanks. In predicting the survival of micro-organisms during disinfection in a continuous scale reactor, Severin *et al.* (1984) report: "In the scale up of inactivation data from batch data to a flow-through reactor with complete mixing, it was found that the use of simple mixed, second order kinetics leads to severe errors due to the effects of initial resistance on survival under the completely mixed, flow-through reactor regime. The errors encountered are so severe as to completely miss the prediction that the relative resistance of organisms can change due to the mixing condition". Li (2004) reports: "It has been realised that a plug flow reactor is the most efficient reactor in disinfection facilities and a continuously stirred tank reactor (CSTR) is probably the poorest possible configuration for efficient disinfection". In reality, all continuous flow systems will have a flow characteristic that lies between a CSTR and complete plug flow.

The series event model can therefore be applied to a series of CSTRs by (Severin *et al.*, 1984)

$$\frac{N_t}{N_0} = \left(\frac{1}{1 + kC\tau'}\right)^N \sum_{i=0}^{j-1}\left[\frac{i + N - 1}{N - 1}\right]\left(\frac{kC\tau'}{1 + kC\tau'}\right)^i \qquad (3\text{-}18)$$

Where: τ = Residence time in one CSTR, s N = Number of CSTRs

The number of CSTRs that is representative of the continuous flow system is attained by fitting the 'Tanks in Series model' (TISM) to a residence time distribution determined using a pulse injection of tracer through the continuous flow system.

The TISM with one CSTR is equivalent to a completely mixed flow regime. As the number of tanks increases, the mixing characteristics approach plug flow. It can be seen that as the number of CSTRs in Equation 3-18 increases, the survival rate decreases, which agrees with Li (2004) in that a plug flow reactor is more efficient than a CSTR.

Hence, in the study by Pretorius and Pretorius (1999) the residence time distribution of both bench scale reactors was determined using a pulse injection of lithium as a tracer. Samples of the tracer were taken at time intervals and analysed using an atomic absorption spectrophotometer and the tanks in series model then used to fit a distribution to the residence time data.

Experimental disinfection data was acquired for a continuous flow through the bench scale reactors and compared with predicted survival using Equation 3-18. By comparison of the predicted and measured data, an R_t^2 value of 0.94 was acquired, which was reported by Pretorius and Pretorius (1999) to be a good fit.

Hence, the data from the batch inactivation studies by Pretorius and Pretorius (1999) can be combined with residence time data acquired for a HDVS and therefore used to predict the disinfection performance of a HDVS.

3.7   Summary

- HDVSs for the removal of particulates from wastewater were developed in the 1950s and 1960s.

- The majority of the research literature on HDVSs is from just over the last decade.

- Little still seems to be known about the detailed flow patterns within the HDVS. A shear zone has been detected where there is downward flow along the walls and upward flow along the axis and the position of the shear zone is said to vary around the HDVS and does not lie directly under the dip plate. It is has also been observed that there is downward flow along the central shaft of the Grit King®.

- An efficiency formula has been derived for the retention of particulates in a HDVS operating with an underflow component.

- It is thought that the settling velocity and rise velocity are the main parameters controlling the efficiency.

- A formula for scaling retention efficiency has also been derived for a HDVS operating without an underflow component.

- There are a number of ways to characterise the settling velocity of particles. Some of these involve the use of settling columns and others are more sophisticated, mainly where the characterisation of slurries is concerned.

- In characterising the settling velocity of sewage, it has been shown that the volume of suspended solids, the nature of the water in which the settling tests are carried out and storage of the sample prior to characterisation all affect the settling velocity.

- It is said that for the Eff-Pac™ Clarifier neither the TISM nor the ADM can accurately represent the RTD, hence a combined mathematical model was developed whose application relies upon knowledge of the operational characteristics of the HDVS in order to set appropriate boundary conditions for the model.

- Scaling of residence time has been undertaken using the Froude number to scale the flow and a scaling protocol to scale the residence time.

- Although the primary purpose of the HDVS was for the removal of particulates, the hydraulics of the HDVS are reported to be suitable for performing disinfection processes. There is very little research reported on the application of the HDVS to disinfection. Kinetic rate constants for the disinfection of primary sewage don't seem to be widely reported.

4 Investigating variables that influence the efficiency of a HDVS

A sensitivity study was undertaken using CFD to investigate variables that influence the predicted efficiency of a HDVS using the Discrete Phase Model (see Section 2.3.4.3). The variables investigated may be categorised into two groups; model and physical. Model variables are solution controls within the CFD code. Physical variables are those that will influence the velocity and trajectory of a particle. Although the results of this study were not to be validated against experimental data, the results were seen as a guide to what parameters might have the greatest influence on the retention efficiency and also what variables within the CFD code might require careful consideration for improved modelling when predicting retention efficiency.

Luyckx *et al.* (1998) suggest that the particle settling velocity is one of the most influential parameters that affect the efficiency of a HDVS. Thus, prior to investigating variables that influence the HDVS efficiency, an initial study was carried out to verify that the CFD software can accurately predict the settling velocity of the simplest particle, a sphere.

4.1 CFD validation of the settling velocity of a sphere

4.1.1 Experimental setup and procedure

Experimental testing was carried out whereby the settling velocities of a variety of precision cellulose acetate balls were measured in water. The specific gravity of cellulose acetate is 1.28. A settlement length of 1m in a 0.25m internal diameter settling column was used to measure the settling velocity using a stop-watch. By comparing the particle-column diameter ratio with Figure 2-2, adapted from Fidleris & Whitmore (1961), the diameter of the column was sufficient to say that wall effects were negligible.

A distance of 0.3m was provided for the ball to reach the terminal settling velocity. From a theoretical calculation of the settling velocity of the particle using knowledge of the particle size, density and fluid temperature such that the density and viscosity could be determined, the number of time constants, derived from Newton's second law of motion applied to a sphere, can be calculated for the particle to reach 99.9% of the terminal settling velocity (see Section 2.1.3). Hence, an estimate of the distance required for the particle to achieve the

terminal settling velocity can be made. It was estimated that for the largest particle, a distance of 0.3m was more than 5 times the distance required.

4.1.2   Grid setup and boundary conditions

Using the FLUENT CFD simulation software, coarse and fine hexahedral grids aligned with the trajectory of the particle were used as well as coarse and fine tetrahedral grids which due to the nature of a tetrahedral cell cannot be aligned with the trajectory of a particle. A hexahedral grid aligned at 45° to the direction of the particle trajectory was also investigated to see if grid alignment in a hexahedral mesh has any influence on the predicted settling velocity.

Figure 4-1 shows the coarse hexahedral grid that was used. The settling column was split so that a mapped region was present in the centre of the column where the particle trajectory was computed. Here the cells had a skewness of 0 and aspect ratio of 1. The cell size was 11mm in the mapped region. The geometry was split in an identical way for a fine hexahedral grid with a cell size of 4.5mm. A coarse tetrahedral grid was constructed with a cell size of 20mm and a fine tetrahedral grid with a cell size of 8.5mm. Due to the nature of hexahedral and tetrahedral elements, identical cell sizes were not used because a hexahedral grid with the same cell size as a tetrahedral could be constructed with fewer cells. Thus, the fine hexahedral and tetrahedral grid sizes were between approximately 700 000 and 800 000 cells and the coarse hexahedral and tetrahedral grid sizes were between approximately 50 000 and 70 000 cells.
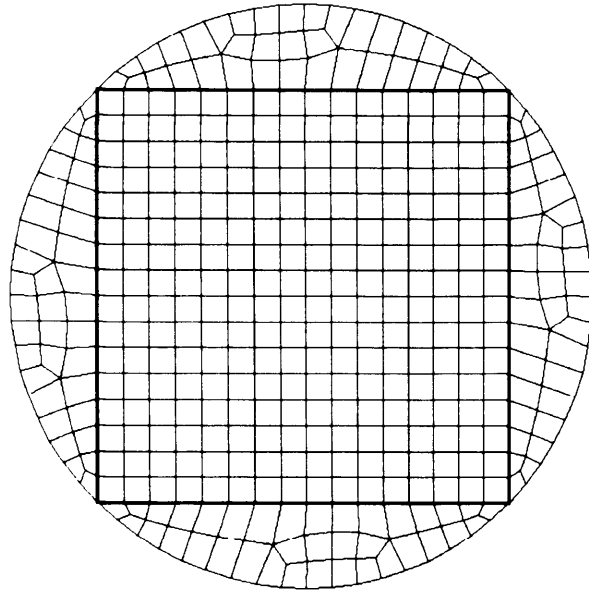
Figure 4-1. Coarse hexahedral grid used for investigating CFD settling velocity predictions.

As the fluid velocity was zero, solution of the fluid transport equations was not necessary. Within the CFD model two planes were monitored, 1m apart, so that the time the particle passes through each plane could be recorded, and hence the settling velocity determined. The particle was released at a point 0.3m above the first surface to replicate the experimental setup. The length scale specified in all models was 1mm i.e. the equations of motion for the particle were updated every millimetre.

4.1.3 Results

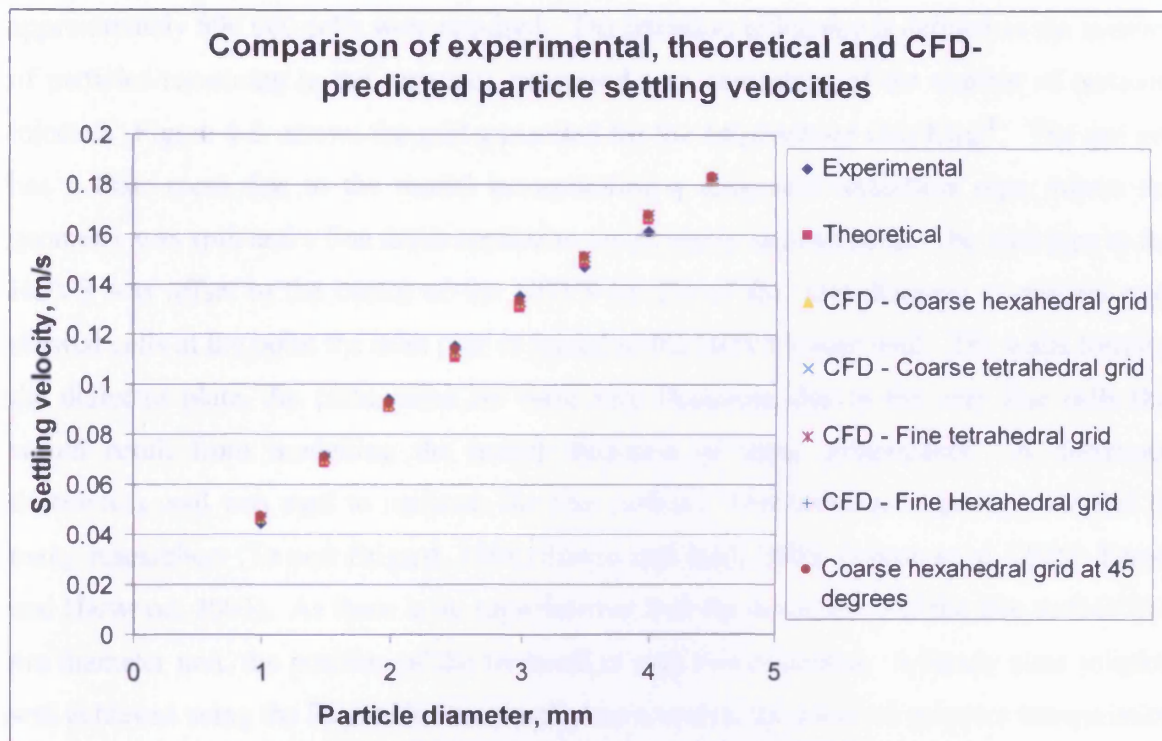The results comparing CFD with experimental data are presented in Figure 4-2.

Figure 4-2. Comparison between theoretical, experimental and CFD-predicted particle settling velocities.

As can be seen from Figure 4-2, FLUENT CFD predictions compare very well with experimental results. These also compare well with theoretical settling velocities computed using Equations 2-4, 2-5 and 2-6. Calculation of the particle Reynolds number at a water temperature of 20°C reveals that all the particles are in the intermediate drag regime.

One reason that the CFD predictions are very good is probably due to the fluid inside the settling column being stationary. If velocity gradients were present in the fluid, then one would expect cell shape and grid resolution to influence the results. This would require further work to look at the effect of cell shape, mesh alignment, grid dependency and for a turbulent flow the choice of turbulence model.

4.2 Sensitivity study

4.2.1 Grid setup and boundary conditions

A 4m diameter Grit King® was modelled with an inlet flowrate of 452 litres per second which was considered a typical flowrate. Different sizes of tetrahedral grids were applied to the separator where it was found for grid independency of retention efficiency a mesh size of

approximately 500 000 cells were required. The retention efficiency is defined as the number of particles remaining in the separator expressed as a percentage of the number of particles injected. Figure 4-3 shows the grid generated for the 4m diameter Grit King[®]. The grit pot has a finer mesh due to the model incorporating a tangential underflow pipe, where the geometry was split and a fine mesh applied to avoid highly skewed cells. The inlet pipe to the HDVS was offset to the centre of the HDVS by 5% of the inlet diameter to prevent over skewed cells at the point the inlet pipe is joined to the HDVS vessel wall. The walls forming the deflector plate, dip plate, cone etc were zero thickness, due to the very fine cells that would result from modelling the actual thickness of these components. A horizontal frictionless wall was used to replicate the free surface. This technique has been adopted by many researchers (Ta and Brignal, 1998; Stovin and Saul, 2000; Greene *et al.*, 2002; Faram and Harwood, 2003). As there is no experimental data for the position of the free surface in a 4m diameter unit, the position of the frictionless wall was estimated. A steady state solution was achieved using the Reynolds Stress turbulence model, the standard pressure interpolation scheme, the SIMPLE pressure-velocity coupling algorithm and first order terms were solved for momentum, turbulent kinetic energy and turbulent dissipation rate.
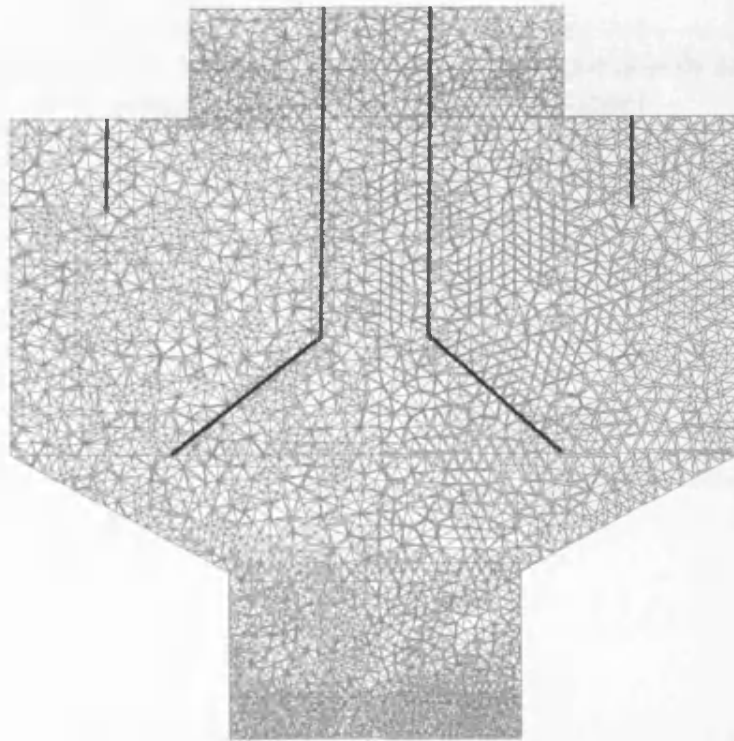

Figure 4-3. The tetrahedral mesh applied to the 4m diameter Grit King[®].

4.2.2   Model variables

Turbulent dispersion model

To look at the effect of injecting particles without a turbulent dispersion model, five surface injections were carried out where the number of particles injected started at 135 and was increased in increments of 135 up to 675. A surface injection is such that a particle is released from each data point on the surface, in this case the inlet to the HDVS model. Due to the resolution of the grid, the face of the inlet contained 135 data points. To increase the number of particles injected, an integer value is used to define the number of particles released from each data point. Hence, the number of particles injected increased in increments of 135. The results were such that there was no variation in the efficiency. This is because without any dispersion of particles, each particle that is released from a data point follows the same path as the previous particle.

Comparison of results with and without a turbulent dispersion model

The turbulent dispersion model used was Stochastic Tracking which computes the particle trajectory using the instantaneous value of the fluctuating velocity. Figure 4-4 shows predicted retention efficiencies with and without the dispersion model.
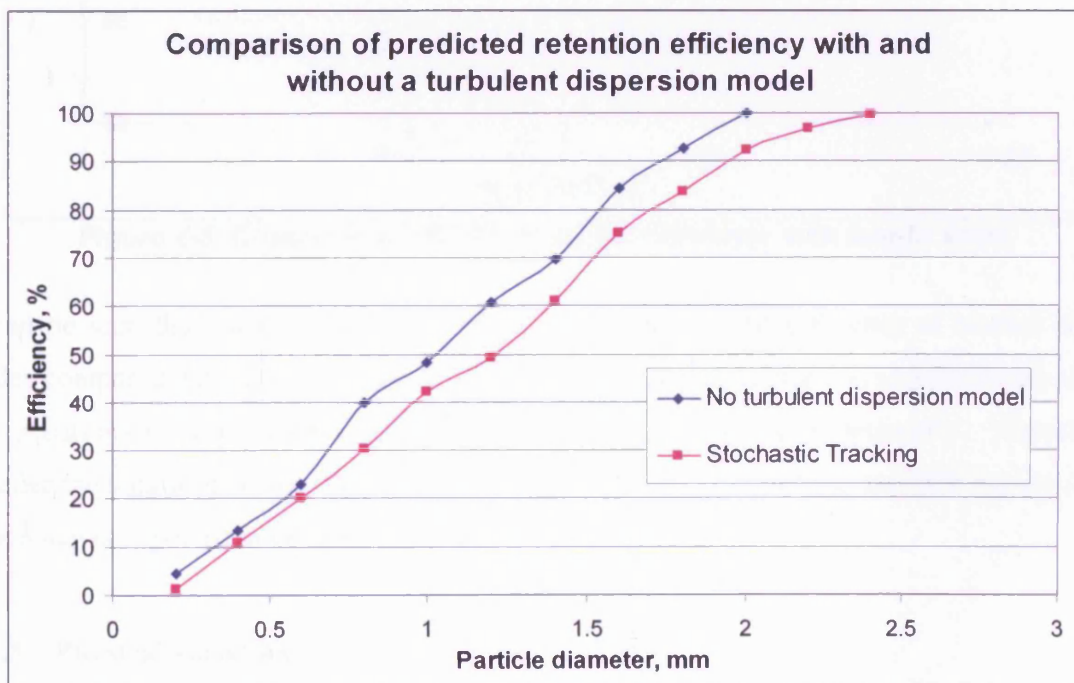

Figure 4-4. Predicted retention efficiency with and without a turbulent dispersion model.

There is a discrepancy between the two sets of results. This is because eddies will affect particles with identical properties in different ways and it is therefore reasonable to assume a certain amount of stochastic behaviour.

Length scale

The length scale determines the time step used to integrate the equations of motion for the particle (see Equation 2-67). Figure 4-4 shows how the predicted efficiency of a particle changes with length scale.
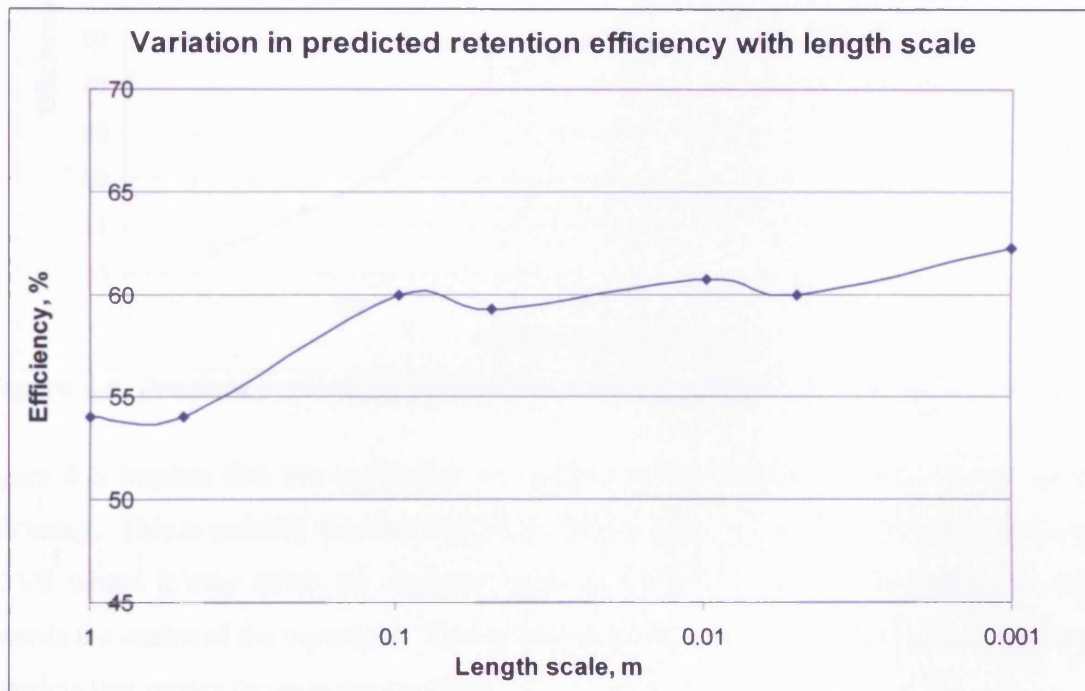

Figure 4-5. Change in predicted retention efficiency with length scale.

It can be seen that there is approximately 8% difference in the efficiency at smaller length scales compared with those at larger values. This is probably because at smaller length scales the equations of motion for the particles are being updated more frequently. Hence, the smaller the length scale, the more accurate the trajectory of the particle and thus the predicted efficiency is expected to be more accurate.

4.2.3   Physical variables

Coefficient of restitution

The coefficient of restitution defines the momentum that is retained or lost by a particle when it strikes a wall. Figure 4-6 shows the difference between predictions where the default value

in both the normal and tangential component is one and predictions where the coefficient of restitution in both the normal and tangential component is zero.
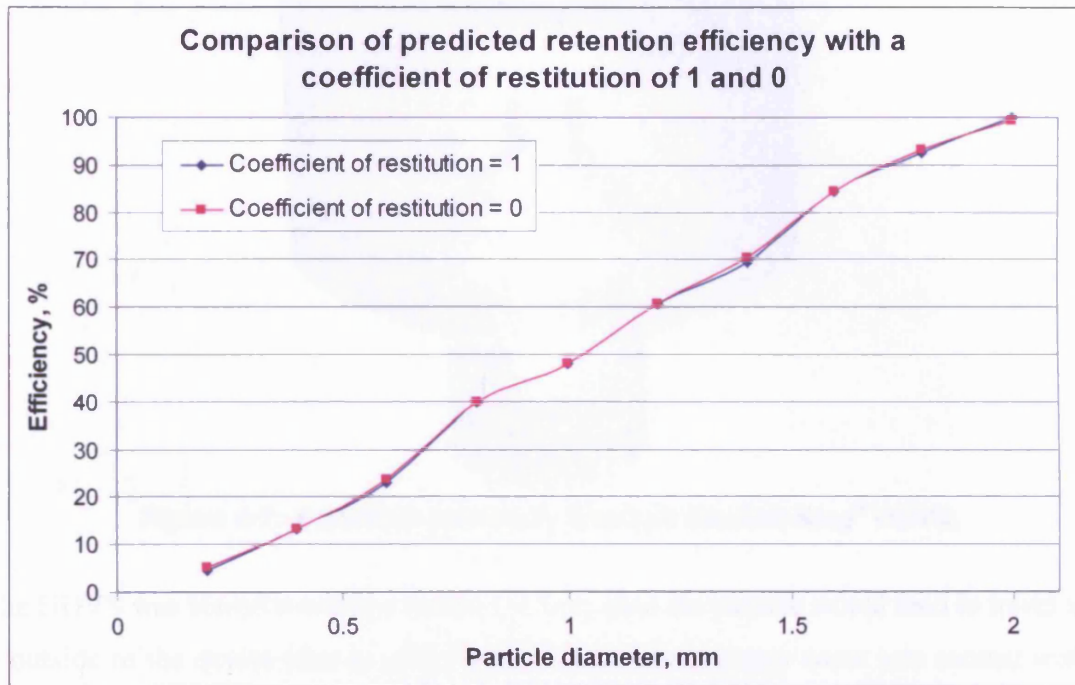

Figure 4-6. Predicted retention efficiencies with a coefficient of restitution of 0 and 1.

Figure 4-6 implies that the coefficient of restitution has negligible effect on the retention efficiency. This is possibly because a particle is most likely to strike a wall when it enters the HDVS where it may strike the deflector plate and after this the particle tends to migrate towards the centre of the separator. This is shown in Figure 4-7 which shows the trajectory of a particle that passes through the overflow.
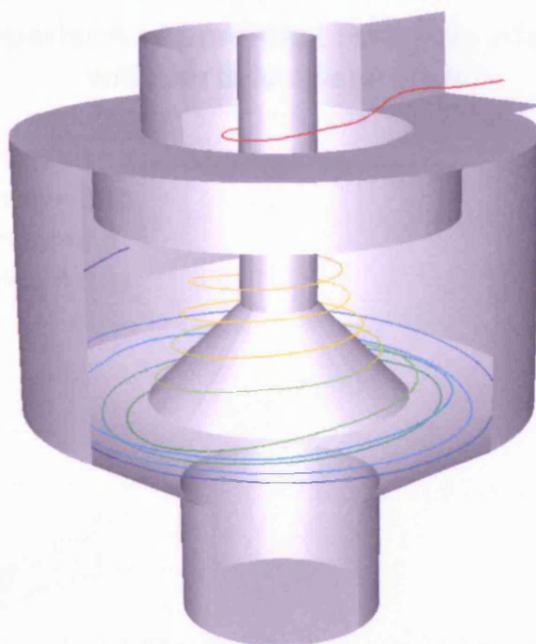
Figure 4-7. A particle trajectory through the Grit King® HDVS.

If the HDVS was biased towards a forced cyclone, then the particle would tend to travel along the outside of the device (due to centrifugal effects) where it may come into contact with the outside wall, in which case the coefficient of restitution could be critical. However, this is not the case here.

Shape factor

The shape factor of a particle has a direct impact on its settling velocity. Shape factor is defined by the sphericity. As the shape factor tends towards zero, the particle becomes flatter and hence the drag will increase and the settling velocity decrease. The lower the settling velocity, the lower the expected efficiency. This has been investigated with a sphericity of 1, 0.75, 0.5 and 0.25. A sphericity of 1 corresponds to a sphere. Table 4-1 indicates how the remaining shape factors correspond to the shape of cylinders.

Table 4-1. Comparison between the shape of a cylinder and the sphericity.

Sphericity	Cylinder	
	Diameter, D	Length, L
0.75	1	3.5D
0.5	1	16.5D
0.25	1	142.5D

Figure 4-8 shows CFD-predicted retention efficiencies for the various particle shapes.
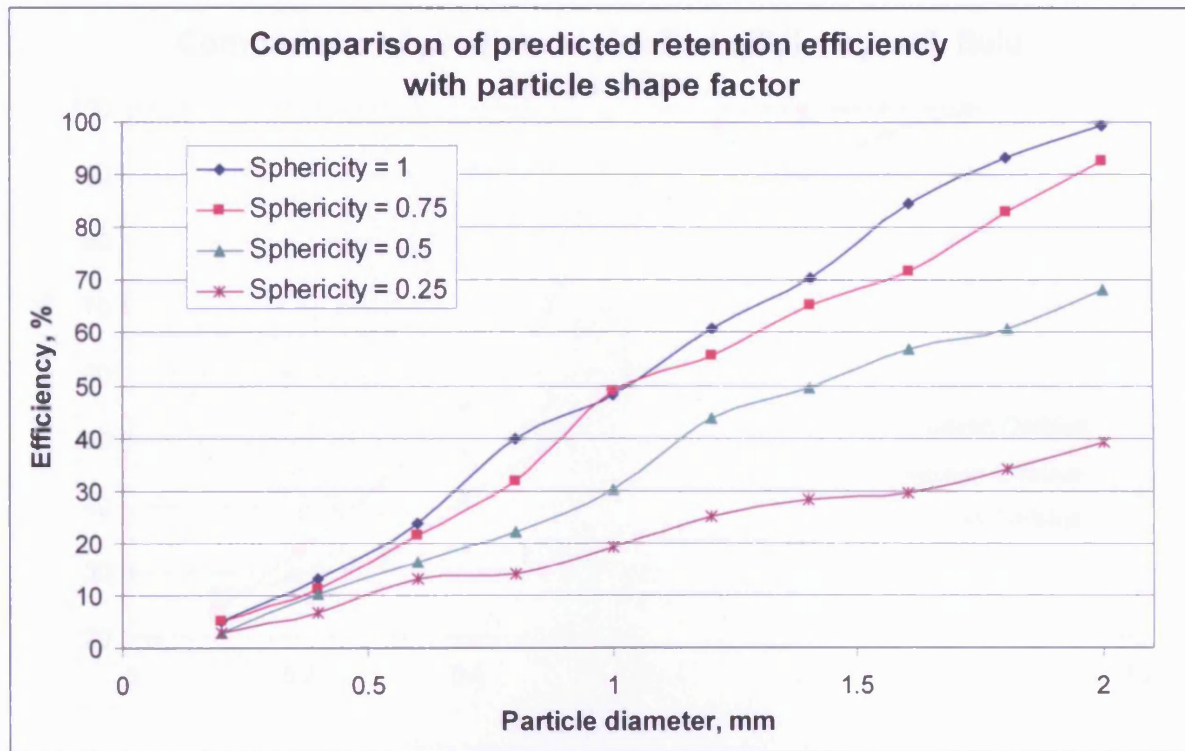
Figure 4-8. Predicted retention efficiencies for particles with four different shape factors.

Clearly the particle shape is predicted to have a significant impact on the retention efficiency of the HDVS. The shape factor is therefore an important parameter because grit is irregular in shape making prediction of the efficiency quite a complex task.

Fluid temperature

The temperature of the fluid has a direct influence upon the viscosity and density of the fluid and hence the settling velocity of a particle. Figure 4-9 shows predicted efficiencies at 0.2, 16 and 25°C.
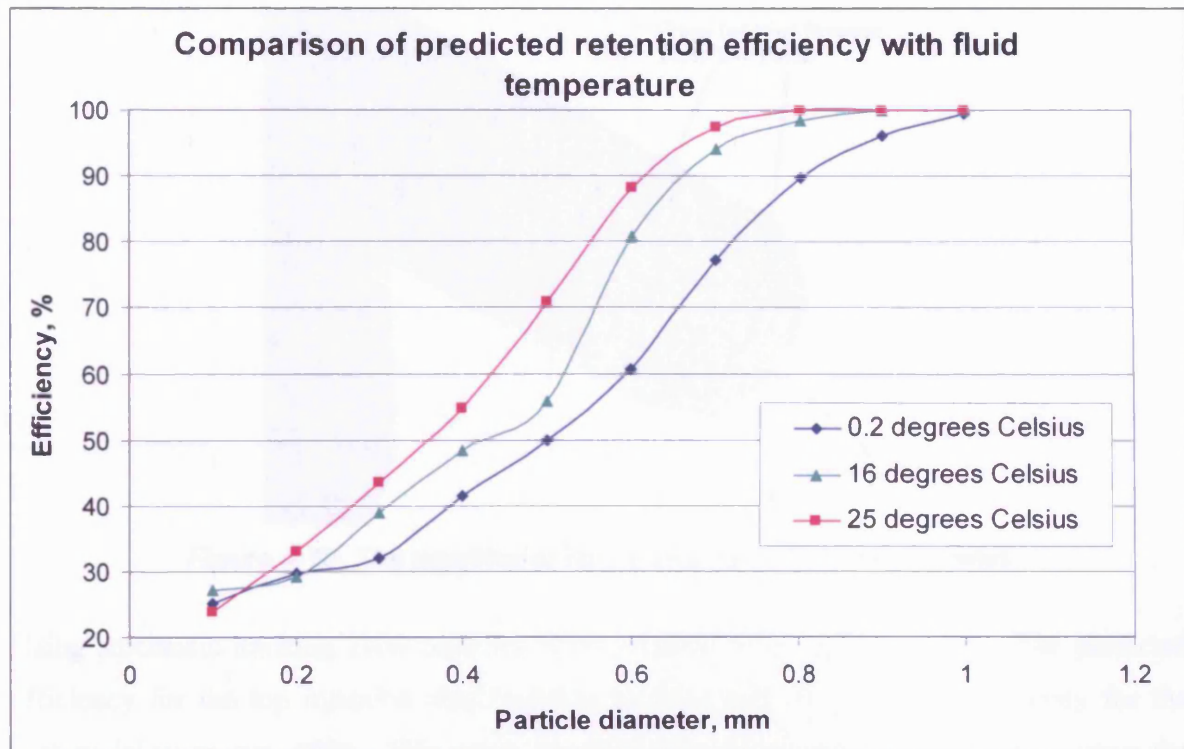
Figure 4-9. Predicted retention efficiencies at 0.2, 16 and 25°C.

As might be expected, at a higher fluid temperature the efficiency is greater due to the fluid having a lower viscosity and density, which means that the particle has a higher settling velocity.

Initial Particle Position

Two group injections were created where one was between two horizontal points in the top half of the inlet and the other between two horizontal points in the bottom half of the inlet, as shown in Figure 4-10.
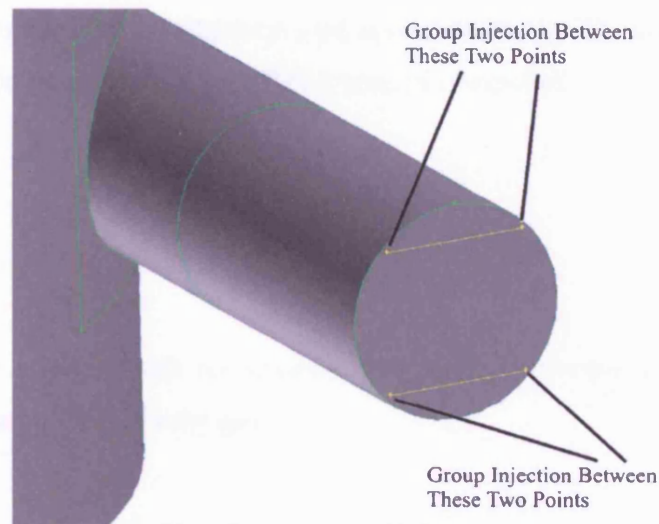
Figure 4-10. The position of two group injections on the inlet.

Using stochastic tracking 2000 particles were released from each injection. The predicted efficiency for the top injection was found to be 54% and the predicted efficiency for the bottom injection was 98%. This result suggests that the efficiency is dependent upon the initial position of the particle.

4.3   Discussion

It has been shown that the CFD software can accurately predict the settling velocity of a sphere. In a stationary body of fluid where no velocity gradients exist, the predicted settling velocity is independent of the cell type, the grid resolution and the alignment of the grid. Further work to investigate the settling velocity of a sphere in a settling column in which there is upward moving fluid was considered but given the time required to design and manufacture an appropriate test rig this aspect was considered to be beyond the scope of the work.

A 4m diameter Grit King® has been modelled and relative effects studied to gain an insight into the parameters that may have an influence on the retention efficiency of this type of separator. It has been predicted that the coefficient of restitution has negligible effect on the retention efficiency of this type of separator at the flowrates investigated. Those variables that may have a significant impact include the position of the particle at entry into the separator, the particle shape and the fluid temperature and hence, the fluid density and viscosity. During experimentation, this highlights the need to record the fluid temperature

and also the configuration of the upstream pipe layout so that if CFD modelling is undertaken, then the velocity profile at entry to the HDVS may be computed.

4.4   Summary

- For a body of fluid with no velocity gradients the predicted settling velocity of a sphere made by CFD is very good.

- The length scale and the use of a turbulent dispersion model should be given consideration when attempting to validate retention efficiencies.

- The position of the particle at entry to the separator, the particle shape and the fluid temperature are predicted to have a significant affect on the retention efficiency.

5 Experimental study of a 0.75m diameter Grit King®

A 0.75m diameter Grit King® was designed by scaling a 4m diameter unit[4]. A HDVS with a diameter of 0.75m has been considered by previous researchers to be of such a size to be able to class as a prototype (Higgins, 2000; Alkhaddar *et al.*, 1999). The 0.75m diameter Grit King® unit was to be tested in a laboratory at Cardiff University where it was decided that a custom built rig would be used. Detailed drawings of the Grit King® and the rig are found on Pages 95 to 99. The internal components and principle of operation are described in Section 1.2. Figures B1 and B2 in Appendix B are photographs of the test rig in the laboratory.

5.1 Rig design

Water was pumped by a Grundfos CR30 centrifugal pump to a header tank whose base was at a height of approximately 3.3m, marked 'A' in Figure 5-1. This method of delivering fluid to the Grit King® was preferred to delivery straight from the pump as a header tank could be used to maintain a constant head of water and thus a steady flow was achieved somewhat faster than waiting for the oscillatory flowrate from a pump to dampen out.

If sand was to be used, or any other media that could get into the system and cause wear through abrasion etc, the option to fit filters was designed such that a bypass space was provided by two sweeping tee sections in the section of pipe work immediately after the pump, marked 'B' in Figure 5-1. A valve was fitted to the pipe work leading up to the header tank to isolate that side when using the filters, Figure 5-1 'C'.

---

[4] It should be noted that during the design of the 0.75m diameter Grit King® the tangential underflow was placed at the wrong side of the separator. This went unnoticed until well into the testing period by the author and Hydro International Plc who inspected the unit prior to it being installed in the rig. It has been suggested through computational modelling that the fluid velocity in this region is very low (Faram *et al.*, 2003). Thus, it is expected that this design fault will have little influence on the experimental results when operating without a base flow and adjustment of the tangential underflow when studying scaling effects with CFD can therefore be made with confidence that the models will still be valid without requiring further validation.

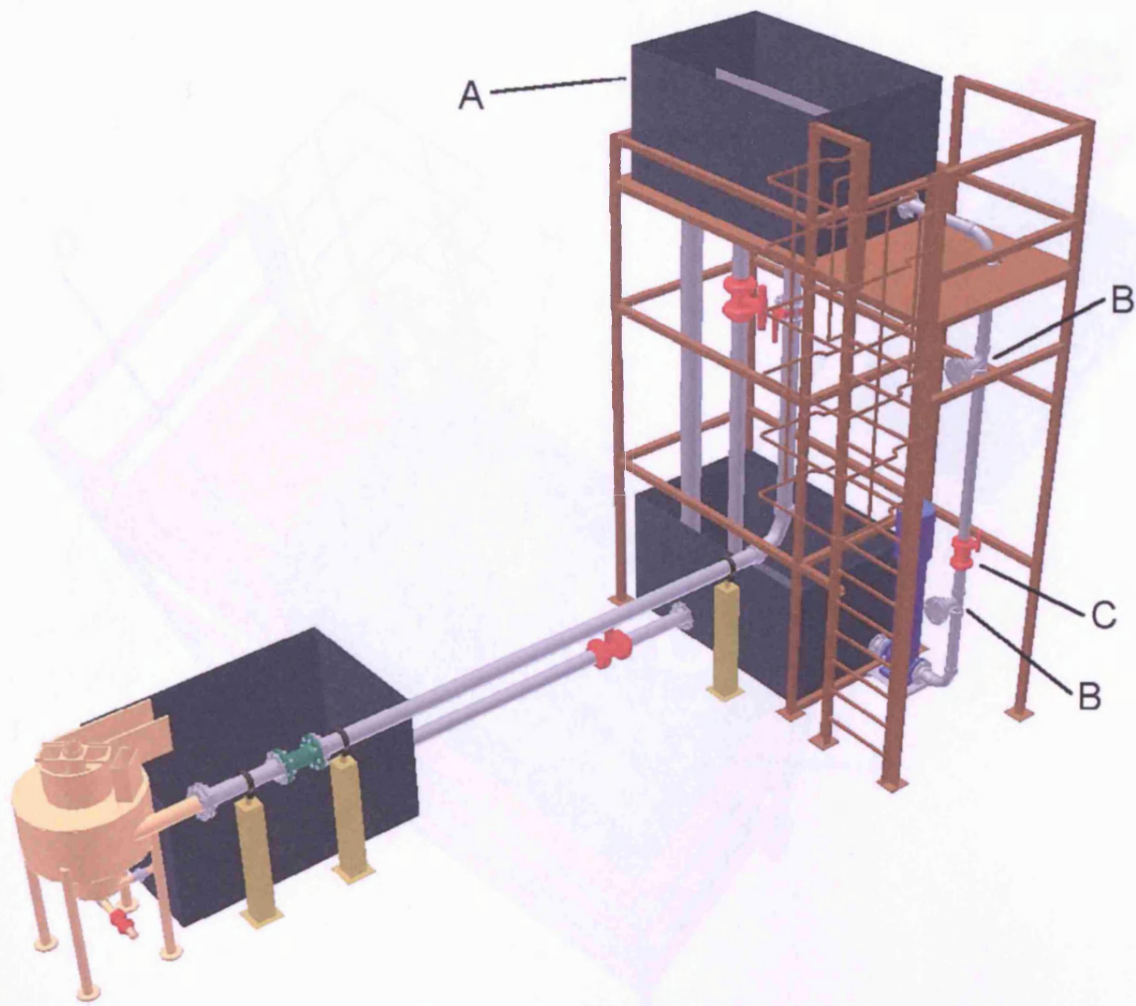**Figure 5-1. Conceptual view of the test rig design.**

The pipe work entered the header tank at a height where it was below the water level, Figure 5-2 'D'. This was to reduce the number of air bubbles created from the jet entering the header tank. Should any air bubbles be created, there was a baffle plate, Figure 5-2 'E' that acted as a weir to eliminate bubbles from being drawn through the rest of the system.
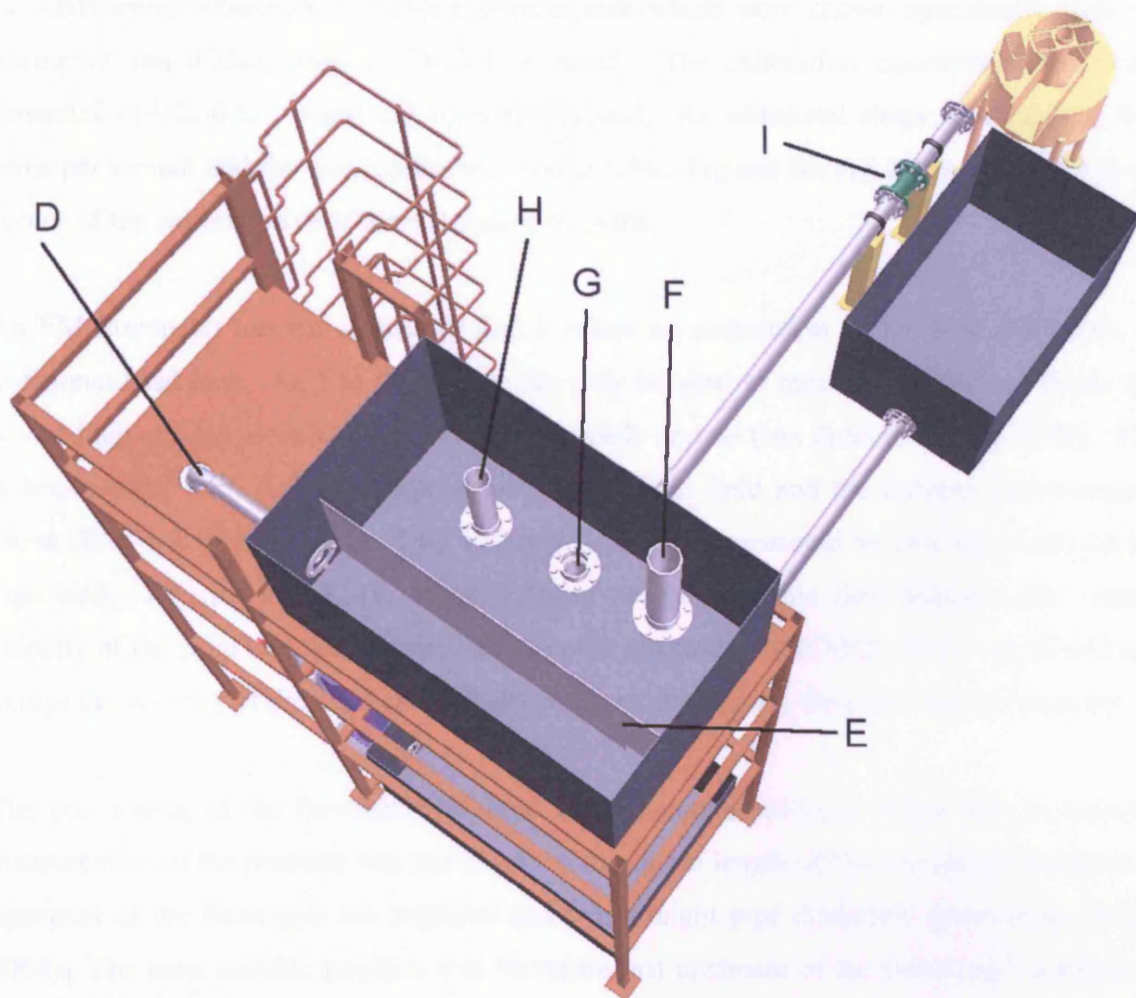
Figure 5-2. Conceptual view of the test rig design.

In the header tank was a vertical pipe, marked 'F' in Figure 5-2, whose purpose was to maintain a constant head of water. A second pipe marked 'G' passed to the tank below whose purpose was to drain the header tank. A third pipe 'H' was used for feeding water to the Grit King®. Two possibilities were considered regarding the release of particles into the flow for studying retention efficiencies. The first was a standpipe, which was not favourable because in Section 4.2.3 it has been shown that the position of a particle at entry to a HDVS may influence the efficiency and thus, placing a standpipe close to the HDVS may not give an adequate residence time for particles to find a realistic position at entry into the separator. A second possibility was to release the particles into the flow at the header tank through pipe 'H'. This was favourable as it would provide realistic mixing of the particulate matter over the pipe length.

An Electromagnetic flowmeter was supplied courtesy of ABB. This flowmeter was calibrated by ABB using volumetric flowrate measurements which were chosen specifically with the testing of the 0.75m diameter HDVS in mind. The calibration concentrated on lower flowrates of 0.2, 0.5, 1.0 and 2.0 litres per second. An additional check was made at 20.0 litres per second and the maximum error was 0.52%. Figures B3 and B4 in Appendix B are copies of the calibration certificate supplied by ABB.

An EM flowmeter has the advantage that it offers no obstruction to the flow and hence, no additional head loss. An EM flowmeter can only be used to measure the flow of fluids that have a high enough electrical conductivity, typically no less than $2\mu S/cm$ (Miller, 1976). This is because the fluid flows through an electromagnetic field and the induced Electromotive Force (EMF), which is insulated by Teflon or rubber, is measured by two electrodes on the pipe wall. This induced EMF "is proportional to the magnetic field strength, the average velocity of the fluid and the distance between the electrodes" (BS7405:1991). As all of these except the velocity of the fluid can be held constant, the average flowrate may be measured.

The positioning of the flowmeter required careful consideration to ensure that an accurate measurement of the flowrate was achieved. A minimum length of five straight pipe diameters upstream of the flowmeter are required and two straight pipe diameters downstream (ABB, 2004). The most suitable position was therefore just upstream of the Grit King®, marked 'I' in Figure 5-2, where 45 diameters of straight pipe were located.

When the rig was assembled, the only pipe that extended into the header tank was that marked 'F' in Figure 5-2. This was to ensure that on pipe 'H', a vortex was not created between the inlet to the pipe and the free surface which could have entrained air through the pipe to the Grit King® and result in an erroneous reading in the Electromagnetic flowmeter. In the vertical section of pipe 'H' was a butterfly valve, marked 'J' in Figure 5-3, chosen for ease of controlling the flow.

Once water passes through the Grit King®, marked 'K' in Figure 5-3, it discharged into a third tank 'L' which is connected to tank 'M' below the header tank. Hence the flow circulates through the system instead of going straight to drain. A modification that was later made was to add a second pipe between tanks 'L' and 'M' which allowed a higher flowrate between the

tanks and also helped balance the water level which reduced the chance of air being entrained through the pump if the quantity of water in the system was a little low.

To prevent contaminants entering into the header tank a lid was used (not shown in figures). Access to the pipe delivering fluid to the rig for releasing the particles was easily provided by removing a circular disc in the lid. Particulates were released into the system by pouring the particles through a slim cylindrical piece of tubing placed into the top of pipe 'H'.
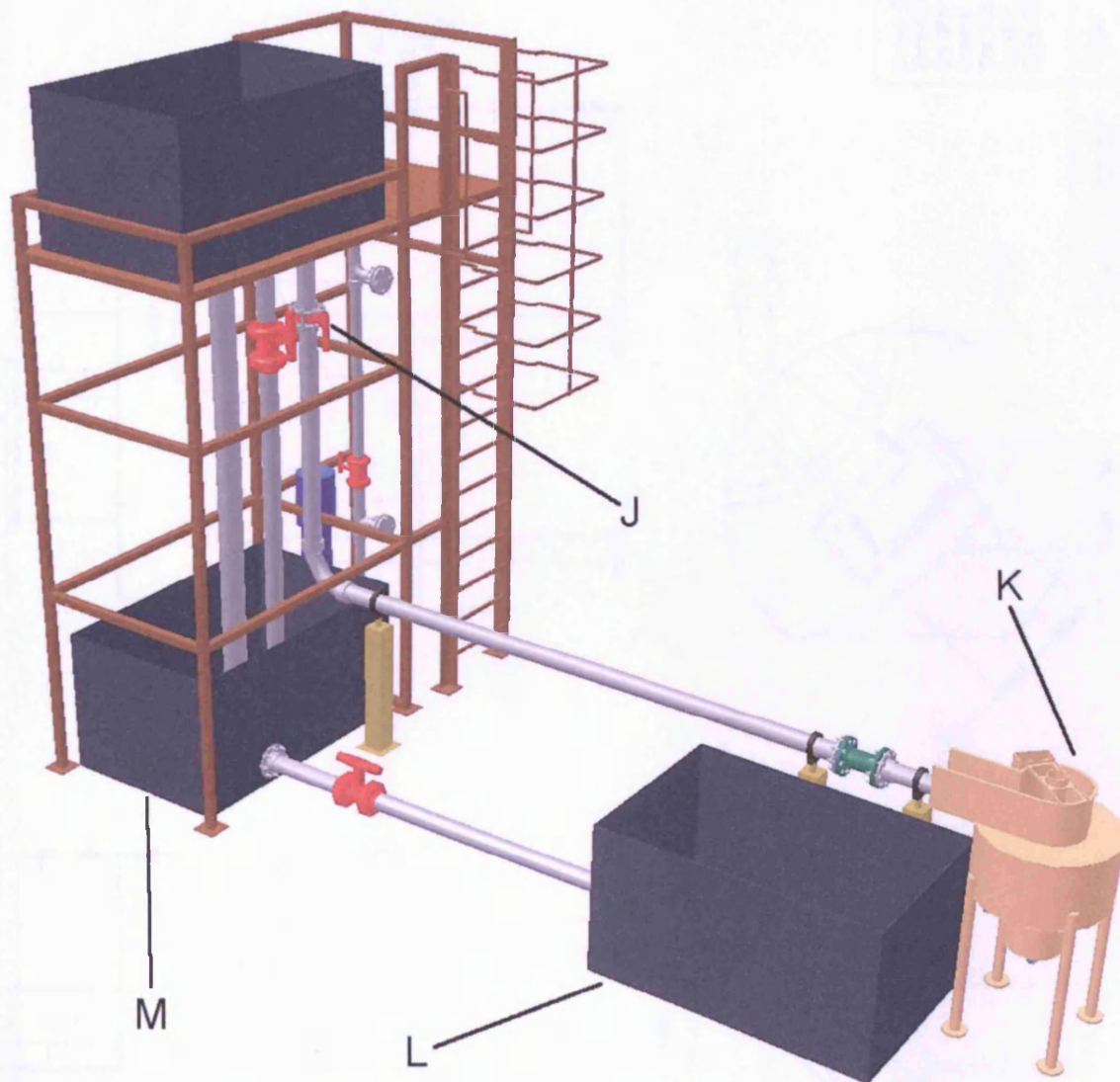
Figure 5-3. Conceptual view of the test rig design.

Internal ⌀97

245

Material: Polypropylene, 5mm thk

693

⌀40

50

195

170

1010

25

⌀760

R650
R540

87

A

135°

180

300

262

A (1:8)

Full dimensions omitted at the
request of Hydro International

Dimensions: mm

Scale: 1:16

Paper Size: A4

Date: 02/02/03

Title:
0.75m diameter Grit King(R)
External Dimensions

B–B

A–A

C–C

B ▸◂ A

C

B ▸◂ A
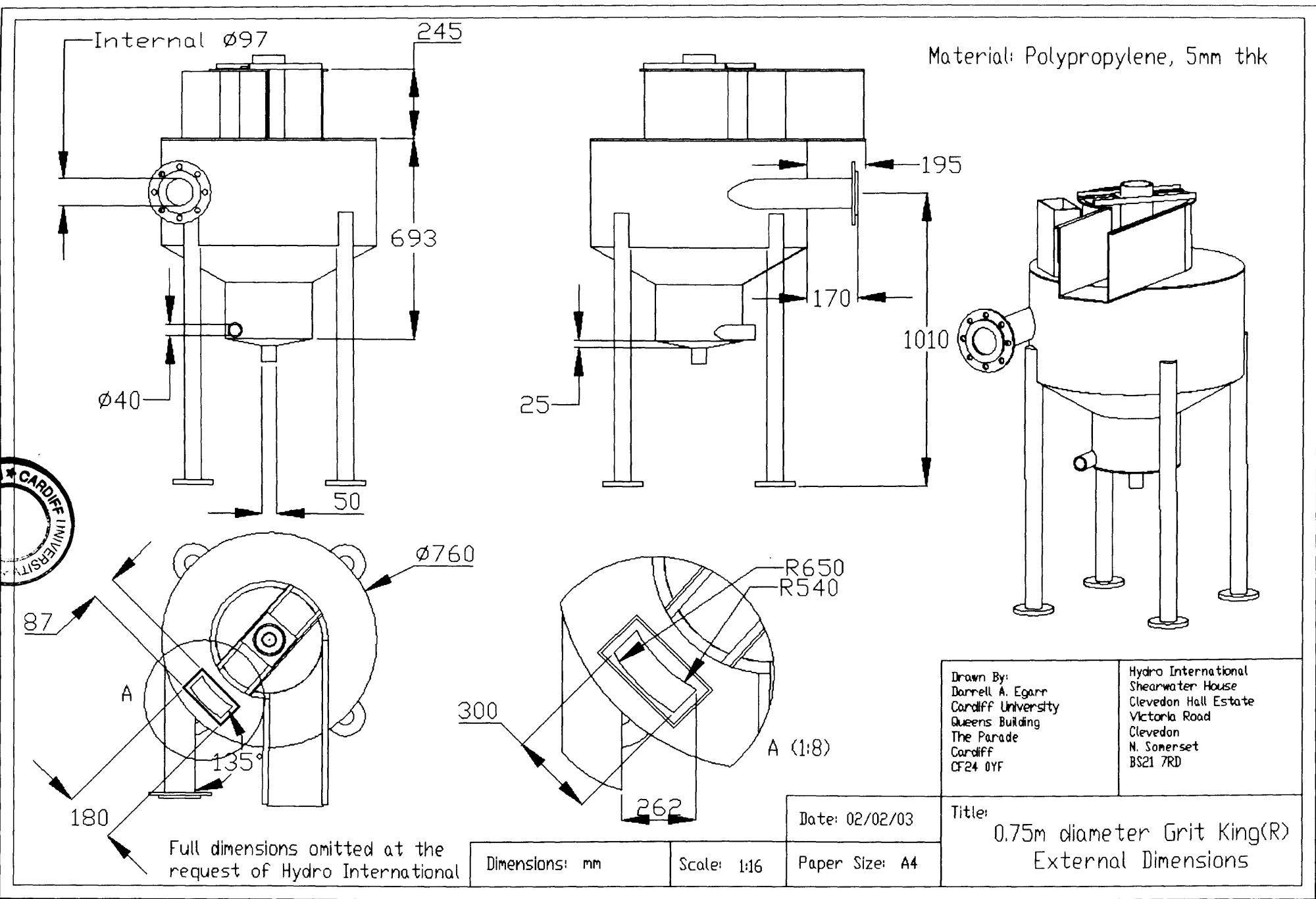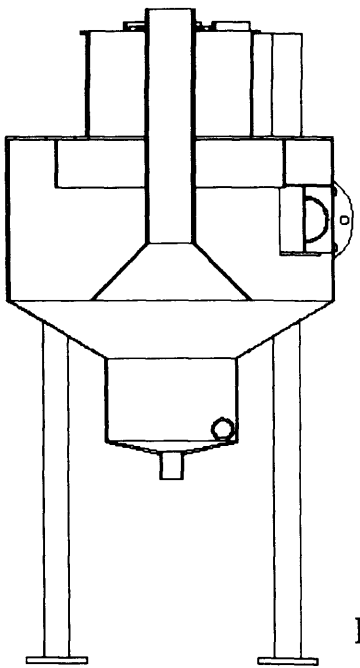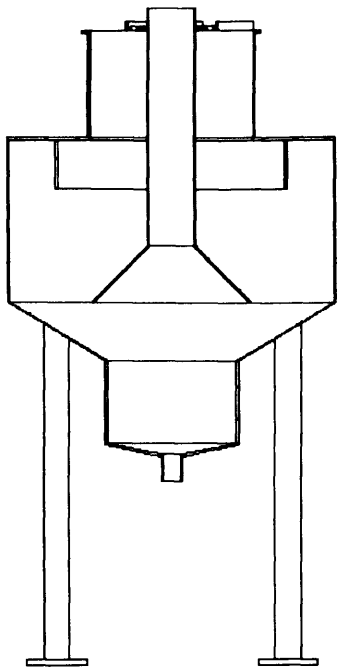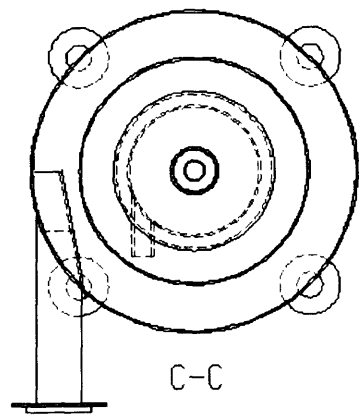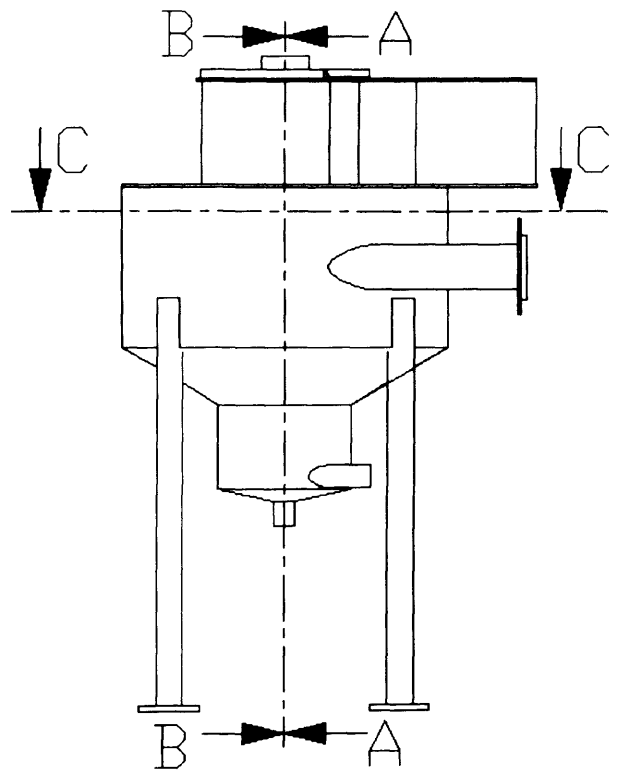
Full dimensions omitted at the
request of Hydro International

Material: Polypropylene, 5mm thk

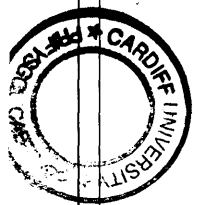| Drawn By: Darrell A. Egarr Cardiff University Queens Building The Parade Cardiff CF24 0YF	Hydro International Shearwater House Clevedon Hall Estate Victoria Road Clevedon N. Somerset BS21 7RD

			Date: 02/02/03	Title: 0.75m diameter Grit King(R) Internal View
Dimensions: mm	Scale: 1:16	Paper Size: A4		

4340

4200

EM Flowmeter

Header Tank

Grit King(R)

630

Pump

6340

All dimensions are
approximate

Drawn By: Darrell A. Egarr Cardiff University Queens Building The Parade Cardiff CF24 0YF	Hydro International Shearwater House Clevedon Hall Estate Victoria Road Clevedon N. Somerset BS21 7RD
Date: 02/02/03	Title:
	0.75m diameter Grit King(R) Test Rig (Side View)

Dimensions: mm	Scale: 1:50	Paper Size: A4

630

EM
Flowmeter

Constant
Head Pipe

Drainage Pipe

Feed Pipe

6340

2975

Platform

Header Tank

Grit King(R)

Discharge
Tank

Sump Tank

Pump

All dimensions are
approximate

Drawn By:	Hydro International
Darrell A. Egarr	Shearwater House
Cardiff University	Clevedon Hall Estate
Queens Building	Victoria Road
The Parade	Clevedon
Cardiff	N. Somerset
CF24 0YF	BS21 7RD

Date: 02/02/03	Title:
	0.75m diameter Grit King(R)
Dimensions: mm	Scale: 1:45	Paper Size: A4	Test Rig (Top View)

Drainage Pipe

Feed Pipe

Constant Head Pipe

Header Tank

Grit King(R)

4200

3300

1380

Discharge Tank

Sump Tank

1925

1050

All dimensions are
approximate

Drawn By:	Hydro International
Darrell A. Egarr	Shearwater House
Cardiff University	Clevedon Hall Estate
Queens Building	Victoria Road
The Parade	Clevedon
Cardiff	N. Somerset
CF24 0YF	BS21 7RD

Date: 02/02/03	Title:
	0.75m diameter Grit King(R)
Dimensions: mm	Scale: 1:40	Paper Size: A4	Test Rig (Rear View)

5.2 Experimental investigation

5.2.1 Free surface measurements

Validation of experimental data ideally requires knowledge of the position and shape of the free surface. This has been achieved for the 0.75m diameter Grit King® by taking measurements of the distance from the free surface to the top of the device at particular points on the separator shown in Figure 5-4. Points 1 to 4 are positioned approximately 90° from each other on the annulus of the overflow. Point 5 is on the central shaft. Point 6 is the height of the fluid at the end of the overflow. Measurements were also taken within the vent box.

The measurements are given in Table C1, Appendix C, which includes approximate measurements of the fluctuations.
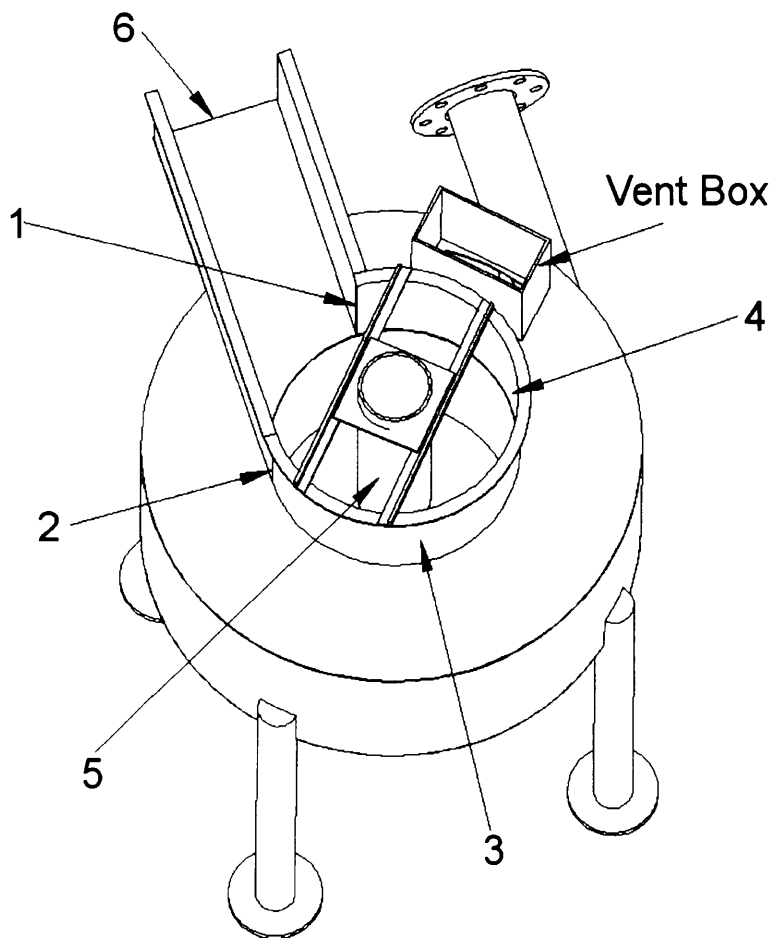
Figure 5-4. Points at which measurements were taken for the free surface on the 0.75m diameter Grit King®.

5.2.2 Static pressure measurements

The use of pressure tapping points was considered as a means for validating the flow field predictions being computed by FLUENT.

For procedures on the placement of pressure tapping points, BS EN ISO 5167 outlines guidelines for placing pressure tapping points on Venturi tubes:

- The upstream pressure tappings shall be made in the form of separate pipe wall pressure tappings interconnected by annular chambers or piezometer rings.

- The diameter of these tappings shall be between 4 mm and 10 mm.

- At least four pressure tappings shall be provided for the upstream measurements. The centre-lines of the pressure tappings shall meet the centre-line of the pipe, shall form equal angles with each other and shall be contained in planes perpendicular to the centre-line of the pipe. Hence, unless otherwise stated, the static pressure at the inlet is the average of four tapping points placed at the inlet.

- At the point of break-through, the hole of the pressure tapping shall be circular. The edges shall be flush with the pipe wall, free from burrs and generally have no peculiarities.

- The pressure tappings shall be cylindrical over a length at least 2.5 times the internal diameter of the tapping, measured from the inner wall of the pipeline.

With these guidelines in mind, pressure tappings were connected to vertical manometers via tubing. A junction in each pipe connecting the pressure tapping point to the glass tube was used to bleed air out of the line.

In taking pressure readings, the procedure undertaken was:

1. Turn on pumps and set valve to allow highest possible flowrate.

2. Allow to run for several minutes until air does not pass through the vent box.

3. Bleed the interconnecting pressure tapping points at the inlet.

4. Bleed the pipes connecting the pressure tapping to the vertical glass tubes.

5. Close inlet valve to Grit King®.

6. At a flowrate of 0 litres per second, note the height, h_0, of the fluid in the vertical glass tube.

7. Increase flowrate at inlet and allow several minutes for flow to stabilise.

8. Note the height of the fluid, h, in the vertical glass tubes.

9. Repeat (7) and (8) over a range of flowrates.

The pressure at a tapping point at an arbitrary flowrate is thus given by

$$p = \rho g(h - h_0)$$ (5-1)

Where: h = Fluid height in manometer, m h_0 = Fluid height in manometer at $Q = 0\text{m}^3/\text{s}$

Figure 5-5 shows the location of each pressure tapping point. Points 1 to 4 at the inlet were placed in a plane that is 0.375m from the centreline of the Grit King®. Points 5 to 8 are located on the same plane as points 2 and 4 at the inlet. Points 9 and 10 on the central shaft are situated opposite point 5 and 7 respectively. Points 11 and 12 are located half way down the grit pot, in the same plane as point 5 and 7.
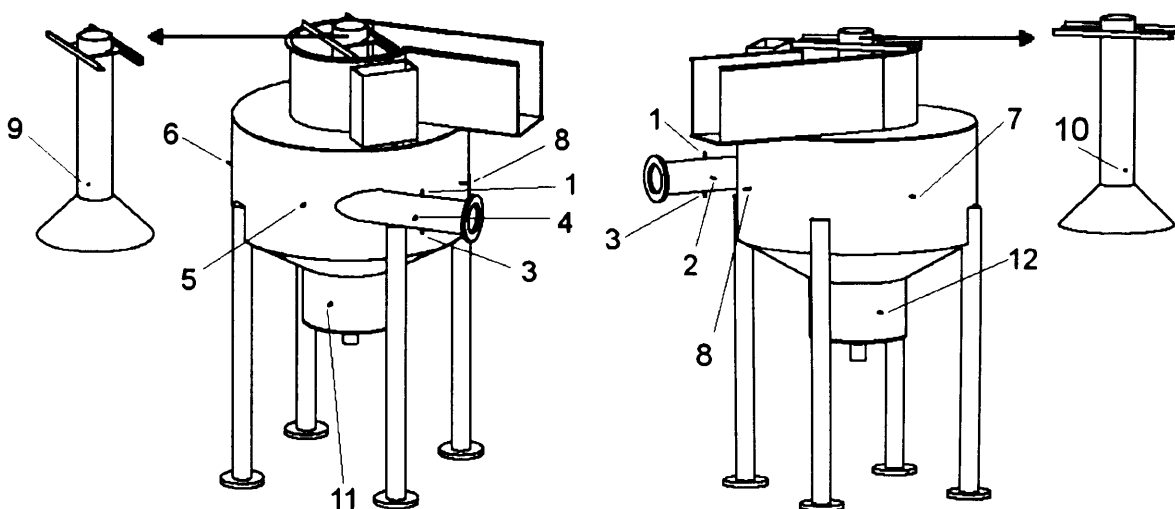

Figure 5-5. Location of pressure tapping points on the 0.75m diameter Grit King®.

Tables D1 to D4 in Appendix D present the static pressure readings taken on the 0.75m diameter Grit King[®].

5.2.3   Retention efficiency testing

The particulate required for retention efficiency should ideally be uniform in shape. Spherical particles eliminate the need to compute a shape factor and the obvious media for testing was precision balls, available from 'The Precision Plastic Ball Co., Ltd'. However, using small samples of the lowest settling velocity particles available (Cellulose acetate, specific gravity 1.28, 1mm diameter) retention efficiencies of almost 95% were achieved at 12 litres per second, the highest flowrate that could be achieved.

A media already being used by Hydro International Plc and also Fenner and Tyack (1997) is pre-expanded polystyrene ('Styrocell'). A second media that was observed by Hydro International Plc at an exhibition demonstrating particle-liquid separation, is an ion exchange resin used in water treatment applications ('Purolite'). Two samples of Purolite were obtained; A100 and PPC-100H. The main difference between the two is the specific gravity. All particles were dried if necessary and sieved to reduce the size range of particles in a sample. The volume of particles used in retention efficiency testing given in Table 5-1, determined by measurement using a measuring cylinder, ranged from 100ml to 900ml, this being dependent on the volume of particles available after sieving.

Table 5-1. Volume of particles, determined using a measuring cylinder, used in retention efficiency testing.

Particle type and sieve size range	Volume of particles used in retention efficiency testing, / ml
Purolite (PPC-100H) 500-600microns	330
Purolite (A100) 500-710microns	360
Purolite (A100) 710-1000microns	410
Styrocell 1.4-2.0mm	330
Styrocell 2.0-2.8mm	900
Styrocell 2.8-5.6mm	170

Samples of dry particles have been observed under an optical microscope. Figure 5-6 shows particles of Styrocell in a 2.8-5.6mm sieve size range. Clearly some particles deviate slightly in shape from a perfect sphere. It can also be seen that not all particles have a smooth surface, particularly those marked 'A' and 'B'. Figure 5-7 shows the surface of a particle of Styrocell.

The surface is not smooth and the surface imperfections look similar to scratches. A limitation in obtaining these images is the shallow depth of field. The depth of field is defined as the region of the image that appears to be of acceptable focus.
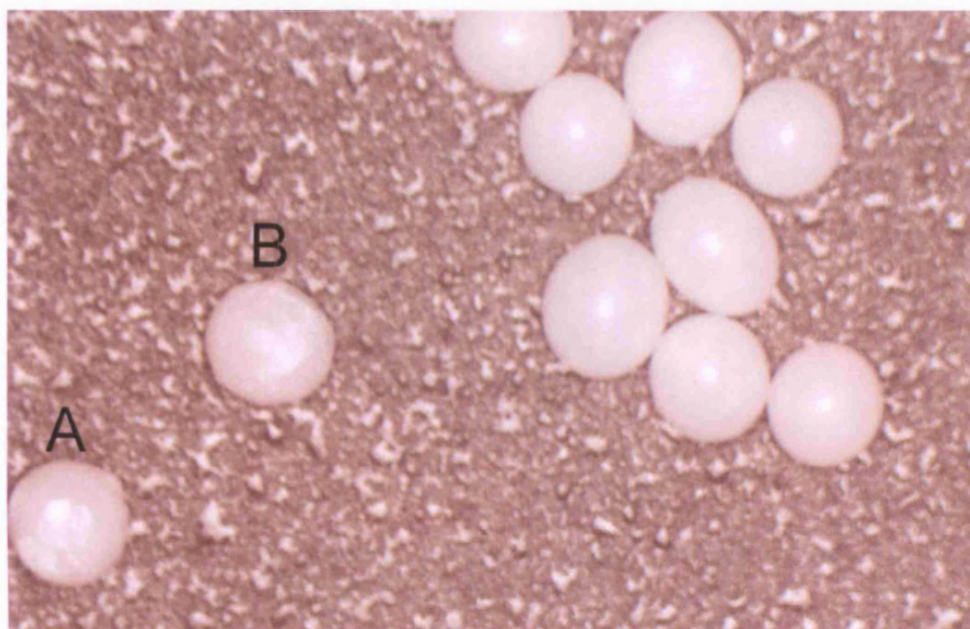
Figure 5-6. Particles of Styrocell in the 2.8-5.6mm sieve size range taken under an optical microscope.
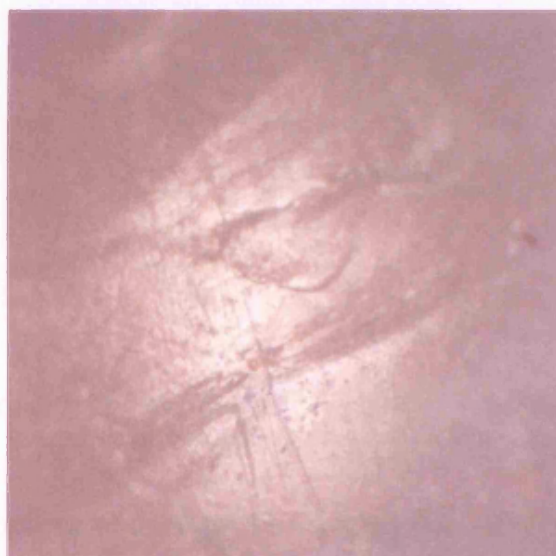
Figure 5-7. The surface of a particle of Styrocell taken under an optical microscope.

Figure 5-8 shows a silhouette of a particle of Purolite A100 in the 710-1000micron sieve size range. Clearly the particle appears to be perfectly spherical for the plane in which the photograph was taken. The surfaces of these particles were examined and the surface appears

to be smooth with very few imperfections that can be seen using the optical microscope. Figure 5-9 shows a slight imperfection but the detail is difficult to elaborate on. Clearly the surface around the imperfection appears to be very smooth.
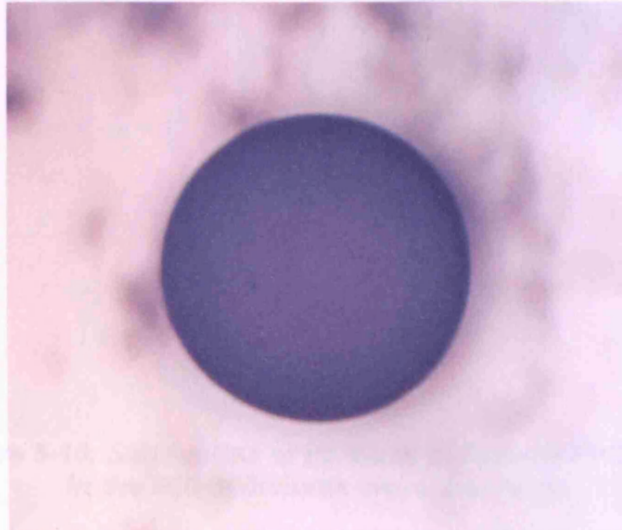
Figure 5-8. A silhouette of a particle of Purolite A100 in the 710-1000micron sieve size range.

Figure 5-9. The surface of a particle of Purolite A100 taken under an optical microscope.

Figure 5-10 shows a silhouette of three particles of Purolite PPC-100H in the 500-600micron sieve size range. Again, the particles appear to be spherical. Figure 5-11 shows the surface of a particle of Purolite PPC-100H. Again, the photograph is limited by the depth of field, but the uneven surface on the top of the particle is clearly visible.
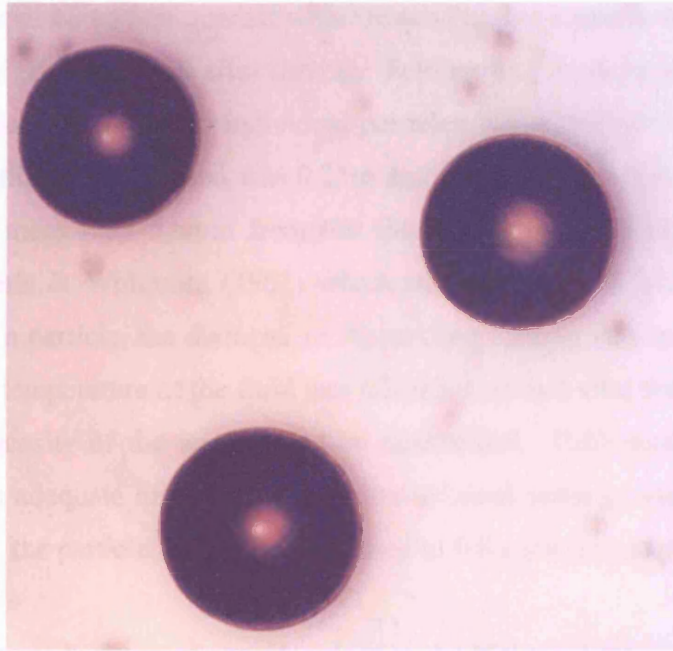
**Figure 5-10. Silhouettes of particles of Purolite PPC-100H
in the 500-600micron sieve size range.**

**Figure 5-11. The surface of a particle of Purolite PPC-100H
taken under an optical microscope.**

All types of particles are generally spherical, and hence a sphericity of 1 is assumed. Although the density is supplied by the manufacturer/supplier of the particles, the figure is an approximation. In the case of Styrocell, it is thought that pores of air may be trapped in the particle during the manufacturing process, which would explain why a fraction of particles float in water, despite the density being stated as being in the range 1020-1050kg/m³. Purolite expands when wet and because it is an ion exchange resin, the density depends upon what

ions the particles have come into contact with. Since Purolite expands when wet, it was left in water for approximately a week after sieving. Settling velocity tests were then carried out on a random sample of typically 50 individual particles in a sieved size range. The internal diameter of the settling column used was 0.25m and the maximum particle diameter can be assumed to be no more than 5.6mm from the sieve sizes used. Hence, from Figure 2-2, adapted from Fidleris & Whitmore (1961) which accounts for wall effects on the terminal settling velocity of a particle, the diameter of the settling column was sufficient to be able to neglect these. The temperature of the fluid was taken before and after the settling tests so that the density and viscosity of the water could be determined. Each settling test allowed the particle to settle an adequate distance to allow the terminal settling velocity to be achieved. Using a stop watch, the particle would then be timed to fall a predetermined distance.

Characterising the particle size was considered using the Malvern Mastersizer. This apparatus can characterise the size distribution of particles through laser diffraction. The instrumentation has several limitations however that made it unsuitable for this. Firstly, the measurement of particle size is limited to a maximum of 2mm and the smallest sieve size range of Styrocell is 1.4-2.0mm, which borders on this limit. Purolite has the complication that it expands when wet and characterising dry samples would not give a representative size distribution. The Malvern Mastersizer does have the means to characterise wet samples. However, using tap water, dissolved gases are released from the fluid and bubbles start to form which stick to the cell through which the laser passes and measurements taken. The bubbles can also cause the particles to flocculate. A further complication is that if the analysis is carried out before the gases have time to be released from solution, the cell window mists, due to the air adjacent to the cell window being cooled below the dew point which results in the formation of condensation on the cell window and an erroneous measurement. A possibility to overcome this is to use distilled water. However, distilled water will not contain the same ions present in tap water and this could affect the properties of the particles which in turn could affect the size.

The diameter was therefore determined by measuring a random sample of typically 50 individual water soaked particles in a sieved size range using Vernier Callipers, taking care not to squash the particle whilst taking its diameter. Ideally the diameter of all the particles in the sample used in the settling velocity tests would be taken, but due to the size of the particles, ease of handling did not allow this. Assuming the sphericity to be 1 and with the

mean settling velocity and mean particle diameter known, as well as the fluid density and viscosity, a mean particle density can be calculated. This involves calculating the particle Reynolds number, Equation 2-5, which is then used to calculate the drag coefficient from Equation 2-6 proposed by Turton and Levenspiel (1986). The drag coefficient is then used in Equation 2-4 to calculate the particle density. This has been done for all the particle sieve size ranges used in retention efficiency testing. The settling velocity data and particle diameters measured are presented in Tables F1 to F6, Appendix F. Each table also details the standard deviation as a percentage of the mean where it can be seen that the standard deviation is on average approximately 9% for both settling velocity and particle diameter. Table 5-2 presents the particle properties where the mean settling velocity is calculated at 20°C so that a direct comparison of the settling velocity of the particles can be made. It has been found by calculating the particle Reynolds number for all the particles in Table 5-2 that each has a terminal settling velocity that is in the intermediate drag regime at 20°C.

By timing the particle over a sufficiently large distance such that the average time for the particles to descend was of the order of 21 seconds, the error in the terminal settling velocity is estimated to be less than 1.5%. The Vernier callipers measure to 0.01mm. The smallest particles are Purolite 500-600 microns, hence, assuming the Vernier callipers are accurate to 0.01mm, the largest error in the particle diameter is also estimated to be of the order of 1%. It is therefore assumed that the errors introduced in measurement are small and the 99.8% confidence interval has therefore been determined for the settling velocity and particle diameter. Using the upper 99.8% confidence value for settling velocity and lower value for diameter (fast settling particle with small diameter and hence low drag) gives an upper value for the particle density. The inverse gives a lower value for particle density. This is a conservative estimate for the range of the particle density as it was observed during the settling tests that smaller particles tended to settle slower.

The data for the 99.8% confidence interval is presented in Tables F7 to F12, Appendix F.

Table 5-2. Derived particle properties used for testing a 0.75m diameter Grit King$^®$.

Particle type and sieve size range	Mean settling velocity at 20°C, / m/s	Mean diameter, / m	Mean density, / kg/m^3
Purolite (PPC-100H) 500-600microns	0.03073	0.57×10^{-3}	1372
Purolite (A100) 500-710microns	0.00742	0.55×10^{-3}	1064
Purolite (A100) 710-1000microns	0.00999	0.72×10^{-3}	1057
Styrocell 1.4-2.0mm	0.02144	1.74×10^{-3}	1036
Styrocell 2.0-2.8mm	0.02910	2.28×10^{-3}	1037
Styrocell 2.8-5.6mm	0.03519	2.80×10^{-3}	1036

Due to the sieve sizes available at the time of grading, Purolite A100 could not be sieved from 500 to 600microns. The significant difference in density between Purolite A100 and PPC-100H is due to each being produced from different materials to produce two different types of resin.

At the start of each retention efficiency test, the Grit King$^®$ was allowed to fill with water and left to run until air had stopped passing through the vent box. This was air that was trapped between the dip plate and the walls of the Grit King$^®$ when the water level rose above the bottom of the dip plate. The butterfly valve was then adjusted to attain the desired flowrate and the system was again left to run for several minutes to allow a steady flow to develop. Faram *et al.* (2003) have shown through experimentation that the efficiency of such devices is time dependent as particles captured in the grit pot may be re-entrained into the flow. Each retention efficiency test was therefore carried out for a duration of 10 minutes and the temperature of the fluid was taken at the start and end of each test. At the end of each test the butterfly valve was closed before switching off the pump to prevent particulates remaining in the HDVS from being flushed out by water remaining in the header tank. The HDVS efficiency is defined as the volume of particles remaining in the HDVS after 10 minutes expressed as a percentage of the volume released into the HDVS. Measuring the volume of particles instead of mass was justified by the fact that excess water held between the particles by surface tension would be included in the mass and would therefore be erroneous. Drying the particles after each test would have been extremely time consuming. As the total volume of particles collected was the same as the volume introduced at the inlet then the error in determining the efficiency by volumetric measurement would be negligible.

The particles of Styrocell were collected by placing around the overflow a pair of Lycra$^®$ opaque tights (70 Denier, XL), which will be referred to as a 'sock'. The Purolite was

collected by placing a filter bag around the overflow made from Petex 07-225/42 Polyester (PET) monofilament precision fabric manufactured by Sefar. The filter bag allowed the fluid to pass more freely over the overflow and quite clearly did not present any additional head loss across the separator. A disadvantage was that the filter bag required a second person to hold it around the overflow due to the nature of the material in that it could not be easily tied without it slipping under the force of the fluid discharging from the Grit King®. To assess whether the sock caused backfilling to occur, a set of measurements of the distance from the free surface inside the central shaft to the top of the central shaft were made at a number of flowrates with and without the sock. These are shown in Figure 5-12 and clearly, backfilling did not occur and the head loss across the separator was unaffected.
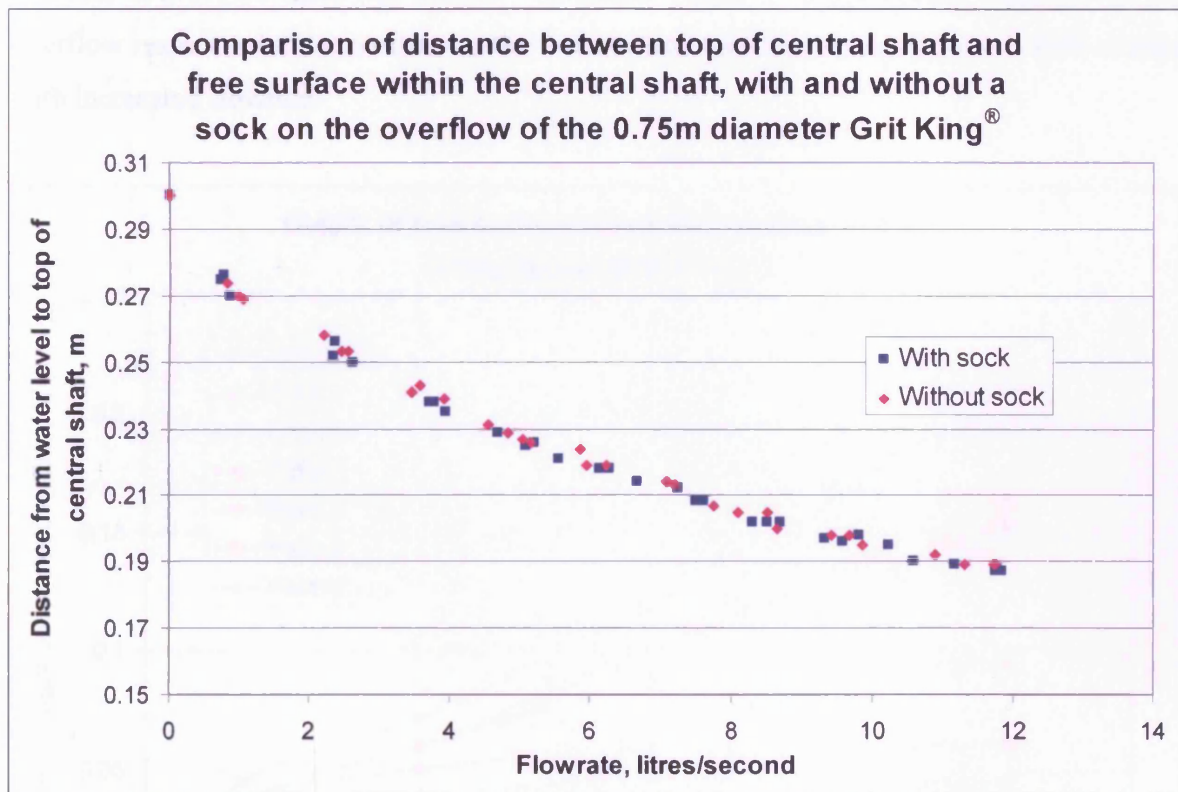
Figure 5-12. Comparison of distance between the top of the central shaft and the water level within the central shaft with and without a sock on the overflow.

Comparison of retention efficiency using approximately 90ml and 410ml of Purolite A100 710-1000microns was made where it was found that the efficiency was independent of the volume of particles used. The same result was also obtained when a comparison was made between volumes of approximately 330ml and 900ml of Styrocell 1.4-2.0mm. Hence, it is assumed that for all tests, the efficiency is independent of the volume of particles used.

5.3   Results

5.3.1   Free surface measurements

Figure 5-13 shows how the height of the free surface varies with flowrate at points 1 to 6 and in the vent box. Error bars indicating the fluctuation in the free surface are not shown for clarity. Due to the fluctuations, although fairly small, the height of the fluid was measured at just a few flowrates so that the general trend in the behaviour of the free surface could be established. From Figure 5-13, at Point 1, where the overflow annulus joins the overflow channel, there is a slow but steady increase in the height of the free surface with increasing flowrate. At points 2, 3 and 4 located on the rear half of the overflow annulus and within the vent box, there appears to be a linear trend in the height of the free surface with increasing flowrate above 1.38 litres per second. At points 5 and 6 on the central shaft and at the overflow respectively, the position of the free surface soon plateaus and there is little change with increasing flowrate.

Height of free surface above the overflow in the 0.75m diameter Grit King®
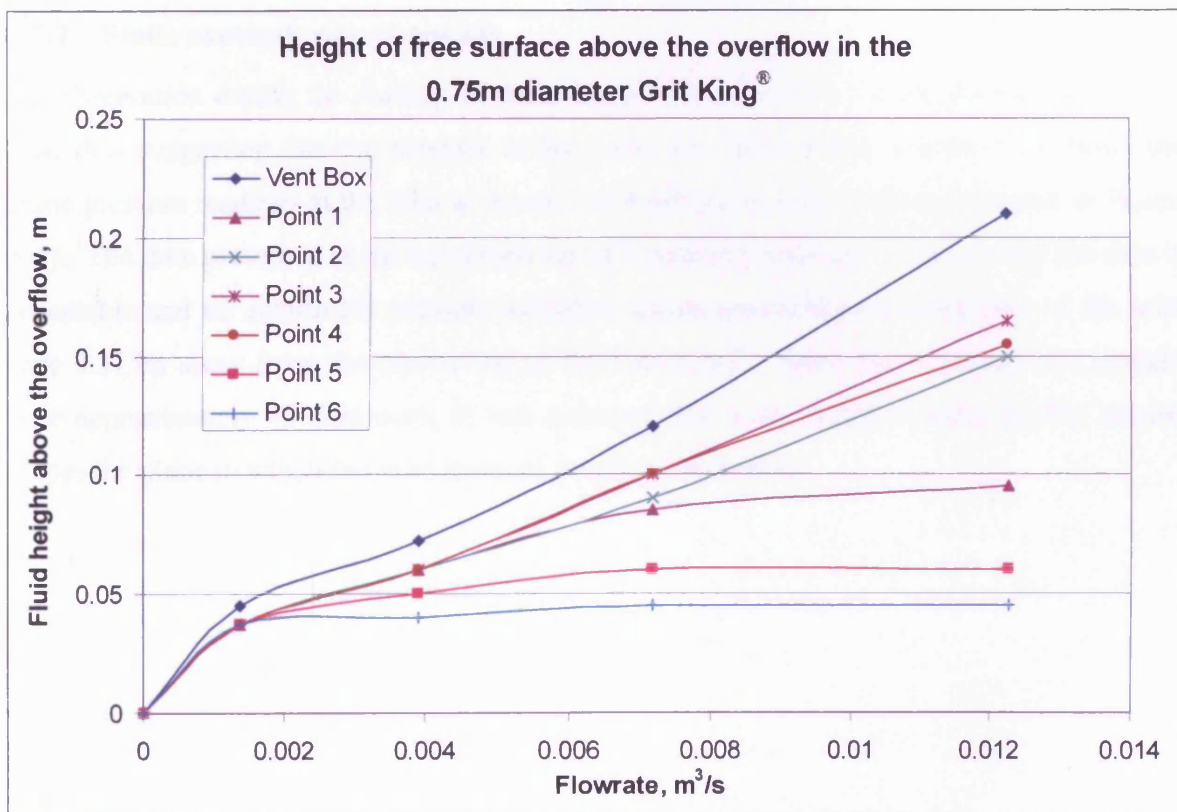
Figure 5-13. Variation of the height of the free surface above the overflow in the 0.75m diameter Grit King®.

Equations 5-2 to 5-8 in Table 5-3 have been derived from least square fits to the data presented in Figure 5-13 and each describes the height, h (m), of the free surface at each

point in Figure 5-4 as a function of the inlet flowrate, Q (m³/s). Each equation in Table 5-3 is valid between inlet flowrates of 1.38 and 12.25 litres per second. The minimum R_t^2 value for the fits was 0.971. Hence, each of Equations 5-2 to 5-8 gave a good fit to the data.

Table 5-3. Equations that describe the height of the fluid above the overflow in the 0.75m diameter Grit King®.

Point	Equation		
Vent Box	$h = 457.94Q^2 + 9.0042Q + 0.0312$	(5-2)	$R_t^2 = 0.998$
1	$h = -551.5Q^2 + 12.937Q + 0.0195$	(5-3)	$R_t^2 = 0.998$
2	$h = 10.4Q + 0.0201$	(5-4)	$R_t^2 = 0.995$
3	$h = 11.929Q + 0.0169$	(5-5)	$R_t^2 = 0.996$
4	$h = 11.009Q + 0.02$	(5-6)	$R_t^2 = 0.998$
5	$h = -365.67Q^2 + 7.107Q + 0.0279$	(5-7)	$R_t^2 = 1.000$
6	$h = -109.42Q^2 + 2.2751Q + 0.0337$	(5-8)	$R_t^2 = 0.971$

5.3.2 Static pressure measurements

An observation during the reading of the static pressure was that the fluctuations were very low, thus suggesting that the pressure at the walls was fairly stable. Figure 5-14 shows the static pressure readings at the inlet at points 1 to 4 (all points refer to those indicated in Figure 5-5). The data presented is the combined set of 3 series of readings. Quite clearly the data is repeatable and no significant pressure variation occurs around the circumference of the inlet pipe 0.375m away from the centre line of the Grit King®. Since the inlet pipe is a straight pipe approximately 45 diameters, it was assumed that a developed velocity profile existed across the plane in which the inlet pressure readings were taken.
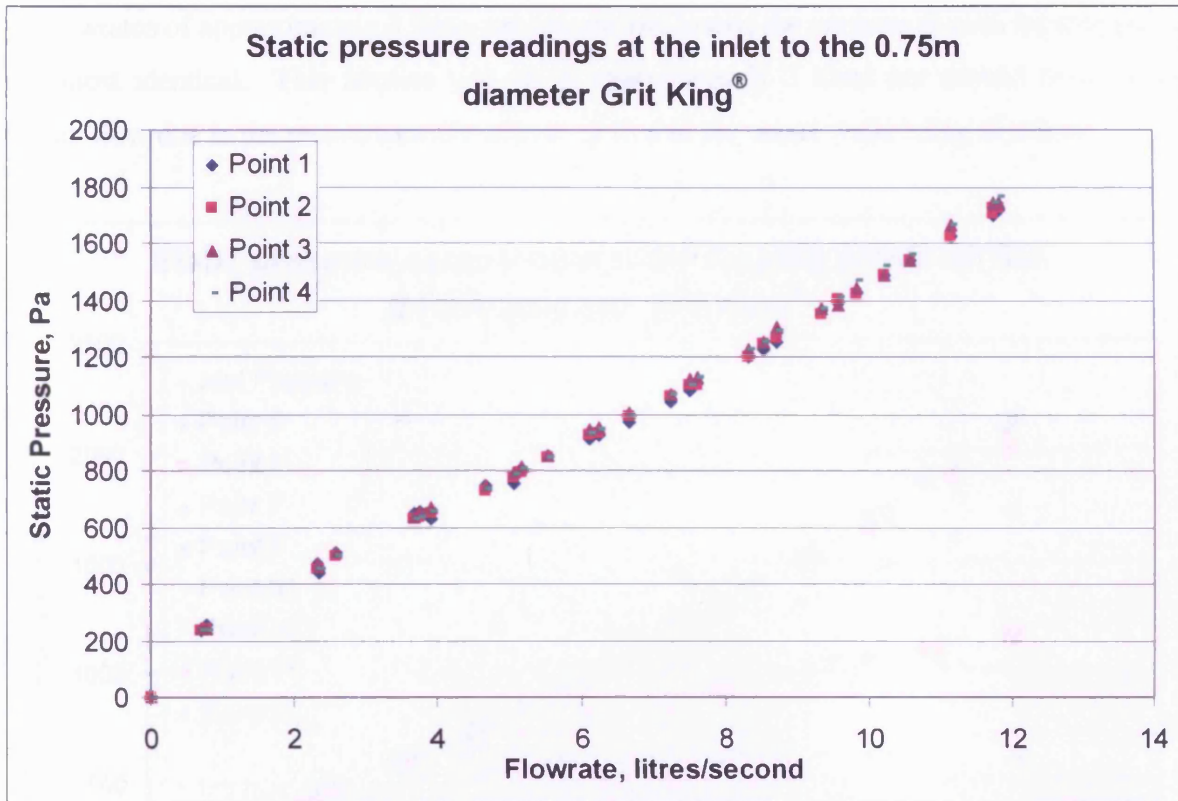
Figure 5-14. Static pressure readings at the inlet to the 0.75m diameter Grit King®.

Figure 5-15 presents the static pressure readings taken on the walls of the HDVS. The data are the combined set of 3 series of readings and the repeatability of the data is consistent. Points 5 to 8 are located around the central drum of the separator and the readings indicate that there is an equal pressure distribution around the outer circumference of the device which is slightly higher than the pressure at the inlet. This could be due to the reduced velocity of the fluid upon expansion from the inlet into the HDVS. The static pressure readings taken at points 9 and 10 are located on the central shaft which is at the centre of the separator. Here the static pressure is low compared with the pressure on the central drum of the separator, as would be expected from a vortex flow where the pressure increases radially outwards (Svarovsky, 1984) and the rotation of the fluid creates a low pressure axial core (Bradley, 1965). The pressure distribution in a free and forced vortex has been derived in Appendix E, which in both cases, results in a pressure distribution that increases radially outwards and is in agreement with both Svarovsky (1984) and Bradley (1965). At points 11 and 12, situated on the grit pot, the static pressure is lower than at the inlet. This may be expected due to the diameter of the grit pot being less than the vessel. Hence, due to a pressure distribution which increases radially outwards, the pressure at the wall of the main vessel would be expected to be higher than in the grit pot.

At flowrates of approximately 3 litres per second and lower, the pressure at each tapping point is almost identical. This implies that up to approximately 3 litres per second there is no vortex flow due to the pressure on the central shaft and the vessel walls being identical.

Static pressure comparison at the tapping points on the 0.75m diameter Grit King®

Legend:
+ Inlet Pressure
♦ Point 5
■ Point 6
▲ Point 7
× Point 8
- Point 9
– Point 10
✳ Point 11
● Point 12
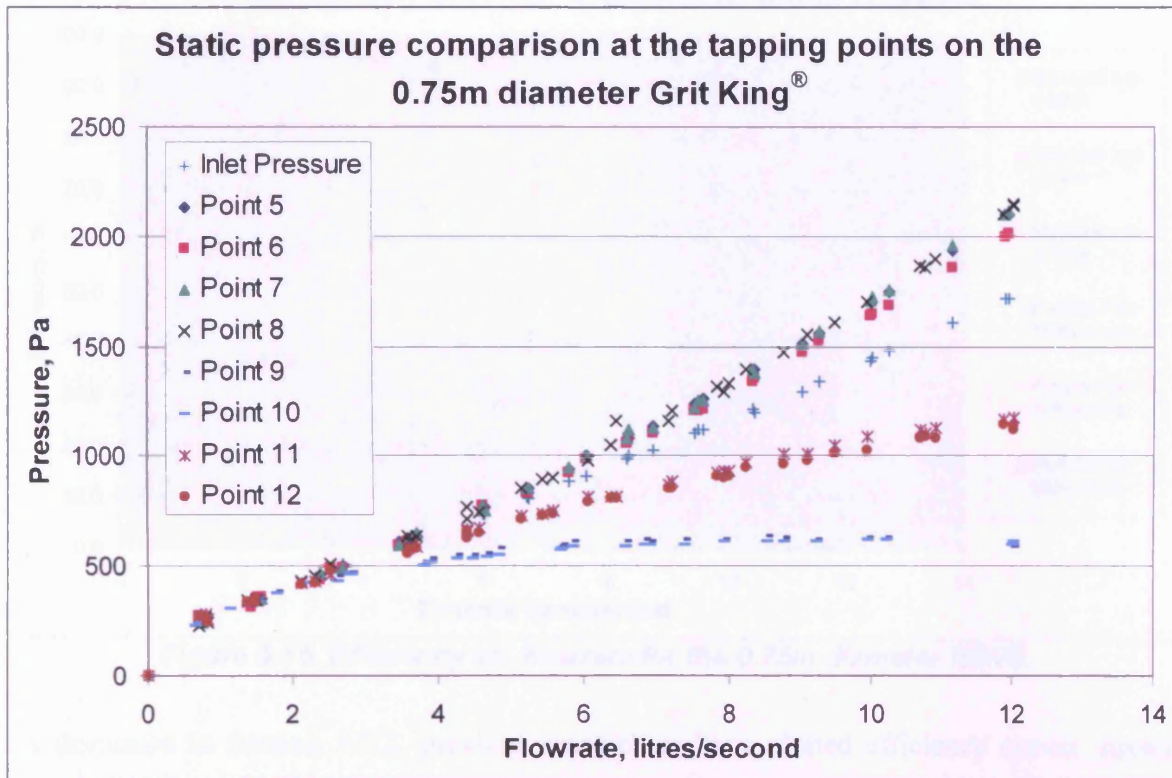
Figure 5-15. Comparison of the static pressure readings taken from the 0.75m diameter Grit King®.

5.3.3 Retention efficiency results

Tables G1 to G6, Appendix G, contain the observed retention efficiency of the 0.75m diameter Grit King®.

Plotting the retention efficiency against the inlet flowrate gives a series of curves as shown in Figure 5-16. Each efficiency curve follows a definite trend and the repeatability of the data is consistent. The data for the Purolite 500-710micron range was not repeated due to the time required to collect all the particulate. Efficiencies for Styrocell 1.4-2.0mm below 4.25 litres per second cannot be achieved because at lower flowrates, the particles tend to flocculate and begin to float. At higher flowrates, the turbulence in the flow prevents the flocs forming. Flowrates higher than 12 litres per second cannot currently be achieved due to the limitation of the pump. Initially the trend in the efficiency appears to be with the settling velocity of the particles but upon closer inspection it can be seen that the particles, Purolite 500-600microns,

have the highest efficiency despite having a settling velocity lower than Styrocell 2.8-5.6mm, as detailed in Table 5-2.

0.75m diameter Grit King® experimental efficiency results
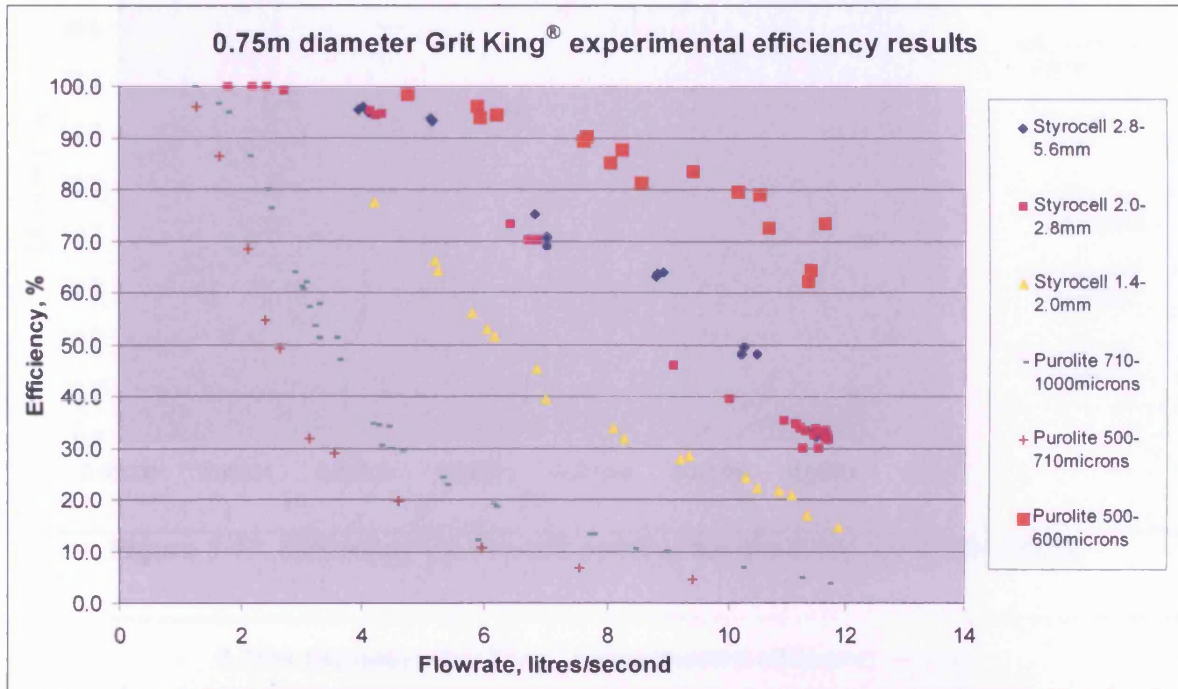
Figure 5-16. Efficiency vs. flowrate for the 0.75m diameter HDVS.

As discussed in Section 3.3.2, previous researchers have plotted efficiency curves against dimensionless groups to try and reduce the spread of the data to a single curve, which would then aid fitting a function to the data. Figures 5-17 to 5-19 show the efficiency as a function

of $\dfrac{Q^2}{D_{HDVS}^5 g}$ (Froude Number), $\dfrac{u_{p\infty} C_D^{0.5}}{U}$ (Frederick and Markland, 1967) and $\dfrac{u_{p\infty}}{U}$ (Halliwell and Saul, 1980).
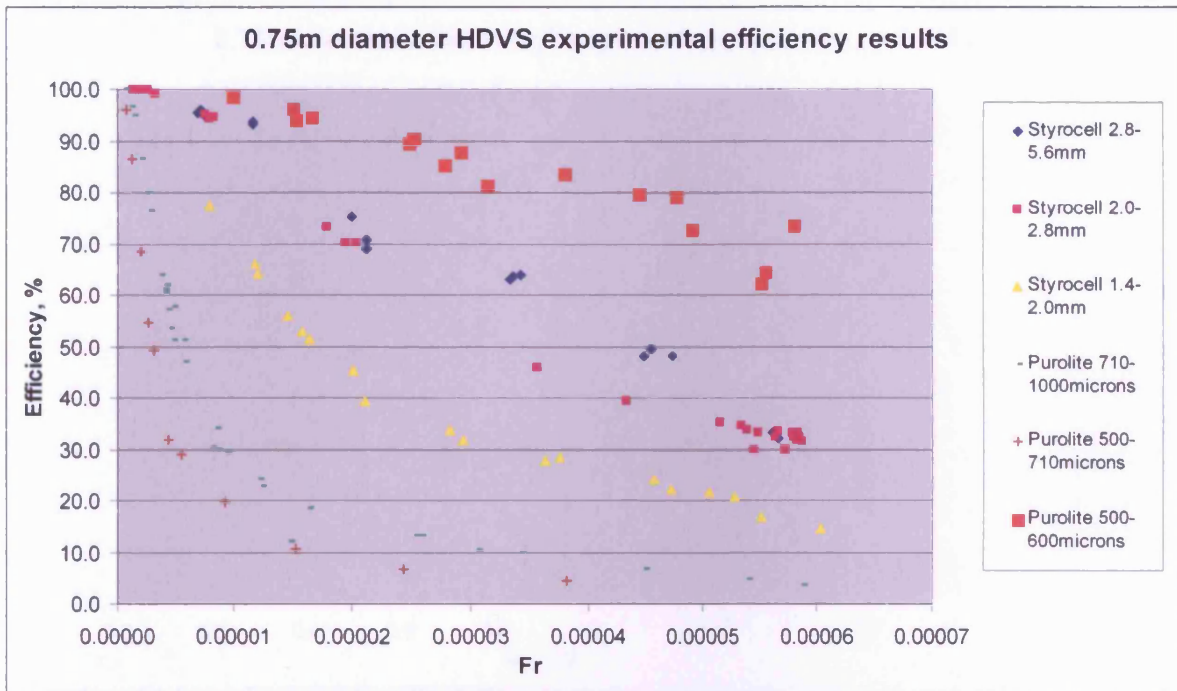
Figure 5-17. Efficiency vs. Froude number for the 0.75m diameter HDVS.
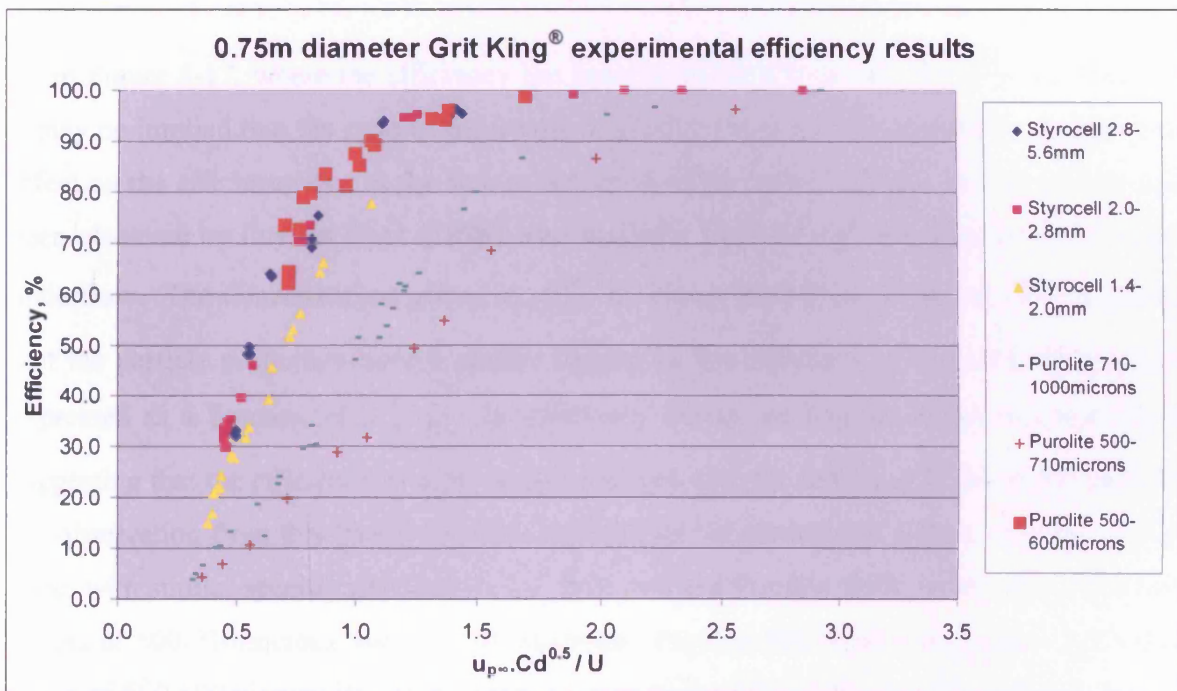
Figure 5-18. Efficiency vs. $\dfrac{u_{p\infty} C_D^{0.5}}{U}$ **for the 0.75m diameter HDVS.**

0.75m diameter Grit King® experimental efficiency results

Figure legend:
- ♦ Styrocell 2.8-5.6mm
- ■ Styrocell 2.0-2.8mm
- ▲ Styrocell 1.4-2.0mm
- - Purolite 710-1000microns
- + Purolite 500-710microns
- ■ Purolite 500-600microns
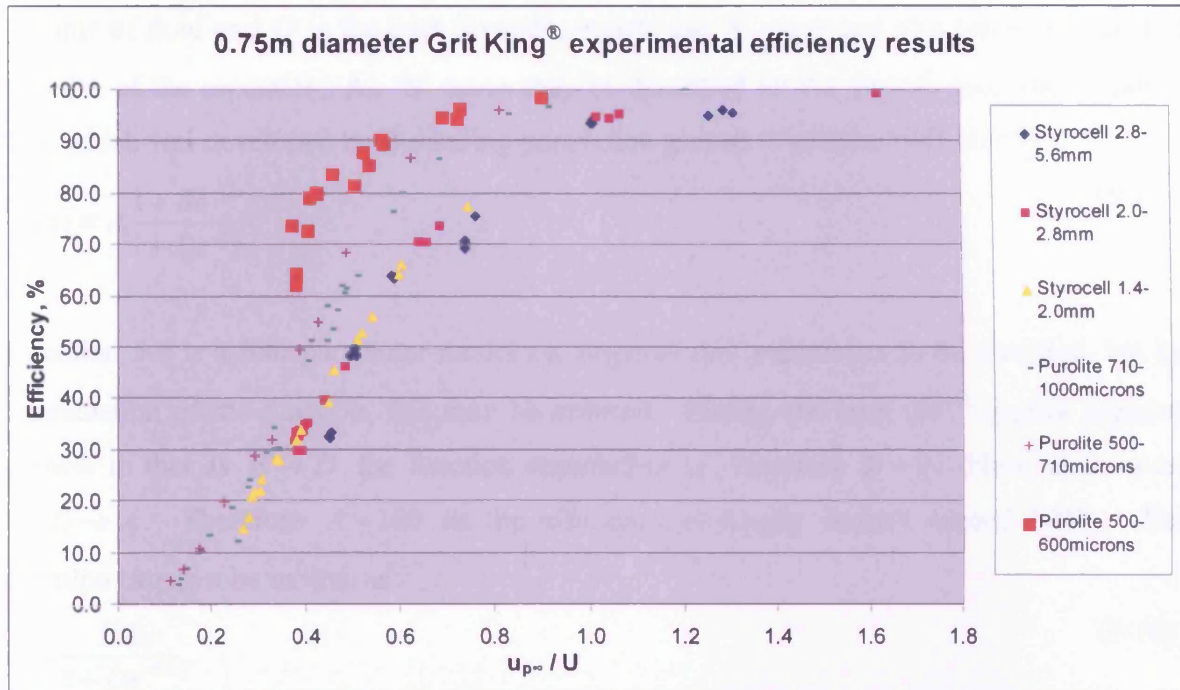
Figure 5-19. Efficiency vs. $\dfrac{u_{p\infty}}{U}$ for the 0.75m diameter HDVS.

From Figure 5-17, where the efficiency has been plotted as a function of the Froude number, it may be implied that the ratio of the inertia to gravity forces in the separator have negligible effect on the efficiency due to the lack in reduction of the spread of data. This result has also been observed by Luyckx *et al.* (1998) who studied a Storm King® operating with a constant underflow. The dimensionless group $u_{p\infty} C_D^{0.5} / U$ brings the curves closer together, implying that the particle properties have a greater impact on the efficiency. When the efficiency is expressed as a function of $u_{p\infty} / U$ the efficiency curves are brought closer together, again suggesting that the efficiency is more strongly linked with the settling velocity of the particle. An observation from this plot is that although not all the particulates align on a single curve, those with similar specific gravities do i.e. Styrocell and Purolite A100 which is in sieve size ranges of 500-710microns and 710-1000microns. Purolite PPC-100H which has a sieve size range of 500-600microns lies on a separate curve to Purolite A100 due to a different specific gravity.

Although the data has been brought closer together, a satisfactory single curve is not achieved. Figure 5-16 shows a series of curves that are in the form of a backward 'S'. Plotting efficiency as a function of V/Q, the theoretical residence time, where V is the

volume of fluid and Q is the inlet flowrate, inverts the 'S' curve and also takes into account the size of the separator. An 'S' curve may be described by the logistic function, Equation 5-9, which was developed for modelling population growth (Verhulst, 1845, 1847).

$$f(x) = A\frac{1 + Be^{-Cx}}{1 + De^{-Cx}}$$
(5-9)

Equation 5-9 is a four parameter model i.e. requires four parameters to be specified, but by examination of the function, this may be reduced. Firstly, the term Be^{-Cx} applies negative growth in that as $B \to D$ the function approaches A, therefore $B = 0$. Now, as $x \to \infty$, $f(x) \to A$. Therefore $A = 100$ as the efficiency obviously doesn't exceed 100%. The function can now be written as

$$\eta = \frac{100}{1 + De^{-Cx}}$$
(5-10)

Where: η = HDVS efficiency, %

Equation 5-10 is now a two parameter model. The coefficients that give the best fit in a two parameter model may be determined using an optimisation technique by Guymer (2002) (see Section 2.2.3). This has been done for each efficiency curve when plotted against V/Q and Table 5-4 lists the R_t^2 value and the values for C and D for each class of particle.

Table 5-4. The parameters C and D derived for the fit of the logistic function to each efficiency curve and the R_t^2 value defining the quality of the fit.

Particle type and sieve size range	C	D	R_t^2
Purolite (A100) 500-710microns	0.036	37.1	0.999
Purolite (A100) 710-1000microns	0.046	32.8	0.998
Styrocell 1.4-2.0mm	0.074	21.8	0.998
Styrocell 2.0-2.8mm	0.100	20.1	1.000
Styrocell 2.8-5.6mm	0.109	18.5	0.996
Purolite (PPC-100H) 500-600microns	0.120	6.9	0.998

If it is assumed that at an arbitrary flowrate, the fluid viscosity, fluid density, particle shape, chamber volume and gravity are all constant, then the only variables are the particle diameter and particle density. It has been found by plotting various quantities for the full range of particles used, that the quantity that appears to be controlling the efficiency is given by Equation 5-11 and has units of kg/m^2. This is therefore analogous to a particle surface load.

$$m_d = d(\rho_p - \rho_f)$$ (5-11)

Where: m_d = Particle surface load, kg/m^2

Table 5-5 compares the average particle surface load defined by Equation 5-11 with the average settling velocity of the particles.

**Table 5-5. Comparison of the average
particle surface load with the average particle settling velocity at 20°C.**

Particle type and sieve size range	Particle surface load, / kg/m^2	Mean settling velocity at 20°C, / m/s
Purolite (A100) 500-710microns	0.035	0.00742
Purolite (A100) 710-1000microns	0.041	0.00999
Styrocell 1.4-2.0mm	0.063	0.02144
Styrocell 2.0-2.8mm	0.084	0.02910
Styrocell 2.8-5.6mm	0.101	0.03519
Purolite (PPC-100H) 500-600microns	0.211	0.03073

Hence, by comparison of the average particle surface load in Table 5-5 with the efficiency curves in Figure 5-16, it can be seen that the greater the average particle surface load, the higher the expected efficiency. Thus, plotting C and D in the logistic equation against the particle surface load, it can be seen from Figures 5-20 and 5-21 that a clear function exists, which also gives confidence in the derived properties from the settling velocity tests. Those points that have been circled are 'dummy' points, used to aid fitting a trendline. These points are justified in that they aid the function to consistently predict efficiency curves that increase as the particle surface load increases, as observed with the experimental data.

Relationship between C (logistic function) and the particle surface load for the 0.75m diameter Grit King®

$$y = 19922x^6 - 19636x^5 + 7349.3x^4 - 1304.5x^3 + 106.87x^2 - 2.5485x + 0.041$$
$$R^2 = 0.9993$$
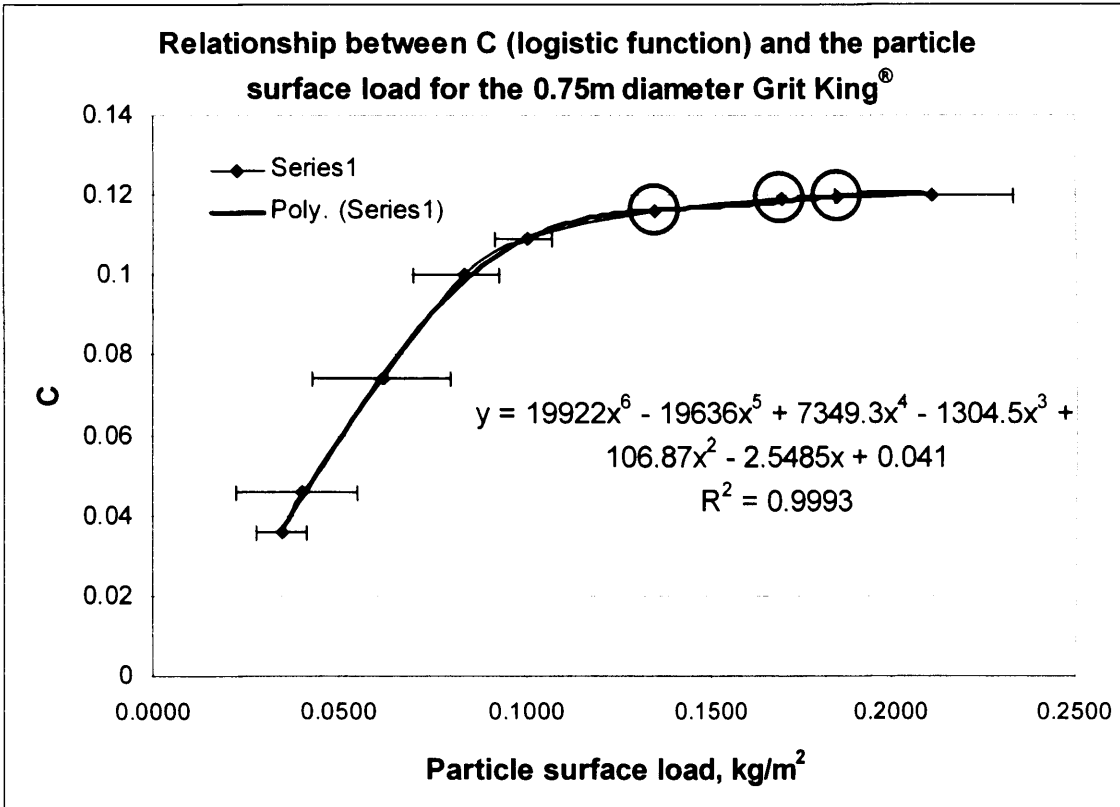
Figure 5-20. Relation between the parameter 'C' and the particle surface load.

Relationship between D (logistic function) and the particle surface load for the 0.75m diameter Grit King®

$$y = -3E+06x^5 + 2E+06x^4 - 479244x^3 + 61092x^2 - 3808.4x + 113.86$$
$$R^2 = 0.9983$$
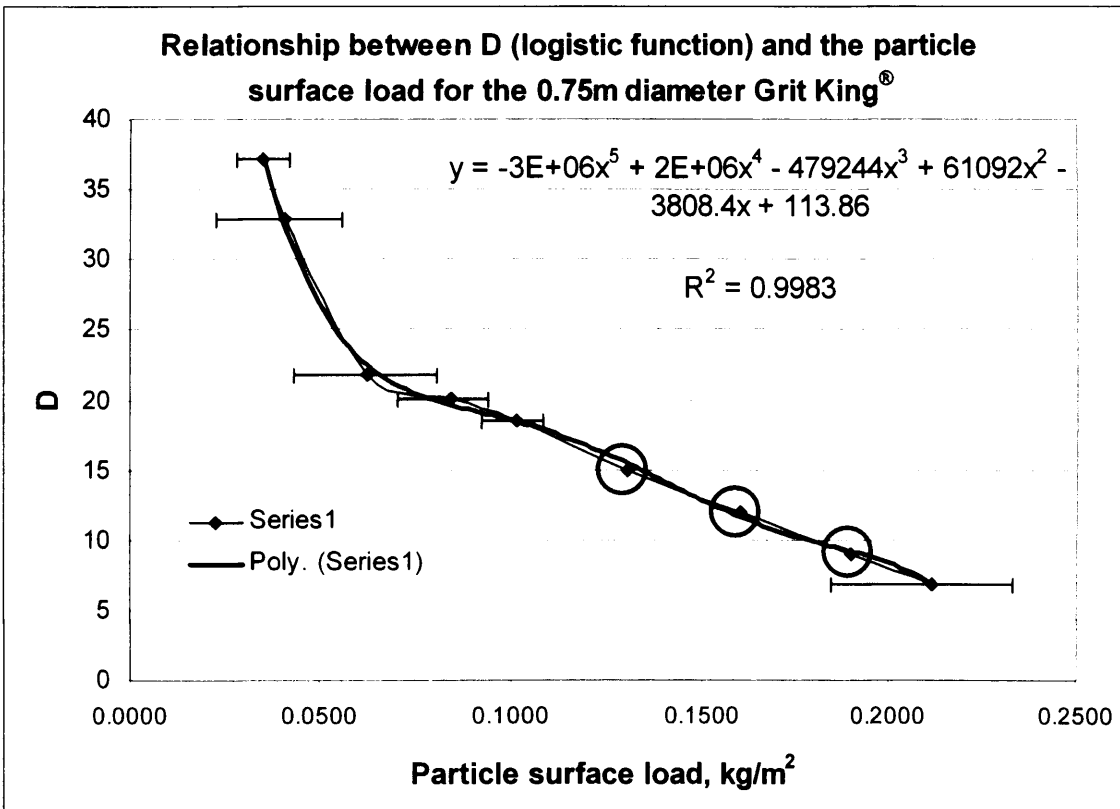
Figure 5-21. Relation between the parameter 'D' and the particle surface load.

Hence, with functions for the two parameters in the logistic function, the efficiency may be predicted for the 0.75m diameter HDVS for any particle with a surface load in the range for which experimental testing has been carried out. The model, Equations 5-10, 5-12 and 5-13, are thus dependent on the inlet flowrate which is the same as the overflow flowrate, the volume of fluid and the particle density and diameter. The fluid volume is taken as 0.26m³ as the experimental test duration of 10 minutes included the time taken for the particles to pass through the inlet pipe.

$$\eta = \frac{100}{1 + De^{-C\frac{V}{Q}}} \tag{5-10}$$

$$C = 19922m_d^6 - 19636m_d^5 + 7349.3m_d^4 - 1304.5m_d^3 + 106.87m_d^2 - 2.5485m_d + 0.041 \tag{5-12}$$

$$D = -2590788m_d^5 + 1797185m_d^4 - 479244m_d^3 + 61092m_d^2 - 3808.4m_d + 113.86 \tag{5-13}$$

Figures 5-22 to 5-27 shows a good fit by the model to each efficiency curve.

0.75m diameter Grit King® efficiency results

Legend:
- ■ Purolite 500-600microns
- ♦ Styrocell 2.8-5.6mm
- ■ Styrocell 2.0-2.8mm
- ▲ Styrocell 1.4-2.0mm
- - Purolite 710-1000microns
- + Purolite 500-710microns
- × Model (Purolite 500-710microns)

X-axis: Fluid volume / Inlet flowrate, s
Y-axis: Efficiency, %

Figure 5-22. Comparison of the model and experimental retention efficiency results for the 0.75m diameter HDVS.

Figure 5-23. Comparison of the model and experimental retention efficiency results for the 0.75m diameter HDVS.

Figure 5-24. Comparison of the model and experimental retention efficiency results for the 0.75m diameter HDVS.
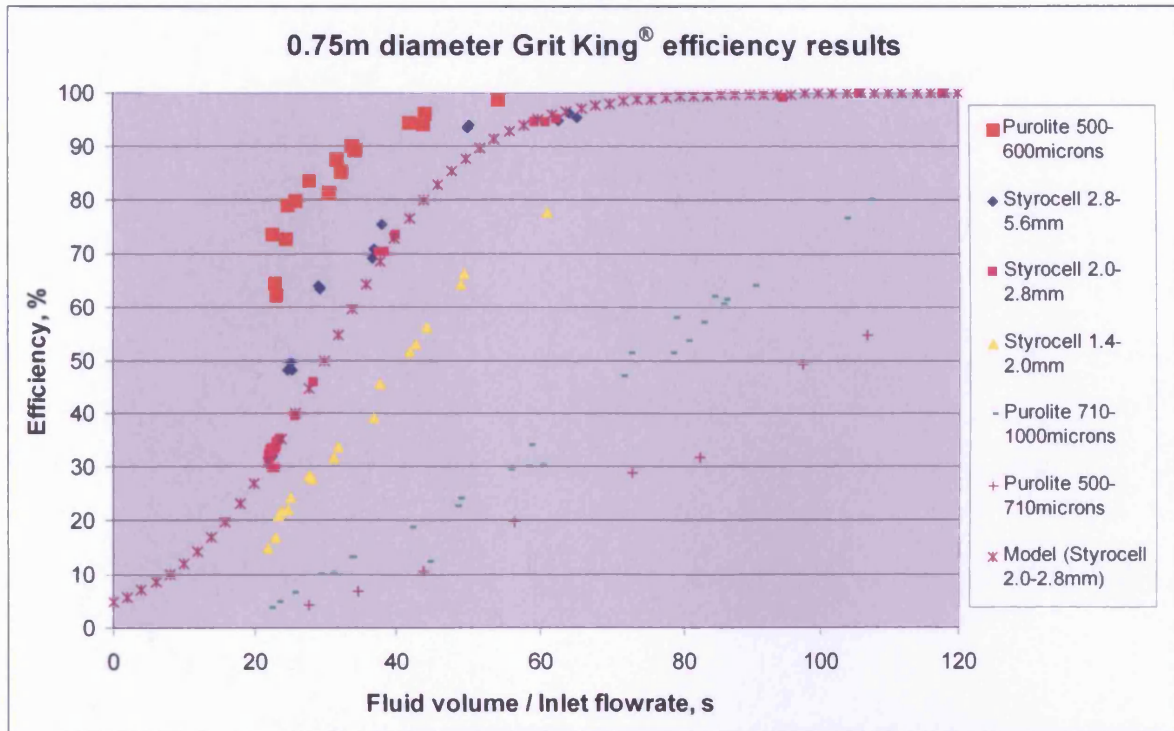
Figure 5-25. Comparison of the model and experimental retention efficiency results for the 0.75m diameter HDVS.
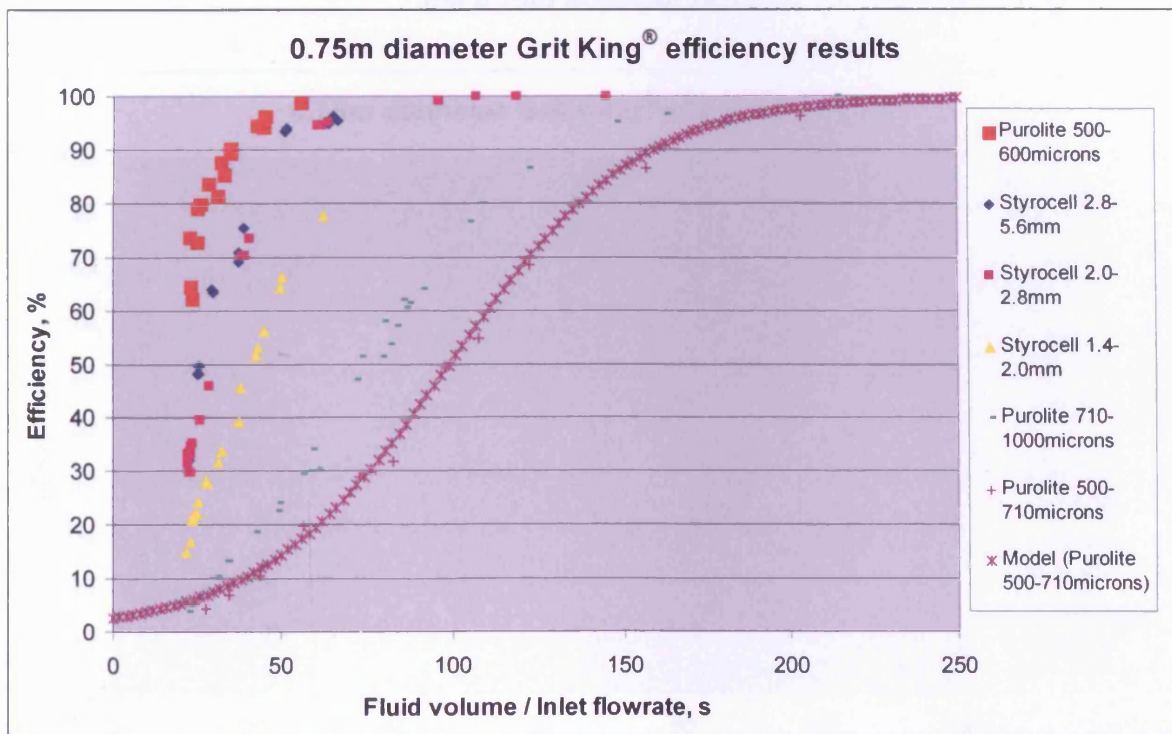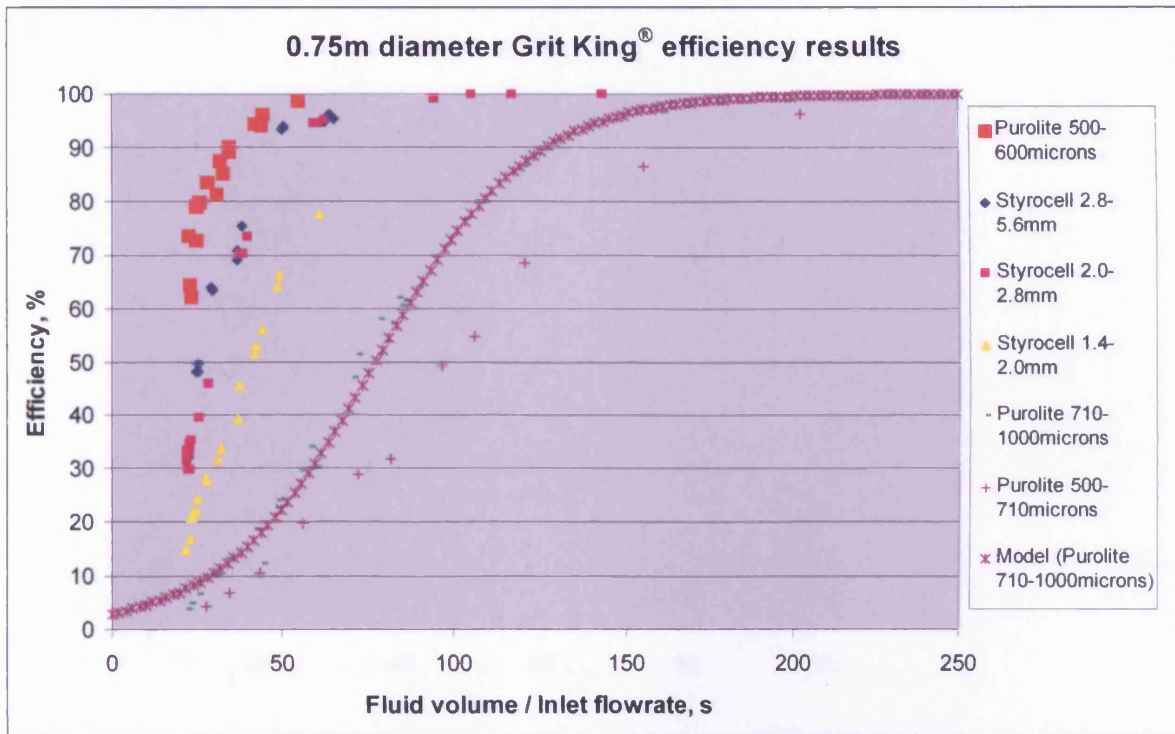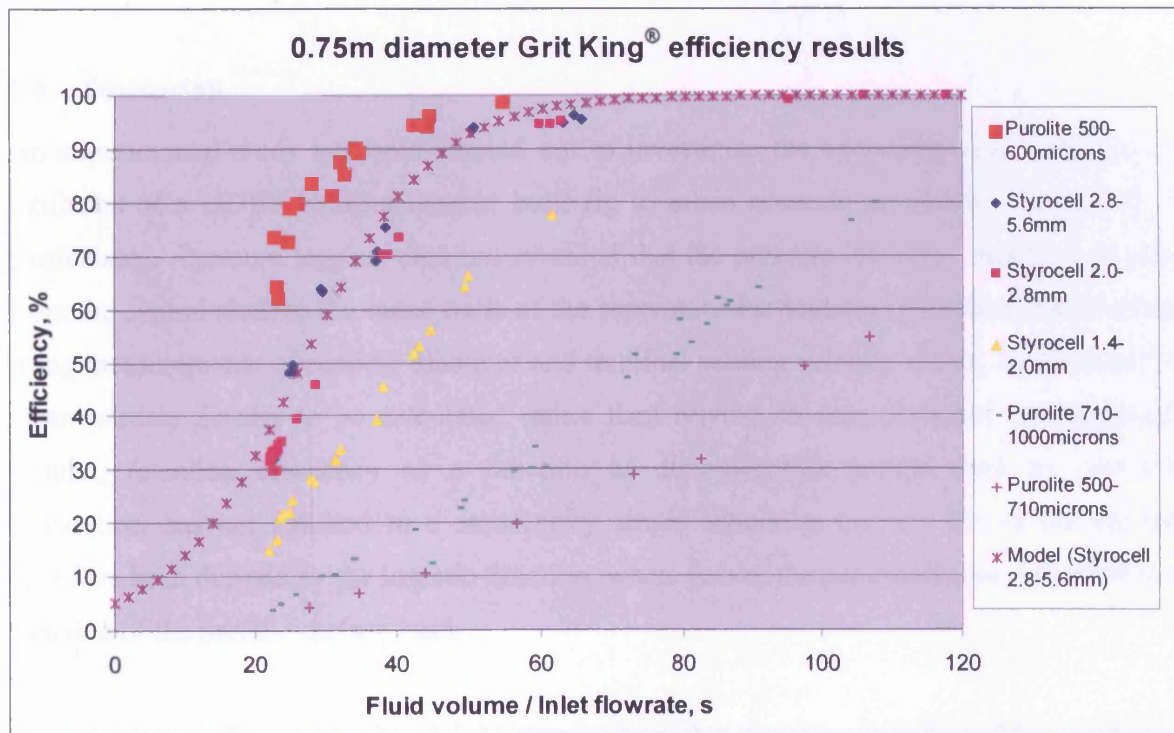

Figure 5-26. Comparison of the model and experimental retention efficiency results for the 0.75m diameter HDVS.
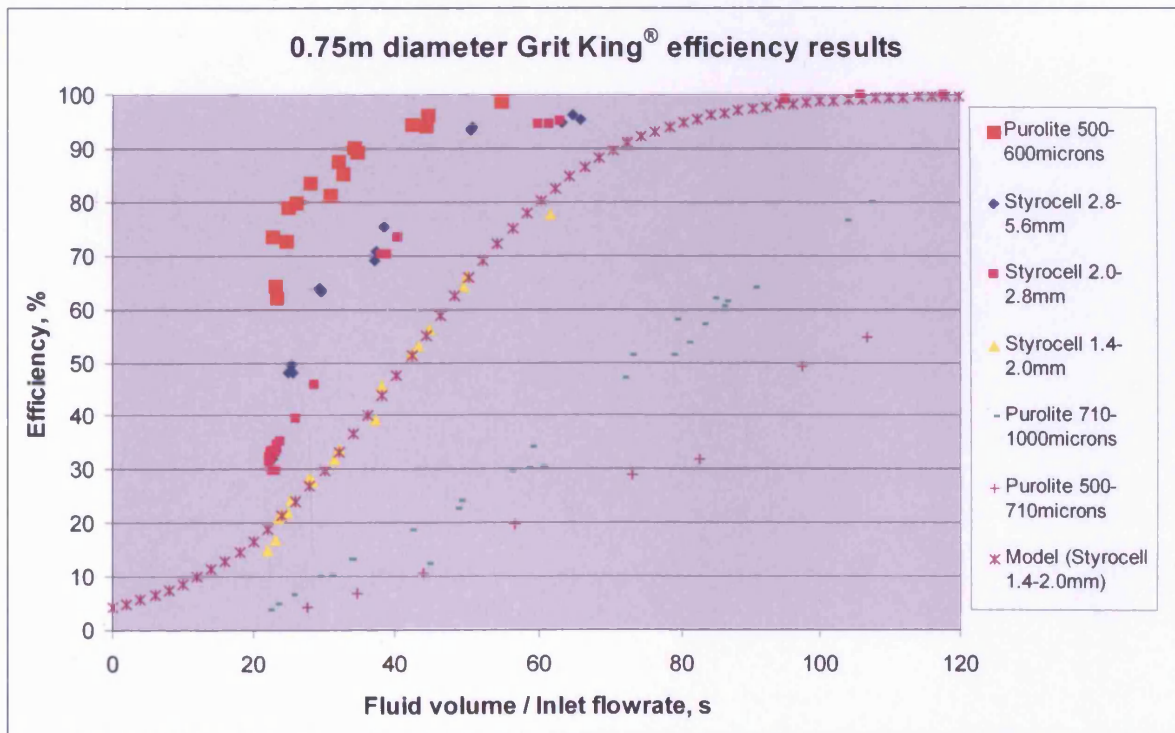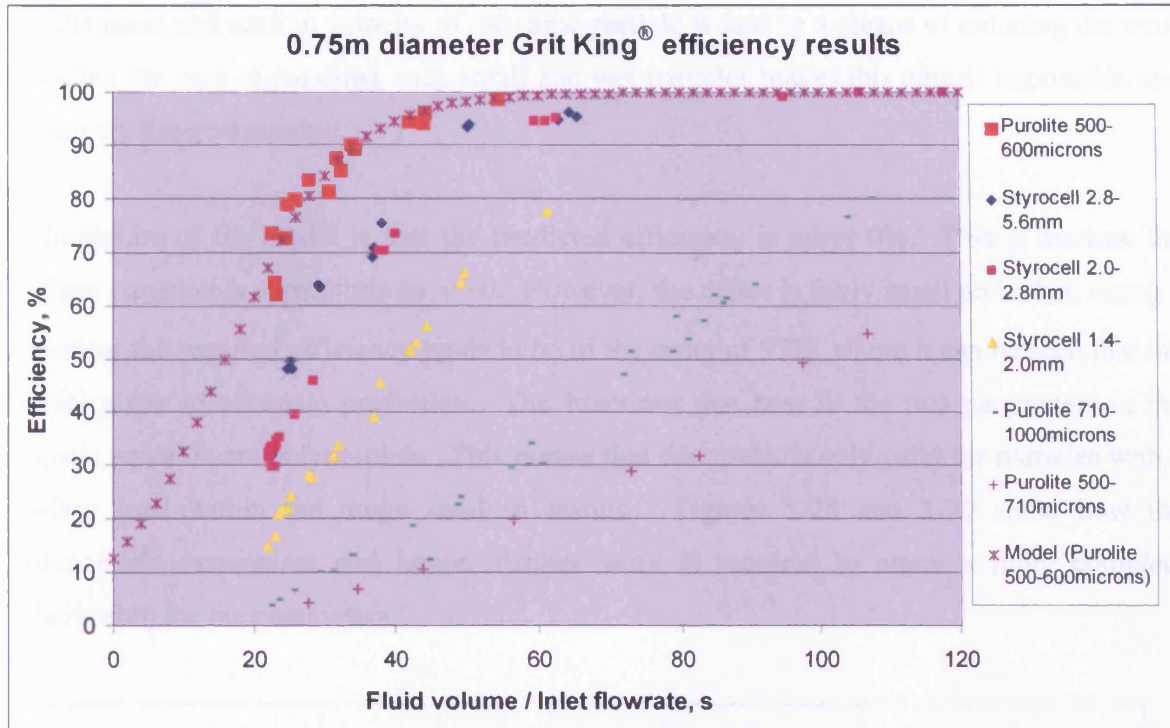
Figure 5-27. Comparison of the model and experimental retention efficiency results for the 0.75m diameter HDVS.

5.4 Discussion

An experimental study has been carried out to investigate the operational and performance attributes of a HDVS using a custom built rig to attain accurate separation efficiencies of particulates. Pressure tapping data has revealed that the pressure increases radially outwards from the central shaft to the outer walls of the separator. Particulates have been characterised using measurements of particle diameter and terminal settling velocity which has allowed the mean particle density to be calculated rather than relying on manufacturers specifications. Plotting retention efficiency as a function of dimensionless groups used by previous researchers has not resulted in a satisfactory single efficiency curve. The efficiency has therefore been defined by the logistic function, where two of the parameters are described as a function of the particle surface load.

The error bars in Figures 5-20 and 5-21 clearly show that by taking a high confidence interval and using the upper limit of settling velocity with the lower limit of the particle diameter to calculate the upper limit of the particle density and vice versa for the lower limit, the range in which the particle surface load lies can be quite generous. As already discussed, measuring

the diameter and settling velocity of the same particle would be a means of reducing the error bars, but the ease of handling such small and wet particles makes this almost impossible and extremely time consuming.

A limitation of the model is that the predicted efficiency is never 0%. This is because the logistic equation is asymptotic to $y = 0$. However, the offset is fairly small and when sizing a separator the required efficiency tends to be of the order of 95%, where it can be seen that the model gives an adequate prediction. The functions that best fit the two parameters in the logistic equation are polynomials. This means that the model is only valid for particles with a surface load within the range used in testing. Figures 5-28 and 5-29 show how the polynomials extrapolate and hence, further work is required to attain a more complete relationship for the parameters.
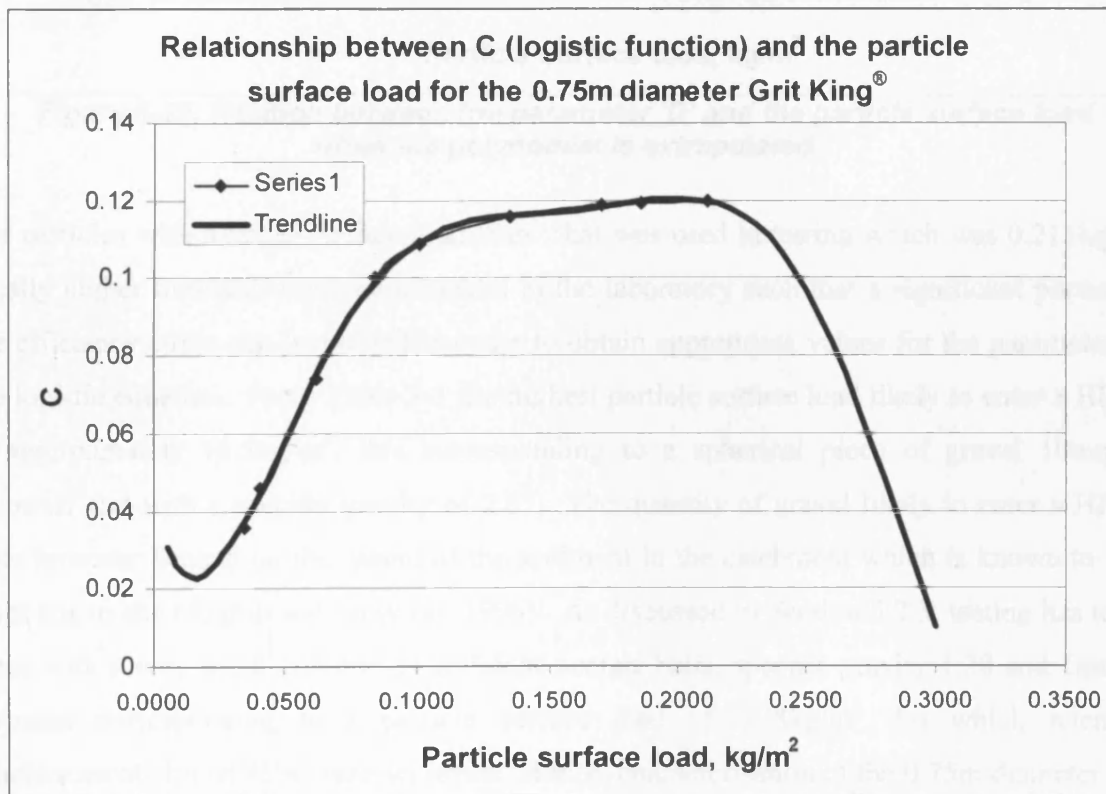
Figure 5-28. Relation between the parameter 'C' and the particle surface load when the polynomial is extrapolated.
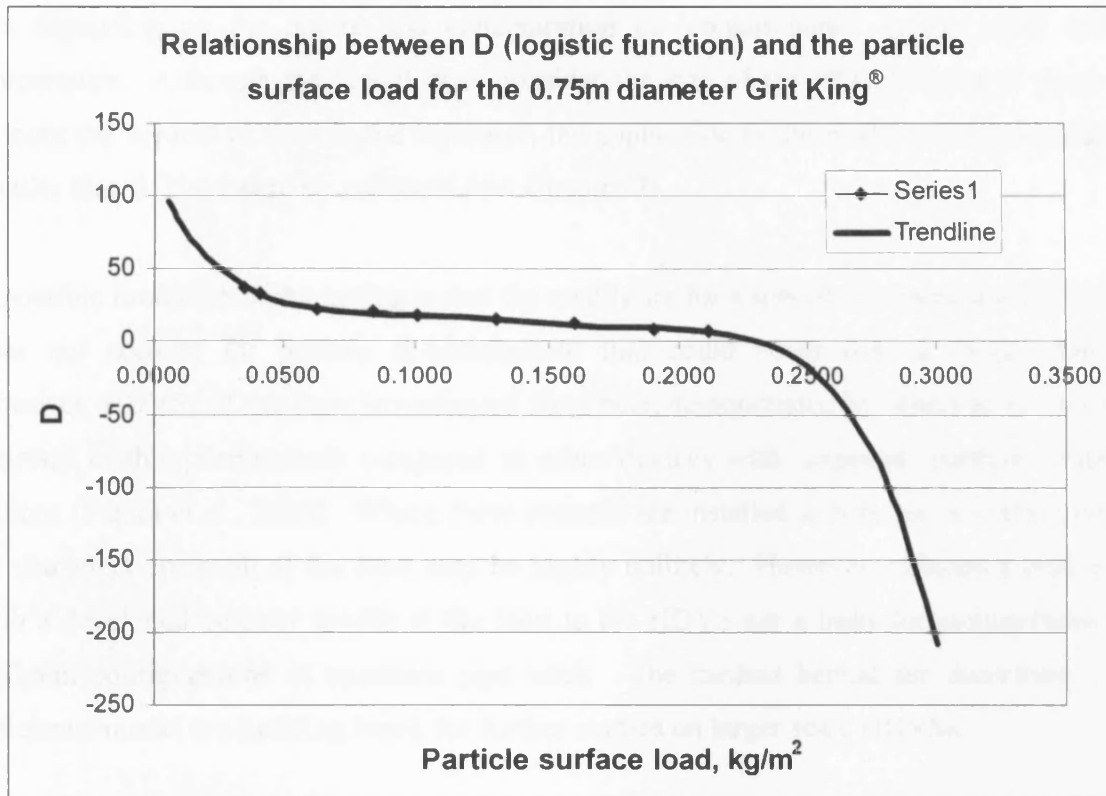
Figure 5-29. Relation between the parameter 'D' and the particle surface load when the polynomial is extrapolated.

For particles with a larger surface load than what was used in testing which was 0.211kg/m^2, ideally higher flowrates must be achieved in the laboratory such that a significant portion of the efficiency curve can be plotted in order to obtain appropriate values for the parameters in the logistic equation. From Table 3-1 the highest particle surface load likely to enter a HDVS is approximately 16.5kg/m^2, this corresponding to a spherical piece of gravel 10mm in diameter and with a specific gravity of 2.65. The quantity of gravel likely to enter a HDVS does however depend on the nature of the sediment in the catchment which is known to vary from site to site (Andoh and Smisson, 1996). As discussed in Section 5.2.3, testing has taken place with a very small quantity of cellulose acetate balls, specific gravity 1.28 and 1mm in diameter corresponding to a particle surface load of 0.28kg/m^2, for which retention efficiencies of almost 95% were achieved. Hence, characterisation of the 0.75m diameter Grit King® does not need to be undertaken using particles with a particle surface load much greater than 0.28kg/m^2 as efficiencies of almost 100% are likely to be achieved for the 0.75m diameter Grit King® operating at the design flowrate of 13.25 litres per second.

The model does not take into account the shape factor of the particle, as it is assumed that the particles used in testing are spherical. The viscosity of the fluid is also not taken into account,

this depending on the nature and concentration of 'contaminants' in the water and its temperature. Although the model does consider the size of the HDVS in that it takes into account the volume of fluid in the separator, the application of the model to HDVSs larger or smaller than 0.75m has to be validated (see Chapter 7).

A possible limitation of the testing is that the results are for a specific test period and therefore does not account for particle re-entrainment that could occur over a longer duration. However, HDVSs of the form investigated have been demonstrated by others to be relatively resistant to this phenomenon compared to other devices with 'exposed' particle collection regions (Faram *et al.*, 2003). Where these systems are installed in practice, a straight pipe of 45 diameters upstream of the inlet may be highly unlikely. However, efficiency predictions with a developed velocity profile at the inlet to the HDVS are a basis for comparisons with different configurations of upstream pipe work. The method behind the derivation of the efficiency model is a building block for further studies on larger scale HDVSs.

5.5 Summary

- A 0.75m diameter Grit King® has been tested under laboratory conditions.

- From static pressure measurements it has been found that below approximately 3 litres per second, there is no vortex flow due to the pressure on the central shaft and the vessel walls being identical.

- A relationship has been found between the retention efficiency and a parameter described as the particle surface load, m_d, given by $m_d = d(\rho_p - \rho_f)$.

- Using the logistic equation, a model has been developed that predicts the retention efficiency of the 0.75m diameter Grit King®.

6 CFD modelling of a 0.75m diameter Grit King®

Validation of the 0.75m diameter Grit King® retention efficiencies (see Section 5.3.3) has been made, using the pressure tapping data (see Section 5.3.2) as a means of validating the predicted flow field.

6.1 Grid setup and boundary conditions

The inlet pipe to the HDVS was modelled as being the full length (45 diameters) present in the laboratory with the 90 degree swept bend preceding the horizontal section and a further two pipe diameters upstream of the bend, as shown in Figure 6-1. This was to allow the particles injected at the model inlet to establish a realistic position at the inlet to the HDVS, as it has been shown in Section 4.2.3 that the position of the particle at entry to the separator may have an impact on the retention efficiency.
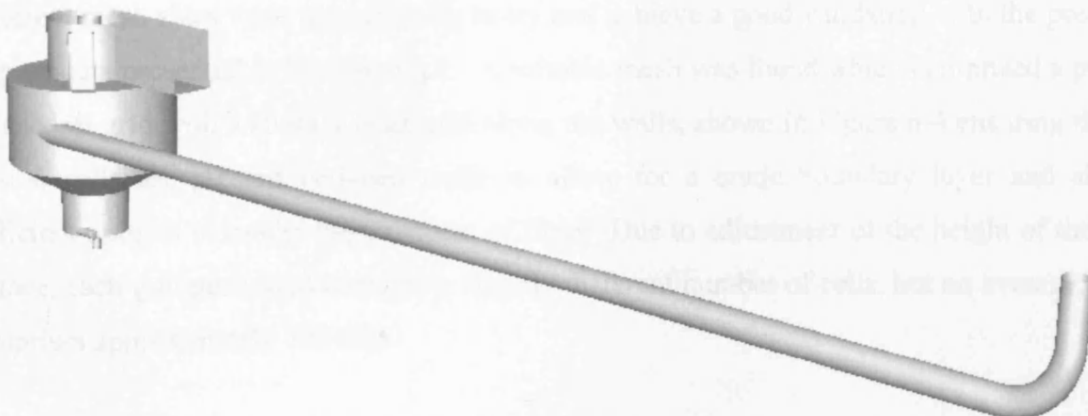
Figure 6-1. 0.75m diameter Grit King® and the complete length of inlet pipe in the CFD model.

The HDVS has a tangential inlet which has been offset by 5% of the inlet diameter in the CFD model to prevent over skewed cells at the point the inlet meets the vessel wall. The overflow was specified as a pressure outlet for which all the flow quantities, except pressure, are extrapolated from the interior. A frictionless wall was used to represent the free surface, for which the position and shape were based on Equations 5-2 to 5-8. For modelling a flowrate of 1 litre per second the position of the free surface was approximated based on Figure 5-13. Figure 6-2 shows the height of the free surface at 2 litres per second and Figure 6-3 shows how the shape differs at a flowrate of 11 litres per second.
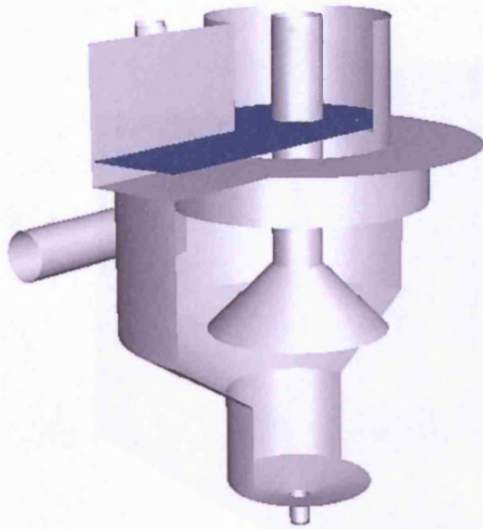
Figure 6-2. Free surface created for modelling the Grit King® at 2 litres per second.
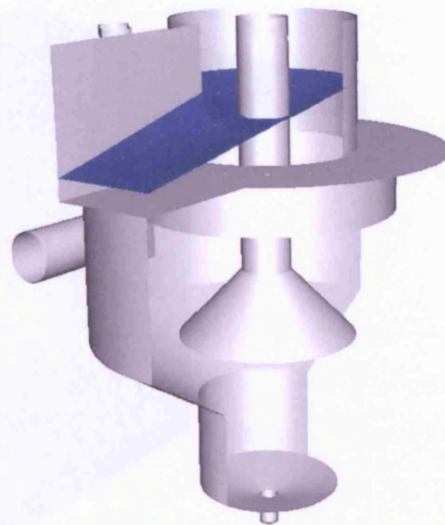
Figure 6-3. Free surface created for modelling the Grit King® at 11 litres per second.

Different mesh sizes were used initially to try and achieve a good validation with the pressure tapping data presented in Section 5.3.2. A suitable mesh was found which comprised a purely tetrahedral grid with a slightly finer grid along the walls, shown in Figure 6-4 ensuring that at least 6 cells are present between walls to allow for a crude boundary layer and also a sufficient number to model the transport of fluid. Due to adjustment of the height of the free surface, each grid generated contains a slightly different number of cells, but on average, each comprises approximately 770 000.

Figure 6-4. A slice through the tetrahedral mesh used for modelling an inlet flowrate of 11 litres per second.

The fluid density and viscosity were based on the average fluid temperature at the time of testing which was 21°C. (Subsequent tests over a winter period have meant that the average fluid temperature for all the tests was 18.5°C. This variation is thought to have negligible effect on the efficiency as can be seen from Table G5, Appendix G, that the maximum and minimum fluid temperature for the tests carried out using Purolite A100 710-1000microns was 14.5°C and 22.0°C and it can be seen from Figure 5-16 that all the results for Purolite 710-1000microns lie on a single curve). Hence, the retention efficiency may not be as sensitive to changes in temperature of tap water as was found in Section 4.2.3, but requires more investigation to be conclusive. The Reynolds Stress turbulence model has been used along with the standard pressure interpolation scheme and the SIMPLE pressure-velocity coupling algorithm. Second order terms for momentum, turbulent kinetic energy, turbulent dissipation rate and Reynolds stresses have been solved as it was found that by solving the second order terms, the validation of the pressure tapping data improved.

The volume of the fluid in the model was approximately 0.26m^3 and the volume of particles used in testing was of the order of 100 to 900ml, hence, efficiency predictions have been

obtained using the Discrete Phase Model, as the maximum volume fraction of particles at 0.34% is significantly lower than the maximum recommended for modelling discrete particles which is 10%. Hence, the need for either the 'Mixture Model'[5] (see Section 2.3.4.1) or the 'Eulerian Model' (see Section 2.3.4.2) is thought to not be justified as the volume fraction of particles is less than 10%.

As stated in Section 5.2.3, each retention efficiency test was carried out for a duration of 10 minutes. The trajectory time of 10 minutes is replicated in CFD using a DPM scalar update UDF, given in Appendix A, titled 'DPM trajectory termination'. This UDF terminates the trajectory by evaporating the particles (by setting the diameter and mass to zero) once the trajectory time exceeds 10 minutes. The length scale was changed from 0.01m to 0.001m for a higher resolution in the particle trajectory. Stochastic tracking was enabled and the time scale constant changed to 0.3 in accordance with the recommendation by the FLUENT manuals (Fluent Inc., 2003) for stochastic tracking with the Reynolds Stress model. Fifty tries were used in the stochastic tracking which results in 3600 particles being tracked for the majority of models.

Volumetric separation efficiencies were measured in the laboratory. A size distribution for the particles was not used as this would not allow a good comparison to be made between experimental efficiency results that have been determined on a volumetric basis and efficiencies determined using CFD on a numbers basis. The efficiency using CFD is given by

$$\eta = 100 \cdot \frac{Number\ of\ particles\ injected - Number\ of\ particles\ that\ escape}{Number\ of\ particles\ injected} \qquad (6\text{-}1)$$

i.e. the percentage of particles remaining in the separator at the end of the DPM iterations.

Particle injections were created based on the mean particle size and density. To estimate the range in which the predicted retention efficiency could lie based on error in the characterisation of the particle properties, error bars on the CFD-predicted efficiency have also been predicted by varying the particle properties. Using the upper 99.8% confidence value for settling velocity and lower 99.8% confidence interval for particle diameter (fast

---

[5] It may be argued that if the volume fraction exceeds 10%, that this type of system should be modelled using the Eulerian model which is more suited to sedimentation (which will occur in the grit pot). However, Okamoto *et al.* (2002) used the Mixture Model.

settling particle with small diameter and hence low drag) gives an upper value for the particle density. The inverse gives a lower value for particle density. This is a conservative estimate for the range of the particle density as it was observed during the settling tests that smaller particles tended to settle slower. Hence, three injections of particles have been carried out for each particle sieve size range. The first injection comprises the mean particle properties. The second injection uses the lower limit of the 99.8% confidence interval for particle diameter and the upper limit of the particle density to give a particle with a faster settling velocity than the average particle in a particular sieve size range. A third injection used the upper 99.8% confidence interval of the particle diameter and lower limit of the particle density to give a slower settling particle than the average particle in a particular sieve size range.

6.2 Results

6.2.1 Static pressure validation

In situations where the fluid density is constant, the mass flux is set in the CFD models by setting the velocity at the inlet. The CFD software then determines, iteratively, the pressure drop required between the inlet and outlet to drive the fluid through the system being modelled. Hence, to validate the static pressure measurements, the pressure difference between the point at which the pressure reading was taken and the inlet must be compared. Figures 6-5 to 6-12 show a comparison between the experimental pressure difference and the predicted values, where it can be seen that in general, CFD predictions are quite reasonable.
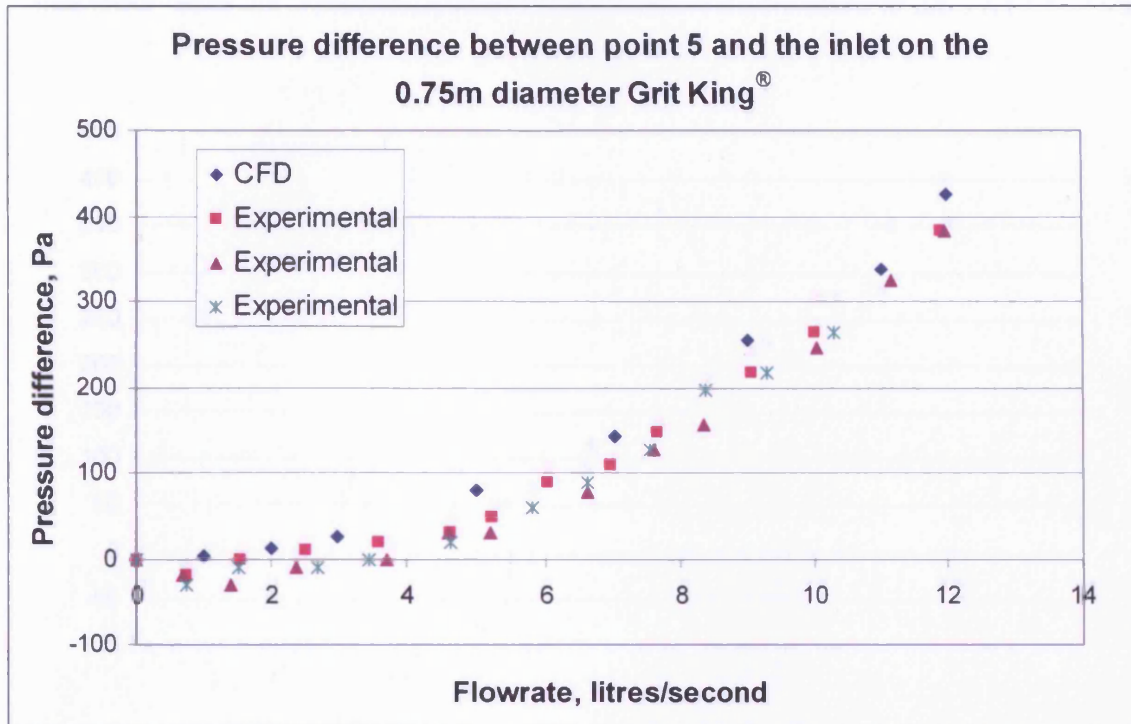
Figure 6-5. *Experimental and CFD pressure difference between point 5 and the inlet.*
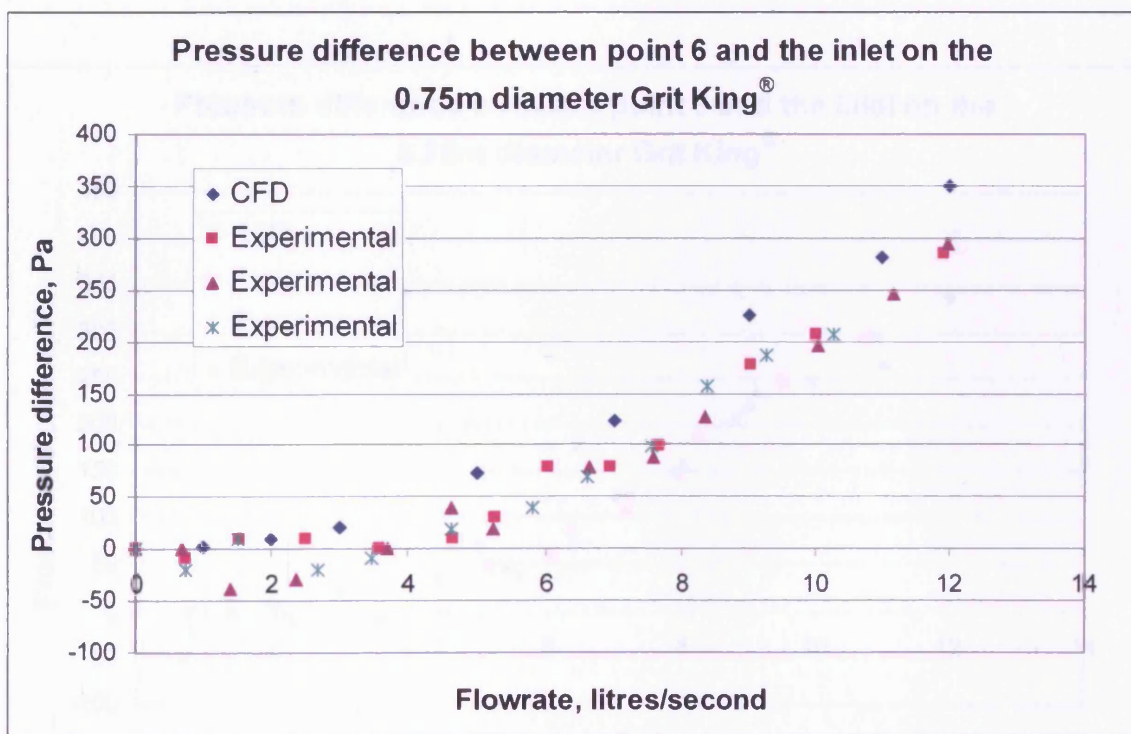
Figure 6-6. *Experimental and CFD pressure difference between point 6 and the inlet.*
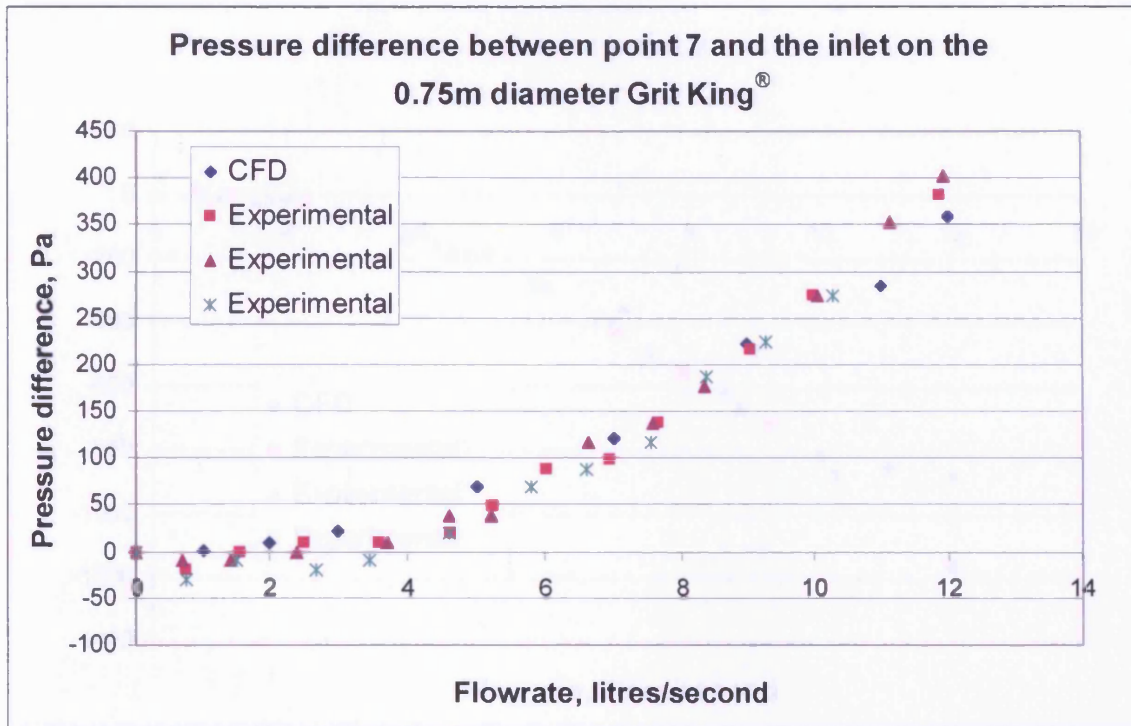
Figure 6-7. Experimental and CFD pressure difference between point 7 and the inlet.
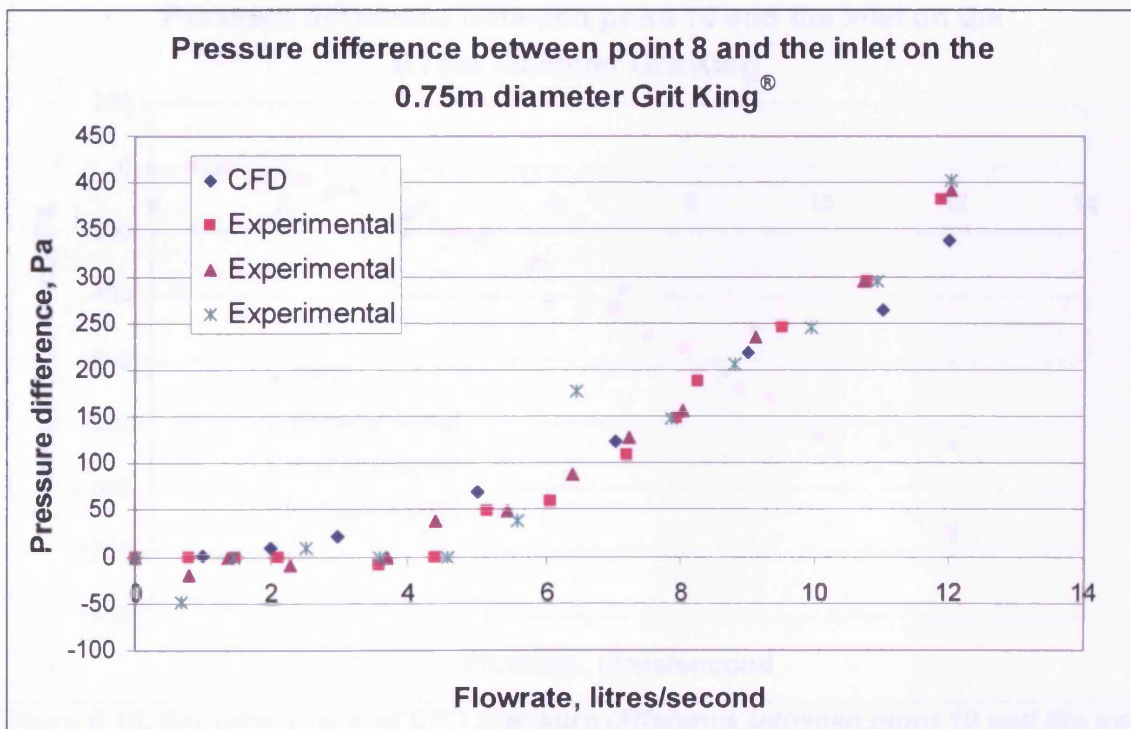
Figure 6-8. Experimental and CFD pressure difference between point 8 and the inlet.
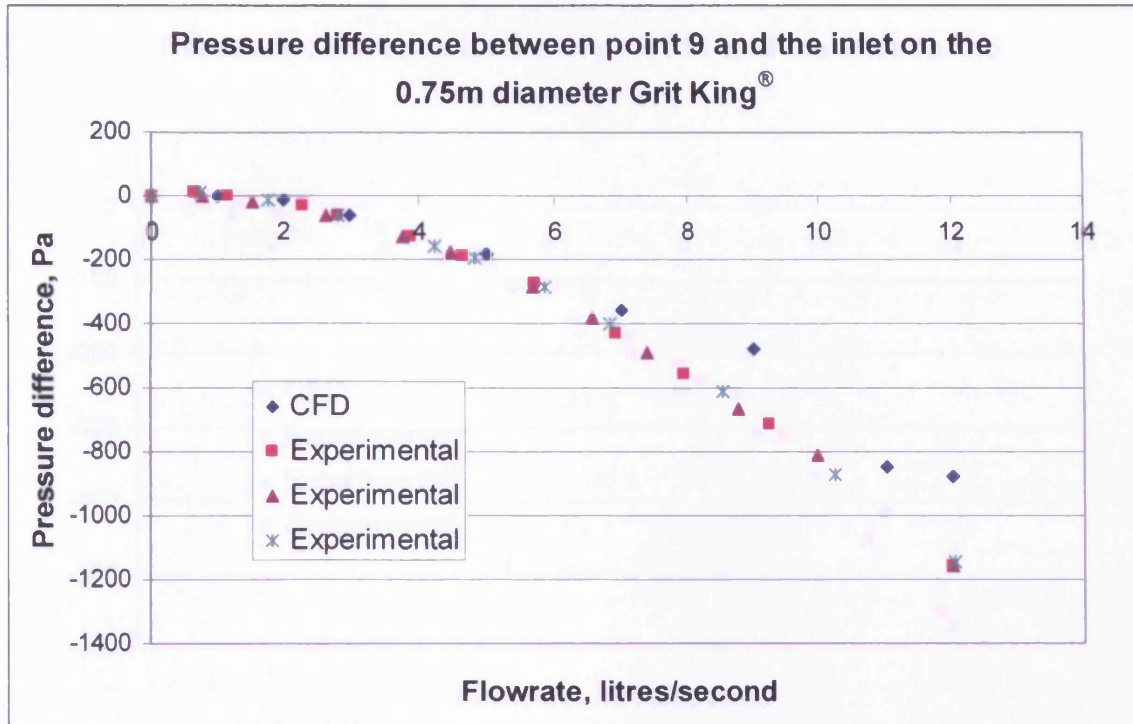
Figure 6-9. Experimental and CFD pressure difference between point 9 and the inlet.
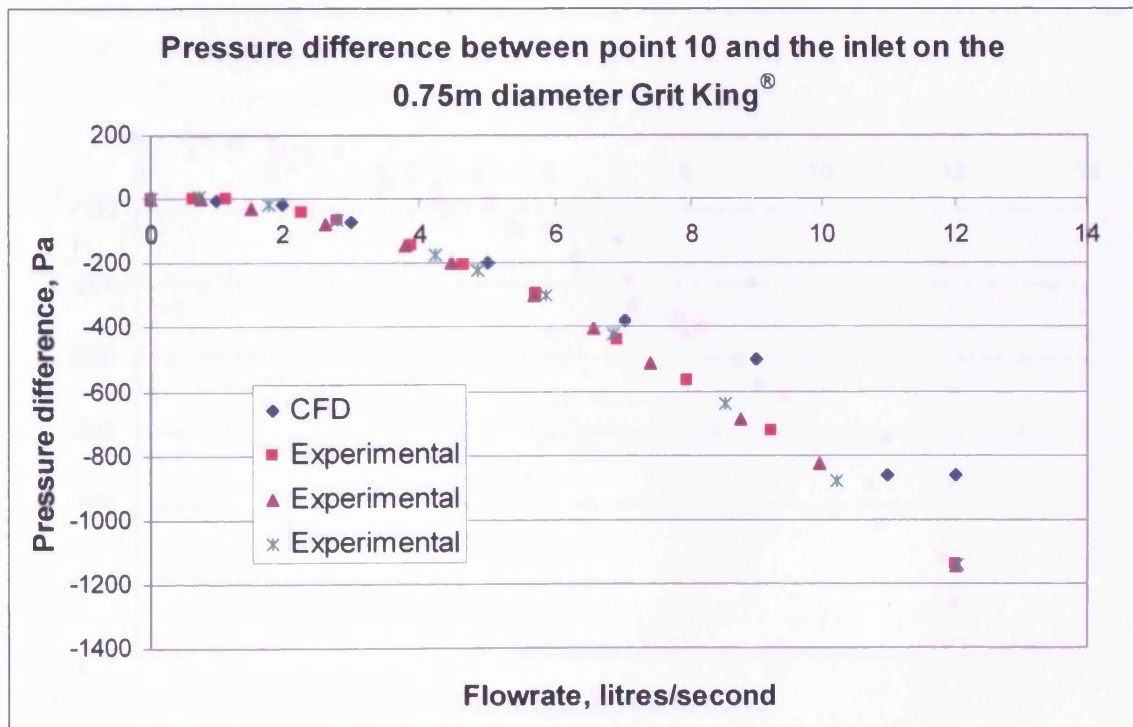
Figure 6-10. Experimental and CFD pressure difference between point 10 and the inlet.
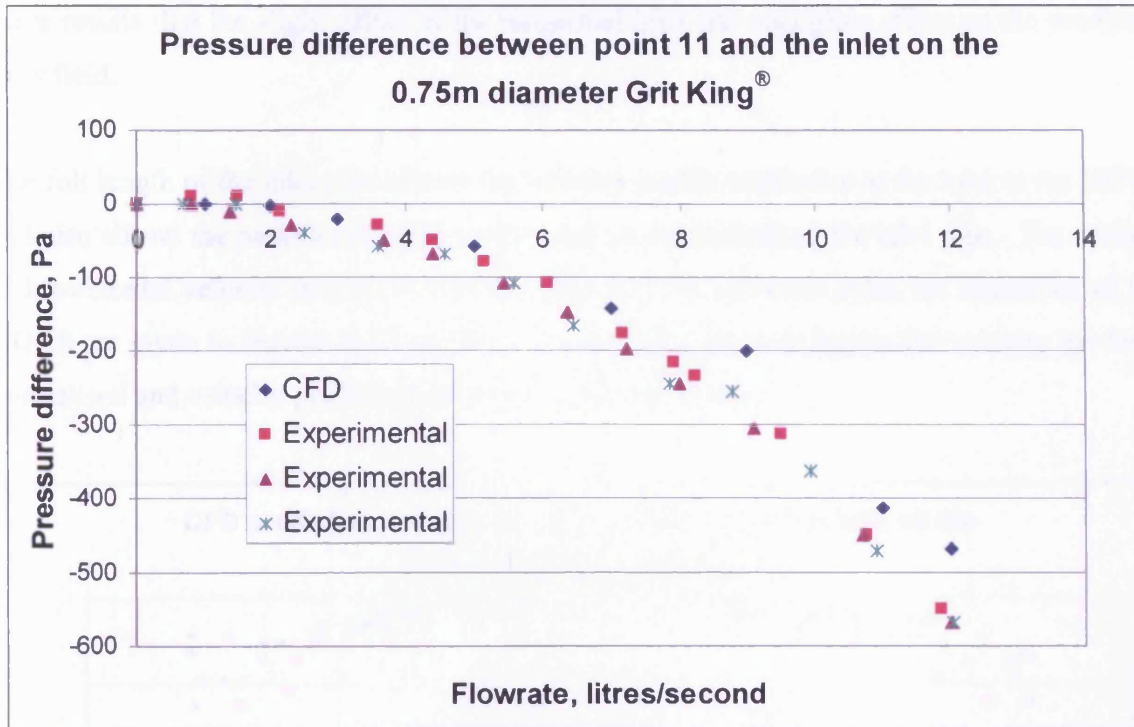
Figure 6-11. Experimental and CFD pressure difference between point 11 and the inlet.
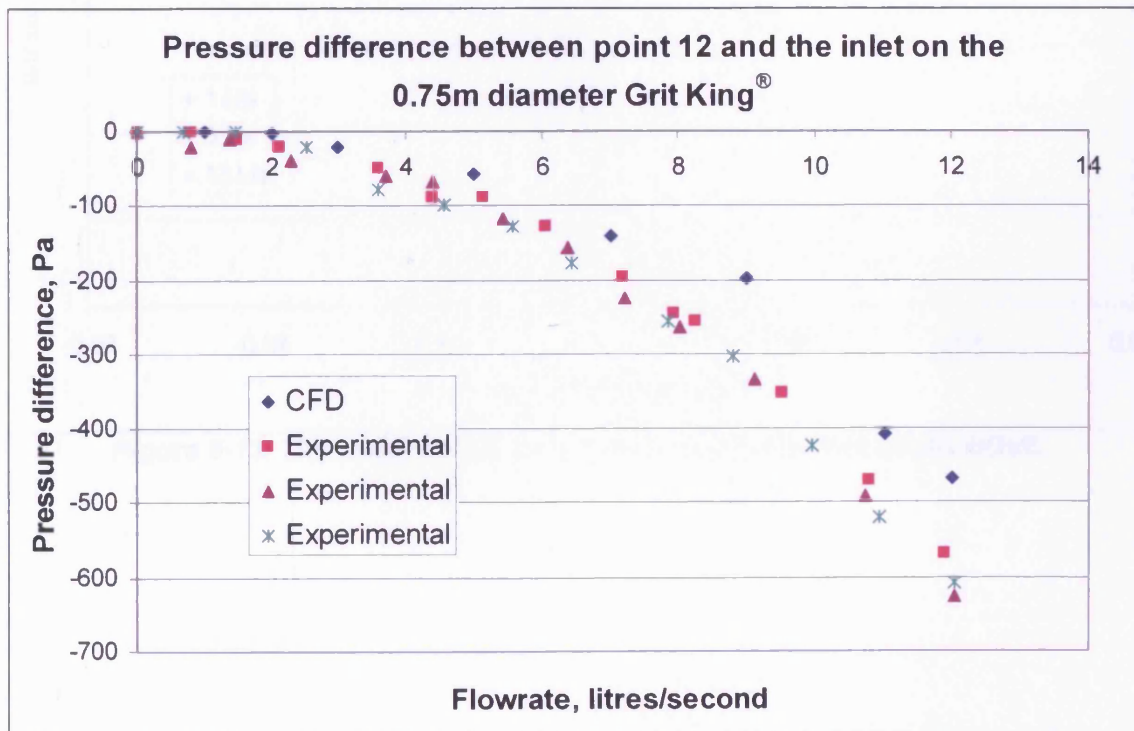
Figure 6-12. Experimental and CFD pressure difference between point 12 and the inlet.

6.2.2 Retention efficiency validation

Having acquired a reasonable validation of the pressures at the walls of the separator, it is assumed that the predicted flow field in general is reasonable. It could also be implied from

these results that the slight offset of the tangential inlet has negligible effect on the predicted flow field.

The full length of the inlet pipe allows the velocity profile to develop at the inlet to the HDVS and also allows the particles to settle as they are transported along the inlet pipe. The vertical and horizontal velocity profiles across the inlet 0.375m upstream from the centreline of the HDVS are given in Figures 6-13 and 6-14 respectively. In both figures the velocity has been normalised and velocity profiles plotted for various flowrates.
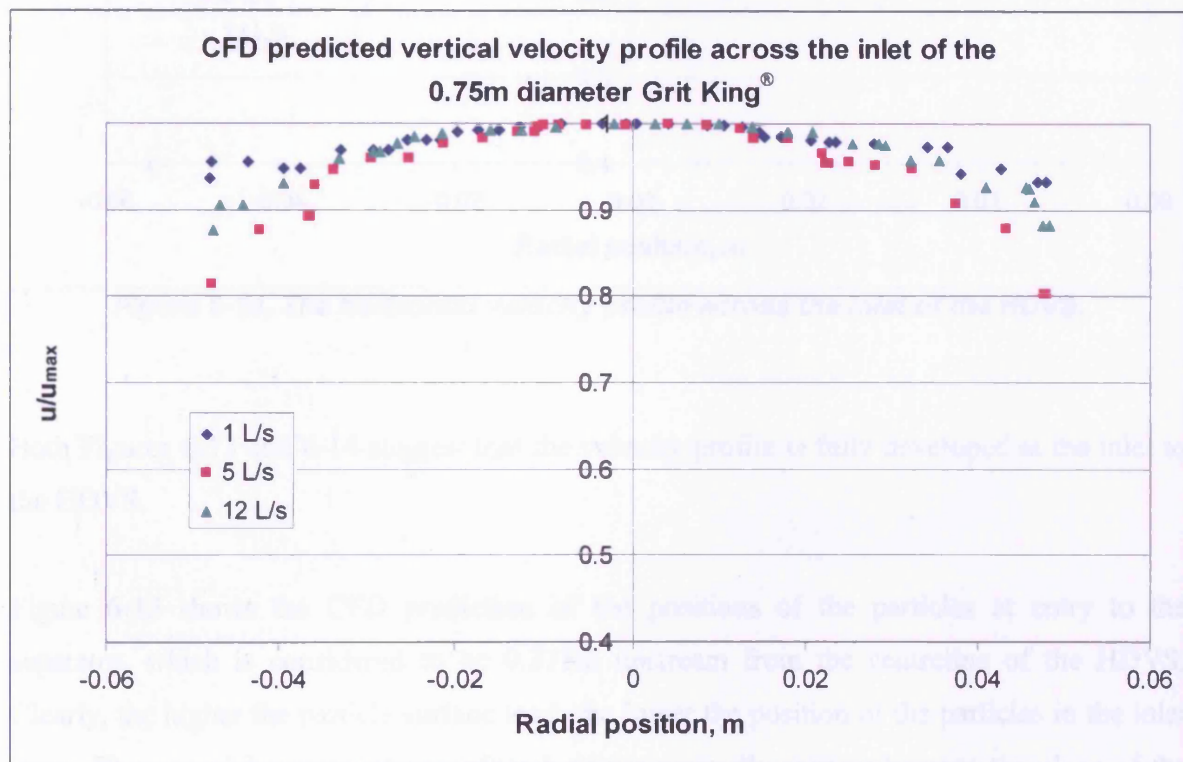
Figure 6-13. The vertical velocity profile across the inlet of the HDVS.

CFD predicted horizontal velocity profile across the inlet of the 0.75m diameter Grit King®
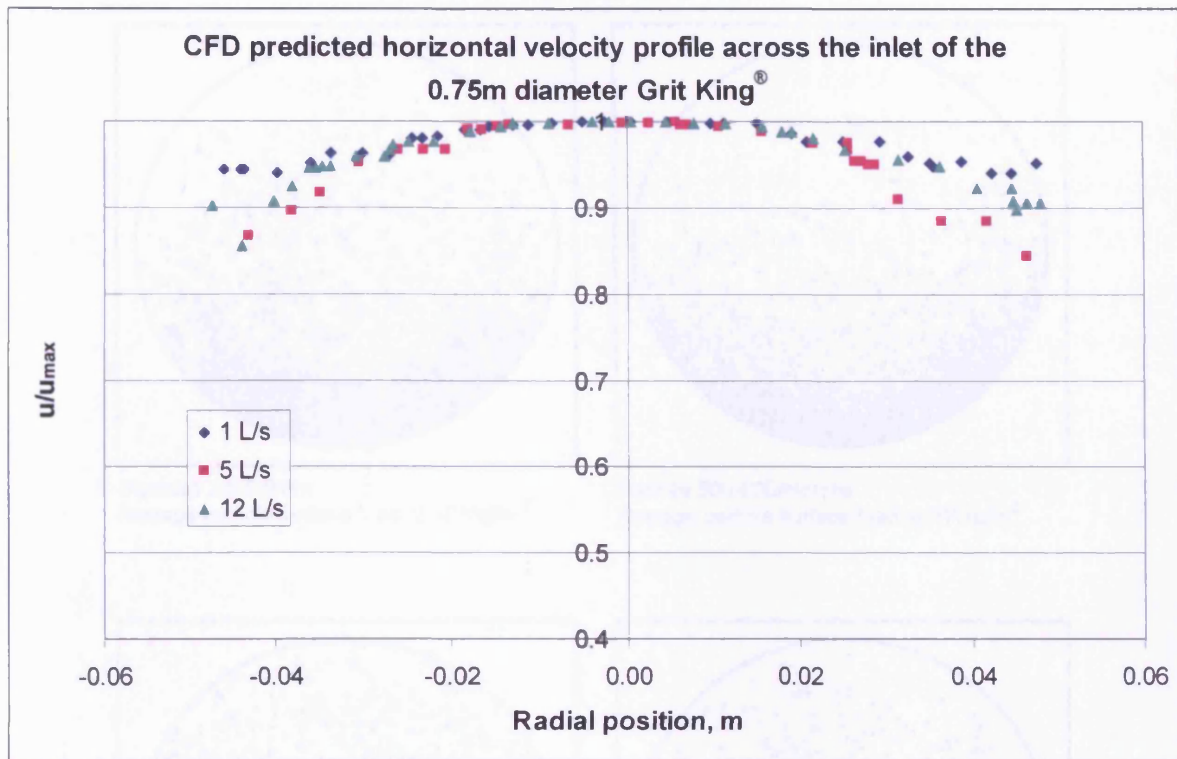
Figure 6-14. The horizontal velocity profile across the inlet of the HDVS.

Both Figures 6-13 and 6-14 suggest that the velocity profile is fully developed at the inlet to the HDVS.

Figure 6-15 shows the CFD prediction of the positions of the particles at entry to the separator, which is considered to be 0.375m upstream from the centreline of the HDVS. Clearly, the higher the particle surface load, the lower the position of the particles in the inlet pipe. Those particles with a low surface load are generally scattered across the plane of the inlet, e.g. Purolite 500-710microns. Particles with a high surface load tend to lie at the bottom of the inlet, e.g. Purolite 500-600microns. With reference to the results obtained in Section 4.2.3 this could therefore be a factor that contributes to the efficiency of the separator.
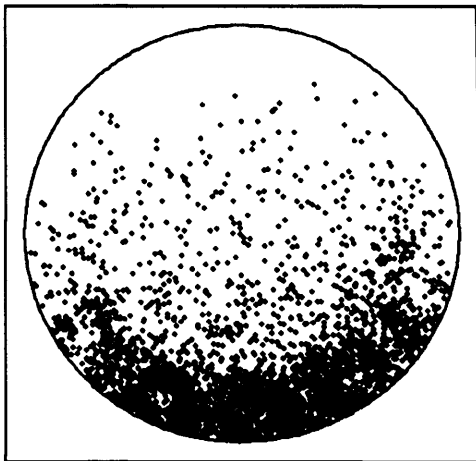
Styrocell 2.8-5.6mm
Average particle surface load: 0.101kg/m²
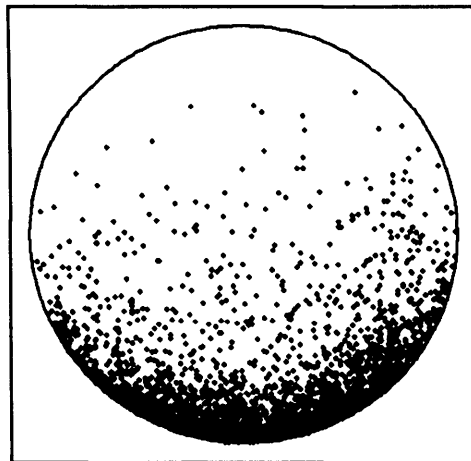
Purolite 500-600microns
Average particle surface load: 0.211kg/m²
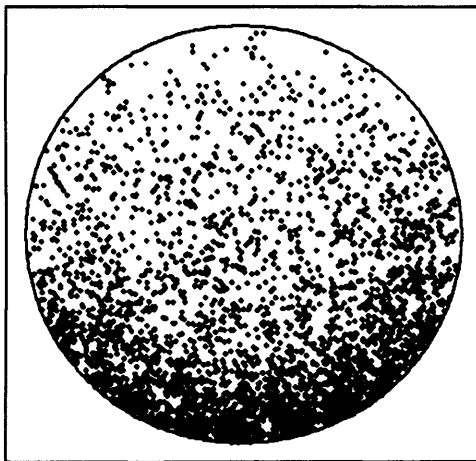
Styrocell 1.4-2.0mm
Average particle surface load: 0.063kg/m²
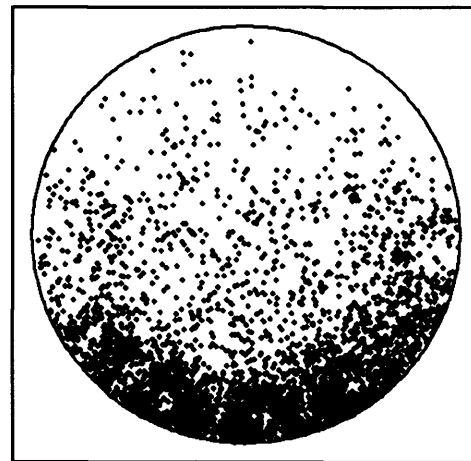
Styrocell 2.0-2.8mm
Average particle surface load: 0.084kg/m²
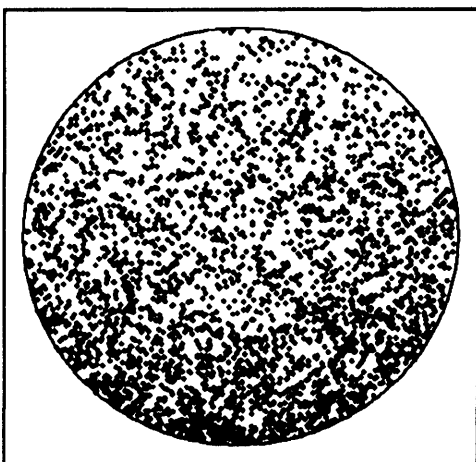
Purolite 500-710microns
Average particle surface load: 0.035kg/m²
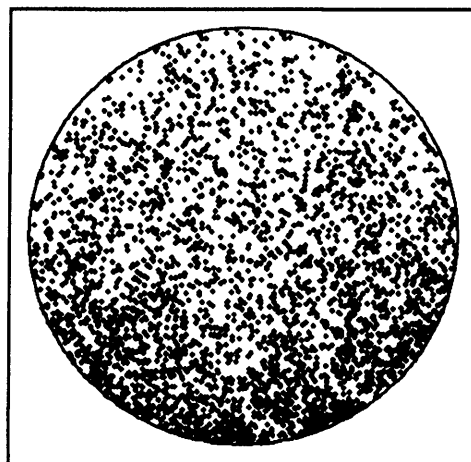
Purolite 710-1000microns
Average particle surface load: 0.041kg/m²

Figure 6-15. CFD prediction for the particle positions at entry to the 0.75m diameter Grit King® at 11 litres per second.

Figures 6-16 to 6-21 present the CFD-predicted retention efficiency. Error bars are not displayed on the experimental data as efficiency has been determined by measurement of the volume of particles captured and as the total volume of particles collected was the same as the volume introduced at the inlet then the error is negligible. The error in the flowrate measurement is also assumed to be minor based on the calibration of the flowmeter (Figures B3 and B4). Each experimental retention efficiency curve follows a definite trend and where practical, repeat tests have been made where the variability in the data at a particular flowrate has been shown to be small.
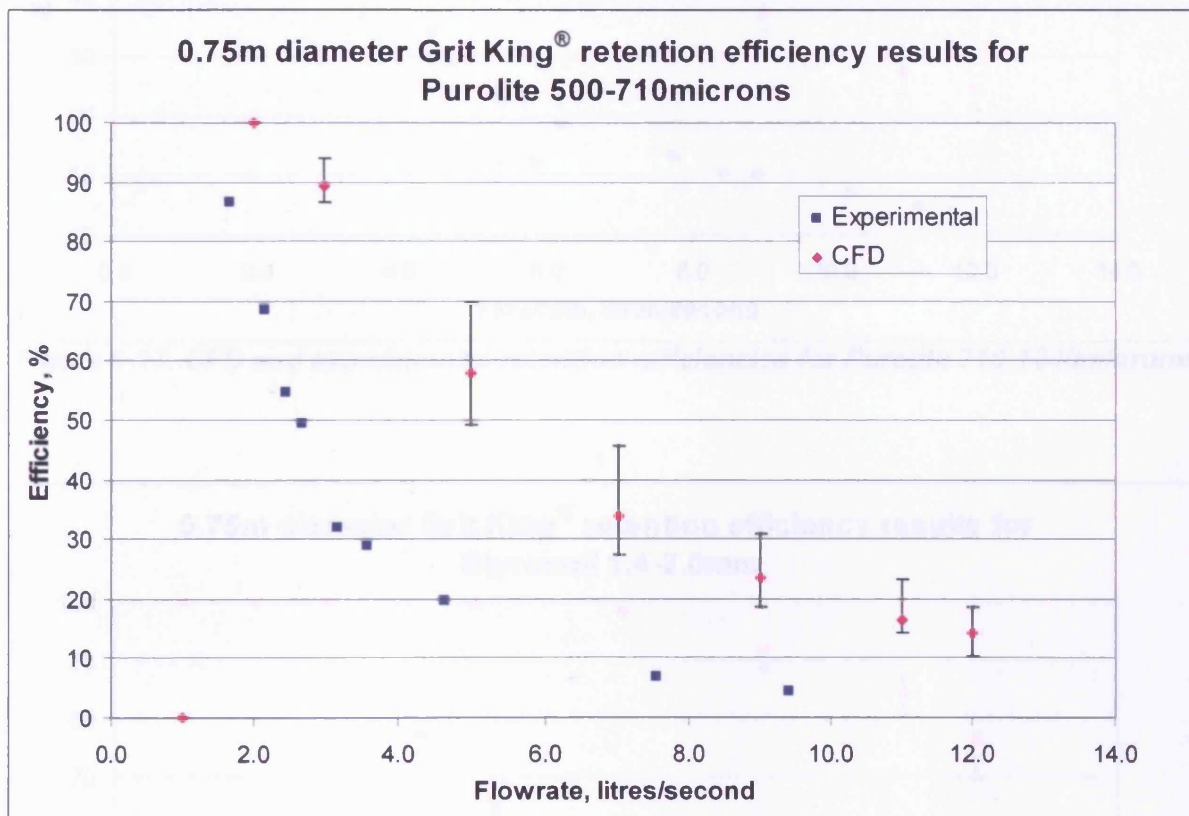
Figure 6-16. CFD and experimental retention efficiencies for Purolite 500-710microns.
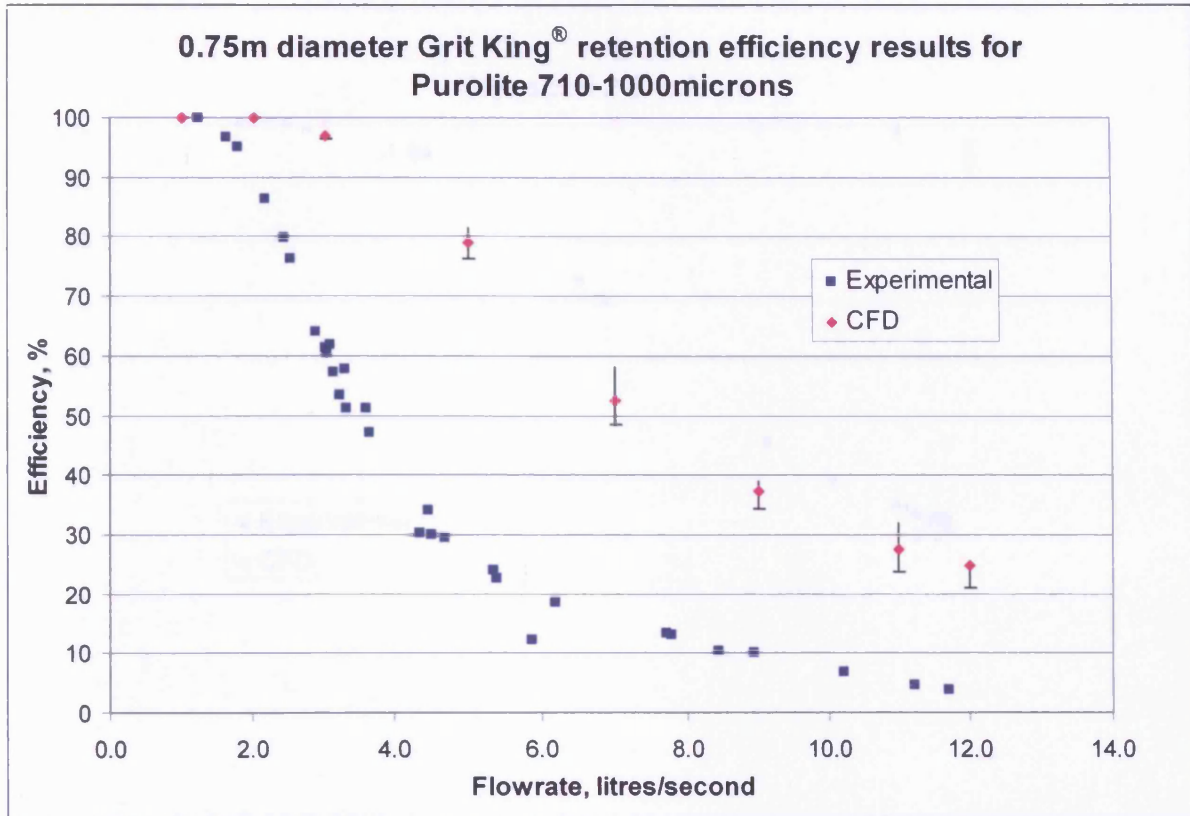
Figure 6-17. CFD and experimental retention efficiencies for Purolite 710-1000microns.
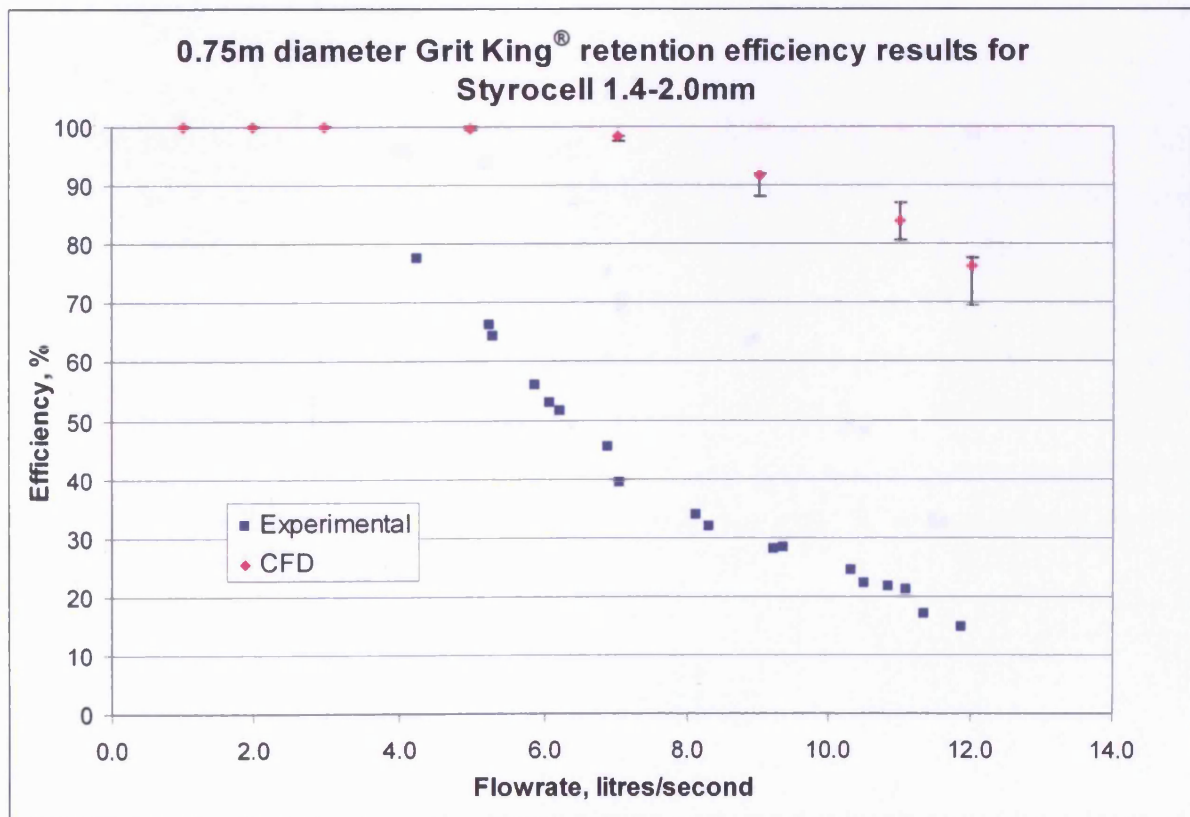
Figure 6-18. CFD and experimental retention efficiencies for Styrocell 1.4-2.0mm.
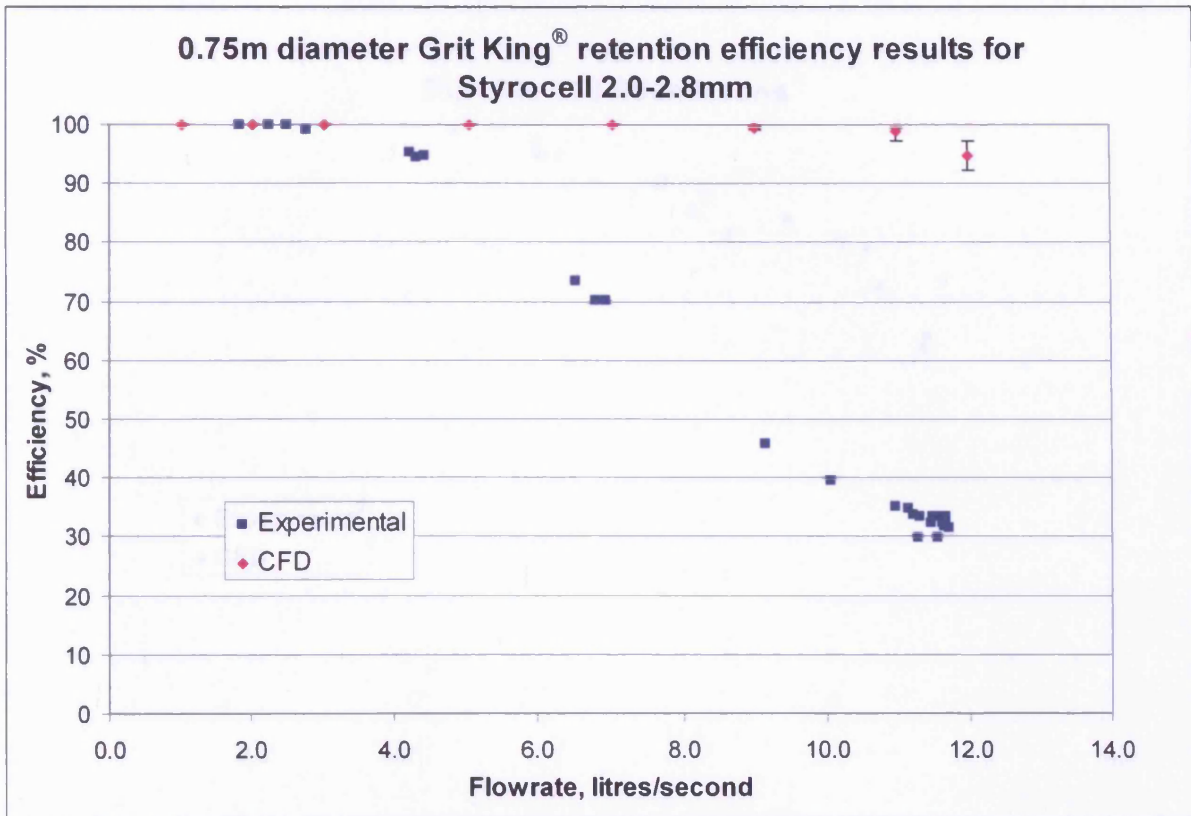
Figure 6-19. CFD and experimental retention efficiencies for Styrocell 2.0-2.8mm.
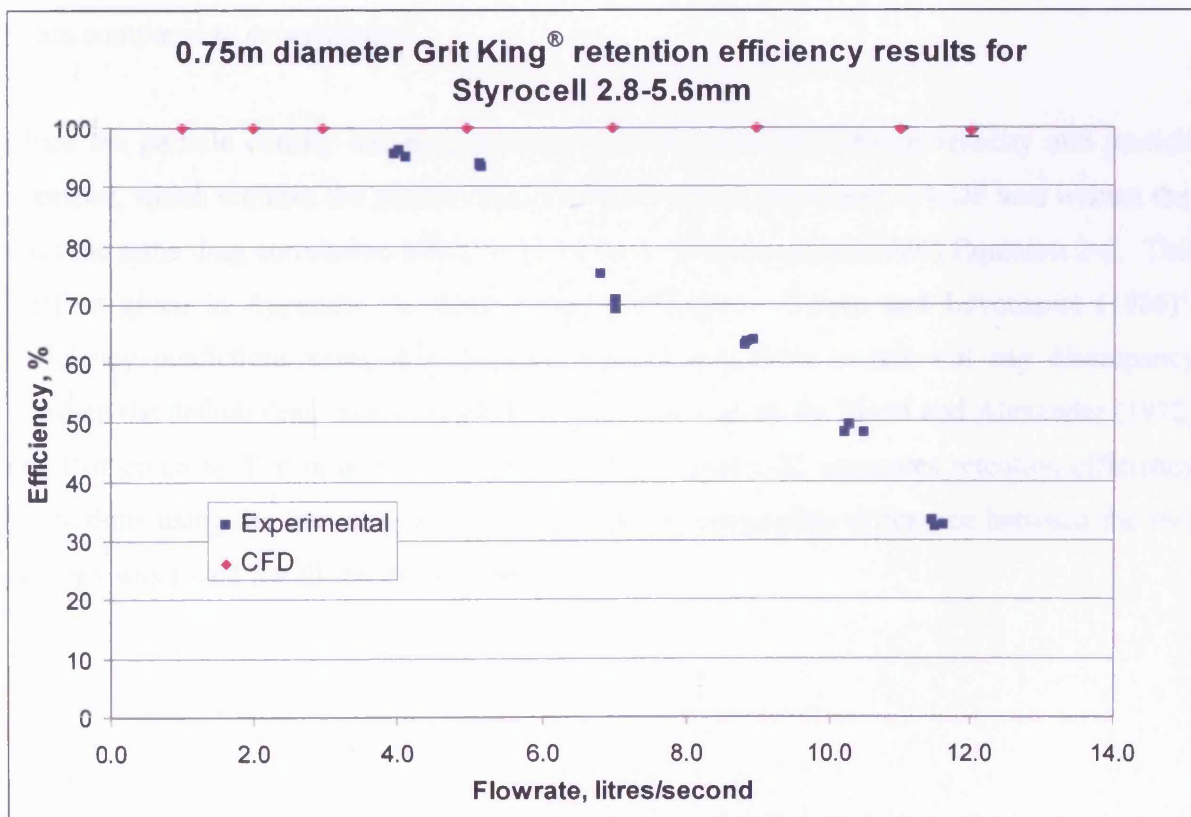
Figure 6-20. CFD and experimental retention efficiencies for Styrocell 2.8-5.6mm.
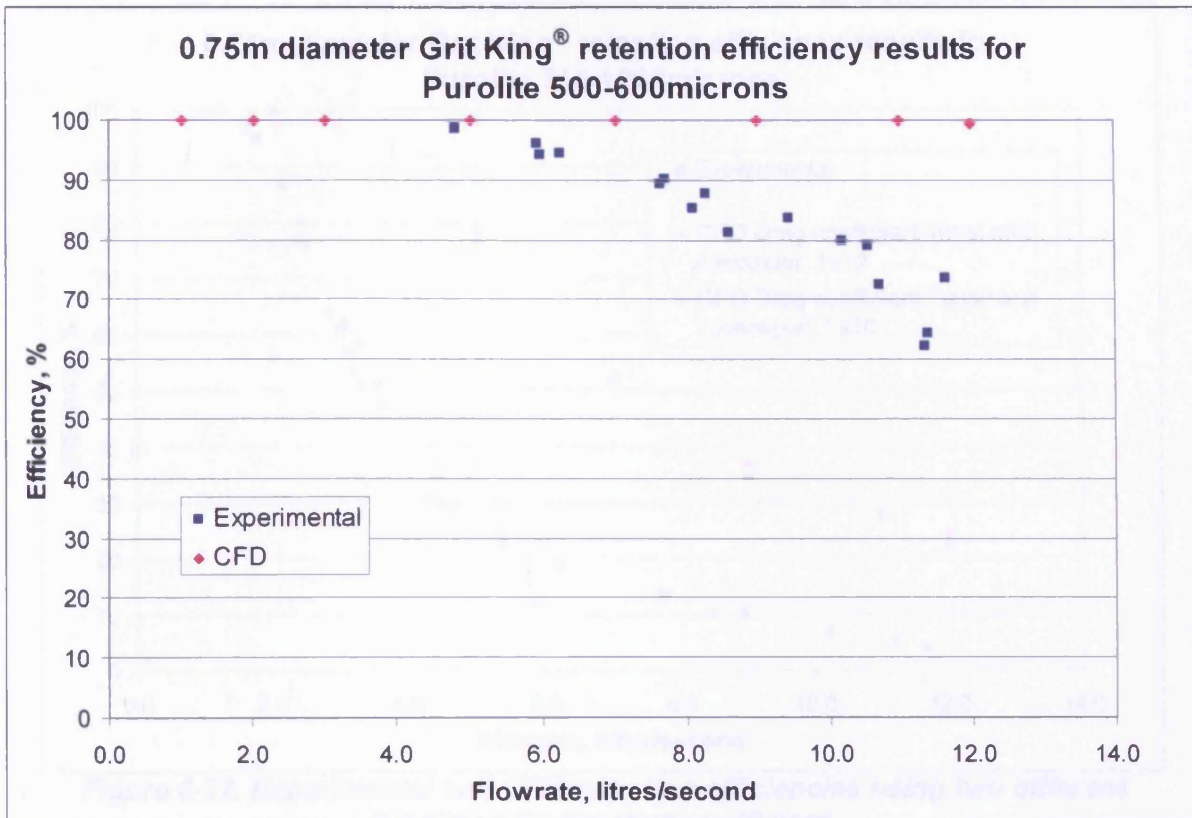
Figure 6-21. CFD and experimental retention efficiencies for Purolite 500-600microns.

From Figures 6-16 to 6-21 it can be seen that CFD-predicted retention efficiencies are poor when compared to experimental.

Since the particle density has been determined from both the settling velocity and particle diameter, which requires the particle drag coefficient to be calculated, a UDF was written that uses the same drag correlation which is by Turton and Levenspiel (1986) Equation 2-6. This UDF is given in Appendix A, titled 'Drag coefficient – Turton and Levenspiel (1986)'. Efficiency predictions using this drag correlation were done to rule out any discrepancy between the default drag correlation used by FLUENT given by Morsi and Alexander (1972) and that given by Turton and Levenspiel (1986). Figure 6-22 compares retention efficiency predictions using the two drag correlations. There is negligible difference between the two and this was found for all the particulates.
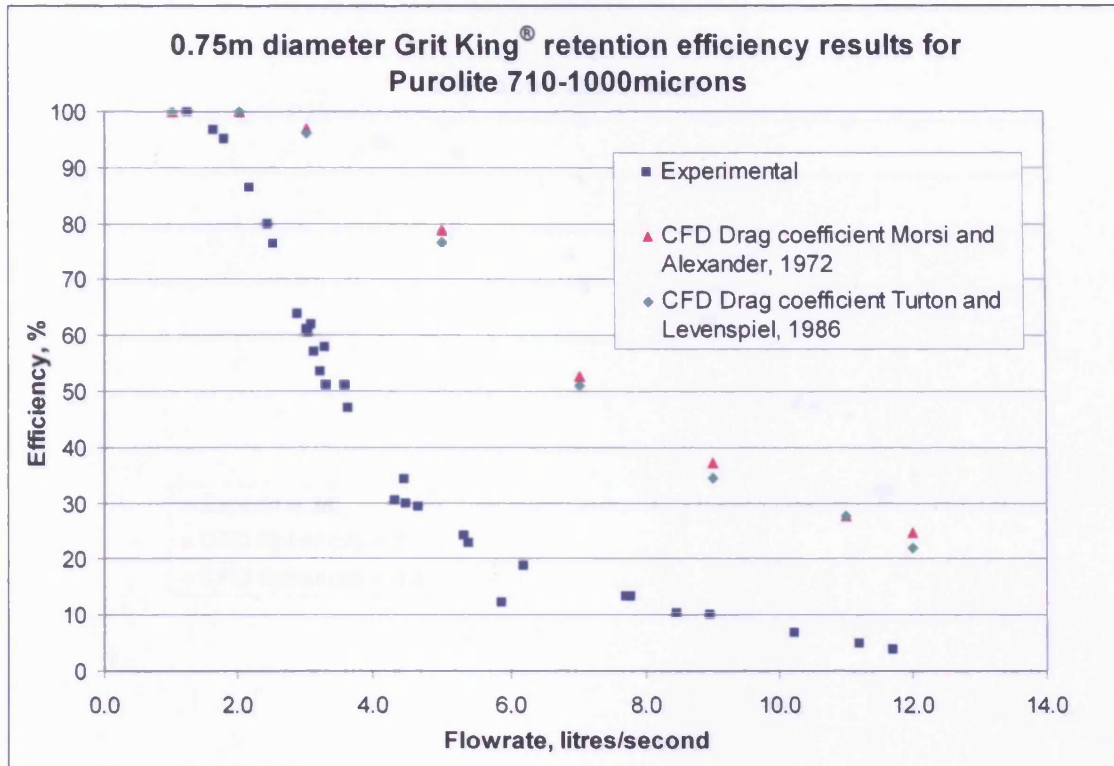
Figure 6-22. Experimental and CFD retention efficiencies using two different functions for the drag coefficient.

Although the particles appear to be spherical to the human eye, there will be some discrepancy compared with a perfect sphere, particularly in the case of Styrocell 2.8-5.6mm as shown in Figure 5-6. An attempt to fit the predicted retention efficiency with those observed was achieved by adjusting the shape factor. This was done for Styrocell 2.8-5.6mm and it was found that a sphericity of 0.5 gave a reasonable fit as shown in Figure 6-23.
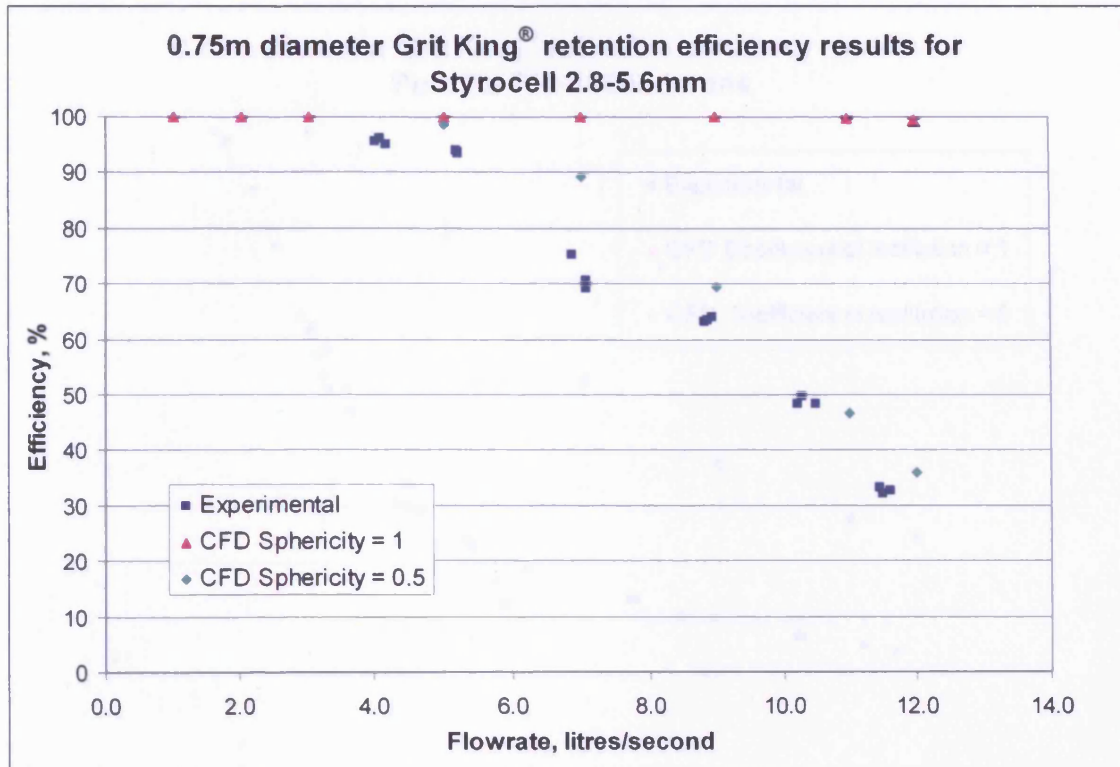
Figure 6-23. Experimental and CFD retention efficiencies using two different shape factors.

However, it may be found from Equation 2-7 that a shape factor of 0.5 corresponds to a particle the shape of a cylinder with a length of 16.5 diameters. It can be seen that a shape factor of 0.5 does not correspond to the particles of Styrocell in the 2.8-5.6mm sieve size range shown in Figure 5-6.

The effect of the coefficient of restitution has been re-examined by comparing results between the default setting and zero for both the normal and tangential components. This gives results between the two extremes where momentum is completely conserved and where it is completely lost in the impact on the wall. Figure 6-24 shows that this has no effect on the predicted efficiency, as found in Section 4.2.3 and this was found for all the particulates.
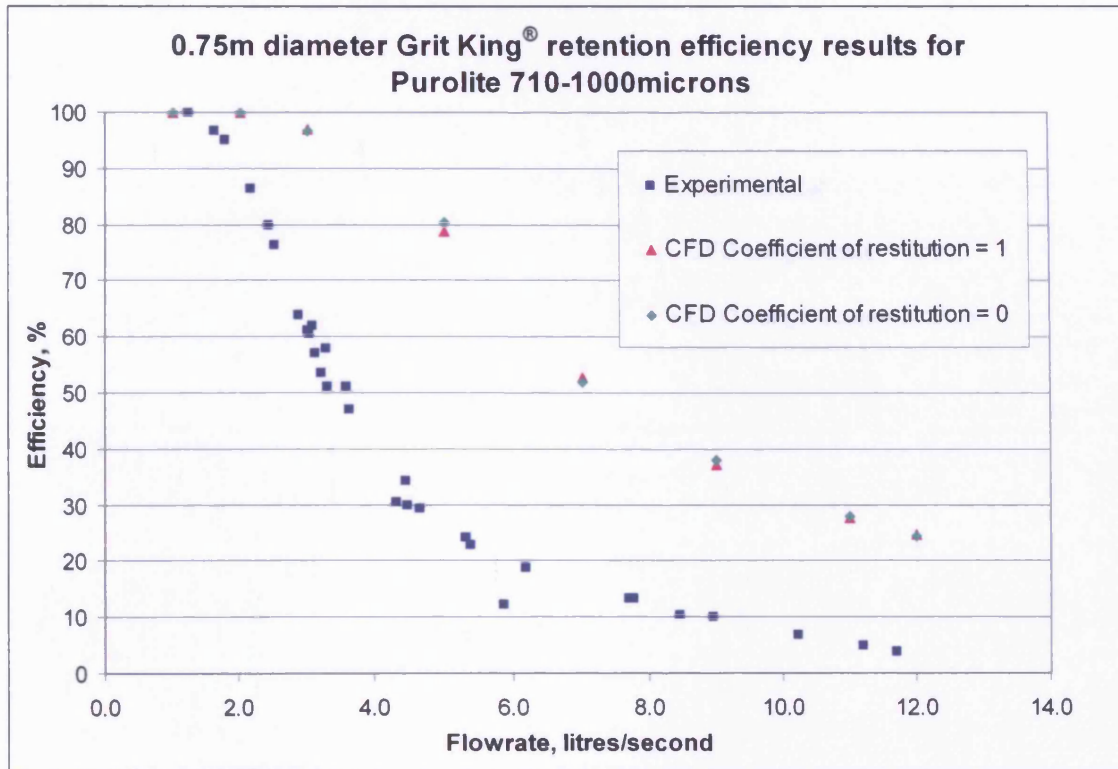
Figure 6-24. Experimental and CFD retention efficiencies using two different values for the coefficient of restitution.

The length scale, defined by Equation 2-67, has been set such that the equations of motion for the particle are updated every millimetre. To verify that the length scale has been set at a solution independent value, a comparison has been made, shown in Figure 6-25, between retention efficiencies predicted using a length scale of 1mm compared to 0.1mm.

0.75m diameter Grit King® retention efficiency results for Purolite 710-1000microns
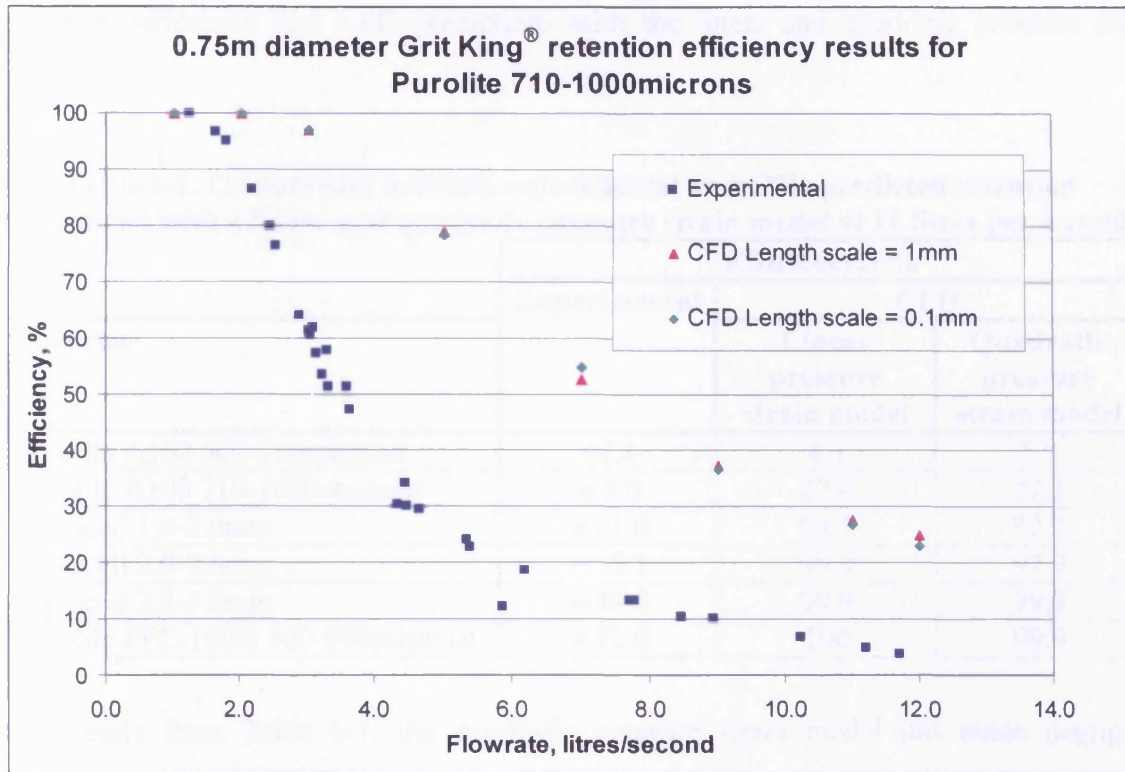
Figure 6-25. Experimental and CFD retention efficiencies using two different length scales.

Quite clearly, a length scale of 1mm gives a solution independent prediction of the retention efficiency.

Having investigated many of the variables within the DPM, then attention must be turned to the predicted flow field. Although validation of the static pressure on the walls is reasonable, the predicted flow field has not been validated.

Section 2.3.3.6 notes that the default method of modelling the pressure strain is by a linear pressure strain model. This may however be replaced by a quadratic pressure strain model and has been demonstrated to give better performance in a range of basic shear flows (Fluent Inc., 2003). It is known from Andoh and Smisson (1993) that shear occurs between downward flow along the walls and upward flow along the axis, hence, the quadratic pressure strain model was used on the model at 11 litres per second as this was considered to be a good test where there is a large discrepancy between CFD predictions and observed efficiencies e.g., Styrocell 1.4-2.0mm (Figure 6-18), Styrocell 2.0-2.8mm (Figure 6-19), Styrocell 2.8-5.6mm (Figure 6-20), Purolite 500-600microns (6-21). Table 6-1 presents a comparison

between experimental and CFD predictions with the linear and quadratic pressure strain model.

Table 6-1. Comparison between experimental and CFD-predicted retention efficiencies with a linear and quadratic pressure strain model at 11 litres per second.

Particles	Efficiency, / %		
	Experimental	CFD	
		Linear pressure strain model	Quadratic pressure strain model
Purolite A100 500-710microns	<4.4	4.3	5.0
Purolite A100 710-1000microns	≈5.0	27.6	27.1
Styrocell 1.4-2.0mm	≈21.0	84.0	82.7
Styrocell 2.0-2.8mm	≈35.1	99.0	97.9
Styrocell 2.8-5.6mm	≈48.0	99.9	99.8
Purolite PPC-100H 500-600microns	≈72.0	100	99.9

Quite clearly from Table 6-1, the quadratic pressure strain model has made negligible difference to the CFD predictions. The difference that is present is most likely due to the stochastic tracking which includes the effects of turbulence on the particles such that each particle that is released from a data point does not follow the same trajectory exactly.

The PRESTO! pressure velocity coupling scheme has also been tested as this is suited to highly swirling flows and flows in strongly curved domains. Table 6-2 presents a comparison between the predicted retention efficiency using the PRESTO! and standard pressure interpolation schemes on the model at 11 litres per second.

Table 6-2. Comparison between experimental and CFD-predicted retention efficiencies with the standard and PRESTO! pressure scheme.

Particles	Efficiency, / %		
	Experimental	CFD	
		Standard pressure scheme	PRESTO! pressure scheme
Purolite A100 500-710microns	<4.4	4.3	3.8
Purolite A100 710-1000microns	≈5.0	27.6	21.4
Styrocell 1.4-2.0mm	≈21.0	84.0	76.2
Styrocell 2.0-2.8mm	≈35.1	99.0	97.2
Styrocell 2.8-5.6mm	≈48.0	99.9	99.7
Purolite PPC-100H 500-600microns	≈72.0	100	99.9

Although the PRESTO! scheme has caused predicted retention efficiencies to reduce slightly, in the case of Styrocell 1.4-2.0mm approximately 8%, the difference between predicted and observed is still significant. The lack of improvement using the PRESTO! scheme is possibly due to the swirl being fairly low as solid-liquid separation is aided by the time gravity has to act on the particle (Andoh and Smisson, 1993) rather than the centrifugal flow present in a hydrocyclone (Svarovsky, 1984).

Although the comparison between experimental and CFD static pressures are quite good, a grid dependency check was performed at 11 litres per second, whereby the grid in the main vessel of the separator was made finer increasing the total number of cells to approximately 1 608 000. Table 6-3 compares predicted retention efficiencies between the coarser grid containing 804 000 cells and the finer grid.

Table 6-3. Comparison between experimental and CFD-predicted retention efficiencies with a coarse and fine grid at 11 litres per second.

	Efficiency, / %		
	Experimental	**CFD**	
Particles		**Coarse grid (804 000 cells)**	**Fine grid (1 608 000 Cells)**
Purolite A100 500-710microns	<4.4	4.3	4.6
Purolite A100 710-1000microns	≈5.0	27.6	23.5
Styrocell 1.4-2.0mm	≈21.0	84.0	80.6
Styrocell 2.0-2.8mm	≈35.1	99.0	97.3
Styrocell 2.8-5.6mm	≈48.0	99.9	99.8
Purolite PPC-100H 500-600microns	≈72.0	100	99.9

From Table 6-3, the finer grid has had a very small effect on the predicted retention efficiency. In some cases e.g. Styrocell 1.4-2.0mm, there has been a reduction of 3.5%, but this is negligible in comparison to the observed efficiency which in this case is approximately 21% compared with a prediction of approximately 80%. Hence, the solution of the model with a coarse grid can be considered to be suitably grid independent.

Many parameters have been investigated to try and achieve a reasonable validation of the retention efficiency. With measurements of particle diameter and the derived particle density, the correct fluid density and viscosity, particle shape accounted for, as well as the drag correlation, efforts turned to the solution controls, such as the pressure strain model and the pressure interpolation scheme, which have not improved the predictions to give a reasonable

validation. A grid dependency check has been made in the event that the grid in the main body of the separator was not of a sufficient resolution for the computation of the particle trajectories. Using the transient solver, no unsteady behaviour has been detected which would be evident by a significant change in the residuals each time step.

To reduce numerical diffusion in the model, a grid that is predominantly hexahedral in the main body of the separator where separation takes place has been generated for modelling a flowrate of 11 litres per second. The grid has been fitted to the geometry of the separator by arranging the cells in a polar orientation, thus aligning them with the flow to reduce numerical diffusion. Tetrahedral elements have been placed at the overflow and at the inlet in the region of the deflector plate where hexahedral elements could not be meshed. This is shown in Figures 6-26 and 6-27.
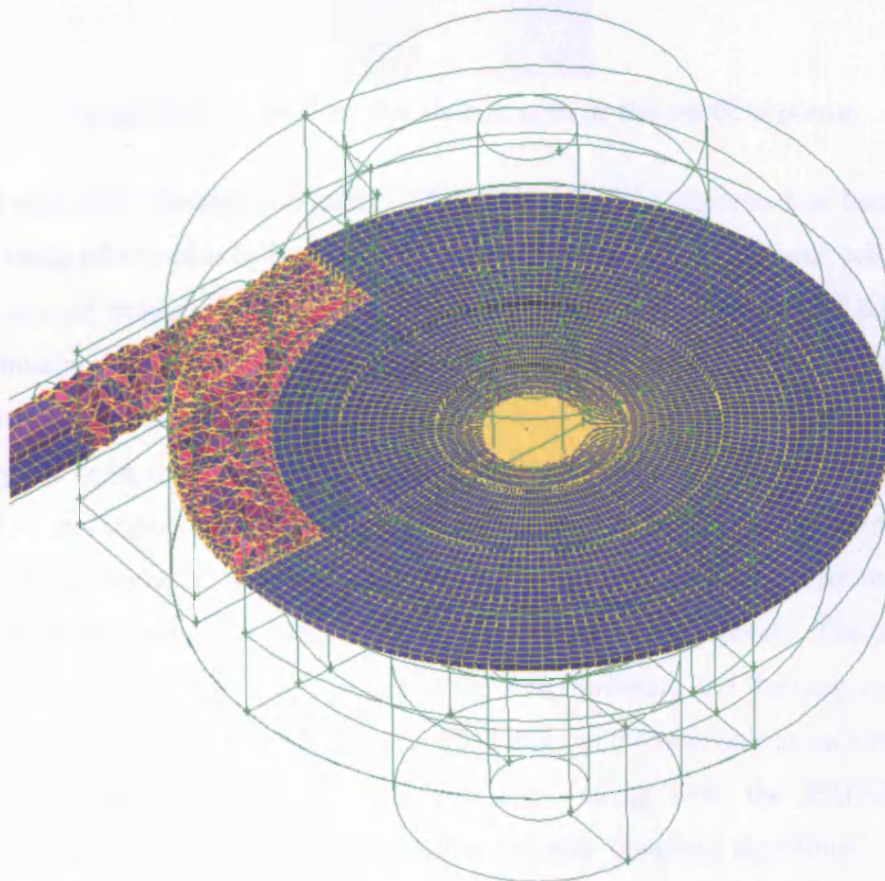
Figure 6-26. A view of the hybrid grid in the horizontal plane.
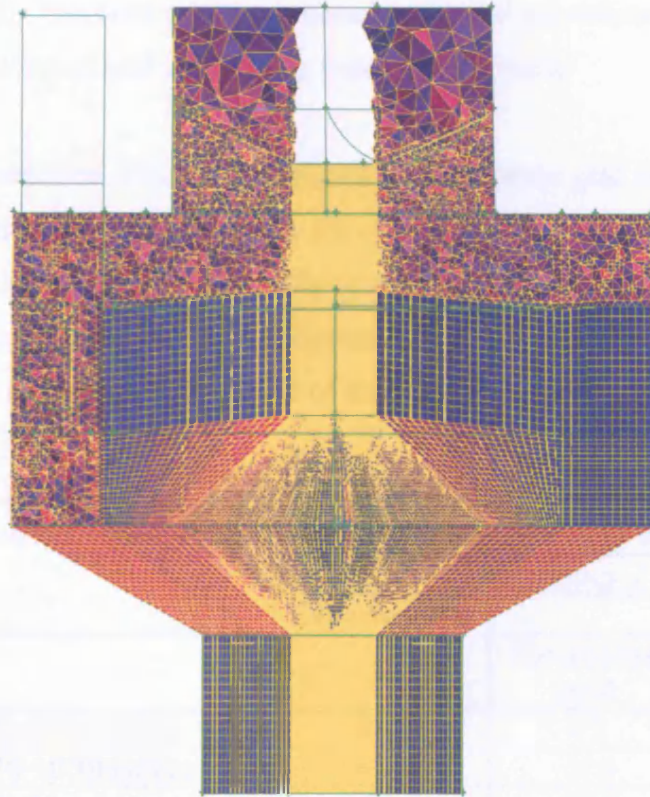
Figure 6-27. A view of the hybrid grid in the vertical plane.

The hybrid grid size was approximately 1 311 000 cells. As discussed in Section 2.3.1.1 a tetrahedral mesh allows cells to be clustered whereas hexahedral grids force cells to be placed where they are not needed. This can be seen in the centre of the meshed Grit King® in Figure 6-27. A converged solution was achieved using the transient solver and monitoring the static pressure on the centreline and the tangential velocity 0.1m off the centreline in the region enclosed by the cone, as here the flow becomes established towards the end of the solution. This is due to this region of fluid being enclosed and the predicted flow field relies upon the convection of the predicted flow field throughout the grid. The transient solver was used as the residuals were more stable compared to using a steady state solver. The predicted flow field is steady state due to the convergence of the static pressure and the tangential velocity at the points where it was monitored and the small change in the residuals at each time step. The Reynolds Stress turbulence model has been used along with the PRESTO! pressure interpolation scheme and the SIMPLE pressure-velocity coupling algorithm. Second order terms were solved for momentum only. According to Fluent Inc. (Fluent Inc., 2005, Private Communication) "Experience suggests that there isn't significant change between first order and higher order on the turbulent quantities" for these types of system and the use of first order terms on the turbulent quantities aids the speed of convergence. Due to the large grid

size and the use of the transient solver a processing time of approximately three weeks was required and examination of grid dependency was not undertaken.

Table 6-4 lists the retention efficiency predicted by the hybrid grid at 11 litres per second compared to the tetrahedral grid and clearly the change in predicted efficiency is small. The largest change is for Styrocell 1.4-2.0mm, where the prediction has reduced by approximately 16% to 68.1%. However, the observed efficiency is approximately 21% and the hybrid mesh is still unable to give a reasonable prediction of the retention efficiency.

Table 6-4. Comparison between experimental and CFD-predicted retention efficiencies with a hybrid and tetrahedral grid at 11 litres per second.

	Efficiency, / %		
	Experimental	**CFD**	
Particles		**Tetrahedral grid**	**Hybrid grid**
Purolite A100 500-710microns	<4.4	4.3	3.8
Purolite A100 710-1000microns	≈5.0	27.6	18
Styrocell 1.4-2.0mm	≈21.0	84.0	68.1
Styrocell 2.0-2.8mm	≈35.1	99.0	92.0
Styrocell 2.8-5.6mm	≈48.0	99.9	97.8
Purolite PPC-100H 500-600microns	≈72.0	100	99.0

Figure 6-28 compares the predicted axial, tangential and radial velocity in the tetrahedral and hybrid mesh in the plane of the inlet pipe within the 0.75m diameter Grit King®. Figure 6-29 compares the magnitude of the RMS velocity fluctuations. Although the axial velocity predicted using the tetrahedral mesh follows a similar trend to the hybrid mesh, whereby there is upward flow to the right of the central shaft and downward flow to the left, the hybrid mesh has predicted higher values for the positive velocity and hence, this is likely to reduce the predicted efficiency. The distribution of axial velocity in the hybrid mesh is more complex, as indicated by the shear zone, marked in olive green. The tetrahedral mesh suggests that the trail of fluid from the inlet tends to flow downwards. In the case of the hybrid grid, the trail of downward flow from the inlet is less pronounced and downward flow is predominantly to the left of the plane. In both cases downward flow along the central shaft is predicted and this behaviour has been observed by Tyack and Fenner (1998a) in a 1.6m diameter Grit King®.
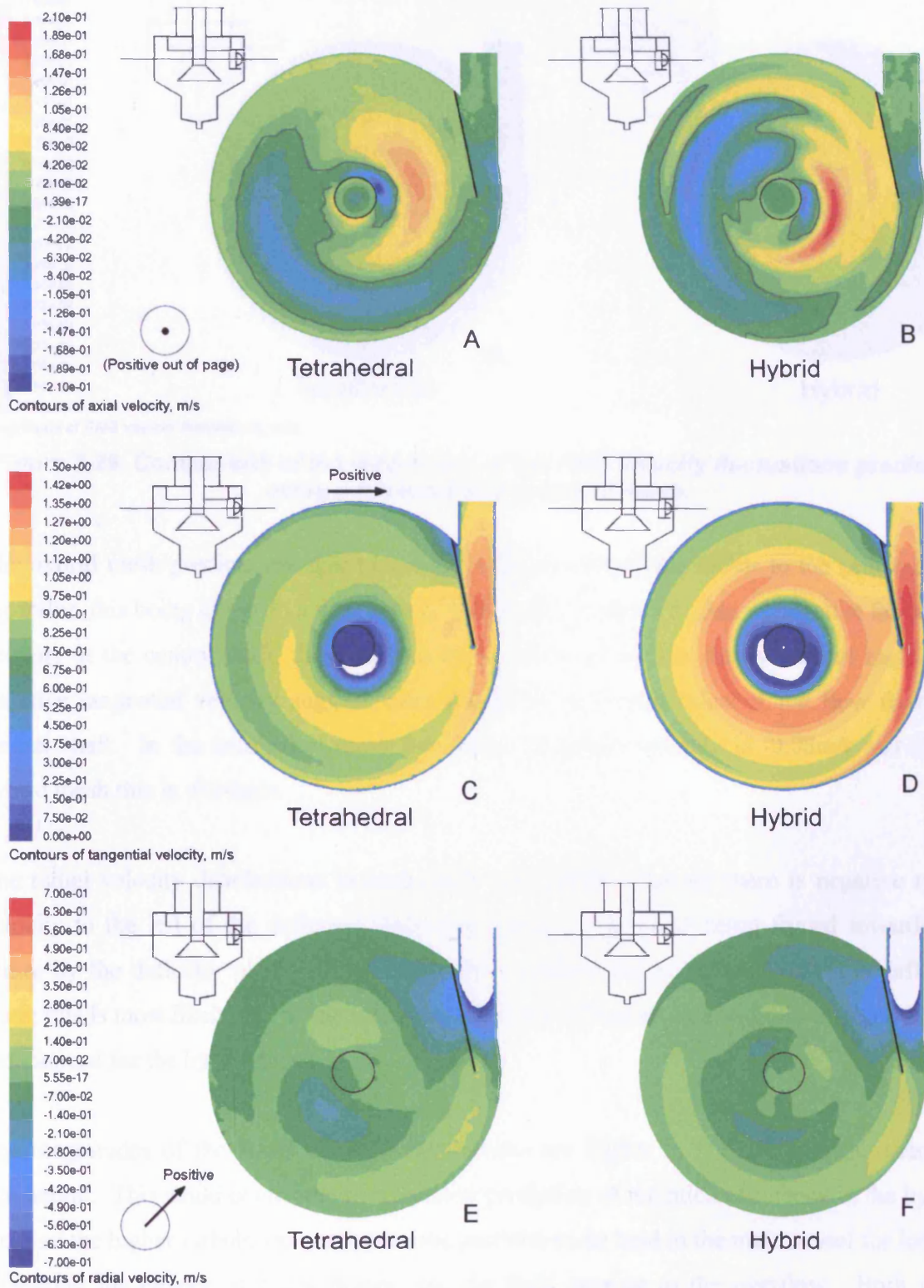
Figure 6-28. Comparison between predicted axial, tangential and radial velocity using a tetrahedral and hybrid mesh.

1.50e-01	
1.43e-01	
1.35e-01	
1.27e-01	
1.20e-01	
1.13e-01	
1.05e-01	
9.75e-02	
9.00e-02	
8.25e-02	
7.50e-02	
6.75e-02	
6.00e-02	
5.25e-02	
4.50e-02	
3.75e-02	
3.00e-02	
2.25e-02	
1.50e-02	
7.50e-03	
0.00e+00	

Magnitude of RMS velocity fluctuations, m/s
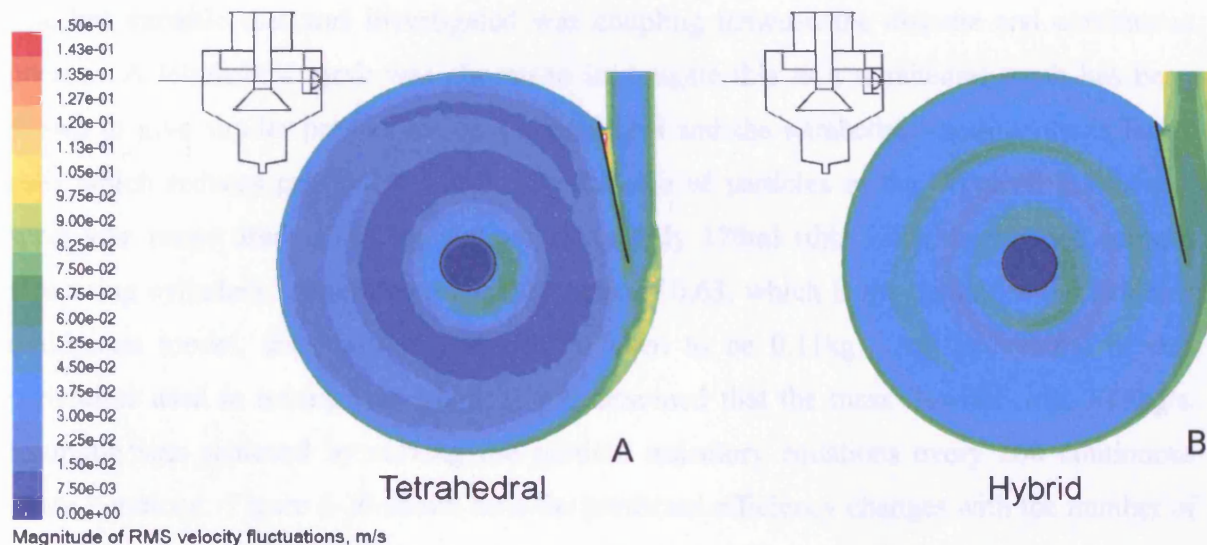
Figure 6-29. Comparison of the magnitude of the RMS velocity fluctuations predicted using a tetrahedral and hybrid mesh.

The hybrid mesh predicts stronger tangential velocities which are closer to the centre of the separator, this being closer to a free vortex. Both grids predict a region of negative tangential velocity at the central shaft, these regions being whitened out for clarity. These regions of negative tangential velocity suggest there might be some separation of the flow from the central shaft. In the tetrahedral mesh the lowest tangential velocity is -0.08m/s and in the hybrid mesh this is -0.04m/s.

The radial velocity distributions in both grids are similar, whereby there is negative radial velocity to the left of the deflector plate, this owing to the fluid being forced towards the centre by the deflector plate. There is a trail of positive radial velocity from the deflector plate; this is most likely due to the inlet flow from the deflector plate and this is slightly more pronounced for the hybrid mesh.

The magnitudes of the RMS velocity fluctuations are higher in the hybrid mesh than the tetrahedral. This could contribute to a reduced prediction of retention efficiency in the hybrid mesh as the higher turbulence may cause the particles to be held in the main vessel for longer, increasing the chance of being drawn into the fluid passing to the overflow. Both grids predict a high fluctuation adjacent to the HDVS vessel wall where the fluid emerges from the deflector plate and this region decays quite rapidly.

The last variable that was investigated was coupling between the discrete and continuous phases. A tetrahedral mesh was chosen to investigate this as a tetrahedral mesh has been shown to give similar predictions to a hybrid grid and the tetrahedral mesh contains fewer cells which reduces processing time. The volume of particles in the Styrocell 2.8-5.6mm sieve size range used in testing was approximately 170ml (this value determined using a measuring cylinder). Assuming a packing limit of 0.63, which is the default in the Eulerian multiphase model, the mass of particles is taken to be 0.11kg. As the volume of this particulate used in testing was small, it was assumed that the mass flowrate was 0.11kg/s. Coupling was achieved by solving the particle trajectory equations every 200 continuous phase iterations. Figure 6-30 shows how the predicted efficiency changes with the number of continuous phase iterations during the discrete phase coupling.
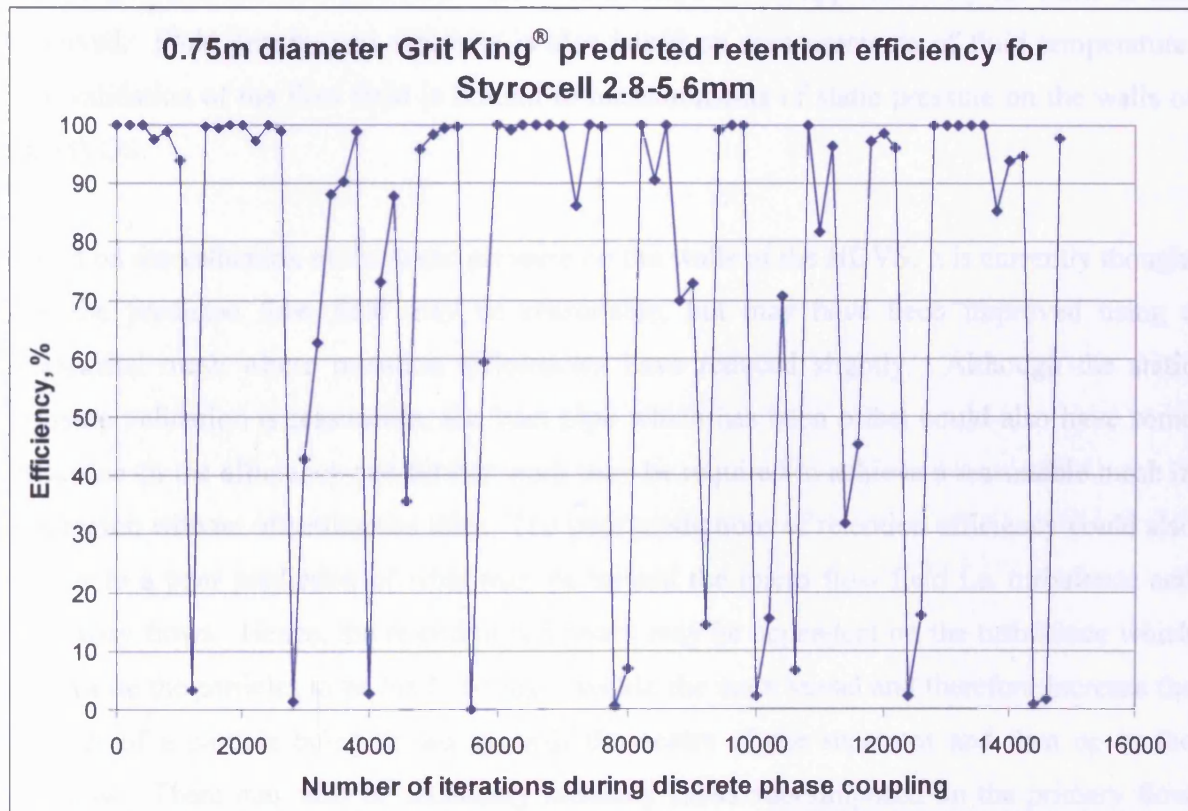
Figure 6-30. CFD-predicted retention efficiency for Styrocell 2.8-5.6mm with coupling between the discrete and continuous phases.

Quite clearly from Figure 6-30 the solution for the discrete phase has not converged. In general the predicted retention efficiency is in excess of 80%, with spikes occurring where the efficiency frequently drops to less than 20%. The spikes appear to occur periodically which would imply that a transient solver may be more suitable for achieving a converged solution.

Another limitation of using a steady state solver is that the mass flowrate is assumed to be a constant 0.11kg/s. Using a transient solver, the mass flowrate of particles injected can be set at 0.11kg/s for the first second of the solution and zero thereafter, which would be a more realistic representation of conditions in the laboratory. However, using a transient solver to compute the particle trajectories would be considerably time consuming and this requires more work to see if a reasonable validation can be made.

6.3 Discussion

CFD models have been created to try and replicate, as far as possible, the conditions present in the laboratory. This includes the full length of horizontal pipe preceding the HDVS as well as trying to generate a free surface which has a shape that is approximately the same as that observed. Fluid density and viscosity is also based on measurements of fluid temperature. The validation of the flow field is limited to measurements of static pressure on the walls of the HVDS.

Based on the validation of the static pressure on the walls of the HDVS, it is currently thought that the predicted flow field may be reasonable, but may have been improved using a hexahedral mesh where retention efficiencies have reduced slightly. Although the static pressure validation is reasonable, the inlet pipe which has been offset could also have some influence on the efficiency and further work may be required to achieve a reasonable mesh in this region without offsetting the inlet. The poor predictions of retention efficiency could also be due to a poor prediction of what may be termed the micro flow field i.e. turbulence and secondary flows. Hence, the retention efficiency may be dependent on the turbulence which may cause the particles to be held up longer within the main vessel and therefore increase the chances of a particle being drawn towards the centre of the separator and then up to the overflow. There may also be secondary unsteady flows superimposed on the primary flow which causes the particles to be held within the main vessel for an extended period of time compared with the flow field without secondary flows. Using a transient solver secondary unsteady flows have not been detected. For example in the hybrid grid where a transient solver was used to give better convergence also resulted in convergence of the static pressure and tangential velocity.

Numerous steps have been taken to try and achieve a reasonable validation of the HDVS retention efficiency. This includes examination of the relationship used for calculating the drag coefficient, the effect of shape factor, the coefficient of restitution, the length scale used for updating the equations of motion for the particle, the pressure strain model used in the RSM, the pressure interpolation scheme, grid dependency, the effect of a hybrid mesh and coupling between the discrete and continuous phases.

An option that has not been examined is to use a transient solver with coupling between the discrete and continuous phases. Another possibility is to refine the mesh in the near wall region. Secondary flows may result from pressure gradients in the boundary layers and this will require near wall modelling where the mesh in the boundary layer is of a sufficient resolution such that the y^+ value is less than 10, which will most likely result in a mesh size larger than any used in this work i.e. greater than 1 300 000 and hence a considerable processing time.

Further work would be desirable to attain measurements of the fluid velocity within the HDVS and if Laser Doppler Anemometry (LDA) was to be used, then the fluctuating components of the velocity can also be investigated and hence the turbulence. This could then be used to increase the validation of the computed flow field. Using Particle Image Velocimetry (PIV) in the laboratory, the fluid behaviour within the HDVS may be studied and may give an insight into whether CFD is predicting a similar flow pattern. However, LDA and PIV were beyond the scope of this work. Retention efficiencies are over predicted and this could be due to the prediction of the particle positions at entry to the HVDS. A method of characterising the particle distributions at the inlet to the HDVS would therefore be desirable.

6.4   Summary

- CFD predictions of the pressure difference between the inlet and various points on the separator compare reasonably well.

- CFD predictions of retention efficiency are poor.

- Further work is required to look at grid dependency of the hybrid grid and if there is no improvement in the validation then modelling the HDVS using a transient solver with coupling between the discrete and continuous phases as well as refinement of the grid in the near wall region may be required.

- Further work is required to take measurements and observations of the flow field within the HDVS.

7 Retention efficiency testing of a 6' diameter Grit King®

It was the opinion of Hydro International Plc (Hydro International Plc, 2005, Private Communication) that a 6' (1.83m) diameter Grit King® in the research laboratory in Portland, Maine, USA, provided the opportunity to study scaling of retention efficiency. It was the intention that the testing media, Purolite, would be dried, sieved and soaked prior to the author's arrival in Portland. Due to a clerical error, this was not the case and the 2 week test period was consequently reduced to only a week.

Figure 7-1 details the internal components and the pipe layout preceding the unit in the laboratory.

A Inlet
B Standpipe
C Deflector plate
D Vessel wall
E Dip plate
F Cone   K Underflow
G Central Shaft L Annulus
H Cut outs   M Overflow channel
I Benching skirt N Overflow
J Grit pot   O Ventbox
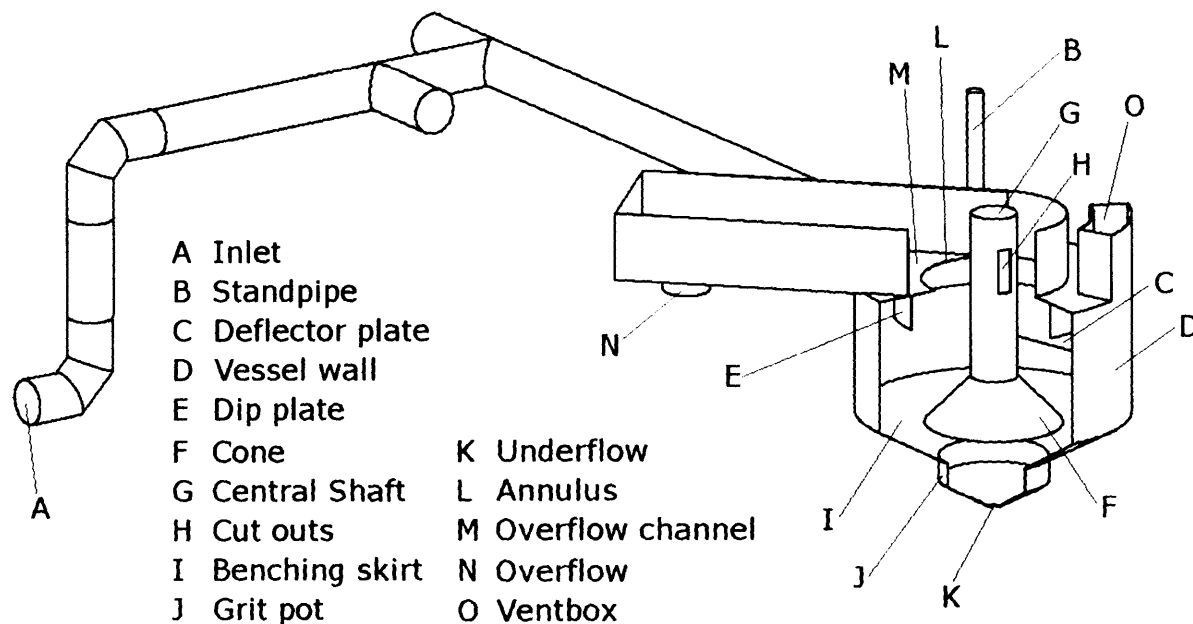
Figure 7-1. The layout of the 6' diameter Grit King® and the preceding pipe work.

The 6' diameter Grit King® contains similar internal components to the 0.75m diameter unit (see Section 5.1) such as the deflector plate 'C', dip plate 'E' central shaft 'G' and cone 'F'. Noticeable differences are that the overflow channel 'M' of the 6' unit is positioned at 45° to the inlet pipe, whereas the overflow of the 0.75m diameter unit is parallel to the inlet pipe. The overflow of the 6' unit is central and has a width equal to the diameter of the annulus of the overflow 'L'. The overflow of the 0.75m diameter unit is tangential and has a width that is 0.53 times the diameter of the overflow annulus. The base of the cone is 0.086m below the top of the benching skirt whereas the base of the cone in the 0.75m diameter unit is level with the top of the benching skirt 'I'. Table 7-1 summarises the aspect ratio of the main

components of the two HDVSs, excluding the deflector plate and each dimension being compared is indicated in Figure 7-2. The aspect ratio is defined as the dimension of the component in the 6' diameter unit divided by the dimension in the 0.75m diameter unit.
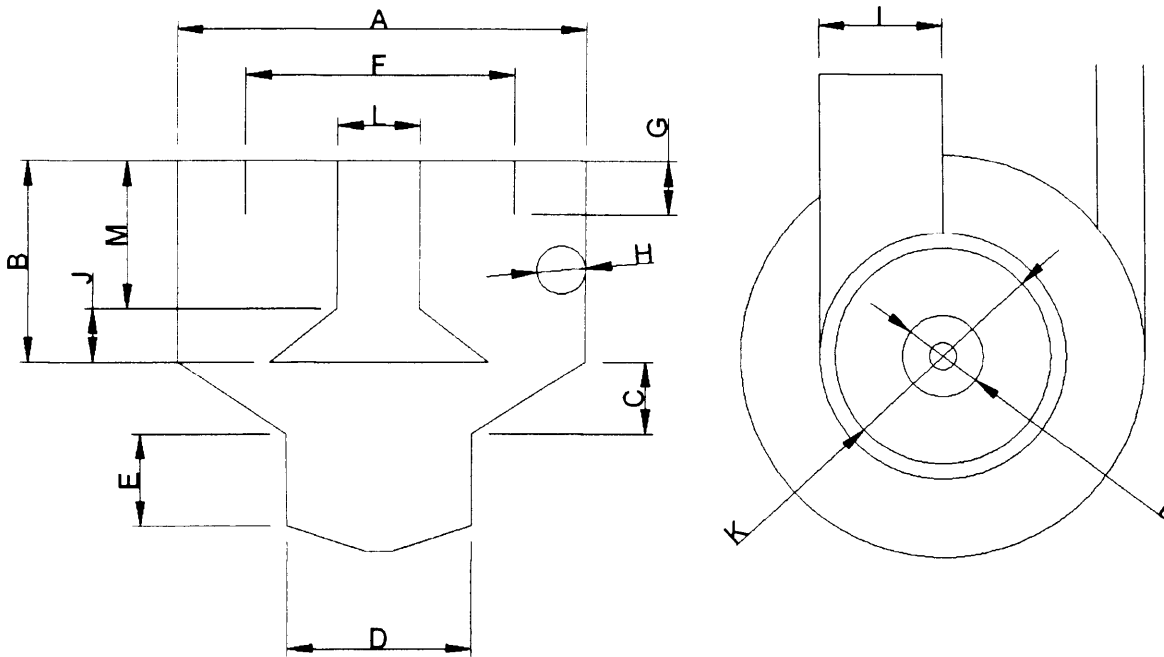
Figure 7-2. Dimensions of the main components forming the Grit King®.

Table 7-1. The aspect ratio between the components in the 6' and 0.75m diameter Grit King®.

Component	Dimension	Aspect ratio
Vessel diameter	A	2.4
Vessel height	B	2.4
Benching skirt height	C	2.4
Grit pot diameter	D	2.4
Grit pot height	E	0.8
Dip plate diameter	F	2.5
Dip plate height	G	2.2
Inlet diameter	H	3.1
Overflow width	I	4.9
Cone height	J	2.5
Cone base diameter	K	2.5
Cone top diameter	L	3.0
Central shaft height	M	2.8

The ideal aspect ratio of each component is 2.4 based on scaling the HDVS diameter. From Table 7-1 it can be seen that the vessel and benching skirt height as well as the grit pot diameter are scaled in proportion. The dip plate diameter, dip plate height, cone height and

the diameter of the cone base are satisfactory for studying scaling. The central shaft height, the diameter of the top of the cone, the grit pot height and the inlet diameter are not ideal due to the aspect ratio of each deviating from 2.4. As already discussed, the overflow width is not satisfactory and may influence efficiencies due to the design deviating from the 0.75m diameter unit.

7.1 Experimental setup and procedure

7.1.1 Facility layout

The preceding pipe work to the 6' diameter Grit King® comprises a 0.305m (12 inch) diameter pipe which is fed from a FLYGT submersible pump positioned at 'A' in Figure 7-1. The pump is located in a storage tank 7.92m in diameter. Just downstream of point 'A' is a 90° bend which feeds the fluid vertically upwards to a height of 1.7m where a second 90° bend turns the pipe back into the horizontal plane. Further downstream at 2.3m is a junction that comprises a 90° bend to the right which just downstream is sealed by a valve. Further downstream at 0.9m from the junction is a T-section which is sealed to the left by a second valve and the fluid is thus forced to pass through the T-section to the right which forms the inlet to the 6' diameter Grit King®. A standpipe 'B' is positioned 5.6m downstream from the T-section and was used for releasing the particles into the inlet pipe. Positioned on the inlet pipe just upstream of the standpipe are the sensors to a Sono-Trak™ ultrasonic flowmeter.

Detailed dimensions of the Grit King® and rig layout are given on Pages 162 to 164. Figures H1 and H2, Appendix H, show additional photographs of the test rig.

460

1395

197

24°

46.2°

2438

384

R914

45°

∅305

305

60

1828

Drawn By:	Hydro International
Darrell A. Egarr	94 Hutchins Drive
Cardiff University	Portland
Queens Building	ME 04102
The Parade	
Cardiff	
CF24 0YF	

Full dimensions omitted at the request of Hydro International

	Date: 26/04/05	Title:
		6' Grit King(R) External
Dimensions: mm	Scale: 1:40	Paper Size: A4	Dimensions

Cut outs on central shaft
See detail C

A

A

A-A

C (2 : 35)

Cut outs on each side
of central shaft

B

B (1 : 20)

Full dimensions omitted at the
request of Hydro International

Drawn By:	Hydro International
Darrell A. Egarr	94 Hutchins Drive
Cardiff University	Portland
Queens Building	ME 04102
The Parade	
Cardiff	
CF24 0YF	

| Date: 26/04/05 | Title: 6' Grit King(R) Internal View |
| Dimensions: mm | Scale: 1:35 | Paper Size: A4 | |
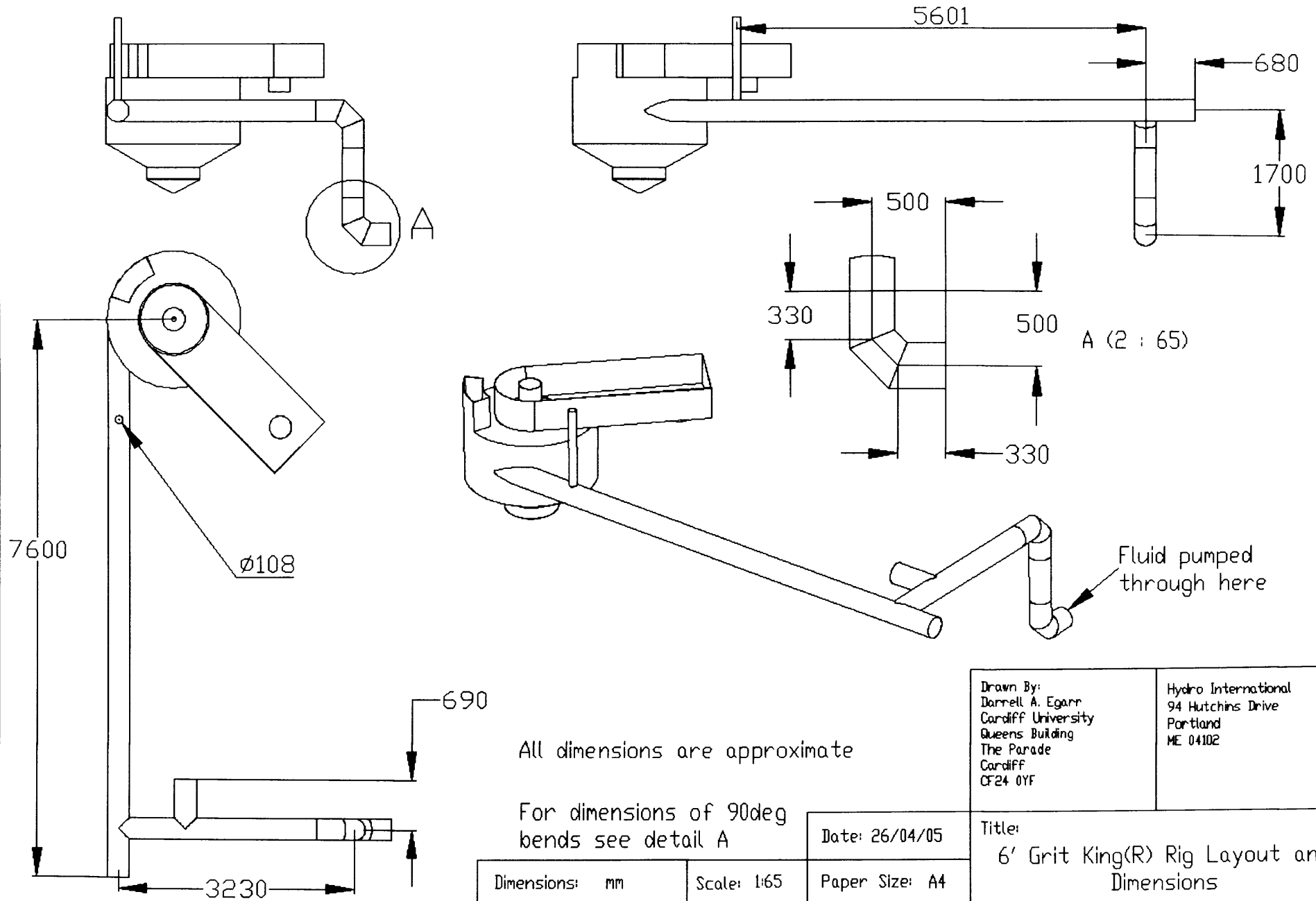
5601

680

1700

500

330

330

500

A (2 : 65)

A

7600

Ø108

690

3230

Fluid pumped through here

All dimensions are approximate

For dimensions of 90deg bends see detail A

Drawn By: Darrell A. Egarr Cardiff University Queens Building The Parade Cardiff CF24 0YF	Hydro International 94 Hutchins Drive Portland ME 04102	
	Date: 26/04/05	Title:
Dimensions: mm	Scale: 1:65	Paper Size: A4

6' Grit King(R) Rig Layout and Dimensions

The overflow channel is approximately 0.8m above the free surface of the fluid in the storage tank. Hence, when the Grit King® is discharging fluid, switching the pump off results in all the fluid above the free surface of the reservoir to drain back, which could result in a proportion of the particulates remaining in the HDVS being drawn back through the inlet and into the storage tank.

The particles were collected at the overflow by placing a piece of mesh (Petex 07-225/42 Polyester (PET) monofilament precision fabric) between the flange on the overflow and the overflow pipe, as shown in Figure 7-3.

Figure 7-3. The placement of the mesh at the overflow in the 6' diameter Grit King®.

7.1.2   Particle characterisation

The particulate used for testing the HDVS was 'Purolite' as used for testing the 0.75m diameter Grit King®. Types A100 and PFC-100H were used. Both types were dried and sieved to reduce the size range of particles in a sample and then left for a period of 5 days in fluid from the storage tank to allow expansion and adjustment to the fluid which contains a

small amount of chlorine to prevent algae growth. The particles were characterised in the same way as the samples used for testing the 0.75m diameter unit, by taking measurements of particle diameter of 50 water soaked particles using Vernier callipers taking care not to squash the particle whilst taking its diameter. Determination of settling velocity on the same number of particles was also carried out. The diameter of the settling column used was 59mm and the maximum particle diameter can be assumed to be no more than 850microns from the sieve sizes used. Hence, from Figure 2-2, adapted from Fidleris & Whitmore (1961) which accounts for wall effects on the terminal settling velocity of a particle, the diameter of the settling column is sufficient to be able to neglect these. The temperature of the fluid was taken before and after the settling tests so that the density and viscosity of the water could be determined. Each settling test allowed the particle to settle an adequate distance to allow the terminal settling velocity to be achieved. Using a stop watch, the particle was then timed to fall a pre-determined distance. The particle density was then calculated using the procedure described in Section 5.2.3.

The settling velocity data and particle diameters measured are presented in Appendix I. It can be seen from Tables I1 and I3 that the average standard deviation for the settling velocity is approximately 13% and for the particle diameter 11%. These values are slightly higher than what was achieved for the particles for testing the 0.75m diameter Grit King® due to time constraints for sieving the particles. Table 7-2 presents the average settling velocity, diameter and calculated density. The mean settling velocity is at 20°C so that a direct comparison of the settling velocity of the particles can be made. It has been found by calculating the particle Reynolds number for all the particles in Table 7-2, that each has a terminal settling velocity that is in the intermediate drag regime at 20°C.

In the characterisation of the particles it is assumed that the errors introduced in measurement are small and the 99.8% confidence interval has therefore been determined for the settling velocity and particle diameter. Using the upper 99.8% confidence value for settling velocity and lower value for diameter (fast settling particle with small diameter and hence low drag) gives an upper value for the particle density. The inverse gives a lower value for particle density. This is a conservative estimate for the range of the particle density as it was observed during the settling tests that smaller particles tended to settle slower. The data for the 99.8% confidence interval is presented in Appendix I.

Table 7-2. Derived particle properties used for testing the 6' diameter Grit King®.

Particle type and sieve size range	Mean settling velocity at 20°C, / m/s	Mean diameter, / m	Mean density, / kg/m^3
Purolite (PFC-100H) 425-600microns	0.01527	0.5932×10^{-3}	1137
Purolite (A100) 600-850microns	0.00862	0.6332×10^{-3}	1059

The density of the Purolite A100 is similar to that used for testing the 0.75m diameter Grit King® as would be expected. Type PFC-100H has not been characterised previously and no comparison can be made.

7.1.3 Head loss due to mesh at overflow

To assess whether the placement of the mesh at the overflow caused an additional head loss and hence backfilling to occur, a set of measurements of the height of the fluid in the overflow channel were made at a number of flowrates with and without the mesh. The data is tabulated in Table C2, Appendix C and presented in Figure 7-4 and backfilling does not seem to have occurred.
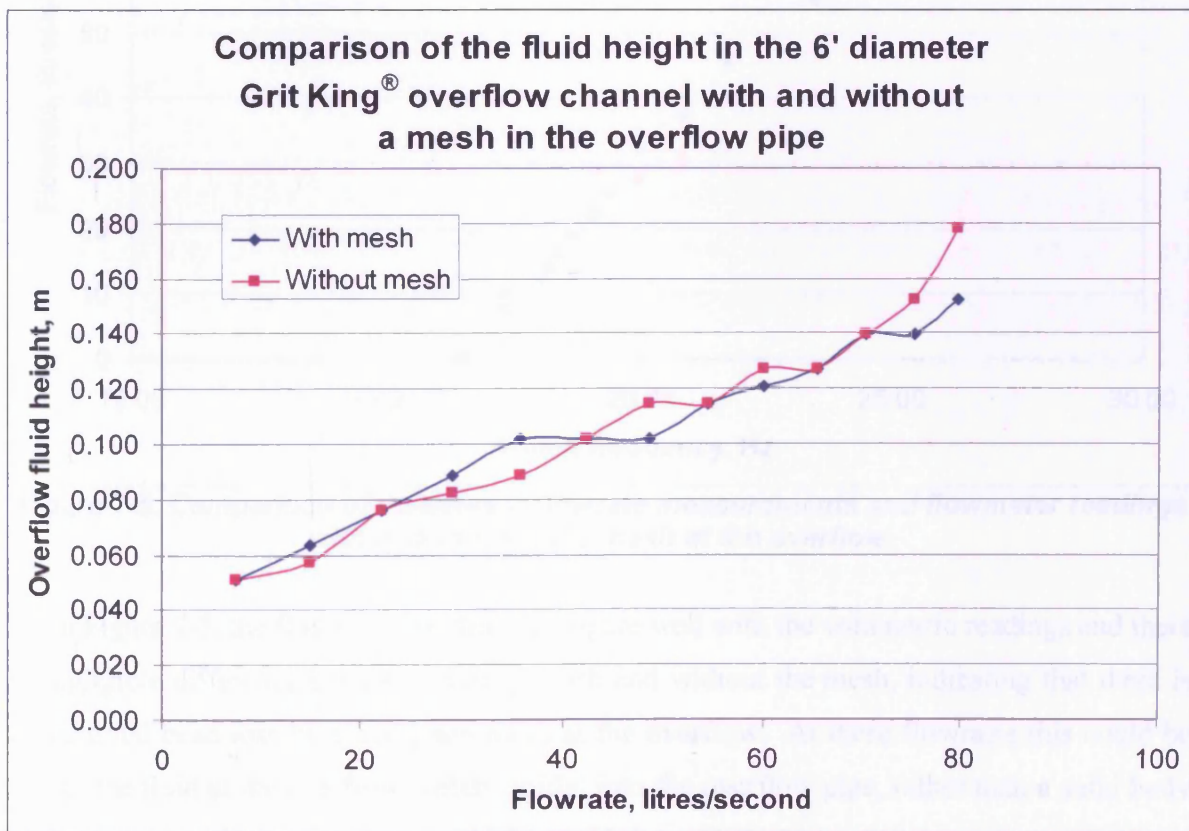
Figure 7-4. Comparison of the fluid height in the 6' diameter Grit King® overflow channel with and without the mesh in the overflow pipe.

Volumetric flowrate measurements, supplied by Hydro International Plc, were compared to flowmeter readings. The volumetric flowrate measurements were taken in the range of 12.6 and 25.5 litres per second. A comparison can only be made at low flowrates as the container available for volumetric measurement was 568 litres (150 US gallons) and floated on the free surface of the fluid in the storage tank; hence, at higher flowrates, keeping the container horizontal is difficult and the time to fill is reduced significantly such that an accurate measurement cannot be taken. Figure 7-5 compares the pump frequency with the volumetric flowrate measurements. An additional check for head loss was made by comparing the flowmeter readings with and without the mesh at the overflow.
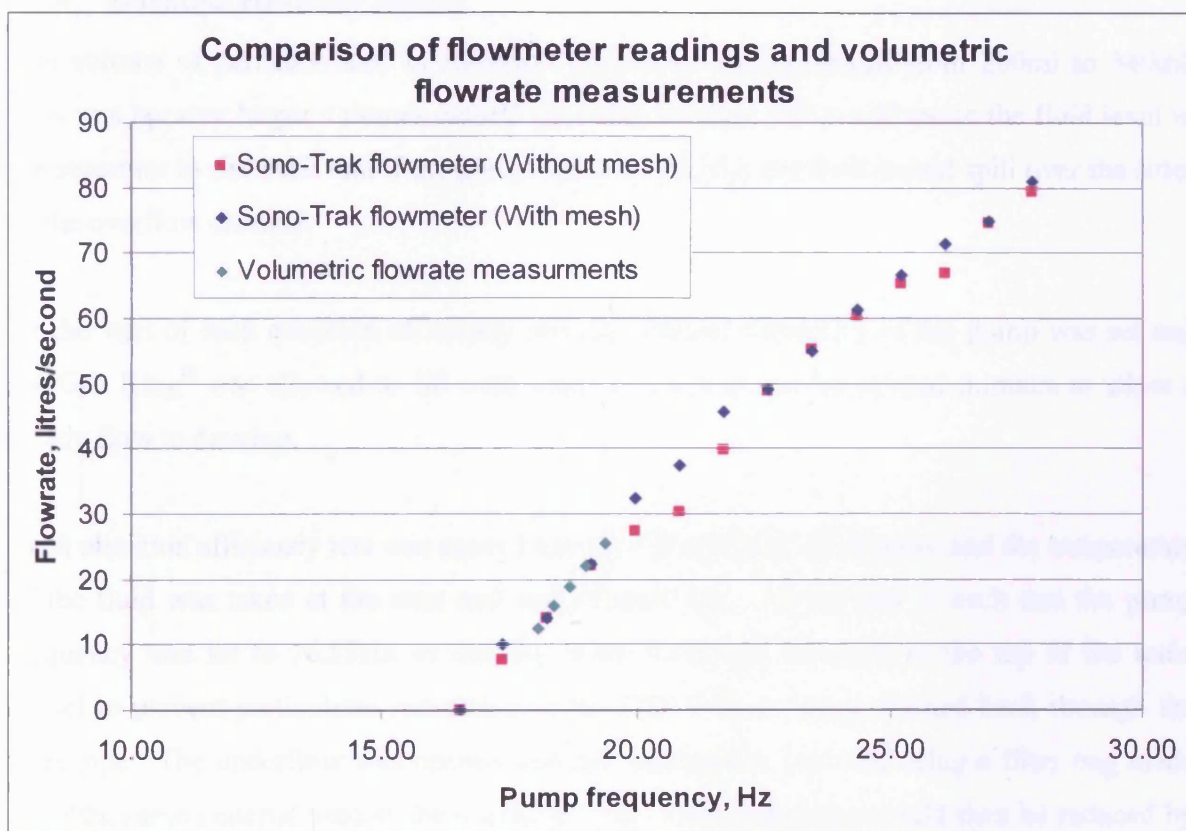
Figure 7-5. Comparison of volumetric flowrate measurements and flowmeter readings with and without the mesh at the overflow.

From Figure 7-5, the flowmeter readings compare well with the volumetric readings and there is negligible difference between readings with and without the mesh, indicating that there is no incurred head loss by placing the mesh at the overflow. At these flowrates this could be due to the fluid at the overflow which 'spills' into the overflow pipe, rather than a solid body of fluid passing through the mesh which would more likely have a head loss associated with it. Taking the average of the ultrasonic flowmeter readings at each pump frequency, a

relationship between the pump frequency and flowrate has been found to be given by Equation 7-1 and fits the data with an R_t^2 value of 0.999.

$$Q = -0.1796f^2 + 15.024f - 199.58 \qquad (7\text{-}1)$$

Where: f = Frequency of pump, Hz

Hence, the flowrate may be determined for a pump frequency in the range of 0 to 27.8Hz. At 16.55Hz the water level is balanced at the top of the main vessel with no discharge at the overflow.

7.1.4 Retention efficiency testing

The volume of particles used in retention efficiency testing ranged from 200ml to 340ml. This was because larger volumes caused the mesh to blind and would cause the fluid level in the separator to rise such that if the pump was left running, the fluid would spill over the sides of the overflow channel.

At the start of each retention efficiency test, the desired frequency of the pump was set and the Grit King® was allowed to fill with water and left to run for several minutes to allow a steady flow to develop.

Each retention efficiency test was carried out for a duration of 10 minutes and the temperature of the fluid was taken at the start and end of each test. At the end of each test the pump frequency was set to 16.55Hz so that the water level was balanced at the top of the main vessel to prevent particulates remaining in the HDVS from being drained back through the inlet pipe. The underflow was opened and the particulates captured using a filter bag made from the same material used at the overflow. The pump frequency would then be reduced by 1Hz every 2 minutes so that the fluid level reduced gradually. At the end of each test the inside of the HDVS was washed down using a hose to rinse any particulates that were remaining in the separator.

The HDVS efficiency is defined as the volume of particles remaining in the HDVS after 10 minutes expressed as a percentage of what was released into the HDVS. Measuring the volume of particles instead of mass was justified by the fact that excess water held between the particles by surface tension would be included in the mass and would therefore be

erroneous. Drying the particles after each test would have been extremely time consuming. As the total volume of particles collected was the same as the volume introduced at the inlet then the error in determining the efficiency by volumetric measurement would be negligible.

7.2 Results

Tables J1 and J2, Appendix J, contain the retention efficiency data for the 6' diameter Grit King®. Figure 7-6 shows the retention efficiency plotted against V/Q, the theoretical residence time. The data for Purolite A100 is a little scattered. The logistic equation has been fitted to the data to give a best fit curve and an R_i^2 value of 0.982 has been achieved, indicating a good fit. The data for Purolite PFC-100H, Figure 7-7, is fairly consistent and the R_i^2 value is 0.999. Ideally more data on each efficiency curve, as well as data for different particles would be acquired but due to time constraints this was not possible.

In Section 5.3.3 an efficiency model, Equations 5-10, 5-12 and 5-13, was developed for the 0.75m diameter Grit King® which included a volume term that may make the model suitable for scaling retention efficiencies. Figure 7-6 compares the efficiency curve for Purolite A100 to the prediction made by the 0.75m diameter Grit King® efficiency model. Figure 7-7 compares the model's prediction with the efficiency curve for Purolite PFC-100H.

6' diameter Grit King® retention efficiency results

Efficiency, % (y-axis: 0, 10, 20, 30, 40, 50, 60, 70, 80, 90, 100)

Fluid volume / Inlet flowrate, s (x-axis: 0, 100, 200, 300, 400, 500, 600, 700)

- ◆ Purolite A100 600-850microns
- ◇ Purolite A100 600-850microns BEST FIT
- ■ 0.75m Diameter Grit King® Model
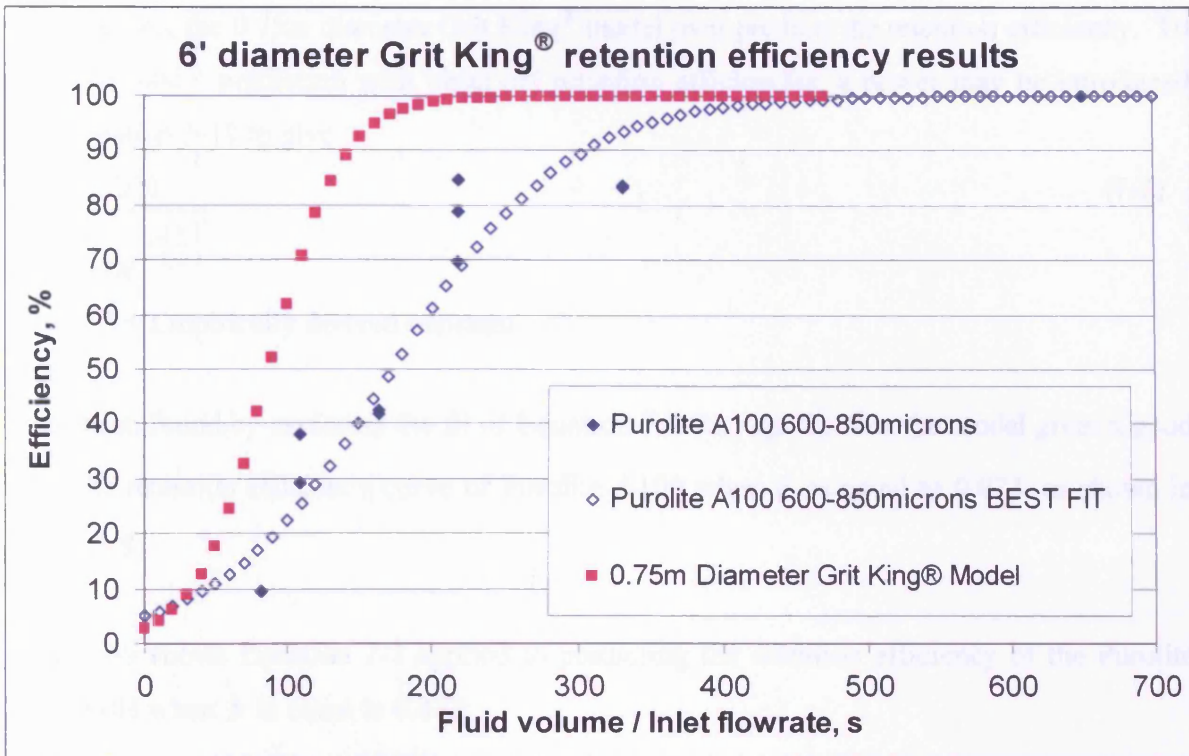
Figure 7-6. Comparison of the experimental retention efficiencies and those predicted using the efficiency model developed for the 0.75m diameter Grit King®.

6' diameter Grit King® retention efficiency results

Efficiency, % (y-axis: 0, 10, 20, 30, 40, 50, 60, 70, 80, 90, 100)

Fluid volume / Inlet flowrate, s (x-axis: 0, 50, 100, 150, 200, 250, 300)

- ◆ Purolite PFC-100H 425-600microns
- ◇ Purolite PFC-100H 425-600microns BEST FIT
- ■ 0.75m Diameter Grit King® Model
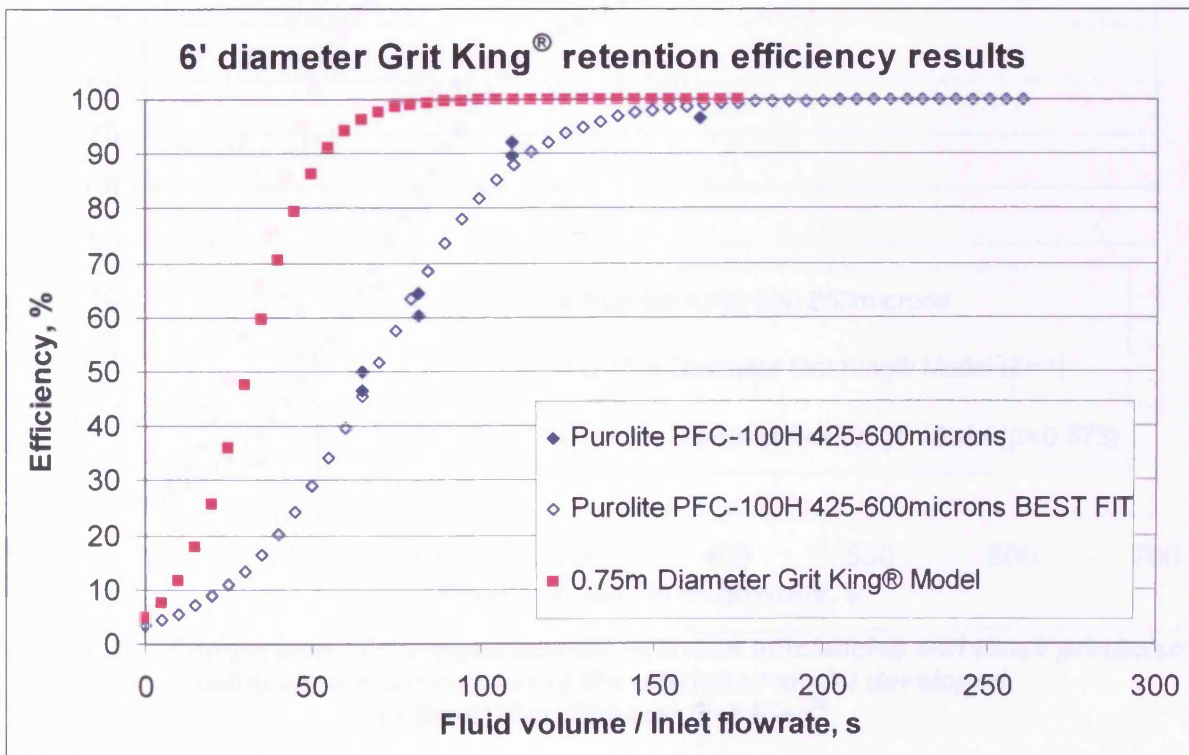
Figure 7-7. Comparison of the experimental retention efficiencies and those predicted using the efficiency model developed for the 0.75m diameter Grit King®.

In both cases, the 0.75m diameter Grit King® model over predicts the retention efficiency. To align the model prediction with observed retention efficiencies, a power may be introduced into Equation 5-10 to give

$$\eta = \frac{100}{1 + De^{-C\left(\frac{V}{Q}\right)^{\beta}}}$$

(7-2)

Where: β = Empirically derived constant

It has been found by assessing the fit of Equation 7-2 through R_t^2 that the model gives a good fit to the retention efficiency curve of Purolite A100 when β is equal to 0.873, as shown in Figure 7-8.

Figure 7-9 shows Equation 7-2 applied to predicting the retention efficiency of the Purolite PFC-100H when β is equal to 0.873.
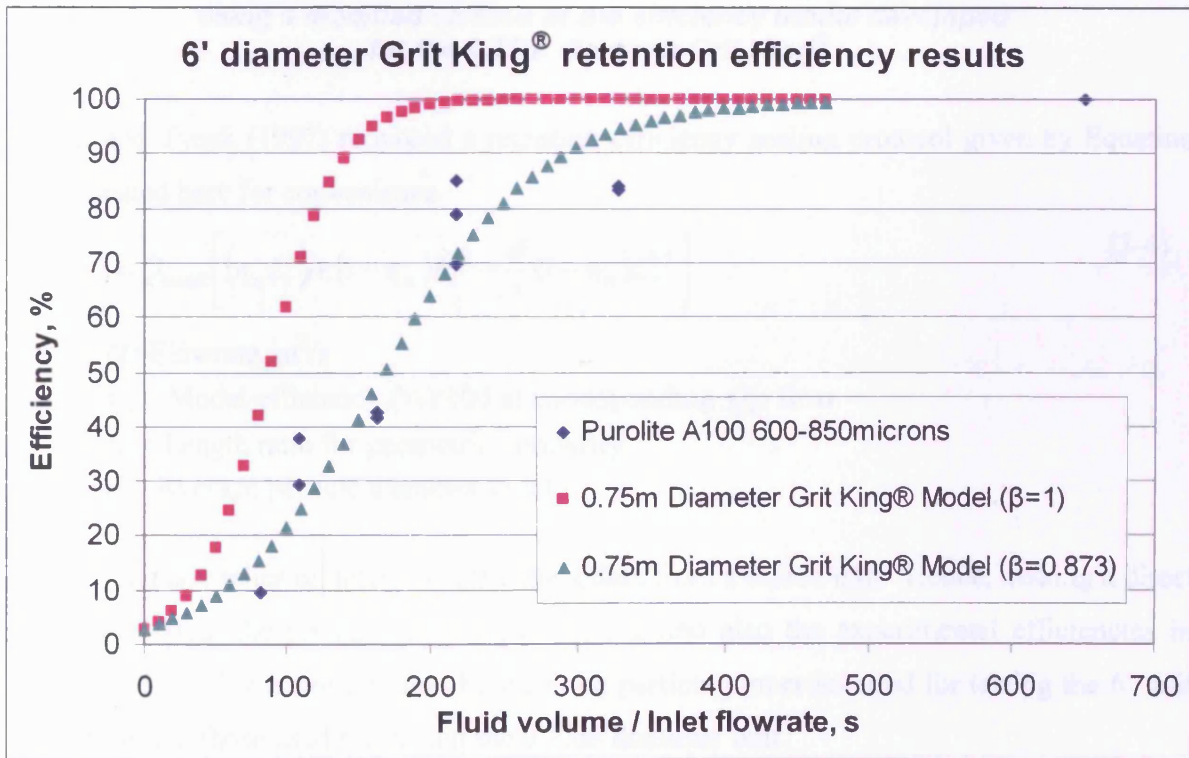
Figure 7-8. Comparison of the experimental retention efficiencies and those predicted using a modified version of the efficiency model developed for the 0.75m diameter Grit King®.
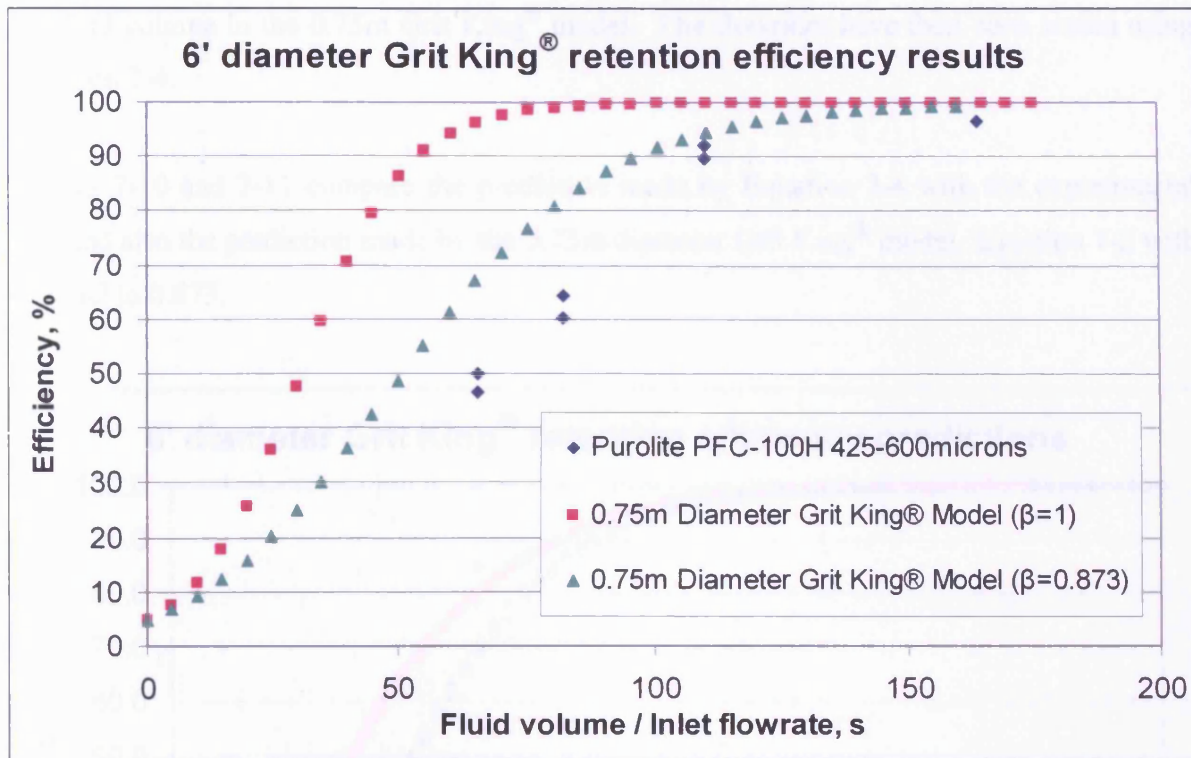
Figure 7-9. Comparison of the experimental retention efficiencies and those predicted using a modified version of the efficiency model developed for the 0.75m diameter Grit King®.

Fenner and Tyack (1997) proposed a retention efficiency scaling protocol given by Equation 3-4, repeated here for convenience

$$Q_{\text{prototype}} = Q_{\text{model}}\left[\left(\eta_m L_r^2\right) + \left(1 - \eta_m\right)L_r^{2.5} + \frac{d}{3}\left(1 - \eta_m\right)L_r^{2.5}\right]$$

(3-4)

Where: Q =Flowrate, m³/s

η_m = Model efficiency (%)/100 at corresponding Q_m flow

L_r = Length ratio for geometric similarity

d = Average particle diameter in mm

This scaling law relies on retention efficiency data from a scaled unit. Hence, making a direct comparison with the prediction by Equation 7-2 and also the experimental efficiencies in Figures 7-6 and 7-7 is not possible because the particle properties used for testing the 6' unit are different to those used for testing the 0.75m diameter unit.

An estimation of the suitability of Equation 3-4 has been made in the following way: A prediction of the retention efficiency of the particulates used for testing the 6' unit has been made for a 0.75m diameter unit using the 0.75m diameter Grit King® model with β equal to 1. The flowrate at which each predicted efficiency occurs has also been calculated knowing

the fluid volume in the 0.75m Grit King® model. The flowrates have then been scaled using Equation 3-4.

Figures 7-10 and 7-11 compare the prediction made by Equation 3-4 with the experimental data and also the prediction made by the 0.75m diameter Grit King® model, Equation 7-2 with β equal to 0.873.

6' diameter Grit King® retention efficiency predictions

- ◆ Purolite A100 600-850microns
- ◇ Purolite A100 600-850microns BEST FIT
- ■ Fenner and Tyack, 1997
- ▲ 0.75m diameter Grit King® Model (β=0.873)
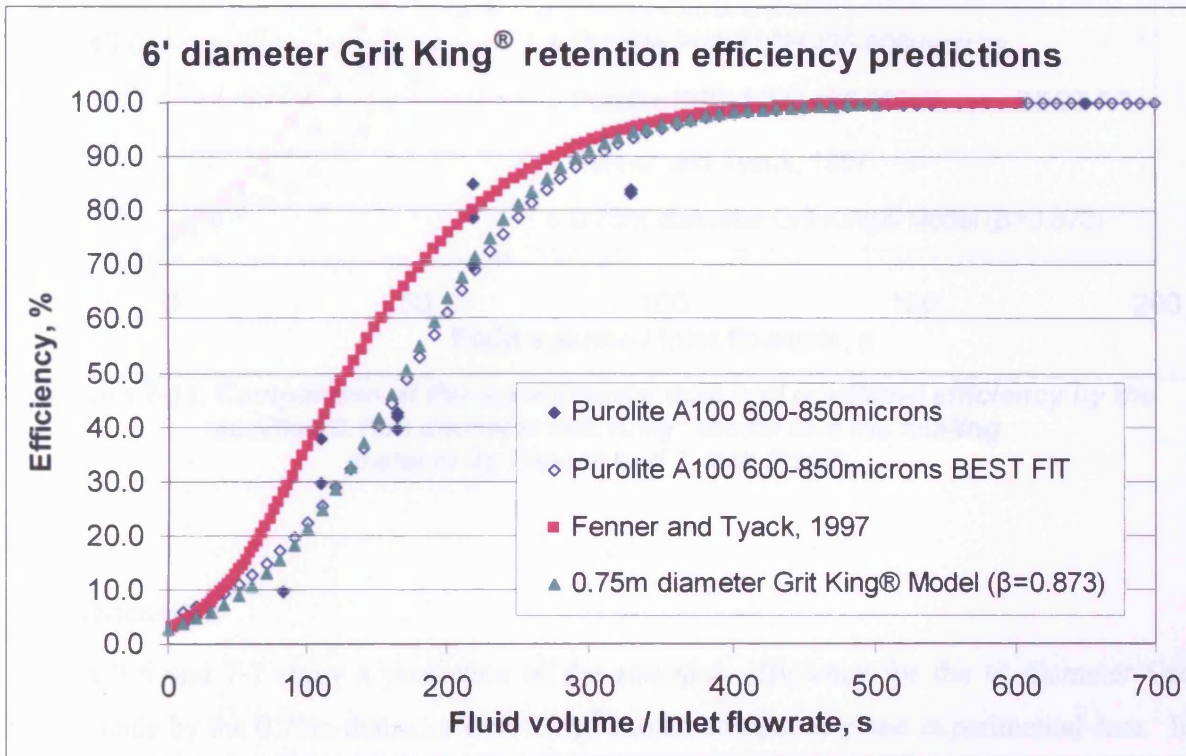
Figure 7-10. Comparison of the experimental data and predicted efficiency by the modified 0.75m diameter Grit King® model and the scaling protocol by Fenner and Tyack (1997).

6' diameter Grit King® retention efficiency predictions

Legend:
- ◆ Purolite PFC-100H 425-600microns
- ◇ Purolite PFC-100H 425-600microns BEST FIT
- ■ Fenner and Tyack, 1997
- ▲ 0.75m diameter Grit King® Model (β=0.873)

X-axis: Fluid volume / Inlet flowrate, s
Y-axis: Efficiency, %
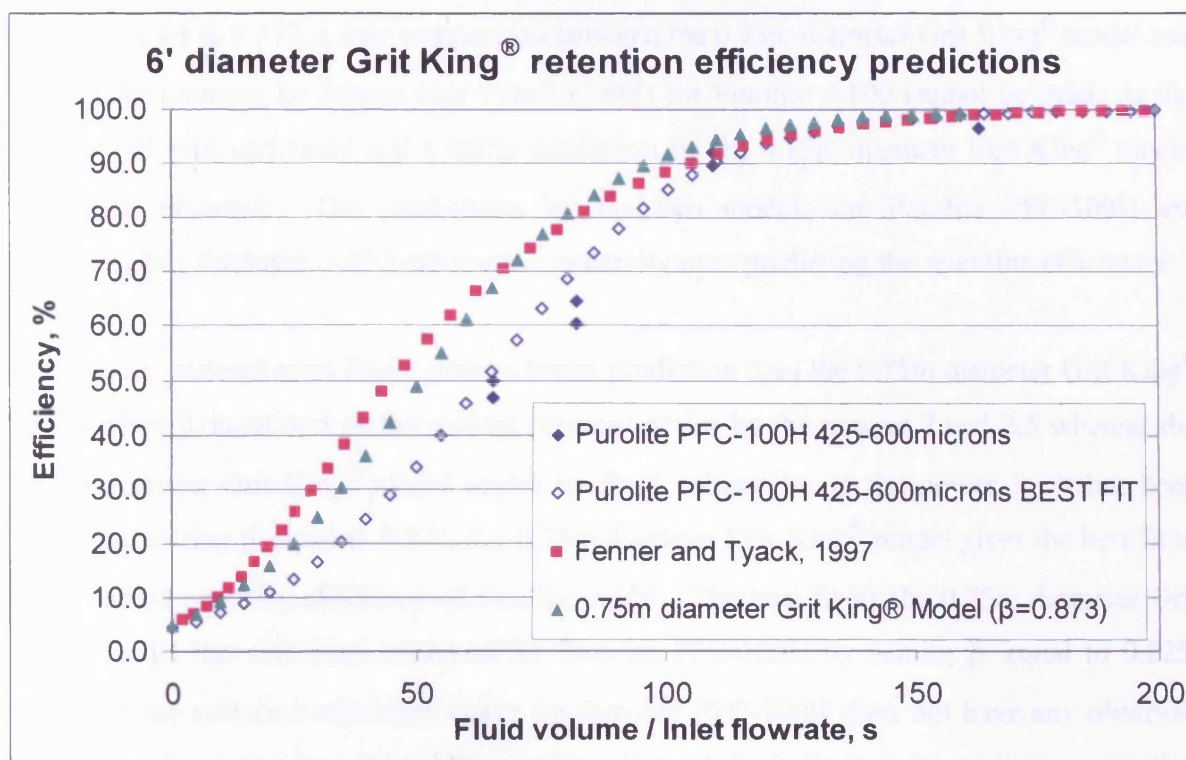
Figure 7-11. Comparison of the experimental data and predicted efficiency by the modified 0.75m diameter Grit King® model and the scaling protocol by Fenner and Tyack (1997).

7.3 Discussion

Figures 7-6 and 7-7 show a prediction of the retention efficiency for the 6' diameter Grit King® made by the 0.75m diameter Grit King® model compared to the experimental data. In both cases the efficiency model over predicts the retention efficiency. When β is equal to 0.873 the predicted efficiency by the Grit King® model is aligned with the experimentally determined efficiencies of Purolite A100, as shown in Figure 7-8. When the same constant is applied to predicting the retention efficiency of Purolite PFC-100H, the predicted efficiency is higher as shown in Figure 7-9. This could be due to geometric differences between the 0.75m diameter and 6' units. Alternatively, a function may exist for the power used to scale the theoretical residence time, β. The function may need to consider the size of the separator as well as the particle properties which will be affected by the fluid dynamics within the HDVS.

The scaling protocol by Fenner and Tyack (1997) has been used to assess its suitability for scaling. In both of Figures 7-10 and 7-11, the scaling protocol gives a better prediction of the retention efficiency compared to the 0.75m diameter Grit King® model when β is set to 1.

When β is set to 0.873, a true comparison between the 0.75m diameter Grit King® model and the scaling protocol by Fenner and Tyack (1997) for Purolite A100 cannot be made as the value for β was optimised and a better prediction by the 0.75m diameter Grit King® model would be expected. The predictions by the two models for Purolite PFC-100H are approximately the same, with both models generally over predicting the retention efficiency.

The scaling protocol most likely gives a better prediction than the 0.75m diameter Grit King® model when β is set to 1 as the scaling protocol scales by the powers 2 and 2.5 whereas the 0.75m diameter Grit King® model scales by fluid volume i.e. to the power 3. It has been found that setting β equal to 0.873, the 0.75m diameter Grit King® model gives the best fit to the observed retention efficiency of Purolite A100. The best fit by the 0.75m diameter Grit King® model has also been achieved for Purolite PFC-100H by setting β equal to 0.825. However, the retention efficiency curve for Purolite PFC-100H does not have any observed retention efficiencies less than 47% so this value of β is limited to predicting retention efficiencies higher than this. However, this gives a guide in that for scaling retention efficiencies using the 0.75m diameter Grit King® model, a value for β in the range of 0.825 to 0.873 is required.

The scaling protocol predicts the efficiency by taking the same efficiencies as those observed in a scaled unit and scales the flowrates. Since the efficiencies are influenced by the shape factor, particle density, particle diameter, fluid viscosity, fluid density etc, then a reason that the predicted efficiency of Purolite PFC-100H is not as good as Purolite A100 is that there may be a function for the power used to scale the flowrates as suggested for the 0.75m diameter Grit King® model. Again, this could also be due to geometric differences between the units. A third possibility for the predicted retention efficiency of Purolite A100 being better than the prediction made for Purolite PFC-100H is that the density of the Purolite A100 is 1059kg/m^3 which is close to the density of Styrocell, 1040kg/m^3, used by Fenner and Tyack (1997) for validating the scaling protocol. The density of Purolite PFC-100H has been found to be 1137kg/m^3, hence, density could be a missing parameter from the scaling protocol and predictions by the scaling protocol may diverge for particles whose densities are greater than this.

It would have been ideal to have more observations of the retention efficiency to have greater confidence in the data but due to time constraints this was not possible. These results also emphasise the need to study retention efficiency scaling effects with at least three to six different particle characteristics i.e. particles whose surface loads, m_d, are different, in order to attain good relationships between the relevant parameters. Studying scaling effects with at least 3 different sizes of separator which are geometrically scaled would reveal any non-linearity in the trends i.e. it would be confirmed whether the 0.75m diameter Grit King® efficiency model can be applied to scaling and if a constant or function for β is required.

However, it has been shown that when the particle properties are known, predictions by the scaling protocol by Fenner and Tyack (1997) may be obtained in combination with the 0.75m diameter Grit King® model which is used to predict the retention efficiency in a 0.75m diameter unit and then the scaling protocol applied to scale the flowrates.

7.4 Summary

- A 6' diameter Grit King® has been tested under laboratory conditions.

- Scaling of retention efficiencies in proportion to the fluid volume over predicts the efficiency and a scale factor for theoretical residence time of 0.873 to 0.825 seems more appropriate.

- Experimental studies of retention efficiency should be undertaken using at least three to six different particle characteristics and three different sizes of HDVS which are geometrically scaled.

- Due to testing with only two different types of particles and geometrically different units, suggested improvements to the scaling protocol and 0.75m diameter Grit King® model cannot be made.

8   CFD modelling of a 0.75m diameter Eff-Pac™ Clarifier

Alkhaddar *et al.* (1999) and Higgins (2000) have characterised the residence time distribution of a 0.75m diameter Eff-Pac™ Clarifier, shown in Figure 8-1, operating with a base flow component. The results from this provide the opportunity to assess whether CFD can be used to predict residence time characteristics and whether CFD predictions of residence time can be further applied to study the inactivation of micro-organisms using a HDVS as a contact vessel.

The internal components and principle of operation of the Eff-Pac™ Clarifier are described in Section 1.2.

A   Inlet
B   Cone
C   Dip Plate
D   Baffle Plate
E   Weir
F   Spill Way
G   Overflow
H   Underflow
I   Vessel Wall
J   Sludge Hopper
K   Benching skirt

Experimental
Sampling Point
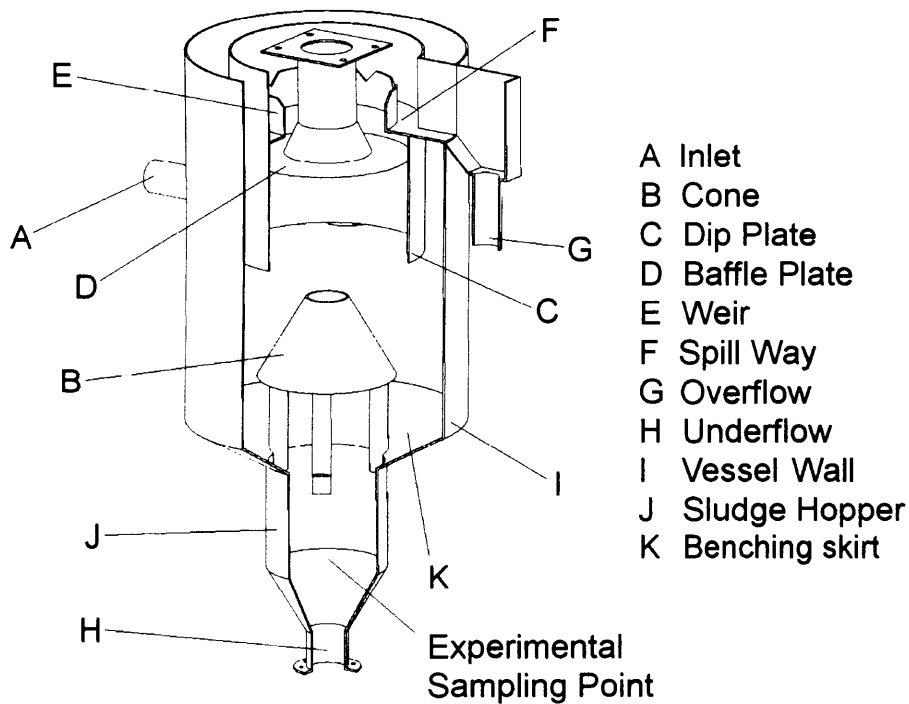
Figure 8-1. 0.75m diameter Eff-Pac™ Clarifier characterised by Alkhaddar et al. (1999) and Higgins (2000).

Detailed drawings of the Eff-Pac™ Clarifier are given on Pages 179 to 181.

140

160

80

1472.5

112

750

Ø102.2

Ø80

R375

120

500

Full dimensions omitted at the
request of Hydro International

Drawn By:
Darrell A. Egarr
Cardiff University
Queens Building
The Parade
Cardiff
CF24 0YF

Hydro International
Shearwater House
Clevedon Hall Estate
Victoria Road
Clevedon
N. Somerset
BS21 7RD

Date: 02/02/03

Title:
0.75m Diameter Eff-Pac(TM)
Clarifier External Dimensions
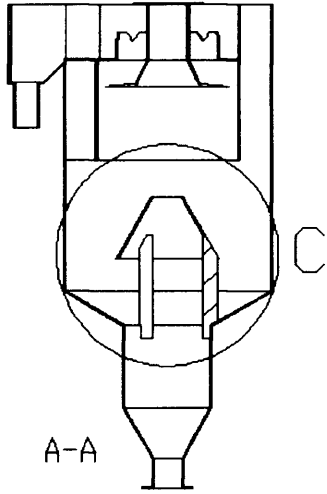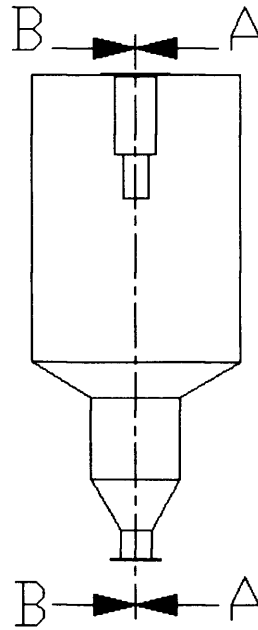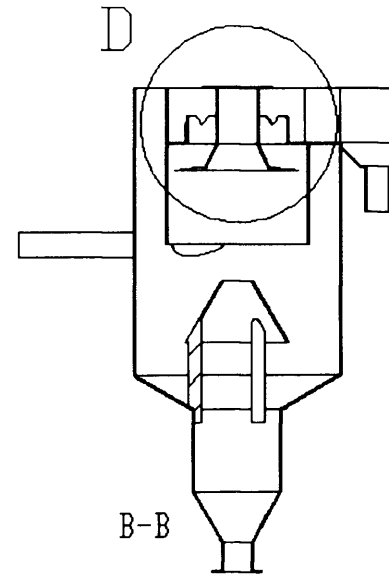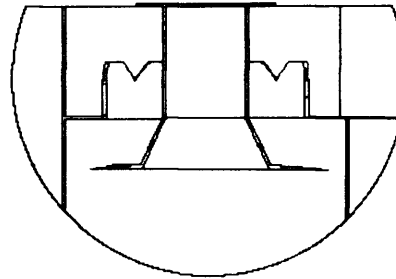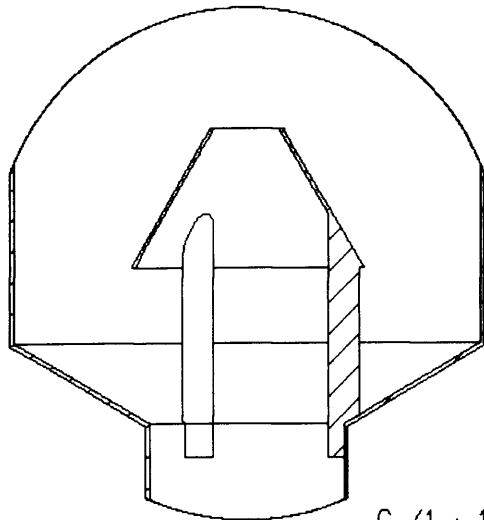
Dimensions: mm

Scale: 1:22

Paper Size: A4

A-A

C

B — A

B — A

D

B-B

D (2 : 25)

Full dimensions omitted at the
request of Hydro International

C (1 : 11)

| Dimensions: mm | Scale: 1:25 | Date: 02/02/03 | Title: |
| | | Paper Size: A4 | 0.75m Diameter Eff-Pac(TM) Internal View |

A →

45°

100

64.6

A-A

A →

22.5°

11.25°

45°

Full dimensions omitted at the
request of Hydro International

Drawn By: Darrell A. Egarr Cardiff University Queens Building The Parade Cardiff CF24 0YF	Hydro International Shearwater House Clevedon Hall Estate Victoria Road Clevedon N. Somerset BS21 7RD	
Date: 02/02/03	Title: 0.75m Diameter Eff-Pac(TM) Clarifier Weir Dimensions	
Dimensions: mm	Scale: 1:5	Paper Size: A4

8.1 Experimental setup and procedure

The experimental setup and procedure is outlined by Alkhaddar *et al.* (1999). In brief, the inlet pipe to the HDVS was a straight pipe extending 24 diameters upstream of the HDVS and a dosing point positioned at 12 diameters upstream. A sampling point was present below the sludge hopper, shown in Figure 8-1. The inlet flow was controlled by a gate valve and flow measurement made by a calibrated turbine style flowmeter. The flow rate was also checked by recording the time taken to fill a container of a known volume. The HDVS discharged straight to drain i.e. a closed pumped system was not used and the chance of recirculation of the tracer through the system was therefore eliminated. The study involved the use of an injection of lithium chloride, assumed to be a perfect pulse input and samples were taken manually from the underflow and overflow. The samples were analysed using an atomic absorption spectrophotometer. Flow splits of 10, 20, 30 and 40% were investigated where the flow split is expressed as a percentage of the inflow, Q_i i.e. $100.Q_b/Q_i$ where Q_b is the base flow. Inlet flowrates were between 0.75 to 6 litres per second. The 'method of moments' was used to characterise the residence time distribution of the HDVS, Equations 2-24 and 2-25.

8.2 Grid setup and boundary conditions

The inlet pipe to the HDVS in Figure 8-1 was offset by 5% of the inlet diameter to prevent over-skewed cells at the point the inlet pipe is joined to the HDVS vessel wall as this would result in appreciable error and possible convergence problems during computation of the flow. The walls forming the dip plate, baffle plate, cone etc were zero thickness.

A mesh was constructed, shown in Figure 8-2, which comprised of approximately 750 000 cells and the geometry was split such that a finer mesh was present along the side of the dip plate marked 'A' in Figure 8-2, due to the very slim gap between the baffle plate and the dip plate where all the fluid leaving the device through the overflow has to pass. The faces forming the 'V' notches in the weir 'B' also had a finer mesh. In general it was also ensured that a minimum of six cells were present between two faces that formed a channel e.g. between the weir and baffle plate 'C', or between the dip plate and the walls of the vessel 'D' and in the underflow. This was to ensure that a crude boundary layer could be represented whilst also allowing for fluid to pass through the cells in the centre of the channel. Due to the

geometry of the HDVS, these requirements utilised a large number of cells, leaving few cells to refine other regions without increasing processing time even further.
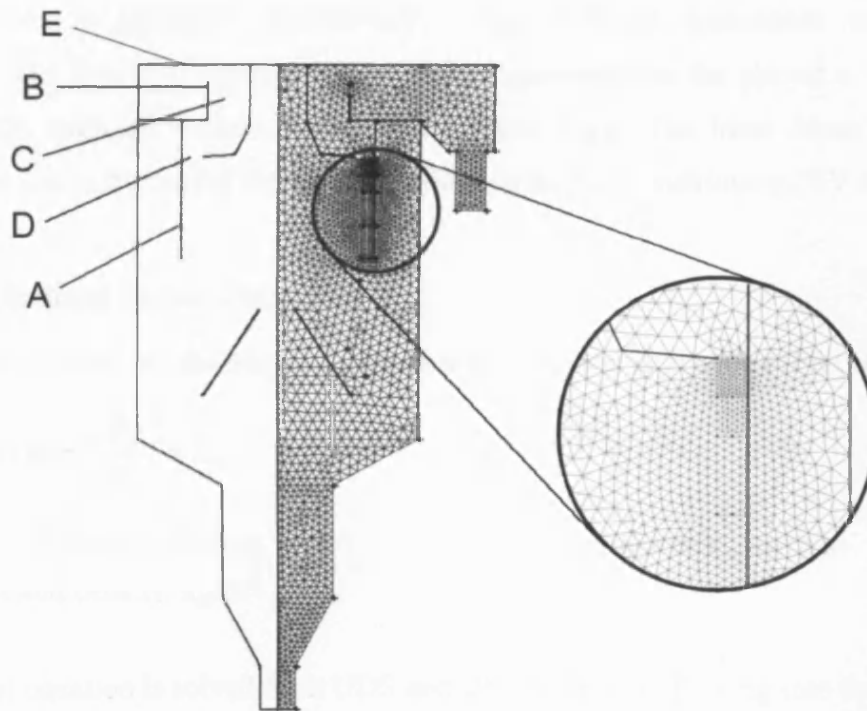
Figure 8-2. The mesh used to model the 0.75m diameter Eff-Pac™ Clarifier.

The free-surface between the water and air was modelled as a frictionless wall, marked 'E' in Figure 8-2. The overflow was specified as a pressure outlet for which all the flow quantities excluding pressure are extrapolated from the interior. The underflow was specified as a velocity inlet for which a negative velocity was applied to obtain the required flow split. A steady state solution was achieved for all the models using the Reynolds Stress Model. The standard pressure interpolation scheme was used along with the SIMPLE pressure-velocity coupling algorithm and first order terms were solved for momentum, turbulent kinetic energy and turbulent dissipation rate.

The determination of residence time distributions using numerical methods has been attempted previously. One of these methods was by introducing a second species which acts as the tracer and this species can be monitored at the outlet and an RTD curve plotted. Sherwin and Ta (2002) used this to investigate short circuiting in an anaerobic zone consisting of a baffle plate and two mixers. Ta and Brignal (1998) used the same technique to study the residence time of a storage reservoir. Contours of species concentration can be viewed within the domain being modelled which will reveal the path of the fluid through the system. It is

known that in using a species transport approach to study residence time that a small time step must be set to aid conservation of the second species (Grimm, J., 2003, Private Communication). This is not desirable when the system has a large residence time as the processing time is increased significantly. Two different approaches were therefore undertaken. The first is a 'Discrete Phase Model' approach and the second a 'User Defined Scalar' (UDS) approach which is essentially taken from 'The local Mean Age of Air' developed for use in modelling Heating, Ventilation and Air Conditioning (HVAC).

8.2.1 User Defined Scalar (UDS) theory

For an arbitrary scalar, φ, the transport equation to be solved is given by (Fluent Inc., 2003)

$$\frac{\partial \rho \varphi}{\partial t} + \frac{\partial}{\partial x_i}\left(\rho u_i \varphi - \Gamma \frac{\partial \varphi}{\partial x_i}\right) = S_\varphi \qquad (8\text{-}1)$$

Where: Γ = Diffusion coefficient, kg/ms $\qquad$ S_φ = Source term, kg/m³s

ρ = Fluid density, kg/m³

This transport equation is solved for a UDS and allows the fluid flowing into the HDVS to be marked in such a way that the UDS acts as a tracer i.e. the response to different inputs can be monitored to yield a 'C', 'F' and 'I' curve.

The diffusivity of the UDS is defined as being the same as the fluid flowing through the HDVS and in a turbulent flow is a function of the binary diffusivity, turbulent and laminar viscosity and turbulent Schmidt number, given by (Fluent Inc., 2003)

$$Diffusivity = D_h \rho + \frac{\mu_L + \mu_T}{Sc_t} \qquad (8\text{-}2)$$

Where: D_h = Binary diffusivity, m²/s $\qquad$ μ_L = Laminar viscosity, kg/ms

μ_T = Turbulent viscosity, kg/ms $\qquad$ Sc_t = Turbulent Schmidt Number

The turbulent Schmidt number is defined as

$$Sc_t = \frac{\mu_T}{\rho D_t} \qquad (8\text{-}3)$$

Where: D_t = Turbulent diffusivity, m²/s

The mean residence time of a fluid may be computed using a steady state solver and is solved such that the fluid enters the control volume, in this case the HDVS, where it is split into

finite control volumes. At time t the mass flowrate of fluid into a cell is $\overset{\bullet}{m}$, such that the value of the scalar when it enters a cell is $\overset{\bullet}{m}t$. When the fluid leaves the cell its age will have increased by Δt such that the value of the scalar when it leaves the cell is $\overset{\bullet}{m}(t + \Delta t)$ (Fluent Inc., 2003, Private Communication). In order to find the time at which the fluid leaves, a source term is required equivalent to:

$$S_\varphi = \frac{\overset{\bullet}{m}\,\Delta t}{V} \qquad (8\text{-}4)$$

Where: $\overset{\bullet}{m}$ = Mass flow rate, kg/s $\qquad V$ = Volume, m^3

The source term is divided by the cell volume since it is applied on a volumetric basis. However, the time is not known nor is the mass flowrate through the cell; hence by considering the following relationships, the source term is simplified:

$$\overset{\bullet}{m} = \rho A u = \rho \overset{\bullet}{V} \qquad (8\text{-}5)$$

Where: u = Velocity, m/s $\qquad A$ = Area, m^2 $\qquad \overset{\bullet}{V}$ = Volumetric flowrate, m^3/s

Rearranging Equation 8-5 gives

$$\overset{\bullet}{V} = \frac{\overset{\bullet}{m}}{\rho} \qquad (8\text{-}6)$$

and since

$$\Delta t = \frac{V}{\overset{\bullet}{V}} \qquad (8\text{-}7)$$

then by substituting Equation 8-7 into 8-6 gives

$$\Delta t = \frac{V\rho}{\overset{\bullet}{m}} \qquad (8\text{-}8)$$

Now substituting Equation 8-8 into 8-4 gives

$$S_\varphi = \rho \qquad (8\text{-}9)$$

A detailed discussion and mathematical derivation is given by Roos (1999).

Using the source term, Equation 8-9, the exact mean residence time of the fluid within the CFD model can be evaluated using a steady state solver. This may be achieved either by specifying a constant value in the case of incompressible fluids at a constant temperature and pressure, or by using a UDF which applies the source term on a cell by cell basis and which may also be applied to fluids where the density is not constant. This UDF is given in Appendix A titled 'Mean residence time'. The diffusivity is also applied using a UDF and is given in Appendix A titled 'Diffusivity of water'.

8.3   Results

8.3.1   Discrete Phase Model (DPM)

When a salt such as lithium chloride is dissolved to produce an aqueous solution, the bonds between the sodium and chlorine ions break and produce a solution containing chlorine ions and lithium ions. Using CFD it would be ideal to model each and every ion that was released into the HDVS, but in practice this is not possible due to computational processing time. The discrete phase model was used initially to inject 1 micron neutrally buoyant particles after solving the continuous phase of water. Coupling between the interactions of the particles and the fluid was not necessary because it was the residence time of the fluid that was required i.e. momentum exchange between the particles and fluid was not required.

Figure 8-3 shows an RTD curve produced from particle tracking by plotting the number of particles that leave the outlet in a time step decided by the user. The smaller the time step, the more accurate the plot, but more particles have to be tracked in order to make the curve as smooth as possible and this results in a greater, undesired, processing time. Despite injecting 10 000 particles into the system, the plot in Figure 8-3 is not smooth which makes characterising the HDVS using CFD harder. A curve was fitted to the data, shown in Figure 8-3 which provides a trade-off between a high processing time and accuracy.
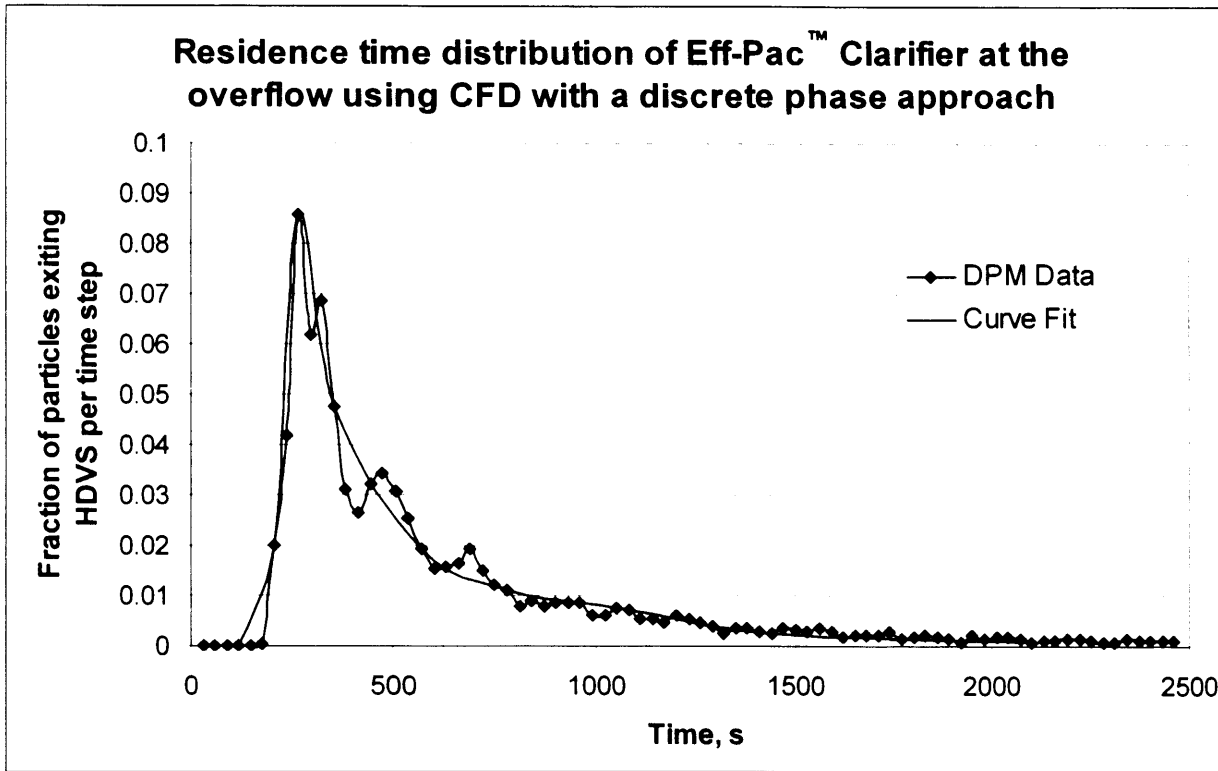
**Figure 8-3. An RTD curve for the Eff-Pac™ Clarifier using a
discrete phase model approach.**

When using a discrete phase model there is a calculation for drag on the particle; ideally the particle will always have the same velocity as the fluid. A particle with a diameter of zero cannot be specified so that the particle follows the fluid perfectly. The particle trajectory is given by Fluent Inc. (2003) (Equation 2-63) repeated here for convenience.

$$\frac{du_p}{dt} = F_D(u - u_p) + \frac{g(\rho_p - \rho)}{\rho_p} \tag{2-63}$$

Where:

$$F_D = \frac{18\mu}{\rho_p d_p^2} \frac{C_D \, \text{Re}}{24} \tag{2-64}$$

The particle density is a function of the particle's diameter, thus, when the particle has a diameter of zero, Equation 2-63 reduces to zero. The FLUENT software therefore classes a particle with a diameter of zero as a particle that has evaporated.

Due to computational expense, only a relatively small finite number of particles can be tracked; ideally the same number of particles would be monitored as ions produced in the tracer solution. Particles that get close to walls can get stuck due to boundary layer effects.

Hence, provided an alternative method can be used that simulates more realistically a tracer in solution, this method of describing the residence time distribution is not preferable.

8.3.2   User Defined Scalar

Mixing characteristics

By 'patching' or marking a region of fluid in the CFD model with a scalar close to the inlet, the transient response can be computed and a concentration curve or 'C' curve produced.

Although the processing time for a pulse input is longer than for calculating the mean, a much smoother and more accurate curve is produced compared to the discrete phase method. Processing time can be reduced by disabling calculation of the flow and turbulence equations, once a converged solution has been acquired and solving the UDS transport equation only. However, the choice of time step will also affect the accuracy and speed in which a solution can be computed. A small time step will increase the accuracy but increase processing time and conversely a large time step will decrease the accuracy but reduce processing time. To determine time step dependency, comparison of the RTDs will be made and any significant change in the RTD will imply a dependency in the time step. A comparison of the RTD has been made using 100, 350 and 600 time steps. This is shown in Figures 8-4 and 8-5.
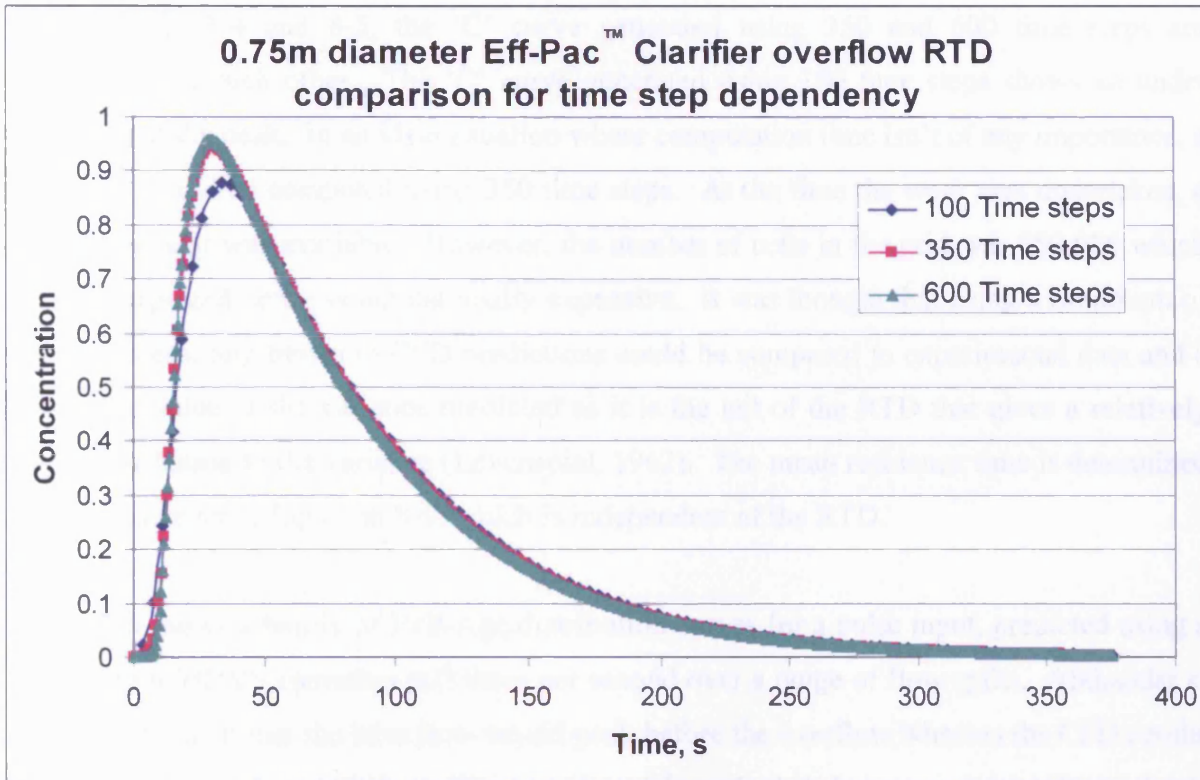
Figure 8-4. CFD RTD prediction comparison for time step dependency at the Eff-Pac™ Clarifier overflow.
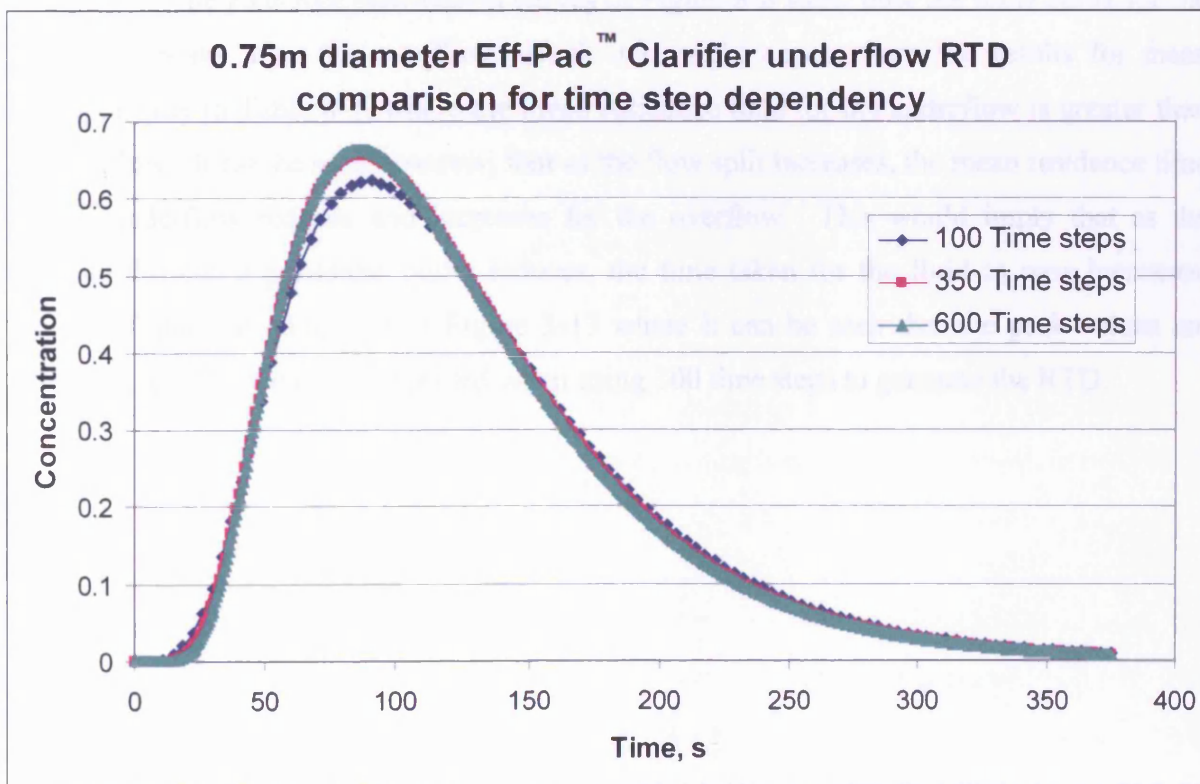
Figure 8-5. CFD RTD prediction comparison for time step dependency at the Eff-Pac™ Clarifier underflow.

From Figures 8-4 and 8-5, the 'C' curve generated using 350 and 600 time steps are independent of each other. The 'C' curve generated using 100 time steps shows an under prediction at the peak. In an ideal situation where computation time isn't of any importance, a 'C' curve would be computed using 350 time steps. At the time the work was undertaken, a 2GHz processor was available. However, the number of cells in the grid was 750 000 which is fairly large and hence computationally expensive. It was thought that using a minimum of 100 time steps, any trends in CFD predictions could be compared to experimental data and a reasonable value of the variance predicted as it is the tail of the RTD that gives a relatively large contribution to the variance (Levenspiel, 1962). The mean residence time is determined using a source term, Equation 8-9, which is independent of the RTD.

Figure 8-6 shows a family of Exit-Age distribution curves for a pulse input, predicted using a UDS, for the HDVS operating at 2 litres per second over a range of flow splits. Alkhaddar *et al.* (1999) thought that the base flow would peak before the overflow whereas the CFD results show otherwise. In contrast to the experimental methods where a point in the outlet is monitored, using CFD the average concentration of the UDS over the outlet surface is monitored. The Exit-Age distribution curves in Figure 8-6 show how the RTD curve for the underflow peaks after the overflow, which one might expect from the results for mean residence time in Table 8-1, where the mean residence time for the underflow is greater than the overflow. It can be seen however, that as the flow split increases, the mean residence time for the underflow reduces and increases for the overflow. This would imply that as the flowrate through a particular outlet reduces, the time taken for the fluid to pass increases. Figure 8-6 may be compared to Figure 3-13 where it can be seen that the peak values are under predicted as would be expected when using 100 time steps to generate the RTD.
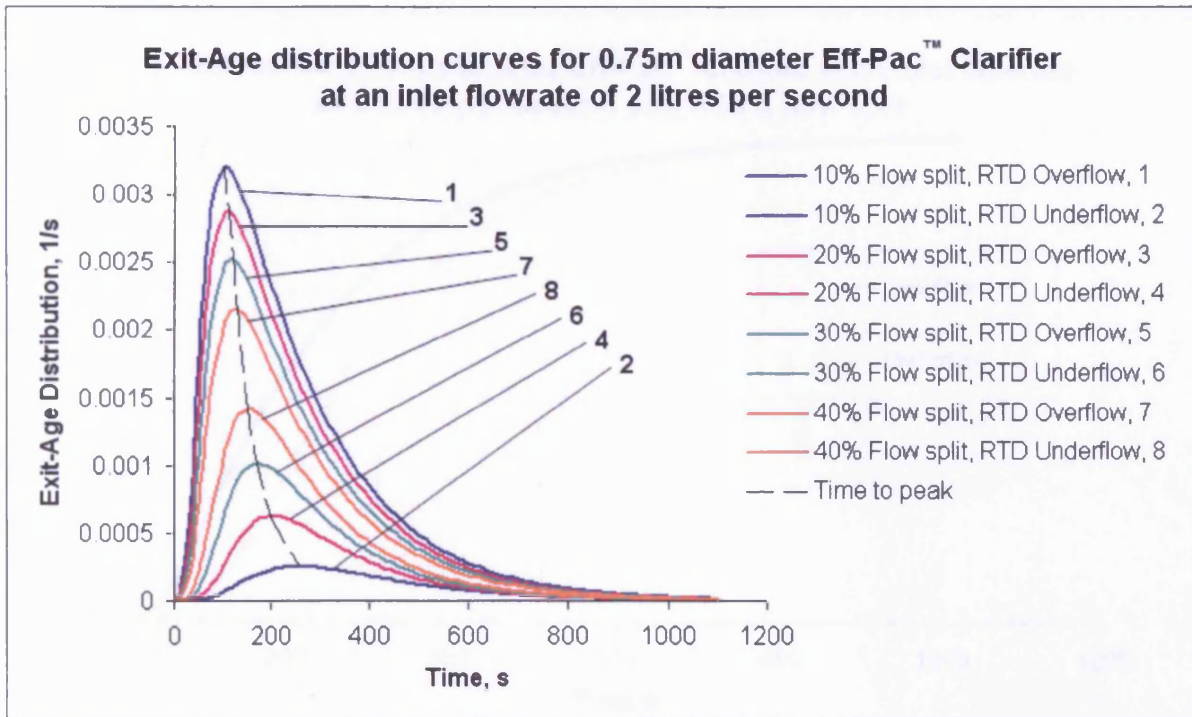
Figure 8-6. CFD-predicted Exit-Age distribution curves for the 0.75m diameter Eff-Pac™ Clarifier.

Table 8-1. CFD-predicted mean residence times of the HDVS at 2 litres per second.

Flow split, / %	10	20	30	40
Overflow mean residence time, / s	239.5	240	241	246.5
Underflow mean residence time, / s	365	304	275	260

Using a UDS it is also possible to simulate the response to a step input. Figure 8-7 shows a plot of an 'F' curve using a UDS. As expected, due to the mean residence time in the overflow being shorter, the concentration of UDS in the overflow increases faster than in the underflow. The short circuiting in the HDVS is seen due to the sharp rise in the curves and the mixing is indicated by the way in which the curves plateau as the concentration of UDS in the outlets approach 1 i.e. the steeper the curve the less mixing that has occurred. Figure 8-8 shows four contour plots of tracer concentration in response to a step input. At 15 seconds the onset of UDS around the circumference of the HDVS can be seen and at 75 seconds the concentration of UDS is greatest around the circumference of the HDVS vessel walls. By 285 seconds it is clear that mixing is occurring as contours of UDS greater than zero are present throughout the HDVS and by 585 seconds, the tracer is almost completely dispersed throughout the HDVS and this is ideal for chemical disinfection or flocculation.
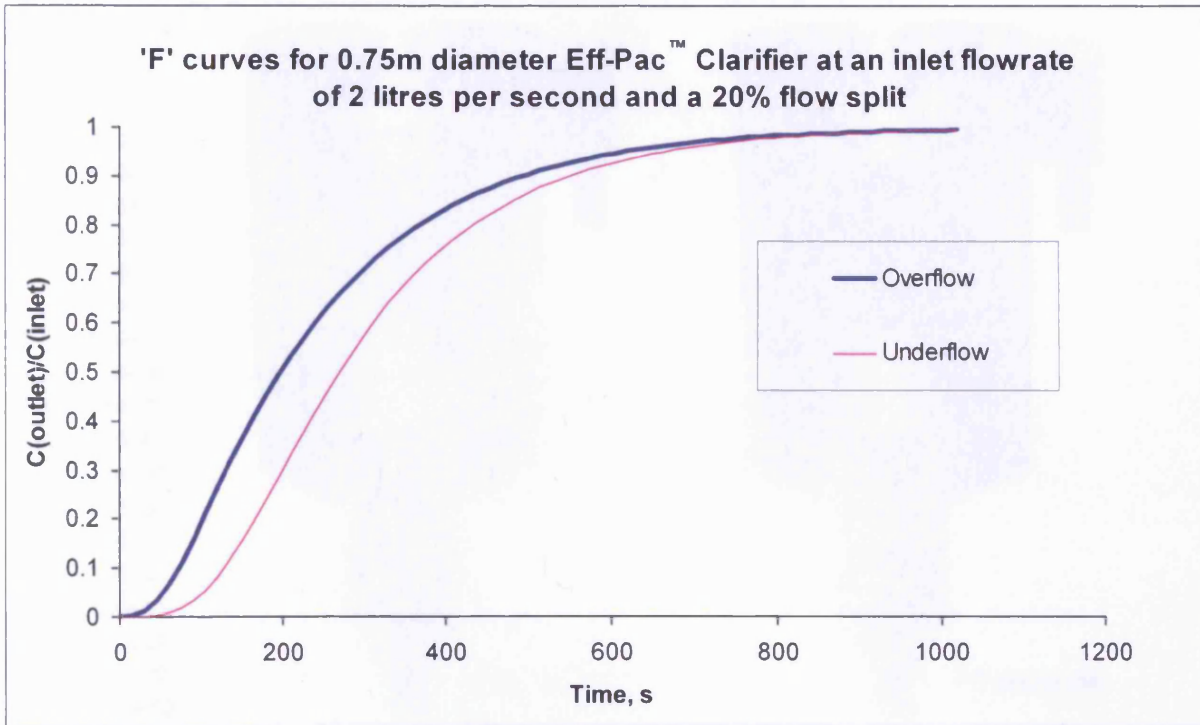
Figure 8-7. Predicted 'F' curves for the 0.75m diameter Eff-Pac™ *Clarifier.*
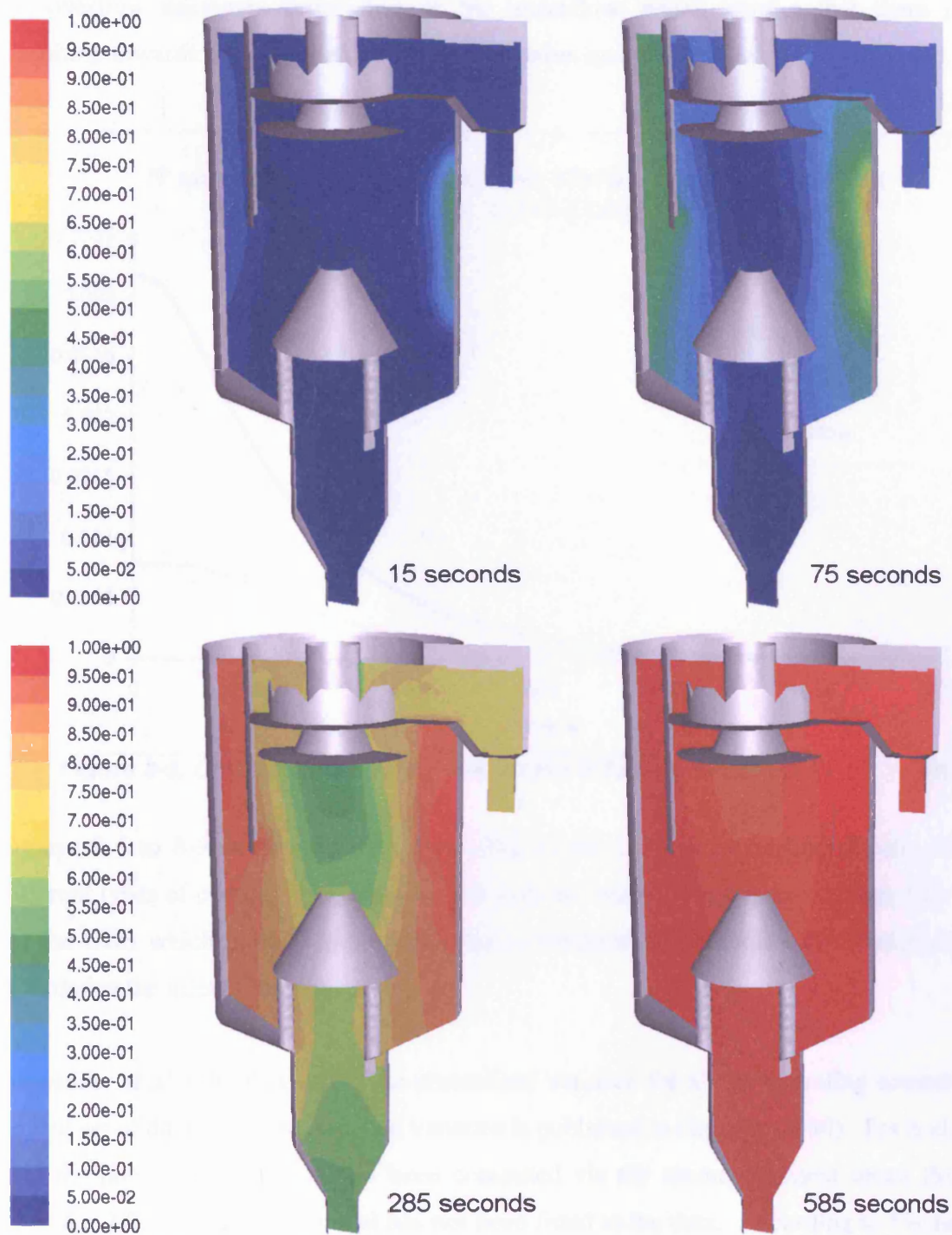
Contours of UDS concentration

Figure 8-8. Contours of tracer concentration in response to a step input at 2 litres per second and a 20% flow split.

Again using a UDS it is possible to predict the Internal Age distribution function and produce an 'I' curve, shown in Figure 8-9. Again the plug flow characteristics can be seen by the steep gradient between 50 and 250 seconds in the overflow and then the mixing where the plot starts to plateau towards a concentration of 0 in the outlet. The concentration of UDS in

the overflow decreases faster than in the underflow, which implies that there is short circuiting towards the overflow for the configuration modelled.
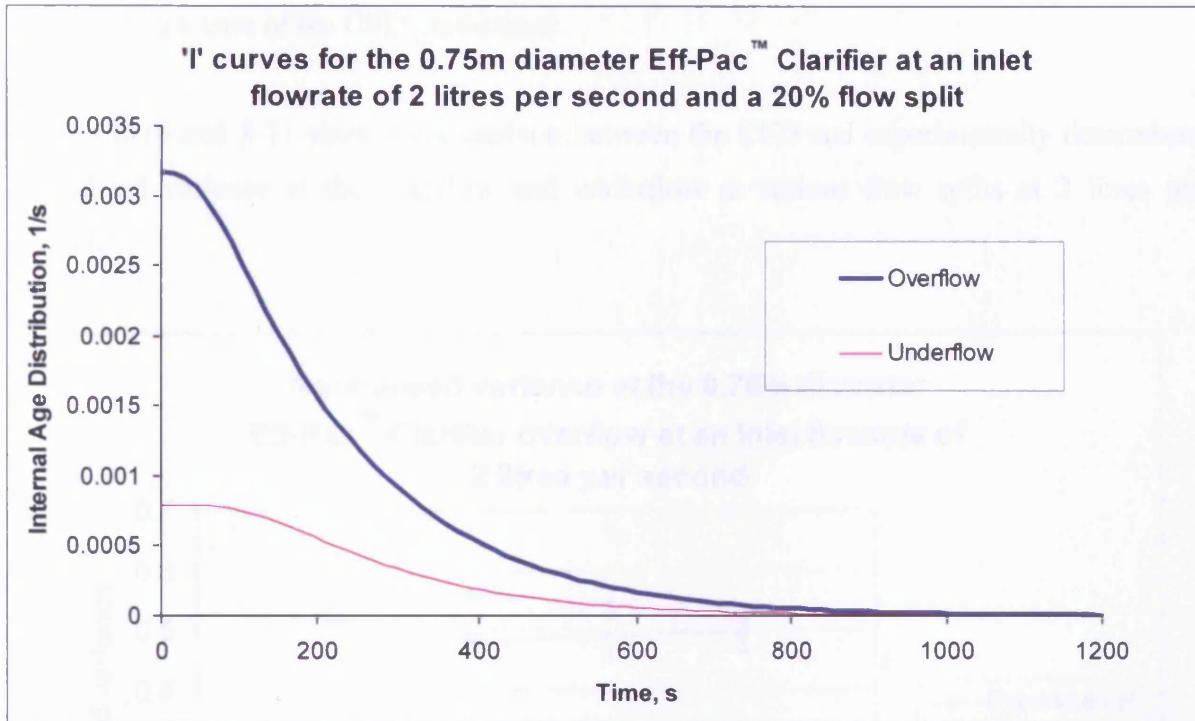
Figure 8-9. CFD-predicted 'I' curves for the 0.75m diameter Eff-Pac™ Clarifier.

Figures 8-6 to 8-9 demonstrate the flexibility of the UDS to generating directly the three different types of curves. If desired, a UDF may be written to generate a custom inlet profile for the UDS which may be applicable when a temporal concentration distribution has been recorded at the inlet to the separator.

Alkhaddar *et al.* (1999) reported the normalised variance for all the operating conditions. A second set of data for the normalised variance is published in Higgins (2000). For both sets of data the normalised variance has been computed via the second moment about the mean, Equation 2-25 i.e. an RTD model has not been fitted to the data. According to Fischer *et al.* (1979) the long 'tails' on observed distributions make it difficult to calculate a meaningful value of the variance and this can be overcome by fitting an RTD model to the observed temporal concentration distribution.

Using the UDS, the normalised variance has been determined from the RTD curves at the underflow and overflow using a pulse input. The normalised variance for the CFD-predicted RTDs is calculated via the second moment about the mean, Equation 2-25. In the case of

CFD the mass balance of the tracer is almost conserved based on integrating the area under the 'E' curve which reveals a mass conservation of approximately 99.9%. The variance computed from the second moment about the mean is therefore expected to be a reasonable estimate in the case of the CFD predictions.

Figures 8-10 and 8-11 show a comparison between the CFD and experimentally determined normalised variance at the overflow and underflow at various flow splits at 2 litres per second.
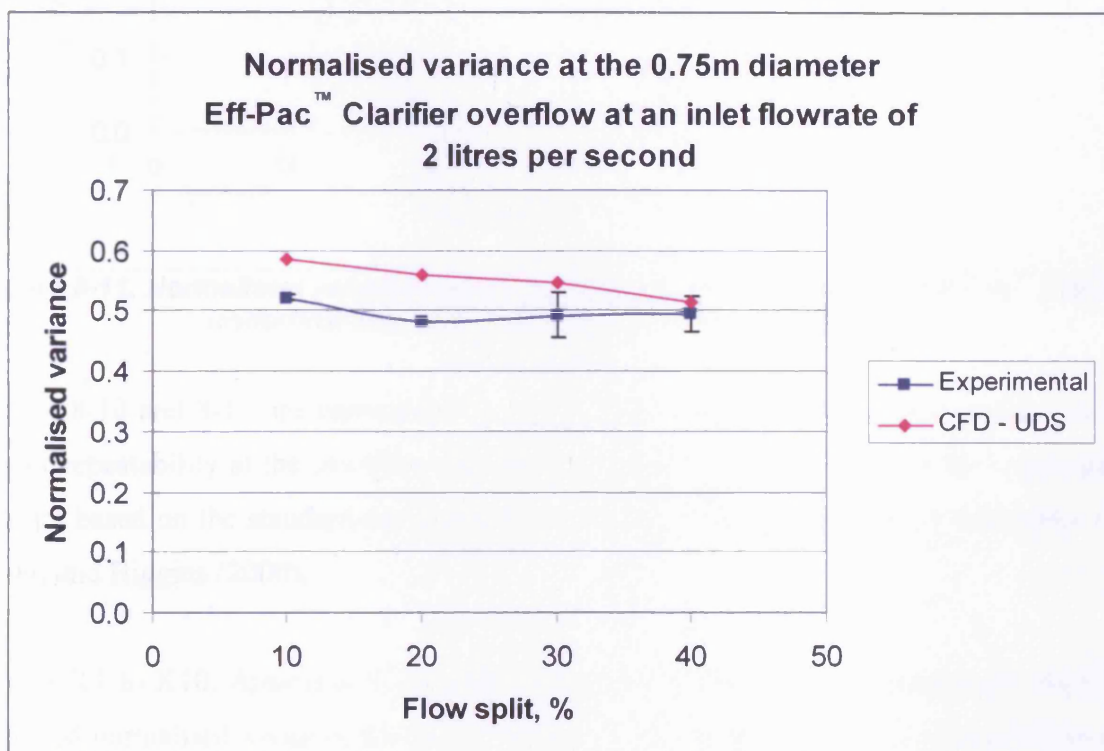
Figure 8-10. Normalised variance comparison at the 0.75m diameter Eff-Pac™ Clarifier overflow at an inlet flowrate of 2 litres per second.
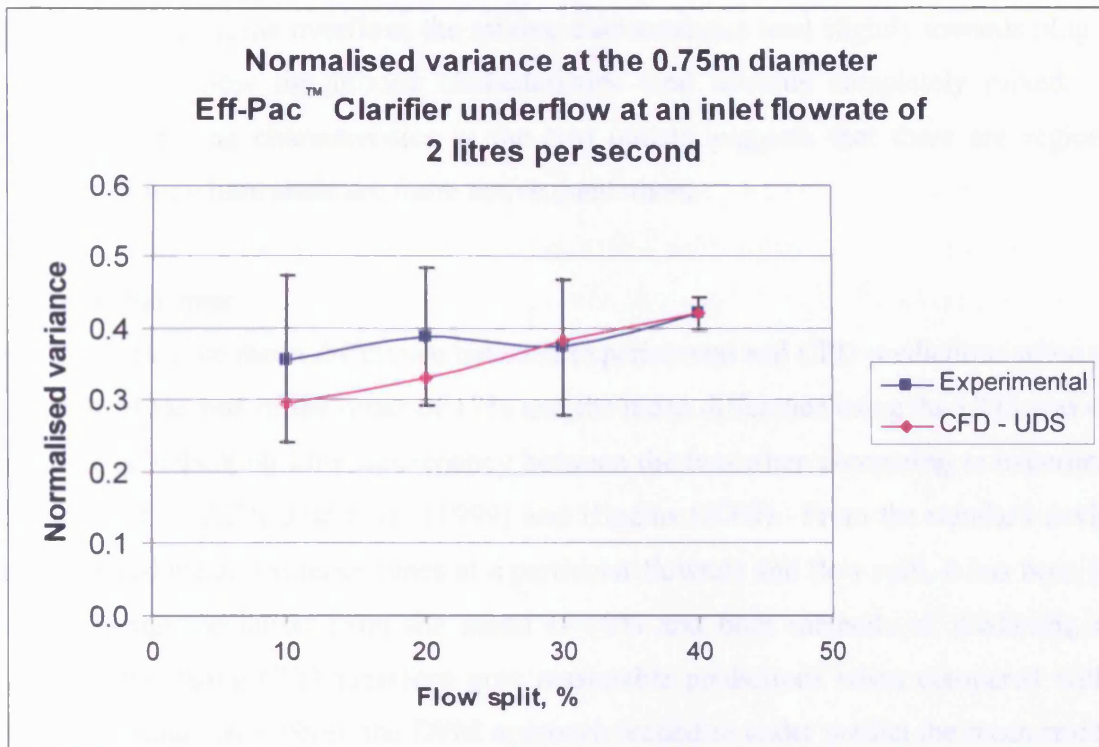
Figure 8-11. Normalised variance comparison at the 0.75m diameter Eff-Pac^{TM} Clarifier underflow at an inlet flowrate of 2 litres per second.

Figures 8-10 and 8-11 are representative of the entire data set, where there appears to be a greater repeatability at the overflow than the underflow. The error bars on the experimental data are based on the standard deviation of the two sets of data reported by Alkhaddar *et al.* (1999) and Higgins (2000).

Figures K1 to K10, Appendix K, contain comparisons between the experimental and CFD-predicted normalised variance for all the operating conditions (0.75, 1, 2, 4 and 6 litres per second at flow splits between 10 and 40%). The data is also presented in Table K1. From the standard deviation of the normalised variance for the two sets of experimental data, it has been found that the average deviation of the normalised variance from the mean is 16.2%. The average difference between the CFD normalised variance and the experimental average is 22.4%. Thus, given the repeatability of the experimental data, it is felt that CFD predictions compare reasonably well to the calculated values. Hence, using 100 time steps in the generation of the 'C' curve gives a reasonable prediction of the variance and a compromise between accuracy and processing time.

The general trend for the normalised variance is to decrease with increasing flow split at the overflow and to increase with increasing flow split at the underflow. This suggests that as the

flowrate decreases at the overflow, the mixing characteristics tend slightly towards plug flow and at the underflow the mixing characteristics tend towards completely mixed. The difference in mixing characteristics at the two outlets suggests that there are regions of segregated flows where some are more active than others.

Mean residence time

It was found that the mean difference between experimental and CFD predictions when using the discrete phase was of the order of 17% and the mean difference using the UDS was of the order of 16%, indicating little discrepancy between the two when comparing to experimental data published by Alkhaddar *et al.* (1999) and Higgins (2000). From the standard deviation of the observed mean residence times at a particular flowrate and flow split, it has been found that the average deviation from the mean is 10% and both methods of predicting mean residence times using CFD therefore give reasonable predictions when compared with the experimental data. In general, the DPM approach tended to under predict the mean residence time and this may be due to injecting only 10 000 particles. It has been found from a study at the highest flowrate of 6 litres per second that if the number of particles injected exceeds 30 000, then the difference between experimental and CFD predictions in the mean residence time is of the order of 4% above the experimental, compared to 20% under with an injection of 10 000 particles. (The UDS approach at this particular flowrate has a difference of 6% when compared to the experimental data). However, the UDS determines the exact mean residence time of the fluid in the CFD model. When injecting 30 000 particles, the mean residence time prediction using the DPM was 10% greater than the UDS value. This suggests that the DPM method over predicts the mean residence time of the fluid in the CFD model when a sufficiently large number of particles are tracked. A further consideration that should be taken prior to using the DPM is that processing the trajectory of 30 000 particles is time consuming, especially when the mean residence time is high. The quantity of data also becomes increasingly harder to process using a spreadsheet package such as MS-Excel®. Thus, a method that determines the exact mean residence time of the fluid within the model is more desirable than a method whose prediction is approximately correct.

For completeness, Figures K11 to K20, Appendix K, show experimental and CFD-predicted mean residence times using a UDS for all the operating conditions at which experimental data was observed. Error bars are based on the standard deviation of the data published by Alkhaddar *et al.* (1999) and Higgins (2000). The data is also presented in Table K2. Table

K3 presents the mean residence time data predicted using the DPM when injecting 10 000 particles.

Using the UDS, contours of mean residence time can also be plotted. An example is shown in Figure 8-12, for the Eff-Pac™ Clarifier operating at 2 litres per second and a 20% flow split. The figure highlights regions of segregated flows such as the region enclosed by the baffle plate where the residence time is high in contrast to a region of low residence time on the outside of the main vessel. This can be compared to the plot of contours of velocity magnitude also in Figure 8-12 which is for the same operating conditions and can be used for estimating the regions where the mean residence time will be low or high. On the outer part of the vessel the velocity is high after the fluid enters the HDVS through the inlet. In this region the mean residence time is low. In the region at the top of the HDVS below the baffle plate the velocity is very low and here one would expect a high residence time due to the fluid being stagnant; this can be seen to be true in Figure 8-12.

3.80e+02
3.64e+02
3.48e+02
3.32e+02
3.16e+02
3.00e+02
2.84e+02
2.68e+02
2.52e+02
2.36e+02
2.20e+02
2.04e+02
1.88e+02
1.72e+02
1.56e+02
1.40e+02
1.24e+02
1.08e+02
9.20e+01
7.60e+01
6.00e+01

4.04e-01
3.83e-01
3.63e-01
3.43e-01
3.23e-01
3.03e-01
2.83e-01
2.62e-01
2.42e-01
2.22e-01
2.02e-01
1.82e-01
1.61e-01
1.41e-01
1.21e-01
1.01e-01
8.07e-02
6.05e-02
4.04e-02
2.02e-02
0.00e+00

Contours of mean residence time, s   Contours of velocity magnitude, m/s

Figure 8-12. Contours of mean residence time and velocity magnitude at 2 litres per second and a 20% flow split.

8.4 Application to disinfection

When investigating residence times experimentally, the decomposition of a chemical that decays predictably with time can be used (Higgins, 2000), or a non pathogenic strain of bacteria such as E-Coli can be used together with a disinfectant (Alkhaddar *et al.*, 2000). Consider for example, a constant stream of wastewater and disinfectant into the HDVS containing a concentration of bacteria of say 1000cfu/ml (colony forming units/millilitre) and that the concentration of disinfectant remains constant with time, as may be the case where pure culture bacteria are introduced into a HDVS with tap water in a laboratory. Then a suitable kinetic model to describe the decay of bacteria with time could be a first order process, Chick (1908), for which the integrated form is given by Equation 3-13 repeated here for convenience

$$\frac{N_t}{N_0} = e^{-kt} \qquad\qquad (3\text{-}13)$$

Where: N_t = Number of bacteria at time t N_0 = Number of bacteria at entry into the HDVS
        k = Decay rate, s^{-1} t = Time, s

If the rate constant for a particular strength of disinfectant is found to be $0.0028s^{-1}$, Figure 8-13 'B' shows contours of the survival of bacteria, where 50% is being killed by the overflow. It can also be seen that where the mean residence time is high below the baffle, a lower survival rate exists, as would be expected. If for another strength of disinfectant, the rate constant is found to be $0.0093s^{-1}$, Figure 8-13 'C' shows that at the overflow approximately 2% of bacteria survive. Thus, CFD can be used to find the required rate constant of disinfectant, or alternatively for a fixed rate constant the desired flowrate, given that a suitable kinetic model is chosen that describes the survival rate of bacteria. CFD could also be used to compare directly with alternative experimental methods of investigating RTDs such as those mentioned previously.

Figure 8-13. Contours of mean residence time and mean survival rates at 2 litres per second and a 20% flow split.

Pretorius and Pretorius (1999) have determined kinetic rate constants for the inactivation of micro-organisms in secondary treated effluent from a typical biological nutrient removal wastewater treatment plant (see Section 3.6.3). This data can be applied to residence time data from a full scale HDVS in order to determine if the application of a HDVS as a disinfection vessel is viable (see Section 9.5).

8.5 Discussion

The classical 'Method of Moments' was used to determine the experimental mean residence time and variance. Fitting an RTD model such as the ADM or the TISM to the RTD would be preferable because the long 'tails' on observed distributions make it difficult to calculate a meaningful value of the variance (Fischer *et al.,* 1979). Although a request for the raw data was made, the data was assumed to be unavailable. It should also be noted that there is no information reported on the accuracy of the flowrate measurement. It can therefore only be assumed that each flowrate was at that reported, but a flowrate of 2 litres per second could potentially range, to 1 decimal place, from 1.5 to 2.4 litres per second.

The DPM and a UDS have been compared as a means to predict the residence time characteristics of a HDVS. The grid shown in Figure 8-2 was the evolution of a mesh from 6 months work in an attempt to obtain a reasonable validation between CFD and experimental data. Many of the parameters within the DPM were investigated, such as using different particle sizes which affect the drag on the particle, different length scales which control the frequency that the equations of motion are updated for the particle, as well as using different

grids. A grid comprising of approximately 750 000 cells was considered the maximum possible in terms of processing time. With the grid shown in Figure 8-2, using a 2GHz processor and the RSM each simulation took approximately two to three days to complete. Twenty simulations have been undertaken to compare against the matrix of operating conditions for which the mean and normalised variance are reported by Alkhaddar *et al.* (1999) and Higgins (2000), resulting in an extensive processing time for all simulations to complete. Although all twenty simulations may not have been required for validation, it was felt that this was necessary to have confidence in the CFD predictions. Hence, using a finer grid with a larger number of cells wasn't an option once a reasonable validation had been acquired due to the processing time. Although it would have been ideal to model the Eff-Pac™ Clarifier using the Volume of Fluid Model (VOF) to estimate the position of the free surface, it was felt that the validation using the frictionless wall and mesh depicted in Figure 8-2 was reasonable.

The DPM injects neutrally buoyant particles and the mean residence time is calculated from a report of the time at which each particle leaves through the outlet. The processing time for an injection of 10 000 particles can be of the order of two hours or more and generates a considerable amount of data. The processing time for generating a 'C' curve using a UDS may be of the order of twelve hours. However, less data is generated and the curve is smoother and hence easier to interpret than a similar curve produced using the DPM where the number of particles leaving through the outlet in a time step is plotted. Using a UDS as a source to evaluate the mean takes approximately ten minutes, which is considerably faster than the DPM. Although the peak values in Figure 8-6 generated using a UDS have been under predicted when compared to Figure 3-13, the trend of the data is similar. Although two sets of data exist, the repeatability of the RTD is unknown and although the normalised variance and the mean residence time are known for two sets of data, Alkhaddar *et al.* (2001) state the neither the TISM nor the ADM can be used to describe the mixing characteristics. Hence, comparing the CFD-predicted RTD with the ADM using the reported values of the normalised variance and the mean residence time which have been calculated using the method of moments would not give a true comparison. Measurement of the tracer concentration in the laboratory is also at a single point and assumes well mixed conditions. Alkhaddar *et al.* (1999) report that it was initially thought that the base flow RTD curve would peak before the underflow RTD. Sampling at a different position revealed that this was the case. This highlights the presence of poorly mixed conditions of the tracer.

An advantage of the UDS is that a contour plot of mean residence time can be viewed to study regions of high and low residence time within the device. Although this work is not concerned with design optimisation, this feature of the UDS could be used to make a decision on design modifications to increase or decrease the residence time in a particular region of the HDVS as required and hence, reduce or increase the presence of low velocity regions. The UDS also allows the characterisation of a HDVS by producing directly from the model 'C', 'F' and 'I' curves. Figure 8-8 shows contours of UDS in response to a step input and clearly shows the mixing of the tracer in the device with time. The general trend for the normalised variance appears to be a decrease at the overflow and an increase at the underflow with increasing flow split.

A simple application of residence time to disinfection has been demonstrated, using a simple first order kinetic model to describe the rate of inactivation of micro-organisms. A UDS is thus a suitable method to aid the determination of a scaling law for fluid residence time in a HDVS.

8.6   Summary

- A method for characterising a HDVS using a UDS has been utilised from that for determining the mean age of air in HVAC.

- Using a UDS has advantages over the discrete phase approach in that it is faster in determining the mean residence time, gives the exact mean residence time of the fluid independent of the RTD curve and involves less manual processing of data.

- The UDS allows contours of mean residence time to be viewed within the CFD model and when studying disinfection, contours of micro-organism survival rates, which reveals an insight into the hydraulic behaviour within the system.

- This UDS is the only method from this point forth used to determine residence time characteristics.

- All mean residence time predictions in subsequent sections are made using the source term, as this in independent of the RTD curve where errors are introduced such as the time step size.

9 CFD modelling of a 3.4m diameter Storm King®

A 3.4m diameter Storm King® was installed in a laboratory at the University of Bradford. Residence time testing was contracted to Ian Guymer of the University of Warwick and these results provided the opportunity to validate CFD models on a large scale unit. Initially the raw data wasn't available for validating CFD models and validation was based on a summary of the results reported by Guymer (2004).

9.1 Experimental setup and procedure

A 3.4m diameter Storm King® was fed from a header tank using a 0.178m internal diameter pipe marked 'A' in Figure 9-1. Due to limited space within the laboratory, the 0.178m pipe was attached to the tangential inlet of the HDVS, 'B', with a sudden expansion and was angled downwards at 14°. 3.2 diameters upstream of the HDVS inlet was a stand pipe, 'C', 3.5 diameters upstream of the standpipe a butterfly valve, 'D' and 2.25 diameters further upstream a 90° shoulder, 'E'. The internal components and principle of operation are described in Section 1.2.

The underflow discharge was controlled using a second butterfly valve, 'J' and the fluid discharged into a channel at 'K'. The valve at 'J' therefore allowed the HDVS to operate at any required flow split which is expressed as a percentage of the inflow, Q_i i.e. $100.Q_b/Q_i$ where Q_b is the base flow. The discharge from the overflow 'O' passed into a second channel 'V'. This second channel included a 90° V-Notch weir, 'W' and ruler, 'X', used to measure the flowrate via the head. In a usual installation of this type of system, a self priming siphon is attached to the overflow that produces a backwash, the purpose being to wash floatable material trapped on the screen 'U' into the central underflow 'Q'. However, for testing within the laboratory, the siphon was omitted.

A Inlet
B HDVS inlet
C Standpipe
D Butterfly valve
E 90deg bend
F Deflector plate
G Cone
H Helix
I Tangential underflow
J Valve
K Underflow discharge
L HDVS vessel wall
M Dip plate
N Venturi plate
O Overflow
P Baffle plate
Q Central underflow
R Stiffener
S Baffle
T Weir
U Screen
V Overflow discharge channel
W V-Notch
X Ruler
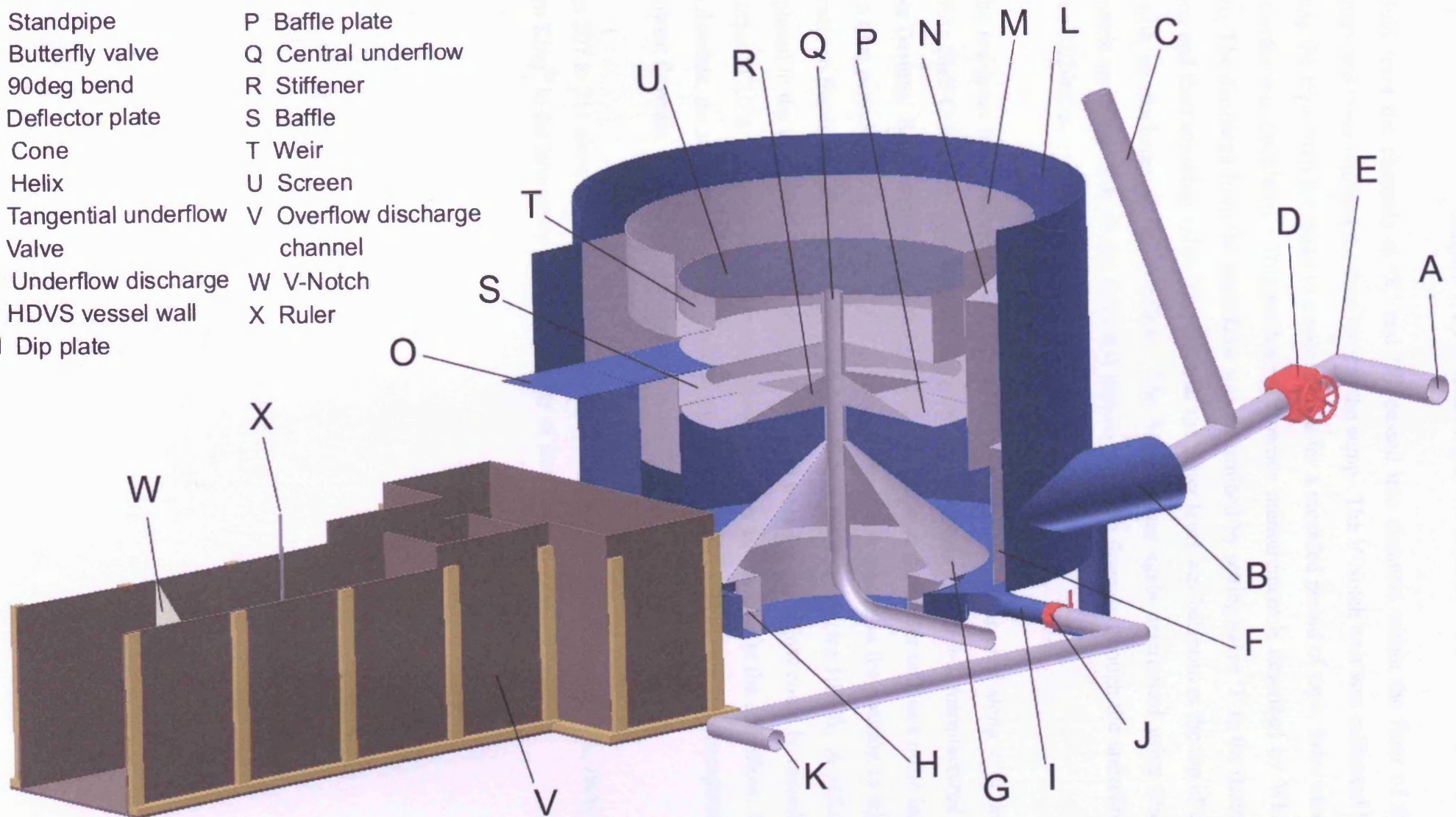
Figure 9-1. A schematic of the test rig setup for the 3.4m diameter Storm King®.

The fluid from the channels at 'K' and 'V' passed into channels within the floor of the laboratory and these returned the flow back to the sump. The V-Notch weir was calibrated by diverting the flow from the sump to a second tank for a recorded period of time, from which the flowrate was calculated. This method of flowrate measurement is described by White (1979). The discharge from the underflow was determined by setting valve 'J' to the desired position and then adjusting valve 'D' such that the water level was balanced at the top of the weir with no discharge at the overflow. The flowrate was again determined using timed volumetric sampling. For all the flowrates investigated, the flowrate through the underflow, Q_b, was 0.020m³/s.

For the residence time testing, Rhodamine WT fluorescent tracer was used along with three SCUFAs (Self-Contained Underwater Fluorescence Apparatus), Figure 9-2, manufactured by Turner Designs. Rhodamine WT was injected into the flow at the header tank as a pulse input over a time period of 15 to 25 seconds. The header tank was chosen as the position to inject the tracer so that it would be as well mixed as possible at the inflow to the HDVS. A SCUFA was placed in the inlet through the standpipe so that a trace for the inflow could be recorded. One other SCUFA was placed at the centre of the overflow and another at the underflow. For each flowrate, the residence time distribution was measured three times, with the exception of the lowest flowrate, where only one repeat was possible.

Pages 207 to 211 show the Storm King® in detail. Figures L1 and L2, Appendix L, show the Storm King® in the laboratory at the University of Bradford.

2850

785

3400

2975

Ø500

Venturi Plate

2254

Ø150

Full dimensions omitted at the
request of Hydro International

Drawn By: Darrell A. Egarr Cardiff University Queens Building The Parade Cardiff CF24 0YF	Hydro International Shearwater House Clevedon Hall Estate Victoria Road Clevedon N. Somerset BS21 7RD	
Dimensions: mm	Date: 02/02/03	Title: 3.4m Diameter Storm King(R) External Dimensions
Scale: 1:55	Paper Size: A4	

C (1 : 30)

Stiffener

(3 : 55)

B-B

Helix

A-A

Full dimensions omitted at the request of Hydro International

Drawn By: Darrell A. Egarr Cardiff University Queens Building The Parade Cardiff CF24 0YF	Hydro International Shearwater House Clevedon Hall Estate Victoria Road Clevedon N. Somerset BS21 7RD

Date: 02/02/03	Title: 3.4m Diameter Storm King(R) Internal View
Dimensions: mm	Scale: 1:55	Paper Size: A4	
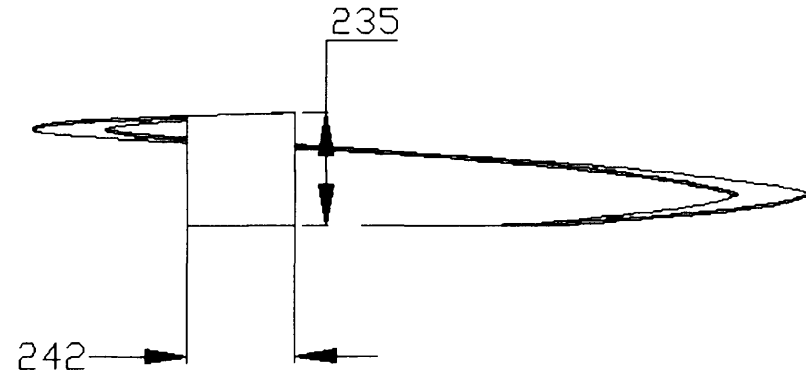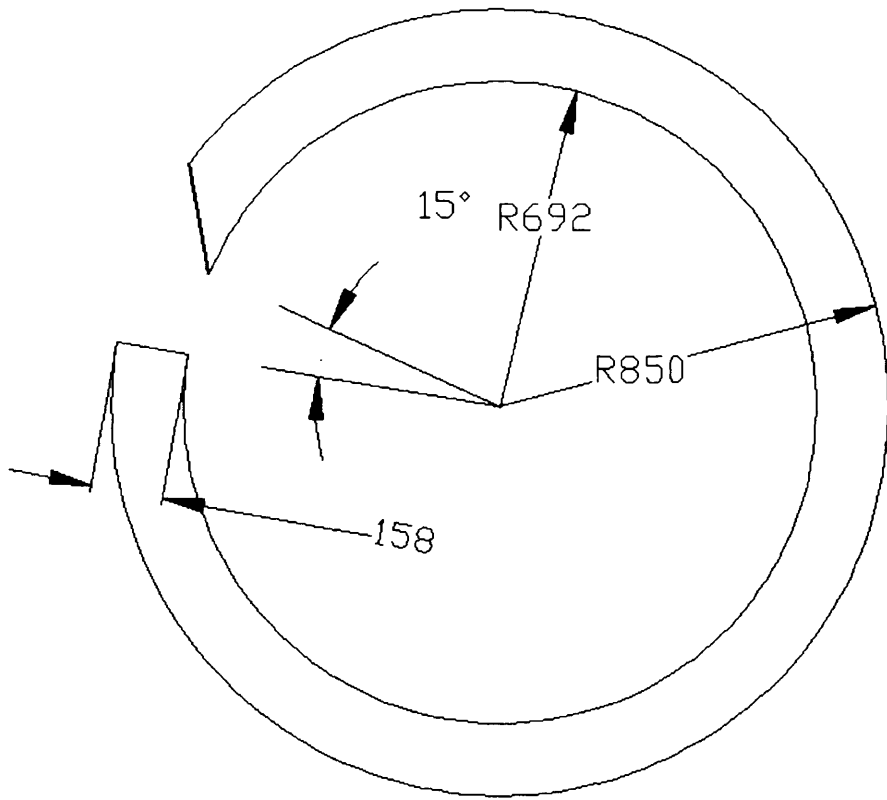
15° R692

R850

158

235

242

Drawn By:	Hydro International
Darrell A. Egarr	Shearwater House
Cardiff University	Clevedon Hall Estate
Queens Building	Victoria Road
The Parade	Clevedon
Cardiff	N. Somerset
CF24 0YF	BS21 7RD

Date: 02/02/03	Title:
	3.4m diameter Storm King(R)
Dimensions: mm	Scale: 1:15	Paper Size: A4	Helix Dimensions
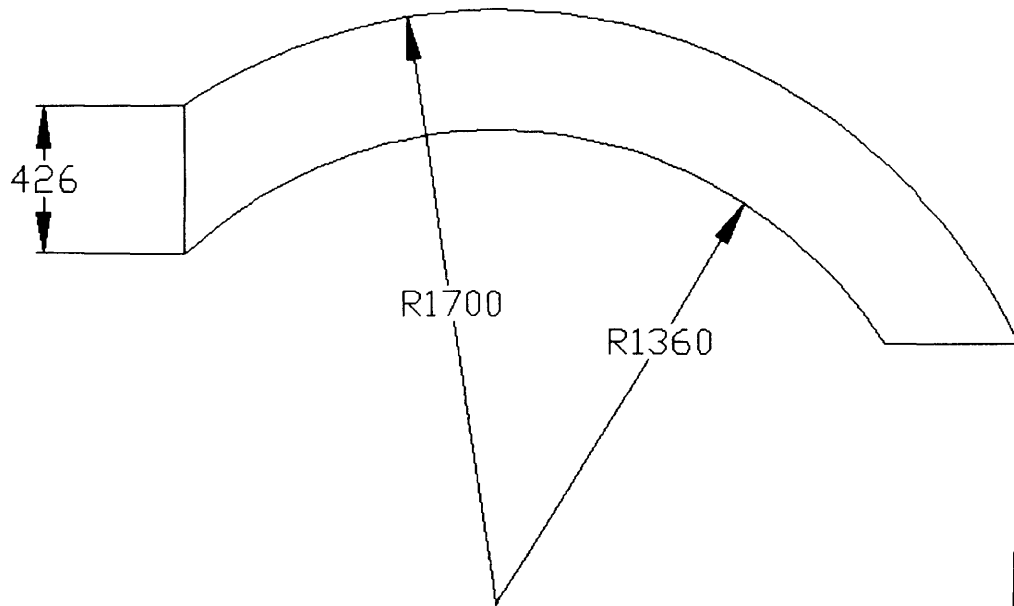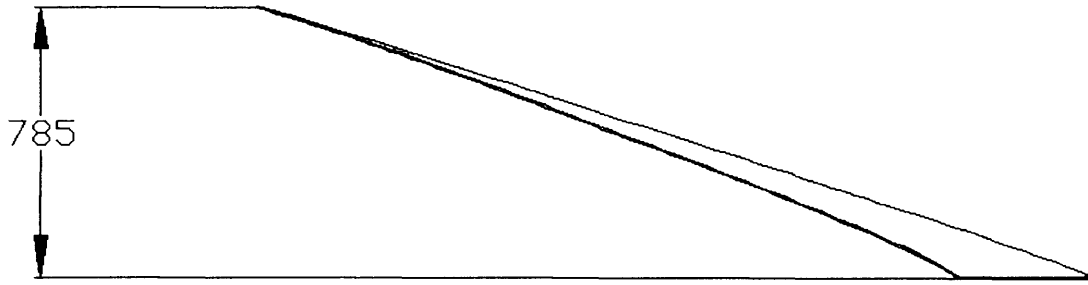
785

426

R1700

R1360

Drawn By: Darrell A. Egarr Cardiff University Queens Building The Parade Cardiff CF24 0YF	Hydro International Shearwater House Clevedon Hall Estate Victoria Road Clevedon N. Somerset BS21 7RD	
Date: 02/02/03	Title: 3.4m Diameter Storm King(R) Venturi Plate Dimensions	
Dimensions: mm	Scale: 1:20	Paper Size: A4

Standpipe

Weir

Overflow

Inlet

1260

3015

14°

V-Notch Weir

4710

2740

9940

2280

3850

1585

Underflow

900

1060

500

1990

1200

All dimensions are approximate

Drawn By:
Darrell A. Egarr
Cardiff University
Queens Building
The Parade
Cardiff
CF24 0YF

Hydro International
Shearwater House
Clevedon Hall Estate
Victoria Road
Clevedon
N. Somerset
BS21 7RD

Date: 02/02/03

Title:
3.4m Diameter Storm King(R)
Test Rig: External Dimensions

Dimensions: mm   Scale: 1:80   Paper Size: A4

9.1.1 The Self-Contained Underwater Fluorescence Apparatus (SCUFA)

Figure 9-2 shows the SCUFA and Figure 9-3 shows the optical component layout.

Figure 9-2. The SCUFA. Adapted from Turner Designs (2004).
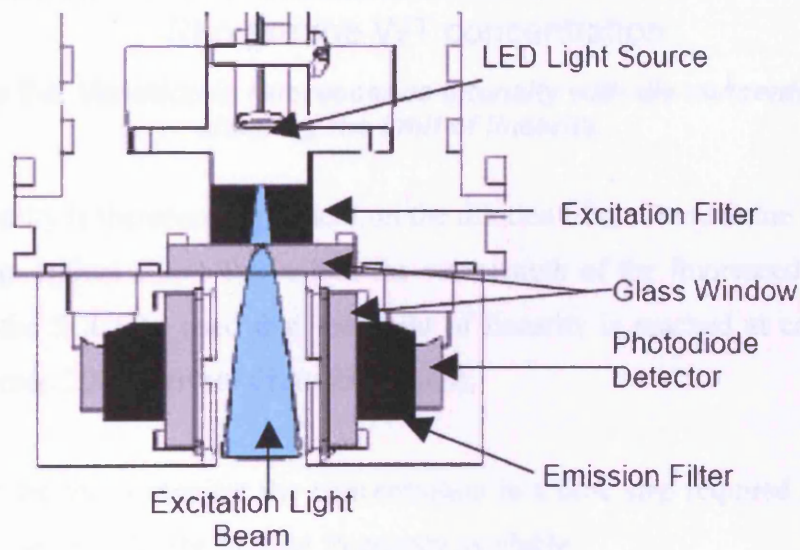
Figure 9-3. Optical component layout in the SCUFA.
(Turner Designs, 2002).

A green LED built into the SCUFA acts as a light source and the fluorescence of the Rhodamine WT is detected by silicon photodiodes positioned at 90° to the light beam. Ambient light is eliminated through "the development of ambient light rejection circuitry" (Turner Designs, 2004). The amount of fluoresced light from the dye is proportional to the concentration up to the limit of linearity. This is reached when the concentration of the Rhodamine WT is such that light cannot pass through the sample to cause excitation and this is known as concentration quenching. When these conditions are achieved, the fluorescence

intensity will be lower indicating a smaller concentration of tracer than what is actually present. Figure 9-4 demonstrates the limit of linearity.
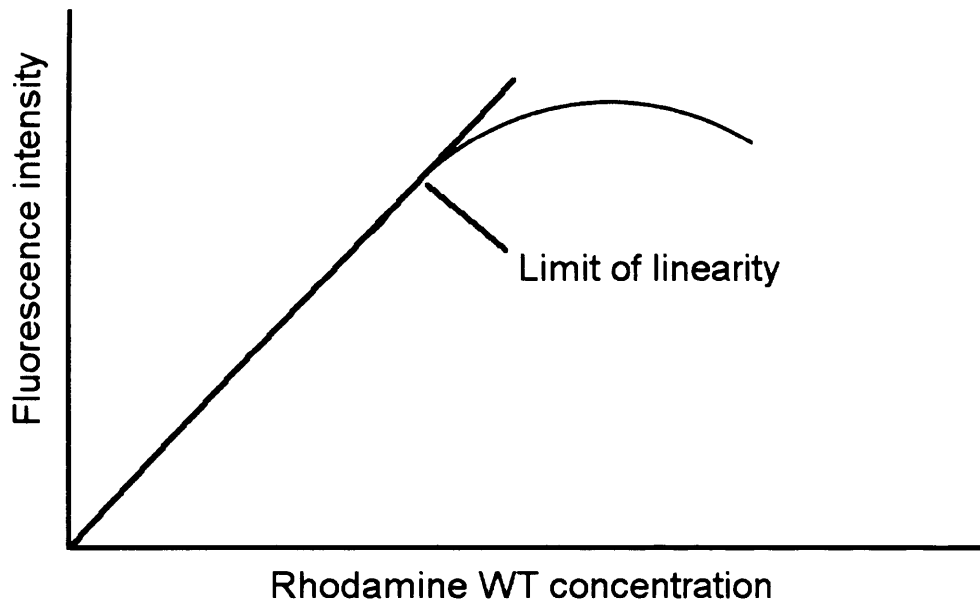
Figure 9-4. Variation in fluorescence intensity with die concentration showing the limit of linearity.

The limit of linearity is therefore dependent on the dilution of the Rhodamine WT and also on the apparatus e.g. optical filters that affect the wavelength of the fluoresced light etc. It is known that for the SCUFAs used that the point of linearity is reached at concentrations of 1000 units (Guymer, 2005, Private Communication).

The SCUFA can be set to monitor the concentration in a time step required by the user. In these tests, it was set to 1Hz, the highest frequency available.

Should any air accumulate on the optical windows a false reading will be recorded and hence the accumulation of air bubbles is undesirable, as well as semi coverage of the optics by the fluid. This was experienced initially by the SCUFA positioned adjacent to the outlet from the underflow, shown in Figure 9-5, but was overcome by positioning the SCUFA into the underflow shown in Figure 9-6.

Figure 9-5. (Provided by Ian Guymer ©2004). SCUFA placed adjacent to the underflow.

Figure 9-6. (Provided by Ian Guymer ©2004). SCUFA placed into the underflow.

Suspended particles will also give an inaccurate reading. However, the hardware has a channel that detects the scattered light due to suspended particles, known as 'turbidity' and adjustments can be made to compensate for this. The effects of suspended particles are assumed to be negligible due to working in laboratory conditions. (This may not be the case however where measurements are taken at sewage treatment works). The fluorescence of Rhodamine WT also varies with temperature. Guilbault (1990) suggests that at higher temperatures, the occurrence of molecular collisions increases, resulting in the loss of energy. The SCUFA is able to measure the temperature of the sample and automatically compensates for changes.

9.2   Grid setup and boundary conditions

The inlet pipe to the HDVS in Figure 9-1 was offset by 5% of the inlet diameter to prevent over skewed cells at the point the inlet pipe is joined to the HDVS vessel wall as this would result in appreciable error and possible convergence problems during computation of the flow. The walls forming the dip plate, baffle plates and cone etc were modelled as having zero thickness, due to the very fine cells that would result from modelling the actual thickness of these components. The free surface between the water and air was modelled as a frictionless

wall. A 'fixed lid' frictionless wall approach was used to represent the free surface and the height of the water at the overflow was based on measurements taken during experimental testing and these are given in Table C3, Appendix C. When the discharge at the overflow was below 0.119m^3/s, the shallow fluid depth at the overflow made accurate representation difficult. In these conditions, the outlet was positioned at the top of the weir, Figure 9-1 'T'. The overflow was specified as a pressure outlet for which all the flow quantities excluding pressure are extrapolated from the interior. The underflow was specified as a negative velocity inlet in order to acquire the desired flow split. However, the point at which the flow leaves the underflow, 'K' in Figure 9-1, is very close to a 90° bend. The profile for the velocity from the underflow was therefore predicted by modelling the underflow between 'I' and 'K' in Figure 9-1 separately, with a flowrate of 0.020m^3/s and then exporting the components of the velocity at the outlet of the underflow, as well as the turbulent quantities, to the full model of the HDVS. The valves at 'D' and 'J' in Figure 9-1 create a disturbance to the flow, so the effects of these were included by representing the valve as a zero thickness face, orientated at an appropriate angle in each model. A steady state solution was achieved for all the models using the Reynolds Stress Model. The standard pressure interpolation scheme was used along with the SIMPLE pressure-velocity coupling algorithm and first order terms were solved for momentum, turbulent kinetic energy and turbulent dissipation rate.

Figure 9-7 shows a slice through the grid applied to the HDVS for modelling a flowrate of 0.187m^3/s, which comprised of approximately 766 000 cells. A combination of the arrangement of internals within the HDVS such as the baffles, stiffeners and Venturi plate in the upper region and the deflector plate and cone which overhangs the base of the main vessel and which also incorporates a very narrow gap for the passage of fluid into the underflow, meant that a purely tetrahedral mesh was chosen over a hexahedral. It was ensured that where the fluid passes between two walls, a sufficient number of cells were present to model a crude boundary layer and to also solve the momentum equation for the transport of the fluid. This is particularly pronounced in the region of the overflow in Figure 9-7.
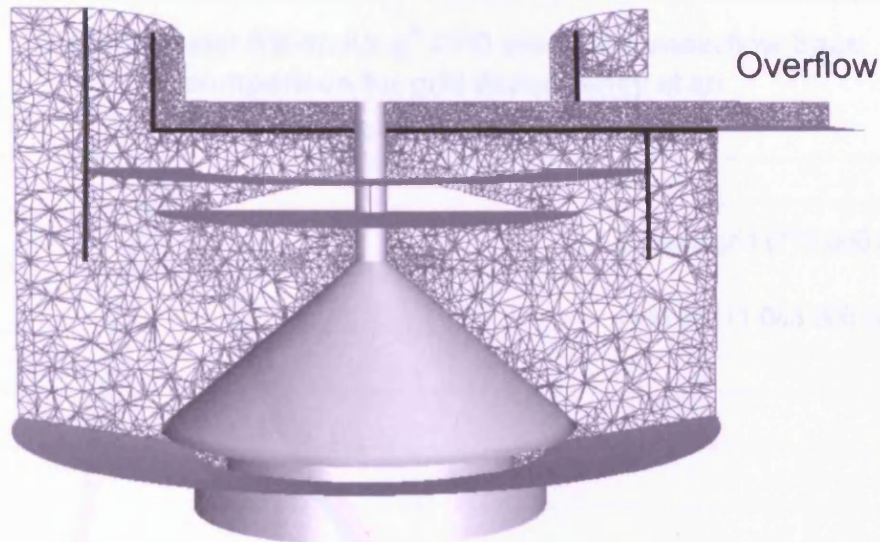
Figure 9-7. Grid for modelling a flowrate of 0.187m³/s.

A grid dependency check for an inlet flowrate of 0.187m³/s was made by increasing the number of cells in the main vessel by approximately 305 000. Figures 9-8 and 9-9 compare CFD-predicted RTDs at the overflow and underflow respectively.
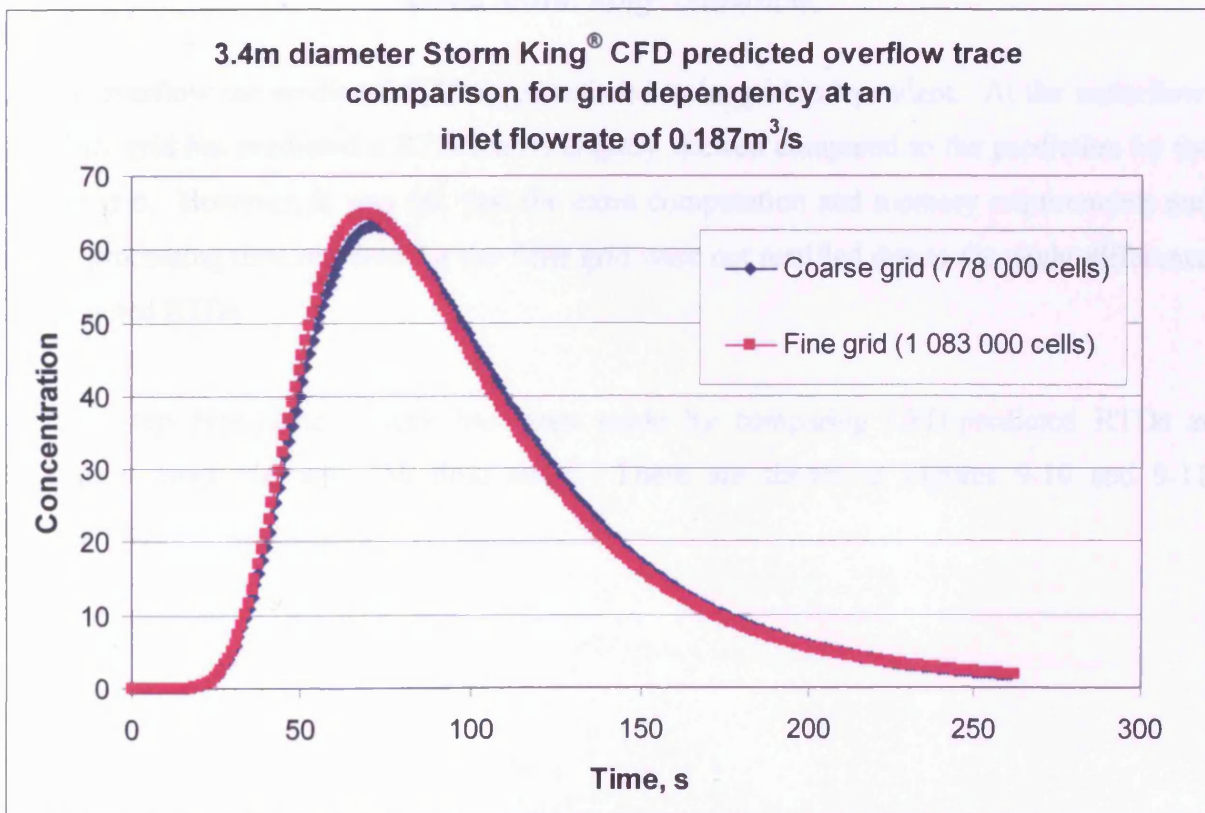
***Figure 9-8. CFD RTD prediction comparison for grid dependency
at the Storm King® overflow.***
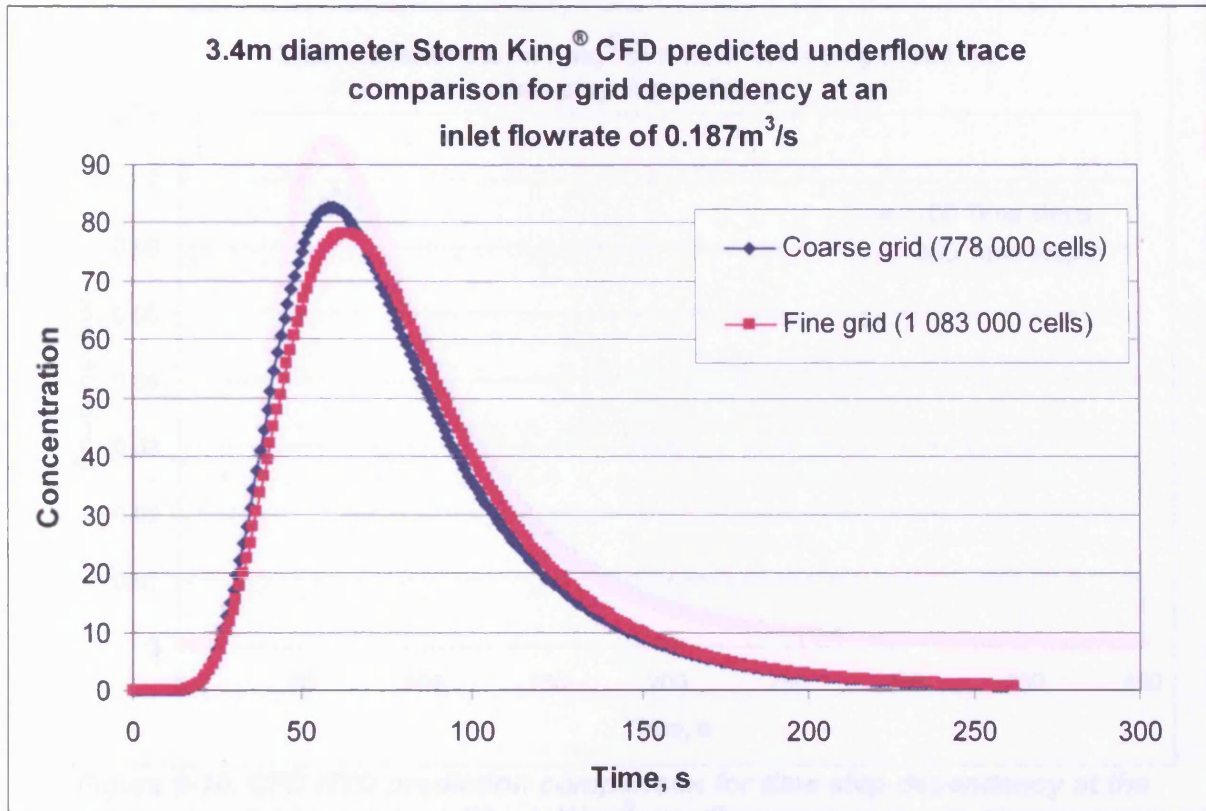
Figure 9-9. CFD RTD prediction comparison for grid dependency at the Storm King® underflow.

At the overflow the predicted RTD is considered to be grid independent. At the underflow, the finer grid has predicted a RTD that is slightly skewed compared to the prediction by the coarse grid. However, it was felt that the extra computation and memory requirements and hence processing time required for the finer grid were not justified due to the slight difference in predicted RTDs.

A time step dependency check has been made by comparing CFD-predicted RTDs at 0.187m³/s using 100 and 350 time steps. These are shown in Figures 9-10 and 9-11 respectively.
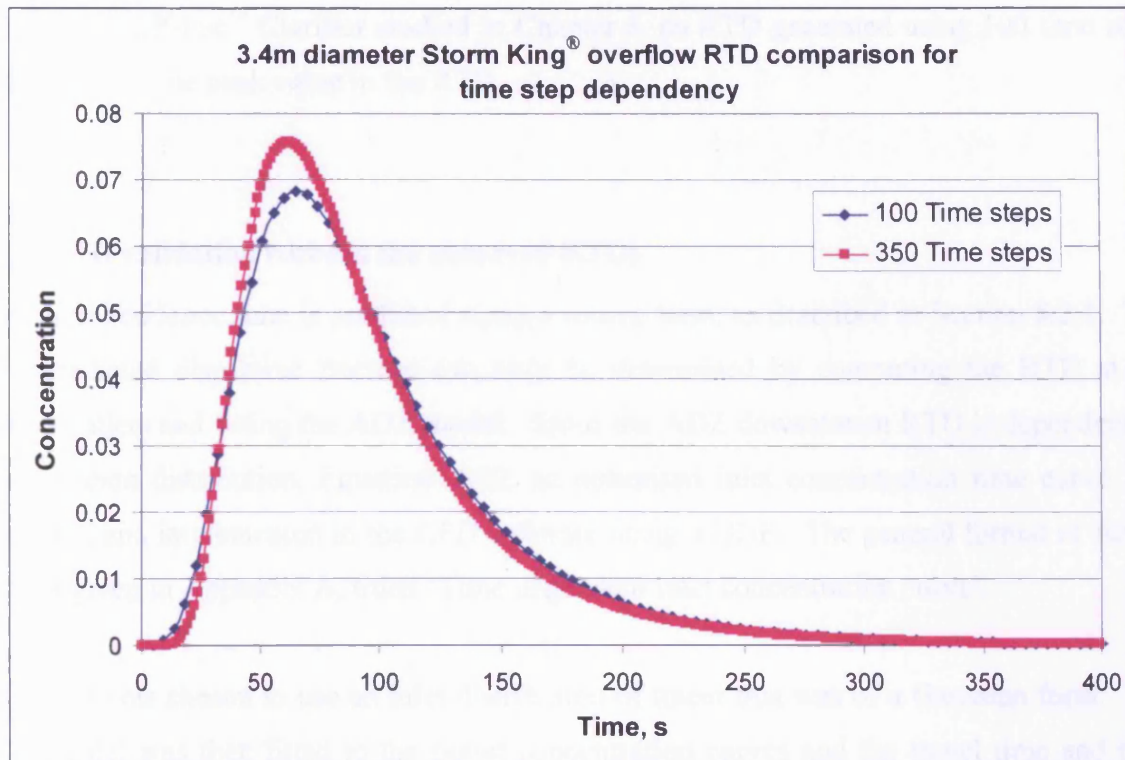
Figure 9-10. CFD RTD prediction comparison for time step dependency at the Storm King® overflow.
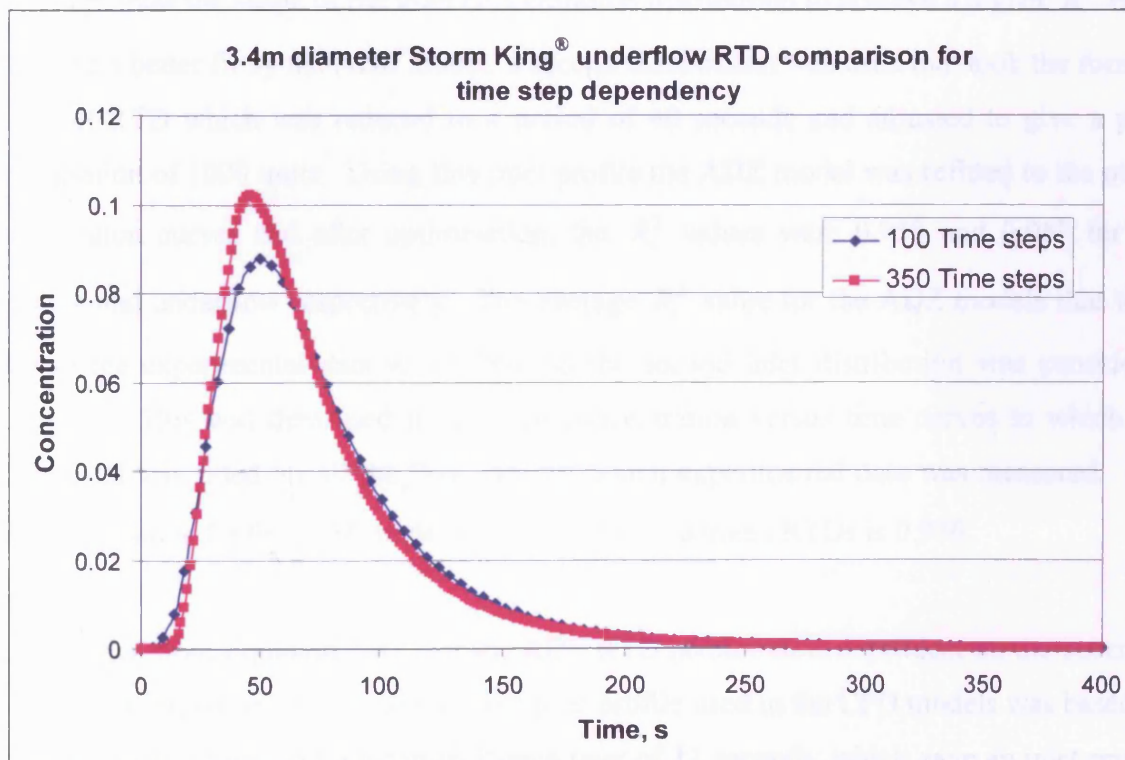
Figure 9-11. CFD RTD prediction comparison for time step dependency at the Storm King® underflow.

As with the Eff-Pac™ Clarifier studied in Chapter 8, an RTD generated using 100 time steps under predicts the peak value in the RTD.

9.3 RTD validation without the observed RTDs

The mean residence time is predicted using a source term, as described in Section 8.2.1. The CFD-predicted dispersive fraction can only be determined by computing the RTD at the HDVS outlets and fitting the ADZ model. Since the ADZ downstream RTD is dependent on the upstream distribution, Equation 2-32, an optimised inlet concentration time curve was generated and implemented in the CFD software using a UDF. The general format of such a UDF is given in Appendix A, titled 'Time dependent inlet concentration curve'.

Initially it was chosen to use an inlet distribution of tracer that was of a Gaussian form. The ADZ model was then fitted to the outlet concentration curves and the travel time and time delay optimised, which gave an R_t^2 value of 0.931 for both the underflow and overflow. To try and optimise the shape of the inlet concentration distribution to achieve a higher R_t^2 value and hence a better fit by the ADZ model, a second distribution was used that took the form of the outlet RTD which was reduced to a period of 40 seconds and adjusted to give a peak concentration of 1000 units. Using this inlet profile the ADZ model was refitted to the outlet concentration curves and after optimisation, the R_t^2 values were 0.958 and 0.967 for the overflow and underflow respectively. The average R_t^2 value for the ADZ models that were fitted to the experimental data was 0.964, so the second inlet distribution was considered acceptable. This was then used to produce concentration versus time curves to which the ADZ model was fitted for all the flowrates for which experimental data was measured. The average R_t^2 value for the ADZ model fit to the CFD-generated RTDs is 0.956.

It can be seen from Equation 2-41 that the ADE RTD prediction is dependent on the observed upstream concentration profile. Hence, the inlet profile used in the CFD models was based on the TISM, with 6 tanks and a mean residence time of 11 seconds, which gave an inlet profile similar to that used for the ADZ model. Thus, with an inlet distribution, a temporal concentration profile was predicted using CFD to which the ADE was fitted and thus, the best fit of the ADE parameters determined.

The time step size in the inlet concentration distributions is 1 second. Hence, the time step in the outlet RTD is also 1 second. This means that in predicting the RTD of the Storm King®, the number of time steps is between 280 and 2900. Processing time was lengthy but reduced with the availability of a 3.4GHz processor.

9.3.1 Results

Figure 9-12 shows a sample of the recorded data measured at the overflow for an inlet flowrate of $0.150m^3$/s. Clearly the sampling frequency, which is 1 second, is sufficient to determine the mean of the distribution and the mixing characteristics.
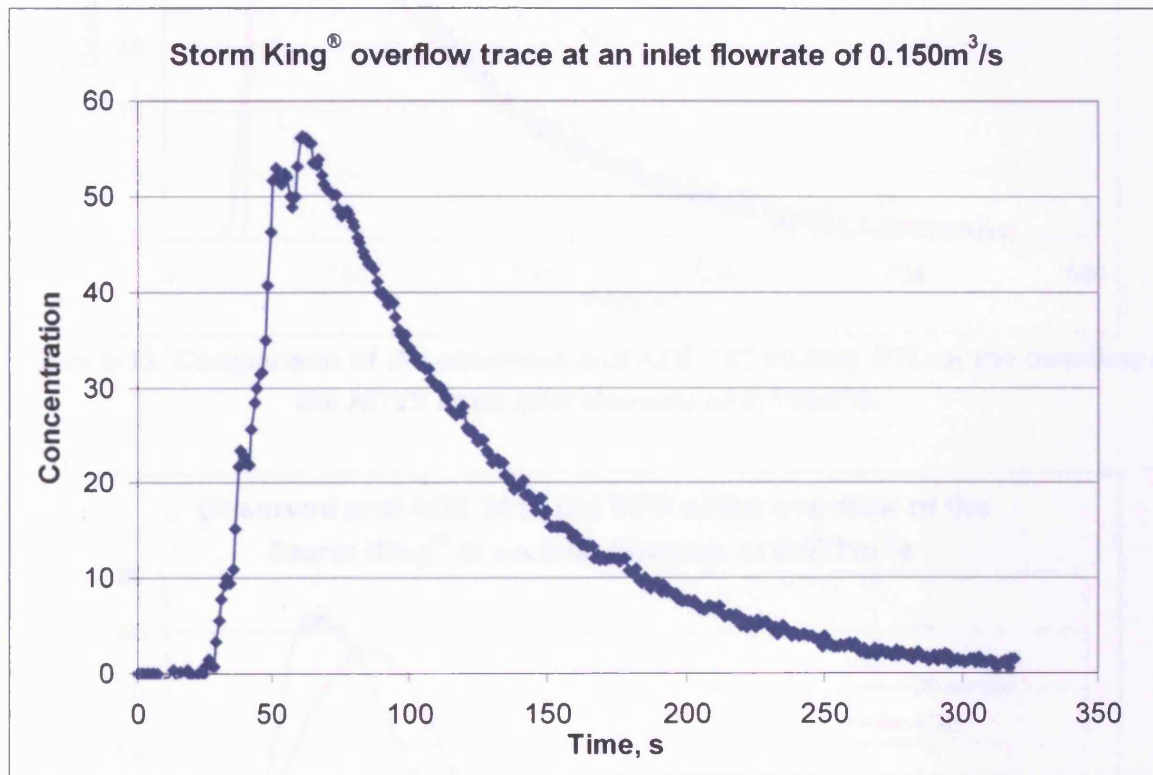
Figure 9-12. Recorded trace at the overflow at an inlet flowrate of 0.150m³/s.

Figure 9-13 shows the fit by the ADZ model to a RTD at the overflow at an inlet flowrate of $0.119m^3$/s where the R_t^2 value is 0.968 and is therefore a representative fit by the ADZ model to all the RTDs.

The average R_t^2 value for the ADE model fit to the observed temporal concentration distributions is 0.916. Figure 9-14 shows the fit by the ADE model to a RTD at the overflow

at an inlet flowrate of $0.077m^3/s$ where the R_t^2 value is 0.920 and is therefore a representative fit by the ADE model to all the RTDs.
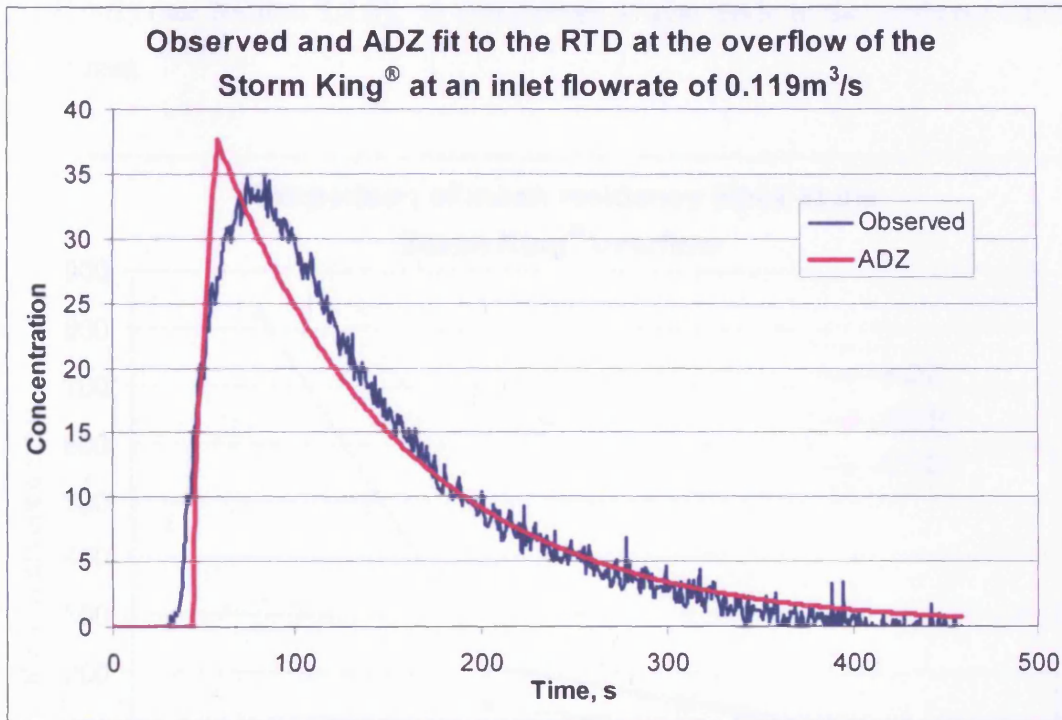
Figure 9-13. Comparison of the observed and ADZ (R_t^2 =0.968) RTD at the overflow of the HDVS at an inlet flowrate of 0.119m³/s.
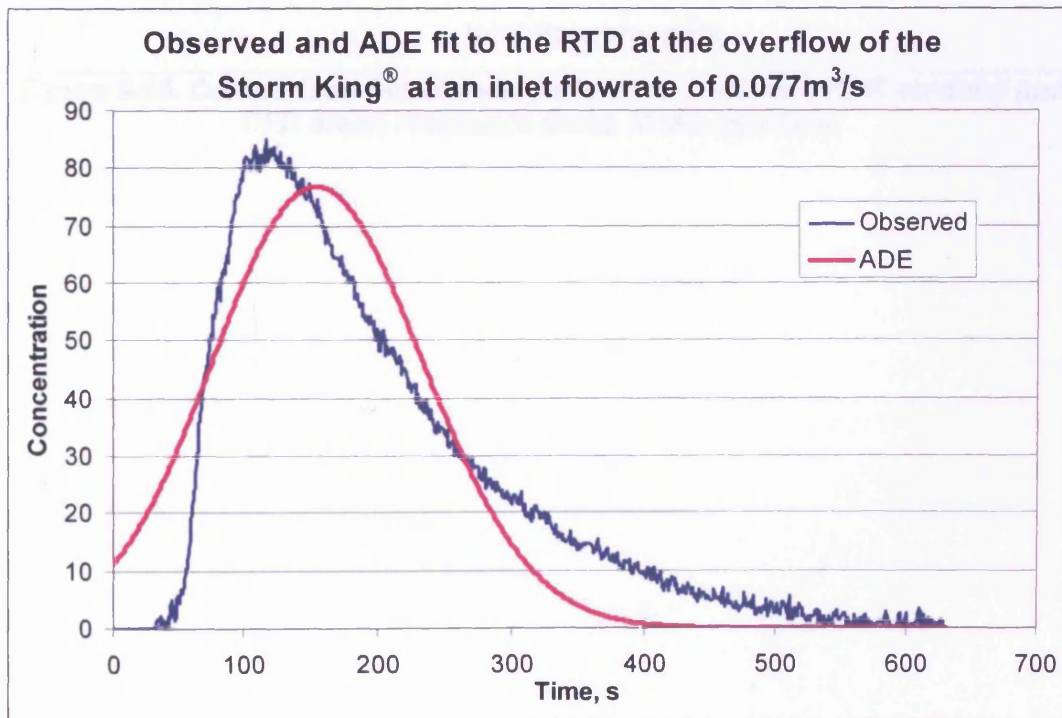
Figure 9-14. Comparison of the observed and ADE (R_t^2 =0.920) RTD at the overflow of the HDVS at an inlet flowrate of 0.077m³/s.

Figures 9-15 and 9-16 show the mean residence times for the overflow and underflow respectively determined by Guymer (2004) deduced from the ADE and ADZ model fits to the experimental data. The best fit of each model is achieved using an optimisation technique by Guymer (2002) (see Section 2.2.3). A comparison is also made to the predicted CFD mean residence times.
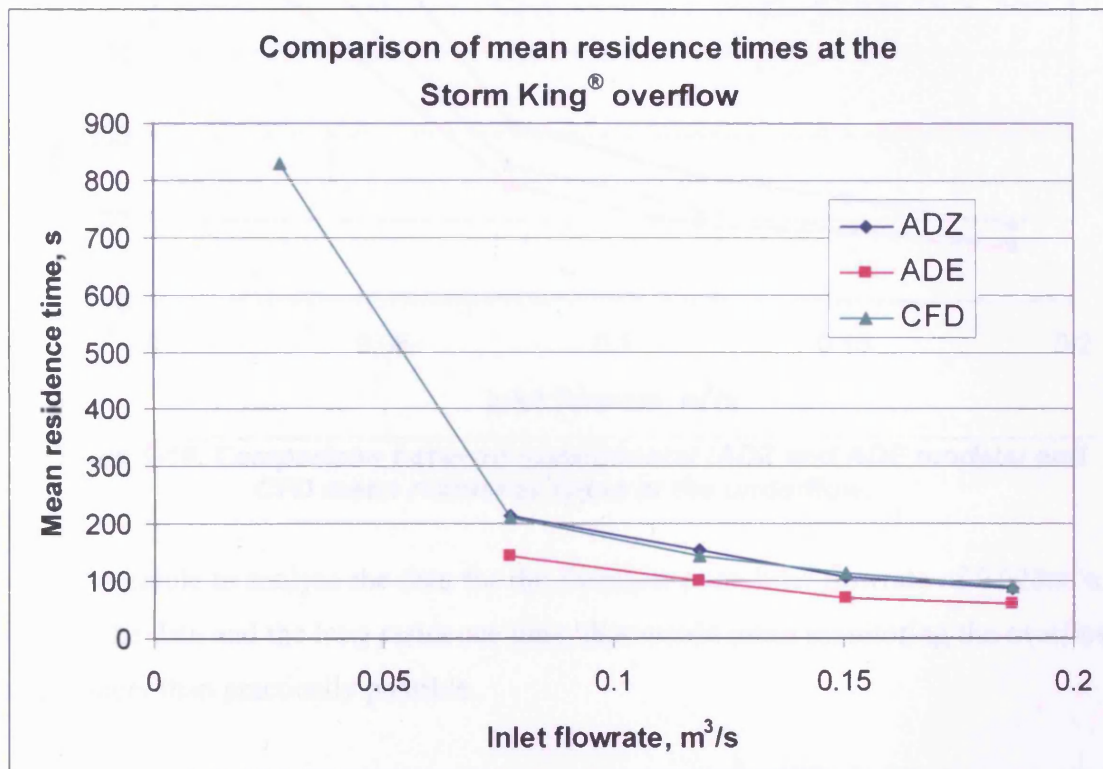
Figure 9-15. Comparison between experimental (ADZ and ADE models) and CFD mean residence times at the overflow.
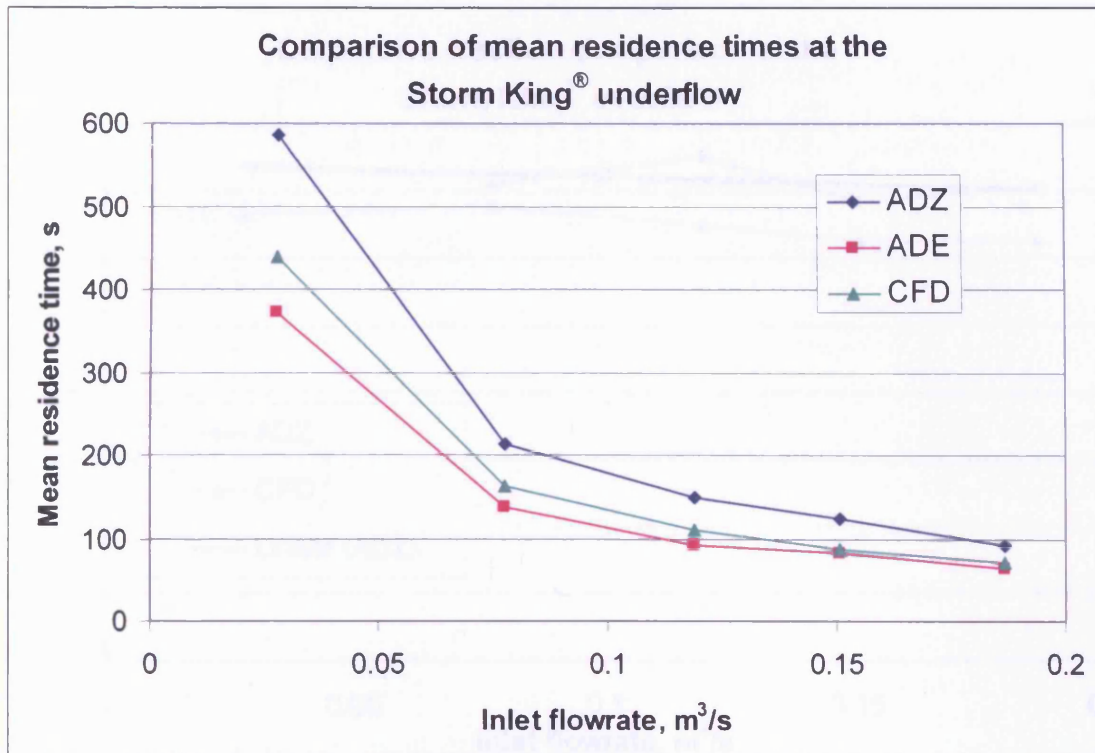
Figure 9-16. Comparison between experimental (ADZ and ADE models) and CFD mean residence times at the underflow.

It was not possible to analyse the data for the overflow at an inlet flowrate of 0.028m³/s, due to noise in the data and the long residence time, that would mean monitoring the overflow for a period longer than practically possible.

The CFD-predicted mean residence time appears to be reasonable for both the overflow and underflow. The CFD mean residence time is biased towards the ADZ model for the overflow and biased slightly towards the ADE model for the underflow.

Figures 9-17 and 9-18 show a comparison between the computed Dispersive Fraction for the experimental and CFD data. The trend in the experimental dispersive fraction from the linear best fit curve is that the dispersive fraction decreases slightly with increasing flowrate. The CFD dispersive fraction prediction is of a similar magnitude to the experimental and the trend in the CFD predictions follows the experimental data.
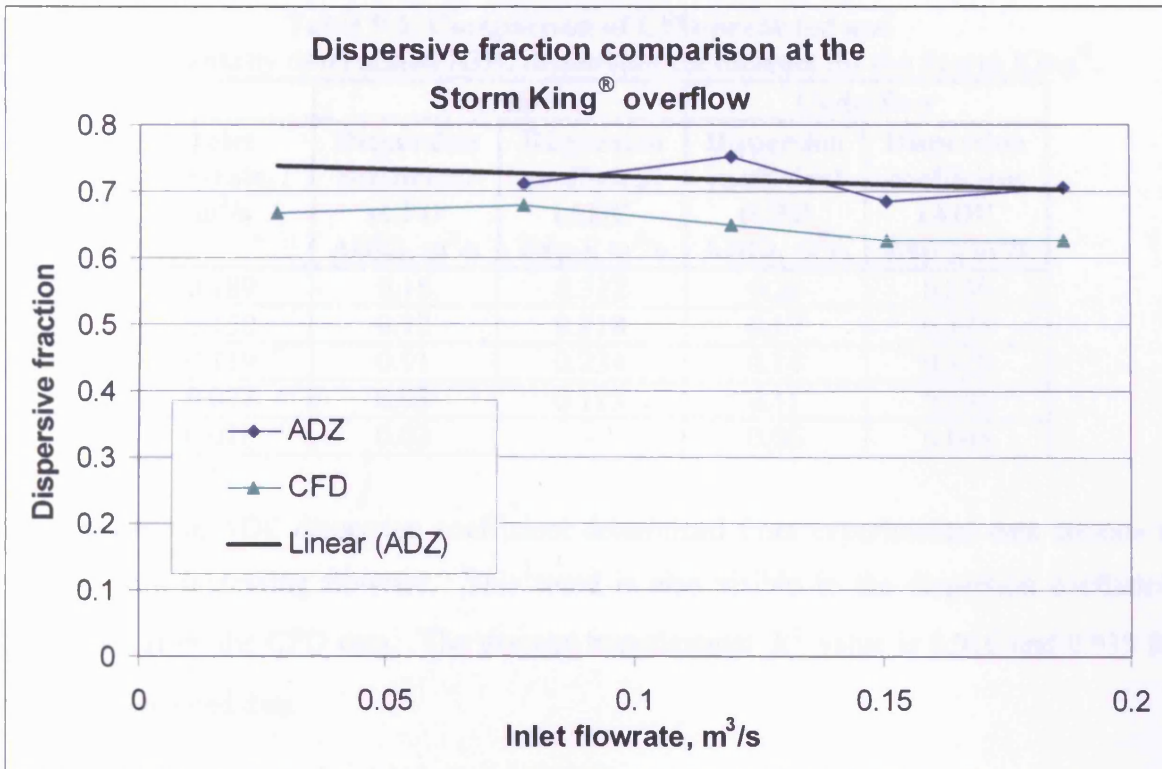
Figure 9-17. Experimental and CFD dispersive fraction at the overflow.
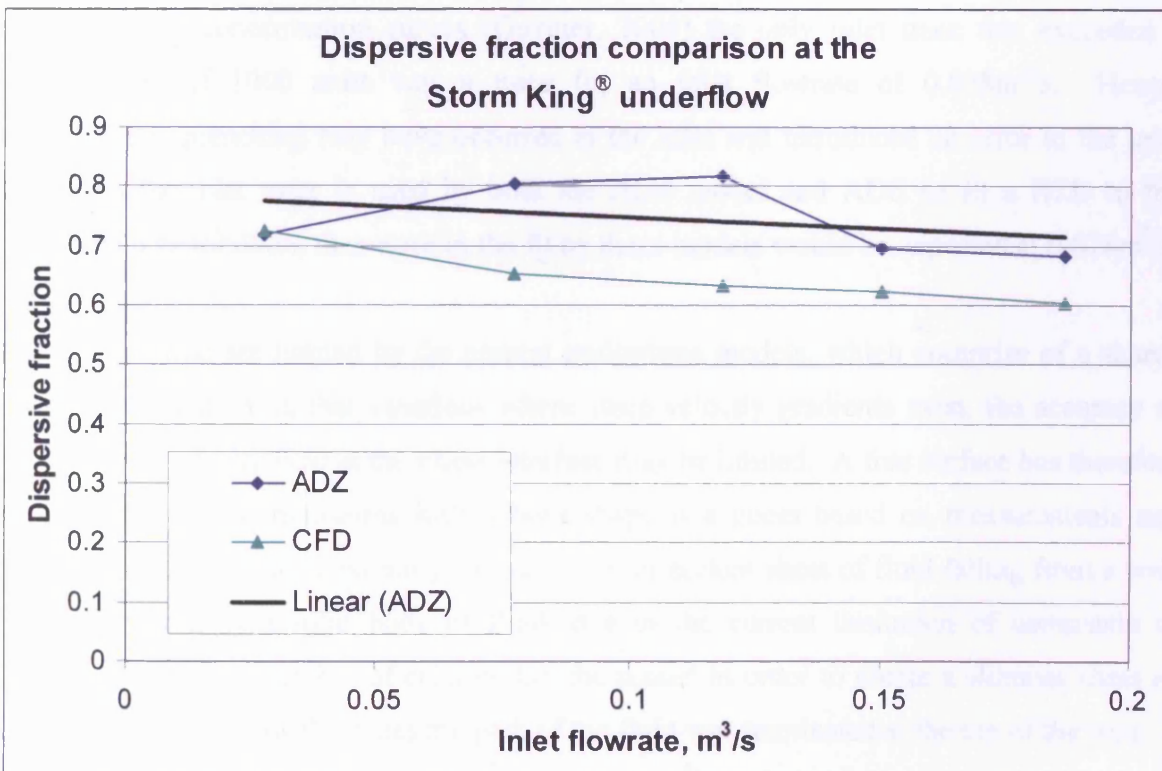
Figure 9-18. Experimental and CFD dispersive fraction at the underflow.

Table 9-1 shows a comparison between the dispersion coefficient determined by fitting the ADE to the observed and CFD-predicted RTDs.

Table 9-1. Comparison of CFD-predicted and experimentally determined ADE dispersion coefficients for the Storm King®.

Inlet flowrate, / m^3/s	Overflow		Underflow	
	Dispersion coefficient (CFD ADE), m^2/s	Dispersion coefficient (ADE Exp.), m^2/s	Dispersion coefficient (CFD ADE), m^2/s	Dispersion coefficient (ADE Exp.), m^2/s
0.189	0.16	0.312	0.20	0.250
0.150	0.12	0.218	0.17	0.175
0.119	0.11	0.234	0.14	0.328
0.077	0.08	0.113	0.11	0.156
0.028	0.02	-	0.06	0.044

The trend in the ADE dispersion coefficient determined from experimental data appears to increase with increasing flowrate. This trend is also visible in the dispersion coefficient determined from the CFD data. The average experimental R_t^2 value is 0.916 and 0.933 for the CFD-generated data.

9.3.2 Discussion

From the inlet concentration curves (Guymer, 2004) the only inlet trace that exceeded a concentration of 1000 units was a trace for an inlet flowrate of 0.028m³/s. Hence, concentration quenching may have occurred at the inlet and introduced an error in the inlet trace. As the inlet trace is used by both the ADZ model and ADE to fit a RTD to the downstream distribution, then error in the fit by these models would be expected at 0.028m³/s.

The CFD models are limited by the current multiphase models, which comprise of a shared momentum equation, in that situations where steep velocity gradients exist, the accuracy of the predicted velocity field at the phase interface may be limited. A free surface has therefore been modelled as a frictionless wall, whose shape is a guess based on measurements and observations taken in the laboratory. A very slim or broken sheet of fluid falling from a weir is approximated by a solid body of fluid, due to the current limitation of computers to incorporate a higher number of cells within the model in order to create a slimmer sheet of fluid. Thus, at very low flowrates the path of the fluid was terminated at the top of the weir.

The flow field computed using CFD was a first order solution. A more accurate solution may be achieved with computation of the second order terms in the governing equations. However, attempts to achieve this were fruitless, in that the solution diverged. This may be

due to the steep velocity gradients in specific regions of the model, such as the valves, particularly the inlet valve, where it is thought that cavitation may have occurred due to the high velocity of the fluid. An obvious region of relatively steep velocity gradient was in the sudden expansion from the inlet pipe, 0.178m in diameter, into the HDVS inlet, 0.5m in diameter, which effectively results in a jet. A possible solution would be to increase the density of the mesh in these areas to reduce the gradients across the cells. However, this would have resulted in a higher processing time.

From Figures 9-15 to 9-18, the CFD-predicted mean residence time and dispersive fraction appear to be reasonable and show the same trends as the values determined from the observed RTDs. The average R_t^2 value for the ADE model fit to the experimental data is lower than the average value for the ADZ model, implying that the ADZ model is a more suitable model for this application which is also visible from Figure 9-13. Despite the ADZ model giving the better prediction it was the author's opinion that a more suitable RTD model may exist which could overcome the angled peak predicted by the ADZ model and hence give a better fit. Alkhaddar *et al.* (2001) state that neither the TISM nor the ADM could represent the RTD of the Eff-Pac™ Clarifier. However, when fitting the ADM and TISM to the observed temporal concentration distribution, the parameters in the TISM and ADM were determined from the raw data via the method of moments, Equations 2-24 and 2-25 (Higgins, 2000). The use of the optimisation technique by Guymer (2002) (see Section 2.2.3) could reveal improved ability of either the ADM or the TISM model to fit RTDs from a HDVS. The results in the previous section illustrate how to validate the dispersive fraction from the ADZ model and the dispersion coefficient from the ADE without access to the raw data.

9.4 Assessment of the most suitable RTD model

The TISM and the ADM have been fitted to the observed temporal concentration profiles by writing a program in MS-Excel® which allows the user to manually determine the most appropriate values for the parameters in the RTD model.

To make a direct comparison between the observed RTDs and CFD predictions at the HDVS outlets, UDFs have been written to define the inlet concentration distributions recorded in the laboratory. Since each inlet concentration distribution recorded is different, 13 inlet profiles

were written. The sampling frequency of all the SCUFAs was 1Hz and hence the time step size in computing the RTD is also 1 second. Again, RTDs have been generated with the number of time steps in the range of 280 to 2900.

9.4.1 Results

An exact solution to the mean residence time of the RTD relies on a full mass recovery of the tracer. When this is not the case, the RTD has effectively been truncated and calculation of the mean residence time based on the first moment about the origin will give an under prediction. However, in a practical sense, provided that at least 95% of the mass of tracer (Rhodamine WT) has passed through then a reasonable estimation may be made.

In the case of the experimental data it is assumed that the tracer follows the fluid perfectly. Thus, with a flow split where 20% of the fluid entering the HDVS passes through the underflow, it is assumed that the same proportion of the tracer will pass through the underflow. Table 9-2 lists the mass balancing correction factors, where a factor less than one reduces the concentration in the downstream RTD curve which is generally the case in the overflow and a value greater than one increases the concentration which is generally the case for the underflow. This could be due to poorly mixed conditions at the inlet and outlets and measurement at a single point and a mass split of the tracer which may not be the same as the volumetric flow split. After mass balancing the RTDs, the majority of the curves did reduce to a concentration of approximately zero, implying that an almost complete mass recovery was achieved.

Table 9-2. Mass balance correction factors.

| Inlet flowrate, m^3/s | Mass balance correction factor | | | | | |
| | Overflow Repeat No. | | | Underflow Repeat No. | | |
	1	2	3	1	2	3
0.187	1.282	0.874	0.849	1.619	1.123	1.090
0.150	0.624	0.637	0.493	0.949	0.985	0.747
0.119	0.865	0.943	0.740	1.135	1.217	0.990
0.077	0.844	0.828	0.881	1.248	1.179	1.166
0.028				1.283		

Table 9-3 shows the average R_t^2 values, mean residence times and standard deviation as a percentage of the mean for the experimental data, CFD predictions and RTD models that have

been fit to the observed RTDs at the overflow and underflow. These results are based on three injections of tracer except at $0.028m^3/s$ where only one repeat was possible. The data at the overflow at this flowrate could not be analysed due to noise in the data and the long residence time, that would mean monitoring the overflow for a period longer than practically possible. The standard deviation of the mean residence time determined using CFD is not given as the mean that is calculated is the exact value.

The CFD predictions fit the residence time distributions with the lowest R_t^2 value. The predicted RTDs are compared to the observed RTDs in Appendix M. Regarding the RTD models, the ADE fits the distributions with the lowest R_t^2 values. The ADZ model and TISM give better fits that are approximately the same based on R_t^2 and the ADM fits with the highest R_t^2 value.

To make a direct comparison between the mixing characteristics computed by each model, Table 9-4 presents the normalised variance of the experimental data, the CFD predictions and the RTD models that have been fit to the observed RTDs. The TISM is a poor comparison as the normalised variance is given by the inverse of the number of tanks, which is generally an integer. The normalised variance of the experimental data, ADZ model and ADE RTDs has been computed via the second moment about the mean, Equation 2-25, as too have the CFD RTD predictions.

Table 9-3. Mean residence time and R_t^2 values based on three injections of tracer.

Inlet flowrate, m³/s			TISM	ADZ	ADE	ADM	CFD	Exp
			OVERFLOW					
0.187	Residence time, s	Mean	71.2	86.5	59.9	76.5	91.9	75.7
		SD(%)	5.8	7.7	5.0	5.8	-	5.8
	R_t^2	Mean	0.977	0.988	0.922	0.995	0.868	-
		SD(%)	0.2	0.1	0.1	0.1	4.3	-
0.150	Residence time, s	Mean	88.6	106.7	71.9	95.6	115.1	92.5
		SD(%)	5.3	4.8	4.6	7.6	-	6.3
	R_t^2	Mean	0.955	0.972	0.894	0.982	0.840	-
		SD(%)	1.8	1.3	3.2	1.2	2.3	-
0.119	Residence time, s	Mean	118.6	153.6	99.8	137.6	144.5	138.4
		SD(%)	7.4	8.1	6.3	14.4	-	12.0
	R_t^2	Mean	0.948	0.978	0.884	0.989	0.870	-
		SD(%)	2.7	1.0	2.5	0.3	5.2	-
0.077	Residence time, s	Mean	165.0	213.8	142.4	180.7	210.7	183.3
		SD(%)	2.2	0.7	0.3	0.9	-	2.2
	R_t^2	Mean	0.975	0.965	0.913	0.995	0.954	-
		SD(%)	0.3	0.4	0.6	0.2	0.4	-
			UNDERFLOW					
0.187	Residence time, s	Mean	89.7	91.8	65.2	94.0	71.2	80.2
		SD(%)	6.5	6.3	6.0	6.5	-	6.5
	R_t^2	Mean	0.974	0.987	0.927	0.995	0.940	-
		SD(%)	0.2	0.1	0.2	0.0	3.0	-
0.150	Residence time, s	Mean	95.3	123.5	83.7	103.0	86.4	102.6
		SD(%)	7.1	8.2	4.3	7.8	-	5.2
	R_t^2	Mean	0.975	0.961	0.928	0.995	0.892	-
		SD(%)	0.5	1.1	1.5	0.3	5.6	-
0.119	Residence time, s	Mean	125.9	149.1	93.0	138.6	110.6	130.7
		SD(%)	14.4	5.3	3.8	12.3	-	9.0
	R_t^2	Mean	0.946	0.979	0.897	0.991	0.825	-
		SD(%)	1.6	1.2	1.6	0.3	7.6	-
0.077	Residence time, s	Mean	159.7	213.2	137.8	185.3	162.9	173.3
		SD(%)	1.9	2.5	2.5	2.4	-	1.8
	R_t^2	Mean	0.969	0.950	0.922	0.988	0.902	-
		SD(%)	0.6	0.7	0.5	0.2	0.8	-
0.028	Residence time, s	-	430.9	586.3	372.2	475.9	439.6	437.7
	R_t^2	-	0.976	0.898	0.955	0.967	0.774	-

Table 9-4. Normalised variance based on three injections of tracer.

Inlet flowrate, / m³/s		TISM	ADZ	ADE	ADM	CFD	Exp
		OVERFLOW					
0.187	Mean	0.250	0.339	0.401	0.300	0.255	0.245
	SD(%)	0.0	3.5	2.7	3.3	6.7	0.6
0.150	Mean	0.214	0.281	0.311	0.270	0.213	0.254
	SD(%)	22.4	21.7	13.8	17.0	23.5	6.6
0.119	Mean	0.250	0.398	0.446	0.407	0.299	0.331
	SD(%)	0.0	10.3	38.1	26.0	12.7	14.1
0.077	Mean	0.250	0.339	0.300	0.313	0.276	0.285
	SD(%)	0.0	4.7	4.7	3.8	3.6	8.9
		UNDERFLOW					
0.187	Mean	0.250	0.318	0.357	0.267	0.328	0.221
	SD(%)	0.0	4.1	4.5	4.5	5.5	5.4
0.150	Mean	0.214	0.257	0.286	0.270	0.296	0.235
	SD(%)	22.4	26.1	11.2	14.8	12.8	1.2
0.118	Mean	0.375	0.432	0.560	0.533	0.373	0.369
	SD(%)	38.4	8.1	34.8	18.9	12.3	5.9
0.077	Mean	0.250	0.356	0.379	0.430	0.344	0.293
	SD(%)	0.0	1.4	2.9	4.0	2.6	2.2
0.028	-	0.250	0.238	0.289	0.350	0.303	0.252

Figures 9-19 and 9-20 summarises the mean residence times in Table 9-3 and Figures 9-21 and 9-22 summarises the normalised variance in Table 9-4.
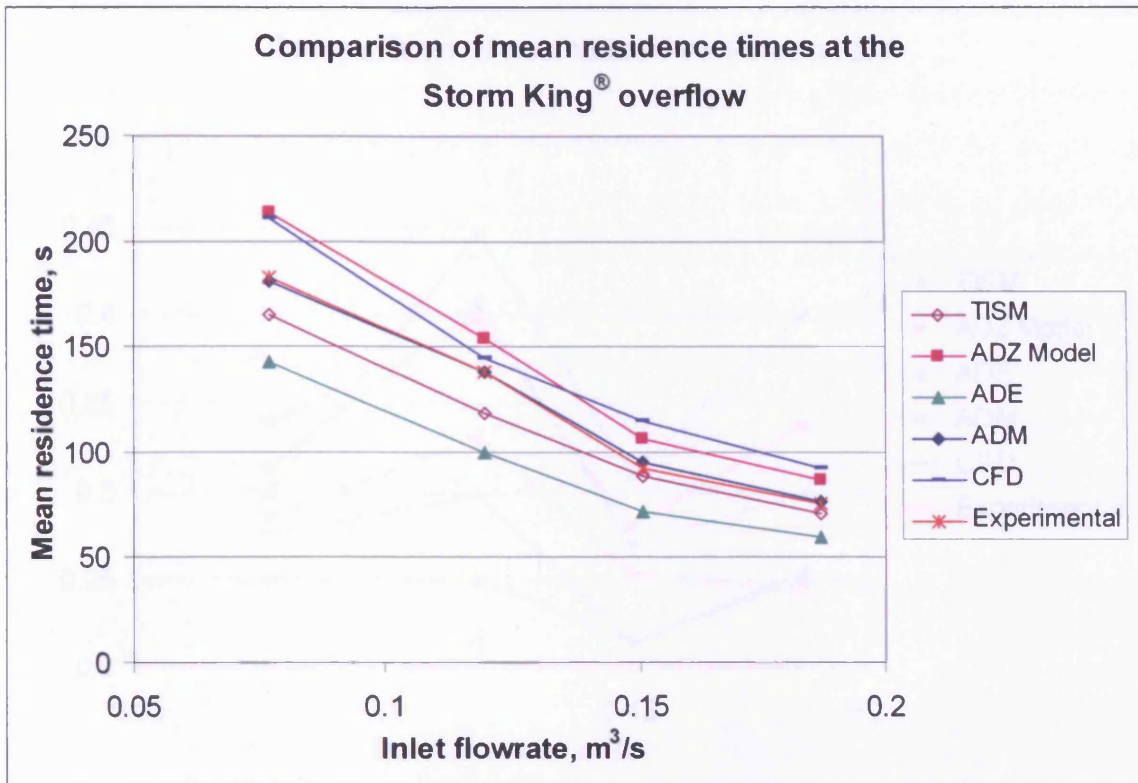
Figure 9-19. Mean residence times at the overflow of the 3.4m diameter Storm King®.
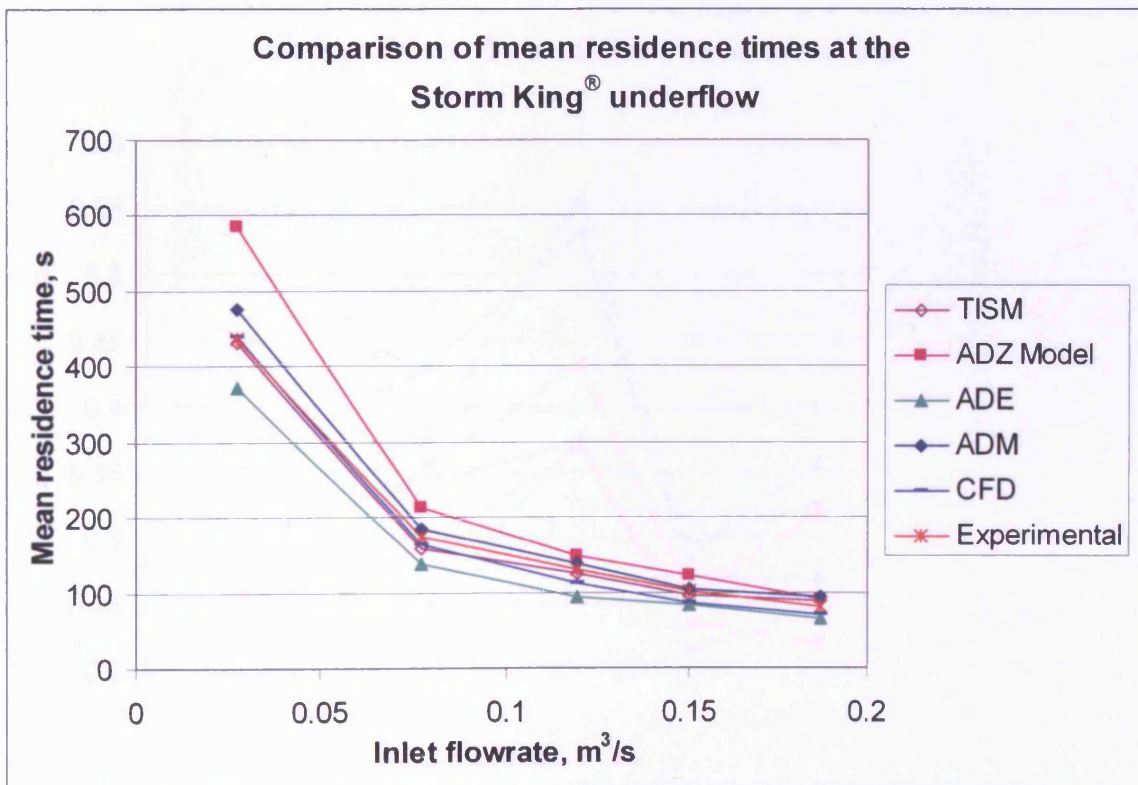
Figure 9-20. Mean residence times at the underflow of the 3.4m diameter Storm King®.
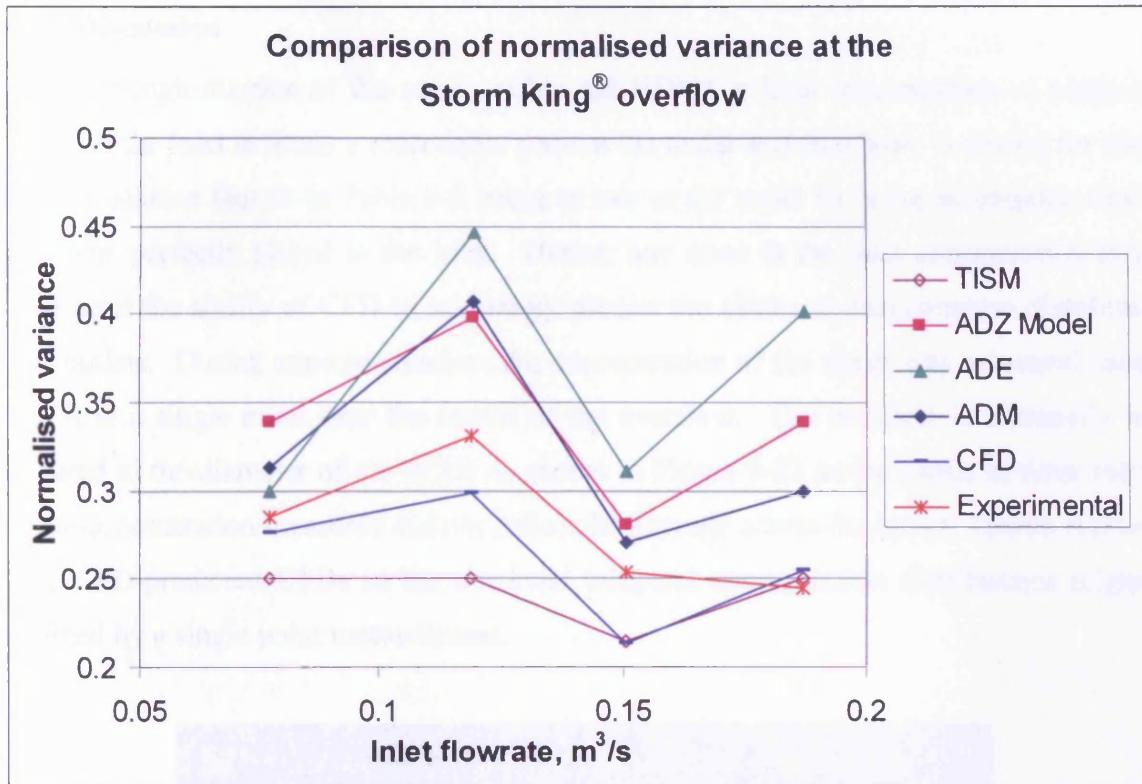
Figure 9-21. *Normalised variance at the overflow of the 3.4m diameter Storm King®.*
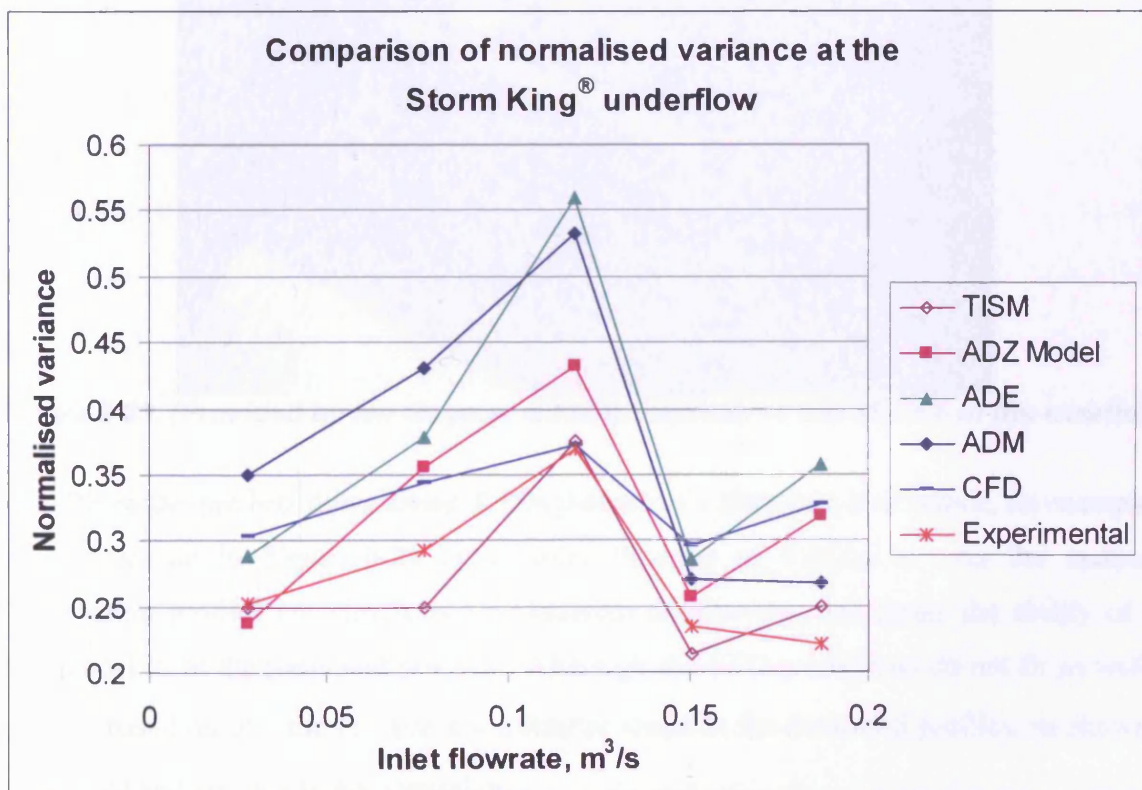
Figure 9-22. *Normalised variance at the underflow of the 3.4m diameter Storm King®.*

9.4.2 Discussion

Due to the high dilution of the tracer within the HDVS, a high concentration of tracer was injected at the inlet to attain a reasonable trace at the under and overflow. A reason for one of the mass balance factors in Table 9-2 being as low as 0.5 could be in the assumption that the tracer was perfectly mixed at the inlet. Hence, any error in the inlet concentration profile would limit the ability of CFD to accurately predict the observed concentration distributions at the outlets. During experimentation, the concentration of the tracer was measured using a SCUFA at a single point near the centre of the overflow. The overflow is extremely wide compared to the diameter of the SCUFA, shown in Figure 9-23 and a source of error may be that the concentration measured did not reflect the average across the outlet. Hence, a poor fit of the CFD-predicted RTDs to the observed temporal concentration distributions might be explained by a single point measurement.

Figure 9-23. (Provided by Ian Guymer ©2004). Position of the SCUFA in the overflow.

The ADE model predicts downstream RTDs that are of a Gaussian distribution, an example of which is shown in Figure 9-24 at an inlet flowrate of 0.077m³/s. As the measured concentration profiles are clearly not a Gaussian distribution, this limits the ability of the ADE model to fit the measured profiles. Although the CFD predictions do not fit as well as the ADE based on R_t^2, the profiles are a similar shape to the measured profiles, as shown in Figure 9-24 and are clearly not Gaussian.
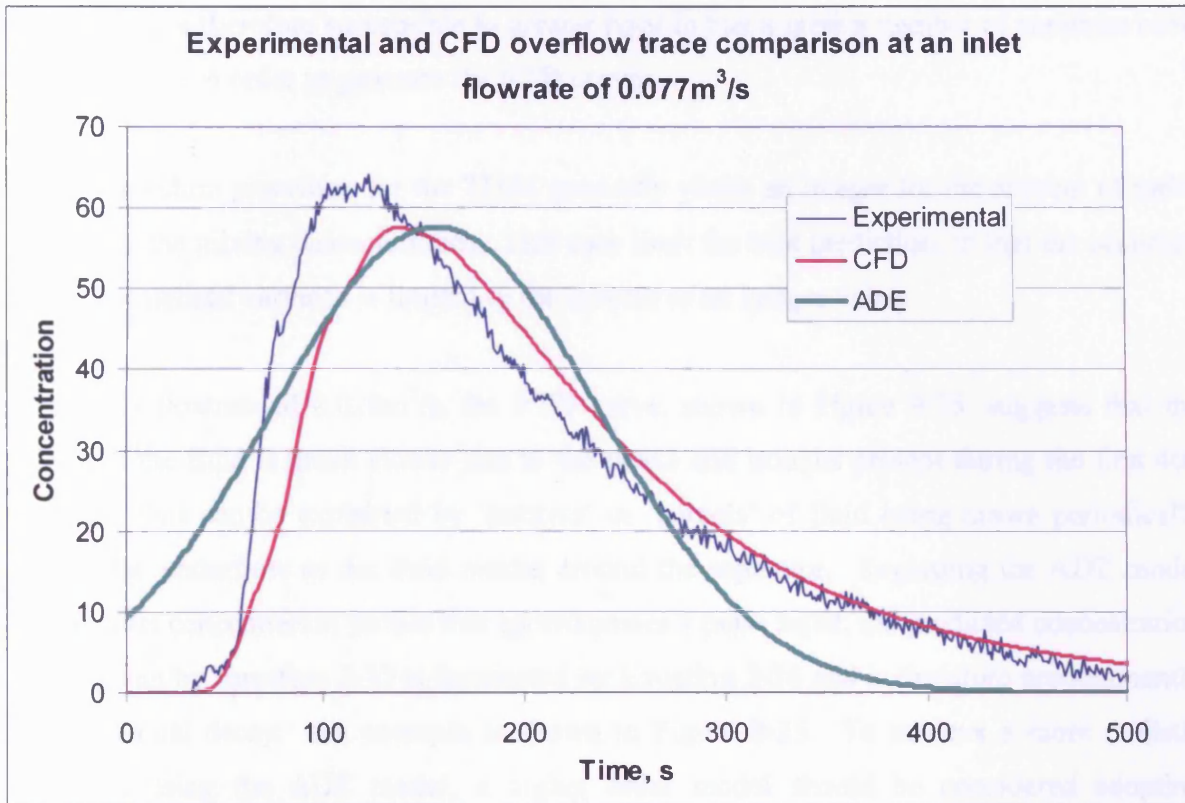
Figure 9-24. ADE (R_t^2 =0.912), CFD (R_t^2 =0.952) and experimental concentration profile comparison at the overflow at an inlet flowrate of 0.077m³/s.

From Figure 9-19, at the overflow the CFD mean residence time prediction compares closest to that predicted using the ADZ model. At the underflow, Figure 9-20, the CFD data compares closest to the TISM at flowrates below 0.120m³/s and the ADE model at flowrates above 0.120m³/s. Despite the R_t^2 value for the CFD being the lowest, prediction of the mean travel time appears to be reasonable compared with the prediction made by the other RTD models. All the models show the same trend in that the mean residence time increases with decreasing flowrate, as would be expected. Although the CFD predictions fit the observed distributions with the lowest R_t^2 value, the RTD models have been fitted to experimentally measured distributions. CFD on the other hand calculates the flow field within the separator over a mesh generated by the user based on a set of boundary conditions and solution options, such as flowrate, the position and shape of the free surface, an estimation of the turbulence at the inlet, all of which are subject to error, as well as the choice of turbulence model and associated solution controls such as pressure-velocity coupling schemes etc. The residence time distribution is then computed from the calculated flow field. Simplistically, the flow field being used to compare the different RTD models is fixed, based on measured RTD curves. CFD predictions are dependent on the boundary conditions and solution methods

chosen and are therefore susceptible to greater error in that a greater number of variables have to be specified in order to generate the RTD curves.

The optimisation procedure for the TISM generally yields an integer for the number of tanks that define the mixing characteristics. This may limit the best prediction, in that the accuracy for the normalised variance is limited to the inverse of an integer value.

At an inlet flowrate of 0.028m³/s, the RTD curve, shown in Figure 9-25, suggests that the mixing of the fluid is much slower due to the peaks and troughs present during the first 400 seconds. This can be explained by 'packets' or 'parcels' of fluid being drawn periodically through the underflow as the fluid rotates around the separator. Regarding the ADZ model with an inlet concentration profile that approximates a pulse input, the predicted concentration profile given by Equation 2-32 is dominated by Equation 2-34 and is therefore predominantly an exponential decay. An example is shown in Figure 9-25. To achieve a more realistic prediction using the ADZ model, a higher order model should be considered adopting multiple cells in parallel and series (Richter, 2004).
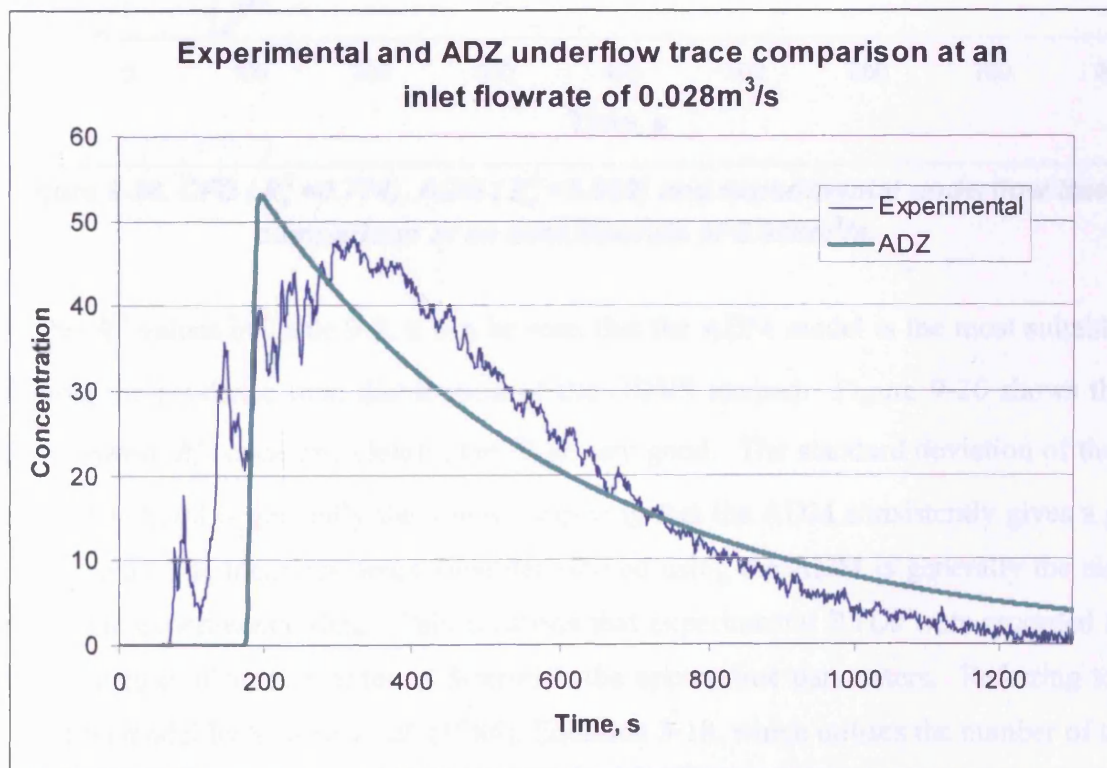
Figure 9-25. ADZ (R_t^2 =0.897) and experimental concentration profile comparison at the underflow at an inlet flowrate of 0.028m³/s.

The RTD models considered are unable to model the peaks and troughs, demonstrated by the ADM model overlaid on the experimental trace in Figure 9-26. The CFD model, which predicts and uses the flow field, achieves a representation of this behaviour, shown in Figure 9-26.
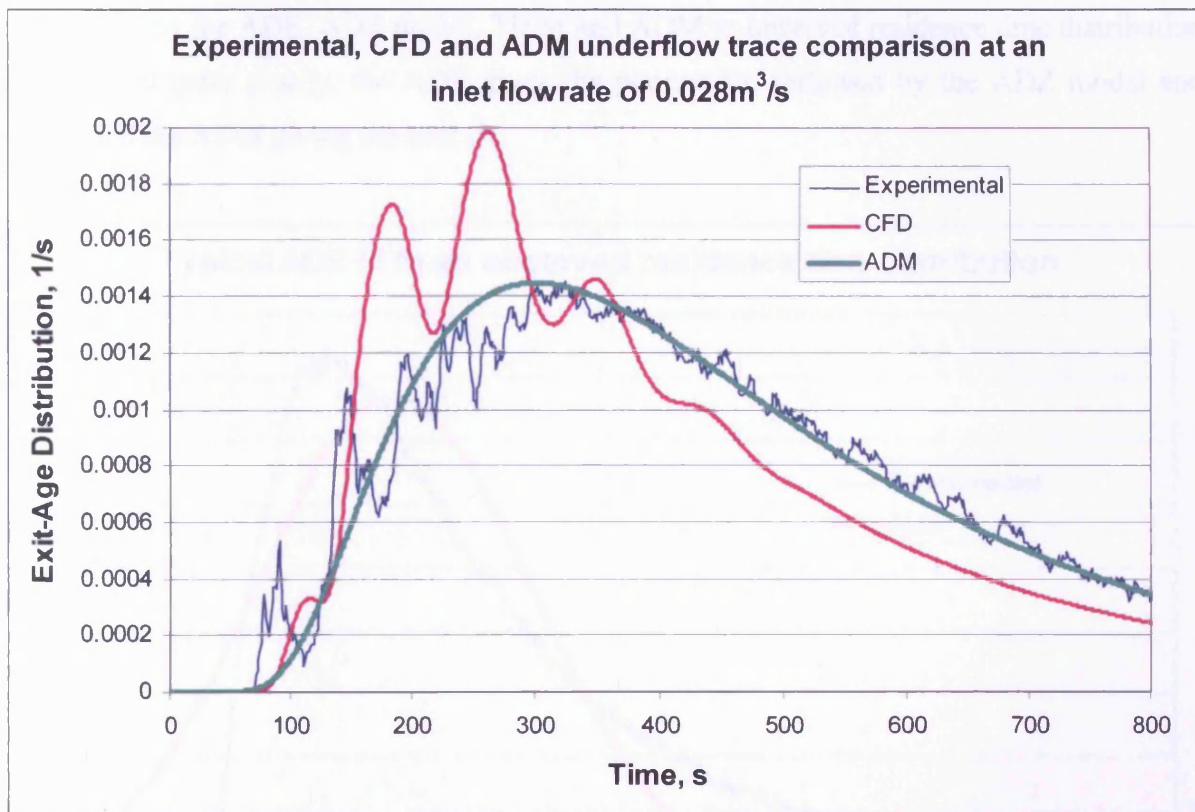
Figure 9-26. CFD (R_t^2 =0.774), ADM (R_t^2 =0.969) and experimental underflow trace comparison at an inlet flowrate of 0.028m³/s.

From the R_t^2 values in Table 9-3, it can be seen that the ADM model is the most suitable for describing the residence time distribution of the HDVS studied. Figure 9-26 shows the fit with the lowest R_t^2 value and clearly, the fit is very good. The standard deviation of the R_t^2 value for the ADM is generally the lowest, implying that the ADM consistently gives a good fit to the data. The mean residence time determined using the ADM is generally the closest match to the experimental data. This confirms that experimental RTDs were recorded for a sufficient period of time in order to determine the appropriate parameters. Referring to the disinfection model by Severin *et al.* (1984), Equation 3-18, which utilises the number of tanks from the TISM, this result highlights that there may be a desire to develop the existing disinfection model for improved disinfection predictions using the ADM rather than the TISM. A possible improvement to the disinfection model could simply be a substitution of

the inverse of the normalised variance, from Equation 2-31, for the number of tanks, predicted using the ADM model. This would have to be confirmed by comparing the disinfection model with experimental disinfection data from an HDVS.

To make a direct comparison between each of the RTD models, Figures 9-27 to 9-30 show typical fits by the ADE, ADZ model, TISM and ADM to observed residence time distribution models and quite clearly, the ADE gives the poorest fit, followed by the ADZ model and TISM and the ADM giving the best fit.
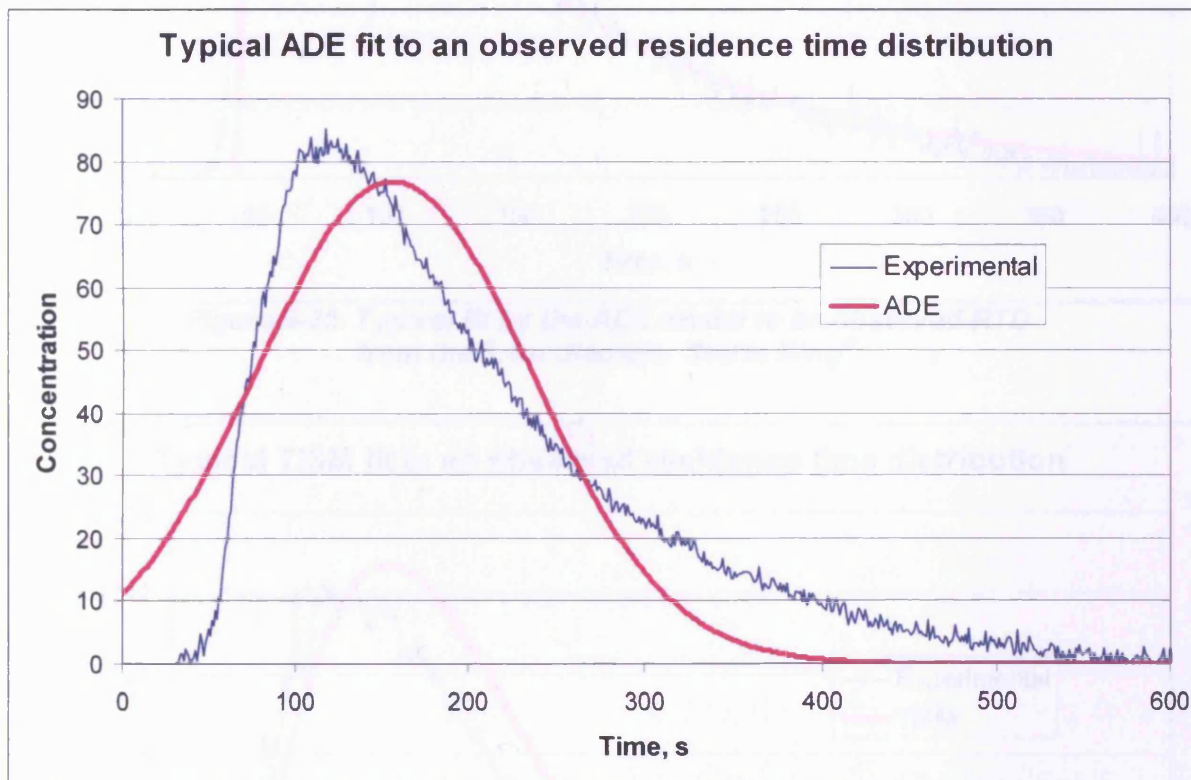
Figure 9-27. Typical fit by the ADE model to an observed RTD from the 3.4m diameter Storm King®.

Typical ADZ fit to an observed residence time distribution
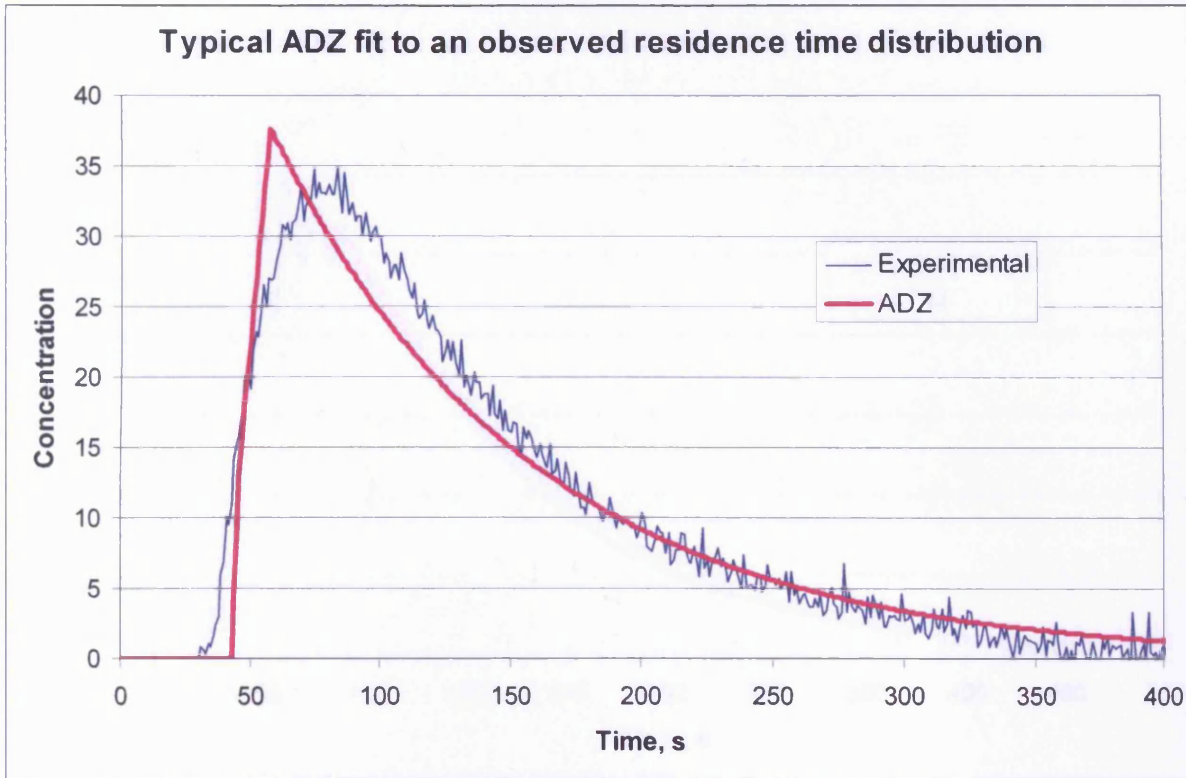
Figure 9-28. *Typical fit by the ADZ model to an observed RTD from the 3.4m diameter Storm King®.*

Typical TISM fit to an observed residence time distribution
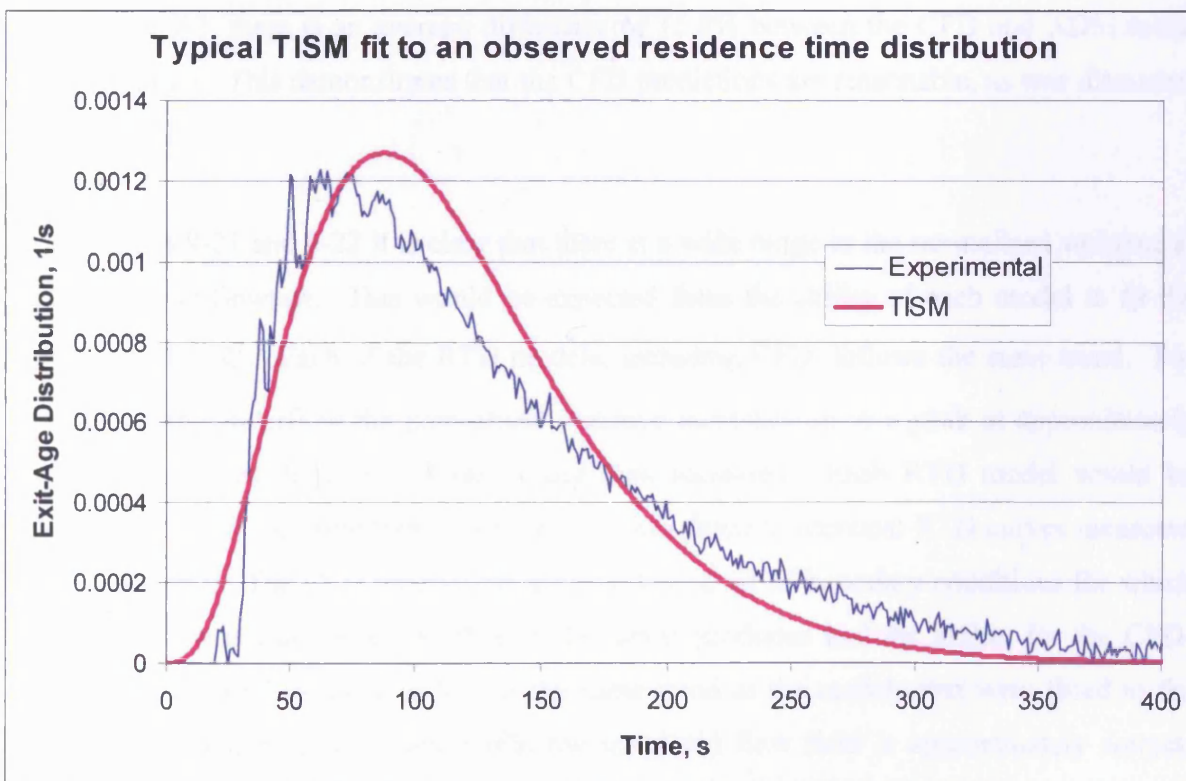
Figure 9-29. *Typical fit by the TISM to an observed RTD from the 3.4m diameter Storm King®.*

Typical ADM fit to an observed residence time distribution
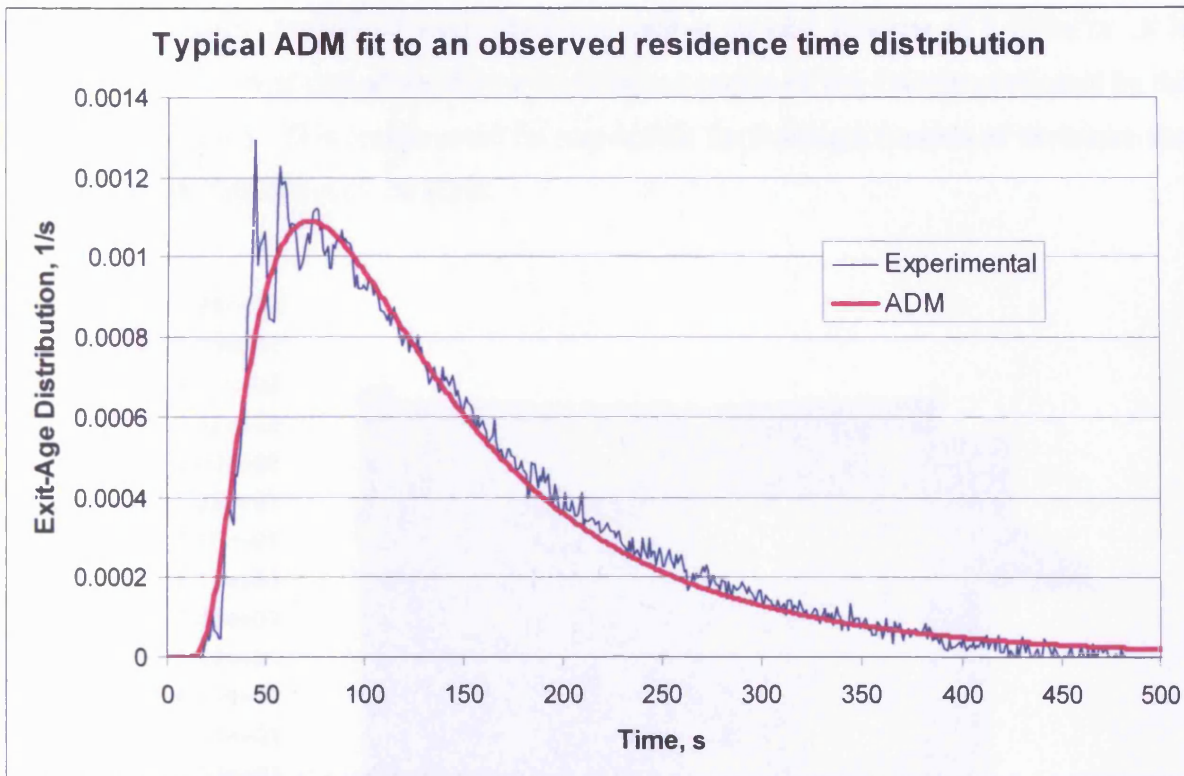
Figure 9-30. Typical fit by the ADM to an observed RTD
from the 3.4m diameter Storm King®.

From Table 9-3, there is an average difference of 15.8% between the CFD and ADM mean residence times. This demonstrates that the CFD predictions are reasonable, as was discussed in Section 9.3.

From Figures 9-21 and 9-22 it is clear that there is a wide range in the normalised variance at any given inlet flowrate. This would be expected from the ability of each model to fit the RTD, given by R_t^2. Each of the RTD models, including CFD, follows the same trend. For example, at the underflow the normalised variance increases up to a peak at approximately $0.120m^3/s$ and then drops at $0.150m^3/s$ and then increases. Each RTD model would be expected to follow the same trend because each was fitted to identical RTD curves measured in the laboratory. The CFD predictions are based on a set of boundary conditions for which the flow field was calculated and then RTD curves produced and the ability for the CFD-predicted normalised variance to follow the same trend as the models that were fitted to the experimental data, gives confidence that the simulated flow field is approximately correct. The CFD-predicted normalised variance is generally within the values predicted by the RTD models.

Figure 9-31 shows contours of mean residence time at an inlet flowrate of $0.187m^3/s$. It is clear that in the central part of the separator, there is a region of low velocity, indicated by the high residence time. This region could be responsible for holding a fraction of the tracer that results in the tailing effect of the RTD.
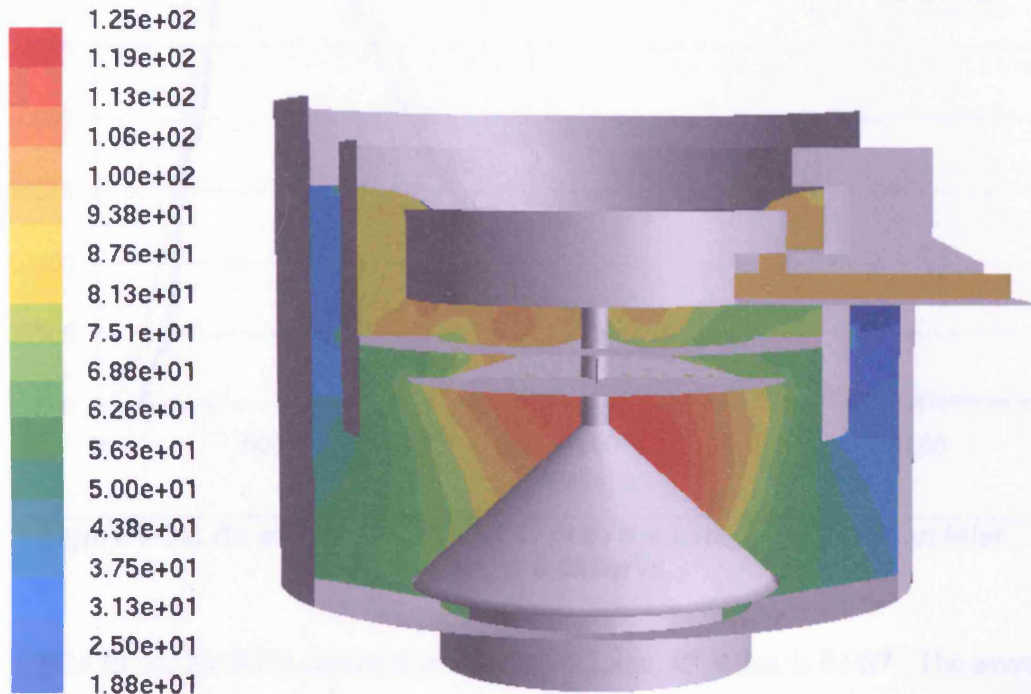
Figure 9-31. Contours of mean residence time at an inlet flowrate of $0.187m^3/s$.

9.5 Disinfection performance

With CFD model predictions that have been found to be reasonable, the application of kinetic rate constants reported by Pretorius and Pretorius (1999) can be applied to predict whether a 3.4m diameter Storm King® is suitable for disinfection processes.

Using a pulse input of tracer at the inlet to the HDVS in the CFD models, a residence time distribution was predicted to which the TISM was fitted and the parameters optimised. An example of a fit of the TISM to the CFD RTD curves is shown in Figure 9-32 for the overflow at an inlet flowrate of $0.028m^3/s$.

TISM fit to the CFD RTD prediction at the overflow at an inlet flowrate of 0.028 m³/s
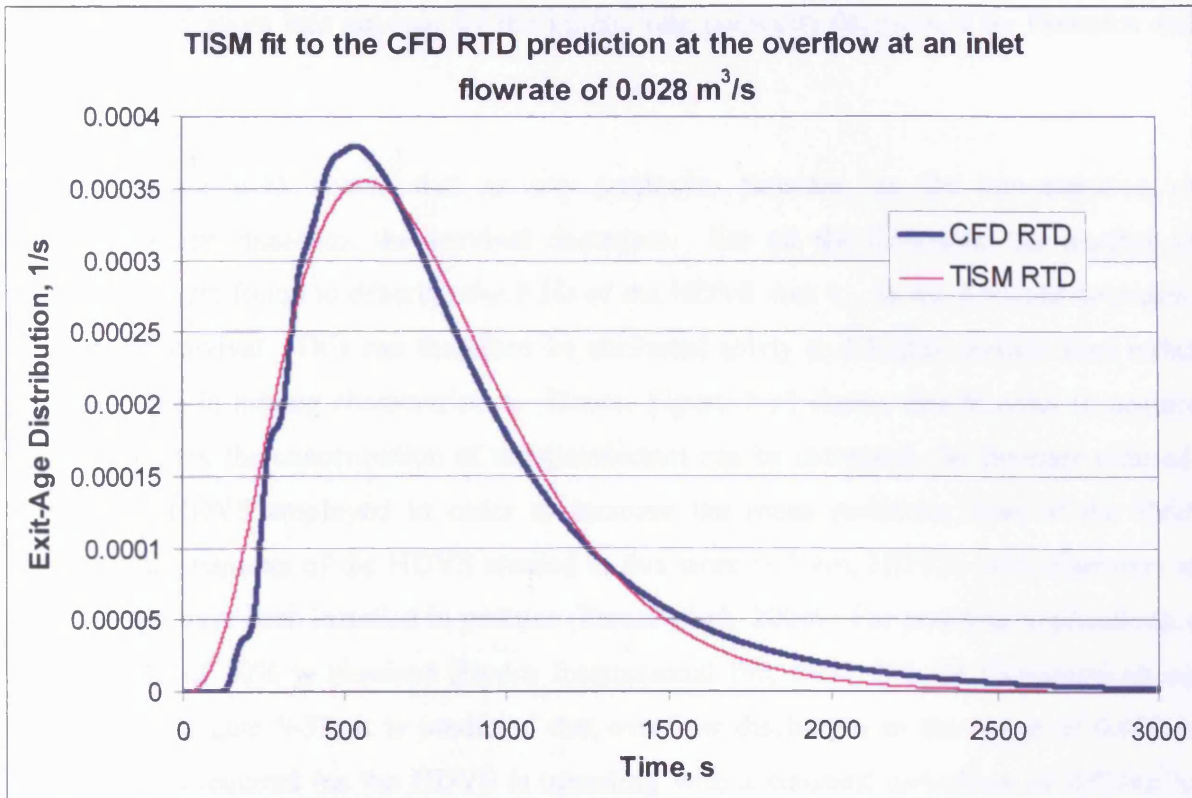
Figure 9-32. An example of the TISM fit to the overflow RTD at an inlet flowrate of 0.028m³/s.

For the TISM fit for the RTD depicted in Figure 9-32, the R_t^2 value is 0.987. The average R_t^2 value is 0.977 for the TISM fit to the CFD-generated RTD curves for all the flowrates, whereby a good fit by the TISM was made for each RTD. Thus, Equation 3-18, which relies on a good fit of the TISM in order to predict survival rates, is an appropriate model for this system.

Using the data from the batch inactivation studies by Pretorius and Pretorius (1999) where the kinetic rate constant and the lethal number of injections required in Equation 3-18 have been determined and the data acquired by fitting the TISM to each of the RTDs determined using CFD, the survival at the outlet of the HDVS can be predicted for a number of flowrates and a range of monochloramine concentrations; monochloramine being the disinfectant used by Pretorius and Pretorius (1999). This is shown in Figure 9-33 for a pH of 7 at 25°C. The performance of the HDVS as a disinfection vessel assumes that a step input of monochloramine has been introduced into the HDVS at the inlet where it is completely mixed and that the disinfectant is uniformly dispersed within the HDVS. Decay of the disinfectant is

assumed to be taken into account by the kinetic rate constants determined by Pretorius and Pretorius (1999)[6].

Clearly, Figure 9-33 shows that at any particular flowrate, as the concentration of monochloramine increases, the survival decreases. For all the flowrates, the number of CSTRs that were found to describe the RTD of the HDVS was 4. As the flowrate decreases, so does the survival. This can therefore be attributed solely to a higher contact time rather than a change in mixing characteristics. Hence, Figure 9-33 shows that in order to acquire higher kill rates, the concentration of the disinfectant can be increased, the flowrate reduced, or a larger HDVS employed in order to increase the mean residence time of the fluid. Although the diameter of the HDVS studied in this work is 3.4m, HDVSs with diameters as large as 16m have been installed in practice (Faram *et al.*, 2004). For practical applications, a survival rate of 10% is required (Hydro International Plc, 2005, Private Communication). Hence, from Figure 9-33, it is predicted that overflow discharges in the range of 0.008 to 0.057m³/s are required (as the HDVS is operating with a constant underflow of 0.020m³/s) and with a concentration of monochloramine in the range of 0.001 to 0.004kg/m³.

With mean residence times at the overflow of the HDVS, predicted using CFD, at a number of flowrates, a function that describes the mean residence time in one CSTR at the overflow as a function of inlet flowrate has found to be

$$\tau' = XQ_{in}^{-Y}$$ (9-1)

Where: Q_{in} = Inlet flowrate, m³/s $X = 2.9363$ $Y = 1.1422$

Inserting the derived numeric values for X and Y, this fits the experimental data with an R_t^2 value of 0.990 and can be used in conjunction with Equation 3-18 to give a model, specific to this 3.4m diameter separator operating with an underflow of 0.020m³/s, that predicts the micro-organism survival at the overflow and is given by

---

[6] It is interesting to note that if the decay of the disinfectant is not accounted for in the kinetic rate constants, then using a User Defined Scalar (UDS), a prediction of the disinfectant concentration throughout the system can be acquired by solving a transient response to a step input of UDS in conjunction with a source term in Equation 8-1 given by $-\rho k_\varphi \varphi$ (Greene *et al.*, 2002).

Where: k_φ = Disinfectant decay rate, s⁻¹

$$\frac{N}{N_0} = \left(\frac{1}{1 + XkcQ^{-Y}}\right)^4 \left[1 + \left(\frac{4}{3}\right)\frac{XkcQ^{-Y}}{1 + XkcQ^{-Y}}\right]$$

(9-2)

Thus, for a given rate constant and disinfectant concentration, Equation 9-2 may be used to predict the disinfection performance as a function of the inlet flowrate of fluid. Alternatively, the disinfection performance may be established as a function of the concentration of disinfectant for a given inlet flowrate of fluid and rate constant. Figure 9-33 shows the prediction made by Equation 9-2 at an inlet flowrate of $0.119m^3/s$, which confirms that Equation 9-2 is a useful design tool for predicting the required conditions for a given survival of micro-organisms.
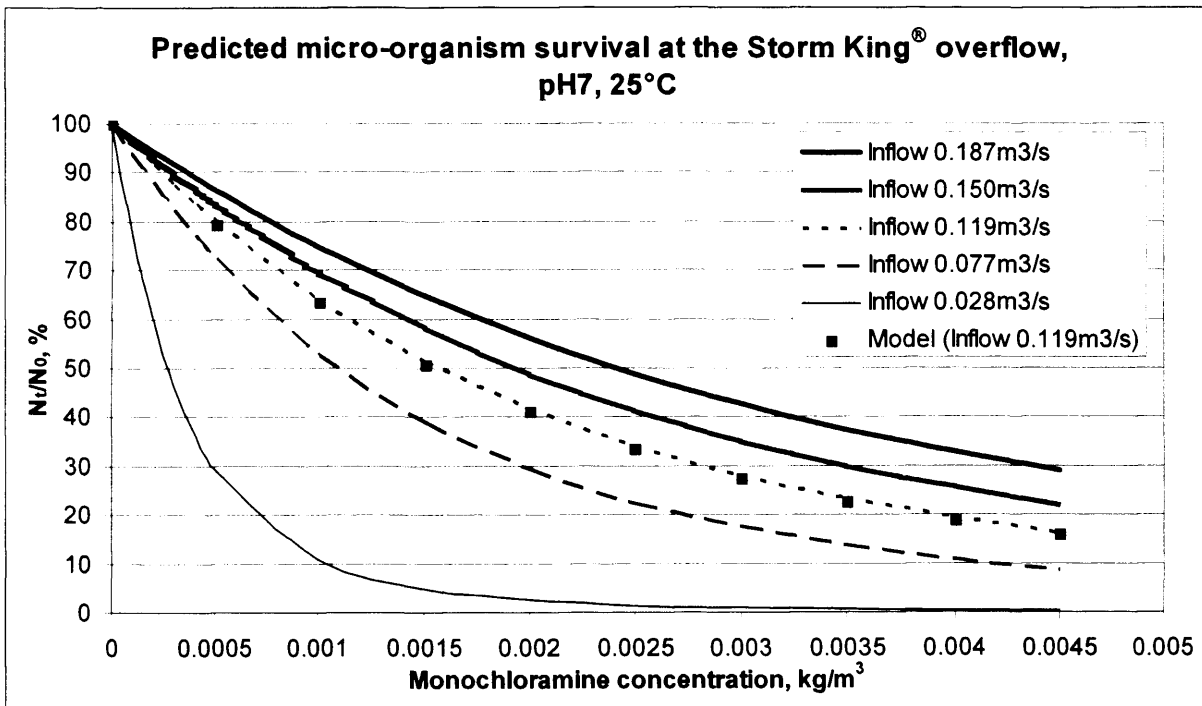
Figure 9-33. Micro-organism survival at the HDVS overflow at pH7 and 25°C.

Figure 9-34 shows how pH influences the survival, for an inlet flowrate of $0.187m^3/s$.
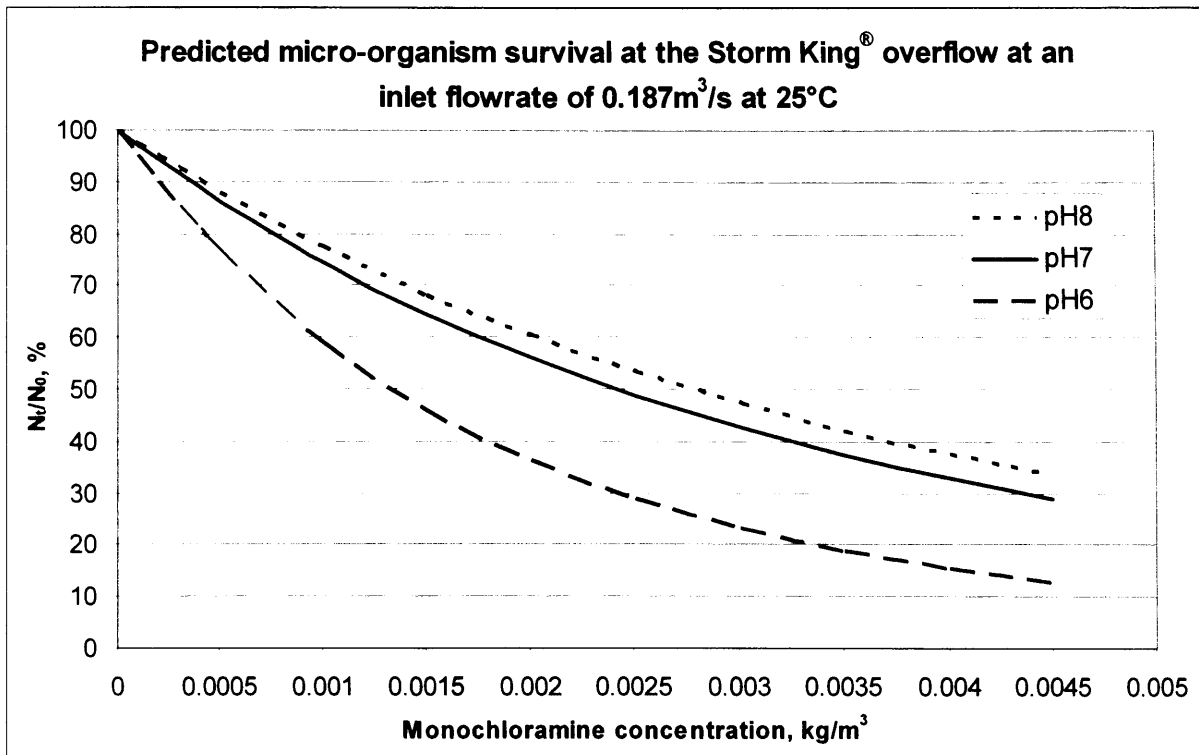
Figure 9-34. Effect of pH on the predicted micro-organism survival at 0.187m³/s.

Clearly the pH of the water within the HDVS has an impact on the survival of micro-organisms. Based on the inactivation studies by Pretorius and Pretorius (1999) a decreased survival occurs for a lower pH i.e. a more acidic fluid. This is therefore a factor that should be taken into consideration when determining the concentration of disinfectant required at any particular flowrate. The reason a much lower survival occurs at a pH6 is due to a much higher kinetic rate constant. Hence, the survival rates in Figure 9-34 would be lower had they been plotted at pH6.

Figure 9-35 shows contours of micro-organism survival at an inlet flowrate of $0.187m^3/s$ with an apparent kinetic rate constant of $0.013s^{-1}$ at pH7. This figure has been plotted using Equation 9-2. It is assumed that the mean residence time, divided by 4, for each cell within the CFD model can be used in Equation 9-2 in place of τ' to predict the survival of micro-organisms in the respective cell.

Contours of micro-organism survival, %
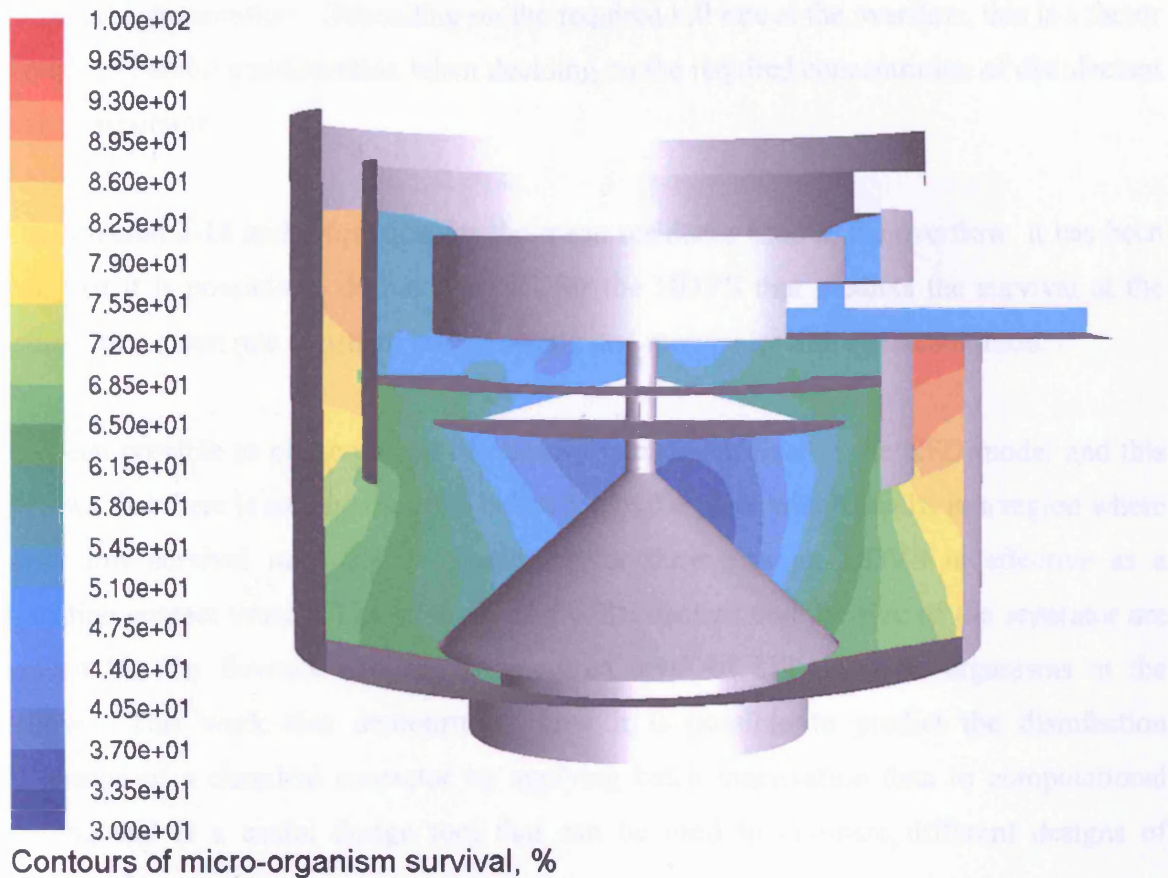
Figure 9-35. Contours of survival at an inlet flowrate of 0.187m³/s at pH7 and 25°C.

It is clear that there is a higher survival in the outer regions of the HDVS where the fluid has a relatively short residence time after entering through the inlet. The survival is higher in the upper portions of the HDVS, implying that in this region the residence time is shortest. In the very centre of the HDVS, the survival is lower than at the overflow, suggesting that there is a region of low activity and hence high residence time in the centre of the HDVS below the baffle plate.

9.5.1 Discussion

The results from the CFD models of a 3.4m diameter Storm King® have been used in conjunction with batch inactivation studies for secondary treated effluent and have allowed the theoretical disinfection performance of a full scale HDVS to be investigated. As the number of CSTRs that characterise the mixing characteristics is constant at all flowrates, it is clear that the increased performance of the HDVS at lower flowrates can be attributed to the higher residence time of the fluid. Predictions of the survival of organisms at pH6, 7 and 8 show that there is a varying survival at the overflow for a given inlet flowrate of fluid and

disinfectant concentration. Depending on the required kill rate at the overflow, this is a factor that requires careful consideration when deciding on the required concentration of disinfectant or size of separator.

Using Equation 3-18 and a function for the mean residence time at the overflow, it has been shown that it is possible to define a model for the HDVS that predicts the survival at the overflow for a given rate constant, inlet flowrate and monochloramine concentration.

It has been possible to plot contours of micro-organism survival in the CFD model and this has shown that there is an inactive zone below the baffle plate which results in a region where a fairly low survival rate exists. These results show that an HDVS is effective as a disinfection contact vessel. The strength of the disinfectant and the size of the separator are dependent on the flowrate and on the required level of kill of micro-organisms at the overflow. This work also demonstrates how it is possible to predict the disinfection performance of a chemical contactor by applying batch inactivation data to computational modelling and is a useful design tool that can be used to compare different designs of continuous flow system.

Further work would be desirable in undertaking an experimental disinfection study on an HDVS for which the results could be used for a more complete validation of CFD models. Scaling residence time predictions would allow the prediction of the disinfection performance to be made for different sizes of HDVS (see Chapter 11). Batch inactivation studies at different temperatures would take into account regional climate variations. Comparison between inactivation studies for effluent from different parts of the world may reveal that the rate constant is influenced by the site from which the effluent is obtained. This could be due to a more acidic fluid due to acid rain in urban areas, or the presence of different strains of micro-organisms that occur in different parts of the world.

9.6 Summary

- It has been shown that CFD predictions of residence time may be validated against the ADZ model and ADE without access to the raw temporal concentration data.

- With the availability of the raw data, it has been shown that the most suitable RTD model for the HDVS is the ADM.

- CFD mean residence time predictions compared to those determined by fitting the ADM confirm that the CFD predictions are reasonable.

- Using kinetic rate constants reported by Pretorius and Pretorius (1999) in conjunction with CFD residence time predictions, it has been predicted that a HDVS as a contact vessel for disinfection processes is a suitable application.

10 CFD modelling of a 1.6m diameter Grit King®

A study of a 1.6m diameter Grit King® was carried out at the University of Hertfordshire between 1995 and 1998 for which there are various publications (Fenner and Tyack, 1997; Tyack and Fenner, 1997, 1998a, 1999). The residence time characteristics which have been derived experimentally provide the opportunity to further validate CFD predictions.

10.1 1.6m diameter Grit King®

Figure 10-1 shows a schematic of the Grit King® and detailed drawings of the modelled Grit King® can be found on Page 249.

A   Inlet
B   Deflector Plate
C   Dip Plate
D   Cone
E   Central Shaft
F   Benching Skirt
G   Grit Pot
H   Vessel wall
I   Overflow Annulus
J   Overflow Channel
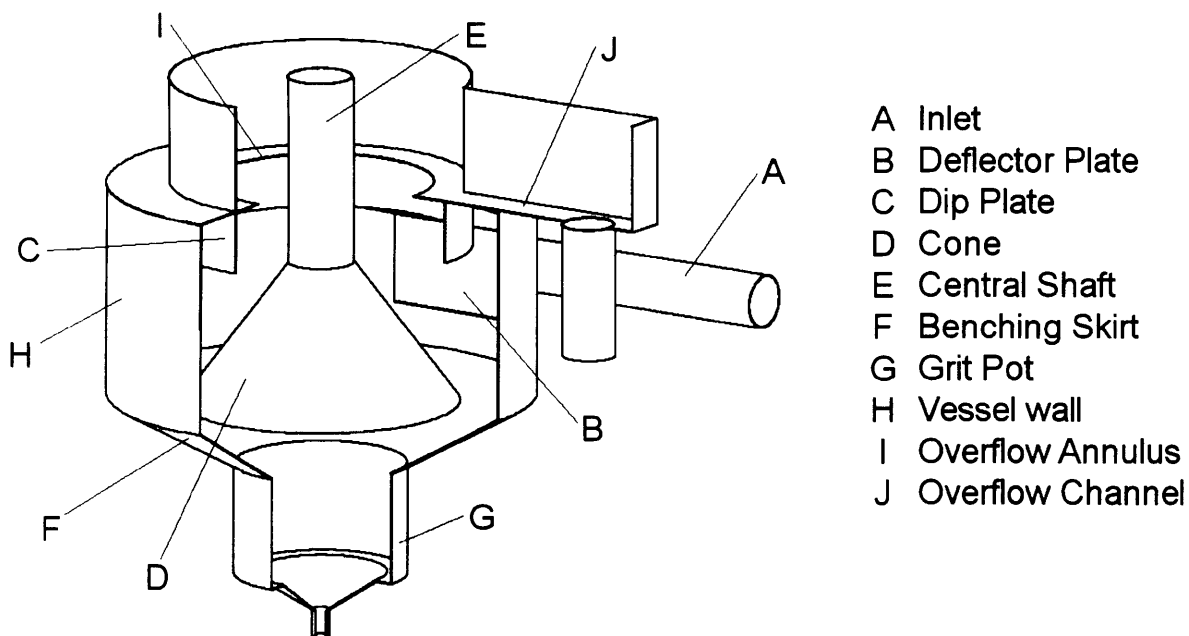
Figure 10-1. Schematic of the 1.6m diameter Grit King® studied at the University of Hertfordshire.

The vent box, which allows trapped air between the dip plate and HDVS wall to escape, has been omitted from this study as details on the dimensions and location are not available. It is thought the vent box will have very little effect on the hydrodynamics.

Tyack and Fenner (1999) report that at the bottom of the central shaft were holes that allowed the fluid to transfer "into and out of the centre of the cone". The number of holes and diameter are unknown and these have also been omitted from this study. Tyack and Fenner (1999) state that there is not a large amount of movement of fluid in this region and the effect of these holes on the flow patterns within the HDVS is assumed to be negligible.

A noticeable difference between the 1.6m diameter Grit King® in Figure 10-1 and the 0.75m diameter unit analysed in Chapter 5 is that the overflow channel marked 'J' in Figure 10-1 is central, whereas the overflow of the 0.75m diameter unit is tangential. Table 10-1 summarises the aspect ratio of the main components of the two HDVSs, excluding the deflector plate and each dimension being compared is indicated in Figure 10-2. The aspect ratio is defined as the dimension of the component in the 1.6m diameter unit divided by the dimension in the 0.75m diameter unit.
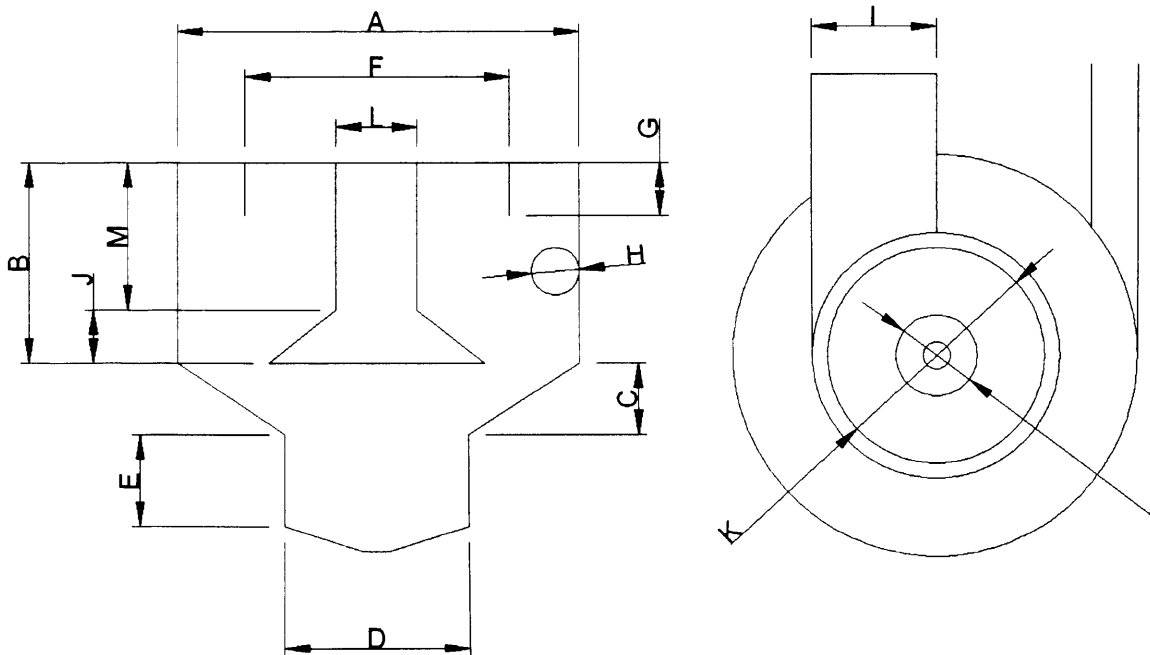
Figure 10-2. Dimensions of the main components forming the Grit King®.

**Table 10-1. The aspect ratio between the
components in the 1.6m and 0.75m diameter Grit King®.**

Component	Dimension	Aspect ratio
Vessel diameter	A	2.13
Vessel height	B	2.17
Benching skirt height	C	2.08
Grit pot diameter	D	2.09
Grit pot height	E	2.17
Dip plate diameter	F	2.15
Dip plate height	G	2.08
Inlet diameter	H	1.97
Overflow width	I	1.51
Cone height	J	4.05
Cone base diameter	K	2.20
Cone top diameter	L	2.36
Central shaft height	M	1.28

Although the scaling and orientation of some of the components within the 1.6m diameter HDVS does not make this unit suitable for studying scaling of observed RTDs, the size of the device is ideal for validating CFD predictions of residence time. A reason that some of the components are out of proportion e.g. the cone height, is that design constraints have been included that make the HDVS suitable for installation and operation at a sewage treatment works.

10.2 Experimental testing

Although residence time testing at Hertfordshire University was carried out with the Grit King® operating with and without a continuous base flow, the focus of this work is to study the Grit King® without an underflow, as this is the condition under which the Grit King® predominantly operates.

Figure 10-3 shows a schematic of the test facility used for studying the 1.6m diameter Grit King®. The facility comprises a flow control valve marked 'B' used to adjust the flowrate into the separator. Situated between the separator and the Grit King® is a stand pipe 'C' used for releasing the tracer into the fluid. The discharge from the Grit King® passes along the overflow channel 'F' and down an overflow pipe 'G', into a stilling box 'I'. After the stilling box is a flowmeter 'J'. The type of meter is unknown. After the fluid passes through the flowmeter, it returns back to the sump.
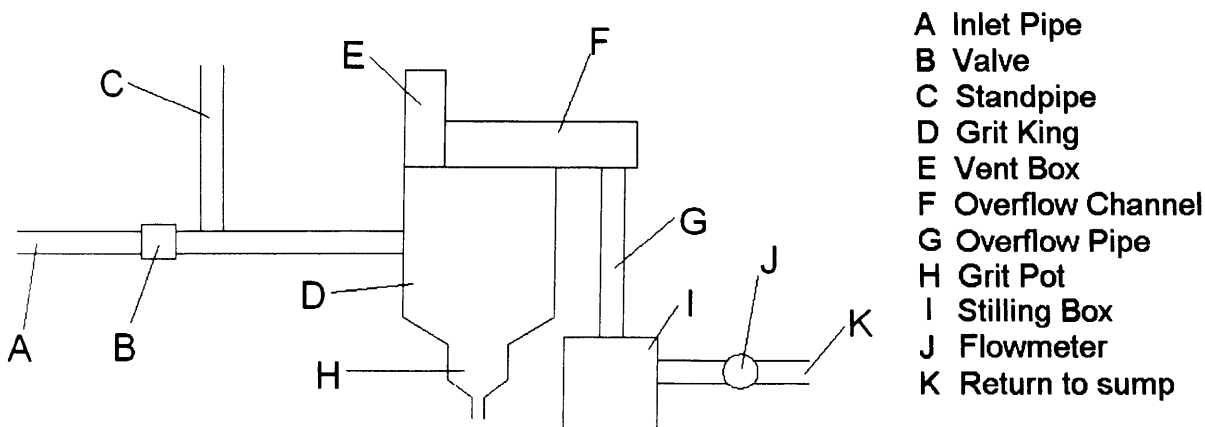
Figure 10-3. Schematic of the 1.6m diameter Grit King® setup at the University of Hertfordshire. Adapted from Tyack and Fenner (1998b).

The RTDs were produced using lithium chloride in solution as a tracer and the concentration at the overflow of the Grit King® detected by taking samples of fluid at predetermined time intervals and analysing using either a flame photometer or an atomic absorption spectrophotometer (Tyack and Fenner, 1998b).

A 'closed' loop was used in the laboratory whereby the discharge from the Grit King® went to the sump and the fluid therefore circulates through the pumped system. Testing was done to look at the recirculation of lithium chloride through the pumped system during a test. It was found that the circulation of lithium chloride was not detectable during individual experiments most likely due to the discharge from the Grit King® being at the opposite end to where the fluid entered the pump and hence, allowing maximum mixing of the tracer in the sump. Between tests the pumps were run continuously to allow maximum mixing of the tracer. Prior to each test, the base level of the lithium chloride in the sump was measured and deducted from the test data (Tyack, 2004, Private Communication).

Appendix N contains the data from which the base level has been subtracted. It is known that the mean residence times and dispersion coefficients reported in Tyack and Fenner (1998a) have been computed using the data in Appendix N. The mean residence time and the variance were computed using the method of moments, Equations 2-24 and 2-25.

A limiting factor for creating a CFD model of the 1.6m diameter Grit King® is that the position of the free surface is unknown. Positioning the free surface too low to the overflow would result in a high fluid velocity due to the reduced volume of liquid and a free surface

that is positioned too high would result in a low fluid velocity due to an increased fluid volume.

Although this unit is still in existence, installation into a test facility would have been expensive. It is also known that modifications to this unit have been made since 1998 and these may alter the outcome of any subsequent tests aimed at supplementing those already carried out at the University of Hertfordshire. The 'Volume of Fluid' (VOF) model available in the CFD code was therefore chosen as a means to estimate the position of the free surface.

In order to assess whether the VOF model can approximately predict the position of the free surface, a simulation of the 0.75m diameter Grit King® (which is analysed in Chapter 5) at an inlet flowrate of 11 litres per second was undertaken using the VOF model. At a flowrate higher than 8 litres per second the fluid on the outer part of the overflow annulus is forced outwards and results in a surface that is angled downwards from the outer walls down to the central shaft. This is caused by the centrifugal force due to the rotation of the fluid and is best illustrated in Figure 10-4 at an inlet flowrate of 11 litres per second. Hence, the nature of the free surface at 11 litres per second was considered a reasonable test at which to validate a CFD prediction.
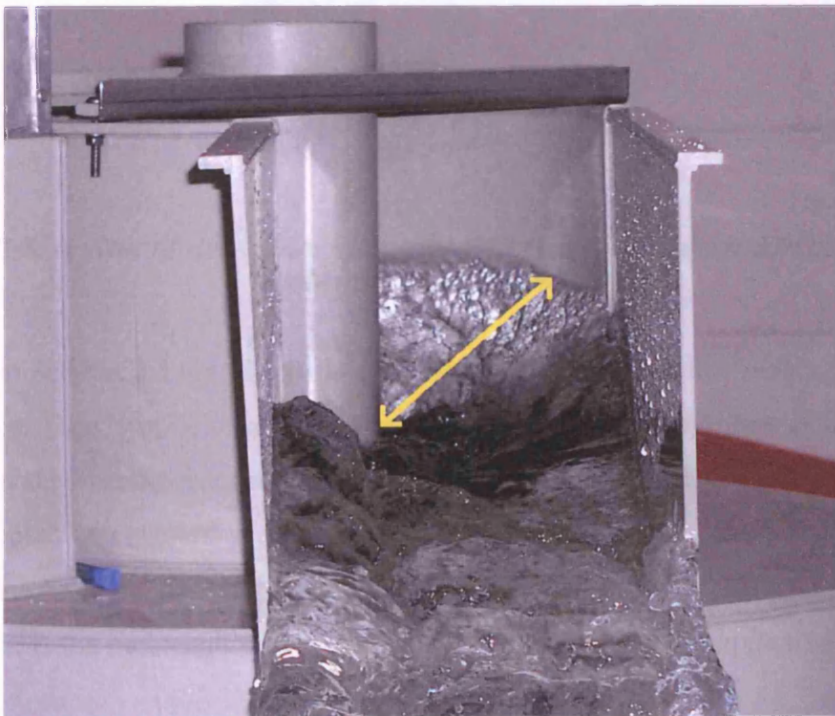
Figure 10-4. A view of the free surface in the 0.75m diameter Grit King® at an inlet flowrate of 11 litres per second.

10.3   CFD free surface predictions

10.3.1   0.75m diameter Grit King®

The grid generated, shown in Figure 10-5, was constructed using a purely tetrahedral mesh which was fairly coarse in the lower part of the separator and finer in the upper part where the free surface will occur. Hence, with a finer mesh where the free surface will occur, a more accurate representation of the free surface is likely to be predicted and the coarser mesh in the lower region of the HDVS reduces processing time.
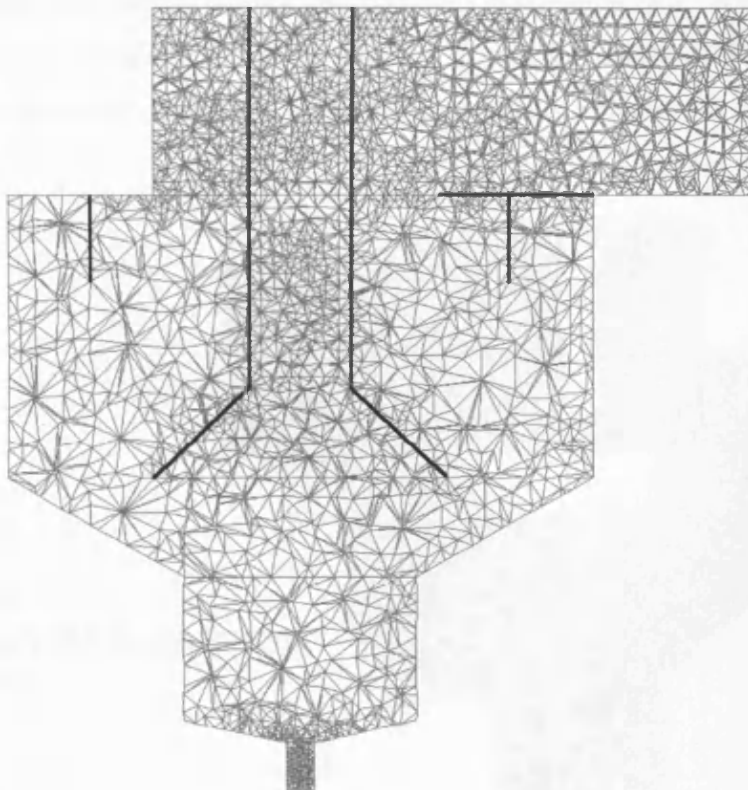
Figure 10-5. A view of the 0.75m diameter Grit King® mesh used in conjunction with the VOF model.

As discussed in Section 2.3.4.4, the CFD code offers three options for tracking the position of the free surface. The 'implicit' scheme was chosen which is the inferior of the three in that computation of the volume fraction is based on the values at the current time step, which are unknown. Hence, "a standard scalar transport equation is solved iteratively for each of the secondary-phase volume fractions at each time step", Fluent Inc. (2003). However, the implicit scheme is the most stable of the three and is also the most computational inexpensive.

Although the CFD code may use a steady state solver with the implicit tracking scheme the transient solver is recommended and was therefore implemented because the solution for the change in shape of a free surface is time dependent and the solution is therefore likely to be more stable. With this in mind, the grid generated, shown in Figure 10-5, comprises 376 000 cells in order to reduce the processing time. The RNG-kε viscous model was also chosen as it is a two equation model that will reduce processing time compared with the Reynolds Stress viscous model. The standard pressure interpolation scheme was used along with the SIMPLE pressure-velocity coupling algorithm and first order terms were solved for momentum, volume fraction, turbulent kinetic energy and turbulent dissipation rate. After initialising the solution, the phases were 'patched' into the domain so that the height of the water was level with the base of the overflow channel. This is demonstrated in Figure 10-6.

1.00

0.00

Contours of volume fraction
of water
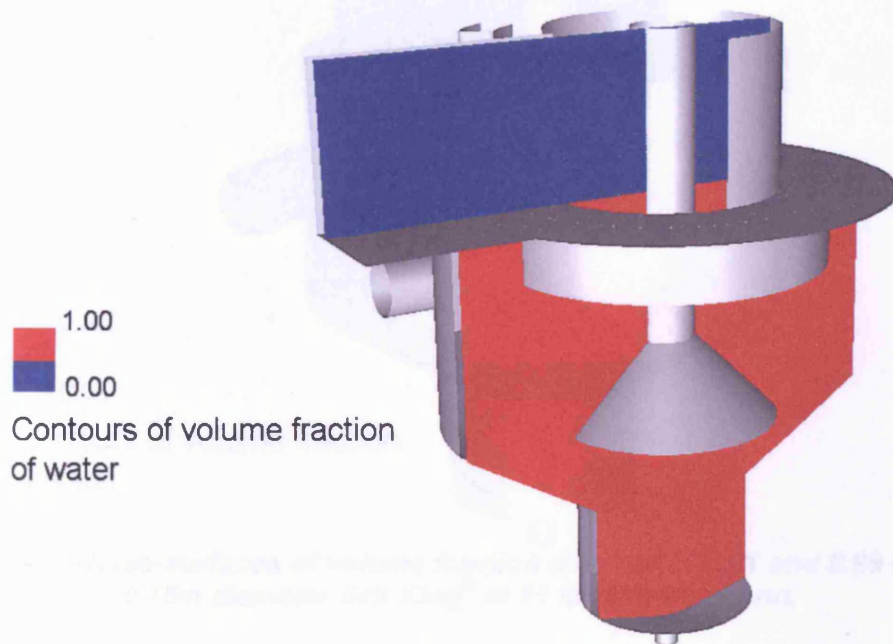
**Figure 10-6. The region of fluid 'patched' in the 0.75m diameter
Grit King® prior to iterating.**

'Patching' the phases into the model prior to iterating gives an initial guess as to where the phases are likely to occur and reduces the processing time. (It would have taken considerably longer for the model to converge if the volume fraction of water was zero at the first time step as the solver has to iterate a solution for water filling the separator).

Convergence of the solution at 11 litres per second was judged visually based on the amount of 'smear' of the interface and the change in shape of the interface. It was found that

provided the solution was given a sufficient run time, the amount of smear was reduced and the free surface takes a shape that does not vary with time.

Despite achieving a limited amount of smear, Figure 10-7 demonstrates the limitation of the implicit scheme by displaying iso-surfaces of volume fraction of water of 0.01 and 0.99 where it is assumed that above and below these surfaces, the phase is either completely water or air. Displaying contour fractions of 0 and 1 is not practical due to rounding error that would place the extremes of the interface further apart.
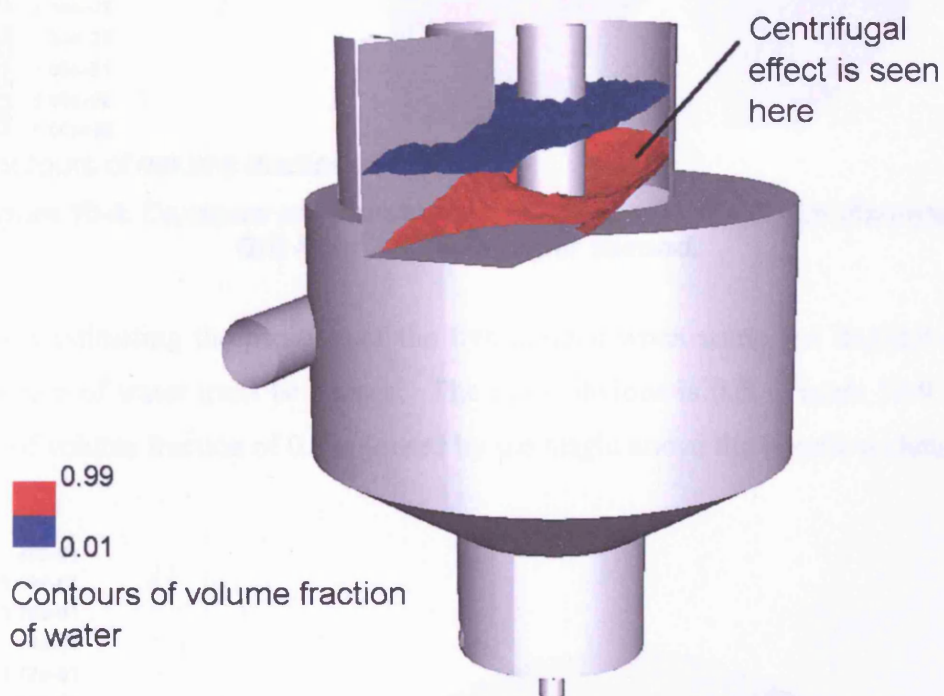
Figure 10-7. Iso-surfaces of volume fraction of water of 0.01 and 0.99 in the 0.75m diameter Grit King® at 11 litres per second.

Figure 10-8 shows that the VOF model has predicted a centrifugal effect on the fluid to the right of the central shaft, as depicted in Figure 10-7 for a volume fraction of 0.99 and is thus most prevalent where the volume fraction of water is highest, as is also seen in Figure 10-8.
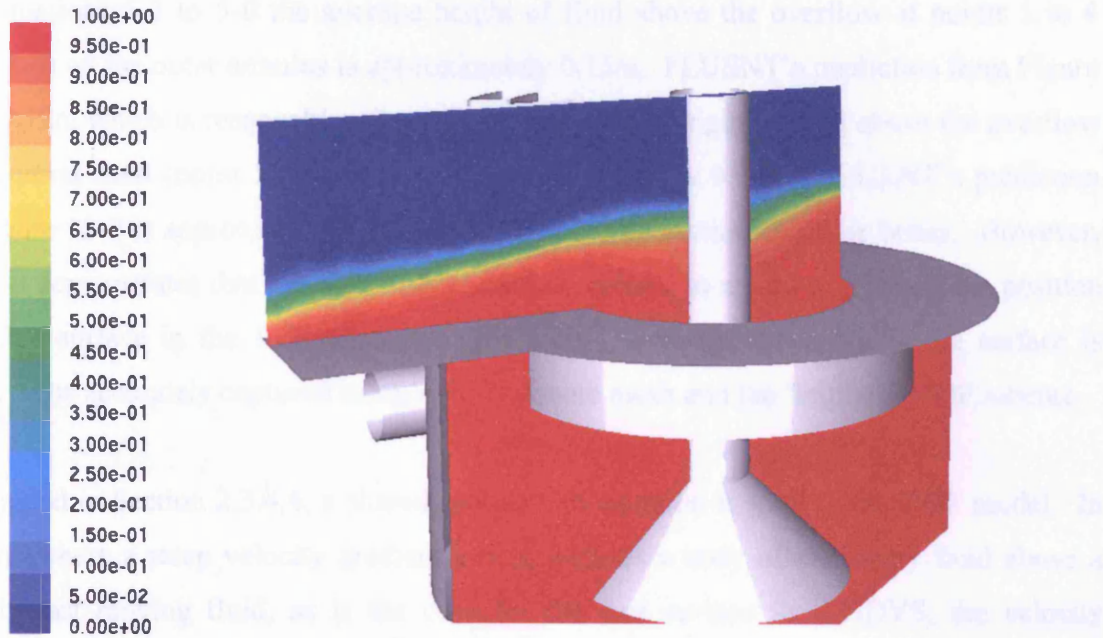
Contours of volume fraction of water

Figure 10-8. Contours of volume fraction of water in the 0.75m diameter Grit King® at 11 litres per second.

Clearly when estimating the position of the free surface when using the implicit scheme a volume fraction of water must be chosen. The most obvious is 0.5. Figure 10-9 shows an iso-surface of volume fraction of 0.5 coloured by the height above the overflow channel.
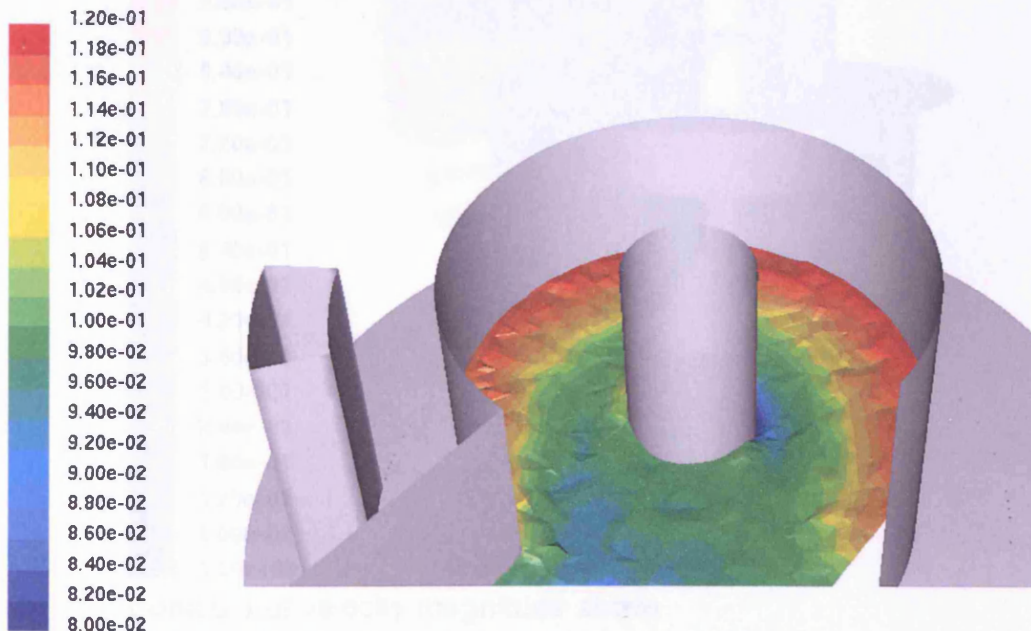
Surface of volume fraction of 0.5 coloured by height above the overflow channel, m

Figure 10-9. Surface of volume fraction of 0.5 coloured by height above the overflow channel in the 0.75m diameter Grit King® at 11 litres per second.

From Equations 5-3 to 5-6 the average height of fluid above the overflow at points 1 to 4 (Figure 5-4) on the outer annulus is approximately 0.13m. FLUENT's prediction from Figure 10-9 is 0.12m which is reasonable. From Equation 5-7 the height of fluid above the overflow on the central shaft (point 5 on Figure 5-4) is approximately 0.06m. FLUENT's prediction from Figure 10-9 is approximately 0.08 to 0.1m. This prediction could be better. However, this result demonstrates that the VOF model may be utilised as means to estimate the position of the free surface in the 1.6m diameter Grit King®, although the detail in the surface is unlikely to be accurately captured using a fairly coarse mesh and the 'implicit' VOF scheme.

As discussed in Section 2.3.4.4, a shared momentum equation is used in the VOF model. In situations where a steep velocity gradient exists, such as a body of stationary fluid above a relatively fast moving fluid, as is the case for the free surface in a HDVS, the velocity prediction at the interface may be affected. This is shown in Figure 10-10, where the fluid velocity is high across the interface of the fluids. Hence, a more accurate prediction is likely to be achieved using a single phase model with a frictionless wall for the free surface.

| 1.20e+00 |
| 1.14e+00 |
| 1.08e+00 |
| 1.02e+00 |
| 9.60e-01 |
| 9.00e-01 |
| 8.40e-01 |
| 7.80e-01 |
| 7.20e-01 |
| 6.60e-01 |
| 6.00e-01 |
| 5.40e-01 |
| 4.80e-01 |
| 4.20e-01 |
| 3.60e-01 |
| 3.00e-01 |
| 2.40e-01 |
| 1.80e-01 |
| 1.20e-01 |
| 6.00e-02 |
| 0.00e+00 |
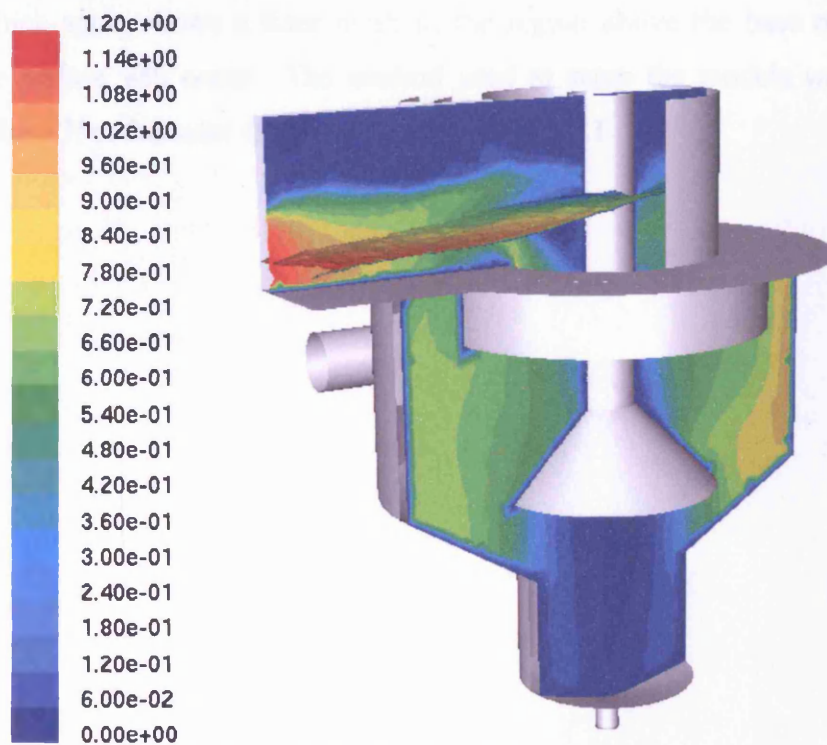
Contours of velocity magnitude above
and below a surface of volume fraction of 0.5, m/s

Figure 10-10. Contours of velocity magnitude demonstrating the adverse velocity field at the phase interface in the 0.75m diameter Grit King®.

10.3.2 1.6m diameter Grit King®

It is known that when the 1.6m diameter Grit King® was installed in the test facility at the University of Hertfordshire the overflow channel was sealed at the end and the flow discharged down a vertical cylindrical pipe through the base of the open channel, as depicted in Figure 10-3. However, the length of the open channel and the diameter and position of the cylindrical pipe is unknown. The conditions at the outlet will influence the water level in the separator. With the configuration described, above a critical flowrate backfilling may have occurred due to the discharge pipe restricting the flow, which may not occur with the flow discharging straight from the open channel as in the 0.75m diameter Grit King® analysed in Chapter 5.

With this in mind, the length of the open channel, position and diameter of the vertical cylindrical pipe in the VOF models were estimated based on the dimensions of the Grit King®.

Figure 10-11 shows the grid generated for predicting the fluid height in the 1.6m diameter Grit King® which again shows a finer mesh in the region above the base of the overflow where the free surface will occur. The method used to setup the models was the same as described for the 0.75m diameter Grit King® in Section 10.3.1.
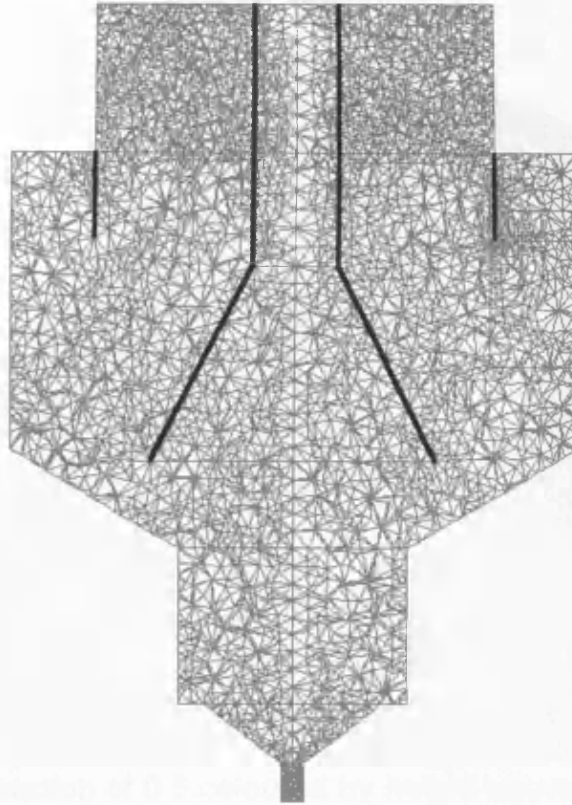
Figure 10-11. The mesh generated for estimating the position of the free surface in the 1.6m diameter Grit King®.

Figure 10-12 shows a prediction of the free surface at 61 litres per second and shows that in contrast to the 0.75m diameter Grit King® there is no centrifugal effect on the shape of the free surface. Instead, the surface appears to slant slightly towards the overflow channel. The centrifugal effect on the fluid in the 0.75m diameter Grit King®, Figure 10-4, is most likely enhanced by the tangential overflow channel.

```
3.00e-01
2.95e-01
2.90e-01
2.85e-01
2.80e-01
2.75e-01
2.70e-01
2.65e-01
2.60e-01
2.55e-01
2.50e-01
2.45e-01
2.40e-01
2.35e-01
2.30e-01
2.25e-01
2.20e-01
2.15e-01
2.10e-01
2.05e-01
2.00e-01
```
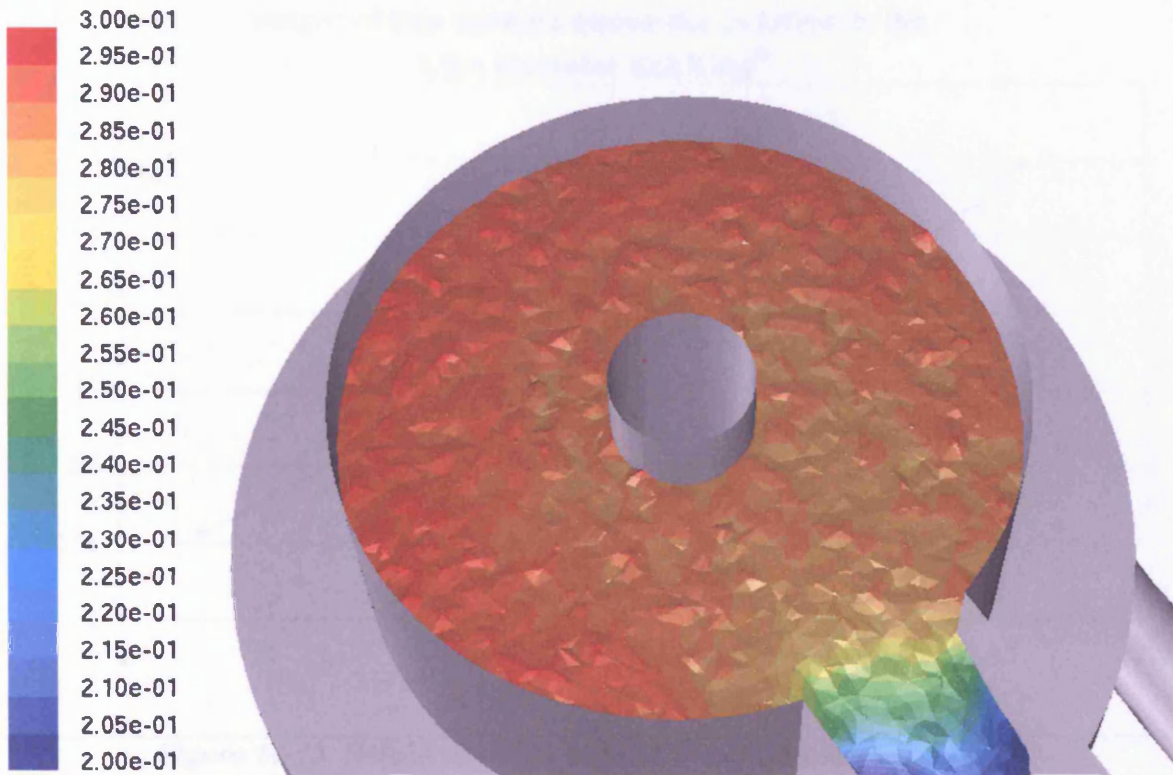
Surface of volume fraction of 0.5 coloured by height above the
overflow channel, m

Figure 10-12. Surface of volume fraction of 0.5 coloured by height above the overflow in the 1.6m diameter Grit King® at 61 litres per second.

Figures 10-13 and 10-14 show a relationship between the height of the fluid and the flowrate.
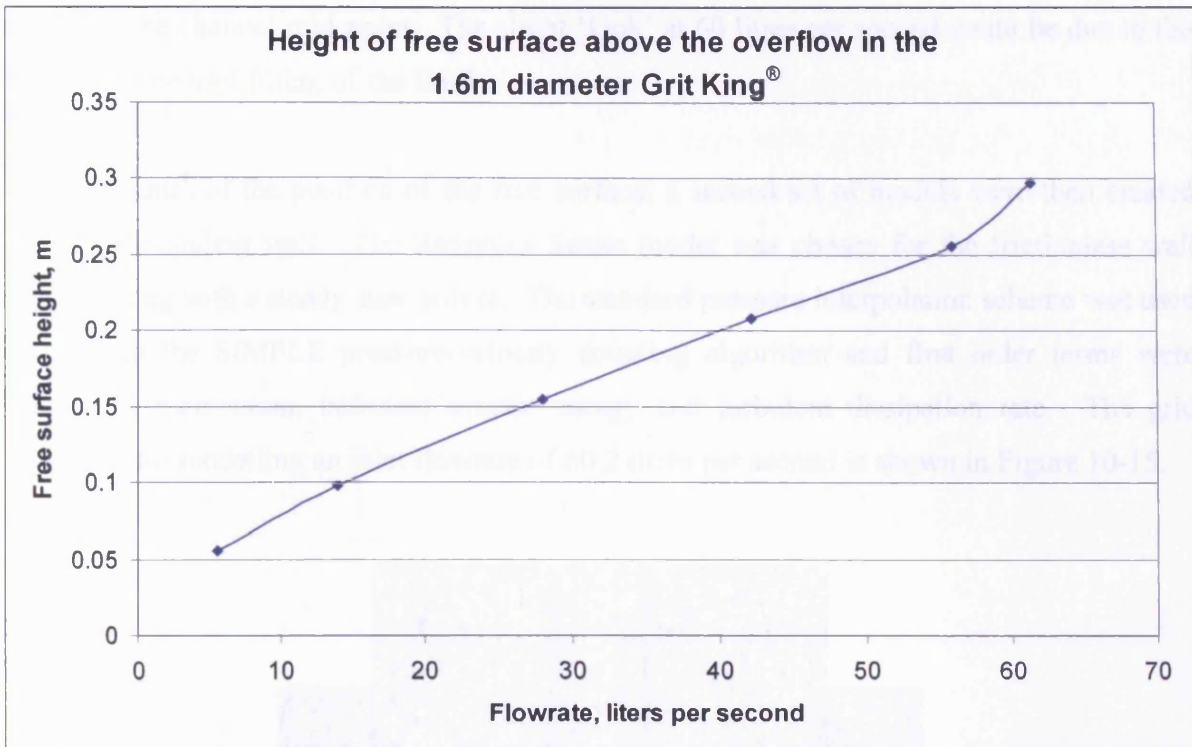
Figure 10-13. Height of fluid above the overflow annulus in the 1.6m diameter Grit King®.
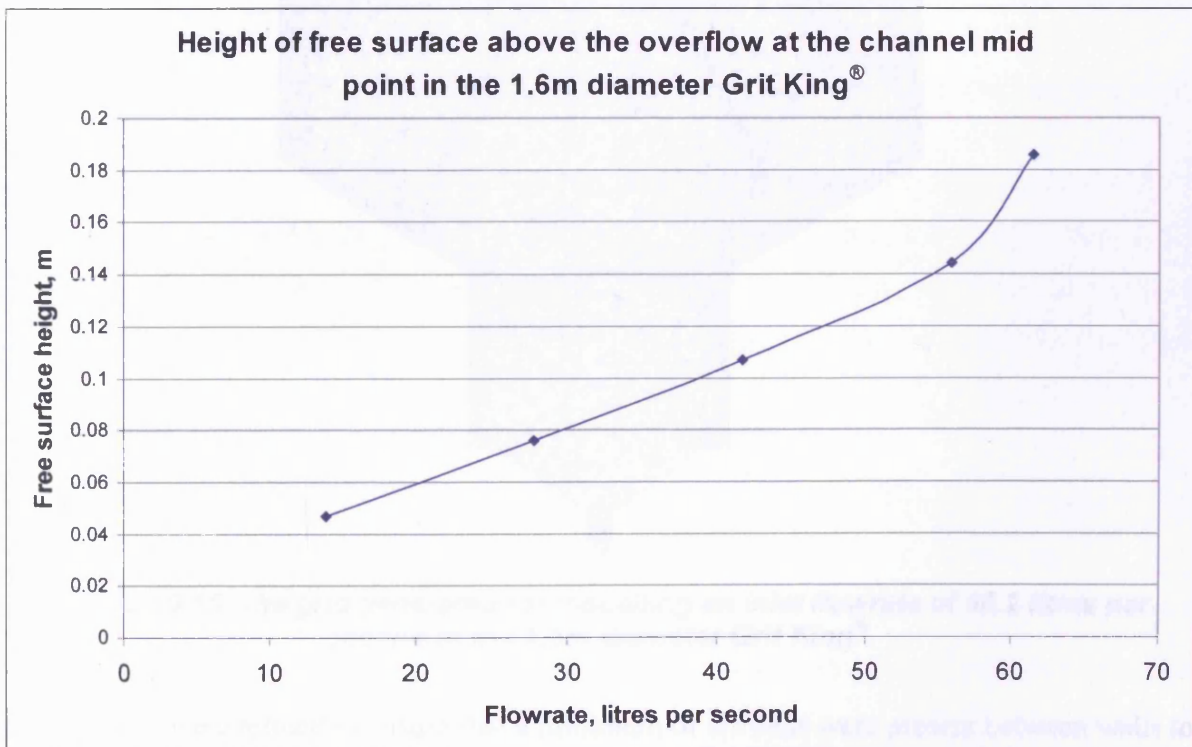
Figure 10-14. Height of fluid above the overflow annulus at the channel mid point in the 1.6m diameter Grit King®.

A prediction at 5 litres per second at the channel mid point was not available due to the 'smear' of the interface which meant that an iso-surface of volume fraction of 0.5 did not

extend to the channel mid point. The slight 'kink' at 60 litres per second could be due to the onset of some backfilling of the fluid.

With estimates of the position of the free surface, a second set of models were then created using a frictionless wall. The Reynolds Stress model was chosen for the frictionless wall models along with a steady state solver. The standard pressure interpolation scheme was used along with the SIMPLE pressure-velocity coupling algorithm and first order terms were solved for momentum, turbulent kinetic energy and turbulent dissipation rate. The grid generated for modelling an inlet flowrate of 60.2 litres per second is shown in Figure 10-15.
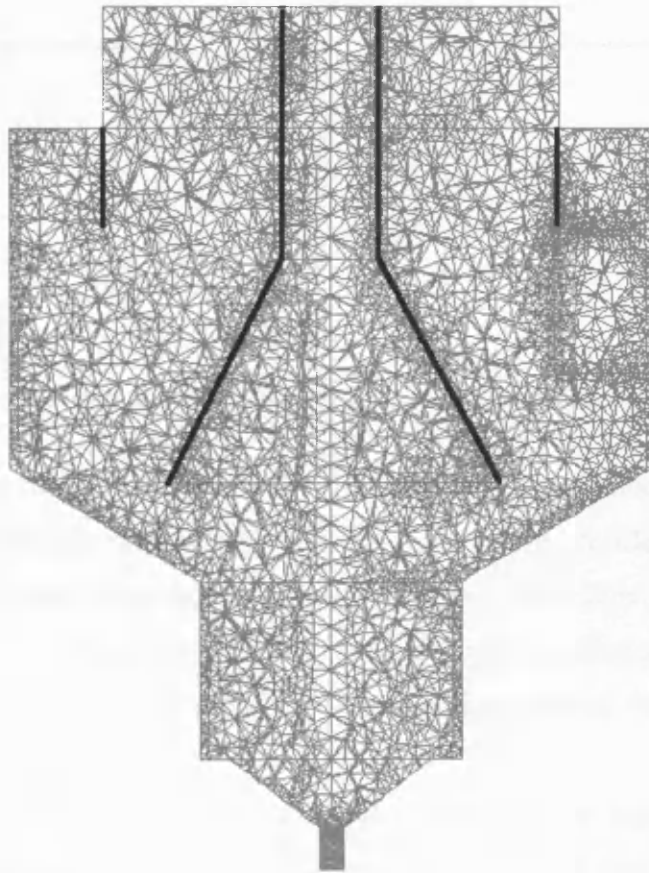
Figure 10-15. The grid generated for modelling an inlet flowrate of 60.2 litres per second in the 1.6m diameter Grit King®.

All the grids were refined to ensure that a minimum of six cells were present between walls to allow a crude boundary layer to be modelled. At higher flowrates such as 60.2 litres per second, the grid generated comprised only 342 000 cells as such a fine mesh was not required at the overflow due to the increased height of the free surface. The grid resolution was increased along the walls and a custom sizing function was used between the top of the

deflector plate and dip plate due to both components being in such close proximity to each other. In these models the outlet has been positioned 1.0m from the centre of the Grit King® as indicated by section C-C on Page 249. This is because when modelling the 1.6m diameter Grit King® with a frictionless wall, only one fluid phase is present (water). When the fluid is modelled as pouring down the vertical cylindrical pipe, a circulation region may be setup at the top of the cylindrical pipe, as depicted in Figure 10-16.
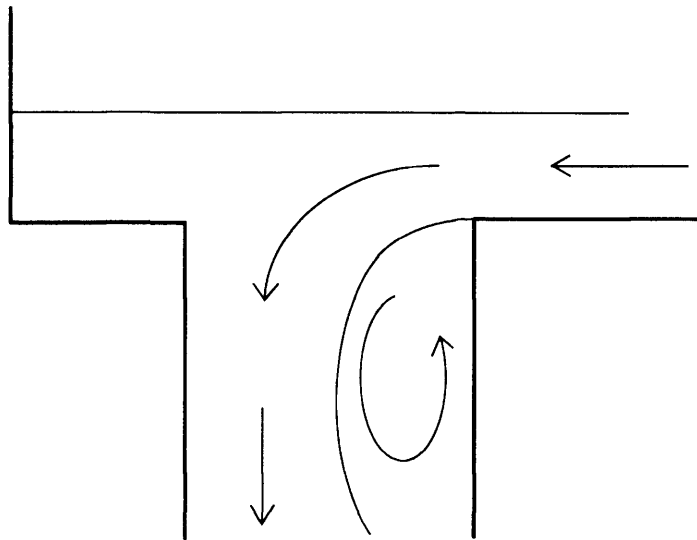
Figure 10-16. An example of a circulation region as fluid spills down a cylindrical pipe.

In practise this region would comprise of air. However, when only one fluid phase is present in the model, this circulation region will increase the predicted residence time. Hence, the outlet was placed midway along the overflow to eliminate this. It is expected that the time taken for the fluid to travel from the overflow channel to the sampling point will be very short compared with the time spent in the separator, thus the error incurred will be small.

At 60.2 litres per second, a grid dependency check was made by increasing the number of cells in the model to approximately 674 000 and it was found that the results were grid independent as demonstrated by the RTD predictions in Figure 10-17. At this flowrate a comparison was also made between an RTD curve generated using 100 time steps and one using 350 which is shown in Figure 10-18. Again, it can be seen that the RTD which is computed using 100 time steps has a smaller peak. However, it was felt that the extra computation time using 350 time steps may not be justified and RTD predictions were therefore made using 100 time steps.
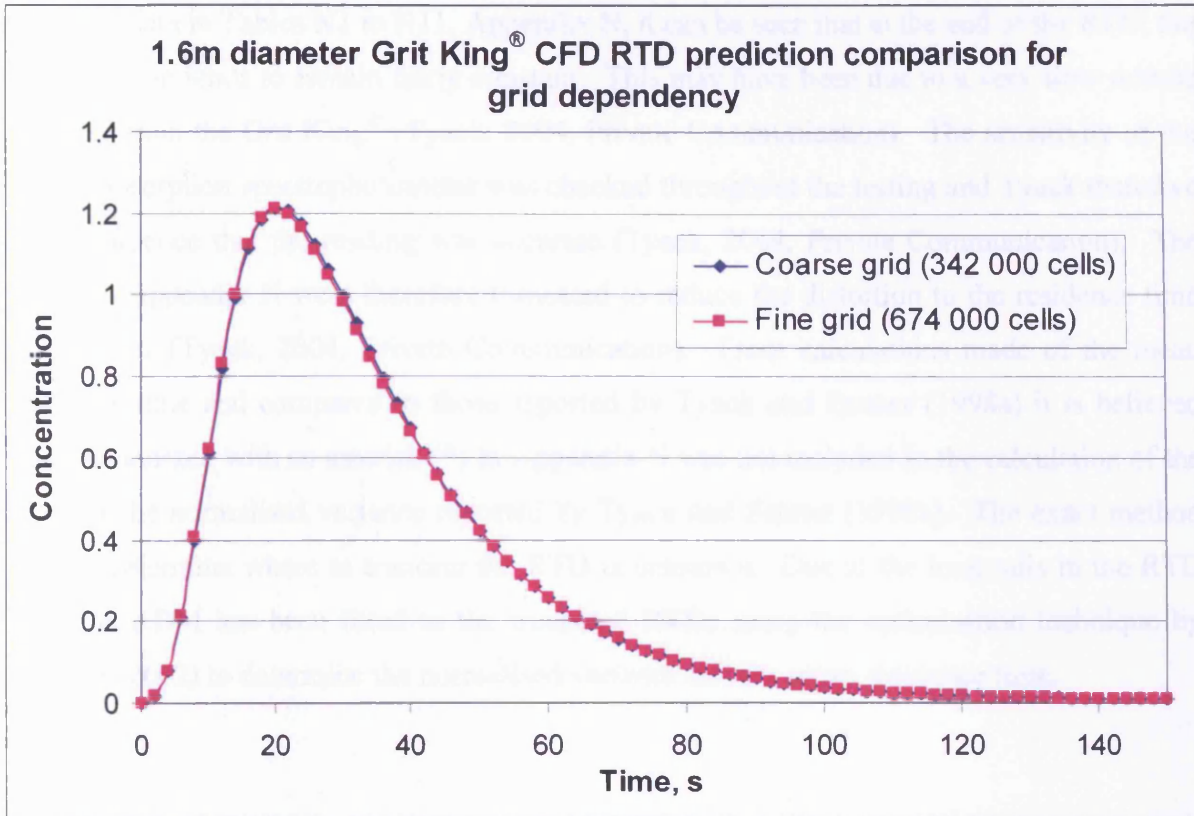
Figure 10-17. CFD RTD prediction comparison for grid dependency at 60.2 litres per second.
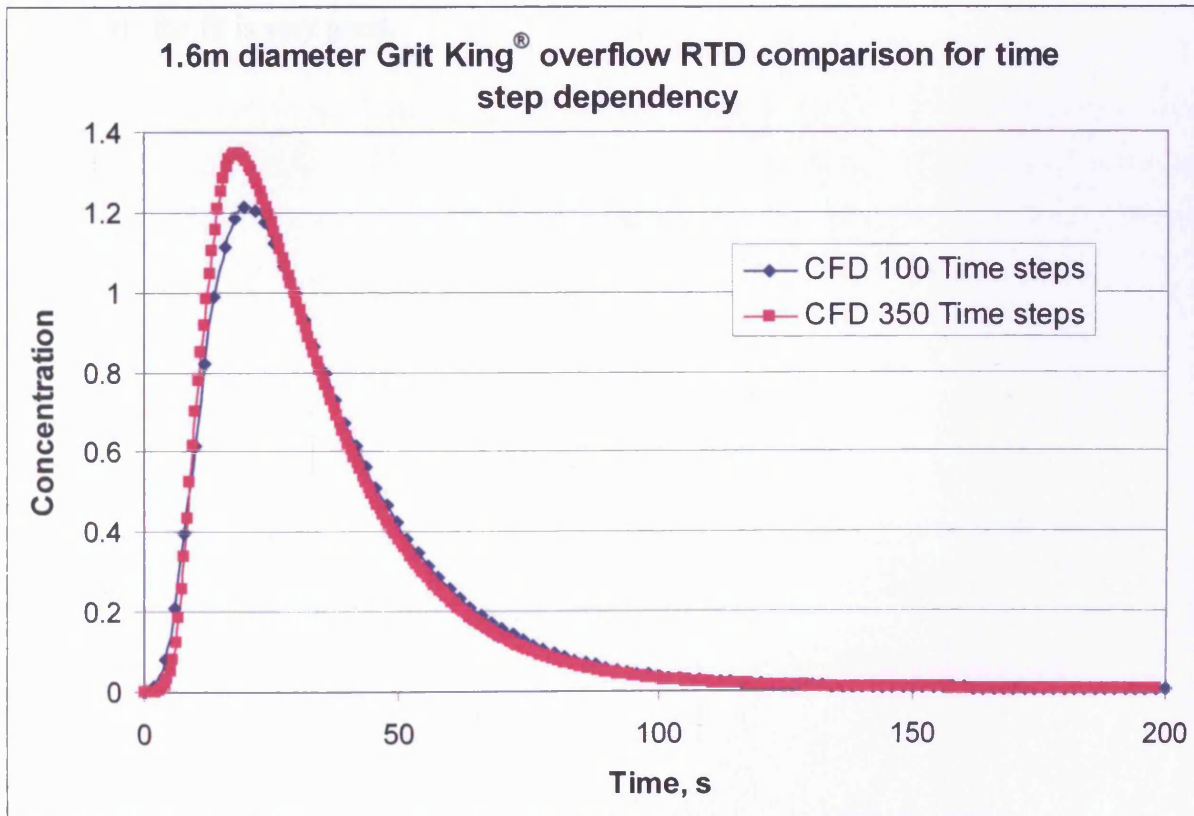
Figure 10-18. CFD RTD prediction comparison for time step dependency at 60.2 litres per second.

From the data in Tables N1 to N11, Appendix N, it can be seen that at the end of the RTD, the concentration tends to remain fairly constant. This may have been due to a very slow release of tracer from the Grit King® (Tyack, 2004, Private Communication). The sensitivity of the atomic absorption spectrophotometer was checked throughout the testing and Tyack therefore had confidence that the reading was accurate (Tyack, 2004, Private Communication). The RTDs in Appendix N were therefore truncated to reduce the distortion to the residence time calculations (Tyack, 2004, Private Communication). From calculations made of the mean residence time and compared to those reported by Tyack and Fenner (1998a) it is believed that data marked with an asterisk (*) in Appendix N was not included in the calculation of the mean or the normalised variance reported by Tyack and Fenner (1998a). The exact method used to determine where to truncate the RTD is unknown. Due to the long tails in the RTD data, the ADM has been fitted to the truncated RTDs using the optimisation technique by Guymer (2002) to determine the normalised variance and the mean residence time.

10.4 Results

An example of the fit of the ADM model at 15.51 litres per second is given in Figure 10-19 and clearly the fit is very good.
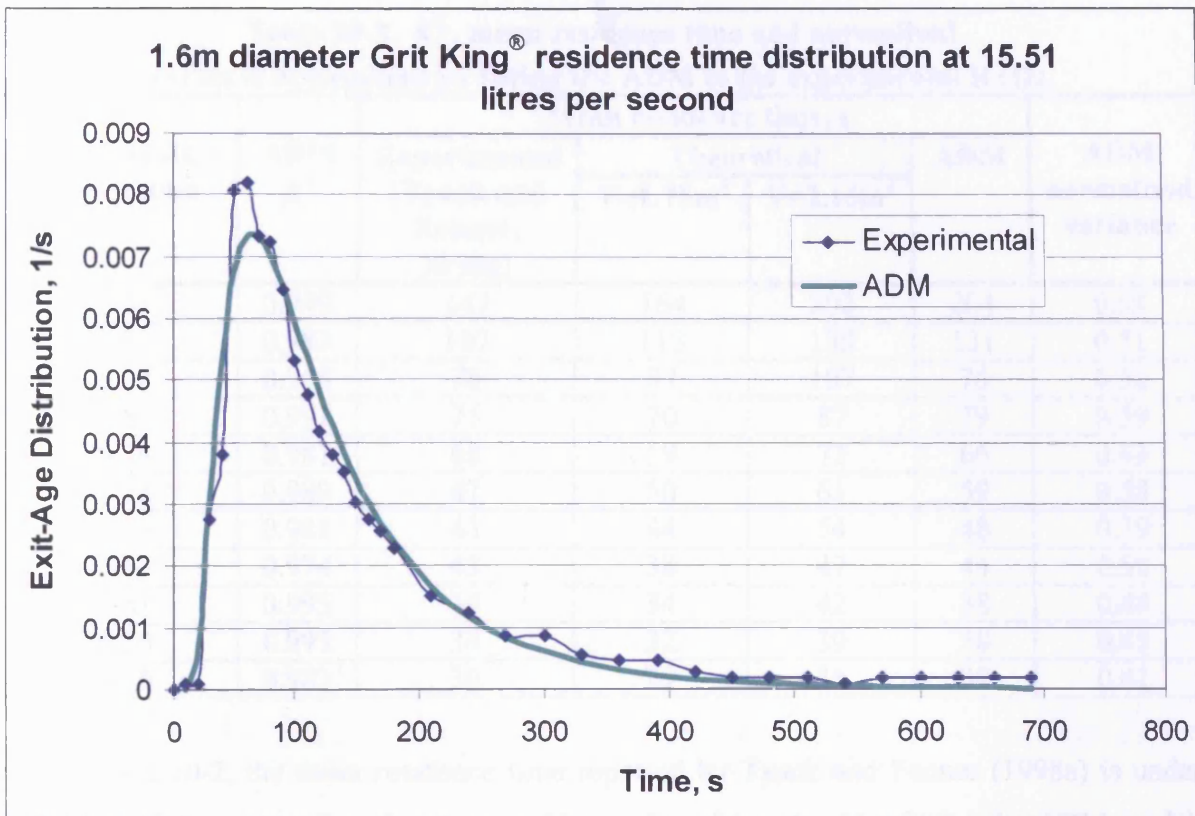
Figure 10-19. The ADM fit (R_t^2 =0.983) to the experimental temporal concentration distribution.

Table 10-2 summarises the mean residence time, normalised variance and the R_t^2 value for the fit by the ADM model to the RTDs. Table 10-2 also compares the mean residence time determined by fitting the ADM model with the theoretical mean residence time computed assuming the fluid volume is 1.75m³, as reported by Tyack and Fenner (1998a) and also the actual volume of fluid which is approximately 2.16m³.

Table 10-2. R_t^2, mean residence time and normalised variance determined by fitting the ADM to the experimental RTDs.

Inlet flowrate, / litres/second	ADM R_t^2	Mean residence time, s			ADM	ADM normalised variance
		Experimental (Tyack and Fenner, 1998a)	Theoretical			
			V=1.75m³	V=2.16m³		
10.67	0.949	147	164	202	204	0.58
15.51	0.983	107	113	139	131	0.51
20.22	0.968	78	87	107	76	0.30
24.85	0.992	75	70	87	79	0.59
29.76	0.981	68	59	73	66	0.43
35.33	0.989	47	50	61	59	0.58
39.93	0.981	43	44	54	48	0.39
45.65	0.974	43	38	47	44	0.50
51.81	0.995	34	34	42	38	0.44
55.20	0.995	34	32	39	38	0.45
60.20	0.983	30	29	36	32	0.41

From Table 10-2, the mean residence time reported by Tyack and Fenner (1998a) is under predicted when compared to the mean residence time determined by fitting the ADM model. Hence, for the mean residence time reported by Tyack and Fenner (1998a) to match a theoretical mean residence time, an active volume must be considered[7]. This active volume is thought to be 1.75m³ whereas the actual volume of fluid in the 1.6m diameter HDVS is approximately 2.16m³. Comparison of the theoretical mean residence time using the actual fluid volume within the 1.6m diameter Grit King® with the mean residence time determined using the ADM, reveals that the residence time of this HDVS is in fact approximately equal to the theoretical residence time. The experimental mean residence time will therefore be considered to be that determined by fitting the RTD model, a method used by Guymer (2002 and 2004) and Boxall *et al.* (2003).

Figure 10-20 compares the CFD-predicted mean residence time with the mean residence time determined by fitting the ADM.

---

[7] It is the author's opinion that the concept of an active volume can be misleading if the active volume is not clearly stated and compared to the actual volume of fluid in the HDVS. This is because the normalised mean residence time is used as a measure to determine any short circuiting or whether the system holds the fluid for an extended period of time. By matching the experimental mean residence time to a theoretical mean residence time where an active volume is considered, the normalised mean residence time will always be 1!

Mean residence time of the 1.6m diameter Grit King®
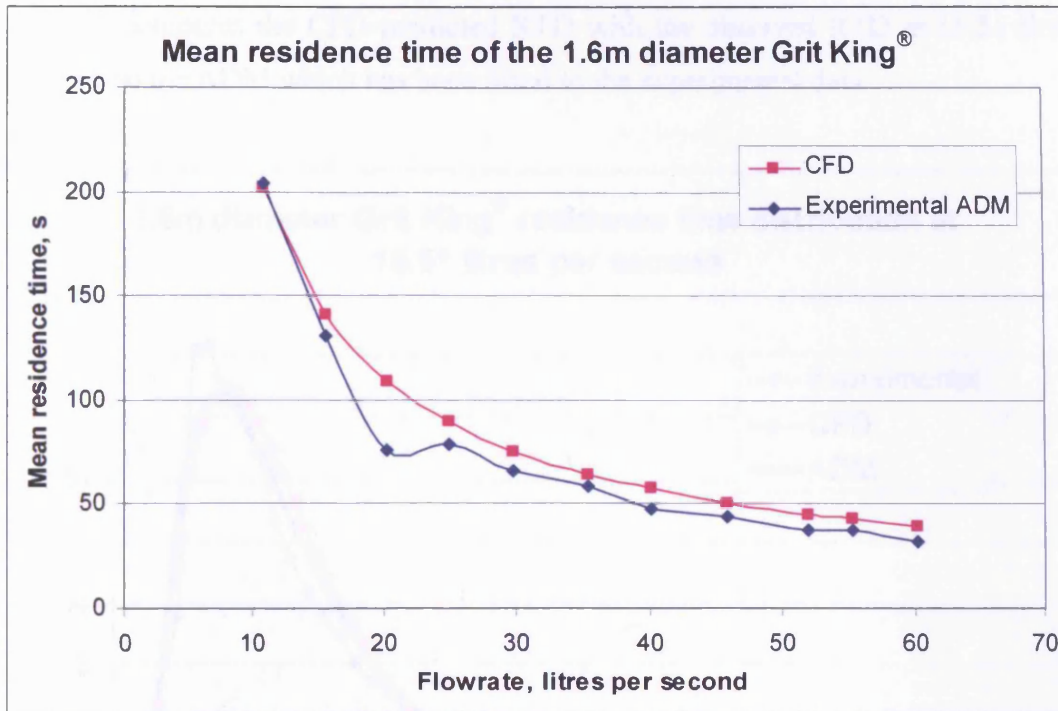
Figure 10-20. Comparison between experimentally determined mean residence times and CFD predictions for the 1.6m diameter Grit King®.

Figure 10-21 compares the CFD-predicted normalised variance, computed via the second moment about the mean, Equation 2-25, with the normalised variance determined by fitting the ADM to the experimental data.

Normalised variance of the 1.6m diameter Grit King®
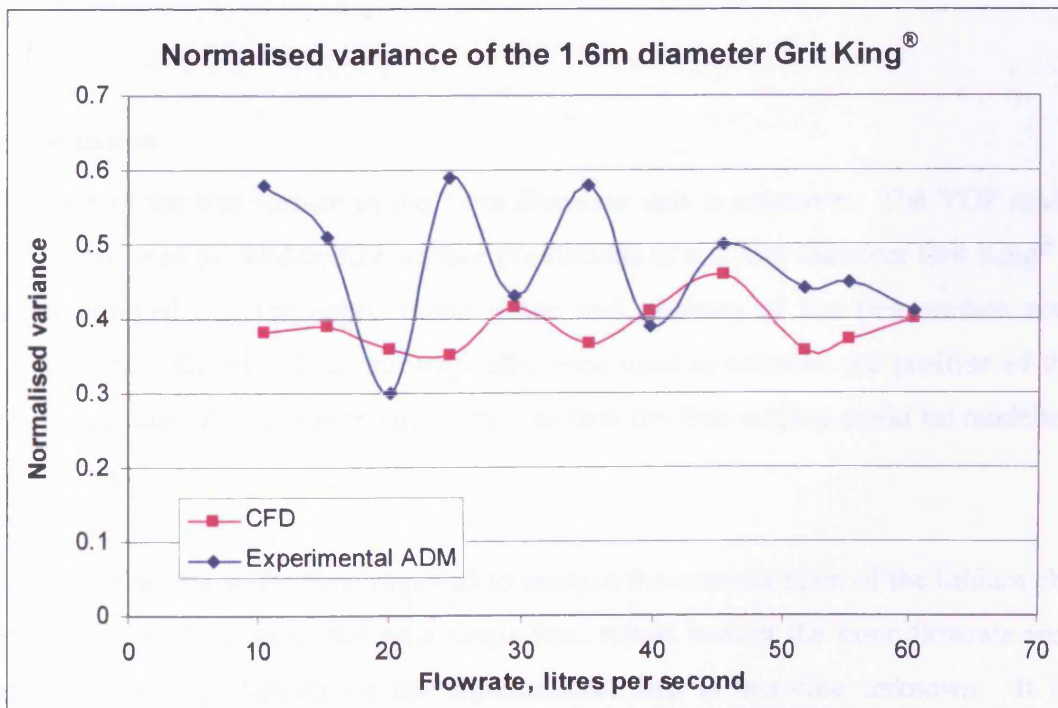
Figure 10-21. Comparison between the experimentally determined normalised variance and CFD predictions for the 1.6m diameter Grit King®.

Figure 10-22 compares the CFD-predicted RTD with the observed RTD at 15.51 litres per second and also the ADM which has been fitted to the experimental data.
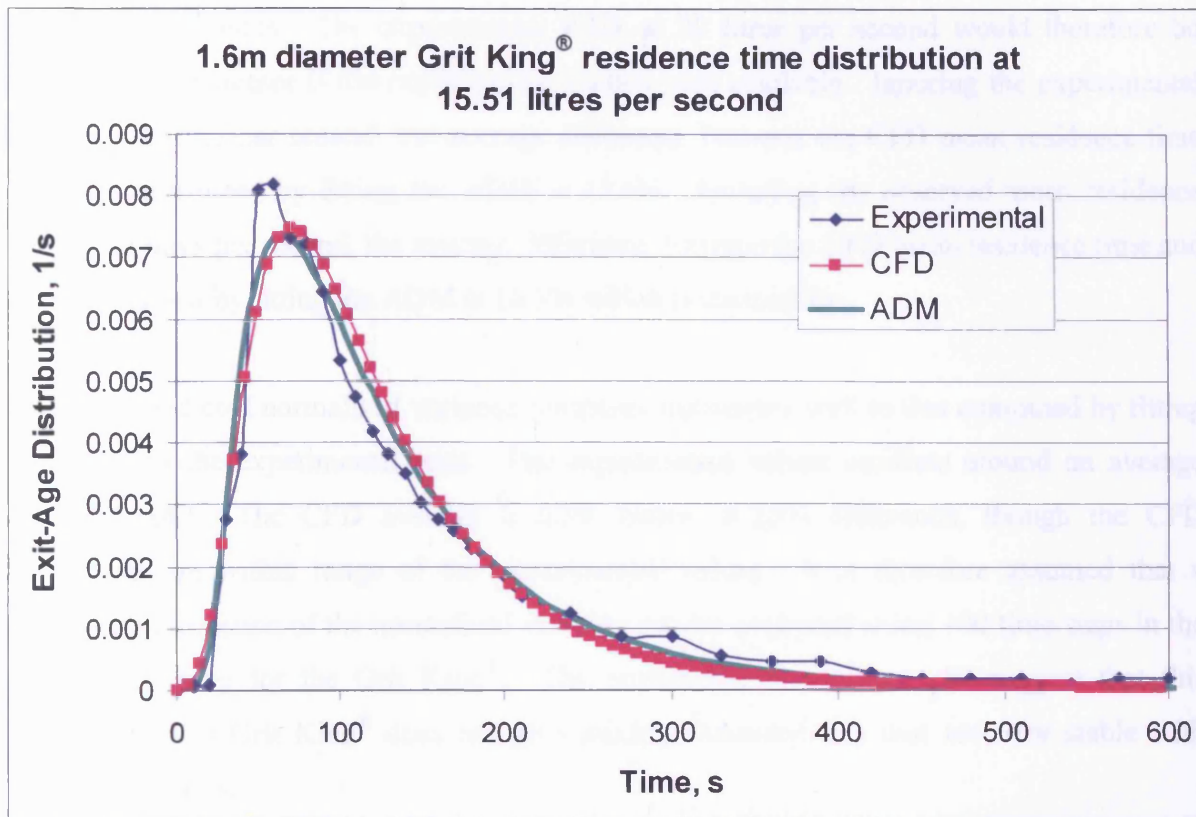
Figure 10-22. CFD-predicted RTD compared to the ADM fitted to the observed temporal concentration distribution.

10.5 Discussion

The position of the free surface in the 1.6m diameter unit is unknown. The VOF model has therefore been used to validate free surface predictions of a 0.75m diameter Grit King® where it was determined that the approximate shape and position of the free surface could be estimated. The VOF model has subsequently been used to estimate the position of the free surface within the 1.6m diameter Grit King® so that the free surface could be modelled as a frictionless wall.

It is believed that due to the time required to analyse the concentration of the lithium chloride in the samples of fluid taken during a single test, repeat tests at the same flowrate were not performed. The repeatability of the experimental data is therefore unknown. It is also assumed that the tracer is well mixed at the sampling point.

Figure 10-20 shows that the CFD predictions generally follow the same trend as the experimental data. The ADM mean residence time at 20 litres per second which is 76 seconds is probably an anomaly since it is less than the mean residence time at 25 litres per second which is 79 seconds. The experimental RTD at 20 litres per second would therefore be repeated by the author if the experimental facility was available. Ignoring the experimental value at 20 litres per second, the average difference between the CFD mean residence time and that determined by fitting the ADM is 13.6%. Including the observed mean residence time at 20 litres per second, the average difference between the CFD mean residence time and that determined by fitting the ADM is 16.3% which is reasonable.

The CFD-predicted normalised variance compares reasonably well to that computed by fitting the ADM to the experimental data. The experimental values oscillate around an average value of 0.49. The CFD average is 0.39, hence, a 25% difference, though the CFD predictions are within range of the experimental values. It is therefore assumed that a reasonable estimation of the normalised variance can be evaluated using 100 time steps in the CFD RTD curve for the Grit King®. The normalised variance results suggest that this configuration of Grit King® does not give mixing characteristics that are very stable with varying flowrates.

Figure 10-22 shows a very good prediction by CFD of the RTD at 15.51 litres per second, despite the difference in the CFD mean residence time being 8% and the normalised variance being 23.5%. This result emphasises how sensitive the normalised variance is to the tail of the temporal concentration distribution. The CFD prediction also compares very well to the ADM which has been fit to the experimental data. Figures N1 to N11, Appendix N, compare the CFD-predicted RTD with the experimental where it can be seen in general CFD gives a good prediction.

10.6 Summary

- The VOF model has been used to estimate the position of the free surface in the 1.6m diameter Grit King®.

- The ADM appears to be a suitable RTD model for the Grit King® based on good fits to the observed RTDs.

- CFD predictions of the mean and normalised variance for the 1.6m diameter Grit King® are reasonable.

11 Scaling laws for HDVSs

Predictions of residence time described in Chapters 8 to 10 are reasonable and CFD has therefore been used in an attempt to derive scaling laws for the residence time in the Eff-Pac™ Clarifier, Storm King® and Grit King®.

To establish accurate scaling laws, reasonable fluid properties must be defined. When an HDVS operates as a CSO, a spill occurs only when the volume of fluid within the sewer system exceeds the design limit. During this stage of operation, it is assumed that the effect of sewage sludge will have little effect on the density and viscosity of the water due to the extra volume of fluid in the system. The density and viscosity of water within the models used to establish a scaling law are therefore defined as the density and viscosity of water at an estimate of the UK average annual temperature.

The average annual UK temperature has been estimated from data available from the World Wide Web, more specifically http://www.worldclimate.com/. This source provides average monthly and annual temperature for specific towns and cities throughout the world based on available data. Table 11-1 lists the towns/cities used in this study to derive an average UK temperature and the location of each is shown in Figure 11-1.

Table 11-1. Average annual temperatures of selected UK towns/cities (Data source: http://www.worldclimate.com/).

Town/City	Years data derived between	Number of months data derived from	Average yearly temp., / °C
Southampton (50.90°N 1.40°W)	1855 – 1978	1477	10.4
Sheffield (53.40°N 1.50°W)	1882 – 1978	1128	9.3
Manchester Airport (53.4°N 2.29°W)	1794 – 1990	1138	9.3
London Heathrow Airport (51.48°N 0.40°W)	1981 – 1990	118	11.0
Glasgow (55.90°N 4.30°W)	1857 – 1978	1453	8.5
Durham (54.80°N 1.60°W)	1847 – 1981	1620	8.3
Dumfries (55.10°N 3.10°W)	1871 – 1969	1184	8.5
Cardiff Airport (51.40°N 3.30°W)	1961 – 1990	358	9.9
Aberporth (52.13°N 4.50°W)	1981 – 1990	117	9.6
Plymouth Mount Batten (50.40°N 4.09°W)	1865 – 1990	1510	10.7
Birmingham Airport (52.45°N 1.70°W)	1951 – 1991	492	9.2
Belfast Aldergrove Airport (54.65°N 6.20°W)	1834 – 1990	1663	9.0
Aberdeen Dyce (57.20°N 2.20°W)	1871 – 1990	1435	7.9
		Average	9.4

Figure 11-1. Location of sites used to derive an average annual yearly temperature (Microsoft, 2003).

From Table 11-1 the collection of data at the various sites is not over the same period. Records of temperature in the British Isles indicate that the average annual temperature over the British Isles have risen by 0.5°C since the turn of the 20th century (Met. Office, 2004). Although there may be some error in that the average annual temperature at some sites has been derived from data for longer periods than others, the average annual UK temperature from Table 11-1 is taken as being 9°C in this study. To confirm further that this value is reasonable, according to the Met. Office, which is assumed to be an independent source from which the data was acquired, "the warmest place in the UK is Scilly, Cornwall, with a mean temperature of 11.5 °C" (Met. Office, 2005). As the Scilly Islands are to the very south of the UK where temperatures are generally higher, the derived UK average temperature in Table 11-1 is considered to be reasonable.

11.1 Grid Setup and boundary conditions

Initially, it was envisaged that a comparison of retention efficiency may be made between the three HDVSs and each model was therefore constructed with an inlet pipe of 40 diameters to allow the particles to settle under the force of gravity to a realistic position at the inlet to the HDVS. Chapter 6 describes how CFD-predicted retention efficiencies do not compare well to observed efficiencies and scaling retention efficiencies has therefore been abandoned.

Chapter 8 describes residence time predictions for a 0.75m diameter Eff-Pac™ Clarifier. Reasonable predictions were obtained over a range of flowrates where the free surface was kept at a constant position. Hence, in this study, the position of the free surface has also been kept in the same position. The largest separator studied is the Storm King® with a diameter of 3.4m (see Chapter 9). The number of cells in each model when scaled to 3.4m is therefore based on the number of cells per metre cube within the Storm King® such that each model has a cell concentration that is approximately equal to or greater than the Storm King®. When modelling an HDVS smaller than 3.4m, the grid has been scaled down as it is assumed that the model will be grid independent. In the case of the Eff-Pac™ Clarifier, the number of cells in the model was increased to 1 113 000 in such a way that the grid described in Section 8.2 was still finer along the edge of the dip plate but was also refined in other regions such as the main body of the separator.

A non-radial pressure distribution was specified on the underflow of the Eff-Pac™ Clarifier and may have restricted the predicted swirl within the body of the separator. This was investigated by specifying a pressure outlet with a radial pressure distribution on a 0.75m diameter Eff-Pac™ Clarifier operating with a rise velocity of 30 litres/m²s and an underflow component equivalent to 2.5 litres/m²s. By comparison of the RTD where a non-radial pressure distribution has been specified, it can be seen from Figures 11-2 and 11-3 that the difference in the RTD is negligible and it is therefore assumed that a non-radial pressure distribution is an appropriate boundary condition for the surface loading rates investigated.
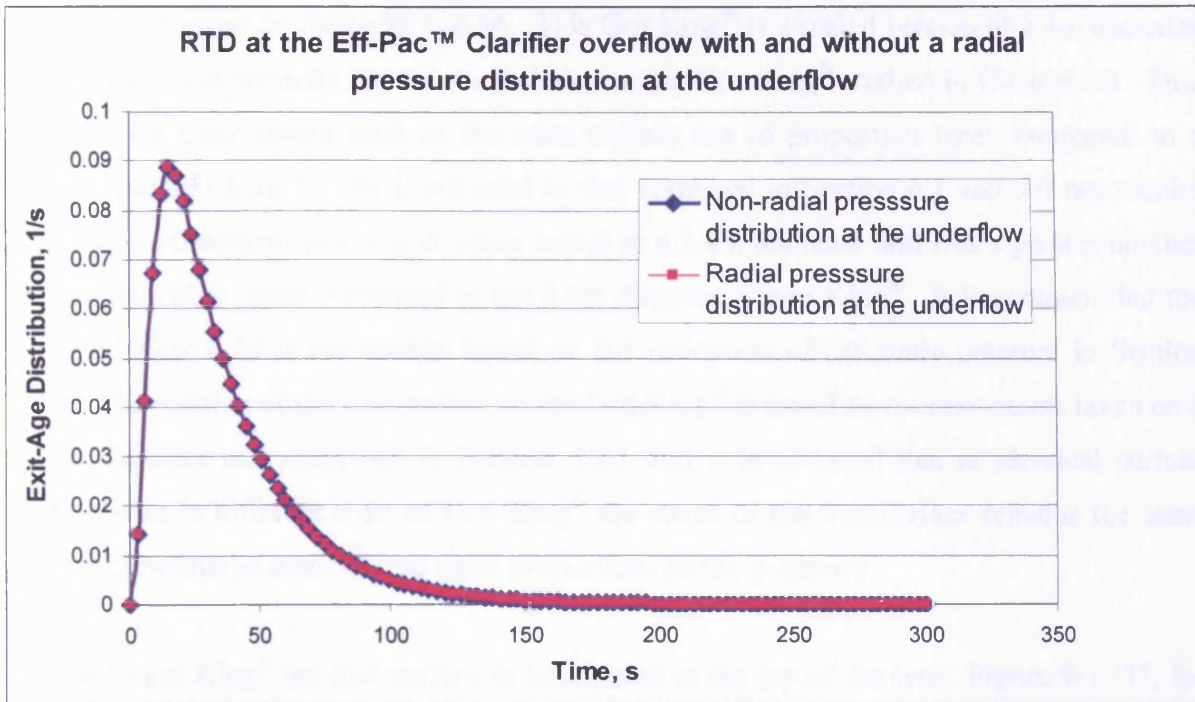
Figure 11-2. Comparison of the CFD-predicted RTD at the Eff-Pac™ Clarifier overflow with and without a radial pressure distribution at the underflow.
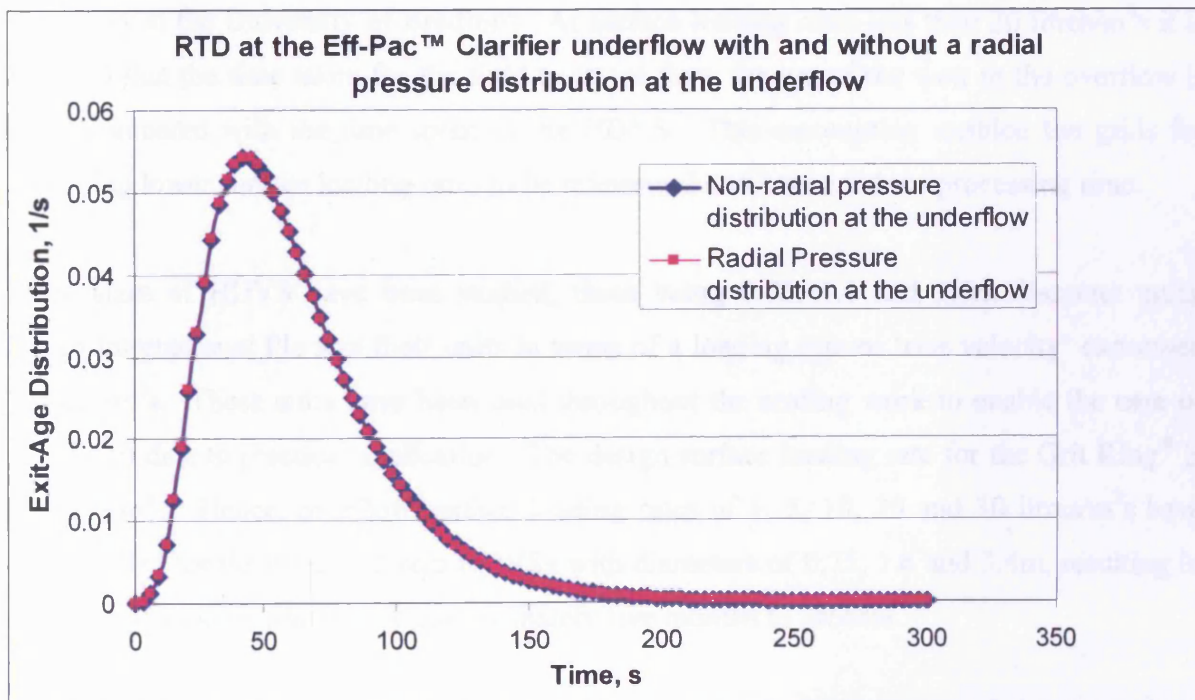
Figure 11-3. Comparison of the CFD-predicted RTD at the Eff-Pac™ Clarifier underflow with and without a radial pressure distribution at the underflow.

For the Grit King® a purely tetrahedral mesh has been used as this gave reasonable validation of residence times in a 1.6m diameter unit described in Chapter 10. The configuration of Grit King® on which scaling is being investigated is that studied in Chapter 5 for which detailed

drawings are given on Pages 95 and 96. This Grit King® is a scaled version of a 4m diameter unit, as design constraints have been included in the Grit King® studied in Chapter 10. This makes some components such as the cone slightly out of proportion when compared to a larger scale Grit King®. The mesh used is that described in Section 6.1 and did not require any further refinement as the grid when scaled to a 3.4m diameter unit had a greater number of cells per cubic metre compared to the 3.4m diameter Storm King®. It is assumed that the predicted flow field is reasonable based on the validation of the static pressure in Section 6.2.1. The position of the free surface in the Grit King® is based on measurements taken on a 0.75m diameter unit described in Section 5.2.1 and it is assumed that at identical surface loading rates in different sizes of Grit King® the shape of the free surface remains the same and can therefore be scaled in the same proportions as the geometry.

For the Storm King® the free surface is terminated at the top of the weir, Figure 9-1 'T', for surface loading rates less than 20 litres/m²s and at higher surface loading rates the depth of fluid at the overflow was 0.12m. This was based on rough measurements taken in the laboratory at the University of Bradford. At surface loading rates less than 20 litres/m²s it is assumed that the time taken for the fluid to travel from the top of the weir to the overflow is small compared with the time spent in the HDVS. This assumption enabled the grids for modelling lower surface loading rates to be minimised and hence reduce processing time.

Three sizes of HDVS have been studied, these being 0.75, 1.6 and 3.4m diameter units. Hydro International Plc size their units in terms of a loading rate or 'rise velocity' expressed as litres/m²s. These units have been used throughout the scaling work to enable the ease of transfer of data to practical application. The design surface loading rate for the Grit King® is 30 litres/m²s. Hence, overflow surface loading rates of 1, 5, 10, 20 and 30 litres/m²s have been studied for the three different HDVSs with diameters of 0.75, 1.6 and 3.4m, resulting in a total of 45 models which took approximately five months to process.

Chapters 8 and 9 describe the Eff-Pac™ Clarifier and the Storm King® operating with an underflow component. To make a direct comparison between each, both are modelled operating with an underflow of 2.5 litres/m²s, this being slightly higher than the 2.1 litres/m²s underflow component that the Storm King® was operating with during residence time studies. The Grit King® has been studied operating without an underflow component. To make a direct comparison between the Grit King® and the two HDVSs operating with an underflow,

each HDVS operates with an identical overflow surface loading rate. Hence, the inlet flowrate to the Storm King® when operating with an overflow surface loading rate of 30 litres/m²s is equivalent to 32.5 litres/m²s allowing for the underflow.

If each HDVS has the same diameter, due to the design of these components, each will hold a different quantity of fluid. For example, the ratio of the diameter to height of the Eff-Pac™ Clarifier is greater than the Storm King® and at identical inlet flowrates the Eff-Pac™ Clarifier would therefore be expected to have a higher residence time based on Equation 2-18 since it has a larger volume of fluid. Table 11-2 lists the average volume of fluid within each size of HDVS.

Table 11-2. Comparison of the volume of fluid within each HDVS.

Diameter, / m	Volume, / m³		
	Eff-Pac™ Clarifier	Storm King®	Grit King®
0.75	0.5	0.2	0.2
1.6	4.9	1.6	2.2
3.4	47.0	15.7	21.3

Validated residence time predictions for the Storm King® and the Eff-Pac™ Clarifier have been obtained with first order solutions. Hence, first order solutions for these models have been acquired when studying scaling effects. Although reasonable validation of residence time of a 1.6m diameter Grit King® was achieved with a first order solution, the validation of the pressure drop from the inlet to pressure tapping points placed on various positions of the HDVS was improved with a second order solution. Hence, for the Grit King® second order solutions have been acquired for momentum, turbulent kinetic energy, turbulent dissipations rate and Reynolds stresses. In some cases, solving the second order terms for the turbulent dissipation rate resulted in a solution that diverged and this had to be set to first order. According to Fluent Inc. (Fluent Inc., 2005, Private Communication) "Experience suggests that there isn't significant change between first order and higher order on the turbulence quantities" for these types of system. The Reynolds Stress Model has been used for all three HDVSs.

Once converged solutions have been acquired, where convergence is judged based on the change in the residuals and also from monitoring the static pressure, the mean residence time has been determined using a UDS as a source term, as described in Section 8.2.1. To describe

the mixing characteristics the TISM and the ADM have been fitted to the Exit-Age distribution function. This will give parameters that can be easily transferred to other applications such as predicting disinfection performance. The best fit of the RTD model has been established through the optimisation procedure by Guymer (2002) described in Section 2.2.3. The Exit-Age distribution function has been predicted using a pulse input at the inlet to the HDVS in the CFD models and monitoring the outlets for a period of time equivalent to five mean residence times of the outlet with the highest mean residence time. A total of 100 time steps have been used to monitor each outlet for each HDVS. Ideally the number of time steps used would be of the order of 350 where it has been shown in Chapters 8 to 10 that using 100 time steps the peak of the RTD is under predicted. However, the processing time for the RTDs alone is estimated to have taken approximately four weeks. Hence, using 350 times steps would have significantly increased the time taken to processes the RTDs and a compromise has to be made. Furthermore it is the tail of the residence time distribution that has a relatively large contribution to the variance (Levenspiel, 1962).

t_{95} has also been determined from the predicted 'C' curve and is defined as the time when C/C_0 has risen to 0.95 for a particular outflow and is analogous to the time it takes for the 'F' curve to plateau. t_{95} is important as it approximates the start up time before predicted survival rates will be achieved when adding disinfectant to the HDVS. This is because predicted survival rates assume that the disinfectant is dispersed throughout the HDVS and t_{95} approximates the time taken to achieve this[8].

The head loss across an HDVS will affect the head of fluid required to drive a given steady state rate of fluid through the separator. The head loss may be determined from the predicted pressure. As discussed in Section 6.2.1, for a fluid with constant density, the mass flux is set in the CFD model by specifying the velocity at the inlet. When the HDVS operates with a flow split a negative velocity is set at one of the outlets. The CFD software then computes the pressure drop required to drive the fluid through the system. Hence, taking the difference

---

[8] It should be noted that under practical circumstances, when an overflow occurs due to a 'flash flood' then a 'first flush' occurs where the quantity of solid matter and hence, micro-organisms, is high compared with the rest of the storm. Therefore when carrying out disinfection, the concentration of disinfectant during the first flush is fairly high and is reduced gradually as the storm proceeds and the number of micro-organisms reduces (Hydro International Plc, 2005, Private Communication). However, the time taken for any concentration of disinfectant to be dispersed throughout the HDVS will remain unchanged.

between the inlet pressure and the outlet pressure, the head loss across the separator may be determined by

$$h_L = \frac{p_1 - p_2}{\rho g}$$ (11-1)

Where: h_L = Head loss, m $\qquad$ p_1 = Inlet pressure, Pa $\qquad$ p_2 = Outlet pressure, Pa

The outlet pressure is taken as being the smallest of the underflow and overflow pressure when the HDVS is operating with a throughflow, hence, giving the greatest head loss. For each HDVS this has been found to be the pressure at the overflow.

Losses have been found to vary as the square of the mean velocity and are frequently expressed in the form (Massey, 1984)

$$h_L = k \frac{u^2}{2g}$$ (11-2)

Where: u = Inlet velocity, m/s $\qquad$ k = Loss coefficient

In deriving a loss coefficient for a system, a long pipe should be installed upstream and downstream. The long pipe before the component ensures a developed flow at the inlet and the long pipe at the outlet ensures that losses caused by flow re-development after the component are debited to the component (Miller, 1978).

Section 6.2.1 presents a reasonable validation of pressure drop between the inlet and static pressure points on the 0.75m diameter Grit King®. It is assumed that the predicted pressure distribution in the Eff-Pac™ Clarifier and the Storm King® are also reasonable having acquired reasonable validation of residence time. Hence, the prediction of the static pressure field can be used to obtain an estimate of the head loss across the separators.

11.2 Results

In the following sections the mean residence time from the TISM and ADM are detailed so that the predicted RTD may be reproduced if desired. Differences between the derived mean residence time using the ADM and TISM and the value straight from CFD are mainly attributable to time step dependency. However, it is the predicted mixing characteristics that are of main interest as reasonable validations have been achieved in Chapters 8 to 10.

11.2.1 Eff-Pac™ Clarifier

Table 11-3 lists the R_t^2 value and the number of tanks for the TISM fit to the predicted RTD of the Eff-Pac™ Clarifier overflow and underflow.

Table 11-4 lists the R_t^2 value and the normalised variance for the ADM fit to the same RTDs.

**Table 11-3. R_t^2 value and the predicted
number of tanks for the TISM fit to Eff-Pac™ Clarifier RTDs.**

Diameter, / m	Rise velocity U_r, / litres/m²s	Eff-Pac™ Clarifier Overflow		Eff-Pac™ Clarifier Underflow	
		Number of tanks (N)	R_t^2	Number of tanks (N)	R_t^2
0.75	1	4.0	0.995	3.0	0.989
	5	2.1	0.975	3.0	0.990
	10	2.1	0.982	4.0	0.996
	20	2.0	0.985	4.0	0.998
	30	2.0	0.986	4.0	0.998
1.6	1	4.0	0.994	3.0	0.990
	5	2.1	0.973	4.0	0.988
	10	2.1	0.981	4.0	0.996
	20	2.0	0.984	4.0	0.997
	30	2.0	0.987	4.0	0.998
3.4	1	4.0	0.993	3.0	0.992
	5	3.0	0.978	4.0	0.989
	10	2.1	0.980	4.0	0.995
	20	2.0	0.984	4.0	0.997
	30	2.0	0.986	4.0	0.998

The average R_t^2 value for the TISM fit to the predicted overflow and underflow RTDs of the Eff-Pac™ Clarifier is 0.989 whereby the TISM produces a good fit.

**Table 11-4. R_t^2 value and the predicted
normalised variance for the ADM fit to Eff-Pac™ Clarifier RTDs.**

Diameter, / m	Rise velocity U_r, / litres/m^{2}s	Eff-Pac™ Clarifier Overflow		Eff-Pac™ Clarifier Underflow	
		Normalised Variance	R_t^2	Normalised Variance	R_t^2
0.75	1	0.33	0.999	0.55	0.997
	5	0.61	0.998	0.40	0.998
	10	0.70	0.997	0.33	0.998
	20	0.76	0.995	0.31	0.997
	30	0.78	0.995	0.33	0.996
1.6	1	0.34	0.998	0.53	0.997
	5	0.60	0.998	0.39	0.999
	10	0.70	0.997	0.32	0.998
	20	0.76	0.996	0.29	0.997
	30	0.78	0.994	0.31	0.996
3.4	1	0.36	0.999	0.51	0.997
	5	0.61	0.998	0.38	0.999
	10	0.71	0.997	0.32	0.999
	20	0.77	0.996	0.29	0.997
	30	0.79	0.995	0.31	0.997

The average R_t^2 value for the ADM fit to the predicted overflow and underflow RTDs of the Eff-Pac™ Clarifier is 0.997 whereby the ADM gives a slightly better fit than the TISM which has an average R_t^2 value of 0.989.

Table 11-5 lists the predicted mean residence time at the Eff-Pac™ Clarifier overflow and underflow and the mean residence time from the fit of the TISM and the ADM to the predicted Exit-Age distribution function.

Table 11-6 lists the predicted t_{95} values for the Eff-Pac™ Clarifier overflow and underflow.

Table 11-5. Predicted mean residence
time at the Eff-Pac™ Clarifier overflow and underflow.

Diameter, / m	Rise velocity U_r, / litres/m²s	Eff-Pac™ Clarifier overflow mean residence time			Eff-Pac™ Clarifier underflow mean residence time		
		CFD, / s	TISM, / s	ADM, / s	CFD, / s	TISM, / s	ADM, / s
0.75	1	368	361	395	309	299	350
	5	145	147	162	168	168	183
	10	86	87	99	114	114	124
	20	48	48	57	76	78	84
	30	33	33	40	59	60	66
1.6	1	781	767	843	662	644	748
	5	307	309	338	360	346	390
	10	183	184	210	243	242	263
	20	102	101	120	160	163	174
	30	71	72	86	123	126	137
3.4	1	1638	1599	1775	1415	1381	1589
	5	649	590	716	773	743	835
	10	387	385	443	521	517	563
	20	216	215	257	343	350	375
	30	151	151	182	264	270	292

Table 11-6. Predicted t_{95} values for the Eff-Pac™ Clarifier overflow and underflow.

Diameter, / m	Rise velocity U_r, / litres/m²s	t_{95}, / s	
		Eff-Pac™ Clarifier Overflow	Eff-Pac™ Clarifier Underflow
0.75	1	792	756
	5	369	387
	10	228	252
	20	128	164
	30	93	126
1.6	1	1720	1640
	5	792	792
	10	481	533
	20	272	336
	30	196	266
3.4	1	3608	3444
	5	1677	1794
	10	1040	1144
	20	594	720
	30	420	560

Table 11-7 list the predicted head loss across the Eff-Pac™ Clarifier.

Table 11-7. Predicted head loss across the Eff-Pac™ Clarifier.

Diameter, / m	Rise velocity U_r, / litres/m²s	Head loss, / m
0.75	1	0.002
	5	0.023
	10	0.084
	20	0.325
	30	0.722
1.6	1	0.003
	5	0.022
	10	0.083
	20	0.319
	30	0.709
3.4	1	0.003
	5	0.023
	10	0.083
	20	0.319
	30	0.709

Plotting the mean residence time predicted using CFD against the rise velocity, the best fit curve from a least squares fit takes the form of

$$\bar{t} = XU_r^{-Y} \qquad (11\text{-}3)$$

Where: X = constant $\qquad Y$ = constant $\qquad U_r$ = Rise velocity, litres/m²s

It has been found that the parameter X increases in proportion to the diameter of the separator and the parameter Y remains approximately constant over the sizes of HDVS modelled. Hence, the mean residence time may be described by

$$\bar{t} = ZD_{HDVS}U_r^{-Y} \qquad (11\text{-}4)$$

Where: Z = constant $\qquad D_{HDVS}$ = HDVS diameter, m

Taking the average value of Z and Y for the different sizes of unit gives for the overflow and underflow respectively

$$\bar{t} = 529.380D_{HDVS}U_r^{-0.701} \qquad (11\text{-}5)$$

$$\bar{t} = 445.862 D_{HDVS} U_r^{-0.491} \tag{11-6}$$

t_{95} may be described in a similar manner for the overflow and underflow respectively

$$t_{95} = 1182 D_{HDVS} U_r^{-0.633} \tag{11-7}$$

$$t_{95} = 1089 D_{HDVS} U_r^{-0.534} \tag{11-8}$$

Where: t_{95} = Time when C/C_0 has risen to 0.95 for a particular outflow, s

From Table 11-7 it can be seen that there isn't any significant variation of head loss with HDVS size. The average head loss at each surface loading rate has been determined and the optimum value of k to describe the head loss found by assessing the R_t^2 value for the fit of Equation 11-2 to the data. Thus, the head loss for the Eff-Pac™ Clarifier can be modelled by Equation 11-2 where k is equal to 1.62 and this gives an R_t^2 value of 0.998 which is a good fit to the data.

These relationships are valid only for predictions of the Eff-Pac™ Clarifier operating with a constant underflow of 2.5 litres/m²s, an overflow surface loading rate in the range of 1 to 30 litres/m²s and for units with a diameter in the range of 0.75m to 3.4m.

An example of the fit of Equation 11-5 and 11-6 to describe the mean residence time and Equation 11-7 and 11-8 to describe t_{95} at the Eff-Pac™ Clarifier outlets for a 1.6m diameter unit is shown in Figures 11-4 to 11-7.

Figure 11-4. The trend in the mean residence time at the Eff-Pac™ Clarifier overflow and a fit of the model to a 1.6m diameter unit.

Figure 11-5. The trend in the mean residence time at the Eff-Pac™ Clarifier underflow and a fit of the model to a 1.6m diameter unit.

Figure 11-6. The trend in t_{95} at the Eff-Pac™ Clarifier overflow and a fit of the model to a 1.6m diameter unit.
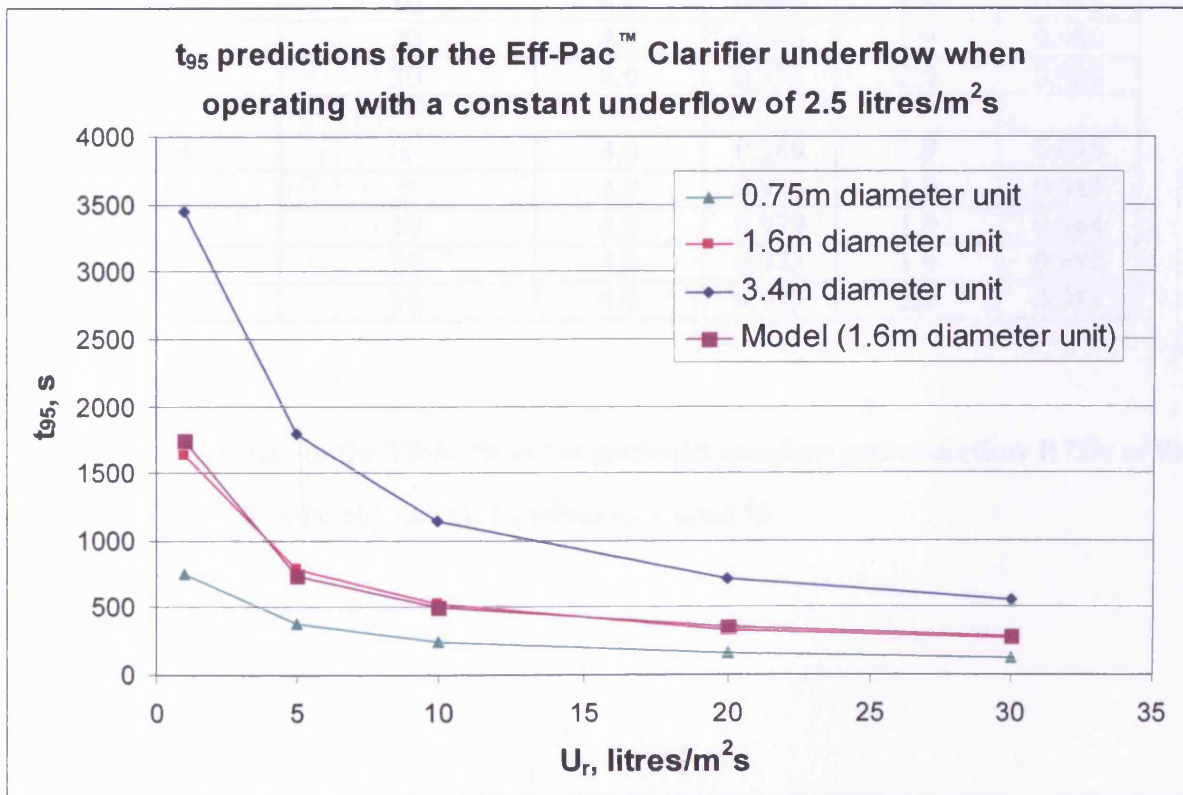
Figure 11-7. The trend in t_{95} at the Eff-Pac™ Clarifier underflow and a fit of the model to a 1.6m diameter unit.

11.2.2 Storm King®

Table 11-8 lists the R_t^2 value and the number of tanks for the TISM fit to the predicted RTD of the Storm King® overflow and underflow. Table 11-9 lists the R_t^2 value and the normalised variance for the ADM fit to the same RTDs.

Table 11-8. R_t^2 value and the predicted
number of tanks for the TISM fit to Storm King® RTDs.

Diameter, / m	Rise velocity U_r, / litres/m^{2}s	Storm King® Overflow		Storm King® Underflow	
		Number of tanks (N)	R_t^2	Number of tanks (N)	R_t^2
0.75	1	4.0	0.989	1.9	0.981
	5	4.0	0.983	1.9	0.986
	10	4.0	0.979	1.9	0.985
	20	4.0	0.972	2.0	0.978
	30	4.0	0.972	2.0	0.976
1.6	1	4.0	0.989	1.9	0.985
	5	4.0	0.984	1.9	0.987
	10	4.0	0.980	1.9	0.985
	20	4.0	0.973	1.9	0.980
	30	4.0	0.973	2.0	0.980
3.4	1	4.0	0.989	1.9	0.986
	5	4.0	0.984	1.9	0.987
	10	4.0	0.979	1.9	0.984
	20	4.0	0.972	1.9	0.980
	30	4.0	0.973	2.0	0.981

The average R_t^2 value for the TISM fit to the predicted overflow and underflow RTDs of the Storm King® is 0.981 whereby the TISM produces a good fit.

Table 11-9. R_t^2 **value and the predicted**
normalised variance for the ADM fit to Storm King® RTDs.

Diameter, / m	Rise velocity U$_r$, / litres/m^{2}s	Storm King® Overflow		Storm King® Underflow	
		Normalised Variance	R$_t$^{2}	Normalised Variance	R$_t$^{2}
0.75	1	0.38	0.999	1.00	0.994
	5	0.37	0.999	1.00	0.988
	10	0.38	0.999	1.00	0.991
	20	0.35	0.994	0.86	0.991
	30	0.35	0.994	0.66	0.988
1.6	1	0.38	0.999	1.00	0.990
	5	0.37	0.999	1.00	0.985
	10	0.39	0.999	1.00	0.992
	20	0.35	0.994	0.92	0.992
	30	0.36	0.995	0.81	0.991
3.4	1	0.38	0.999	1.00	0.988
	5	0.37	0.999	1.00	0.982
	10	0.39	0.999	1.00	0.992
	20	0.36	0.995	0.98	0.994
	30	0.36	0.995	0.88	0.992

The average R_t^2 value for the ADM fit to the predicted overflow and underflow RTDs of the Storm King® is 0.994 whereby the ADM gives a slightly better fit than the TISM which has an average R_t^2 value of 0.981.

Table 11-10 lists the predicted mean residence time at the Storm King® overflow and underflow and the mean residence time from the fit of the TISM and the ADM to the Exit-Age distribution function predicted using CFD.

Table 11-11 lists the predicted t_{95} values for the Storm King® overflow and underflow.

**Table 11-10. Predicted mean residence
time at the Storm King® overflow and underflow.**

Diameter, / m	Rise velocity U_r, / litres/m²s	Storm King® overflow mean residence time			Storm King® underflow mean residence time		
		CFD, / s	TISM, / s	ADM, / s	CFD, / s	TISM, / s	ADM, / s
0.75	1	167	157	177	81	68	89
	5	56	51	57	35	29	38
	10	32	28	32	19	16	21
	20	19	17	19	10	10	12
	30	13	12	13	8	7	8
1.6	1	355	335	377	173	146	192
	5	120	109	122	74	61	80
	10	69	61	69	40	33	43
	20	40	37	41	22	19	25
	30	27	25	28	16	15	18
3.4	1	755	713	801	368	311	409
	5	256	231	259	158	129	169
	10	146	129	147	85	69	91
	20	85	78	88	45	40	53
	30	58	53	60	32	30	38

Table 11-11. Predicted t_{95} values for the Storm King® overflow and underflow.

Diameter, / m	Rise velocity U_r, / litres/m²s	t_{95}, / s	
		Storm King® Overflow	Storm King® Underflow
0.75	1	392	229
	5	134	94
	10	77	50
	20	47	47
	30	32	32
1.6	1	835	488
	5	286	202
	10	165	107
	20	100	100
	30	68	68
3.4	1	1777	1040
	5	608	429
	10	353	227
	20	210	210
	30	140	140

When modelling the Storm King® at surface loading rates less than 20 litres/m²s the outlet was positioned at the top of the weir, as the grid required to model the fluid at the overflow would have been too large due to the very shallow depth of fluid in the overflow channel. Comparing the head loss at two different positions for the outlet over a range of flowrates (i.e. the top of the weir and the overflow outlet) does not give a true comparison due to differences in pressure between the top of the weir and the overflow. Thus, the pressure at the overflow is only available for surface loading rates of 20 and 30 litres/m²s given in Table 11-12.

Table 11-12. Predicted head loss across the Storm King®.

Diameter, / m	Rise velocity U_r, / litres/m²s	Head loss, / m
0.75	20	0.173
	30	0.345
1.6	20	0.168
	30	0.348
3.4	20	0.163
	30	0.351

It has been found that the mean residence time at the overflow and underflow of the Storm King® may be described in a similar way to the Eff-Pac™ Clarifier. Hence, Equation 11-9 and 11-10 describe the mean residence time at the Storm King® overflow and underflow respectively

$$\bar{t} = 233.527 D_{HDVS} U_r^{-0.750}$$ (11-9)

$$\bar{t} = 121.536 D_{HDVS} U_r^{-0.714}$$ (11-10)

t_{95} may be described in a similar manner for the overflow and underflow respectively

$$t_{95} = 545.831 D_{HDVS} U_r^{-0.733}$$ (11-11)

$$t_{95} = 300.478 D_{HDVS} U_r^{-0.578}$$ (11-12)

From Table 11-8 it can be seen that the number of tanks that describe the mixing characteristics at the overflow for all surface loading rates and Storm King® sizes modelled is 4. Since the mixing characteristics are constant, inserting Equation 11-9 into Equation 3-18 yields a general equation to describe the disinfection performance of the Storm King®. This

assumes the disinfection model by Severin *et al.* (1984) is suitable to describe the inactivation of micro-organisms in a particular catchment of wastewater.

$$\frac{N_t}{N_0} = \left(\frac{1}{1 + 58.38kCD_{HDVS}U_r^{-0.750}} \right)^4 \sum_{i=0}^{j-1} \left[\frac{i+3}{3} \right] \left(\frac{58.38kCD_{HDVS}U_r^{-0.750}}{1 + 58.38kCD_{HDVS}U_r^{-0.750}} \right)^i \qquad (11\text{-}13)$$

Although head loss data is only available for two surface loading rates, from Table 11-12 there is no significant variation of head loss with HDVS size. If it is assumed that Equation 11-2 can be used to describe the head loss, then the value of k which gives the best fit may be determined and has been found to be 2.96 which gives an R_t^2 value of 0.942 which is quite a good fit.

These relationships are only valid for predictions of the Storm King[®] operating with a constant underflow of 2.5 litres/m^{2}s, an overflow surface loading rate in the range of 1 to 30 litres/m^{2}s and for units with a diameter in the range of 0.75 to 3.4m.

An example of the fit of Equation 11-9 and 11-10 to describe the mean residence time of the fluid and Equation 11-11 and 11-12 to describe t_{95} at the Storm King[®] overflow and underflow for a 3.4m diameter unit is shown in Figures 11-8 to 11-11.
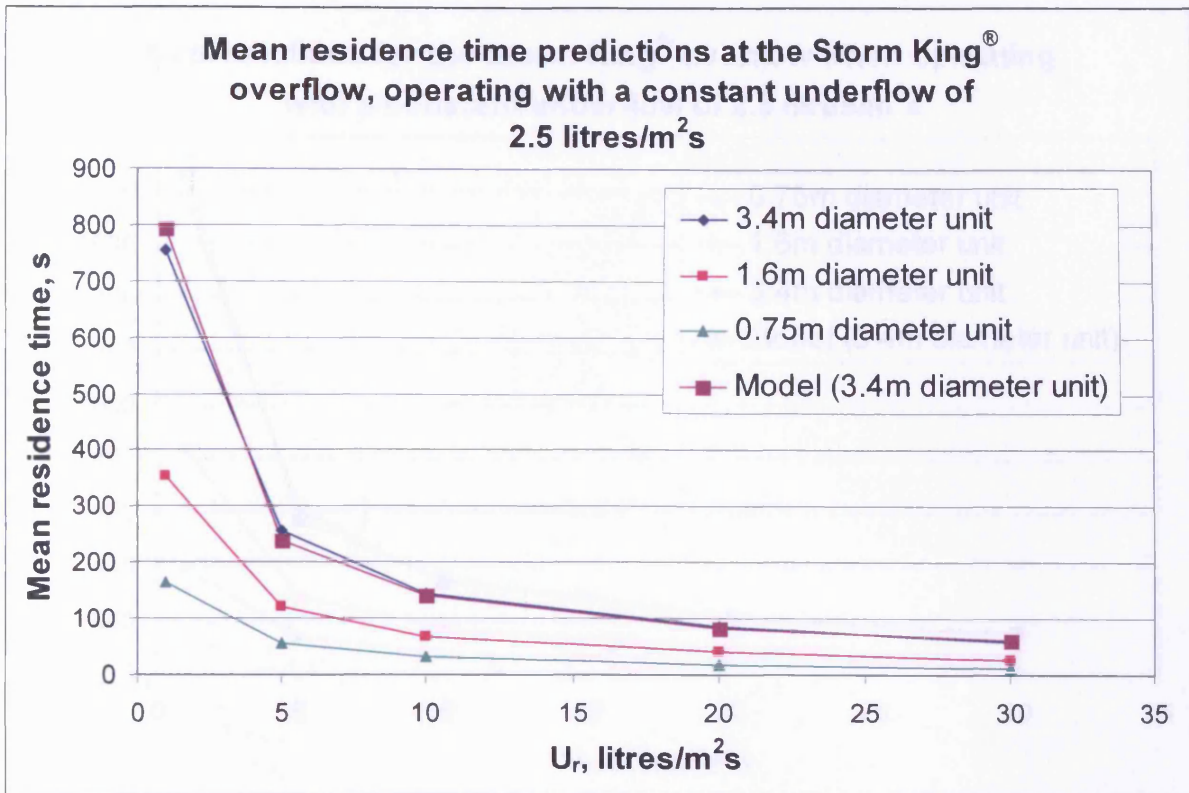
Figure 11-8. The trend in the mean residence time at the Storm King® overflow and a fit of the model to a 3.4m diameter unit.
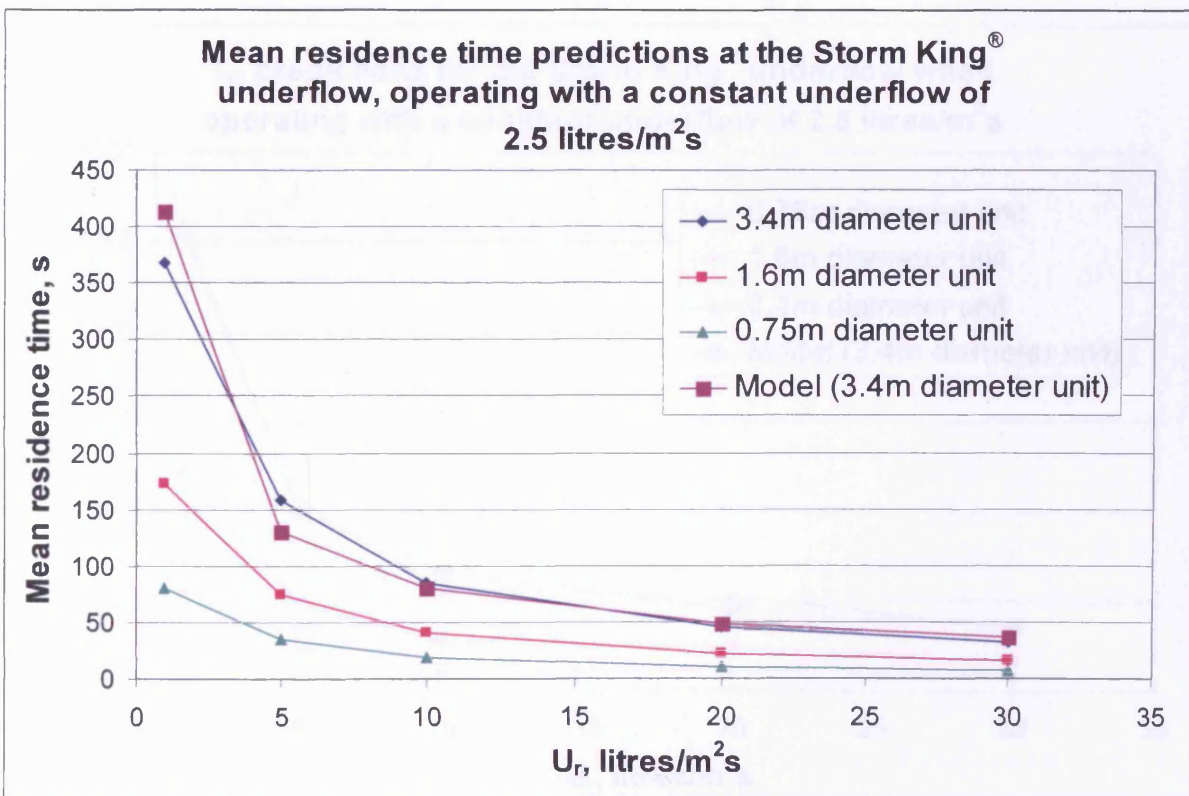
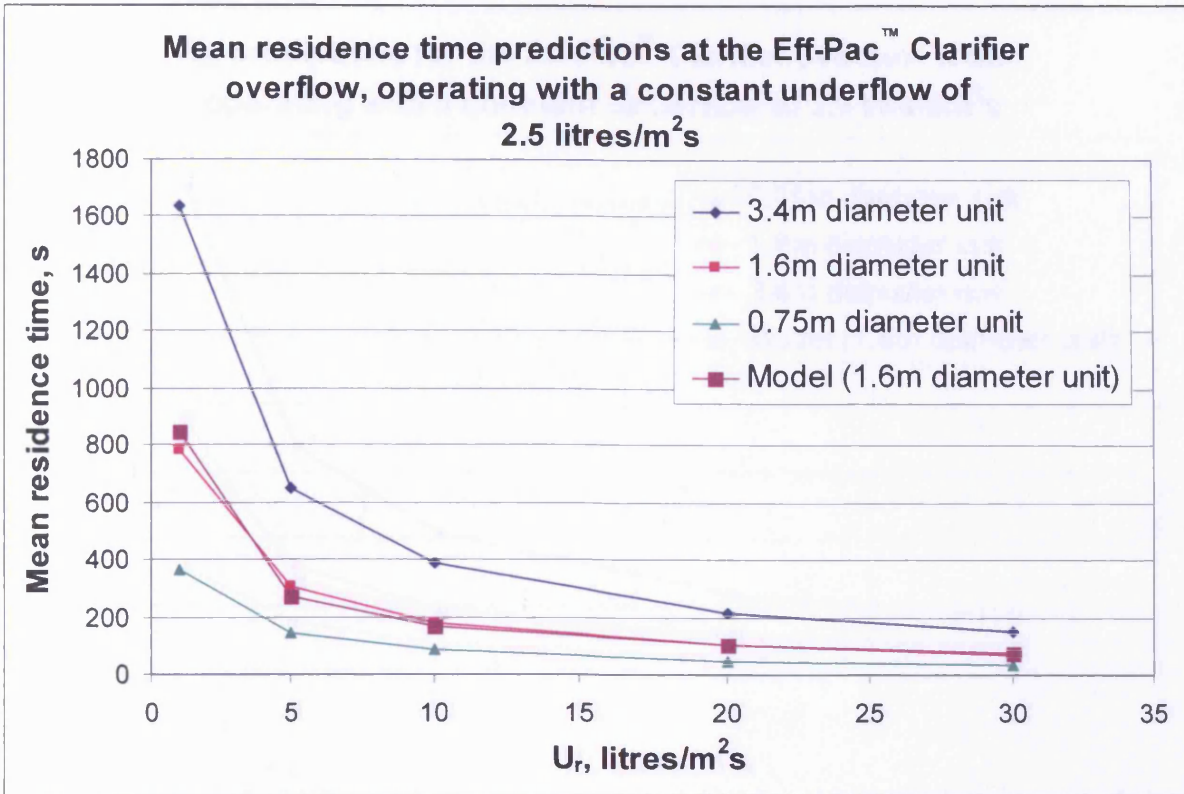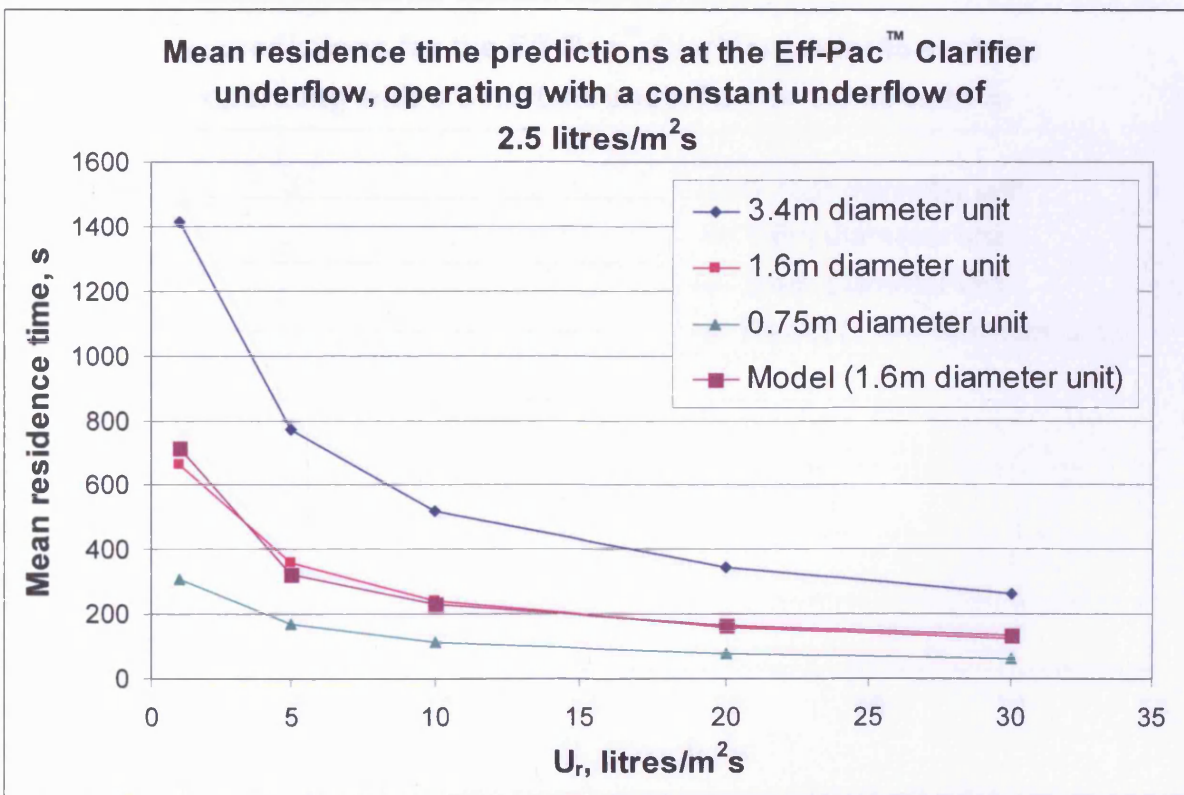**Figure 11-9. The trend in the mean residence time at the Storm King® underflow and a fit of the model to a 3.4m diameter unit.**
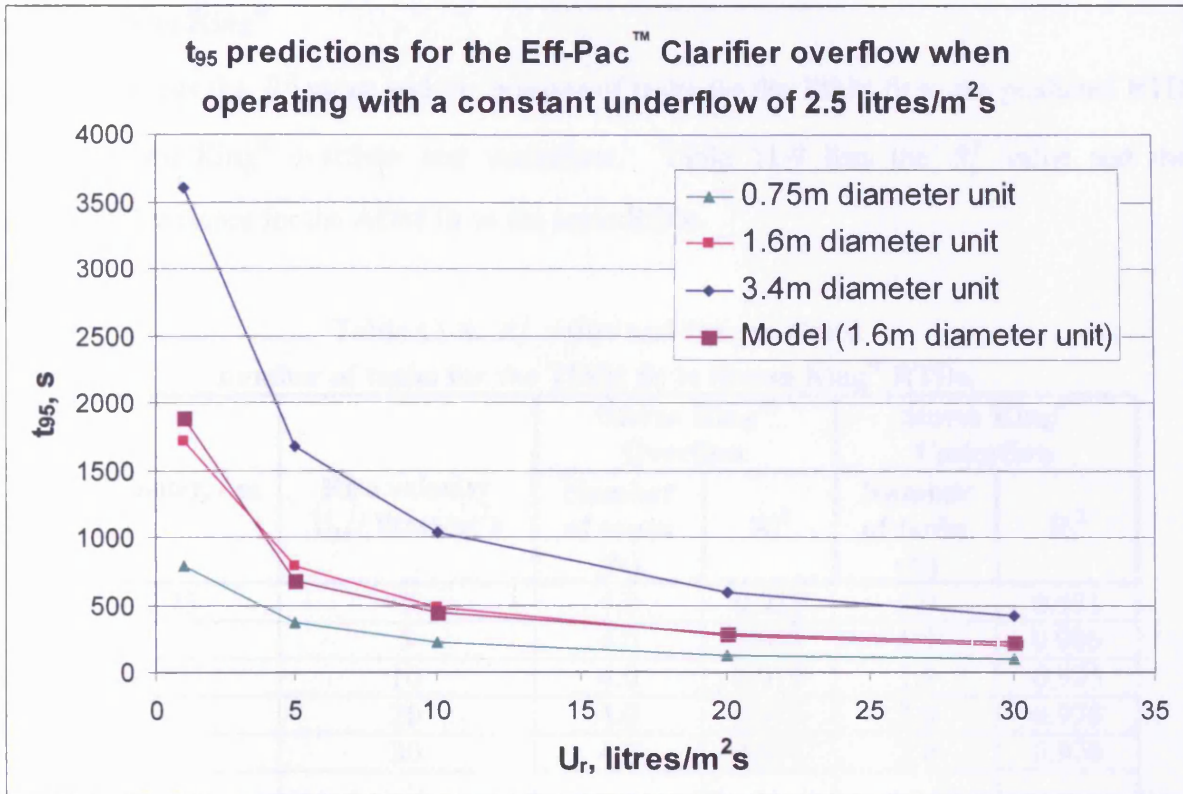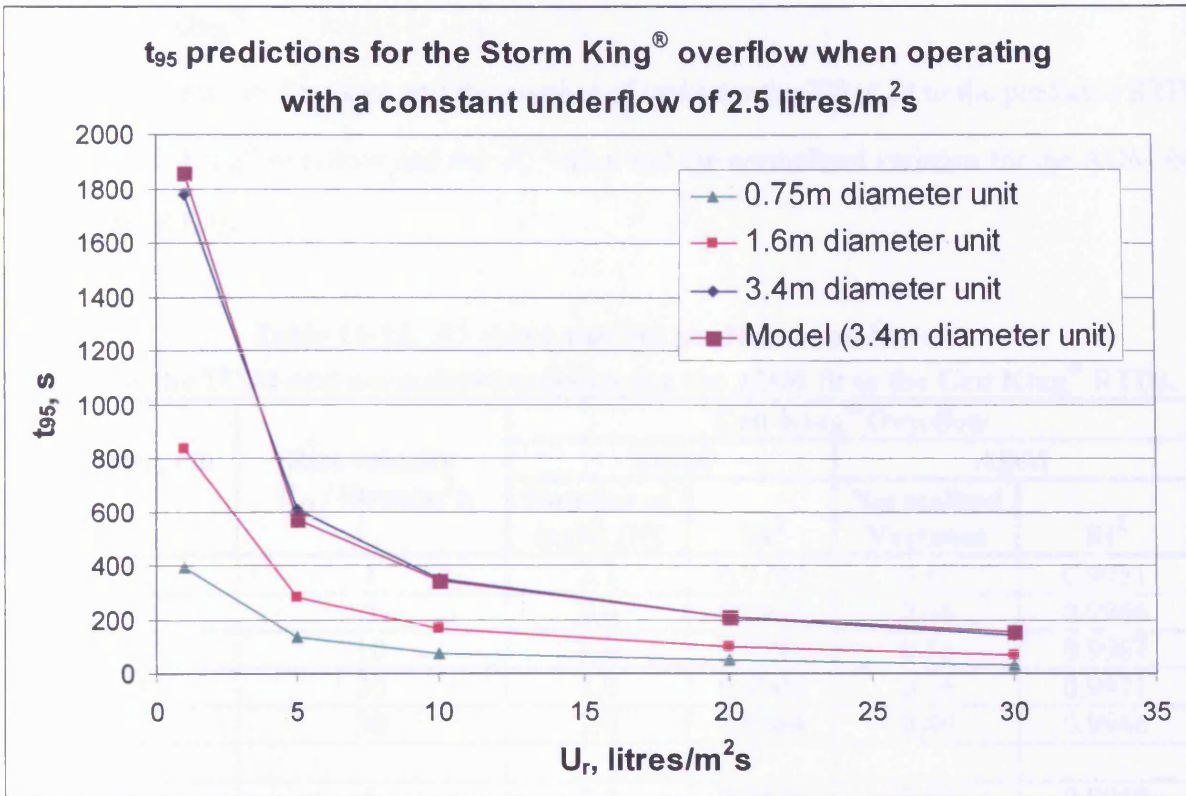
Figure 11-10. The trend in t_{95} **at the Storm King® overflow
and a fit of the model to a 3.4m diameter unit.**
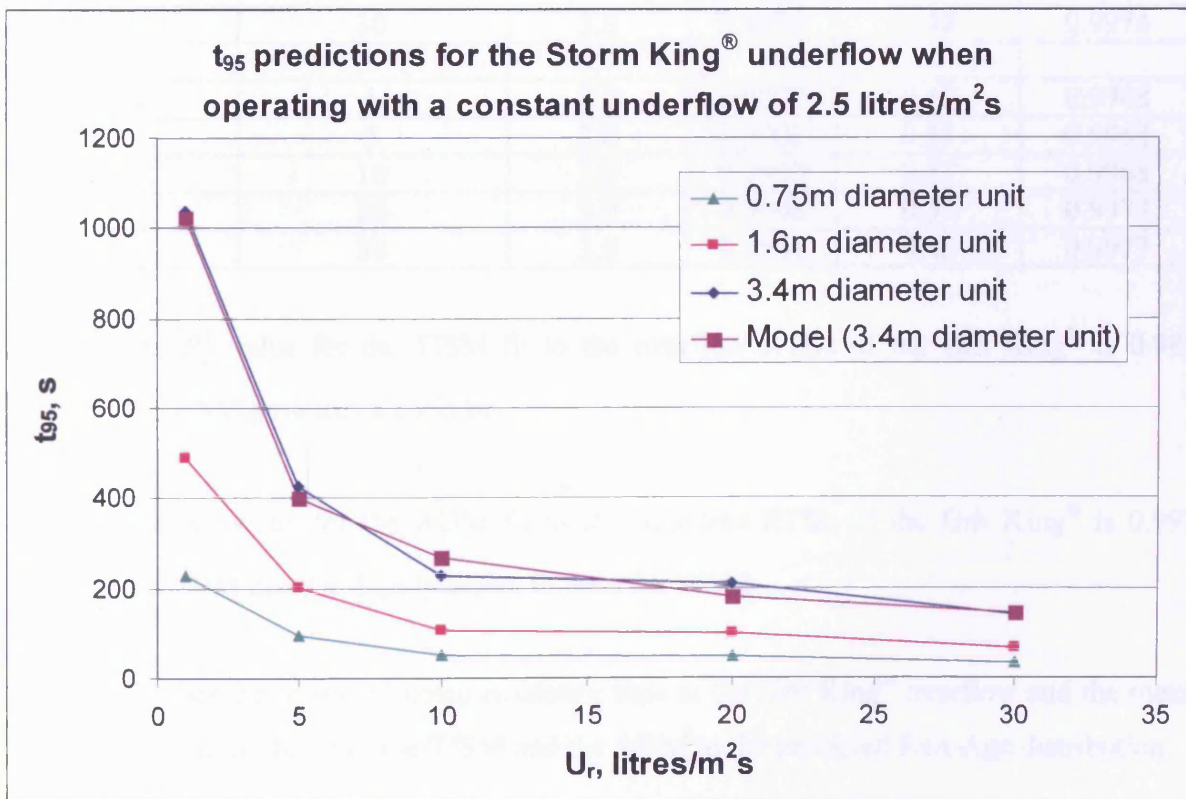
Figure 11-11. The trend in t_{95} **at the Storm King® underflow
and a fit of the model to a 3.4m diameter unit.**

11.2.3 Grit King®

Table 11-13 lists the R_t^2 value and the number of tanks for the TISM fit to the predicted RTD from the Grit King® overflow and the R_t^2 value and the normalised variance for the ADM fit to the same RTDs.

Table 11-13. R_t^2 value and the predicted number of tanks for the TISM and normalised variance for the ADM fit to the Grit King® RTDs.

Diameter, / m	Rise velocity U_r, / litres/m^{2}s	Grit King® Overflow			
		TISM		ADM	
		Number of tanks (N)	Rt^2	Normalised Variance	Rt^2
0.75	1	2.1	0.9784	0.67	0.9951
	5	3.0	0.9913	0.46	0.9966
	10	3.0	0.9896	0.52	0.9967
	20	3.0	0.9906	0.46	0.9971
	30	3.0	0.9884	0.46	0.9966
1.6	1	3.0	0.9829	0.60	0.9960
	5	3.0	0.9898	0.52	0.9969
	10	3.0	0.9849	0.56	0.9970
	20	3.0	0.9908	0.47	0.9971
	30	3.0	0.9899	0.48	0.9974
3.4	1	3.0	0.9807	0.57	0.9948
	5	3.0	0.9901	0.51	0.9968
	10	3.0	0.9902	0.51	0.9968
	20	3.0	0.9908	0.47	0.9973
	30	3.0	0.9901	0.45	0.9977

The average R_t^2 value for the TISM fit to the overflow RTDs of the Grit King® is 0.988 whereby the TISM produces a good fit.

The average R_t^2 value for the ADM fit to the overflow RTDs of the Grit King® is 0.997 whereby the ADM gives a slightly better fit than the TISM.

Table 11-14 lists the predicted mean residence time at the Grit King® overflow and the mean residence time from the fit of the TISM and the ADM to the predicted Exit-Age distribution.

Table 11-14. Predicted mean residence time at the Grit King® overflow.

Diameter, / m	Rise velocity U_r, / litres/m²s	Grit King® overflow mean residence time		
		CFD, / s	TISM, / s	ADM, / s
0.75	1	479	429	490
	5	98	82	93
	10	49	41	48
	20	25	21	24
	30	17	14	16
1.6	1	1024	837	1013
	5	209	172	201
	10	106	86	102
	20	54	45	51
	30	37	31	35
3.4	1	2177	1775	2118
	5	444	366	424
	10	224	185	215
	20	114	96	109
	30	78	66	74

Table 11-15 lists the predicted t_{95} values for the Grit King® overflow.

Table 11-15. Predicted t_{95} values in the Grit King® overflow.

Diameter, / m	Rise velocity U_r, / litres/m²s	t_{95}, / s Grit King® Overflow
0.75	1	1368
	5	245
	10	128
	20	62
	30	43
1.6	1	2808
	5	536
	10	286
	20	135
	30	93
3.4	1	5777
	5	1132
	10	571
	20	285
	30	191

Table 11-16 lists the predicted head loss across the Grit King®.

Table 11-16. Predicted head loss across the Grit King®.

Diameter, / m	Rise velocity U_r, / litres/m²s	Head loss, / m
0.75	1	0.003
	5	0.007
	10	0.020
	20	0.085
	30	0.175
1.6	1	0.002
	5	0.007
	10	0.022
	20	0.086
	30	0.172
3.4	1	0.002
	5	0.007
	10	0.020
	20	0.087
	30	0.165

It has been found that the mean residence time at the overflow of the Grit King® may be described in a similar way to the Eff-Pac™ Clarifier and the Storm King®, hence

$$\bar{t} = 636.418 D_{HDVS} U_r^{-0.981} \qquad (11\text{-}14)$$

t_{95} may be described by

$$t_{95} = 1771.2 D_{HDVS} U_r^{-1.007} \qquad (11\text{-}15)$$

From Table 11-16, there is no significant variation of head loss with separator size. Taking the average values at each surface loading rate and fitting Equation 11-2, the optimum value for k has been found to be 1.01 and fits the data with an R_t^2 value of 0.997.

These relationships are only valid when the Grit King® operates with an overflow surface loading rate in the range of 1 to 30 litres/m²s and for units with a diameter in the range of 0.75 to 3.4m. An example of the fit of Equation 11-14 to describe the mean residence time and

Equation 11-15 to describe t_{95} at the Grit King® overflow for a 3.4m diameter unit is shown in Figures 11-12 and 11-13 respectively.
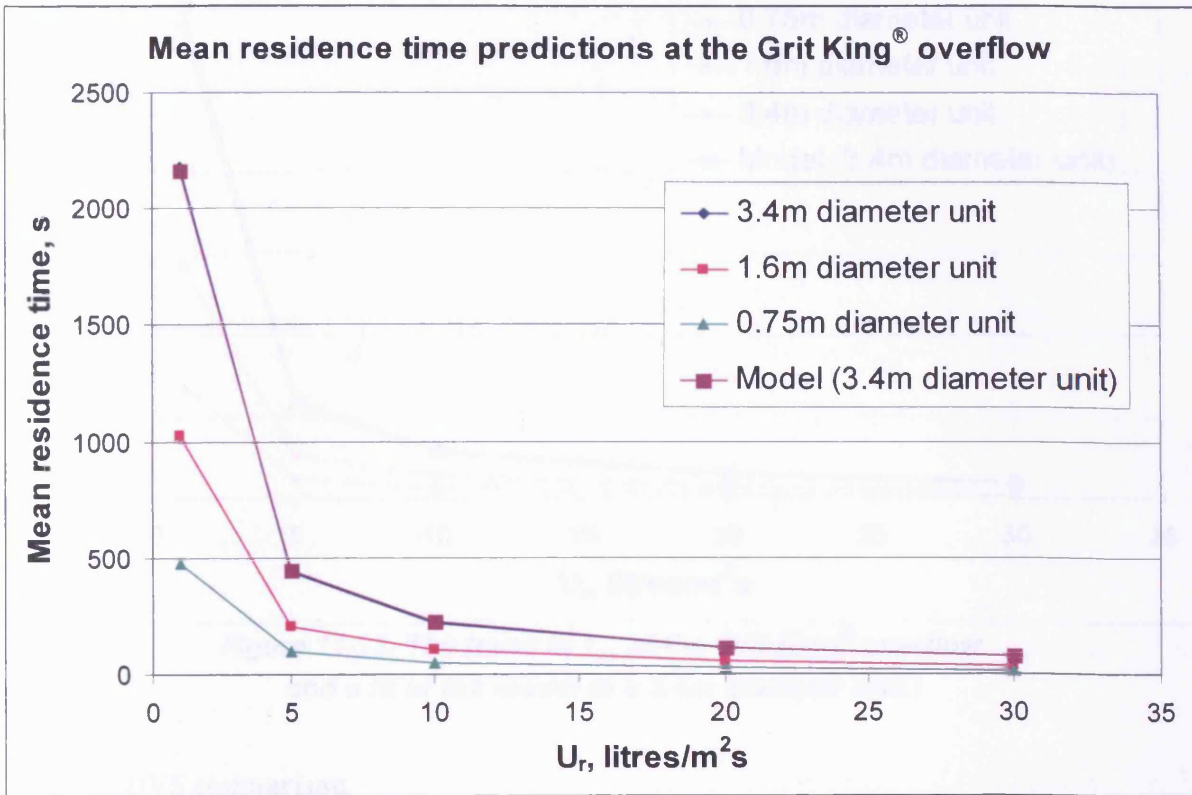
Figure 11-12. The trend in the mean residence time at the Grit King® overflow and a fit of the model to a 3.4m diameter unit.

t95 predictions for the Grit King® overflow

Figure legend:
- 0.75m diameter unit
- 1.6m diameter unit
- 3.4m diameter unit
- Model (3.4m diameter unit)

Y-axis: t_{95}, s
X-axis: U_r, litres/m²s
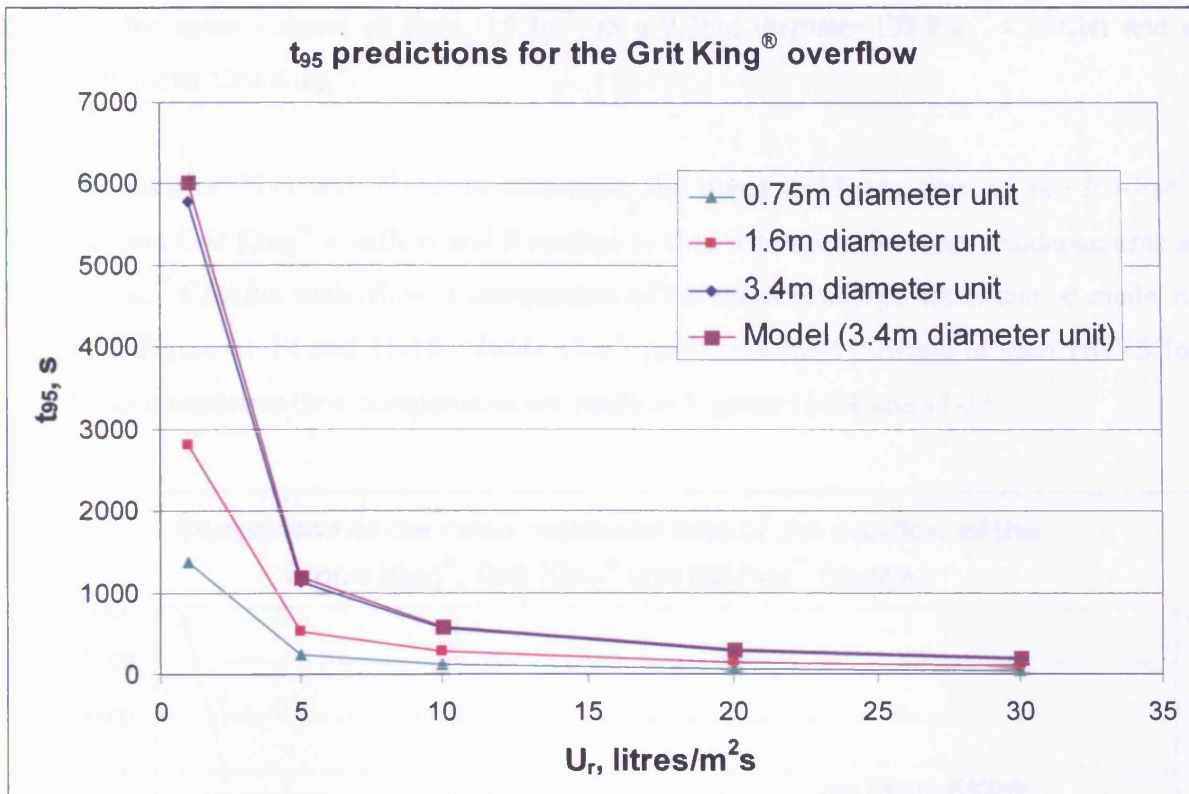
Figure 11-13. The trend in t_{95} at the Grit King® overflow and a fit of the model to a 3.4m diameter unit.

11.2.4 HDVS comparison

Mean residence time

Comparison of mean residence time is difficult to make. Comparisons of identical diameter HDVSs mean each will have a different volume and hence, the greater the fluid volume, the higher the expected mean residence time. Surface loading rate is currently used by Hydro International Plc to size these HDVSs for particle separation processes so identical volumes and surface loading rates will be compared.

A function that describes the volume of fluid in a HDVS with HDVS diameter will take the form of

$$V = KD^3 \qquad (11\text{-}16)$$

Where: K = constant

From Table 11-2 it has been found that for the Eff-Pac™ Clarifier K is approximately 1.195 and for the Grit King® K is approximately 0.543. Hence, a 3.4m diameter Storm King®

contains the same volume of fluid, 15.7m³, as a 2.36m diameter Eff-Pac™ Clarifier and a 3.12m diameter Grit King®.

Using Equations 11-5 and 11-14 to determine the mean residence time of the Eff-Pac™ Clarifier and Grit King® overflow and Equation 11-6 to determine the mean residence time at the Eff-Pac™ Clarifier underflow, a comparison of the mean residence times can be made, as shown in Figure 11-14 and 11-15. Table 11-17 gives the inlet flowrate in each HDVS for which mean residence time comparisons are made in Figures 11-14 and 11-15.
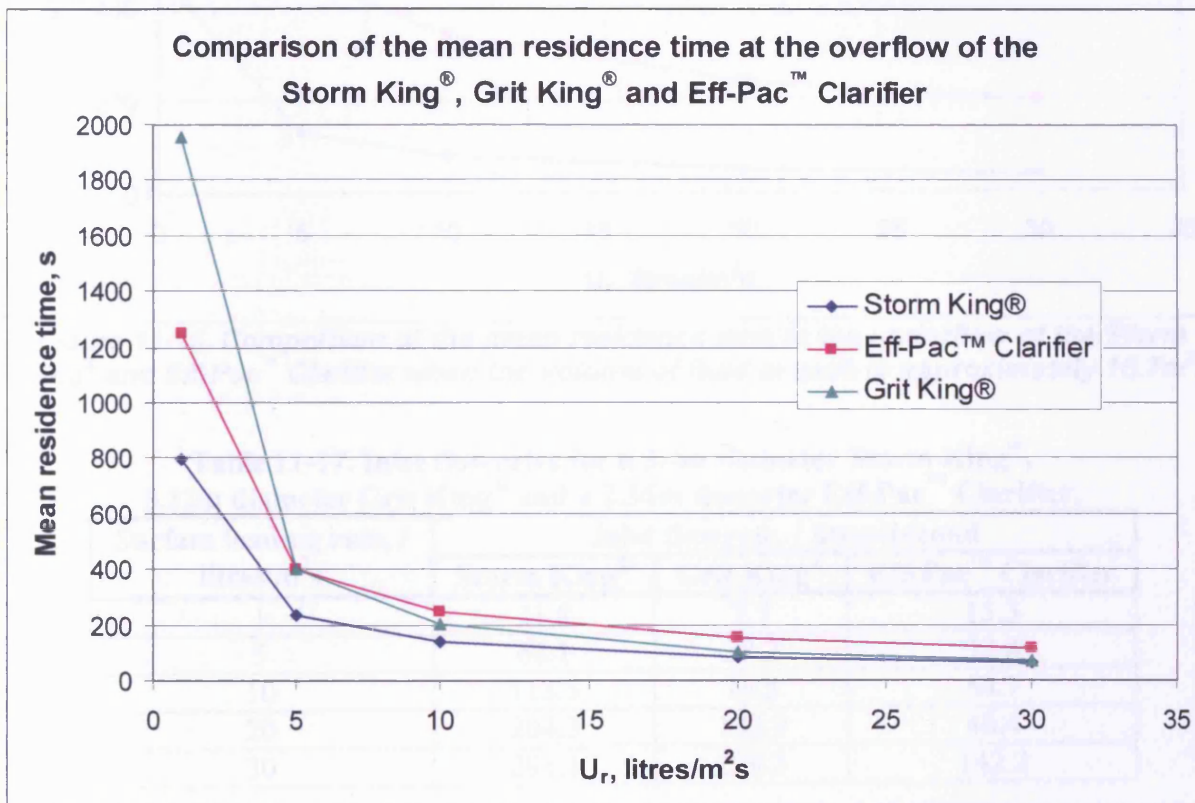
Figure 11-14. Comparison of the mean residence time at the overflow of the Storm King®, Grit King® and Eff-Pac™ Clarifier when the volume of fluid in each is approximately 15.7m³.

Comparison of the mean residence time at the underflow of the Storm King® and Eff-Pac™ Clarifier
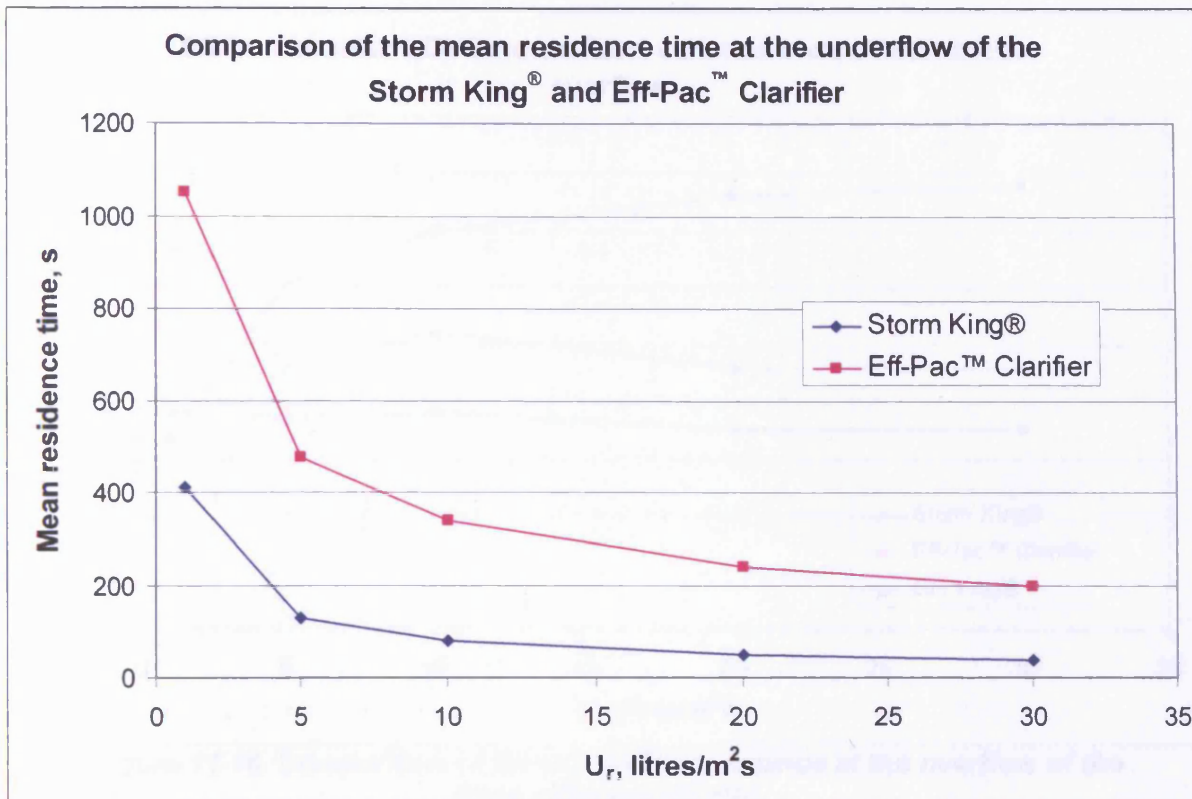
Figure 11-15. Comparison of the mean residence time at the underflow of the Storm King® and Eff-Pac™ Clarifier when the volume of fluid in each is approximately 15.7m³.

Table 11-17. Inlet flowrates for a 3.4m diameter Storm King®, 3.12m diameter Grit King® and a 2.36m diameter Eff-Pac™ Clarifier.

Surface loading rate, / litres/m²s	Inlet flowrate, / litres/second		
	Storm King®	Grit King®	Eff-Pac™ Clarifier
1	31.8	7.7	15.3
5	68.1	38.2	32.8
10	113.5	76.5	54.7
20	204.3	152.9	48.4
30	295.1	229.3	142.2

Normalised variance

It has been found from the results for the normalised variance from the ADM that there are some variations of normalised variance with separator size. These are generally quite small except in the case of the Storm King® underflow. Figure 11-16 compares the normalised variance at the overflow of the 0.75m diameter HDVSs.
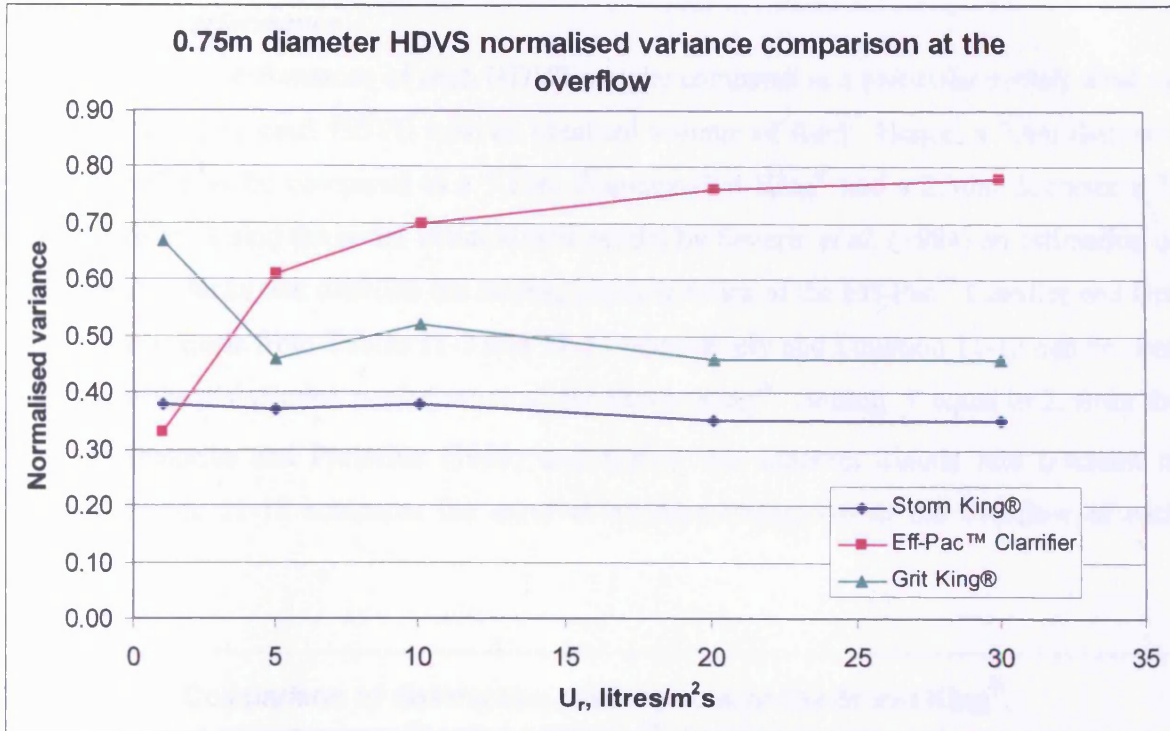
Figure 11-16. Comparison of the normalised variance at the overflow of the three different HDVSs.

Figure 11-17 compares the normalised variance at the underflow of the 0.75m diameter Eff-Pac™ Clarifier and the 3 different sizes of Storm King®.
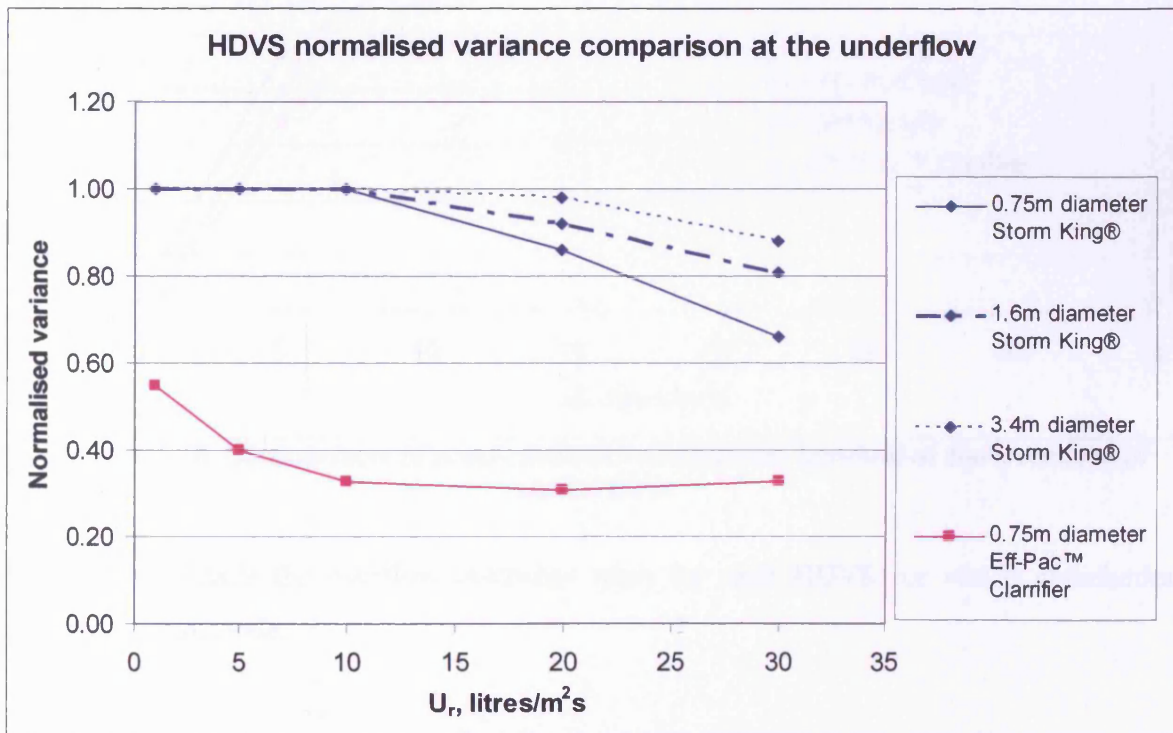
Figure 11-17. Comparison of the normalised variance at the underflow of the Eff-Pac™ Clarifier and the Storm King®.

Disinfection Performance

The disinfection performance of each HDVS may be compared at a particular surface loading rate by considering each HDVS with an identical volume of fluid. Hence, a 3.4m diameter Storm King® may be compared to a 3.12m diameter Grit King® and a 2.36m diameter Eff-Pac™ Clarifier. Using the series event kinetic model by Severin *et al.* (1984) an estimation of the number of tanks that describe the mixing characteristics of the Eff-Pac™ Clarifier and Grit King® can be made from Tables 11-3 and 11-13 respectively and Equation 11-13 can be used to describe the disinfection performance of the Storm King®. Setting j equal to 2, from the work of Pretorius and Pretorius (1999) and setting the apparent kinetic rate constant to $0.005s^{-1}$, Figure 11-18 compares the survival of micro-organisms at the overflow of each HDVS.

Comparison of disinfection performance of the Storm King®, Grit King® and the Eff-Pac™ Clarifier overflow
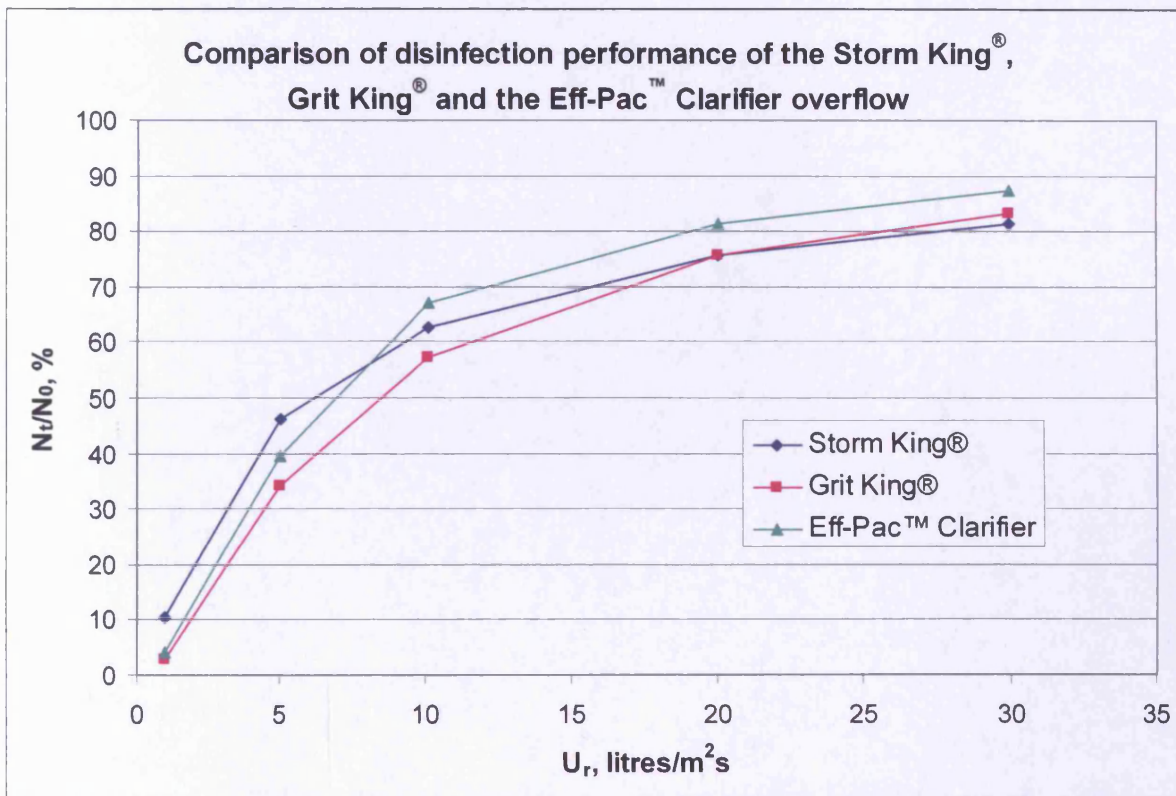
Figure 11-18. Comparison of predicted micro-organism survival at the overflow of each HDVS.

Table 11-18 details the overflow discharge rates for each HDVS for which disinfection comparisons are made.

Table 11-18. Overflow discharge rates for a 3.4m diameter
Storm King®, 3.12m diameter Grit King® and a 2.36m diameter Eff-Pac™ Clarifier.

Surface loading rate, / litres/m²s	Overflow discharge, / litres/second		
	Storm King®	Grit King®	Eff-Pac™ Clarifier
1	9.1	7.6	4.4
5	45.4	38	21.9
10	91.8	76	43.7
20	181.6	153	87.5
30	272.4	229	131.2

Head loss

From Tables 11-7, 11-12 and 11-16 it can be seen that there is negligible change in the head loss with the size of the separator. Hence, Figure 11-19 compares the head loss across the Eff-Pac™ Clarifier, Storm King® and Grit King®. Clearly the Eff-Pac™ Clarifier has the greatest head loss. This is followed by the Storm King® and the Grit King® has the lowest loss.
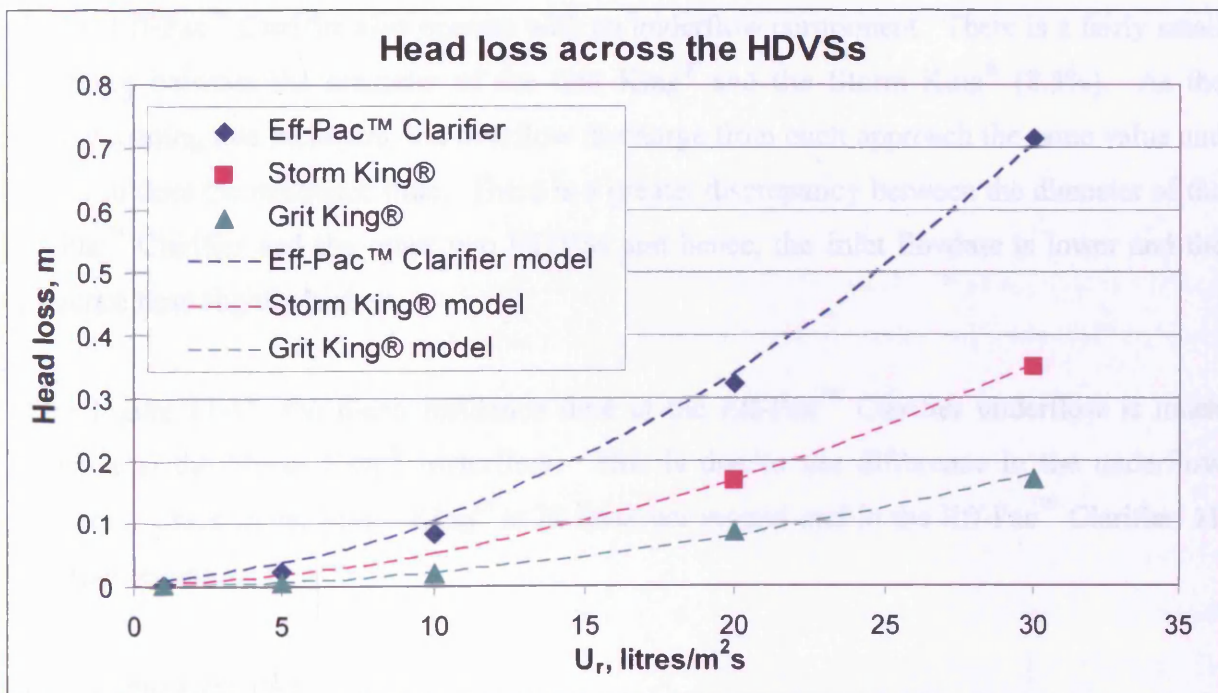
Figure 11-19. Predicted head loss across the HDVSs also showing the fit by the model for each separator.

11.3 Discussion

11.3.1 HDVS comparison

Mean residence time

From Figure 11-14 it can be seen that there is greatest difference in the mean residence time at the overflow of the three HDVSs at a rise velocity of 1 litre/m²s where the Grit King® has the highest residence time, followed by the Eff-Pac™ Clarifier and then the Storm King®. At a rise velocity of 5 litres/m²s the mean residence time of the Eff-Pac™ Clarifier and the Grit King® overflow are approximately the same with the Storm King® having a lower mean residence time. Above 5 litres/m²s the Eff-Pac™ Clarifier has the highest mean residence time. Although the Grit King® has a higher mean residence time than the Storm King® at a rise velocity above 1 litre/m²s, the mean residence time of each almost converge at 30 litres/m²s. The differences in mean residence time at the HDVS overflows appears to be due to the difference in the inlet flowrate, as can be seen by comparison of Table 11-17 with Figure 11-14. Although each HDVS has an identical volume of fluid, each has a different inlet flowrate of fluid due to maintaining a constant surface loading rate. The Storm King® and the Eff-Pac™ Clarifier also operate with an underflow component. There is a fairly small difference between the diameter of the Grit King® and the Storm King® (8.5%). As the surface loading rate increases, the overflow discharge from each approach the same value and hence, so does the residence time. There is a greater discrepancy between the diameter of the Eff-Pac™ Clarifier and the other two HDVSs and hence, the inlet flowrate is lower and the residence time slightly higher.

From Figure 11-15, the mean residence time at the Eff-Pac™ Clarifier underflow is much higher than the Storm King® underflow. This is due to the difference in the underflow discharge, which in the Storm King® is 22 litres per second and in the Eff-Pac™ Clarifier, 11 litres per second.

Mixing characteristics

All three HDVSs have quite different mixing characteristics at the overflow as shown in Figure 11-16. The first trend to note is that variations in mixing characteristics tend to occur at low surface loading rates/rise velocity. From the work carried out on the Grit King® in Section 5.3.2, where measurements of the static pressure have revealed there is not a vortex flow below approximately 3 litres per second, the variations in mixing characteristics at low

flowrates could be due to a diffuse flow within the HDVS. The same applies to the Storm King® and Eff-Pac™ Clarifier, in that as the surface loading rate increases, the segregated regions of flow change and hence so do the mixing characteristics.

The mixing characteristics at the overflow of the Storm King® are approximately constant over the full range of surface loading rates simulated and the mixing characteristics, based on the normalised variance which is just under 0.4, are the most appropriate for a disinfection process since it is the closest to plug flow. In Section 9.4.1 it can be seen that the normalised variance at the overflow of the Storm King® is not constant (Figure 9-21). This could be due to changes in the velocity profile at the inlet to the HDVS in the laboratory. The arrangement of the inlet pipe in the laboratory comprised of a sudden expansion from a 0.178m diameter pipe angled downwards at 14° into the Storm King® inlet which is a 0.5m diameter pipe, hence resulting in a jet. There is also a butterfly valve in the 0.178mm diameter pipe which is used to control the flow and hence, this will also change the velocity profile at the inlet with changes in flowrate. The inlet to the HDVS modelled for scaling is a horizontal 0.5m diameter pipe with a straight length of 40 diameters to allow a velocity profile to develop within the CFD model.

The Grit King® has fairly constant mixing characteristics between 5 and 30 litres/m²s where the normalised variance is just below 0.5. At a surface loading rate of 1 litre/m²s the normalised variance increases to just below 0.7 indicating that at this surface loading rate, a greater amount of mixing is occurring. This could be attributable to a very diffuse flow within the separator which may promote mixing.

The normalised variance at the overflow of the Eff-Pac™ Clarifier is approximately 0.35 at 1 litre/m²s and increases sharply to 0.6 at 5 litres/m²s. The normalised variance then appears to plateau towards 0.8 as the overflow surface loading rate approaches 30 litres/m²s indicating that the mixing characteristics stabilise as the surface loading rate increases. Hence, the Eff-Pac™ Clarifier exhibits a fairly high amount of mixing. A normalised variance of 1 corresponds to a completely mixed CSTR and thus, this configuration of HDVS isn't ideal for disinfection of wastewater at higher rise velocities due to the high mixing characteristics of the flow.

At the underflow of the Eff-Pac™ Clarifier the normalised variance reduces from 0.55 at 1 litre/m²s to approximately 0.33 at surface loading rates between 10 and 30 litres/m²s. At the Storm King® underflow between 1 and 10 litres/m²s the mixing characteristics are equivalent to a CSTR i.e. completely mixed. In the context of a disinfection process, this is not critical, as the fluid that passes through the underflow goes through the system for further treatment when the HDVS is used as a CSO treatment chamber. Above 10 litres/m²s the mixing characteristics tend towards plug flow with increasing surface loading rate and the rate at which the normalised variance changes with surface loading rate appears to vary with the size of the HDVS, where a larger HDVS has a slower rate of change than a small HDVS.

Disinfection

From Figure 11-18 it can be seen that the disinfection performance at the overflow of each HDVS is comparable with the Grit King® giving slightly better performance over the range of surface loading rates investigated.

Although the Eff-Pac™ Clarifier overflow generally has a slightly higher mean residence time than the two other HDVSs, as shown in Figure 11-14, disinfection performance is hindered by mixing characteristics that are generally characterised by 2 tanks in series and hence, closer to being completely mixed. The Storm King® has the lowest mean residence time of the three HDVSs but disinfection performance is enhanced by mixing characteristics that are described by 4 tanks in series which is closer to plug flow than the two other HDVSs. The Grit King® has residence time characteristics that are intermediary between the other two HDVSs where the mixing characteristics are characterised by 3 tanks in series. However, the Storm King® has the highest discharge at the overflow over the full range of surface loading rates, as shown in Table 11-18. Since the disinfection performance of the Storm King® is comparable to the other two HDVSs, the Storm King® is considered to have the best disinfection performance of all three.

Head loss

The loss coefficient is greatest for the Storm King® (2.96) followed by the Eff-Pac™ Clarifier (1.62) and the Grit King® has the lowest loss coefficient (1.01). For hydrocyclones it can be shown that other sources of pressure loss are small when compared to the centrifugal head loss (Bradley, 1965). This would therefore imply that the centrifugal effects are greatest in the Storm King® and lowest in the Grit King®. However, the head loss across the separators

at any particular surface loading rate modelled does not reflect the trend in loss coefficient where the Eff-Pac™ Clarifier has the greatest head loss followed by the Storm King® and the Grit King® has the lowest head loss. This is due to the diameter of the inlet pipe in each HDVS being different which influences the inlet velocity.

A limitation of the predictions for head loss is that a long pipe is not present at the overflow outlets and a possible error is that losses due to flow redevelopment have not been taken into account. This will not be a problem when there is a free falling jet at the overflow which is the case in the Grit King® and Storm King®.

11.3.2 Eff-Pac™ Clarifier

The underflow of the Eff-Pac™ Clarifier was specified as a pressure outlet and the underflow a velocity inlet with a negative velocity to obtain the required flow split. This method gave reasonable validation in Chapter 8. However, in the validation the surface loading rate did not exceed 13 litres/m^{2}s. A possible error in the models at higher loading rates than 13 litres/m^{2}s is that the position of the free surface which is fixed may have an effect on the predicted flow field which may induce error in the RTD predictions. Hence, ideally, studies of this HDVS at higher surface loading rates would be validated first. The same applies to the Storm King® where the highest overflow surface loading rate for which validated CFD data has been acquired is 18.4 litres/m^{2}s.

From the R_t^2 value of the TISM and ADM fit to the predicted RTDs of the Eff-Pac™ Clarifier, the ADM is a more appropriate model for representing the RTD of this HDVS. However, the fit by the TISM is still suitable for applying the number of tanks to predicting disinfection performance using Equation 3-18 by Severin *et al.* (1984) as an average R_t^2 value of 0.989 represents a good fit.

Scaling laws have been proposed that describe the mean residence time at the overflow and underflow of the Eff-Pac™ Clarifier and also t_{95} at each outlet which describes the time taken for the concentration of say disinfectant at the outlet to reach 95% of the inlet concentration in response to a step input. From Figures 11-4 to 11-7, it can be seen that these scaling laws

generally give a good fit and can be used as a useful design tool for estimating the mean residence time and t_{95}.

From Table 11-4, there is not a significant change of the normalised variance with HDVS diameter at the overflow and the underflow. From Table 11-3, the TISM tends to describe the mixing characteristics at the overflow as 2 CSTRs connected in series at surface loading rates of 10 litres/m^{2}s or higher but below this the number of tanks increases to 4 at 1 litre/m^{2}s and the number of tanks that describe the mixing characteristics between 1 and 10 litres/m^{2}s is dependent on the diameter of the HDVS. At the underflow the number of tanks that describe the mixing characteristics is 4 at surface loading rates above 10 litres/m^{2}s and below this surface loading rate the number of tanks is either 3 or 4 depending on the diameter of the HDVS. The dependency on the diameter of the HDVS at low overflow surface loading rates is possibly due to the number of tanks that gives the best fit being close to an integer number and is thus a limitation of the TISM to fit the RTD.

11.3.3 Storm King$^{®}$

From the R_t^2 value of the TISM and ADM fit to the predicted RTDs of the Storm King$^{®}$, the ADM is a more appropriate model for representing the RTD of this HDVS. The fit by the TISM is still suitable for applying the number of tanks to predicting disinfection performance using Equation 3-18 by Severin *et al.* (1984) as an average R_t^2 value of 0.981 represents a good fit.

Scaling laws have been proposed that describe the mean residence time at the overflow and underflow of the Storm King$^{®}$ and also t_{95} at each outlet. From Figures 11-8 to 11-11, it can be seen that these generally give a good fit and can be used as a useful design tool for estimating the mean residence time and t_{95}.

From Table 11-8, the number of tanks that describes the mixing characteristics at the overflow is 4 and is independent of the size of unit and the overflow surface loading rate. The same can be said about the underflow where the number of tanks is approximately 2.

11.3.4 Grit King®

From the R_t^2 value of the TISM and ADM fit to the predicted RTDs of the Grit King®, the ADM is a more appropriate model for representing the RTD of this HDVS. The fit by the TISM is still suitable for applying the number of tanks to predicting disinfection performance using Equation 3-18 by Severin *et al.* (1984) as an average R_t^2 value of 0.988 represents a good fit.

Scaling laws have been proposed that describe the mean residence time at the overflow of the Grit King® and also t_{95}. From Figures 11-12 and 11-13 it can be seen that the scaling laws generally give a good fit to the CFD-predicted data.

The TISM describes the mixing characteristics as being 3 tanks connected in series for all 3 sizes of HDVS over all surface loading rates with the exception of the 0.75m diameter unit operating at 1 litre/m²s where the number of tanks gives a better fit at 2.1.

11.4 Summary

- Scaling laws that predict the mean residence time of the Storm King®, Grit King® and Eff-Pac™ Clarifier have been determined from CFD-predicted residence times and which take the form of $\bar{t} = ZD_{HDVS}U_r^{-Y}$ where Z and Y are constants.

- Scaling laws have been determined for t_{95}, defined as the time when C/C_0 has risen to 0.95 for a particular outflow and this gives an estimate of the time required before predicted disinfection rates occur.

- It has been demonstrated that for a separator diameter between 0.75 and 3.4m, the mean residence time can be predicted and an estimate of the number of tanks that define the mixing characteristics can be made and hence, disinfection rates may be estimated. An example of this has shown that all three HDVSs with identical volumes of fluid give a similar disinfection performance at identical surface loading rates.

- The Grit King® has the lowest head loss compared to the Eff-Pac™ Clarifier and Storm King®.

- For a disinfection application where an underflow component is required, the Storm King® is the most appropriate HDVS as this has the lower head loss compared with the Eff-Pac™ Clarifier and also a higher discharge at the overflow at an identical surface loading rate for a unit with the same fluid volume as the Eff-Pac™ Clarifier.

12 HDVS flow characteristics

A comparison and analysis of the mixing characteristics and flow fields within the three different HDVSs are made to give an insight into the fluid mechanics within these systems. From Section 11.2.4, it has been observed that the predicted mixing characteristics tend to change mainly at very low surface loading rates. To make a comparison between the HDVSs, a surface loading rate of 20 litres/m^{2}s has been chosen, since the mixing characteristics of the devices do not change significantly with higher loading rates with the exception of the Storm King$^®$ underflow. Comparisons are made between HDVSs with identical fluid volumes, hence, a 3.4m diameter Storm King$^®$, 2.36m diameter Eff-Pac$^™$ Clarifier and a 3.12m diameter Grit King$^®$.

Although it has been shown that the predicted flow field may vary for a hybrid mesh as discussed in Section 6.2.2, the results presented are intended to give an insight into the hydraulic behaviour within the three HDVSs. It is believed that the predictions are reasonable based on validation of the residence time of the 3.4m diameter Storm King$^®$, 1.6m diameter Grit King$^®$ and 0.75m diameter Eff-Pac$^™$ Clarifier as well as the validation of the pressure difference between the inlet and tapping points on the 0.75m diameter Grit King$^®$.

The turbulence within the HDVS is not discussed as there has not been any validation of the fluctuating velocity components in any of the vortex separators.

12.1 Mixing characteristics

For each comparison, the UDS has been introduced in the inlet pipe and the times indicated in Figure 12-1 to 12-3 consider the UDS to be introduced in the inlet pipe half a HDVS diameter upstream from the centreline of the HDVS. (The UDS was actually introduced 40 diameters upstream on the inlet boundary as this is the simplest method of defining the boundary condition in the CFD software. However, the time taken for the UDS to travel down the inlet pipe can be computed within the CFD code).

12.1.1 Storm King$^®$

Figure 12-1 demonstrates the mixing characteristics of the Storm King$^®$. The inlet can be seen at the left of the HDVS and is positioned behind the separator with the fluid passing into the HDVS from left to right. At 3 seconds the onset of the UDS can be seen at the right of the

figure due to fluid emerging from the inlet. At 24 seconds, the UDS has dispersed around the outside of the HDVS. A small amount of short circuiting appears to be taking place at the right of the separator where it can be seen that UDS is passing between the baffle plates. This region would therefore be responsible for the onset of tracer in the RTD. At 66 seconds, the UDS is dispersed throughout the HDVS. On the outside between the dip plate and vessel walls the concentration is approaching the inlet concentration. Between the weir and the dip plate and along the overflow channel the concentration of UDS is approximately half the inlet concentration. At the very centre under the baffle plate and stiffeners the UDS concentration is lowest and hence the residence time in this region is comparatively high. This region is therefore quite likely to be responsible for the tailing of the RTD. The UDS is almost uniformly dispersed throughout the Storm King® at 192 seconds.
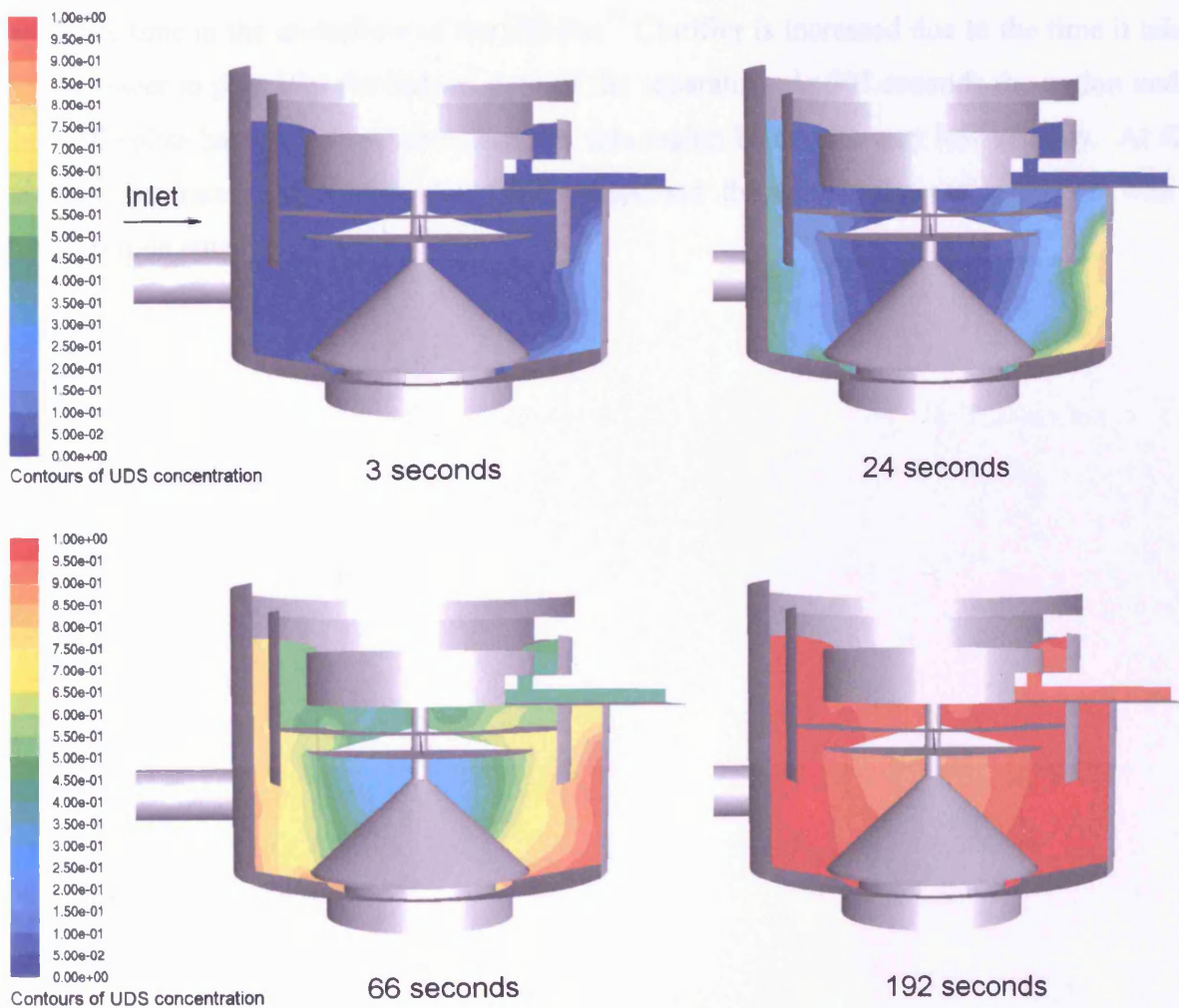
Figure 12-1. A step input of UDS into a 3.4m diameter Storm King® operating with a surface loading rate of 20 litres/m²s.

12.1.2 Eff-Pac™ Clarifier

Figure 12-2 shows a step input of a tracer into the Eff-Pac™ Clarifier. The inlet is positioned behind the separator with fluid entering the HDVS from left to right. At 4 seconds the onset of tracer entering the HDVS can be seen to the right and at 25 seconds, the tracer has dispersed around the outside of the HDVS. At 67 seconds the tracer is mixing around the outside of the HDVS between the dip plate and the vessel walls. The tracer can be seen to be passing up through the HDVS along the inside of the dip plate. A central core extends from the baffle plate down to the underflow where the concentration of UDS is very low. This is in contrast to the Storm King® where only a very small region under the baffle plate has a low concentration of tracer. At 193 seconds the concentration of tracer in the central core is approximately half the inlet concentration whereas in the Storm King®, at 193 seconds, the tracer is almost completely dispersed with a concentration equal to the inlet. Thus, the residence time in the underflow of the Eff-Pac™ Clarifier is increased due to the time it takes for the tracer to pass into the central core of the separator. At 301 seconds the region under the baffle plate has the lowest concentration, this region being of a very low velocity. At 427 seconds the tracer has almost completely dispersed throughout the entire HDVS with a concentration equal to the inlet.
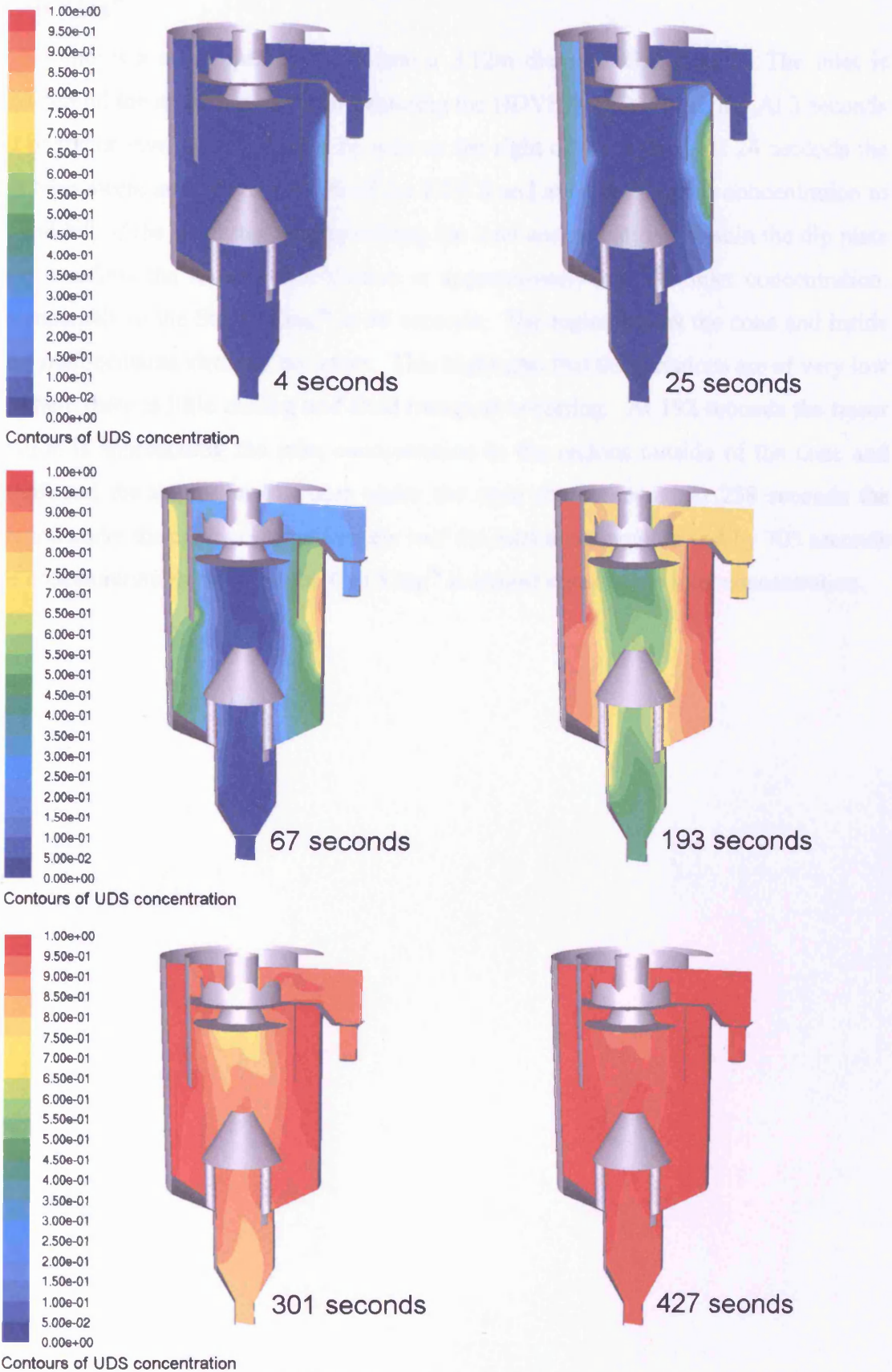
Figure 12-2. A step input of UDS into a 2.36m diameter Eff-Pac™ Clarifier operating with a surface loading rate of 20 litres/m²s.

12.1.3 Grit King®

Figure 12-3 shows a step input of tracer into a 3.12m diameter Grit King®. The inlet is positioned behind the separator with fluid entering the HDVS from left to right. At 3 seconds the onset of tracer into the HDVS can be seen to the right of the figure. At 24 seconds the tracer has been swept around the outside of the HDVS and at 66 seconds the concentration to the right and left of the separator is approaching the inlet concentration. Within the dip plate and at the overflow the tracer concentration is approximately half the inlet concentration. This is comparable to the Storm King® at 66 seconds. The region below the cone and inside the central shaft contains virtually no tracer. This highlights that these regions are of very low velocity where there is little mixing and fluid transport occurring. At 192 seconds the tracer concentration is approaching the inlet concentration in the regions outside of the cone and central shaft and the migration of tracer under the cone can be seen. At 258 seconds the concentration under the cone is approximately half the inlet concentration and by 705 seconds the tracer concentration throughout the Grit King® is almost equal to the inlet concentration.
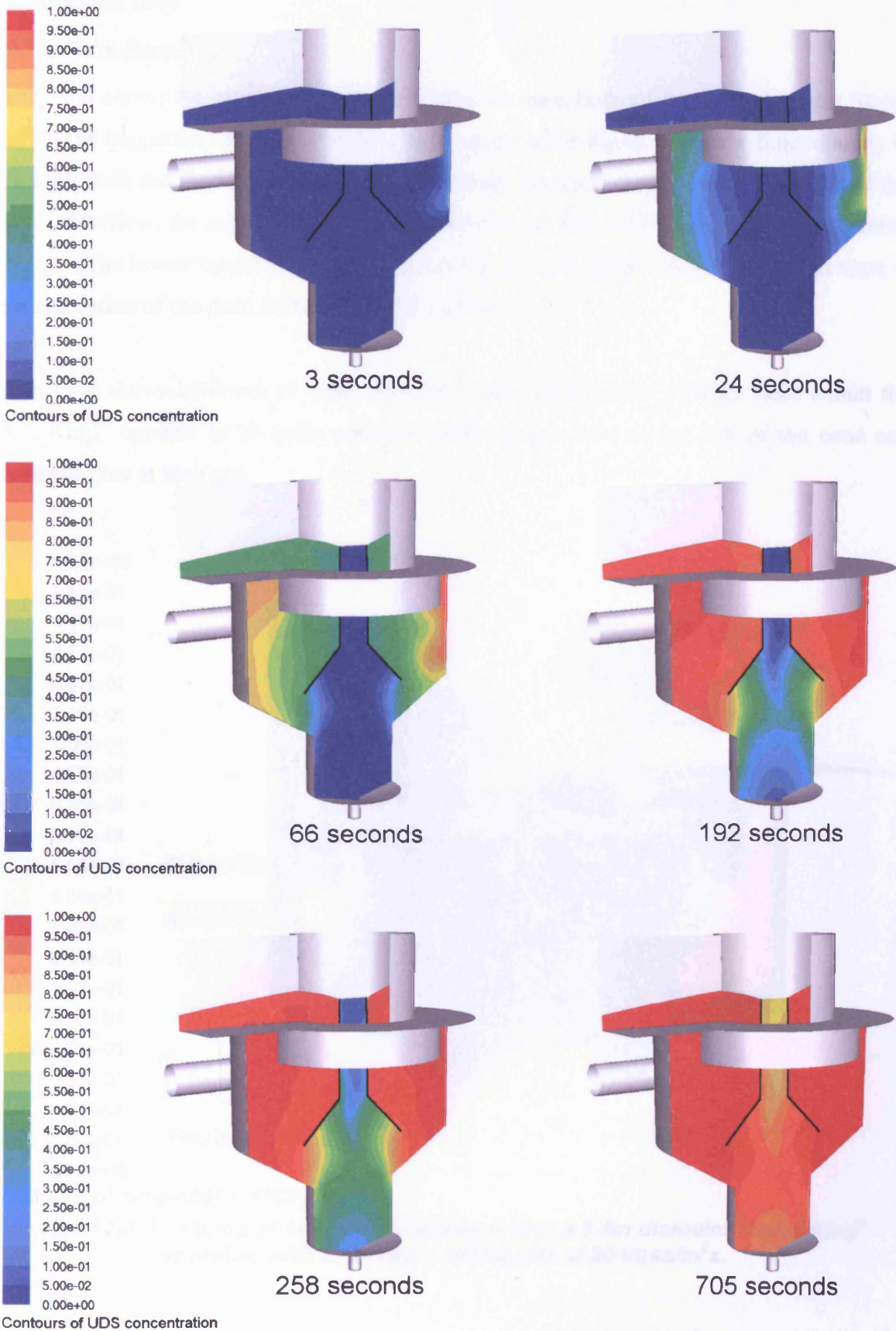
Figure 12-3. A step input of UDS into a 3.12m diameter Grit King® operating with a surface loading rate of 20 litres/m²s.

12.2 Velocity field

12.2.1 Storm King®

Figure 12-4 shows the tangential velocity within the main body of the 3.4m diameter Storm King®. The tangential velocity is highest to the right of the figure where the fluid velocity is quite high from the fluid entering the HDVS through the inlet. At the centre to the left of the central underflow, the region that has been whitened out for clarity has a negative tangential velocity. (The lowest tangential velocity in this region is -0.1m/s). This suggests that there is some separation of the fluid from the central underflow.

Figure 12-5 shows contours of axial velocity. Quite clearly, the velocity field within the Storm King® appears to be quite complex with upward flow to the left of the cone and downward flow at the right.

1.01e+00
9.58e-01
9.07e-01
8.57e-01
8.07e-01
7.56e-01
7.06e-01
6.55e-01
6.05e-01
5.54e-01
5.04e-01
4.54e-01
4.03e-01
3.53e-01
3.02e-01
2.52e-01
2.02e-01
1.51e-01
1.01e-01
5.04e-02 **Positive**
0.00e+00
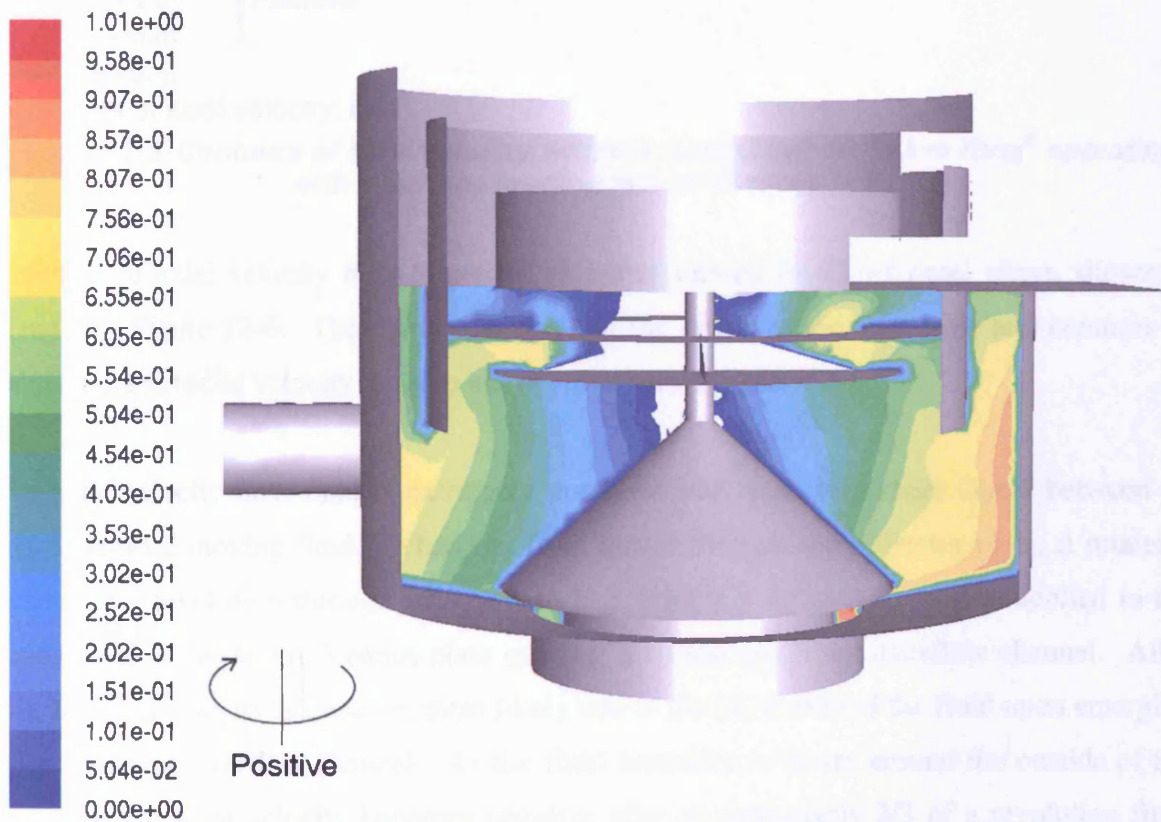
Contours of tangential velocity, m/s

***Figure 12-4. Contours of tangential velocity within a 3.4m diameter Storm King®
operating with a surface loading rate of 20 litres/m²s.***
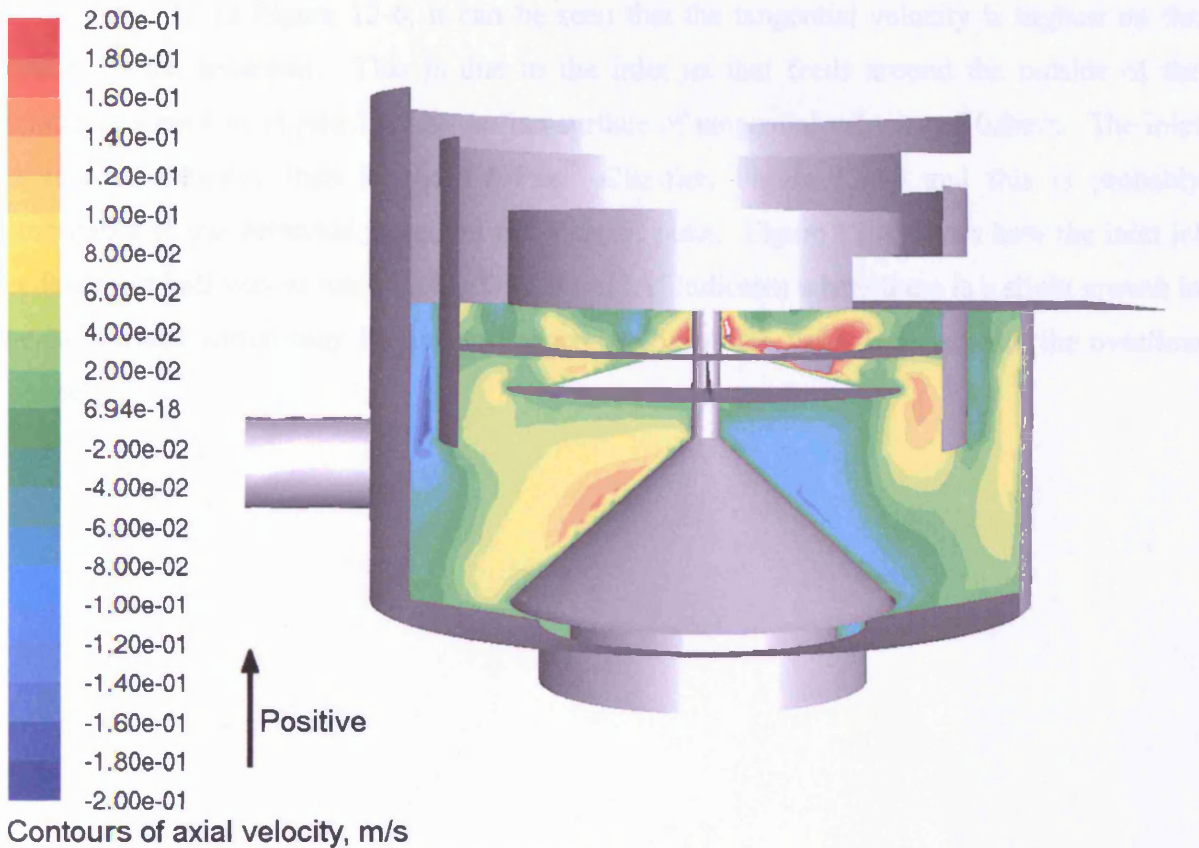
Figure 12-5. Contours of axial velocity within a 3.4m diameter Storm King® operating with a surface loading rate of 20 litres/m²s.

Contours of axial velocity may therefore be better viewed in a horizontal plane, shown in plane 'A', Figure 12-6. The plane cuts through the centre of the inlet pipe and contours of tangential and radial velocity are also shown in planes 'B' and 'C'.

The axial velocity flow field is extremely complex with numerous shear layers between up and downward moving fluid. When the fluid leaves through the deflector plate, it rotates a quarter of a revolution through which there is primarily a downward motion applied to the fluid which is due to the Venturi plate guiding the fluid under the overflow channel. After this, the axial velocity is positive, most likely due to the expansion of the fluid upon emerging from under the overflow channel. As the fluid continues to rotate around the outside of the separator, the axial velocity becomes negative after approximately 2/3 of a revolution from the deflector plate. This is possibly due to the Venturi plate guiding the fluid under the overflow channel. The presence of the deflector plate and the continuous influx of fluid results in a region of positive axial velocity and negative radial velocity as shown in plane 'C' to the left of the cone, as fluid takes the path of least resistance which is up towards the overflow.

From plane 'B' in Figure 12-6, it can be seen that the tangential velocity is highest on the outside of the separator. This is due to the inlet jet that feeds around the outside of the separator, shown in Figure 12-7 by an iso-surface of tangential velocity of 0.8m/s. The inlet jet is less diffusive than in the Eff-Pac™ Clarifier, Figure 12-14 and this is probably attributable to the deflector plate and the Venturi plate. Figure 12-8 shows how the inlet jet feeds almost half way around the HVDS. Point 'A' indicates where there is a slight growth in the iso-surface which may be due to the expansion of the fluid from beneath the overflow channel.
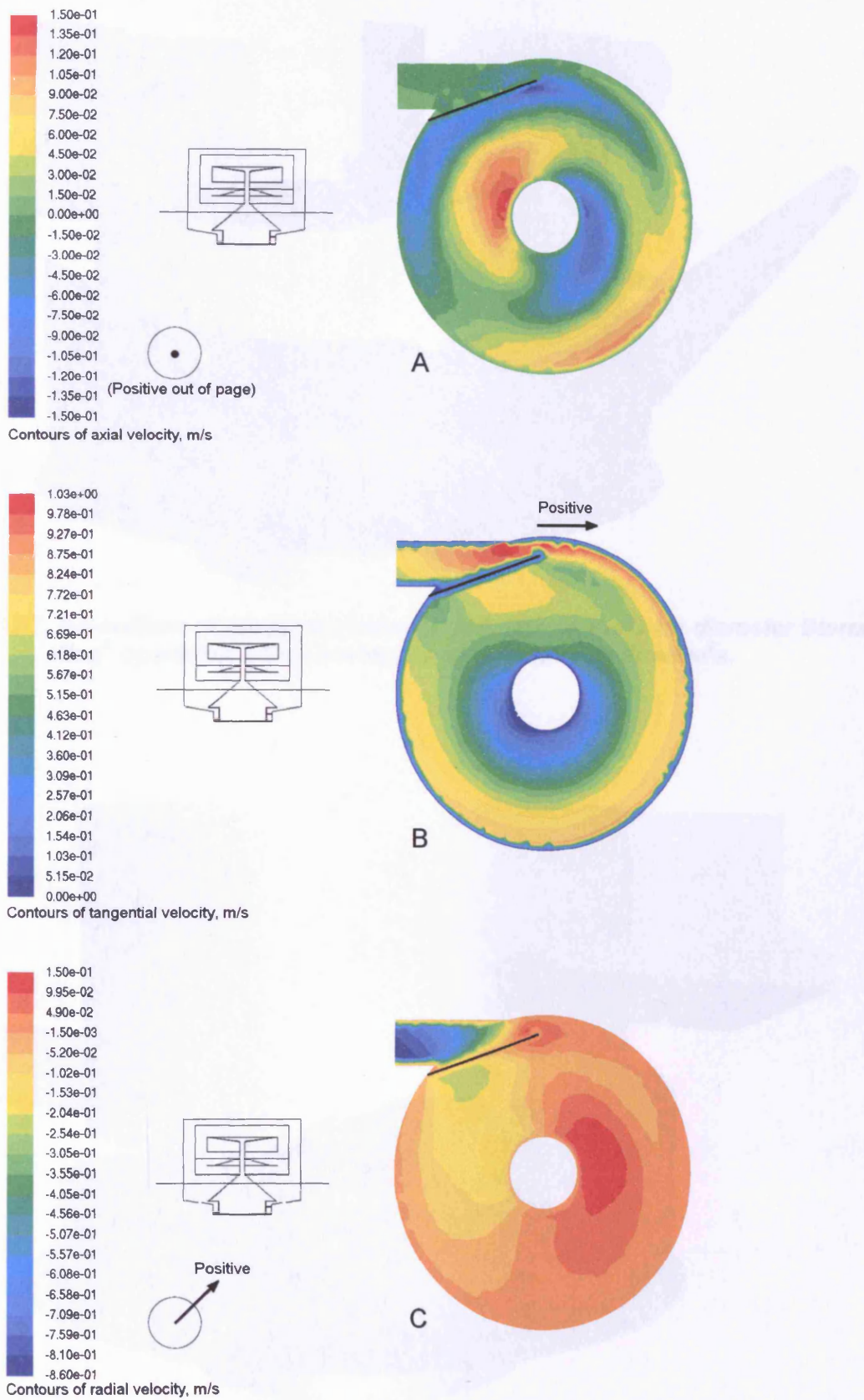
Figure 12-6. Contours of axial, tangential and radial velocity within a 3.4m diameter Storm King® operating with a surface loading rate of 20 litres/m²s.
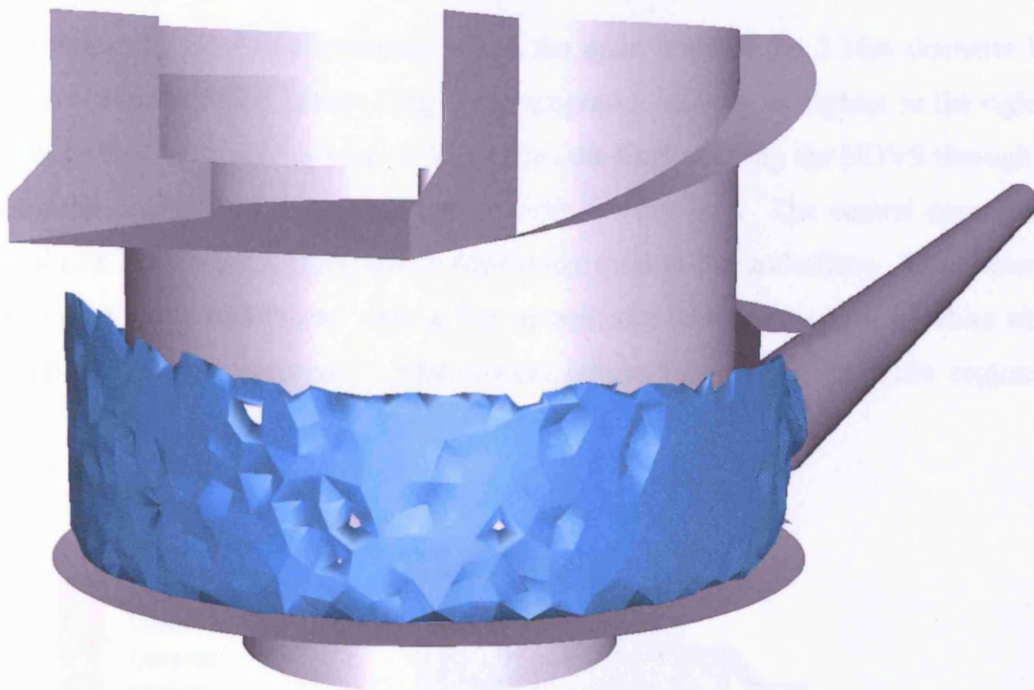
Figure 12-7. Iso-surface of tangential velocity of 0.8m/s in the 3.4m diameter Storm King® operating with a surface loading rate of 20 litres/m²s.
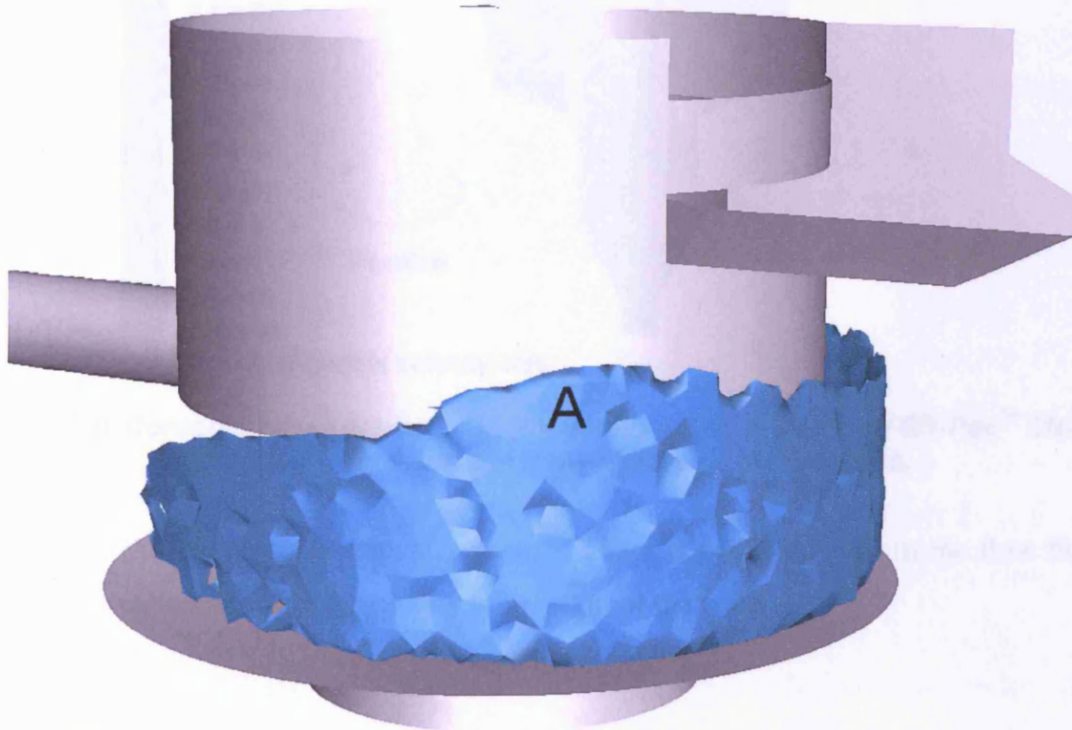
Figure 12-8. Iso-surface of tangential velocity of 0.8m/s in the 3.4m diameter Storm King® operating with a surface loading rate of 20 litres/m²s.

12.2.2 Eff-Pac™ Clarifier

Figure 12-9 shows the tangential velocity within the main body of the 2.36m diameter Eff-Pac™ Clarifier. Similar to the Storm King®, the tangential velocity is highest to the right of the figure where the fluid velocity is quite high from the fluid entering the HDVS through the inlet. Along the central core the tangential velocity is very low. The central core of low velocity fluid fills the sludge hopper, hence restricting fluid to the underflow. This increases the residence time in the underflow. Along the central core there are regions in white where the tangential velocity is negative. (The lowest tangential velocity in these regions is -0.06m/s).

Contours of tangential velocity, m/s

Figure 12-9. Contours of tangential velocity within a 2.36m diameter Eff-Pac™ Clarifier operating with a surface loading rate of 20 litres/m²s.

Figure 12-10 shows contours of axial velocity. There is non-symmetry in the flow field as shown by the region of negative velocity to the right of the cone.
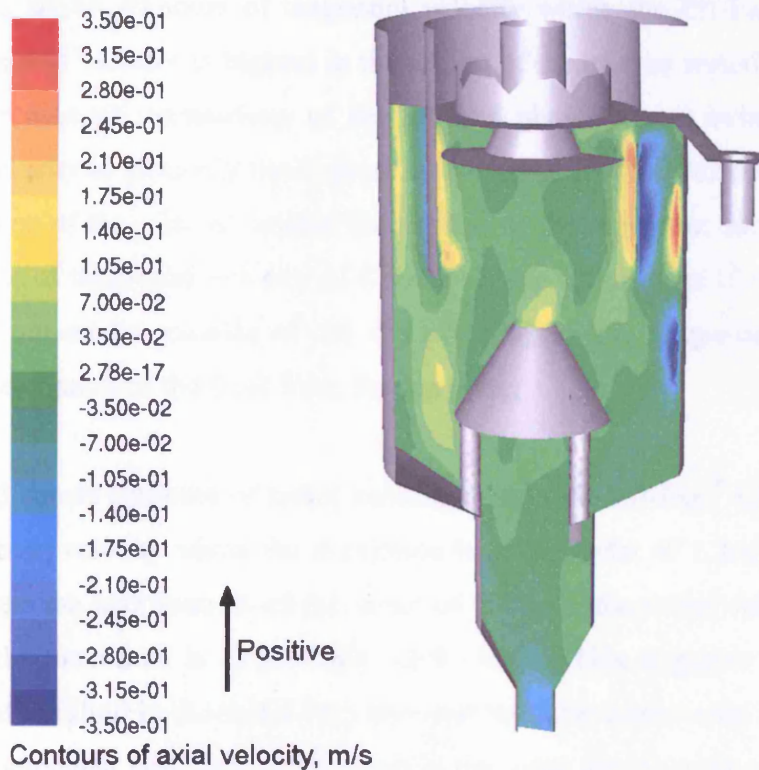
Figure 12-10. Contours of axial velocity within a 2.36m diameter Eff-Pac™ Clarifier operating with a surface loading rate of 20 litres/m²s.

Figure 12-11 shows a series of surfaces of axial velocity within the Eff-Pac™ Clarifier. Plane 'A' shows the axial velocity just below the baffle plate. A high fluid velocity exists on the inside of the dip plate where the fluid is flowing up between the dip plate and baffle plate towards the overflow. On the outside of the dip plate to the right there is a distinct region of upward and downward moving fluid and hence a shear zone exists between these. The axial velocity is positive on the outside of the separator and this is attributable to the expansion of the inlet jet into the HDVS which is shown by an iso-surface of tangential velocity in Figure 12-14. Plane 'B', Figure 12-11, shows that the shear zone on the outside of the dip plate has extended almost all the way round the dip plate. In plane 'C' a shear zone exists between the downward moving fluid and the upward moving fluid below the dip plate. The axial velocity of the fluid from the inlet is approximately zero due to equal expansion of the inlet jet above and below the horizontal plane of the inlet. In the centre of plane 'D' there is some upward moving fluid in the centre of the cone and a region of downward moving fluid at the top of the plane. This downward moving fluid is once again attributable to the expansion of the inlet jet and can be seen to rotate around the separator as the planes extend down through the HDVS as shown in plane 'E' and 'F'. Figure 12-11 shows that there are multiple shear zones within the Eff-Pac™ Clarifier demonstrating the complex flow patterns within the HDVS.

Figure 12-12 shows contours of tangential velocity within the Eff-Pac™ Clarifier. In plane 'C' the tangential velocity is highest in the region of the inlet as would be expected and is out of range for ease of comparison of the various planes hence, being whitened out. The tangential velocity is generally the highest on the outside of the HDVS, this being attributable to the diffusion of the inlet jet around the outside of the separator, shown in Figure 12-14 by an iso-surface of tangential velocity of 0.9m/s. Plane 'A', Figure 12-12, shows a region that is whitened out on the outside of the dip plate where the tangential velocity is negative, suggesting separation of the fluid from the dip plate.

Figure 12-13 shows contours of radial velocity within the Eff-Pac™ Clarifier. In comparison to the tangential velocity where the maximum is of the order of 1.2m/s and contours of axial velocity where the maximum is of the order of 0.35m/s, the radial velocity is generally very low where the maximum is of the order of 0.15m/s. This suggests that there is very little movement of the fluid in the radial direction and the flow can be seen to be dominated by the tangential component with some movement in the axial direction, as would be expected from a vortex flow. The radial velocity component is strongest in the plane of the inlet pipe, plane 'C'. The maximum radial velocity in the region that is whitened out in the top half of the plane is approximately 0.27m/s and in the region to the right of the inlet the minimum radial velocity is approximately -0.31m/s. The reason the radial velocity is very high in the top half of plane 'C' is due to the inlet jet feeding around the outside of the HDVS. The radial velocity to the right of the inlet pipe is negative due to the inlet jet forcing fluid to migrate towards the centre of the HDVS.
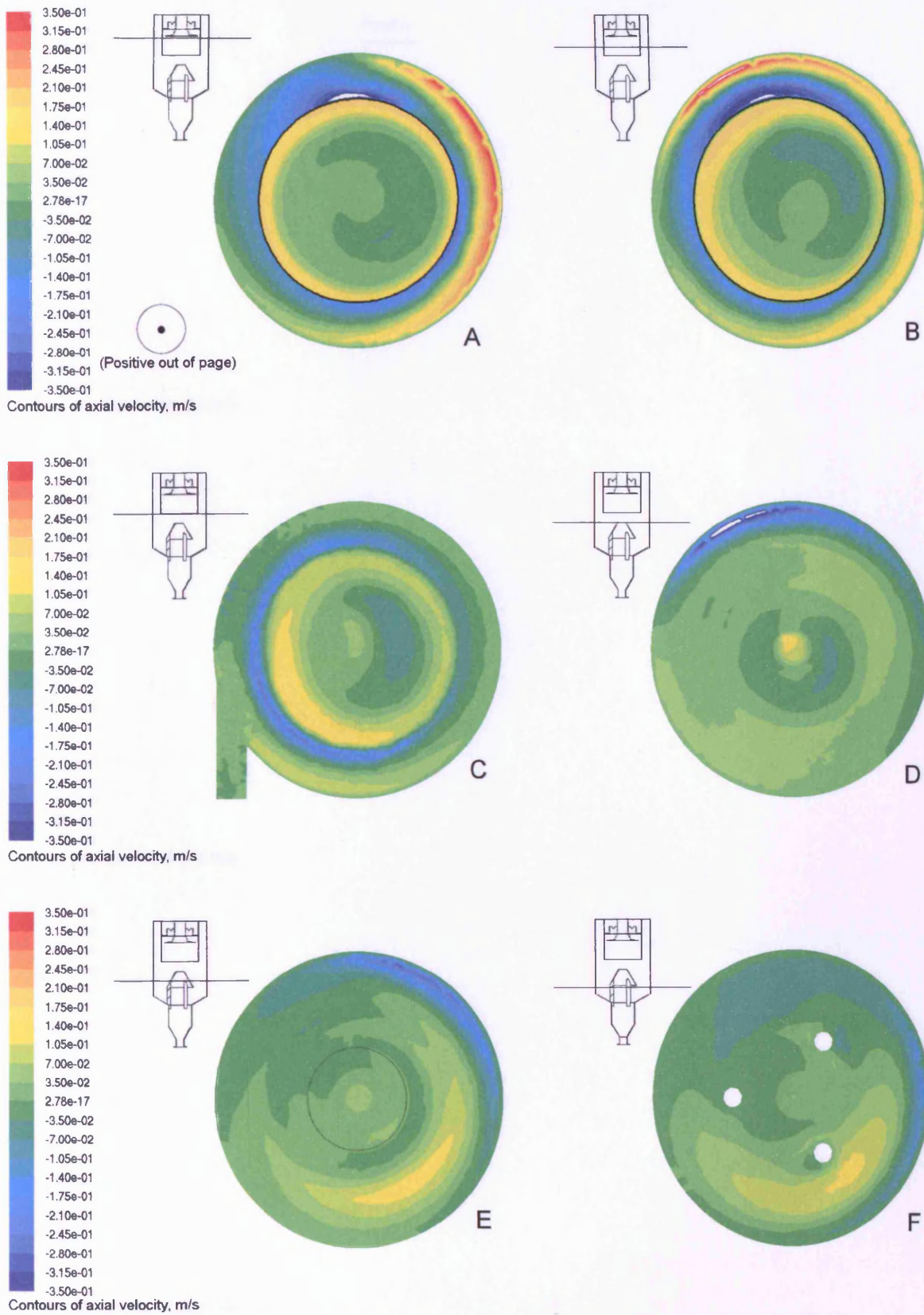
Figure 12-11. Planes of axial velocity within a 2.36m diameter Eff-Pac™ Clarifier operating with a surface loading rate of 20 litres/m²s.
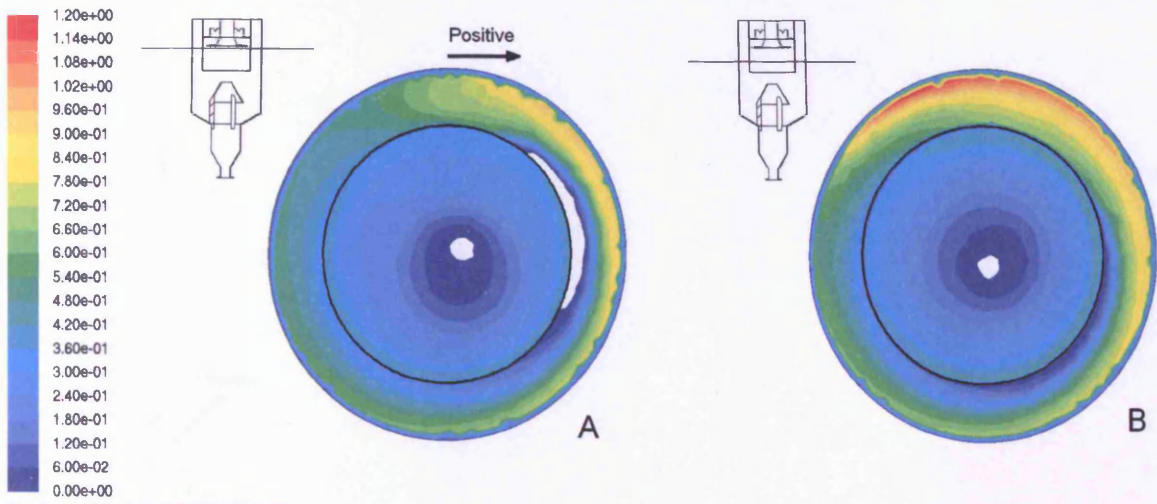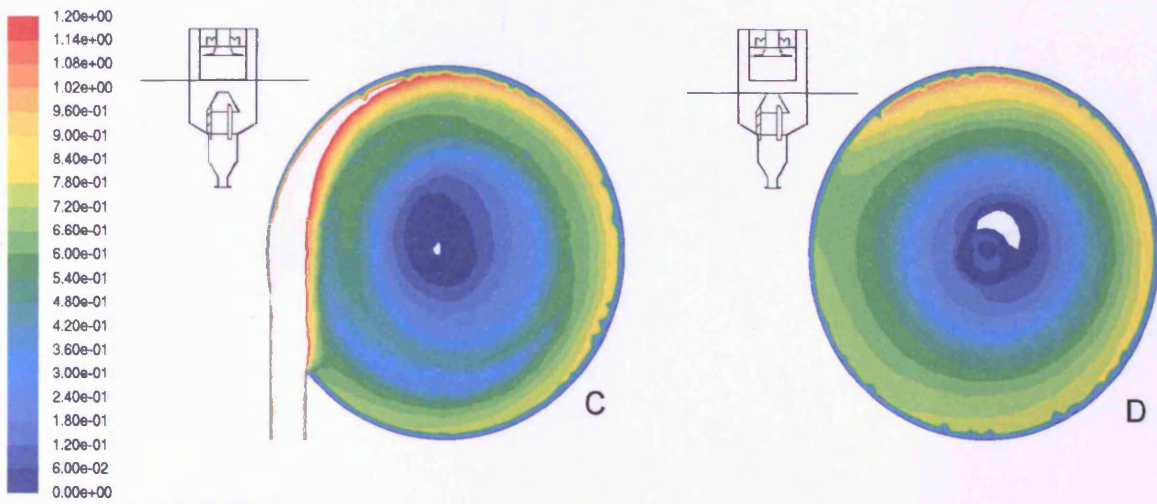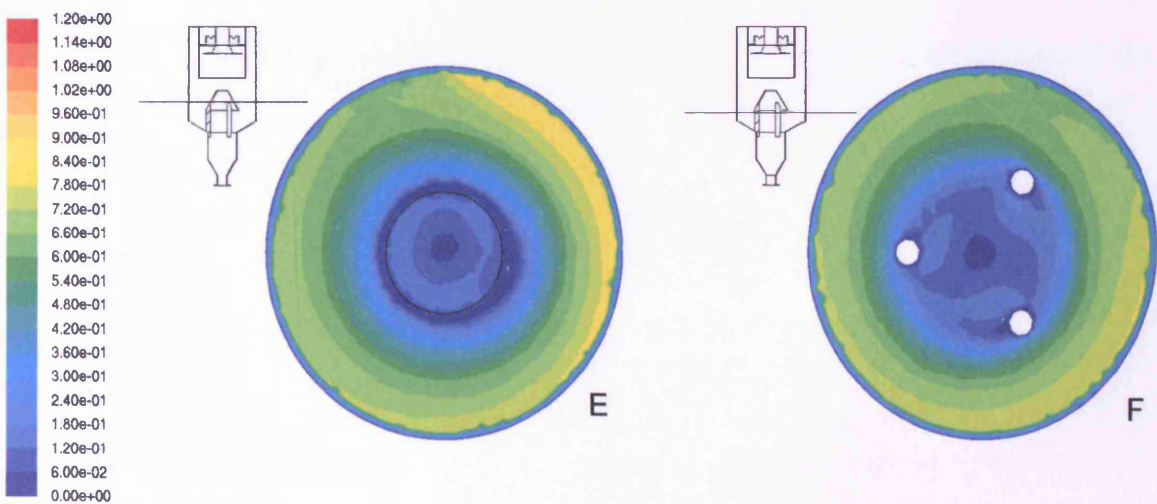
Figure 12-12. Planes of tangential velocity within a 2.36m diameter Eff-Pac™ Clarifier operating with a surface loading rate of 20 litres/m²s.
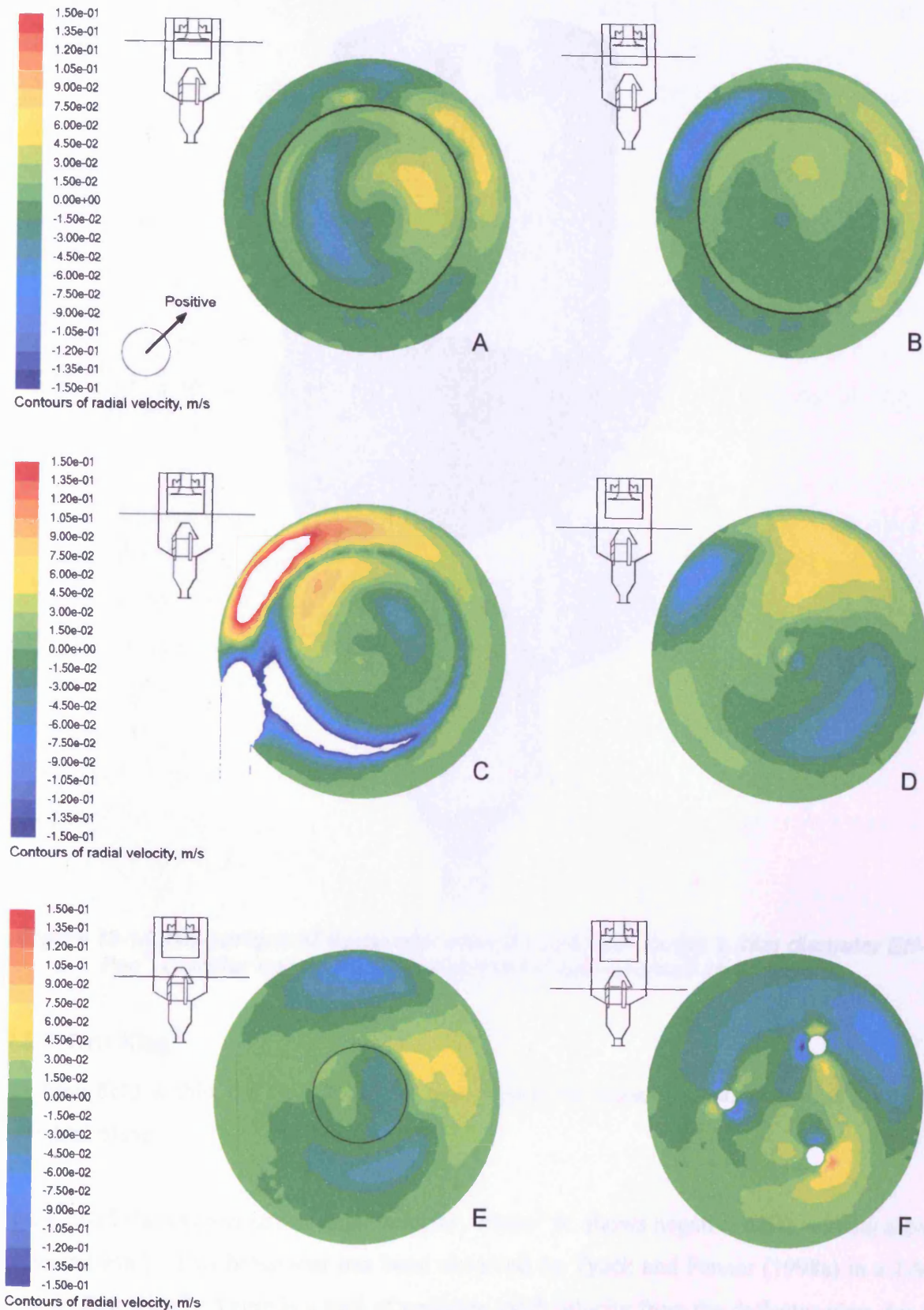
Figure 12-13. Planes of radial velocity within a 2.36m diameter Eff-Pac™ Clarifier operating with a surface loading rate of 20 litres/m²s.
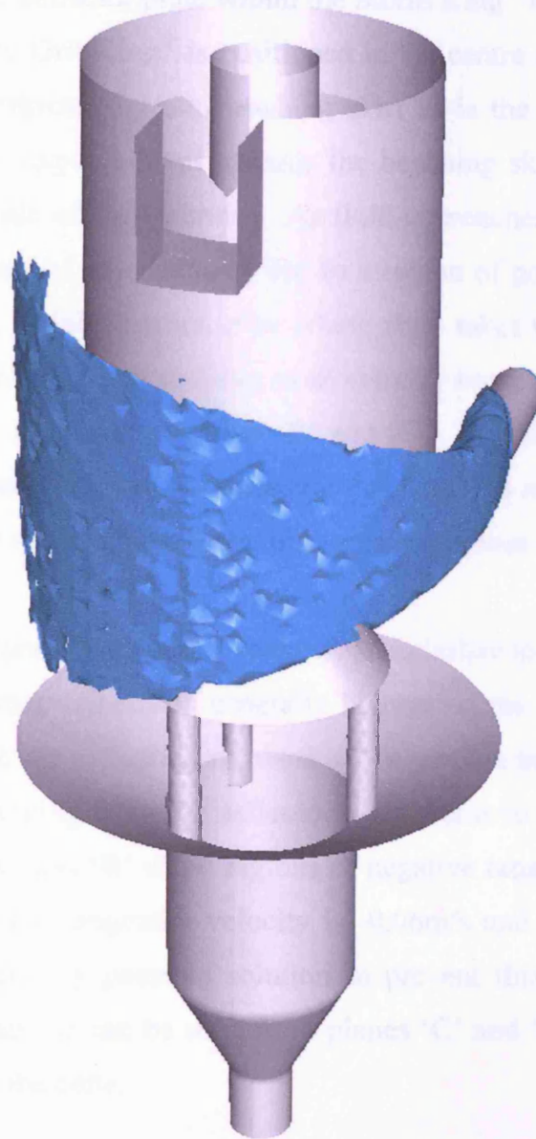
Figure 12-14. Iso-surface of tangential velocity of 0.9m/s in the 2.36m diameter Eff-Pac™ Clarifier operating with a surface loading rate of 20 litres/m²s.

12.2.3 Grit King®

The flow field within the Grit King® is best viewed by examining surfaces that lie in the horizontal plane.

Figure 12-15 shows contours of axial velocity. Plane 'A' shows negative axial velocity above the central shaft. This behaviour has been observed by Tyack and Fenner (1998a) in a 1.6m diameter Grit King®. There is a trail of negative axial velocity from the deflector plate due to the inlet jet of fluid. This is most noticeable in plane 'B' and is possibly a consequence of a section of the base of the deflector plate which is partly cut away allowing the fluid to expand

downwards. Although the deflector plate within the Storm King® is of a similar design to the Grit King®, the inlet of the Grit King® is positioned in the centre of the main vessel and the inlet jet therefore isn't restricted by the benching skirt as is the case in the Storm King®. Hence, the fluid is free to expand down towards the benching skirt. The fluid thus rotates around and down the outside of the separator. As fluid approaches the deflector plate it may be drawn towards the centre of the separator due to a region of positive axial velocity to the left of the deflector plate, which appears to be where fluid takes the path of least resistance towards the overflow. This region of positive axial velocity however twists around the centre of the separator clockwise as shown in planes 'B' and 'C'. In plane 'D' the axial velocity is dominant around the circumference of the cone and this region is responsible for drawing any fluid up through the centre of the separator should it reach the base of the cone.

Figure 12-16 shows contours of tangential velocity. Dissimilar to the Storm King® and Eff-Pac™ Clarifier, the tangential velocity is generally highest on the inner part of the separator and not along the wall with the exception of plane 'A' where the tangential velocity is high in the inlet. The inlet jet emerging from the deflector plate seems to decay rapidly, as shown in plane 'A'. Both planes 'A' and 'B' show regions of negative tangential velocities which are in white. Here the minimum tangential velocity is -0.06m/s and suggests separation of the fluid from the central shaft. A possible solution to prevent this could be to increase the diameter of the central shaft. It can be seen from planes 'C' and 'D' that there is some very low tangential flow within the cone.

Figure 12-17 shows contours of radial velocity. The region of lowest radial velocity, plane 'A', is to the left of the deflector plate where the fluid is forced towards the centre of the separator. The lowest value in the region which is in white is -0.3m/s. Plane 'A' also shows a region of high radial velocity extending from the deflector plate. This is due to fluid from the inlet feeding around the outside of the separator.

2.00e-01
1.80e-01
1.60e-01
1.40e-01
1.20e-01
1.00e-01
8.00e-02
6.00e-02
4.00e-02
2.00e-02
6.94e-18
-2.00e-02
-4.00e-02
-6.00e-02
-8.00e-02
-1.00e-01
-1.20e-01
-1.40e-01
-1.60e-01
-1.80e-01
-2.00e-01

(Positive out of page)

Contours of axial velocity, m/s

A

B

C

D
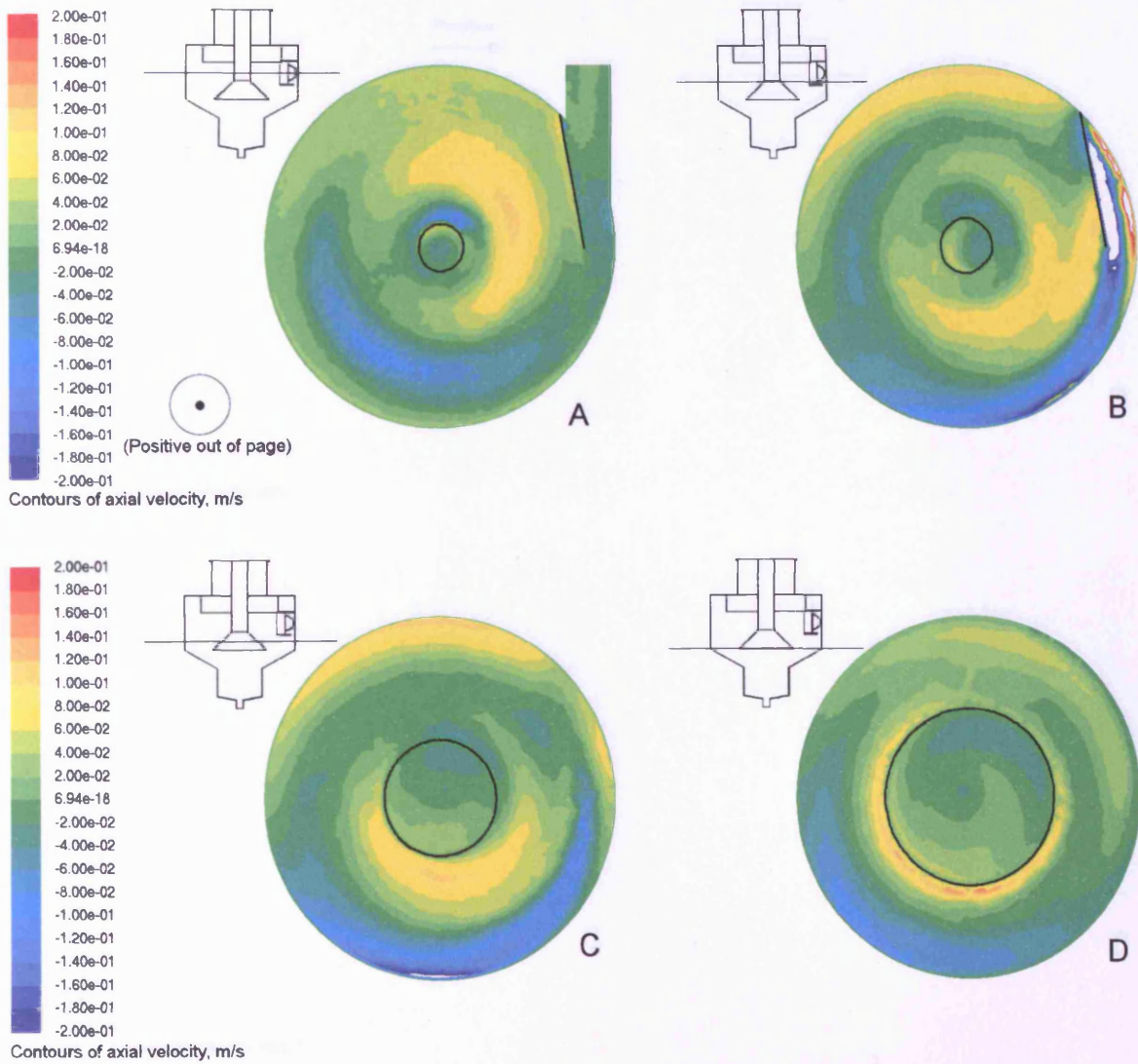
Figure 12-15. Planes of axial velocity within a 3.12m diameter Grit King® operating with a surface loading rate of 20 litres/m²s.
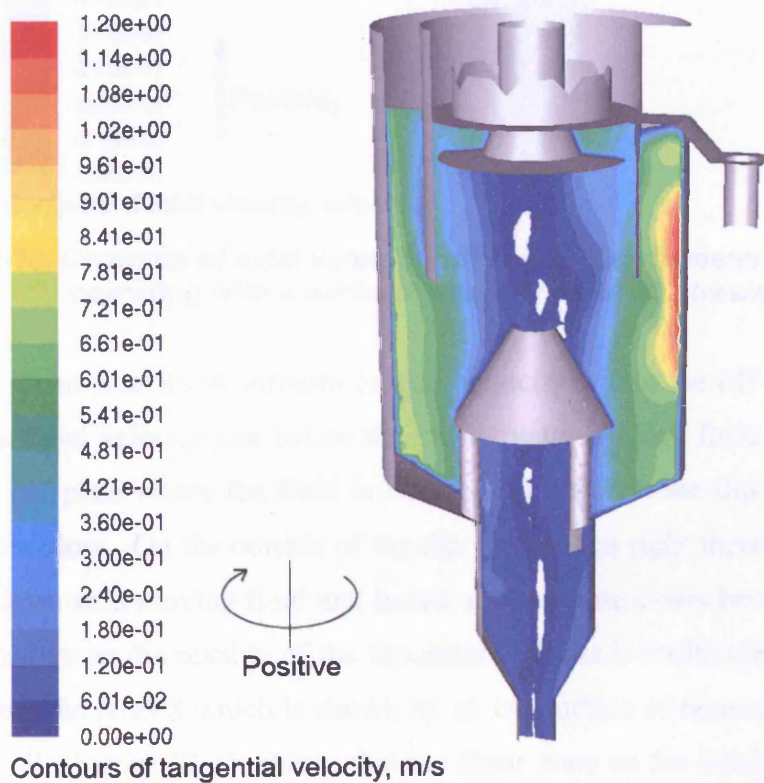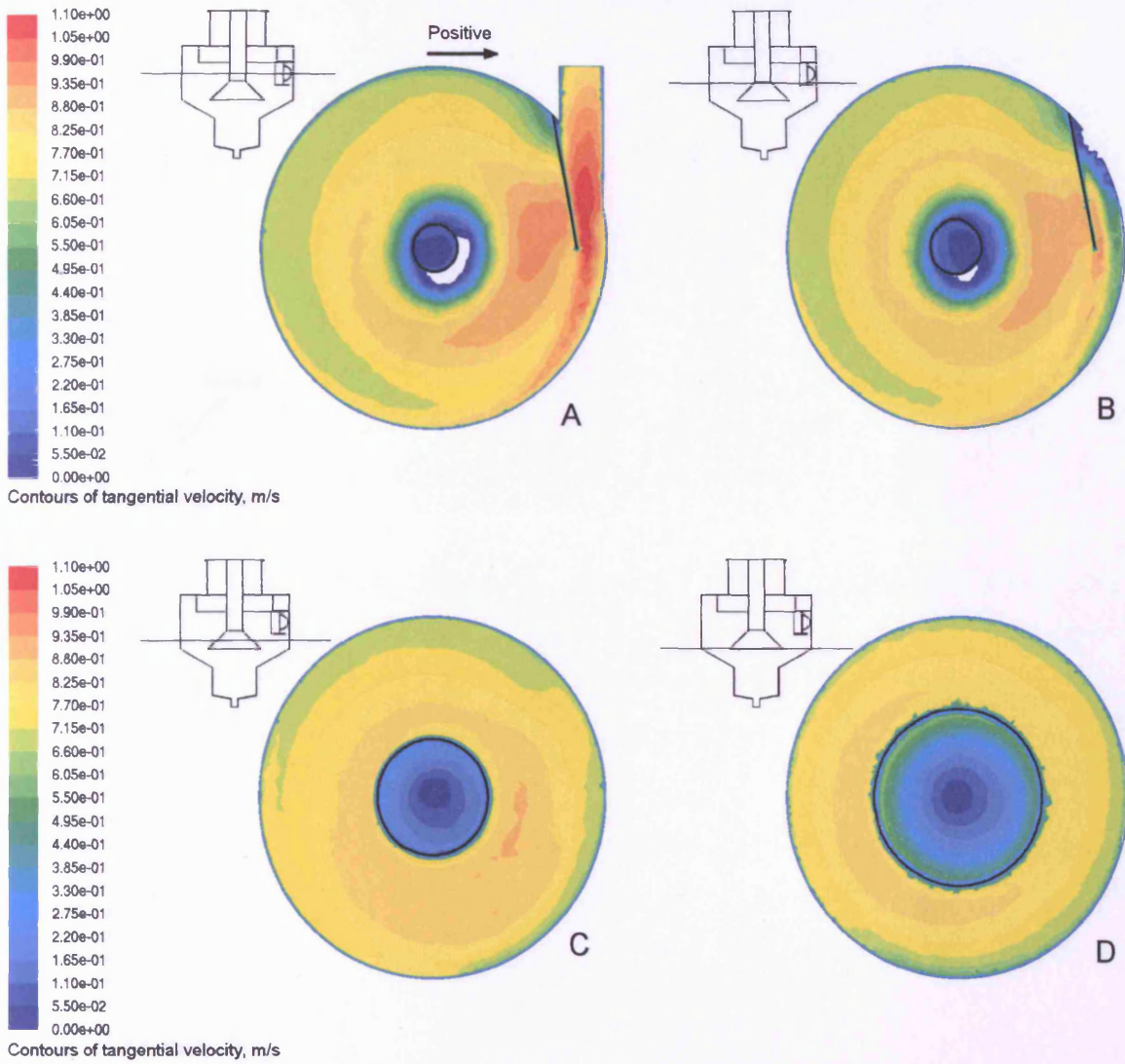
Figure 12-16. Planes of tangential velocity within a 3.12m diameter Grit King®
operating with a surface loading rate of 20 litres/m²s.
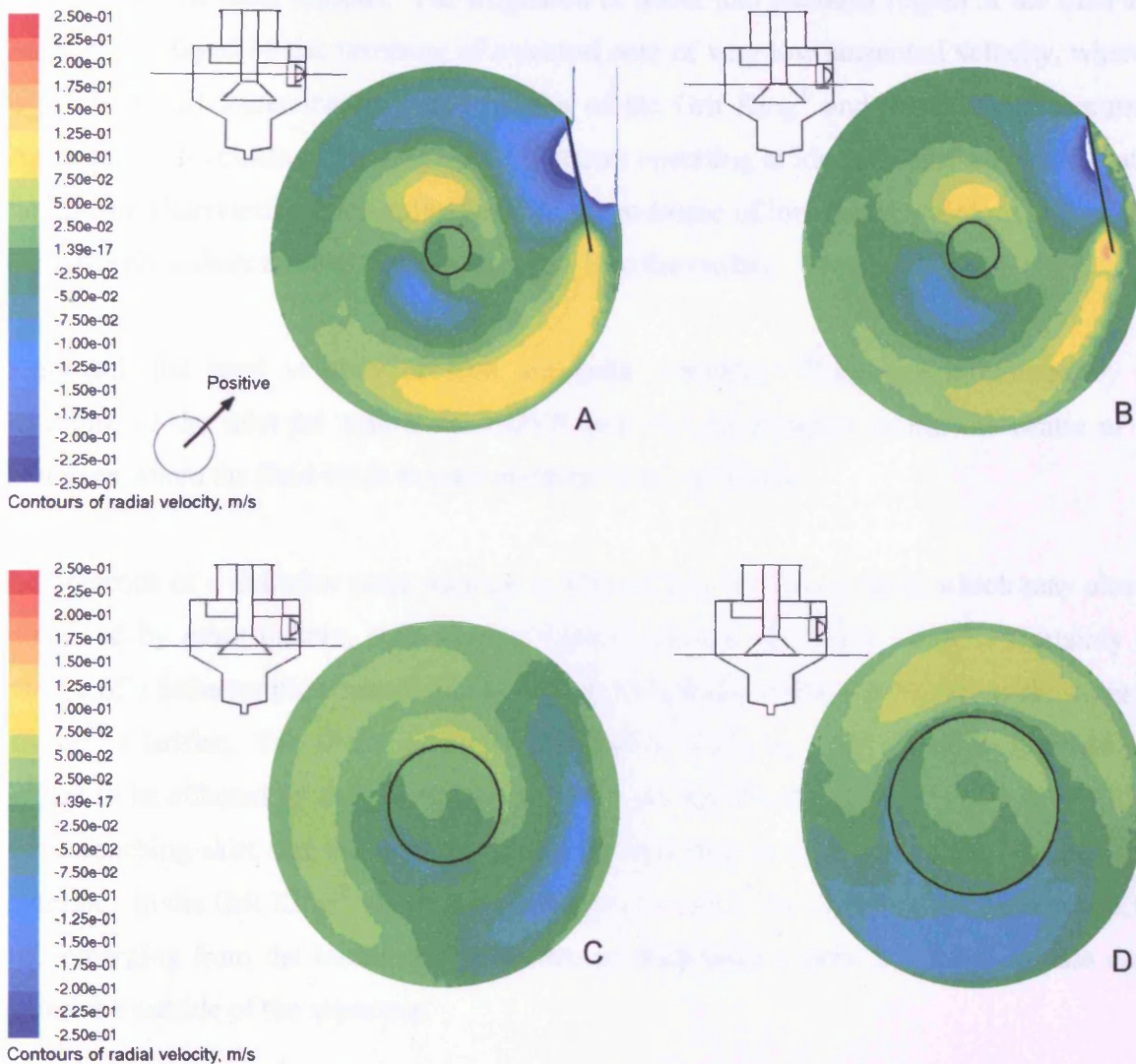
Figure 12-17. Planes of radial velocity within a 3.12m diameter Grit King® operating with a surface loading rate of 20 litres/m²s.

12.3 Discussion

The use of CFD has given an insight into the hydraulic behaviour of the HDVSs. CFD is of course based on theory which can never exactly replicate the actual flow patterns present. However, the general flow patterns are expected to be approximately correct based on validation work undertaken in Chapters 6, 8, 9 and 10.

The use of a step input of tracer is a useful tool to study the path of the fluid throughout the HDVS and highlights regions of low velocity. The path of the fluid through all three HDVSs is similar in that the fluid is swept around the outside of the separator before the tracer

migrates into the inner regions. The migration of tracer into the inner region of the Eff-Pac™ Clarifier is delayed by the presence of a central core of very low tangential velocity, whereas the migration of tracer into the inner region of the Grit King® and Storm King® occurs at similar times in vessels of identical fluid volumes operating at identical surface loading rates. The mixing characteristics are influenced by the presence of low velocity regions and regions where the fluid short circuits through the HDVS to the outlet.

In general, the axial velocity profiles are quite complex. These are influenced by the expansion of the inlet jet within the HDVS and also by a region within the centre of the separators where the fluid tends to pass en route to the overflow.

The presence of a deflector plate appears to control the inlet jet of fluid, which may also be influenced by other factors, such as the Venturi plate in the Storm King®. Certainly the absence of a deflector plate results in the inlet jet expanding within the HDVS as shown in the Eff-Pac™ Clarifier. The direction of the fluid when emerging from the deflector plate also appears to be affected by the position of the inlet. In the Storm King®, the inlet is very close to the benching skirt and the inlet jet appears to just feed its way around the outside of the separator. In the Grit King® where the inlet is positioned in the centre of the main vessel, the fluid emerging from the bottom of the deflector plate takes a path that tends to pass down around the outside of the separator.

It can be seen that as the fluid approaches the deflector plate, or in the case of the Eff-Pac™ Clarifier, the inlet jet, there is a region of negative radial velocity to the left of the inlet due to the fluid being forced towards the centre of the HDVS. A trail of positive radial velocity tends to be present in the inlet jet as the fluid is swept around the outside of the separator.

12.4 Summary

- The flow patterns within the HDVSs, in particular the axial velocity, are very complex.

- The Eff-Pac™ Clarifier has a very low tangential velocity axial core extending through the separator which increases the residence time in the underflow.

- The grit pot in the Grit King® has a very low velocity and appears to be segregated from the flow inside the main vessel. Hence, re-entrainment of particulates from this region is expected to be very low.

- The inlet jet of fluid is controlled by the position of the inlet, the presence of the deflector plate and also the presence of a Venturi plate.

13 Discussion overview

An initial sensitivity study using CFD looking at factors that may influence the efficiency of a HDVS revealed an insight into variables that should be accounted for during experimentation and test rig design. Such variables include measuring the fluid temperature, using regularly shaped particles and in respect of the test rig design, having a long enough inlet pipe such that a developed velocity profile is present at the inlet and particles have sufficient residence time to settle to a realistic position upon entering the HDVS.

The Grit King$^{®}$ HDVS appears to be an effective solid-liquid separator. This is reflected in the difficulty of obtaining suitable test media that are spherical so that the shape factor of the particulates can be accounted for in testing. Test media such as precision balls manufactured by 'The Precision Plastic Ball Co., Ltd' are available in size ranges and densities that the Grit King$^{®}$ is able to separate such that efficiencies of almost 100% are achieved within flowrates obtainable within the laboratory. The use of Styrocell has its limitations such that when the flowrate is low, particle sizes in the range of 1.4-2.0mm or smaller flocculate and float. A second media that has been used is Purolite. This media, although spherical and available in sizes and densities that give an efficiency curve in the range of approximately 0 to 100%, is not as stable as one would prefer, which makes characterisation of the size distribution quite difficult. It has been shown that the parameter controlling the retention efficiency of the Grit King$^{®}$, m_d, which is analagous to a particle surface load, and the relationship between this and the constants in the logistic equation are extremely non-linear. Further work would be desirable to attain efficiency predictions with a wider range of particle surface loads to attain a more complete relationship for the parameters in the logistic function. When the efficiency is expressed as a function of $u_{p\infty}/U$ (particle terminal settling velocity as a fraction of the inlet velocity) only particulates with similar specific gravities align on a single curve. Further work is therefore required to find a dimensionless group which causes all efficiency curves to fall on a single curve. This would allow a single function to be fitted to the data and avoid the need for functions between the particle surface load and the parameters in the logistic equation for a particular size of HDVS. This would consequently simplify the retention efficiency model. Further work is also required to study the effect of particle shape as the shape of grit is irregular. This could be achieved by manufacturing a number of regularly shaped particles made from a suitable material so that efficiencies in the range of 0 to 100% are achieved up to the design flowrate.

Although retention efficiency testing of a 6' diameter Grit King® has been undertaken, due to limited time, only particles having two significantly different characteristics could be tested. With the addition of non geometric similarity between the 6' diameter unit and the 0.75m diameter Grit King®, very few conclusions can be drawn regarding the use of the 0.75m diameter Grit King® model and the scaling protocol by Fenner and Tyack (1997). Scaling residence time predictions by the fluid volume within the HDVS over predicts retention efficiencies and a scale factor has been introduced to account for this. It has also been shown that given knowledge of the particle density and diameter, assuming spherical particles, the 0.75m diameter Grit King® model may be used to predict retention efficiency in a 0.75m diameter unit and the scaling protocol by Fenner and Tyack (1997) may be used to scale the flowrates, hence, predicting the efficiency in a larger HDVS. Further work is required to test the 6' diameter Grit King® with different particle characteristics such that the application of the 0.75m diameter Grit King® model and the scaling protocol by Fenner and Tyack (1997) may be better understood. Ideally, testing of at least three geometrically scaled units should also be undertaken.

Attempts to use CFD to predict the retention efficiency of the 0.75m diameter Grit King® using the DPM have to date failed. The CFD validation of the flow field within the 0.75m diameter Grit King® is limited to static pressure measurements on the walls of the HDVS. Using a hybrid grid the predicted flow field may have been improved. Further work is required to check for grid dependency of such a mesh and which could reveal improved predictions if the solution is not grid independent. Despite achieving a good validation of the static pressure on the HDVS walls, the inlet pipe which has been offset by approximately 5mm may affect the efficiency due to the positions of the particles at entry to the separator. Modifications to the grid are therefore desirable such that the inlet is not offset whilst also achieving reasonable cell skewness and aspect ratio. The use of the transient solver with coupling between the discrete and continuous phases is recommended and the use of enhanced wall treatment might be considered to investigate whether there are any secondary flows within the HDVS caused by pressure gradients at the wall boundaries. A method of predicting retention efficiency using CFD that could be investigated if the DPM continues to fail is the Eulerian model. Although this approach is recommended for solid volume fractions exceeding 10%, this model abandons the use of a Lagrangian frame of reference to compute the particle trajectories. Hence, monitoring the outlet concentration of the solid phase, the retention efficiency would be defined as the outlet concentration expressed as a percentage of

the inlet concentration and this assumes that the outlet concentration plateaus whilst sedimentation occurs in the grit pot. Once the grit pot is full, re-entrainment effects are likely to occur and the overflow concentration will then equal the inlet concentration. Measurements of the fluid velocity within the HDVS using LDA could be used to investigate the velocity fluctuations and hence the turbulence which would also give a better validation of the predicted flow field using CFD. Measurements of velocity profiles at the inlet to the separator are also desirable. A method of characterising the particle distributions at the inlet to the HDVS may also be required to validate CFD predictions. This is because retention efficiencies are over predicted and could be partly attributable to the particles being too low in the inlet pipe as they enter the HDVS. Unless improved predictions can be obtained, scaling retention efficiencies can only be achieved by thorough testing, where a range of particle characteristics are used in geometrically scaled units.

A suitable method for predicting residence time characteristics is one that was developed for HVAC. In terms of predicting mean residence time, this was found to be extremely efficient in terms of processing time. An area that might be improved regarding the characterisation of the mixing characteristics is that with faster computers, the use of say 350 time steps to determine the RTD would be preferable to 100, as using 100 time steps, the peak of the RTD is slightly under predicted. However, where a compromise has to be made between processing time and accuracy, 100 time steps gives a reasonable validation. Each HDVS has been modelled using tetrahedral elements due to the complexity of fitting a hexahedral mesh around the internal components. The use of a tetrahedral mesh increases the numerical diffusion and a hexahedral grid is therefore preferable. However, reasonable validations have been acquired using tetrahedral cells. Where RTD data is applied to predicting disinfection performance, there is likely to be greater error between predicted and actual micro-organism survival rates due to the variable nature of wastewater, where disinfection is influenced by the fluid temperature, pH, the strain of micro-organism and the presence of organic matter in the water which competes for the disinfectant.

It has been shown through an optimisation procedure that the most suitable RTD model for the Storm King® is the ADM. This has also been the case when the ADM and the TISM have been fitted to CFD-predicted RTDs from the Eff-Pac™ Clarifier and the Grit King®. Hence, a combined model such as that proposed by Alkhaddar *et al.* (2001) is not required to

accurately describe the RTD provided the RTD model is fitted to the RTD through optimisation rather than calculating the RTD model parameters via the method of moments.

The disinfection performance of a HDVS may be predicted using kinetic rate constants determined from batch inactivation experiments. Further work is ideally required to validate predicted disinfection rates. Since the ADM is the most appropriate RTD model for a HDVS, a limitation of the disinfection model by Severin *et al.* (1984) is that it uses the number of tanks from the TISM. An improvement for predicting disinfection in a HDVS could be to substitute the number of tanks from the TISM for the inverse of the normalised variance from the ADM. This of course requires validation. However, the disinfection model by Severin *et al.* (1984) may not be the most appropriate model for all wastewaters. Not all disinfection models take into account the effect of the mixing characteristics. Hence, if for a particular catchment of wastewater a more suitable disinfection model is found that does not take into account the mixing characteristics, further work might be required to develop a disinfection model to take this into consideration.

Scaling laws have been derived from CFD predictions for the mean residence time and t_{95} i.e. the time taken for the 'F' curve to plateau. Using the scaling laws for mean residence and the estimates for the mixing characteristics it has been shown that the Grit King®, Eff-Pac™ Clarifier and the Storm King® give a similar disinfection performance at any particular surface loading rate below 30 litres/m²s. If the overflow discharge is taken into consideration then the Storm King® is considered to give the better disinfection performance. The head loss was found to be the lowest across the Grit King®. The Storm King® was found to have the second lowest head loss and this separator may therefore be more desirable than the Eff-Pac™ Clarifier when an underflow component is required. In a usual installation of the Grit King®, the underflow component operates intermittently. However, further work may be desirable to compare the Grit King® operating with an underflow component and to assess the disinfection performance and head loss compared to the Storm King® and Eff-Pac™ Clarifier.

The use of CFD has also given an insight into the hydraulic behaviour of the HDVSs. The presence of a deflector plate appears to control the inlet jet of fluid, which may also be influenced by other factors, such as the Venturi plate in the Storm King®. Certainly the absence of a deflector plate results in the inlet jet expanding within the HDVS as shown in the

Eff-Pac™ Clarifier. The direction of the fluid when emerging from the deflector plate also appears to be affected by the position of the inlet. In the Storm King®, the inlet is very close to the benching skirt and the inlet jet appears to just feed its way around the outside of the separator. In the Grit King® where the inlet is positioned in the centre of the main vessel, the fluid emerging from the bottom of the deflector plate takes a path that tends to pass down around the outside of the separator. Again, the use of LDA and PIV would be ideal to further validate the predicted flow fields.

14 Conclusions

- It was previously thought that the parameter controlling the efficiency of an HDVS was the particle settling velocity. It has been found through experimental testing with particles of different sizes and densities that the parameter controlling the efficiency is given by $m_d = d(\rho_p - \rho_f)$ where m_d is described as the particle surface load, d is the particle diameter and ρ_p and ρ_f are the particle and fluid density respectively.

- A model that predicts the retention efficiency of a 0.75m diameter Grit King® operating without an underflow component has been developed using the logistic equation and takes the form of $\eta = 100/(1 + De^{-C\frac{V}{Q}})$ where V is the volume of fluid in the separator, Q is the inlet flowrate and C and D are polynomials that are a function of the particle surface load.

- The retention efficiency model developed for the 0.75m diameter Grit King® has been applied to predicting retention efficiencies in a 6' diameter Grit King® and a scaling factor, β, introduced so that the model takes the form of $\eta = 100/(1 + De^{-C\left(\frac{V}{Q}\right)^\beta})$ where β in the range of 0.825 to 0.873 gives reasonable predictions. Development of the model was limited to testing taking place with only two different particle characteristics.

- The use of a technique for predicting residence time in HVAC systems has been successfully applied and validated for use with HDVSs. The method has been found to be extremely efficient in processing time and gives the mean residence time of the fluid independent of the RTD curve.

- The Axial Dispersion Model given by $E = \sqrt{\bar{t}/2\pi t^3 \sigma_\theta^2} . \exp\left[-(t - \bar{t})^2 /(2\bar{t}t\sigma_\theta^2)\right]$ where E is the Exit-Age distribution, $\bar{t}$ the mean residence time, t the time, and σ_θ^2 the normalised variance, has been found to be the most suitable RTD model to describe

the mixing characteristics of an HDVS, provided that the ADM is applied by an optimisation technique rather than calculating the parameters via the method of moments. The ADM when applied to RTDs observed at the outlets of a HDVS was found to outperform other RTD models such as the TISM, ADZ model and the ADE.

- Scaling laws, determined from CFD-predicted residence times, have been developed that predict the mean residence time of the Storm King®, Grit King® and Eff-Pac™ Clarifier and which take the form of $\bar{t} = ZD_{HDVS}U_r^{-Y}$ where Z and Y are constants.

- For a disinfection application where an underflow component is required, the Storm King® is the most appropriate HDVS as this has a lower head loss and a higher discharge at the overflow compared with the Eff-Pac™ Clarifier with an identical surface loading rate and volume of fluid.

15 Publications by the author

15.1 Journal papers

Egarr, D.A., Faram, M.G., O'Doherty, T., Phipps, D.A., Syred, N., 2005, Computational fluid dynamic prediction of the residence time of a vortex separator applied to disinfection, Water Science and Technology, Vol. 52, No. 3, pp.29–36.

Egarr, D.A., Faram, M.G., O'Doherty, T., Phipps, D.A., Syred, N., 2005, Computational fluid dynamic prediction of the residence time distribution of a prototype hydrodynamic vortex separator operating with a base flow component, Proceedings of the Institute of Mechanical Engineers, Journal of Process Mechanical Engineering, Vol. 219, No. E1, pp.53-67.

Egarr, D.A., Faram, M.G., Guymer, I., O'Doherty, T., Syred, N., 2005, Residence time study of a hydrodynamic vortex separator applied to predicting disinfection performance, Water Research, Submitted.

Egarr, D.A., Faram, M.G., Guymer, I., O'Doherty, T., Syred, N., 2005, Assessment of residence time distribution models applied to a hydrodynamic vortex separator, Chemical Engineering Journal, Submitted.

Egarr, D.A., Faram, M.G., O'Doherty, T., Syred, N., 2005, Experimental study of a hydrodynamic vortex separator, Chemical Engineering Journal, Submitted.

Egarr, D.A., O'Doherty, T., Morris, S., Bacon., P., 2005, Experimental and computational study of tidal turbines as a renewable energy source, Proceedings of the Institution of Mechanical Engineers, Part A, Journal of Power and Energy, Submitted.

Egarr, D.A., O'Doherty, T., Morris, S., Bacon, P., 2005, Assessment of an array of tidal turbines supported on a free standing structure, Proceedings of the Institution of Mechanical Engineers, Part A, Journal of Power and Energy (Proposed Journal), In preparation.

15.2 Conference papers

Egarr, D.A., Faram, M.G., Guymer, I., O'Doherty, T., Syred, N., 2005, Use of computational fluid dynamics to assess the disinfection performance of a combined sewer overflow treatment chamber, 10th International Conference on Urban Drainage, Copenhagen/Denmark, 21-26th August, CD-ROM.

Egarr, D.A., Faram, M.G., O'Doherty, T., Syred, N., 2005, An efficiency formula for a hydrodynamic vortex separator, International Symposium on EcoTopia Science, Nagoya, Japan, 8-9th August, pp.163-166.

Egarr, D.A., O'Doherty, T., Morris, S., Syred, N., Ayre, R.G., 2005, Computational study of tidal turbines for extracting energy from the tides, International Symposium on EcoTopia Science, Nagoya, Japan, 8-9th August, pp.73-76.

Egarr, D.A., O'Doherty, T., Morris, S., Ayre, R.G., 2004, Feasibility study using computational fluid dynamics for the use of a turbine for extracting energy from the tide, Proceedings of the Fifteenth Australasian Fluid Mechanics Conference, 13-17th December, CDROM, ISBN 1 864 87695 6.

Egarr, D.A., Faram, M.G., O'Doherty, T., Phipps, D.A., Syred, N., 2004, Computational fluid dynamic prediction of the residence time of a vortex separator applied to disinfection, 4th International Conference on Sewer Processes and Networks, Funchal, Madeira, 22nd – 24th November, pp.49-56.

Egarr, D.A., Faram, M.G., O'Doherty, T., Syred, N., 2004, An investigation into the factors that determine the efficiency of a hydrodynamic vortex separator, Novatech, 5th International Conference, Sustainable techniques and strategies in urban water management, Lyon, France, 7-11th June, pp.61-68, ISBN 2-9509337-5-0.

16 References

ABB, 2004, MagMaster instruction manual.

Aiguier, E., Bertrand-Krajewski, J-L., Hedges, P., Tyack, N., 1996, Methods for determining the settling velocity profiles of solids in storm sewage, Wat. Sci. Tech., Vol. 33, No. 9, pp.117-125.

Alder, H.L., Roessler, E.B., 1975, Introduction to probability and statistics, Sixth Edition, W.H. Freeman and Company

Alkhaddar, R, Higgins, P, Phipps, D, 2000, Characterisation for In Situ Disinfection of a Hydrodynamic Vortex Separator (HDVS), Proceedings of the 1st World Congress of the International Water Association, 3-7th July.

Alkhaddar, R.M., Cheong, C.H., Phipps, D.A., Andoh, R., James, A., Higgins, P., 2001, The development of a mathematical model for the prediction of the residence time distribution of a hydrodynamic separator, Novatech, 4th International conference on innovative technologies in urban storm drainage Lyon, France, 25-27th June, pp.835-842.

Alkhaddar, R.M., Higgins, P.R., Phipps, D.A., Andoh, R.Y.G., 1999, The residence time distribution of prototype hydrodynamic vortex separator operating with a baseflow component, 8ICUSD, 30th August – 3rd September, pp.18-25.

Andoh, R.Y.G., Cook, A.P., 1995, The Eff-Pac^{TM} process for industrial wastewater treatment, Filtech Conference, Karlsruhe, 10-12th October, pp.173-189.

Andoh, R.Y.G., Harper, I., Hipwell, P.M., 1996, Meeting the EC urban wastewater treatment directive with the Hydro Swirl-Flo$^{®}$ process, Chemical Water and Wastewater Treatment IV: Proc. 7th Gothenburg Symposium, 23-25th September, Edinburgh, Scotland, pp.241-250.

Andoh, R.Y.G., Saul, A.J., 2003, The use of hydrodynamic vortex separators and screening systems to improve water quality, Wat. Sci. Tech., 47(4), pp.175-183.

Andoh, R.Y.G., Smisson, R.P.M., 1993, High rate sedimentation in hydrodynamic separators, 2nd Int. Conf. on hydraulic modelling development and application of physical and mathematical models, pp.341-358.

Andoh, R.Y.G., Smisson, R.P.M., 1996, The practical use of wastewater characterisation in design, Wat. Sci. Tech., Vol. 33, No. 9, pp.127-134.

Averill, D, Mack-Mumford, D., Marsalek, J., Andoh, R., Weatherbe, D., 1997, Field facility for research and demonstration of CSO treatment technologies, Wat. Sci. Tech., Vol. 36, No. 8-9, pp.391-396.

Boner, M.C., Hides, S.P., Turner, B.G., 1993, High rate treatment of combined sewer overflows in Columbus, Georgia, Proceedings on the Sixth International Conference on Urban Storm Drainage, 12-17th September, pp.1671-1676.

Boxall, J., Shepherd, W., Guymer, I., Fox, K., 2003, Changes in water quality parameters due to in-sewer processes, Wat. Sci. Tech., Vol. 47, No. 7-8, pp.343-350

Bradley, D., 1965, The Hydrocyclone, First Edition, Pergamon Press, Great Britain.

British Standards Institution, 1991, BS7405 Guide to selection and application of flowmeters for the measurements of fluid flow in closed conduits.

British Standards Institution, 1997, BS EN ISO 5167, Measurement of fluid flow by means of pressure differential devices – Part 1: Orifice plates, nozzles, and Venturi tubes inserted in circular cross-section conduits running full.

Brombach, H, 1992, Solids removal from combined sewer overflows with vortex separators, Novatech, Lyon, France, 3-5th November, pp.447-459.

Brown, N.P., Heywood, N.I., 1991, Slurry handling design of solid-liquid systems, Elsevier Applied Science, London and New York.

Burt, D., Corton, M., Hetherington, D., Balmforth, D., 2002, Multiphase modelling and the prediction of retention efficiency in a side weir CSO, 9th International conference on urban drainage: Global solutions for urban drainage, Portland, Oregon, 8-13th September.

Chatfield, C., 1997, Statistics for technology, Third edition (Revised), Chapman & Hall, London.

Chick, H.E., 1908, An investigation of the laws of disinfection, J. Hyg., Vol. 8, pp.92-158.

Choudhury, D., 1993, Introduction to the renormalization group method and turbulence modeling, Fluent Inc., Technical Memorandum TM-107.

Connick, D., Pisano, W.C., 1981, Development and testing of procedures for determination of CSO settleability characteristics, US EPA Edison New Jersey.

Daly, B.J., Harlow, F.H., 1970, Transport equations in turbulence, Phys. Fluids, Vol. 13, pp.2634-2649.

Douglas, J.F., Gasiorek, J.M., Swaffield, J.A., 1998, Fluid mechanics, 3rd Edition, Longman, Singapore.

Douglas, J.F., Gasiorek, J.M., Swaffield, J.A., 2001, Fluid mechanics, 4th Edition, Prentice Hall, Harlow, England.

Egarr, D.A., O'Doherty, T., Morris, S., Ayre, R.G., 2004, Feasibility study using computational fluid dynamics for the use of a turbine for extracting energy from the tide, Proceedings of the Fifteenth Australasian Fluid Mechanics Conference, 13-17th December, CDROM, ISBN 1 864 87695 6.

Egarr, D.A., O'Doherty, T., Morris, S., Syred, N., Ayre, R.G., 2005, Computational study of tidal turbines for extracting energy from the tides, International Symposium on EcoTopia Science, Nagoya, Japan, 8-9th August, pp.73-76.

Faram, M.G., Harwood, R., 2003, A method for the numerical assessment of sediment interceptors, Wat. Sci. Tech., Vol. 47, No. 4, pp.167-174.

Faram, M.G., Harwood, R., Deahl, P.J.D., 2003, Investigation into the sediment removal and retention capabilities of stormwater treatment chambers, StormCon Conference, 28th-31st July, San Antonio, Texas, USA.

Faram, M.G., James, M.D., Williams, C.A., 2004, Wastewater treatment using hydrodynamic vortex separators, CIWEM/AETT 2nd National Conference, Wakefield, UK, September 13-15, pp.79-87.

Fenner, R.A., Tyack, J.N., 1997, Scaling laws for hydrodynamic separators, ASCE Journal of Environmental Engineering, Vol. 123, No. 10, October 1997, pp.1019-1026.

Fidleris, V., Whitmore, R. L., 1961, Experimental determination of the wall effect for spheres falling axially in cylindrical vessels, Brit. J. Appl. Phys., Vol. 12, pp.490-4.

Fischer, H.B., List, E.J.., Koh, R.C.Y., Imberger, J., Brooks, N.H., 1979, Mixing in inland and coastal waters, Academic Press.

Fluent Inc., 2002, Gambit 2.0 Documentation, Lebanon, NH

Fluent Inc., 2003, FLUENT 6.1 Documentation, Lebanon, NH.

Fox, R.W., McDonald, A.T., 1998, Introduction to fluid mechanics, Fifth edition, John Wiley and Sons, New York.

Franzini, J.B., Finnemore, E.J., 1997, Fluid mechanics with engineering applications, Ninth Edition, McGraw-Hill Publishing Co., Boston, Massachusetts.

Frederick, M.R., Markland, E., 1967, The performance of stilling ponds in handling solids, Paper 5 ICE Symposium on Storm Sewage Overflows, pp.51-61.

Fu, S., Launder, B.E., Leschziner, M.A., 1987, Modeling strongly swirling recirculating jet flow with Reynolds-stress transport closures, In Sixth Symposium on Turbulent Shear Flows, Toulouse, France.

Gardner, P. Deamer, A., 1996, An evaluation of methods for assessing the removal efficiency of a grit separation device, Wat. Sci. Tech., Vol. 33, No. 9, pp.269-275.

Gibson, M.M., Launder, B.E., 1978, Ground effects on pressure fluctuations in the atmospheric boundary layer, J. Fluid Mech., Vol. 86, pp.491-511.

Greene, D.J., Haas, C.N., Farouk, B., 2002, Numerical simulation of chlorine disinfection processes, Wat. Sci. Tech: Water Supply, Vol. 2, No. 3, pp.167-173.

Guilbault, G.G., 1990, Practical Fluorescence, Second Edition, Marcel Dekker, Inc., New York.

Guymer, I., 2002, A national database of travel time, dispersion and methodologies for the protection of river abstractions, Environment Agency R & D Technical Report, ISBN 1 85705 821 6.

Guymer, I., 2004, Solute Retention times in a Storm King, Hydro International Plc Internal document.

Guymer, I., O'Brien, R., Harrison, C., 1996, Representation of solute transport and mixing within a surcharged benched manhole using an aggregated dead zone (ADZ) technique, Water Science and Technology, Vol. 34, No. 3-4, pp.95-101.

Guymer, I., Shepherd, W.J., Dearing, M., Dutton, R., Saul, A.J., 2002, Solute retention in storage tanks, 9th International Conference on Urban Drainage: Global solutions for urban drainage, Portland, Oregon, 8-13th September.

Haas, C.N., Joffe, J., 1994, Disinfection under dynamic conditions; modification of Hom's model for decay, Environmental Science and Technology, Vol. 28, No. 7, pp.1367-1369.

Haas, C.N., Joffe, J., Heath, M.S., Jacangelo, J., 1997, Continuous flow residence time distribution function characterisation, J. Envir. Engrg., 123, pp.107-114.

Haider, A., Levenspiel, O., 1989, Drag coefficient and terminal velocity of spherical and nonspherical particles, Powder Technology, Vol. 58, pp.63-70.

Halliwell, A.R., Saul, .J., 1980, The use of hydraulic models to examine the performance of storm-sewage overflows, Proc. Instn Civ Engnrs, Vol. 69, Part 2, June, pp.245-259.

Hedges, P., 1994, The prediction of combined sewer overflow performance from models – a case study, Wat. Sci. Tech., Vol. 29, No. 1-2, pp.373-382.

Hedges, P.D., Lockley, P.E., Martin, J.R., 1992, A field study of an hydrodynamic separator combined sewer overflow, Novatech, Lyon, France, 3-5th November, pp.349-358.

Higgins, P.R., 2000, The characterisation of the hydrodynamic vortex separator using residence time distribution analysis, Ph.D. Thesis, Liverpool John Moores University, Liverpool, UK.

Higgins, P.R., Alkhadar, R., Phipps, D.A., Andoh, R.Y.G., 1998, Residence time distribution of a hydrodynamic vortex separator, IWAQ, Proceedings of the 2nd Int. conference on advanced wastewater treatment, recycling and reuse, Milan, 14-16th September, pp.935-938.

Hinze, J.O., 1975, Turbulence, McGraw-Hill Publishing Co., New York.

Hirt, C.W., Nichols, B.D., 1981, Volume of Fluid (VOF) Method for the Dynamics of Free Boundaries, J. Comput. Phys., Vol. 39, pp.201-225.

Hom, L.W., 1972, Kinetics of chlorine disinfection of an ecosystem, J. of the Sanitary Eng. Div. ASCE 98 (SA1), pp.183-194.

Hydro International Plc, 2002, The middle Chattahoochee river watershed study; CSO Technology Performance Testing, Internal document.

Launder, B.E., 1989a, Second-moment closure: Present... and future?, Inter. J. Heat Fluid Flow, Vol. 10, No. 4, pp.282-300.

Launder, B.E., 1989b, Second-moment closure and its use in modeling turbulent industrial flows, International Journal for Numerical Methods in Fluids, Vol. 9, pp.963-985.

Launder, B.E., Reece, G.J., Rodi, W., 1975, Progress in the development of a Reynolds-stress turbulence closure, J. Fluid Mech., Vol. 68, No. 3, pp.537-566.

Launder, B.E., Shima, N., 1989, Second-moment closure for the near-wall sublayer: Development and Application, AIAA Journal, Vol. 27, No. 10, pp.1319-1325.

Launder, B.E., Spalding, D.B., 1972, Lectures in mathematical models of turbulence, Academic Press, London.

Launder, B.E., Spalding, D.B., 1974, The Numerical Computation of Turbulent Flows, Computer Methods in Applied Mechanics and Engineering, Vol. 3, pp.269-289.

Levenspiel, O, 1962, Chemical reaction engineering, John Wiley and Sons, New York.

Li, L., 2004, Effects of initial microbial density on disinfection efficiency in a continuous flow system and validation of disinfection batch kinetics in a continuous flow system, Ph.D. Thesis, Drexel University.

Lien, F.S., Leschziner, M.A., 1994, Assessment of turbulent transport models including non-linear RNG eddy-viscosity formulation and second-moment closure, Computers and Fluids, Vol. 23, No. 8, pp.983-1004.

Luyckx, G., Vaes, G., Berlamont, J., 1998, Experimental investigation on the efficiency of a hydrodynamic separator, Novatech, 3rd International Conference on innovative technologies in urban storm drainage, Lyon, France, 4-7th May, pp.443-450.

Luyckx, G., Vaes, G., Berlamont, J., 2002, Surface load as a predominant factor for CSO efficiency, 9th International conference on urban drainage: Global solutions for urban drainage, Portland, Oregon, 8-13th September.

Luyckx, G., Vaes, G., Berlamont, J., 2004, Combined sewer overflows: solids separation efficiency, Novatech, 5th International Conference, Sustainable techniques and strategies in urban water management, Lyon, France, 7-11th June, pp.37-44.

Massey, B.S., 1984, Mechanics of fluids, 5th Edition, Van Nostrand Reinhold, UK.

Met. Office, UK Climate, http://www.met-office.gov.uk/education/, Accessed October 2004.

Met. Office, UK Climate, http://www.met-office.gov.uk/education/curriculum/didyouknow.html, Accessed July 2005.

Michelbach, S., Wöhrle, C., 1993, Settleable solids in a combined sewer system, settling characteristics, heavy metals, efficiency of storm water tanks, Wat. Sci. Tech., Vol. 27, No. 5-6, pp.153-164.

Michell, S.J., 1970, Fluid and particle mechanics, Pergamon Press, Oxford.

Microsoft, 2003, Micrsoft Autoroute 2003

Miller, D.S., 1978, Internal flow systems, BHRA Fluid Engineering, ISBN 0 900983 78 7.

Miller, R.W., 1976, Flow measurement engineering handbook, McGraw Hill Book Company.

Miller, I., Freund, J.E., Johnson, R.A., 1990, Probability and statistics for engineers, Fourth Edition, Prentice Hall, Inc..

Mironer, A., 1979, Engineering fluid mechanics, McGraw Hill, New York.

Morsi, S.A., Alexander, A.J., 1972, An investigation of particle trajectories in two-phase flow systems, J. Fluid Mech., September 26th, Vol. 55, No. 2, pp.193-208.

Nauman, E.B., Buffham, B.A., 1983, Mixing in continuous flow systems, John Wiley and Sons, New York.

NIST/SEMATECH e-Handbook of Statistical Methods, http://www.itl.nist.gov/div898/handbook/, Accessed March 2004.

Okamoto, Y., Konugi, M. & Tsuchiya, H., 2002, Numerical simulation of the performance of a hydrodynamic separator, 9th International conference on urban drainage: Global solutions for urban drainage, Portland, Oregon, 8-13th September.

Owen, M.W., 1970, A detailed study of the settling velocity of a estuary mud, Report No. INT 78, Hydraulic Research Station, Wallingford.

Patankar, S.V., 1980, Numerical Heat Transfer and Fluid Flow, Hemisphere, Washington, D.C..

Pisano, W.C., 1996, Summary: United States "Sewer Solids" characterisation methods, results, uses and perspective, Wat. Sci. Tech., Vol. 33, No. 9, pp.109-115.

Pretorius, P.C., Pretorius, W.A., 1999, Disinfection of purified sewage effluent with monochloramine, Water SA, Vol. 25, No. 4, pp.463-471, ISSN 0378-4738.

Reed, D, 1998, Selecting alternatives to chlorine disinfection, Pollution Engineering, Sep, Vol. 30, Part 9, pp.48-58.

Reynolds, W.C., 1987, Fundamentals of turbulence for turbulence modeling and simulation, Lecture Notes for Von Karman Institute Agard Report No. 755.

Richter, K. 2004, Constructed wetlands for the treatment of airport de-icer, Ph.D. Thesis, University of Sheffield, UK.

Roach, L.D., Beecham, S., 2004, Exploring pre-filtering for water sensitive urban design systems in Australia, Novatech, 5th International conference: Sustainable techniques and strategies in urban water management, Lyon, France, 7-11th June, Vol. 1, pp.301-308.

Roos, A, 1999, On the Effectiveness of Ventilation, Ph.D. Thesis, Eindhoven University of Technology, Eindhoven, The Netherlands.

Rutherford, J.C., 1994, River mixing, John Wiley and Sons.

Sánchez-Ruiz, C., Martínez-Royano, S., Tejero-Monzón, I., 1995, An evaluation of the efficiency and impact of raw wastewater disinfection with peracetic acid prior to ocean discharge, Wat. Sci. Tech., Vol. 32, No. 7, pp.159-166.

Schiller, L., Naumann, Z., 1935, Z. Ver. Deutsch. Ing., Vol. 77, pp.318.

Severin, B.F., Suidan, M.T., Engelbrecht, R.S., 1984, Series event kinetic model for chemical disinfection, J. Environ. Eng., Vol. 110, No. 2, pp.430-439.

Shames, I.H., 1992, Mechanics of fluids, Third Edition, McGraw-Hill Publishing Co., New York.

Sherwin, C., Ta, C.T., 2002, Investigation of anaerobic zone short circuiting using computational fluid dynamics, Wat. Sci. Tech., Vol. 46, No. 4-5, pp.333-338.

Shih, T.-H, Liou, W.W., Shabbir, A., Yang, Z., Zhu, J., 1995, A New k- ϵ Eddy-Viscosity Model for High Reynolds Number Turbulent Flows - Model Development and Validation., Computers Fluids, Vol. 24, No. 3, pp.227-238.

Smisson, B., 1967, Design, construction and performance of vortex overflows, Institute of Civil Engineers, Symposium on Storm Sewage Overflows, London, pp.99-110.

Speziale, C.G., Sarkar, S., Gatski, T.B., 1991, Modelling the pressure-strain correlation of turbulence: An invariant dynamical systems approach, J. Fluid Mech., Vol. 227, pp.245-272.

Stovin, V.R., Saul, A.J., 1998, A computational fluid dynamics (CFD) particle tracking approach to efficiency prediction, Wat. Sci. Tech., Vol. 37, No. 1, pp.285-293.

Stovin, V.R., Saul, A.J., 2000, Computational fluid dynamics and the design of sewage storage chambers, J.CIWEM, Vol. 14, pp.103-110.

Svarovsky, L., 1984, Hydrocyclones, Holt, Rinehart and Winston Ltd, East Sussex, England, ISBN 0-03-910562-8.

Ta, C.T., Brignal, W.J., 1998, Application of computational fluid dynamics technique to storage reservoir studies, Wat. Sci. Tech., Vol. 37, No. 2, pp.219-226.

Taylor, J.R., 1982, An introduction to error analysis: The study of uncertainties in physical measurement, University Science Books, Mill Valley, California.

Teefy, S.M., Singer, P.C., 1990, Performance and analysis of tracer tests to determine compliance of a disinfection scheme with the SWTR, Journal of the American Water Works Association (AWWA), Vol. 82, No. 12, pp.88-98.

Turton, R., Levenspiel, O., 1986, A short note on the drag correlations for spheres, Powder Technol., Vol. 47, pp.83-6.

Tyack, J.N., Fenner, R.A., 1997, The use of scaling laws in characterising residence time in hydrodynamic separators, Proceedings of the 2nd International conference of the sewer as a physical, chemical and biological reactor, 25-28th May, Aalborg, Denmark.

Tyack, J.N., Fenner, R.A., 1998a, Identification of flow regimes within a hydrodynamic separator, Novatech, 3rd International Conference on Innovative Technologies in Urban Storm Drainage, Lyon, France, 4-7th May, pp.361-368.

Tyack, J.N., Fenner, R.A., 1998b, An investigation into hydrodynamic separation using physical and computational models, Hydro International Plc Internal Report

Tyack, J.N., Fenner, R.A., 1999, Computational fluid dynamic modelling of velocity profiles within a hydrodynamic separator, Wat. Sci. Tech., Vol. 39, No. 9, pp.169-176.

Tyack, J.N., Hedges, P.D., Smisson, R.P.M., 1992, The use of sewage settling velocity grading in combined sewer overflow design, Novatech, Lyon, France, 3-5th November, pp.341-348.

Tyack, J.N., Hedges, P.D., Smisson, R.P.M., 1996, The relationship between settling velocity grading and the characteristics of the contributing catchment, Wat. Sci. Tech., Vol. 33, No. 9, pp.135-142.

Turner Designs, 2002, SCUFA Users manual.

Turner Designs, SCUFA Brochure, http://www.turnerdesigns.com/, Accessed June 2004.

Uribe-Salas, A., Vermet, F., Finch, J.A., 1992, Apparatus and technique to measure settling velocity and holdup of solids in water slurries, Chemical Engineering Science, Vol. 48, No. 4, pp.815-819.

Vandoormaal, J.P., Raithby, G.D., 1984, Enhancements of the SIMPLE Method for Predicting Incompressible Fluid Flows, Numer. Heat Transfer, Vol. 7, pp.147-163.

Verhulst, P.-F., 1845, Recherches mathématiques sur la loi d'accroissement de la population, Nouv. mém. de l'Academie Royale des Sci. et Belles-Lettres de Bruxelles 18, pp.1-41.

Verhulst, P.-F., 1847, Deuxième mémoire sur la loi d'accroissement de la population, Mém. de l'Academie Royale des Sci., des Lettres et des Beaux-Arts de Belgique 20, pp.1-32.

Vergouw, J.M., Anson, J., Dalhke, R., Xu, Z., Gomez, C., Finch, J.A., 1997, An automated data acquisition technique for settling tests, Wat. Sci. Tech., Vol. 10, No. 10, pp.1095-1105.

Wallis, S.G., Guymer, I., Bilgi, A., 1989, A practical engineering approach to modelling longitudinal dispersion, Proc. of international conference on hydraulic and environmental modelling of coastal, estuarine and river waters, Bradford, Sept. 1989, pp.291-300.

Ward, N.R., Wolfe, R.L., Olson, B., 1984, Effect of pH, application technique, and chlorine-to-nitrogen ratio on disinfectant activity of inorganic chloramines with pure culture bacteria, Appl. Environ. Microbiol. Vol.48, No. 3, pp.508-514.

Wen, C.-Y., Yu, Y. H., 1966, Mechanics of Fluidization, Chem. Eng. Prog. Symp. Series, Vol. 62, pp.100-111.

White, F.M., 1979, Fluid Mechanics, 3rd Edition, McGraw Hill Inc.

Williams, R.A., Xie, C.G., Bragg, R., Amarasinghe, W.P.K., 1990, Experimental techniques for monitoring sedimentation in optically opaque suspensions, Colloids and Surfaces, Vol. 43, Part 1, pp.1-32.

Yakhot, V., Orszag, S.A., 1986, Renormalization Group Analysis of Turbulence: I. Basic Theory, Journal of Scientific Computing, Vol. 1, No. 1, pp.1-51.

Young, P., Jakeman, A., McMurtrie, R., 1980, An instrument variable method for model order identification, Automatica, Vol. 16, pp.281-294.

Youngs, D.L., 1982, Time-dependent multi-material flow with large fluid distortion, In K. W. Morton and M. J. Baines, editors, Numerical Methods for Fluid Dynamics, Academic Press.

Young, P.C., Wallis, S.G., 1986, The aggregated dead zone (ADZ) model for dispersion in rivers, Proceedings of the conference on water quality modelling in the inland natural environment, Bournemouth, 10-13th June, pp.421-433.

Zhu, Y., Wu, J., Shepherd, I.S., Coghill, M., Vagias, N., Elkin, K., 2000, An automated measurement technique for slurry settling tests, Wat. Sci. Tech., Vol. 13, No. 7, pp.765-772.

Appendix A. User Defined Functions (UDFs)

Details on the macros, solver data and implementation are given in Fluent Inc. (2003).

Diffusivity of water

```
/*****************************************************************/
/*  UDF that computes the diffusivity of water for a User        */
/*    Defined Scalar                                             */
/*  UDF written for use with FLUENT 6.1.xx                       */
/*  UDF written by Darrell A. Egarr, August 2003                 */
/*  UDF adapted from fluent 6.1 documentation                    */
/*****************************************************************/

#include "udf.h"

DEFINE_DIFFUSIVITY(water_diffusivity, c, t, i)
{
    return C_R(c,t) * 3.05e-05 + C_MU_EFF(c,t) / 0.7;
}
```

Mean residence time

```
/*****************************************************************/
/*  UDF that defines the source, for a User Defined Scalar, as   */
/*    the density of the fluid                                   */
/*  UDF used for computing the mean residence time of the fluid  */
/*  UDF written by Darrell A. Egarr, August 2003                 */
/*  UDF written for use with FLUENT 6.1.xx                       */
/*****************************************************************/

#include "udf.h"

DEFINE_SOURCE(density, c, ct, dS, eqn)
{
real source;

    source = C_R(c,ct);
    dS[eqn] = 0.0;

return source;
}
```

DPM trajectory termination

```
/***********************************************************/
/* A DPM UDF to evaporate particles after a time period of 10    */
/*  minutes                                                 */
/* UDF written by Darrell A. Egarr, December 2003           */
/* UDF written for use with FLUENT 6.1.xx                   */
/***********************************************************/

#include "udf.h"
#include "dpm.h"
#include "surf.h"
#define P_CELL(p)RP_CELL(&(p->cCell))
#define P_CELL_THREAD(p)RP_THREAD(&(p->cCell))

DEFINE_DPM_SCALAR_UPDATE(terminate_10mins, c, ct, initialize, p)
{
real particle_time;
particle_time = P_TIME(p);
if (particle_time > 600.0)
      {
       P_MASS(p)=0.0;
       P_DIAM(p)=0.0;
      }
}
```

Drag coefficient – Turton and Levenspiel (1986)

```
/***********************************************************/
/* UDF that defines the drag coefficient of a particle as that   */
/*  proposed by Turton and Levenspiel (1986)               */
/* UDF written by Darrell A. Egarr, March 2005             */
/* UDF written for use with FLUENT 6.1.xx                  */
/***********************************************************/

#include "udf.h"
#include "dpm.h"
#include "surf.h"
#define P_CELL(p)RP_CELL(&(p->cCell))
#define P_CELL_THREAD(p)RP_THREAD(&(p->cCell))

DEFINE_DPM_DRAG(Cd_T_and_L, Re, p)
{
real Cd;
real Drag_Force;

if(Re>0.0)
      {
       Cd = (24.0/Re)*(1.0+(0.173*(pow(Re,0.657)))) +
(0.413/(1.0+(16300.0*(pow(Re,-1.09))))));

       Drag_Force = 18.0*Cd*Re/24.0;
       return (Drag_Force);
      }

return 0.0;
}
```

Time dependent inlet concentration curve (General format)

```
/*****************************************************************/
/* UDF defines a time dependent inlet concentration curve    */
/* UDF written by Darrell A. Egarr, September 2004           */
/* UDF written for use with FLUENT 6.1.xx                    */
/*****************************************************************/

#include "udf.h"

DEFINE_PROFILE(Exp_inlet_trace_3_1,ft,i)
{

face_t f;
real t;
t = CURRENT_TIME;

        if( t>0.0 && t<=1.0 )
           {
             begin_f_loop(f,ft)
                {
                  F_PROFILE(f,ft,i) = 0.593;
                }
             end_f_loop(f,ft);
           }

        else if( t>1.0 && t<=2.0 )
           {
             begin_f_loop(f,ft)
                {
                  F_PROFILE(f,ft,i) = 399.393;
                }
             end_f_loop(f,ft);
           }

        else if( t>2.0 && t<=3.0 )
           {
             begin_f_loop(f,ft)
                {
                  F_PROFILE(f,ft,i) = 374.486;
                }
             end_f_loop(f,ft);
           }

        /* (etc) */
        /* (etc) */
        /* (etc) */

        else
           {
             begin_f_loop(f,ft)
                {
                  F_PROFILE(f,ft,i) = 0.000;
                }
             end_f_loop(f,ft);
           }
}
```

Appendix B. 0.75m diameter Grit King® test facility

Figure B1. The 0.75m diameter Grit King® in the laboratory at Cardiff University.

Figure B2. The stand, header tank and inlet pipe to the 0.75m diameter Grit King® in the laboratory at Cardiff University.

CERTIFICATE OF CALIBRATION

World Flow Technology Centres

QSTA 0061 Issue 2

ABB

ABB Automation Oldends Lane, Stonehouse Gloucestershire, GL10 3TA, ENGLAND Tel: +44 (0) 1453 826661 Fax: +44 (0) 1453 821121 e-mail: flow@gb.abb.com	**ABB Automation Inc.** 125 East Country Line Road Warminster, PA 18974 U.S.A. Tel: +1 215 674 6000 Fax: +1 215 674 6394	**ABB Automation** P.O. Box 2083 Taren Point NSW 2229 AUSTRALIA Tel: +61 2 540 0000 Fax: +81 2 540 0001	**ABB Automation GmbH** Dransfelder Str. 2 D-37079 Goettingen GERMANY Tel: +49 (0) 551 905212 Fax: +49 (0) 551 905711

Customer name:	STONEHOUSE MANUFACTURING	Meter code :	MF\E10114110J005ER0000001	Certificate number :	04/57951
Customer ref. :	STEVE MANDEVILLE	Calibration output :	Digital	Date of calibration :	14 May 2004
Serial number :	X/10127/19/1	Customer full scale :	25.000 l/s	Test plant :	Rig 4 70m³/h
Order reference :	X/10127/NKM	Calibration range :	20.00 l/s	Sensor factor 1 :	1.9924
Meter type :	MagMaster	Meter bore :	100 mm	Sensor factor 2/3/4:	-6 / 5 / 1.0000
Tag number :				Transmitter No :	vke403264

Test Run number	Run Time sec	Water Temp °C Int	Water Temp °C Ext	Stream 1 l/s	Stream 2 l/s	Stream 3 l/s	Stream 4 l/s	Stream 5 l/s	Total Flow l/s	Flowrate l/s	% Cal. range	% Error
						Reference				Meter Under Test		
1	100	21.5	–	20.033	0	0	0	0	20.033	20.018	100.1	-0.07
2	301	21.5	–	0	0.19745	0	0	0	0.19745	0.19678	1	-0.34
3	300	21.5	–	0	0.50590	0	0	0	0.5059	0.50327	2.5	-0.52
4	300	21.5	–	0	1.0193	0	0	0	1.0193	1.0186	5.1	-0.06
5	300	21.6	–	0	2.0135	0	0	0	2.0135	2.0139	10.1	0.02

Calibrator   MALCOLM   897   Approved by   ABB   K/T   Witnessed by   Page 1 of 3

Figure B3. Copy of the calibration certificate for the electromagnetic flowmeter, supplied by ABB.

Appendix C. Free surface measurements

Table C1. Height of the free surface
above the overflow in the 0.75m diameter Grit King[®].

Inlet flowrate, / litres/second	Fluid height above the overflow, / mm						
	Vent Box	Point 1	Point 2	Point 3	Point 4	Point 5	Point 6
0.00	0	0	0	0	0	0	0
1.38	45	37	37	37	37	37	37
3.90	72	60	60	60	60	50	40
7.16	120±2	85±10	90±5	100±5	100±5	60±2	45±2
12.25	210±2	95±10	150±7	165±7	155±7	60±5	45±5

Table C2. Comparison of the free surface
height above the base of the overflow channel in the 6' diameter Grit King[®].

Flowrate, / litres/second	Free surface height above the base of the overflow channel	
	With mesh at the overflow	Without mesh at the overflow
	Free surface height, / m	Free surface height, / m
7.60	0.051	0.051
15.11	0.064	0.057
22.37	0.076	0.076
29.26	0.089	0.083
35.97	0.102	0.089
42.40	0.102	0.101
48.57	0.102	0.114
54.39	0.114	0.114
60.01	0.121	0.127
65.37	0.127	0.127
70.39	0.140	0.140
75.20	0.140	0.152
79.73	0.152	0.178

Table C3. Approximate height of the
fluid in the overflow of the 3.4m diameter Storm King[®].

Overflow discharge, / m^3/s	Rise velocity, / litres/m^2s	Fluid height at overflow, / m
0.024	2.6	0.043
0.076	8.3	0.086
0.129	14.2	0.120
0.155	17.0	0.137

Appendix D. Static pressure measurements on the 0.75m diameter Grit King®

**Table D1. Static pressure readings taken at points
1 to 4 at the inlet to the 0.75m diameter Grit King®.**

Inlet flowrate, / litres/second	Pressure, / Pa			
	Point 1	Point 2	Point 3	Point 4
0.00	0	0	0	0
2.35	471	451	471	451
3.71	647	628	638	628
4.69	746	726	746	736
5.55	853	844	853	844
6.67	971	991	1001	991
7.51	1079	1099	1118	1099
8.53	1226	1246	1256	1256
9.58	1393	1403	1383	1413
10.58	1540	1540	1540	1560
11.84	1717	1727	1746	1766
0.00	0	0	0	0
0.77	255	245	245	235
2.36	441	451	461	451
3.94	628	647	667	657
5.08	755	775	795	785
6.26	922	932	952	942
7.25	1040	1059	1069	1069
8.31	1197	1197	1226	1226
9.33	1364	1354	1373	1373
10.23	1491	1491	1491	1521
11.75	1697	1707	1736	1746
0.00	0	0	0	0
0.71	235	235	245	235
2.62	510	500	510	500
3.78	657	638	657	638
5.20	804	795	814	804
6.13	912	922	942	932
7.62	1109	1099	1128	1128
8.70	1256	1265	1305	1295
9.83	1432	1422	1442	1472
11.17	1628	1628	1668	1668
11.77	1697	1727	1746	1746

Table D2. Static pressure readings taken at the inlet and points 5 to 7 on the 0.75m diameter Grit King®.

Inlet flowrate, / litres/second	Pressure, / Pa			
	Inlet	Point 5	Point 6	Point 7
0	0	0	0	0
0.74	265	245	255	245
1.56	353	353	363	353
2.52	481	491	491	491
3.59	608	628	608	618
4.64	736	765	746	755
5.24	804	853	834	853
6.03	912	1001	991	1001
6.95	1030	1138	1109	1128
7.65	1118	1265	1216	1256
9.05	1295	1511	1472	1511
10	1432	1697	1638	1707
11.9	1717	2099	2001	2099
0	0	0	0	0
0.7	275	255	275	265
1.41	353	324	314	343
2.39	471	461	441	471
3.71	638	638	638	647
4.61	736	765	775	775
5.21	814	844	834	853
6.62	1001	1079	1079	1118
7.58	1118	1246	1207	1256
8.34	1216	1373	1344	1393
10.04	1452	1697	1648	1727
11.15	1609	1933	1854	1962
11.96	1717	2099	2011	2119
0	0	0	0	0
0.75	275	245	255	245
1.51	353	343	363	343
2.69	510	500	491	491
3.46	608	608	598	598
4.62	736	755	755	755
5.8	883	942	922	952
6.6	991	1079	1059	1079
7.54	1109	1236	1207	1226
8.37	1197	1393	1354	1383
9.28	1344	1560	1530	1570
10.28	1481	1746	1687	1756

**Table D3. Static pressure readings taken at the inlet
and points 8, 11 and 12 on the 0.75m diameter Grit King®.**

Inlet flowrate, / litres/second	Pressure, / Pa			
	Inlet	Point 8	Point 11	Point 12
0	0	0	0	0
0.81	245	245	255	245
1.5	343	343	353	334
2.12	432	432	422	412
3.6	618	608	589	569
4.41	716	716	667	628
5.15	804	853	726	716
6.07	922	981	814	795
7.18	1050	1158	873	853
7.93	1148	1295	932	903
8.25	1207	1393	971	952
9.51	1364	1609	1050	1010
10.78	1560	1854	1109	1089
11.88	1717	2099	1167	1148
0	0	0	0	0
0.8	284	265	284	265
1.37	343	343	334	334
2.3	461	451	432	422
3.7	638	638	589	579
4.41	726	765	657	657
5.44	844	893	736	726
6.38	961	1050	814	804
7.22	1079	1207	883	853
8.01	1177	1334	932	912
9.11	1315	1550	1010	981
10.71	1570	1864	1118	1079
12.02	1746	2139	1177	1118
0	0	0	0	0
0.7	275	226	275	275
1.48	353	353	353	353
2.52	500	510	461	481
3.59	638	638	579	559
4.58	746	746	677	647
5.58	863	903	755	736
6.44	981	1158	814	804
7.85	1167	1315	922	912
8.79	1265	1472	1010	961
9.95	1452	1697	1089	1030
10.92	1599	1893	1128	1079
12.03	1746	2148	1177	1138

**Table D4. Static pressure readings taken at the inlet
and points 9 and 10 on the 0.75m diameter Grit King®.**

Inlet flowrate, / litres/second	Pressure, / Pa		
	Inlet	Point 9	Point 10
0	0	0	0
0.65	226	235	226
1.13	304	304	304
2.27	461	432	422
2.8	530	471	461
3.9	657	530	515
4.66	746	559	540
5.7	873	598	579
6.91	1040	608	598
7.94	1177	618	608
9.23	1334	618	608
12.02	1746	589	608
0	0	0	0
0.77	245	245	245
1.52	363	343	334
2.63	510	451	432
3.79	647	520	500
4.48	726	549	530
5.67	873	589	569
6.56	991	608	589
7.38	1109	618	598
8.77	1295	628	608
9.96	1442	628	618
12	1746	589	598
0	0	0	0
0.72	235	245	240
1.77	392	383	373
2.81	530	471	461
4.25	706	549	535
4.84	775	579	549
5.85	893	608	589
6.83	1020	618	598
8.53	1246	633	608
10.23	1501	628	618
12.03	1736	589	598

Appendix E. Pressure distribution within a cyclone

In a vortex flow such as that in a HDVS, the pressure increases radially outwards (Svarovsky, 1984) and the rotation of the fluid creates a low pressure axial core (Bradley, 1965). A mathematical proof for this is given below.

When a fluid flows in a curved path, the velocity changes constantly due to a constant change in direction. It can therefore be shown that the total change in energy with radius is given by

$$\frac{dH}{dr} = \frac{u}{g}\left(\frac{u}{r} + \frac{du}{dr}\right)$$

(E1)

The derivation of Equation E1 is documented in fluid mechanics books such as Douglas *et al.* (1998).

Forced vortex

In a forced vortex the fluid rotates as a solid body with a constant angular velocity ω so that at any radius r

$$u = \omega r$$

(E2)

and

$$\frac{du}{dr} = \omega$$

(E3)

Substituting Equation E2 and E3 into Equation E1 and integrating gives

$$H = \frac{\omega^2 r^2}{g} + B$$

(E4)

Where: B = Constant

The head of fluid at a point in the fluid is given by Bernoulli's equation:

$$H = \frac{p}{\rho g} + \frac{u^2}{2g} + z$$

(E5)

Substituting Equation E2 into Equation E5 and equating the resulting equation with E4 gives

$$\frac{p}{\rho g} = \frac{w^2 r^2}{2g} + B - z \qquad \text{(E6)}$$

Hence, from Equation E6 the pressure increases radially outwards.

At the free surface, the pressure is zero, hence the shape of the free surface is given by Equation E6 by setting $p/\rho g$ to zero and is therefore a paraboloid.

Free vortex

In a free vortex, there is no change in total energy per unit weight with radius i.e.

$$\frac{dH}{dr} = 0 \qquad \text{(E7)}$$

Substituting Equation E7 into E1 and rearranging gives

$$\frac{du}{u} + \frac{dr}{r} = 0 \qquad \text{(E8)}$$

Integrating Equation E8 gives

$$\log_e u + \log_e r = B \qquad \text{(E9)}$$

Where: B = Constant

Equation E9 may be simplified to

$$ur = S \qquad \text{(E10)}$$

Where: S = Strength of the vortex at radius r, m^2/s

Substituting Equation E10 into E5 for u and rearranging gives

$$\frac{p}{\rho g} = H - z - \frac{S^2}{2gr^2} \qquad \text{(E11)}$$

Hence, from Equation E11 the pressure increases radially outwards.

Setting $p/\rho g$ to zero in Equation E11 gives the shape of the free surface which is a hyperbola asymptotic to the axis of rotation and to the horizontal plane.

Rankine (Combined) vortex

Real systems are neither a free of forced vortex but are a combination of the two and which may tend towards either a free or a forced vortex. The combination of the two is known as the Rankine vortex and tends to be a forced vortex at the centre where the fluid rotates as a solid body and is surrounded by a free vortex.

Appendix F. Particulate properties used for testing the 0.75m diameter Grit King®

Table F1. Settling velocity and particle diameters for two random samples of a Purolite A100 500-710 micron sieve size range.

Sample 1		Sample 2	
Settling velocity, / m/s		Particle diameter, / mm	
0.00457	0.00295	0.48	0.48
0.00401	0.00415	0.65	0.56
0.00459	0.00331	0.47	0.58
0.00446	0.00392	0.57	0.63
0.00329	0.00427	0.59	0.53
0.00420	0.00312	0.75	0.58
0.00401	0.00429	0.55	0.58
0.00445	0.00346	0.60	0.52
0.00437	0.00445	0.55	0.60
0.00357	0.00374	0.53	0.50
0.00473	0.00363	0.57	0.62
0.00421	0.00388	0.55	0.47
0.00415	0.00284	0.52	0.51
0.00465	0.00503	0.55	0.54
0.00360	0.00391	0.41	0.48
0.00398	0.00420	0.54	0.59
0.00363	0.00429	0.61	0.56
0.00448	0.00347	0.59	0.54
0.00418	0.00437	0.57	0.55
0.00456	0.00371	0.50	0.47
0.00362	0.00377	0.54	0.56
0.00431	0.00404	0.59	0.46
0.00268	0.00399	0.53	0.54
0.00377	0.00387	0.58	0.54
0.00473	0.00305	0.53	0.43
Average	0.0069	Average	0.55
Standard deviation, %	13.3	Standard deviation, %	10.7

Fluid temperature at start of tests: 16.0°C

Fluid temperature at end of tests: 16.0°C

Table F2. Settling velocity and particle diameters for two random samples of a Purolite A100 710-1000 micron sieve size range.

Sample 1		Sample 2	
Settling velocity, / m/s		Particle diameter, / mm	
0.01297	0.00887	0.73	0.73
0.00933	0.00980	0.72	0.64
0.00894	0.00941	0.92	0.67
0.00980	0.01144	0.70	0.73
0.00997	0.00860	0.88	0.66
0.00908	0.01051	0.67	0.67
0.00894	0.01054	0.67	0.77
0.00980	0.00887	0.70	0.69
0.00892	0.01013	0.69	0.67
0.01000	0.00860	0.75	0.67
0.00950	0.00992	0.55	0.71
0.01193	0.00964	0.66	0.65
0.00946	0.00857	0.77	0.68
0.01038	0.00914	0.70	0.63
0.00925	0.00836	0.73	0.73
0.01056	0.01035	0.75	0.75
0.00926	0.00961	0.69	0.71
0.00929	0.00971	0.78	0.81
0.00929	0.00955	0.68	0.55
0.00890	0.01101	0.69	0.89
0.00882	0.00855	0.69	0.74
0.00926	0.01013	0.74	0.86
0.01046	0.00934	0.72	0.68
0.00883	0.00947	0.69	0.86
0.00840	0.01163	0.69	0.68
Average	0.0097	Average	0.72
Standard deviation, %	9.8	Standard deviation, %	10.3

Fluid temperature at start of tests: 18.0°C

Fluid temperature at end of tests: 18.0°C

Table F3. Settling velocity and particle diameters for two random samples of a Purolite PPC-100H 500-600 micron sieve size range.

Sample 1		Sample 2	
Settling velocity, / m/s		Particle diameter, / mm	
0.03030	0.02805	0.55	0.54
0.03111	0.02993	0.53	0.53
0.02655	0.03140	0.62	0.53
0.03007	0.02946	0.58	0.6
0.02756	0.02629	0.57	0.58
0.02562	0.02687	0.62	0.6
0.02725	0.02909	0.54	0.54
0.03010	0.03007	0.55	0.57
0.02951	0.03045	0.56	0.54
0.02562	0.02998	0.63	0.57
0.02640	0.02998	0.56	0.54
0.02852	0.02681	0.61	0.58
0.02909	0.02792	0.59	0.53
0.02810	0.02888	0.58	0.54
0.02524	0.03129	0.54	0.53
0.02562	0.02836	0.61	0.57
0.02571	0.02797	0.6	0.54
0.02623	0.02551	0.66	0.57
0.02573	0.02538	0.64	0.52
0.02918	0.02983	0.6	0.54
0.02836	0.03127	0.56	0.59
0.02939	0.03079	0.55	0.49
0.02497	0.03056	0.59	0.56
0.02904	0.02951	0.54	0.54
0.02779	0.02530	0.59	0.58
Average	0.0283	Average	0.57
Standard deviation, %	6.9	Standard deviation, %	6.1

Fluid temperature at start of tests: 13.5°C

Fluid temperature at end of tests: 14.0°C

Table F4. Settling velocity and particle diameters for two random samples of a Styrocell 1.4-2.0mm sieve size range.

Sample 1		Sample 2	
Settling velocity, / m/s		Particle diameter, / mm	
0.02183	0.02413	1.96	1.79
0.02020	0.02024	1.70	1.69
0.02128	0.01925	1.71	1.58
0.02049	0.01928	1.75	1.87
0.02041	0.02110	1.87	1.75
0.02191	0.01756	1.76	1.76
0.01928	0.02067	1.80	1.79
0.02007	0.02015	1.66	1.65
0.02167	0.02177	1.79	1.82
0.02268	0.02218	1.68	1.72
0.02067	0.02311	1.76	1.81
0.02359	0.02015	1.73	1.78
0.01981	0.01960	1.59	1.62
0.01977	0.02042	1.65	1.65
0.02318	0.02008	1.74	1.87
0.02260	0.01866	1.62	1.66
0.02261	0.02045	1.64	1.79
0.02118	0.01807	1.80	1.68
0.01928	0.02209	1.64	1.68
0.02059	0.01981	1.72	1.71
0.02297	0.02064	1.75	1.82
0.02022	0.02006	1.88	1.74
0.02063	0.02174	1.64	1.67
0.02125	0.02258	1.78	1.85
Average	0.0209	Average	1.74
Standard deviation, %	6.9	Standard deviation, %	4.9

Fluid temperature at start of tests: 18.0°C

Fluid temperature at end of tests: 18.0°C

Table F5. Settling velocity and particle diameters for two random samples of a Styrocell 2.0-2.8mm sieve size range.

Sample 1		Sample 2	
Settling velocity, / m/s		Particle diameter, / mm	
0.02785	0.02781	2.40	2.03
0.03211	0.02706	2.57	2.40
0.03333	0.03231	2.01	2.44
0.02954	0.03093	2.11	2.17
0.02652	0.02905	2.23	2.02
0.02881	0.02738	2.79	2.38
0.02605	0.02830	2.23	2.40
0.02734	0.02318	2.01	2.01
0.02570	0.02515	2.20	2.42
0.03271	0.03139	1.66	2.08
0.02524	0.03241	2.12	2.17
0.01858	0.02713	2.54	2.18
0.03360	0.02774	2.24	2.44
0.03328	0.03404	2.67	2.20
0.02807	0.02921	2.21	2.17
0.03333	0.02570	2.32	2.05
0.03066	0.02975	2.71	2.20
0.02468	0.03066	2.52	2.30
0.02975	0.03437	2.24	2.35
0.03339	0.03547	2.52	2.13
0.02975	0.03088	2.25	2.21
0.02665	0.02881	2.60	2.20
0.02512	0.03465	2.73	2.25
0.02583	0.03107	2.23	2.17
0.03148	0.02849	2.21	2.18
Average	0.0293	Average	2.28
Standard deviation, %	11.7	Standard deviation, %	9.6

Fluid temperature at start of tests: 18.0°C

Fluid temperature at end of tests: 22.0°C

**Table F6. Settling velocity and particle diameters for
two random samples of a Styrocell 2.8-5.6mm sieve size range.**

Sample 1		Sample 2	
Settling velocity, / m/s		Particle diameter, / mm	
0.03561	0.03095	2.75	2.85
0.03822	0.03495	2.00	2.74
0.03793	0.03276	2.74	3.63
0.03390	0.03604	2.86	2.80
0.03390	0.03374	2.48	2.75
0.03495	0.03355	2.80	3.07
0.03677	0.03383	2.98	2.74
0.03435	0.03172	2.67	2.77
0.02217	0.03789	2.82	2.67
0.03422	0.03472	2.87	2.75
0.03425	0.03822	2.78	2.62
0.03492	0.03432	2.76	2.69
0.03579	0.03607	2.84	3.07
0.03793	0.03336	2.86	2.60
0.03529	0.03412	2.74	2.75
0.03475	0.03926	3.29	2.66
0.03150	0.03618	2.86	2.89
0.03575	0.02495	3.28	2.78
0.02922	0.03475	3.12	2.84
0.03673	0.03355	2.85	3.03
0.03512	0.03300	2.65	3.05
0.03561	0.03492	2.57	2.72
0.03336	0.02746	2.86	2.70
0.03396	0.03561	2.63	1.87
0.03723	0.03495	3.19	2.84
Average	0.0343	Average	2.80
Standard deviation, %	9.1	Standard deviation, %	9.7

Fluid temperature at start of tests: 18.0°C

Fluid temperature at end of tests: 18.0°C

Table F7. Derived properties for Purolite A100 500-710micron sieve size range.
(Limits based on a Student t-test with a 99.8% confidence interval).

	Mean	Lower	Upper
Diameter, / mm	0.55	0.49	0.58
Settling velocity, / m/s	0.0069	0.0064	0.0073
Particle density, / kg/m^3	1064	1053	1084

Table F8. Derived properties for Purolite A100 710-1000micron sieve size range.
(Limits based on a Student t-test with a 99.8% confidence interval).

	Mean	Lower	Upper
Diameter, / mm	0.72	0.68	0.75
Settling velocity, / m/s	0.0097	0.0092	0.0101
Particle density, / kg/m^3	1057	1050	1066

Table F9. Derived properties for Purolite PPC-100H 500-600micron sieve size range.
(Limits based on a Student t-test with a 99.8% confidence interval).

	Mean	Lower	Upper
Diameter, / mm	0.57	0.55	0.58
Settling velocity, / m/s	0.0283	0.0274	0.0292
Particle density, / kg/m^3	1372	1344	1410

Table F10. Derived properties for Styrocell 1.4-2.0mm sieve size range.
(Limits based on a Student t-test with a 99.8% confidence interval).

	Mean	Lower	Upper
Diameter, / mm	1.74	1.70	1.78
Settling velocity, / m/s	0.0209	0.0202	0.0216
Particle density, / kg/m^3	1036	1033	1039

Table F11. Derived properties for Styrocell 2.0-2.8mm sieve size range.
(Limits based on a Student t-test with a 99.8% confidence interval).

	Mean	Lower	Upper
Diameter, / mm	2.28	2.18	2.38
Settling velocity, / m/s	0.0293	0.0277	0.0308
Particle density, / kg/m^3	1037	1032	1043

Table F12. Derived properties for Styrocell 2.8-5.6mm sieve size range.
(Limits based on a Student t-test with a 99.8% confidence interval).

	Mean	Lower	Upper
Diameter, / mm	2.80	2.68	2.93
Settling velocity, / m/s	0.0343	0.0328	0.0357
Particle density, / kg/m^3	1036	1031	1041

Appendix G. Retention efficiency data for the 0.75m diameter Grit King®

Table G1. 0.75m diameter Grit King® retention efficiency data for Purolite PPC-100H 500-600micron sieve size range.

Particles: Purolite PPC-100H 500-600microns		
Average water temperature, / °C	Average flowrate, / litres/second	Efficiency, / %
15.8	11.3	62.1
15.5	11.4	64.4
16.0	8.6	81.4
15.3	10.7	72.7
15.8	8.1	85.3
16.3	6.0	94.2
17.3	10.2	79.8
16.8	7.6	89.5
17.8	6.2	94.5
15.0	11.6	73.6
15.8	10.5	79.0
16.5	9.4	83.6
17.3	8.3	87.8
18.0	7.7	90.3
18.8	5.9	96.3
19.3	4.8	98.7

Table G2. 0.75m diameter Grit King® retention efficiency data for Styrocell 2.8-5.6mm sieve size range.

Particles: Styrocell 2.8-5.6mm		
Average water temperature, / °C	Average flowrate, / litres/second	Efficiency, / %
21.5	11.6	32.6
22.3	11.4	33.3
22.5	11.5	32.1
23.3	7.1	69.1
21.8	7.1	70.7
22.5	6.9	75.3
23.0	4.2	94.9
21.3	4.0	95.5
22.3	4.1	96.2
12.0	8.9	63.6
12.5	8.8	63.2
14.3	8.9	64.0
15.3	10.5	48.2
15.8	10.2	48.3
16.3	10.3	49.7
17.0	5.2	93.6
18.0	5.2	93.9
18.8	5.2	93.4

Table G3. 0.75m diameter Grit King® retention efficiency data for Styrocell 2.0-2.8mm sieve size range.

Particles: Styrocell 2.0-2.8mm		
Average water temperature, / °C	Average flowrate, / litres/second	Efficiency, / %
18.5	10.0	39.5
19.5	11.5	29.7
20.0	11.3	29.7
20.0	11.0	35.1
20.5	6.5	73.3
21.5	6.8	70.3
22.0	4.3	94.4
22.5	9.1	45.9
22.5	2.7	99.1
20.8	11.3	33.4
21.0	11.5	32.4
17.8	11.6	32.4
18.8	11.5	33.5
19.3	6.9	70.3
20.5	2.2	100.0
23.0	4.4	94.7
21.8	4.2	95.3
22.5	1.8	100.0
23.5	2.5	100.0
17.5	11.7	31.5
18.3	11.6	31.9
19.3	11.2	33.7
20.3	11.2	34.8
20.8	11.7	32.4
21.3	11.7	33.3
22.3	11.6	33.3

Table G4. 0.75m diameter Grit King® retention efficiency data for Styrocell 1.4-2.0mm sieve size range.

Particles: Styrocell 1.4-2.0mm		
Average water temperature, / °C	**Average flowrate, / litres/second**	**Efficiency, / %**
20.8	11.3	16.9
21.8	11.9	14.8
20.5	7.0	39.3
21.3	4.3	77.5
19.5	10.8	21.7
14.3	10.5	22.2
14.5	9.2	27.9
15.5	8.3	31.8
16.3	6.2	51.5
16.8	5.3	64.2
17.8	5.9	56.1
16.3	11.1	21.0
17.3	10.3	24.2
18.3	9.4	28.4
18.8	8.1	33.8
19.3	6.9	45.5
20.0	6.1	52.9
20.5	5.2	66.2

**Table G5. 0.75m diameter Grit King® retention efficiency data
for Purolite A100 710-1000micron sieve size range.**

Particles: Purolite A100 710-1000microns		
Average water temperature, / °C	**Average flowrate, / litres/second**	**Efficiency, / %**
16.5	4.3	30.3
17.5	4.5	30.0
19.5	2.5	76.4
19.8	2.2	86.5
20.3	1.2	100.0
19.5	5.4	22.7
20.3	7.7	13.3
20.8	8.9	10.0
21.5	3.3	57.8
22.0	3.6	51.2
16.5	1.6	96.7
16.8	11.7	3.8
17.5	5.9	12.2
17.8	4.5	34.1
18.8	3.6	47.1
19.5	3.0	61.2
20.3	2.4	79.9
20.8	1.8	95.1
18.5	7.8	13.2
18.8	3.0	60.5
19.3	2.9	64.0
17.5	3.2	53.5
18.5	3.1	57.1
16.3	3.1	61.9
17.3	3.3	51.2
15.8	4.7	29.4
16.0	5.3	24.1
17.0	6.2	18.7
14.8	8.4	10.3
15.8	10.2	6.7
16.5	11.2	4.8
17.0	6.2	19.3
14.8	4.2	34.8
14.5	4.3	34.5

Table G6. 0.75m diameter Grit King® retention efficiency data for Purolite A100 500-710micron sieve size range.

Particles: Purolite A100 500-710microns		
Average water temperature, / °C	Average flowrate, / litres/second	Efficiency, / %
17.8	3.2	31.9
16.5	1.7	86.6
17.8	2.1	68.5
16.3	2.4	54.7
16.5	2.7	49.4
14.8	3.6	28.9
15.5	4.6	19.7
17.5	7.5	6.8
18.5	9.4	4.4
14.3	6.0	10.7
14.8	1.3	96.2

Appendix H. 6' diameter Grit King® test facility

Figure H1. Photograph showing the position of the stand pipe used for introducing the particles into the Grit King®.

Figure H2. Photograph showing the rear of the Grit King® and the underflow pipe used for removing the particulates.

Appendix I. Particulate properties used for testing the 6' diameter Grit King®

Table I1. Settling velocity and particle diameters for two random samples of a Purolite A100 600-850micron sieve size range.

Sample 1		Sample 2	
Settling velocity, / m/s		Particle diameter, / mm	
0.00897	0.00706	0.72	0.62
0.00725	0.00813	0.69	0.63
0.00615	0.00731	0.63	0.56
0.00763	0.00792	0.57	0.55
0.00870	0.00756	0.60	0.69
0.00826	0.00645	0.56	0.59
0.00732	0.00620	0.56	0.66
0.00726	0.00603	0.64	0.64
0.00890	0.00688	0.56	0.56
0.00935	0.00812	0.62	0.60
0.00683	0.00833	0.60	0.67
0.00694	0.00997	0.51	0.76
0.00833	0.00822	0.58	0.63
0.00826	0.00575	0.62	0.61
0.00827	0.00734	0.62	0.68
0.00793	0.00760	0.68	0.62
0.00935	0.00854	0.58	0.58
0.00745	0.00640	0.73	0.63
0.00666	0.00906	0.74	0.71
0.00726	0.00829	0.70	0.47
0.00855	0.00771	0.59	0.54
0.00855	0.00648	0.76	0.74
0.00718	0.00890	0.59	0.75
0.00649	0.00728	0.75	0.72
0.00892	0.00740	0.58	0.67
Average	0.0077	Average	0.63
Standard deviation, %	12.7	Standard deviation, %	11.1

Fluid temperature at start of tests: 14.0°C

Fluid temperature at end of tests: 14.5°C

Table I2. Derived properties for Purolite A100 600-850micron sieve size range. (Limits based on a Student t-test with a 99.8% confidence interval).

	Mean	Lower	Upper
Diameter, / mm	0.63	0.60	0.67
Settling velocity, / m/s	0.00771	0.00726	0.00816
Particle density, / kg/m^3	1059	1049	1069

Table I3. Settling velocity and particle diameters for two
random samples of a Purolite PFC-100H 425-600micron sieve size range.

Sample 1		Sample 2	
Settling velocity, / m/s		Particle diameter, / mm	
0.02058	0.01505	0.56	0.65
0.01527	0.01552	0.60	0.53
0.01299	0.01436	0.51	0.56
0.01432	0.01407	0.60	0.52
0.01669	0.01305	0.63	0.54
0.01271	0.01186	0.67	0.62
0.01682	0.01290	0.63	0.76
0.01423	0.01314	0.61	0.64
0.01398	0.01448	0.55	0.66
0.01425	0.01460	0.51	0.66
0.01614	0.01128	0.60	0.72
0.01529	0.01182	0.73	0.59
0.01669	0.01333	0.54	0.62
0.01333	0.01376	0.62	0.57
0.01347	0.01174	0.52	0.66
0.01284	0.01727	0.57	0.56
0.01664	0.01358	0.60	0.55
0.01492	0.01577	0.54	0.58
0.01306	0.01200	0.59	0.57
0.01415	0.01314	0.66	0.54
0.01179	0.01210	0.53	0.65
0.01548	0.01168	0.55	0.59
0.01202	0.01396	0.48	0.52
0.01210	0.01202	0.67	0.60
0.01108	0.01225	0.62	0.51
Average	0.0139	Average	0.59
Standard deviation, %	13.5	Standard deviation, %	10.4

Fluid temperature at start of tests: 14.0°C

Fluid temperature at end of tests: 14.5°C

Table I4. Derived properties for Purolite PFC-100H 425-600micron sieve size range.
(Limits based on a Student t-test with a 99.8% confidence interval).

	Mean	Lower	Upper
Diameter, / mm	0.59	0.56	0.62
Settling velocity, / m/s	0.0139	0.0130	0.0148
Particle density, / kg/m^3	1137	1117	1163

Appendix J. Retention efficiency data for the 6' diameter Grit King®

Table J1. 6' diameter Grit King® retention efficiency data for Purolite A100 600-850micron sieve size range.

Particles: Purolite A100 600-850microns		
Average water temperature, / °C	Flowrate, / litres/second	Efficiency, / %
14.5	9.96	83.8
14.5	19.98	42.6
14.5	29.97	29.4
14.5	40.00	9.5
14.5	5.03	100.0
14.5	15.03	84.8
14.5	19.98	41.8
14.5	15.03	78.8
14.5	9.96	83.3
14.5	29.97	37.9
14.5	15.03	69.7
14.5	19.98	39.4
14.5	40.00	Mesh at overflow blinded using 340ml of particles
14.5	50.01	Mesh at overflow blinded using 160ml of particles

Table J2. 6' diameter Grit King® retention efficiency data for Purolite PFC-100H 425-600micron sieve size range.

Particles: Purolite PFC-100H 425-600microns		
Average water temperature, / °C	Flowrate, / litres/second	Efficiency, / %
14	9.96	100.0
14	19.98	96.7
14	29.97	89.8
14	40.00	60.3
14	29.97	92.1
14	40.00	64.5
14	50.01	50.0
14	50.01	46.7
14	79.99	Mesh at overflow blinded using 100ml of particles

Appendix K. Comparison of experimental and CFD residence time predictions for the 0.75m diameter Eff-Pac™ Clarifier

Normalised variance comparison

Experimental based on the average of data published by Alkhaddar *et al.* (1999) and Higgins (2000).
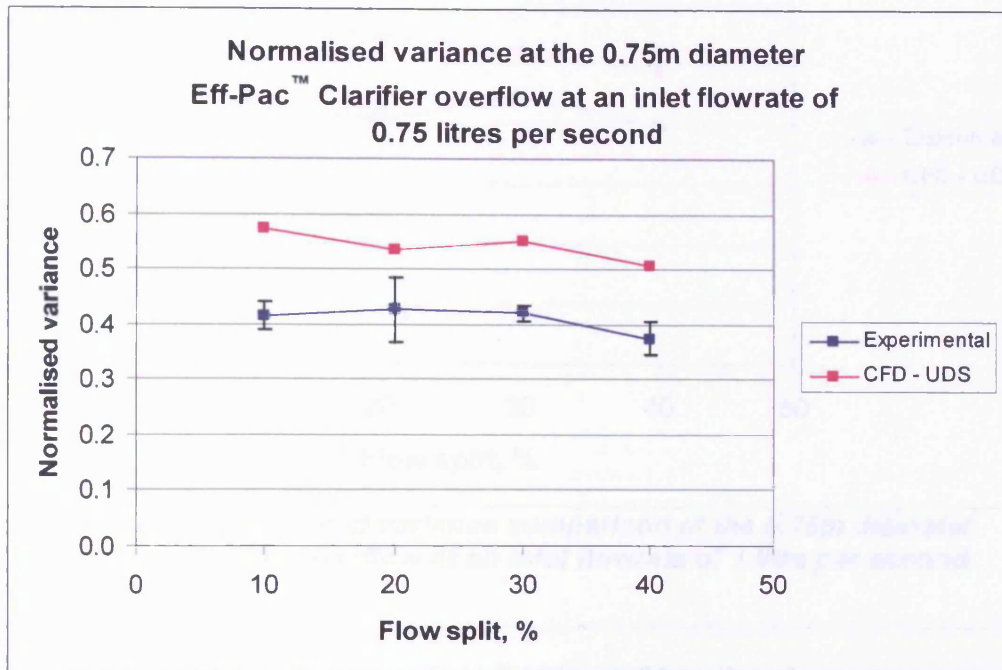
Figure K1. Normalised variance comparison at the 0.75m diameter Eff-Pac™ Clarifier overflow at an inlet flowrate of 0.75 litres per second.
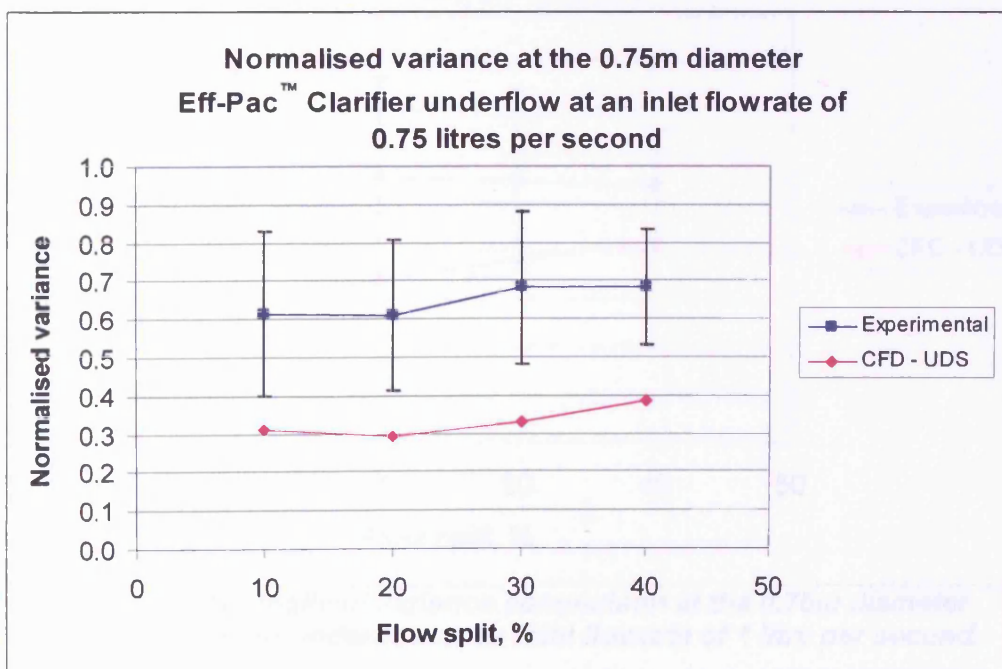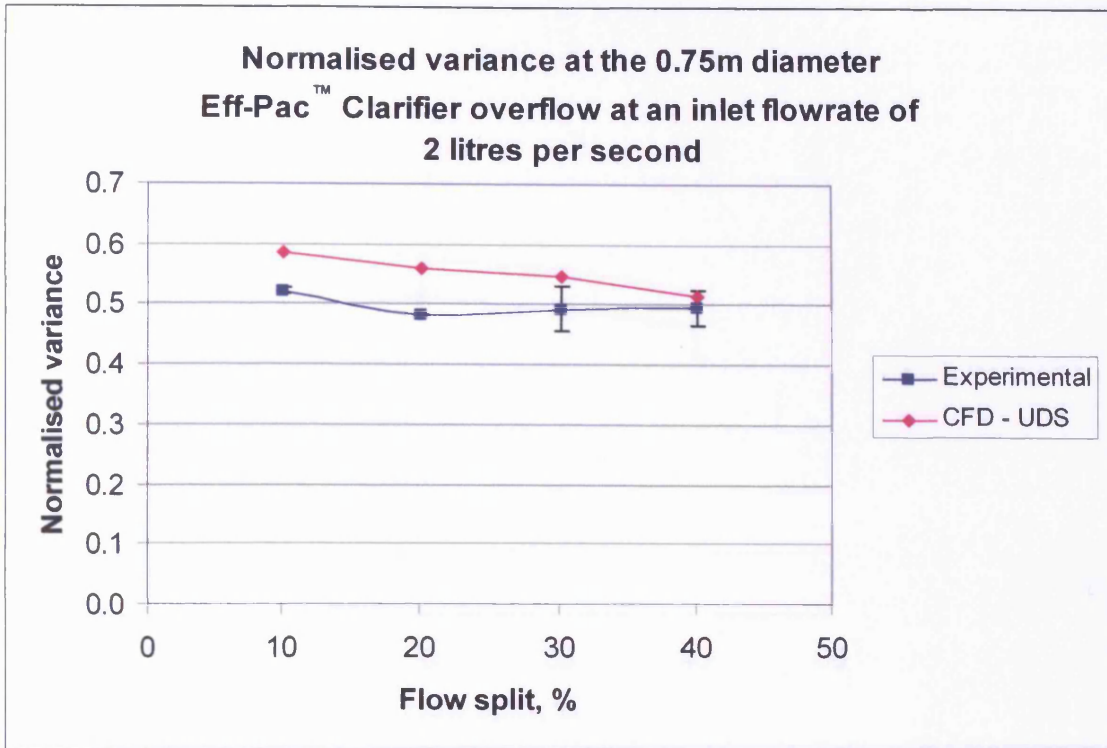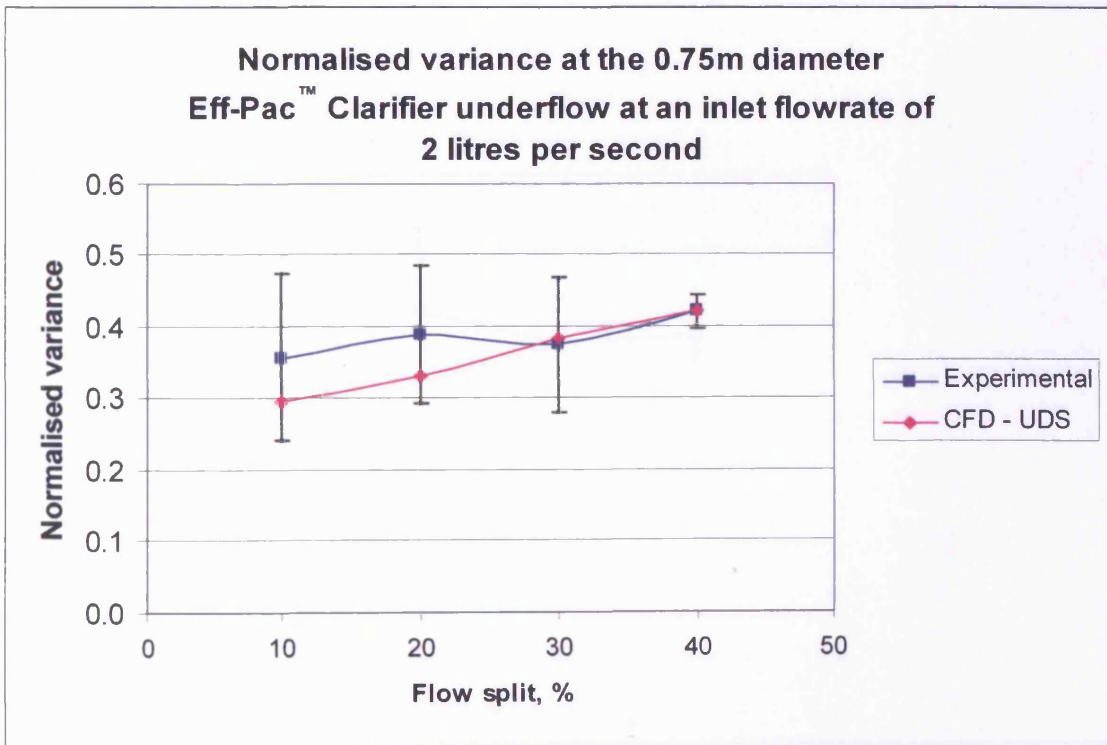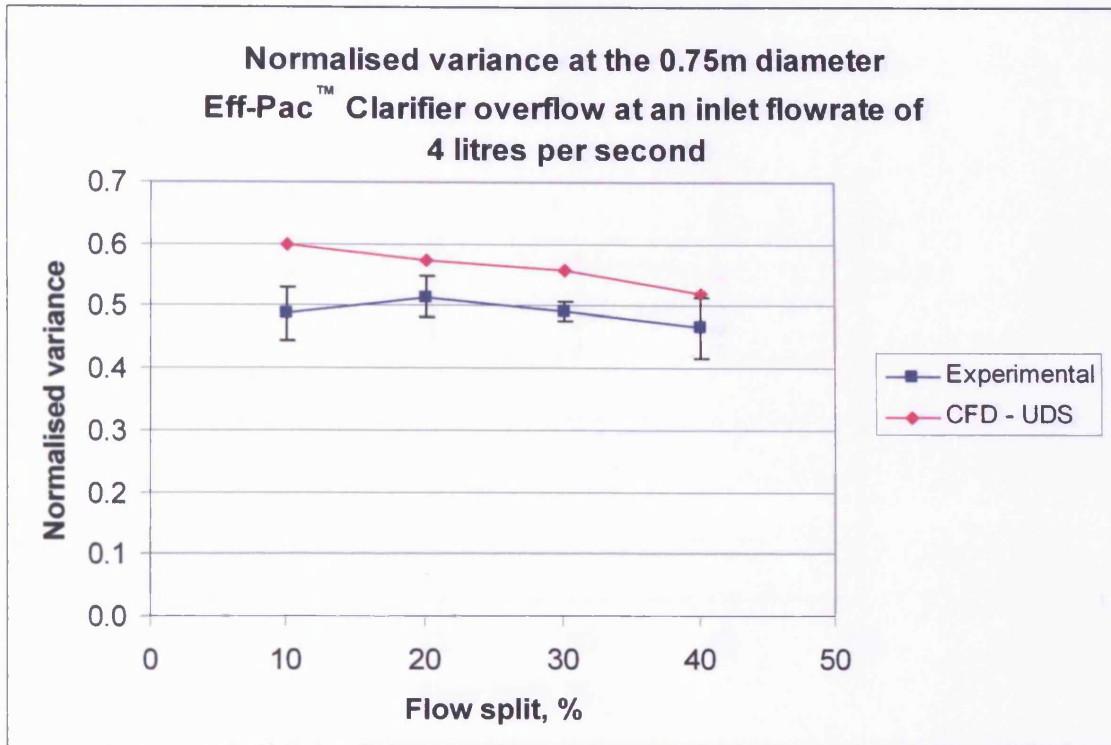

Figure K2. Normalised variance comparison at the 0.75m diameter Eff-Pac™ Clarifier underflow at an inlet flowrate of 0.75 litres per second.

Figure K5. Normalised variance comparison at the 0.75m diameter Eff-Pac™ Clarifier overflow at an inlet flowrate of 2 litres per second.
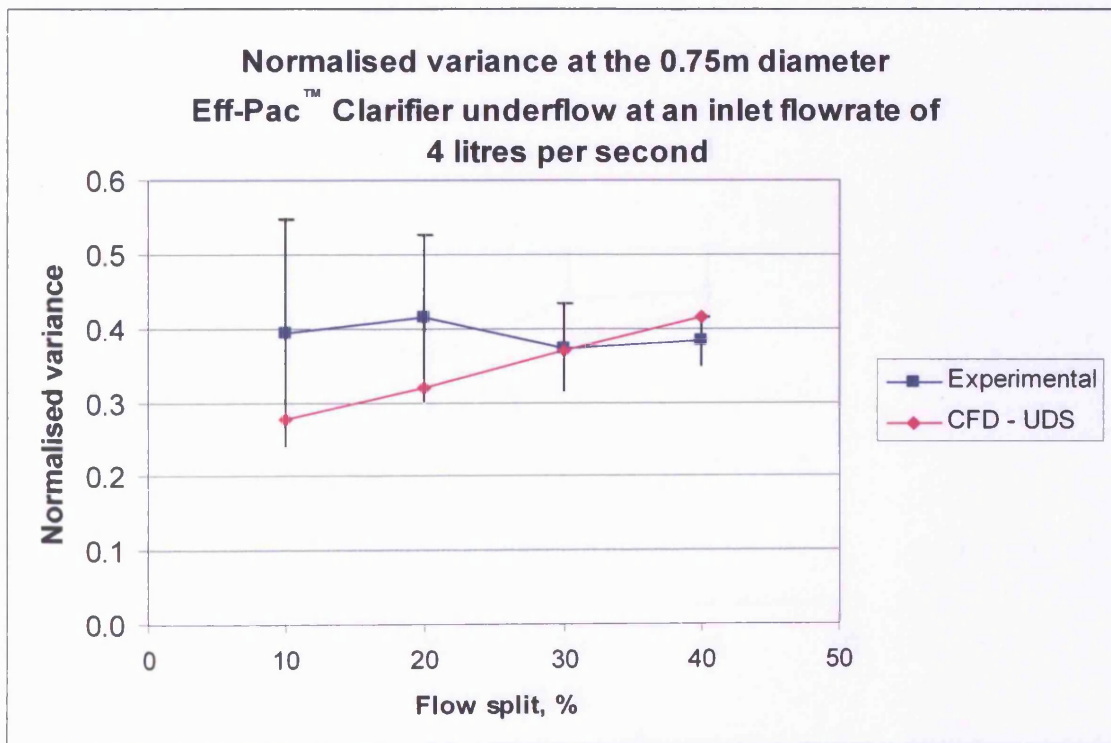

Figure K6. Normalised variance comparison at the 0.75m diameter Eff-Pac™ Clarifier underflow at an inlet flowrate of 2 litres per second.
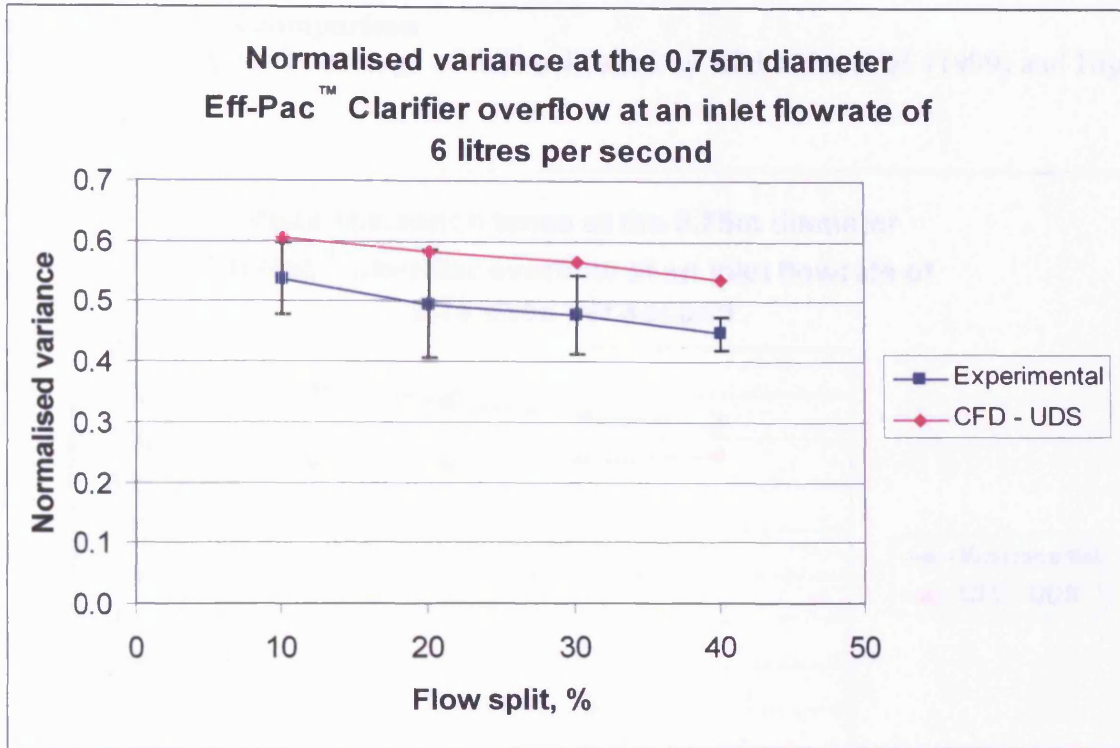
Figure K7. Normalised variance comparison at the 0.75m diameter Eff-Pac™ Clarifier overflow at an inlet flowrate of 4 litres per second.
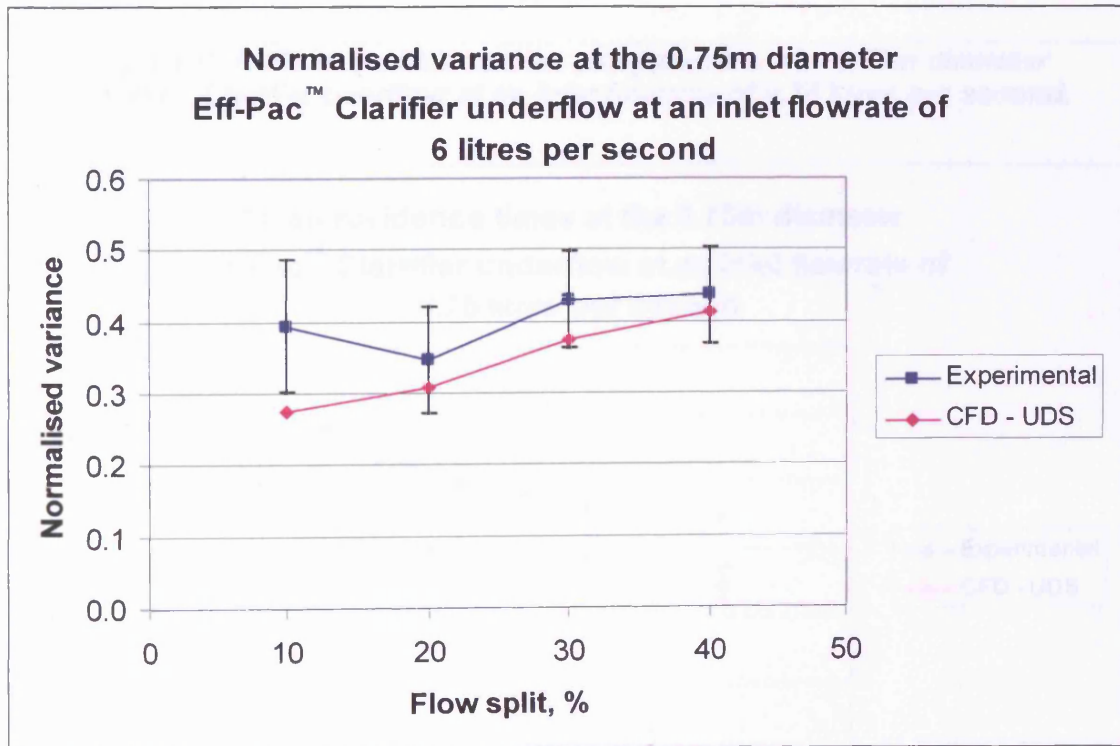

Figure K8. Normalised variance comparison at the 0.75m diameter Eff-Pac™ Clarifier underflow at an inlet flowrate of 4 litres per second.

Figure K9. Normalised variance comparison at the 0.75m diameter Eff-Pac™ Clarifier overflow at an inlet flowrate of 6 litres per second.

Figure K10. Normalised variance comparison at the 0.75m diameter Eff-Pac™ Clarifier underflow at an inlet flowrate of 6 litres per second.

Mean residence time comparison

Experimental based on the average of data published by Alkhaddar *et al.* (1999) and Higgins (2000).
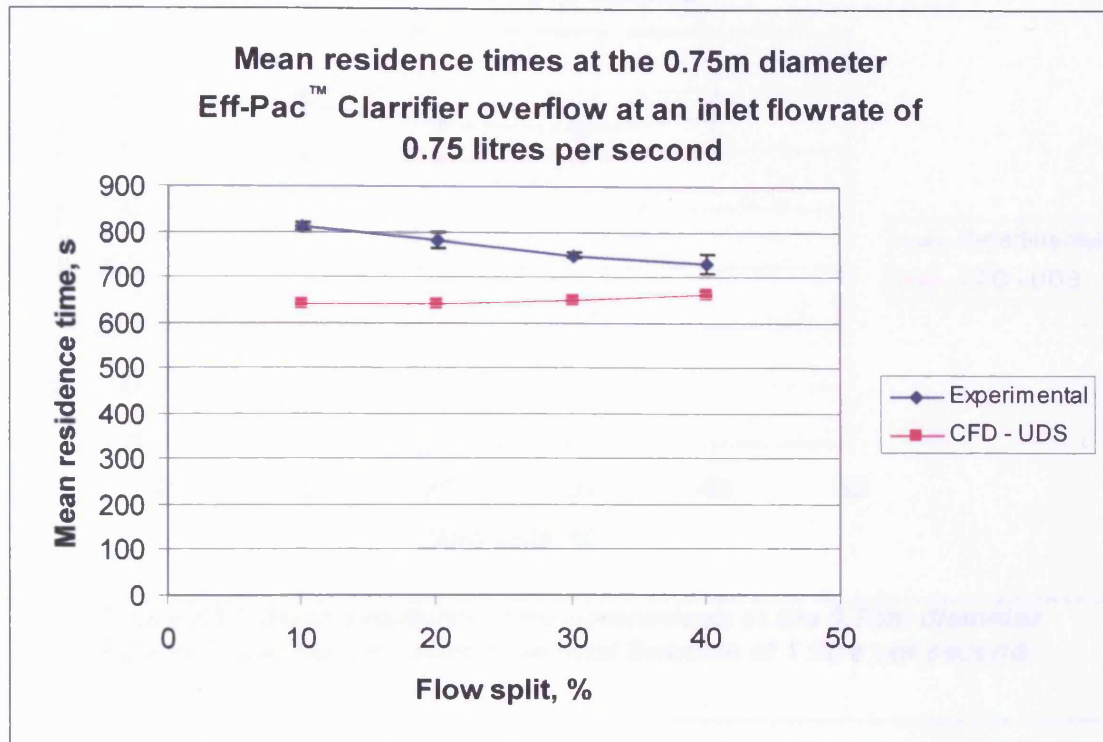

Figure K11. Mean residence time comparison at the 0.75m diameter Eff-Pac™ Clarifier overflow at an inlet flowrate of 0.75 litres per second.
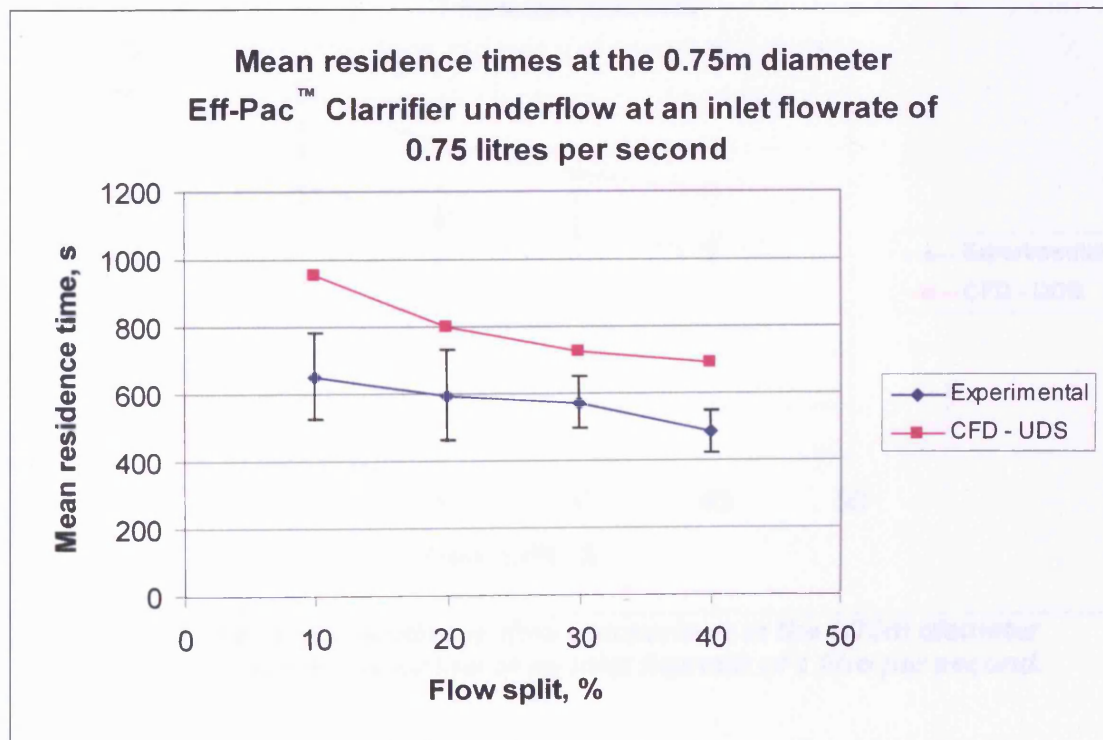

Figure K12. Mean residence time comparison at the 0.75m diameter Eff-Pac™ Clarifier underflow at an inlet flowrate of 0.75 litres per second.
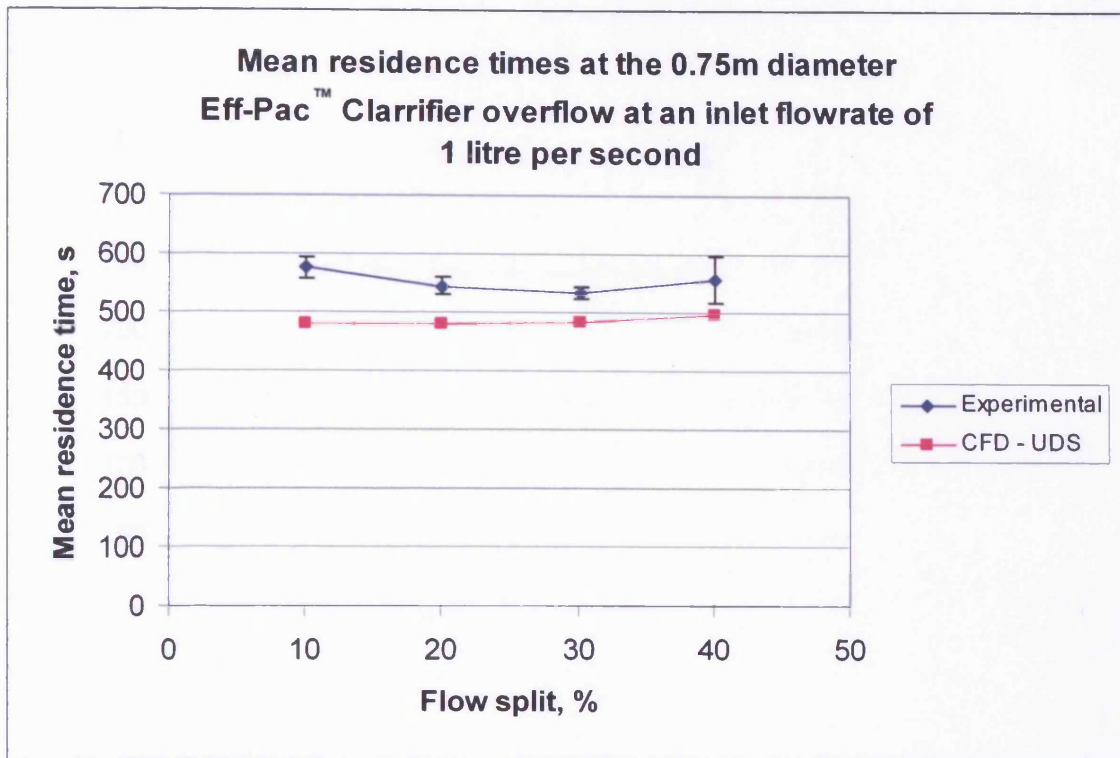
Figure K13. Mean residence time comparison at the 0.75m diameter Eff-Pac™ Clarifier overflow at an inlet flowrate of 1 litre per second.
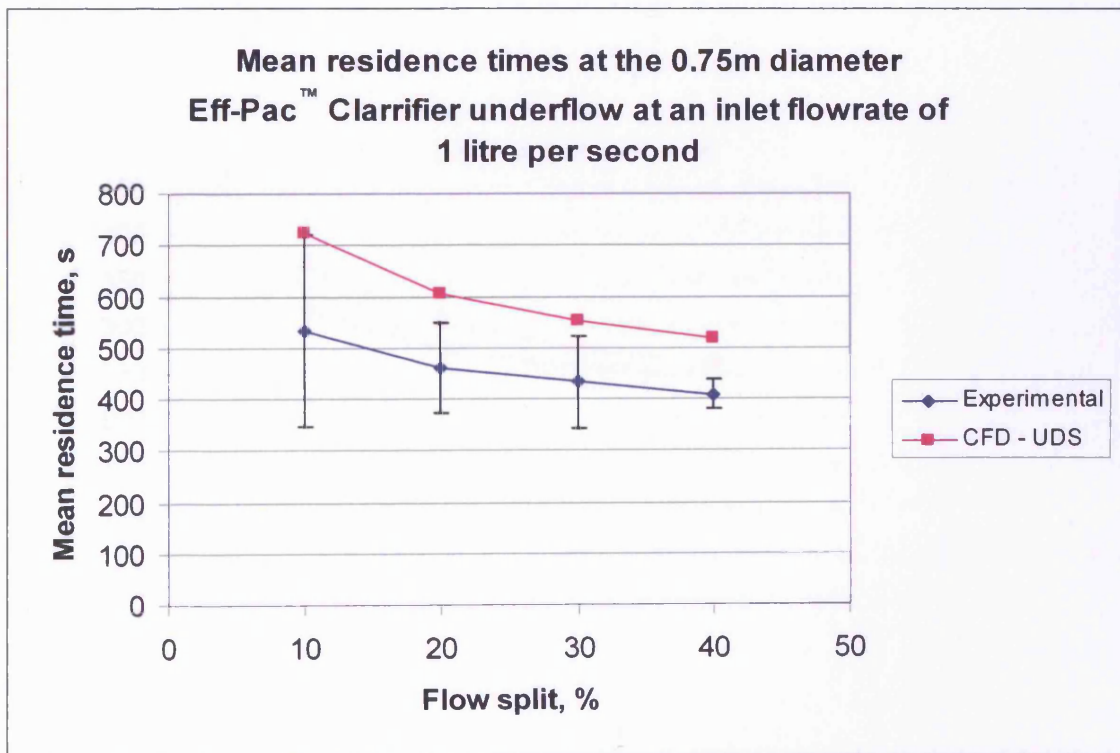

Figure K14. Mean residence time comparison at the 0.75m diameter Eff-Pac™ Clarifier underflow at an inlet flowrate of 1 litre per second.

Figure K15. Mean residence time comparison at the 0.75m diameter Eff-Pac™ Clarifier overflow at an inlet flowrate of 2 litres per second.

Figure K16. Mean residence time comparison at the 0.75m diameter Eff-Pac™ Clarifier underflow at an inlet flowrate of 2 litres per second.
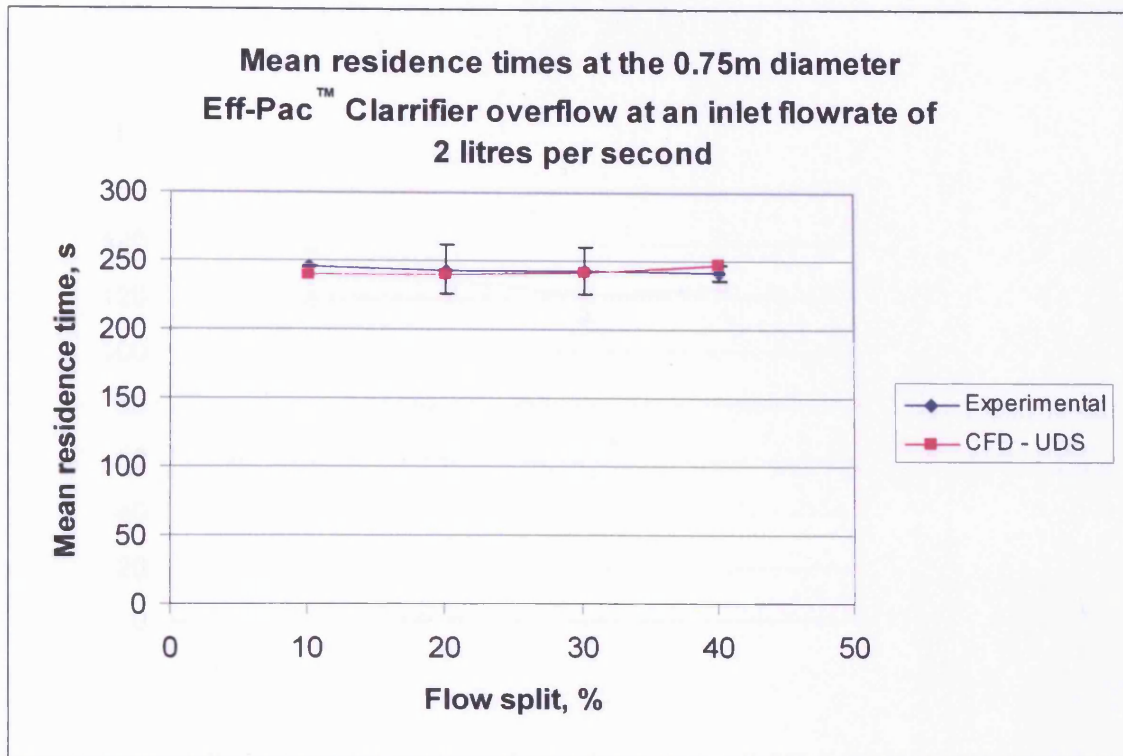
Figure K17. Mean residence time comparison at the 0.75m diameter Eff-Pac™ Clarifier overflow at an inlet flowrate of 4 litres per second.
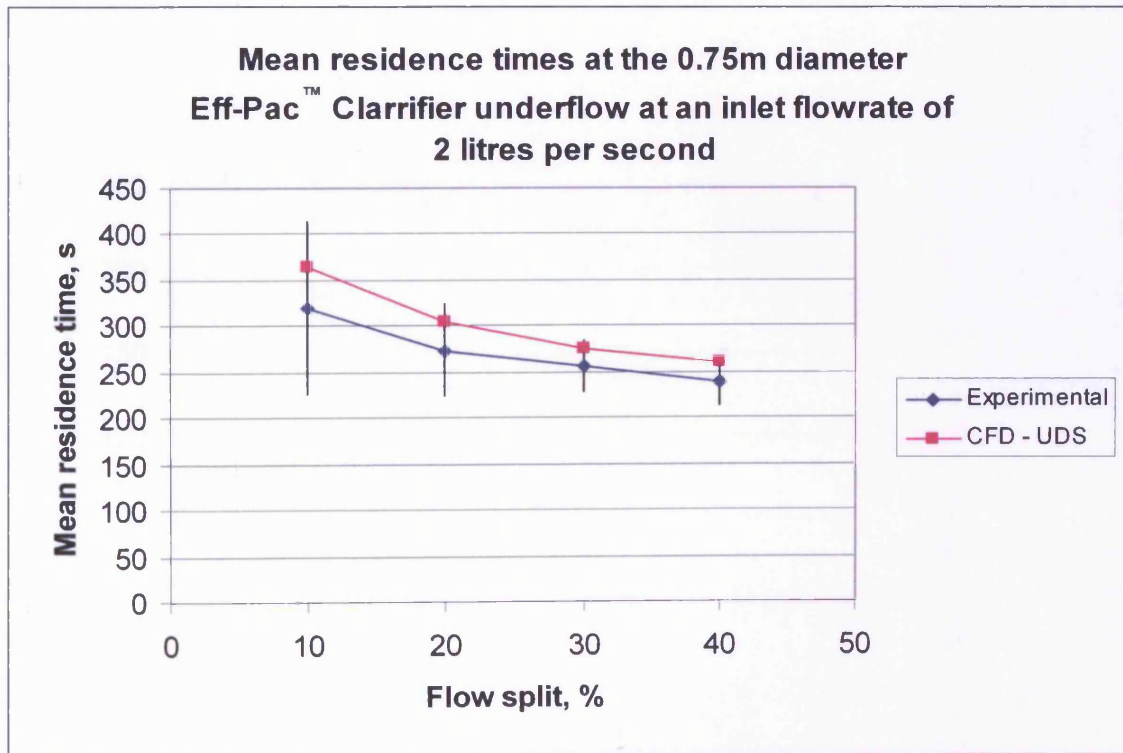

Figure K18. Mean residence time comparison at the 0.75m diameter Eff-Pac™ Clarifier underflow at an inlet flowrate of 4 litres per second.
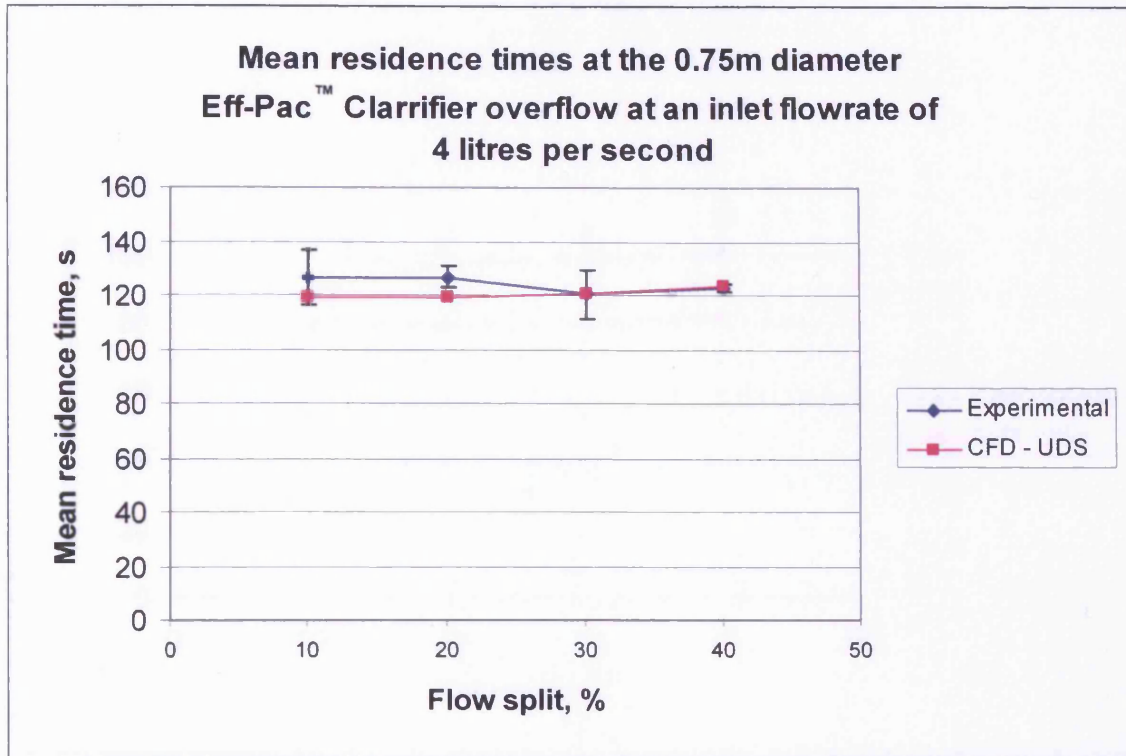
Figure K19. Mean residence time comparison at the 0.75m diameter
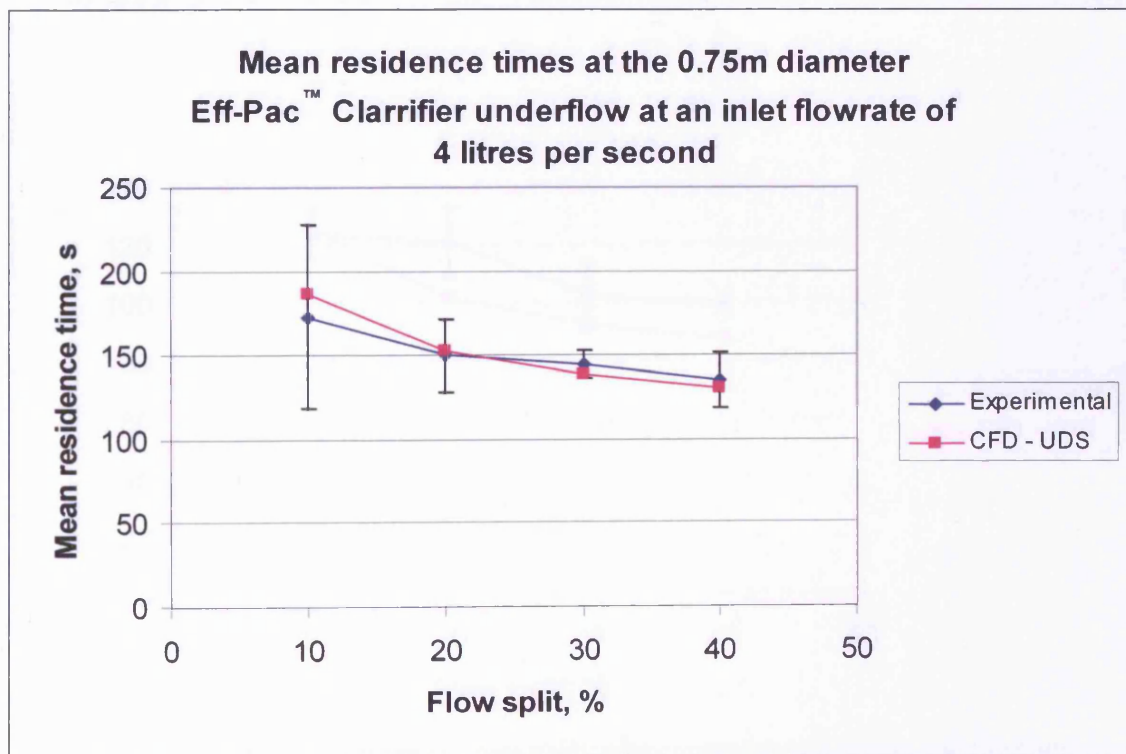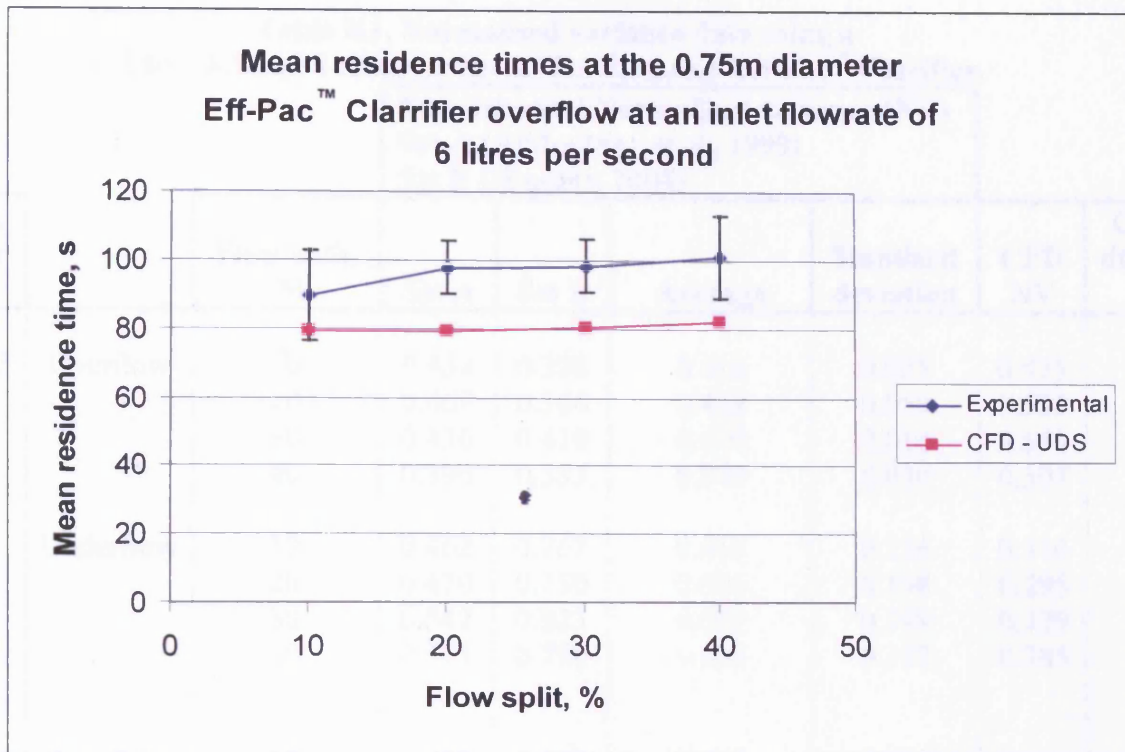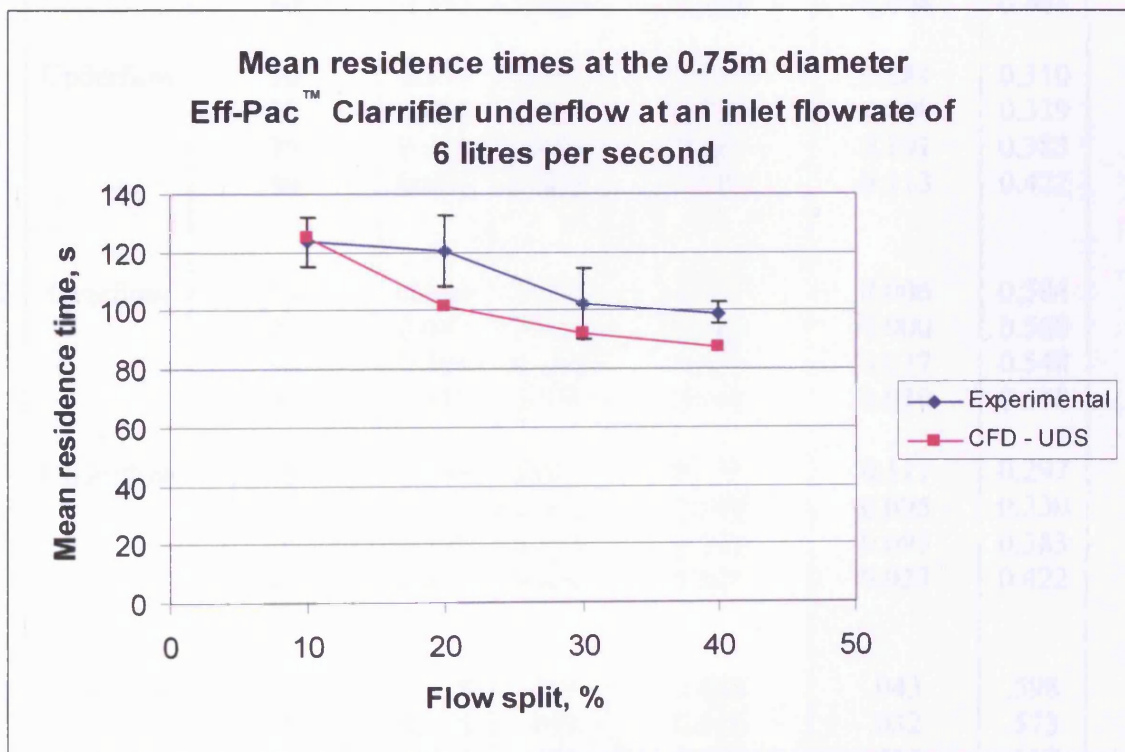*Eff-Pac™ Clarifier overflow at an inlet flowrate of 6 litres per second.*

Figure K20. Mean residence time comparison at the 0.75m diameter
Eff-Pac™ Clarifier underflow at an inlet flowrate of 6 litres per second.

Table K1. Normalised variance data using a
User Defined Scalar for the 0.75m diameter Eff-Pac™ Clarifier.

Flowrate, / litres per second		Flow split, / %	Experimental Normalised variance (NV) Set A (Alkhaddar *et al.*, 1999) Set B (Higgins, 2000)			Standard deviation	CFD NV	CFD NV difference, / %
			Set A	Set B	Average			
0.75	Overflow	10	0.434	0.398	0.416	0.025	0.575	38.2
		20	0.469	0.386	0.428	0.059	0.535	25.2
		30	0.430	0.410	0.420	0.014	0.550	31.0
		40	0.396	0.353	0.375	0.030	0.507	35.5
	Underflow	10	0.462	0.767	0.615	0.216	0.310	49.5
		20	0.470	0.750	0.610	0.198	0.295	51.6
		30	0.542	0.823	0.683	0.199	0.329	51.8
		40	0.575	0.790	0.683	0.152	0.385	43.6
1	Overflow	10	0.432	0.438	0.435	0.004	0.584	34.1
		20	0.400	0.416	0.408	0.011	0.546	33.8
		30	0.447	0.441	0.444	0.004	0.524	17.9
		40	0.395	0.400	0.398	0.004	0.488	22.7
	Underflow	10	0.353	0.755	0.554	0.284	0.310	44.0
		20	0.411	0.705	0.558	0.208	0.339	39.3
		30	0.414	0.684	0.549	0.191	0.383	30.3
		40	0.461	0.621	0.541	0.113	0.422	22.0
2	Overflow	10	0.526	0.518	0.522	0.006	0.584	12.0
		20	0.483	0.483	0.483	0.000	0.560	16.0
		30	0.466	0.519	0.493	0.037	0.548	11.3
		40	0.473	0.516	0.495	0.030	0.515	4.2
	Underflow	10	0.274	0.439	0.357	0.117	0.297	16.8
		20	0.321	0.456	0.389	0.095	0.330	15.0
		30	0.307	0.441	0.374	0.095	0.383	2.5
		40	0.405	0.437	0.421	0.023	0.422	0.3
4	Overflow	10	0.518	.457	0.488	.043	.598	22.6
		20	0.538	.493	0.516	.032	.573	11.2
		30	0.503	.481	0.492	.016	.559	13.6
		40	0.500	.431	0.466	.049	.522	12.1

4	Underflow	10	0.286	0.502	0.394	0.153	0.277	29.6
		20	0.334	0.494	0.414	0.113	0.321	22.5
		30	0.331	0.416	0.374	0.060	0.369	1.2
		40	0.359	0.406	0.383	0.033	0.414	8.3
6	Overflow	10	0.580	0.497	0.539	0.059	0.605	12.4
		20	0.559	0.433	0.496	0.089	0.583	7.4
		30	0.525	0.433	0.479	0.065	0.567	18.4
		40	0.468	0.429	0.449	0.028	0.538	19.8
	Underflow	10	0.329	0.460	0.395	0.093	0.276	30.1
		20	0.293	0.398	0.346	0.074	0.309	10.7
		30	0.383	0.478	0.431	0.067	0.373	13.3
		40	0.389	0.484	0.437	0.067	0.414	5.2

**Table K2. Mean residence time data using a
User Defined Scalar for the 0.75m diameter Eff-Pac™ Clarifier.**

Flowrate, / litres per second		Flow split, / %	Experimental Mean Residence Time (MRT), s Set A (Alkhaddar *et al.*, 1999) Set B (Higgins, 2000)			Standard deviation, / s	CFD MRT, / s	CFD MRT difference, / %
			Set A	Set B	Average, / s			
0.75	Overflow	10	806	816	811	7	641	20.9
		20	794	770	782	16	641	18.0
		30	755	743	749	8	648	13.5
		40	745	716	730	21	662	9.4
	Underflow	10	562	745	654	129	953	45.8
		20	500	690	595	134	798	34.1
		30	519	628	573	77	728	27.0
		40	440	528	484	62	689	42.5
1	Overflow	10	587	563	575	17	479	16.7
		20	556	534	545	15	479	12.1
		30	542	527	534	10	483	9.6
		40	528	586	557	41	496	11.0
	Underflow	10	402	666	534	187	723	35.3
		20	398	524	461	89	604	31.0
		30	370	497	433	89	551	27.1
		40	390	429	409	27	518	26.5
2	Overflow	10	246	245	245	0	240	2.4
		20	256	231	244	17	240	1.5
		30	255	231	243	17	241	0.9
		40	246	237	242	6	247	2.0
	Underflow	10	253	386	319	94	365	14.3
		20	239	309	274	50	304	11.0
		30	236	275	256	28	275	7.5
		40	220	256	238	25	260	9.3
4	Overflow	10	119	134	127	11	119	6.0
		20	130	124	127	4	120	5.7
		30	127	114	121	9	121	0.0
		40	122	124	123	1	124	0.4

4	Underflow	10	134	212	173	55	187	7.8
		20	135	165	150	22	153	1.7
		30	138	150	144	8	139	4.0
		40	124	147	135	16	131	3.5
6	Overflow	10	99	80	90	13	80	11.4
		20	103	92	98	8	80	18.7
		30	104	93	98	8	81	18.2
		40	110	93	101	12	82	18.9
	Underflow	10	118	130	124	8	125	1.1
		20	112	129	121	12	102	15.9
		30	94	111	102	12	92	10.0
		40	96	102	99	4	88	11.7

**Table K3. Mean residence time data using the
Discrete Phase Model for the 0.75m diameter Eff-Pac™ Clarifier.**

Flowrate, / litres per second		Flow split, / %	Experimental Mean Residence Time (MRT), s Set A (Alkhaddar *et al.*, 1999) Set B (Higgins, 2000)			Standard deviation, / s	CFD MRT, / s	CFD MRT difference, / %
			Set A	Set B	Average, / s			
0.75	Overflow	10	806	816	811	7	889	9.6
		20	794	770	782	16	861	10.1
		30	755	743	749	8	858	14.5
		40	745	716	730	21	677	7.3
	Underflow	10	562	745	654	129	754	15.4
		20	500	690	595	134	614	3.2
		30	519	628	573	77	596	3.9
		40	440	528	484	62	533	10.2
1	Overflow	10	587	563	575	17	429	25.4
		20	556	534	545	15	415	23.8
		30	542	527	534	10	488	8.7
		40	528	586	557	41	536	3.8
	Underflow	10	402	666	534	187	523	2.1
		20	398	524	461	89	428	7.1
		30	370	497	433	89	379	12.6
		40	390	429	409	27	381	6.9
2	Overflow	10	246	245	245	0	208	15.3
		20	256	231	244	17	225	7.6
		30	255	231	243	17	226	7.1
		40	246	237	242	6	262	8.4
	Underflow	10	253	386	319	94	291	8.9
		20	239	309	274	50	234	14.5
		30	236	275	256	28	191	25.3
		40	220	256	238	25	182	23.5
4	Overflow	10	119	134	127	11	110	13.1
		20	130	124	127	4	116	8.5
		30	127	114	121	9	123	2.1
		40	122	124	123	1	130	5.7

4	Underflow	10	134	212	173	55	165	4.6
		20	135	165	150	22	114	24.0
		30	138	150	144	8	99.4	31.1
		40	124	147	135	16	98.1	27.5
6	Overflow	10	99	80	90	13	71.7	20.1
		20	103	92	98	8	87.1	10.9
		30	104	93	98	8	89.5	9.1
		40	110	93	101	12	81.1	19.8
	Underflow	10	118	130	124	8	162	31.0
		20	112	129	121	12	71.9	40.4
		30	94	111	102	12	53.2	48.0
		40	96	102	99	4	52.4	47.1

Appendix L. 3.4m diameter Storm King® test facility at the University of Bradford

Figure L1. The 3.4m diameter Storm King® in the laboratory at the University of Bradford (View 1).
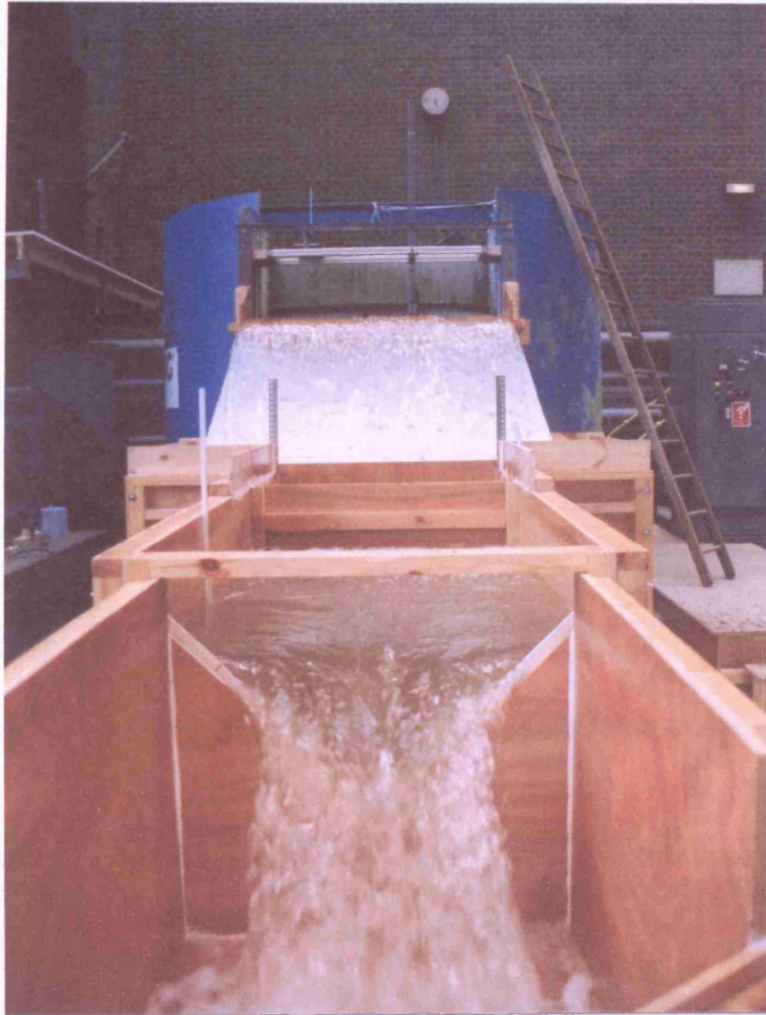
Figure L2. The 3.4m diameter Storm King® in the laboratory at the University of Bradford (View 2).

Appendix M. Comparison of CFD and experimental RTDs for a 3.4m diameter Storm King® operating with a constant underflow of 0.020m³/s
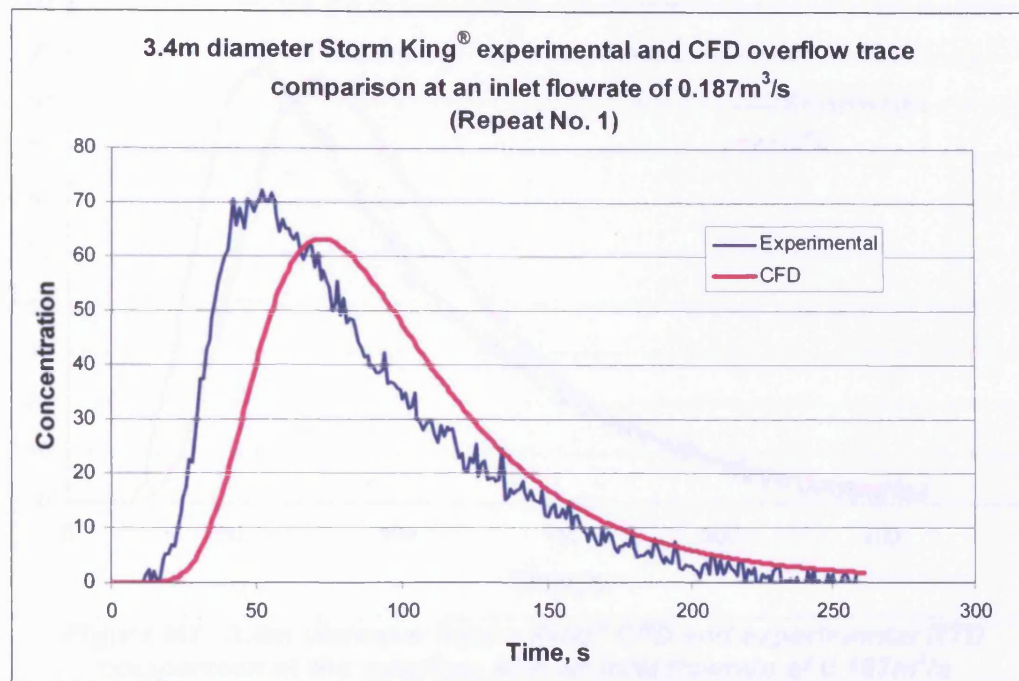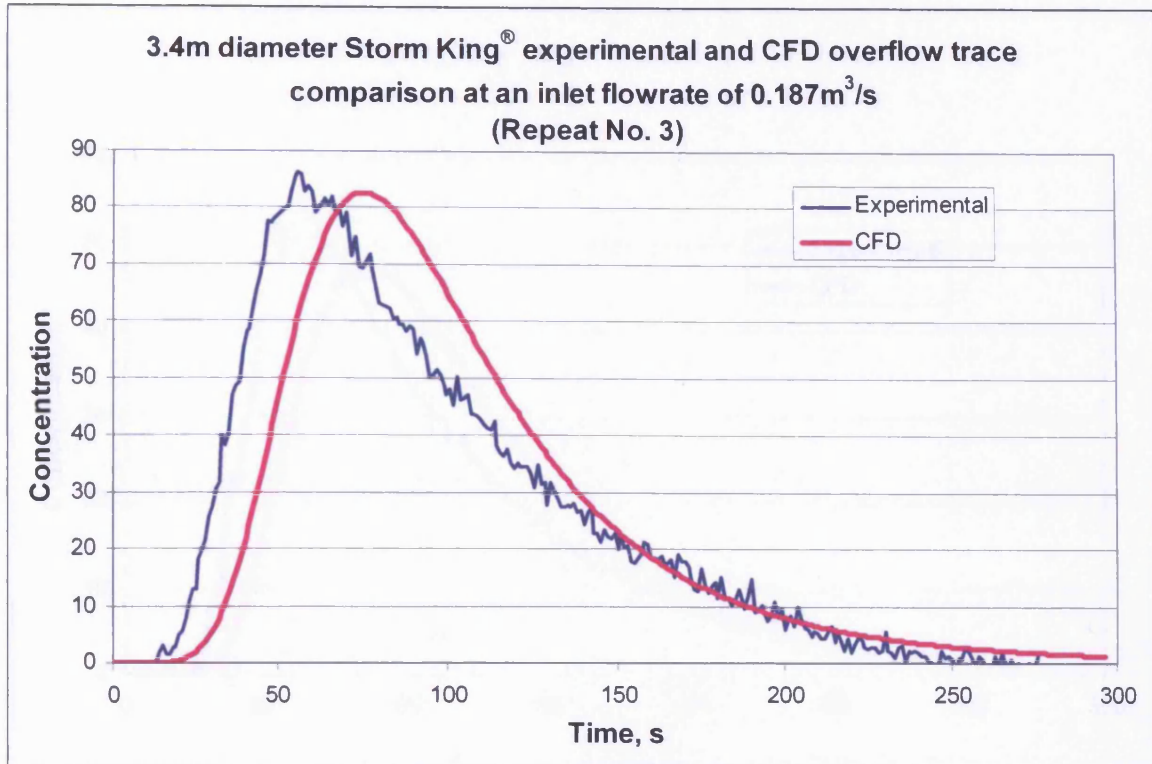

Figure M1. 3.4m diameter Storm King® CFD and experimental RTD comparison at the overflow with an inlet flowrate of 0.187m³/s (Repeat No. 1, R_t^2 =0.825).
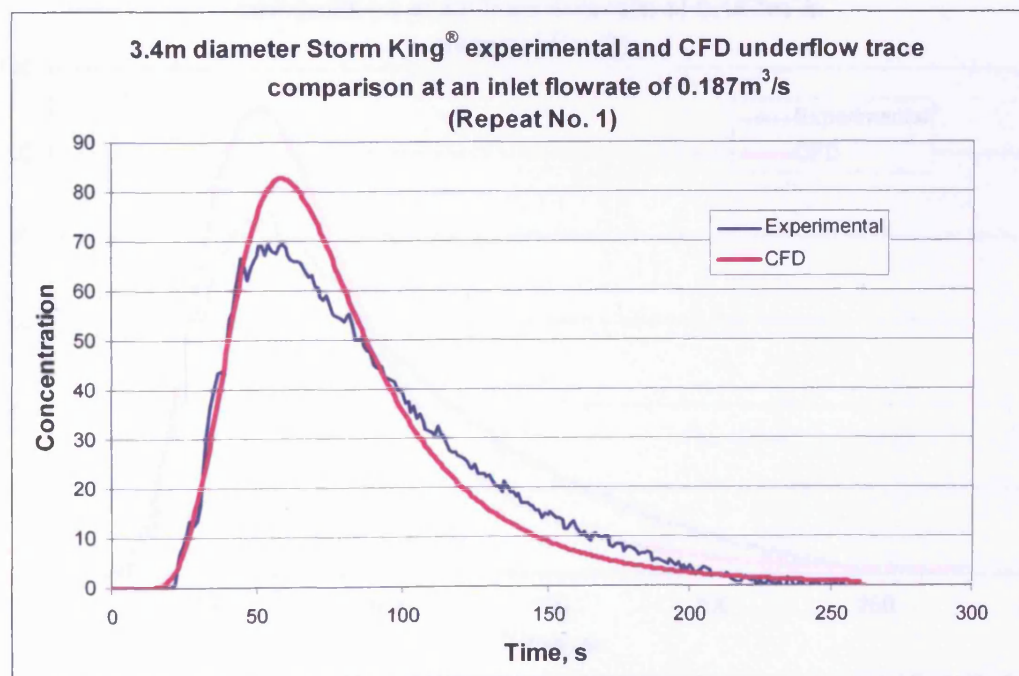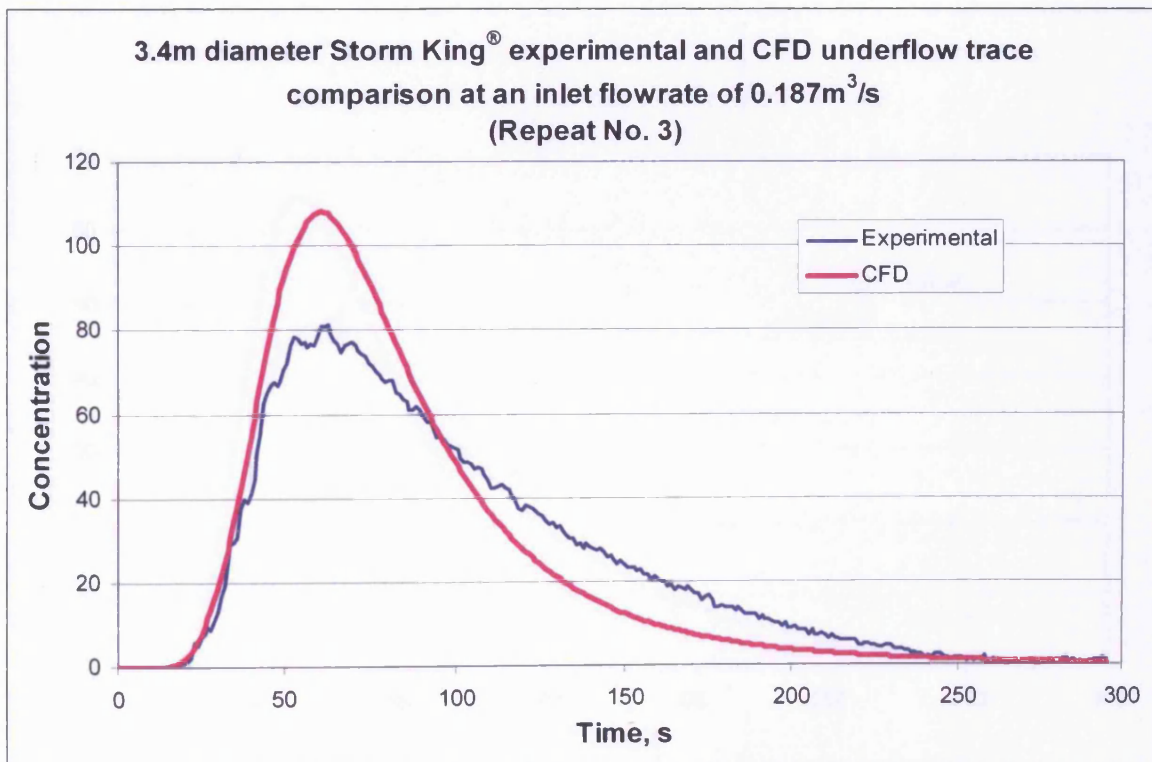

Figure M2. 3.4m diameter Storm King® CFD and experimental RTD comparison at the underflow with an inlet flowrate of 0.187m³/s (Repeat No. 1, R_t^2 =0.970).
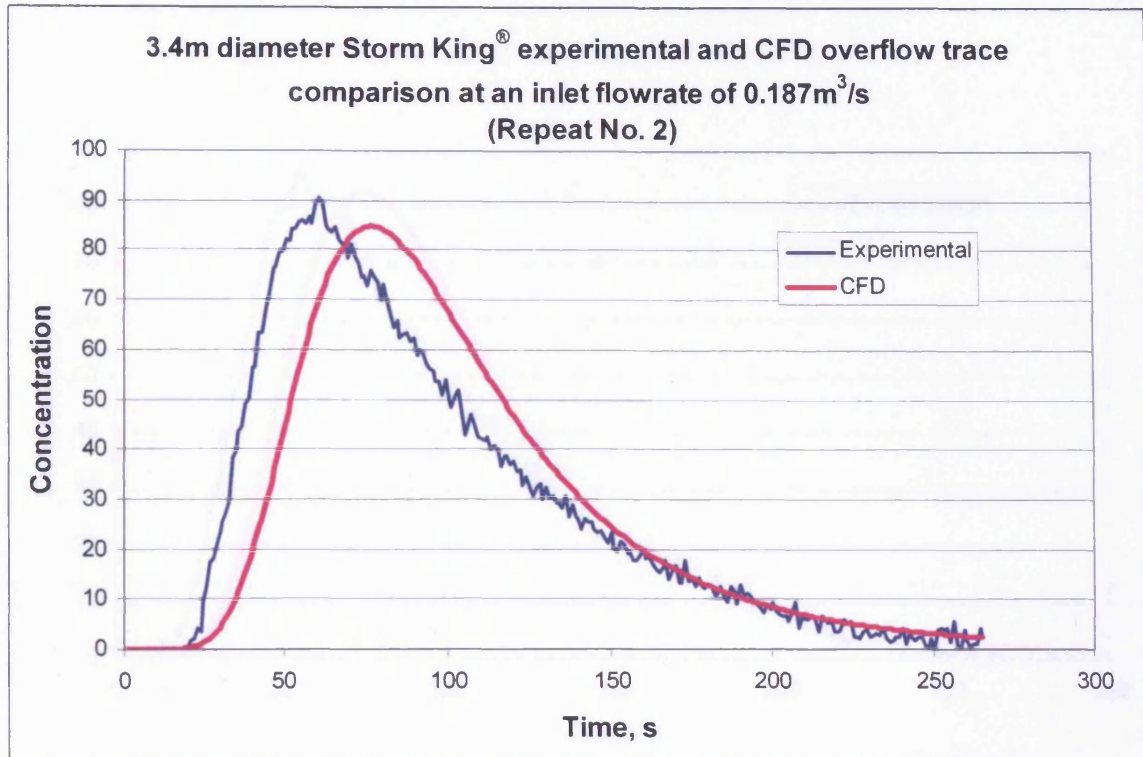
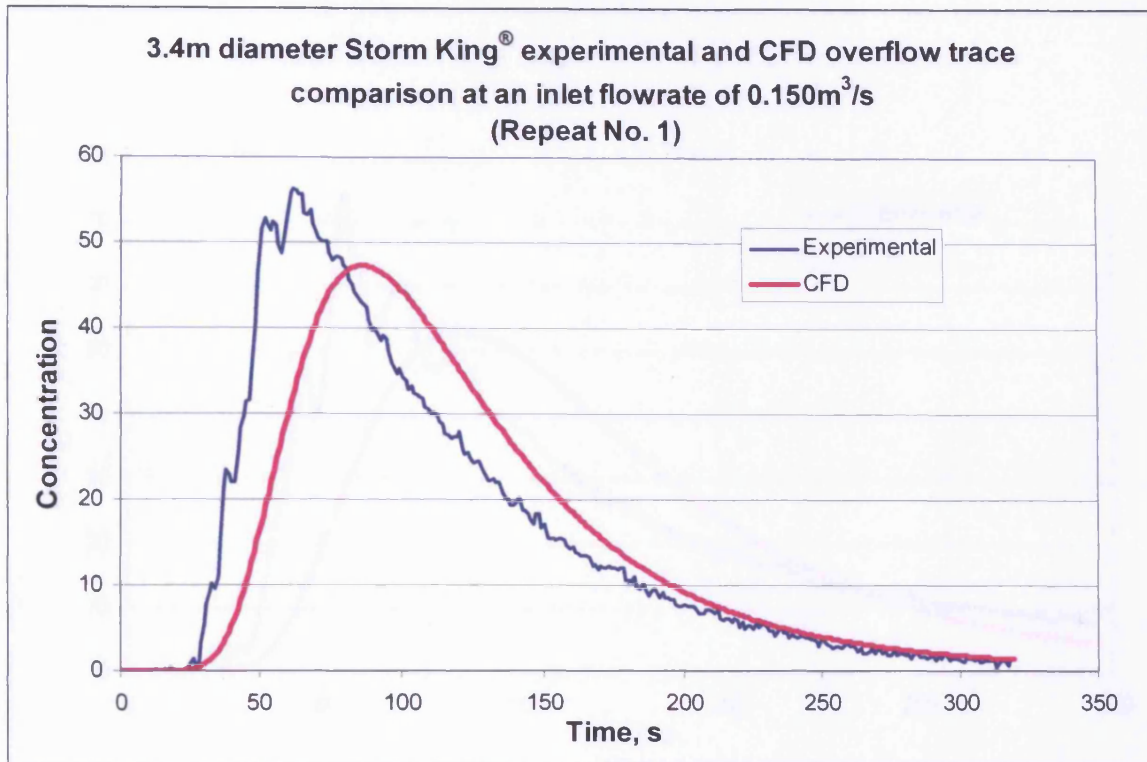**Figure M3. 3.4m diameter Storm King® CFD and experimental RTD comparison at the overflow with an inlet flowrate of 0.187m³/s (Repeat No. 2, R_t^2 =0.890).**
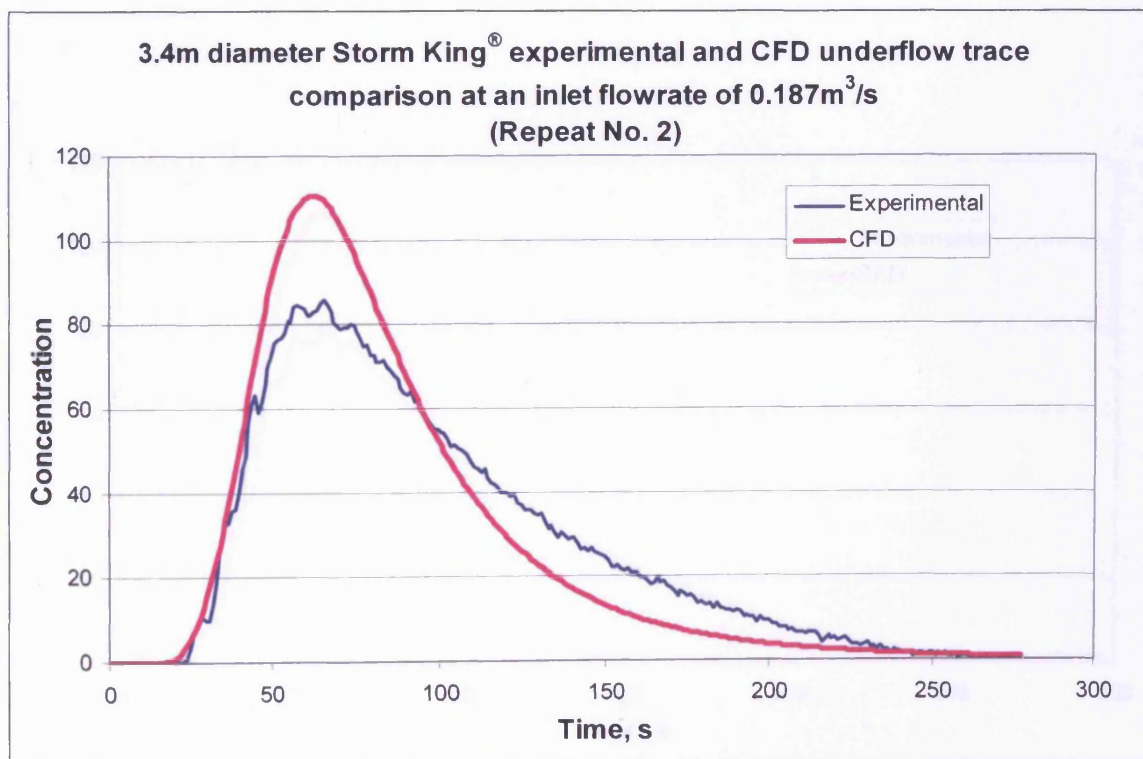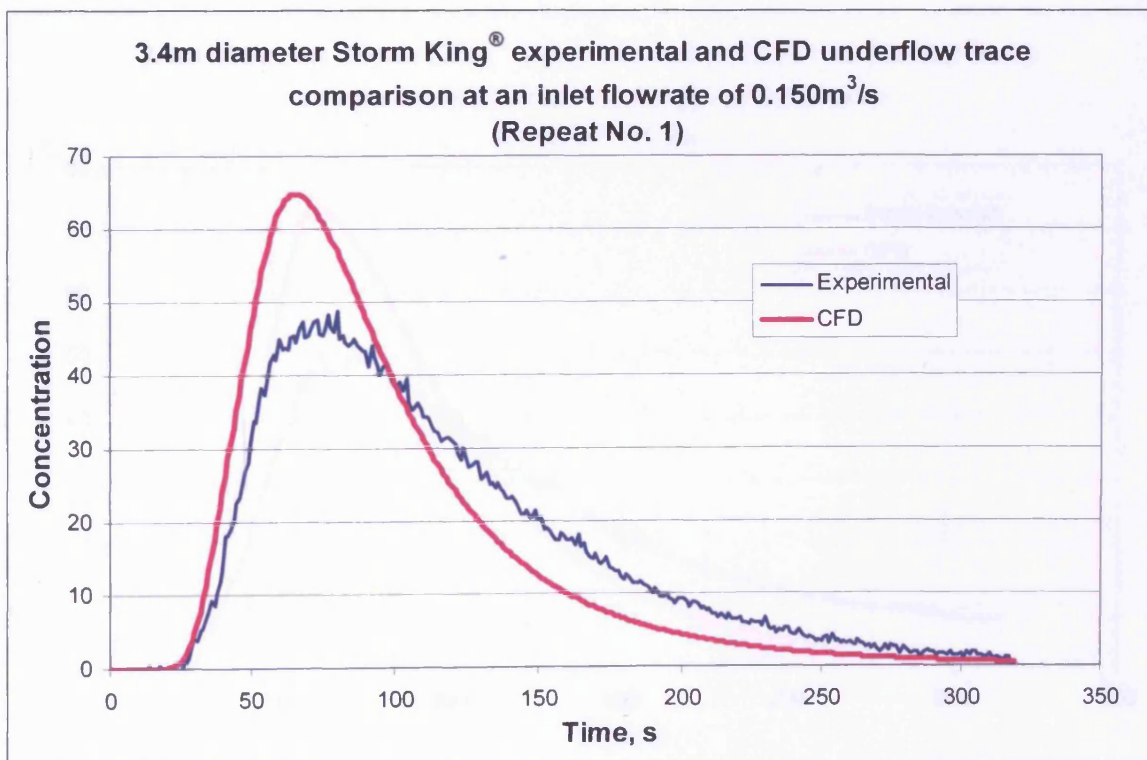

Figure M4. 3.4m diameter Storm King® CFD and experimental RTD comparison at the underflow with an inlet flowrate of 0.187m³/s (Repeat No. 2, R_t^2 =0.934).

Figure M5. 3.4m diameter Storm King® CFD and experimental RTD comparison at the overflow with an inlet flowrate of 0.187m³/s (Repeat No. 3, R_t^2 =0.890).

Figure M6. 3.4m diameter Storm King® CFD and experimental RTD comparison at the underflow with an inlet flowrate of 0.187m³/s (Repeat No. 3, R_t^2 =0.916).
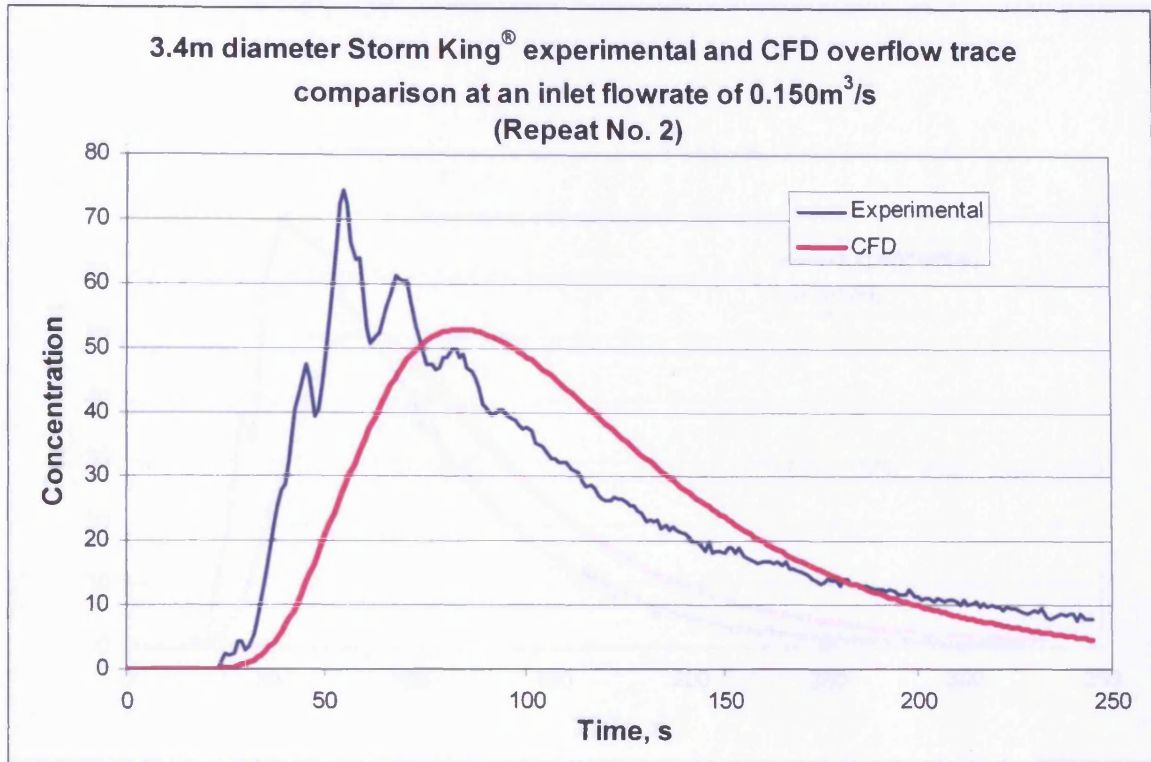
Figure M7. 3.4m diameter Storm King® CFD and experimental RTD comparison at the overflow with an inlet flowrate of 0.150m³/s (Repeat No. 1, R_t^2 =0.859).

Figure M8. 3.4m diameter Storm King® CFD and experimental RTD comparison at the underflow with an inlet flowrate of 0.150m³/s (Repeat No. 1, R_t^2 =0.897).

Figure M9. 3.4m diameter Storm King® CFD and experimental RTD comparison at the overflow with an inlet flowrate of 0.150m³/s (Repeat No. 2, R_t^2 =0.841).
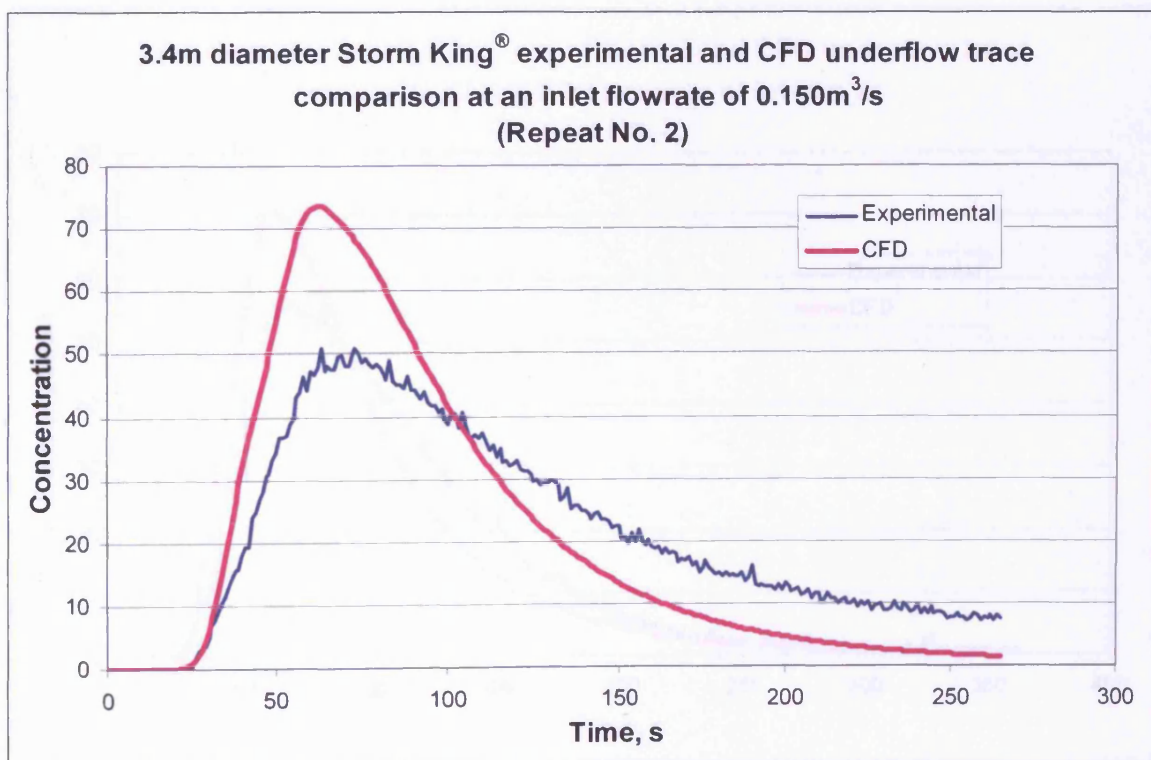

Figure M10. 3.4m diameter Storm King® CFD and experimental RTD comparison at the underflow with an inlet flowrate of 0.150m³/s (Repeat No. 2, R_t^2 =0.839).
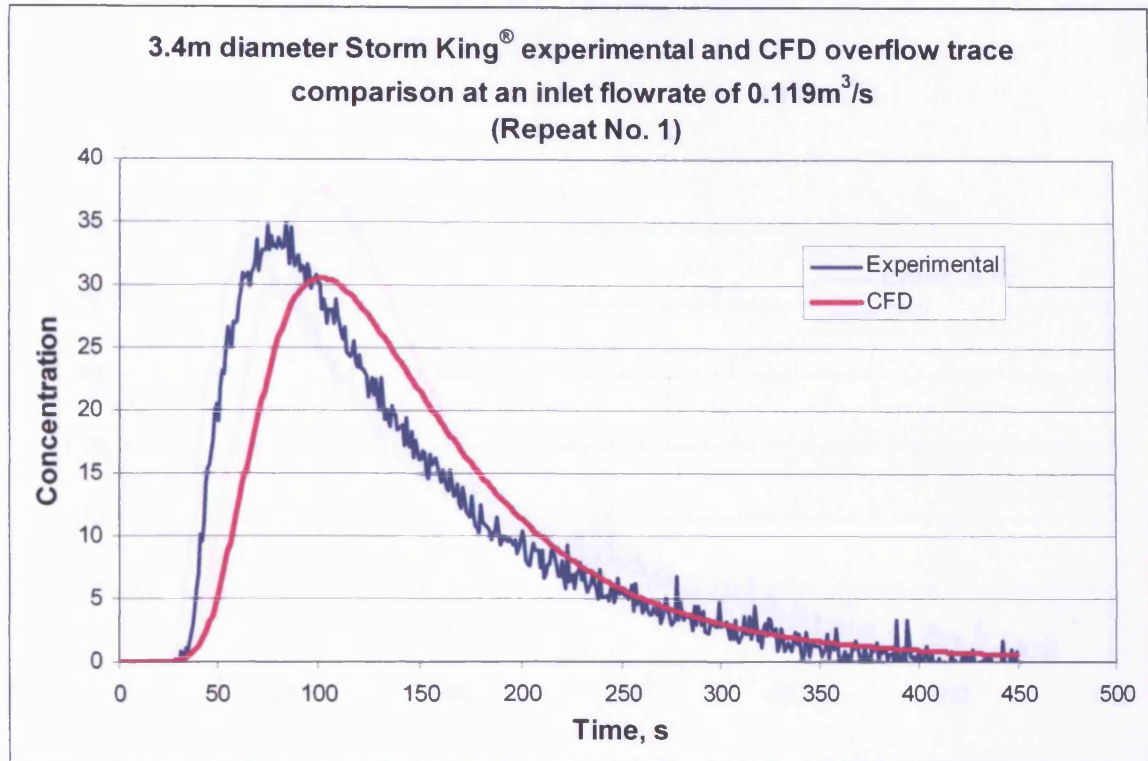
Figure M13. 3.4m diameter Storm King® CFD and experimental RTD comparison at the overflow with an inlet flowrate of 0.119m³/s (Repeat No. 1, R_t^2 =0.888).
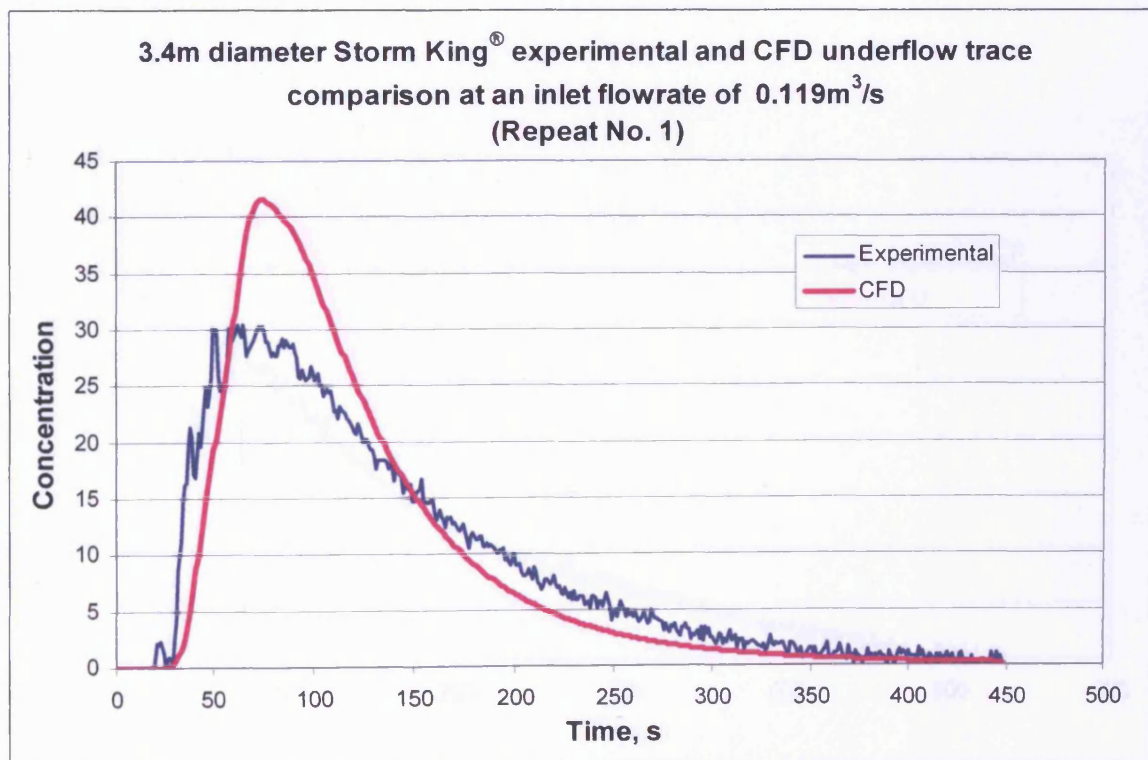

Figure M14. 3.4m diameter Storm King® CFD and experimental RTD comparison at the underflow with an inlet flowrate of 0.119m³/s (Repeat No. 1, R_t^2 =0.891).

Figure M15. 3.4m diameter Storm King® CFD and experimental RTD comparison at the overflow with an inlet flowrate of 0.119m³/s (Repeat No. 2, R_t^2 =0.819).

Figure M16. 3.4m diameter Storm King® CFD and experimental RTD comparison at the underflow with an inlet flowrate of 0.119m³/s (Repeat No. 2, R_t^2 =0.766).
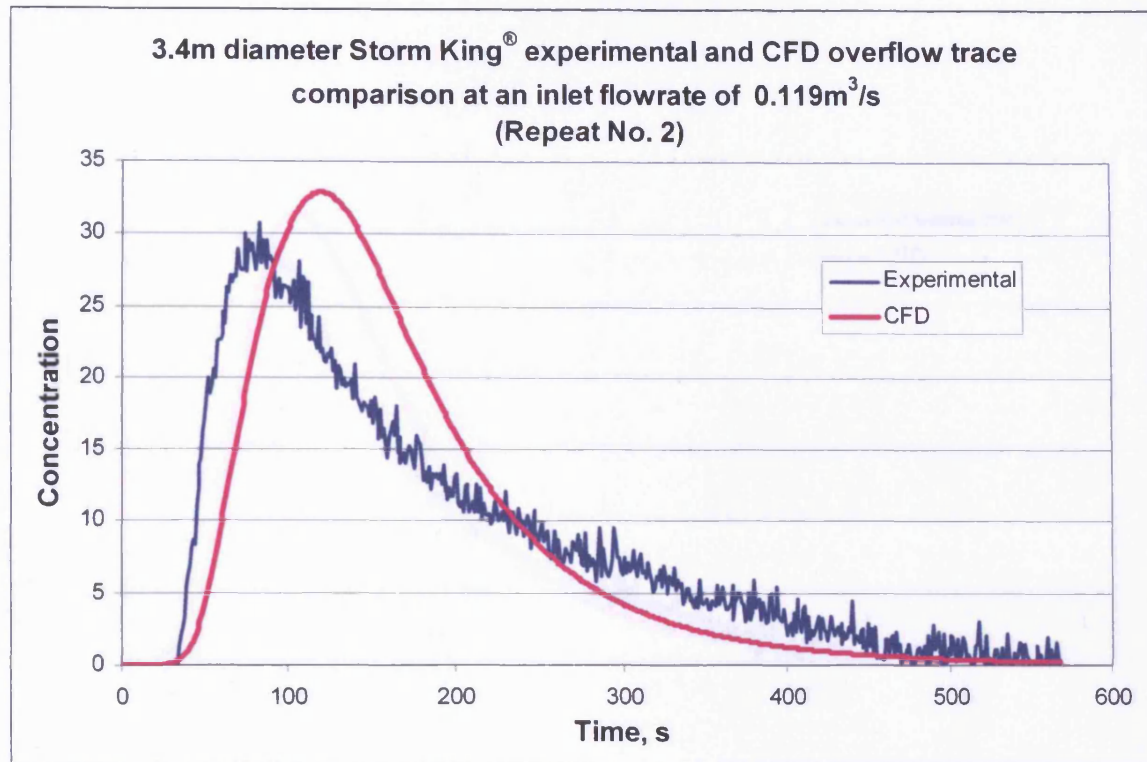
Figure M17. 3.4m diameter Storm King® CFD and experimental RTD comparison at the overflow with an inlet flowrate of 0.119m³/s (Repeat No. 3, $R_t^2 =0.902$).
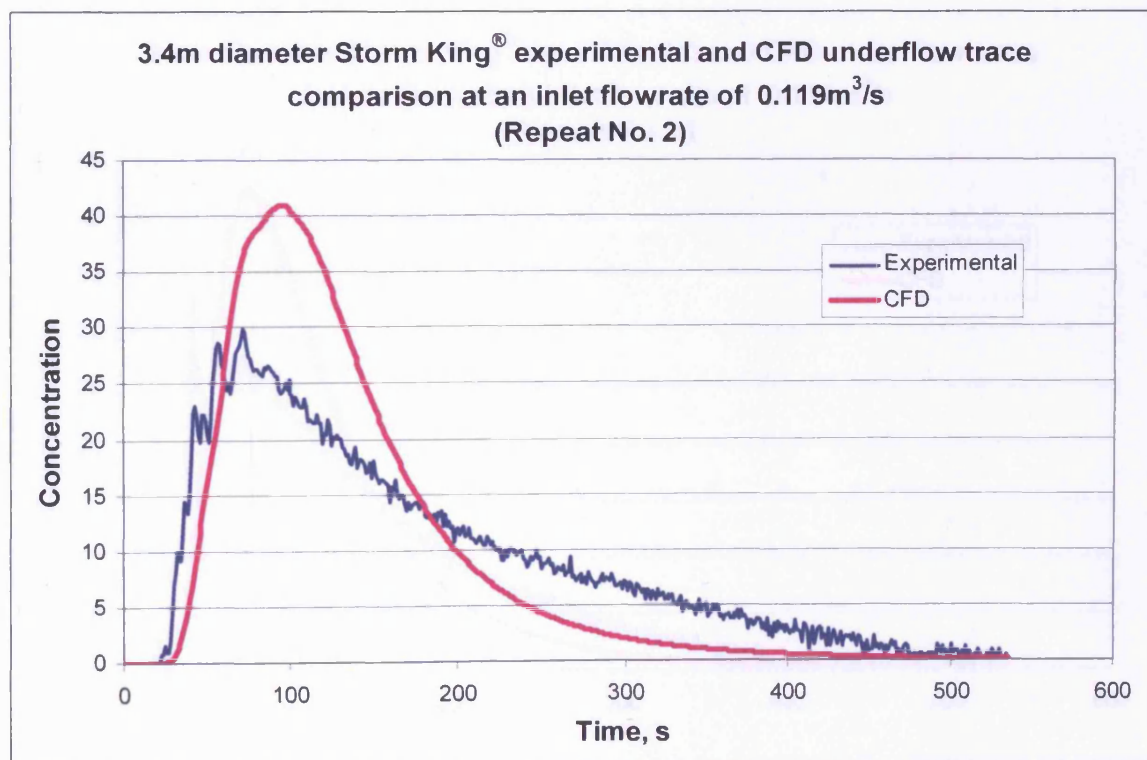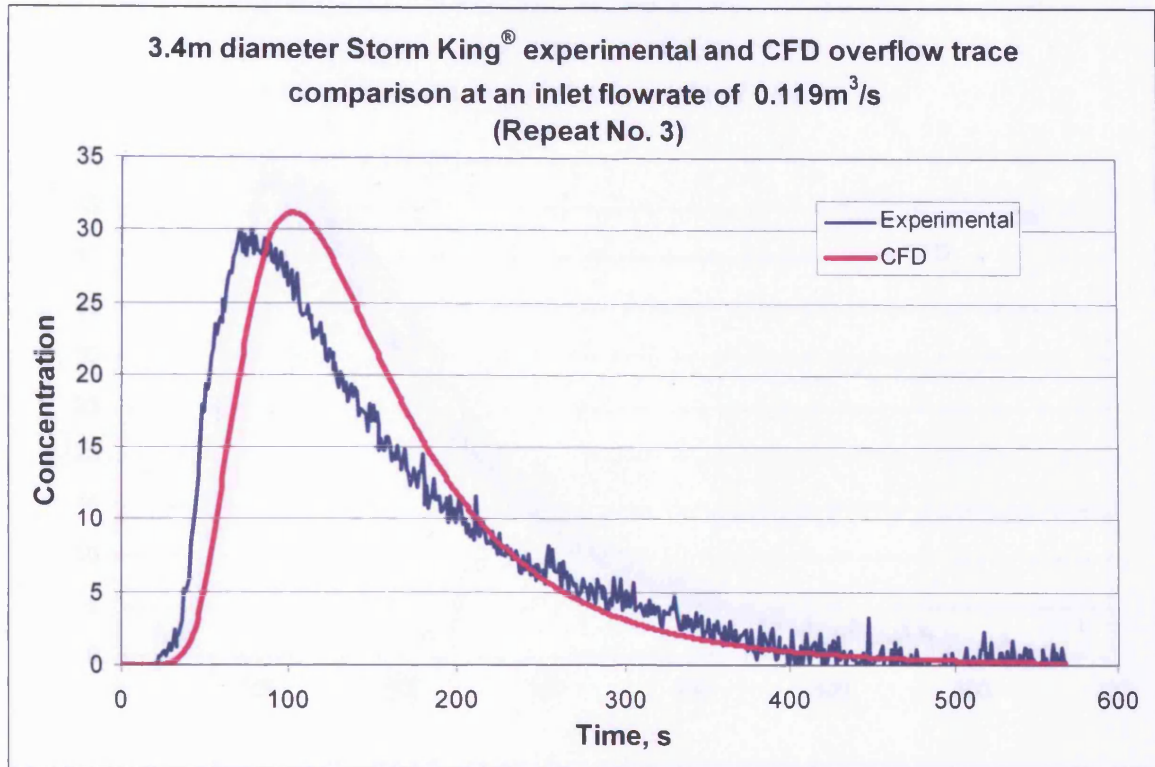

Figure M18. 3.4m diameter Storm King® CFD and experimental RTD comparison at the underflow with an inlet flowrate of 0.119m³/s (Repeat No. 3, $R_t^2 =0.819$).

Figure M19. 3.4m diameter Storm King® CFD and experimental RTD comparison at the overflow with an inlet flowrate of 0.077m³/s (Repeat No. 1, R_t^2 =0.950).

Figure M20. 3.4m diameter Storm King® CFD and experimental RTD comparison at the underflow with an inlet flowrate of 0.077m³/s (Repeat No. 1, R_t^2 =0.905).

Figure M21. 3.4m diameter Storm King® CFD and experimental RTD comparison at the overflow with an inlet flowrate of 0.077m³/s (Repeat No. 2, R_t^2 =0.952).
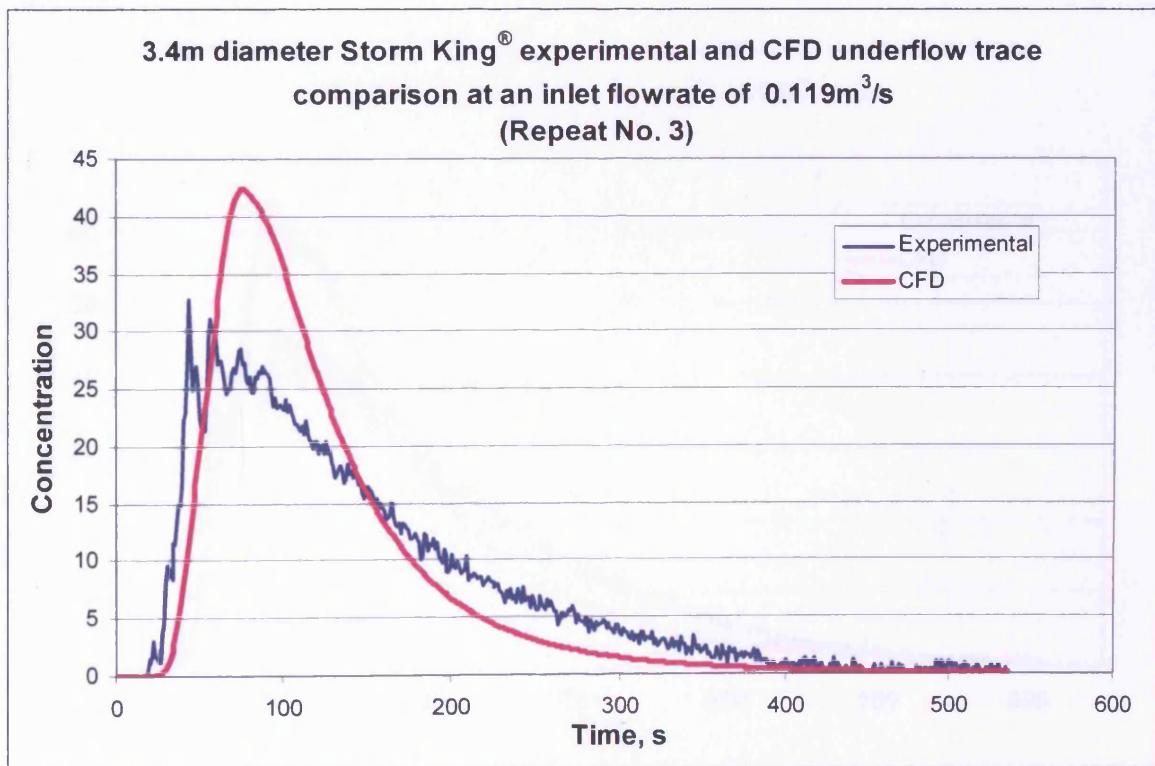

Figure M22. 3.4m diameter Storm King® CFD and experimental RTD comparison at the underflow with an inlet flowrate of 0.077m³/s (Repeat No. 2, R_t^2 =0.893).

3.4m diameter Storm King® experimental and CFD overflow trace comparison at an inlet flowrate of 0.077m³/s (Repeat No. 3)

Figure M23. 3.4m diameter Storm King® CFD and experimental RTD comparison at the overflow with an inlet flowrate of 0.077m³/s (Repeat No. 3, R_t^2 =0.959).
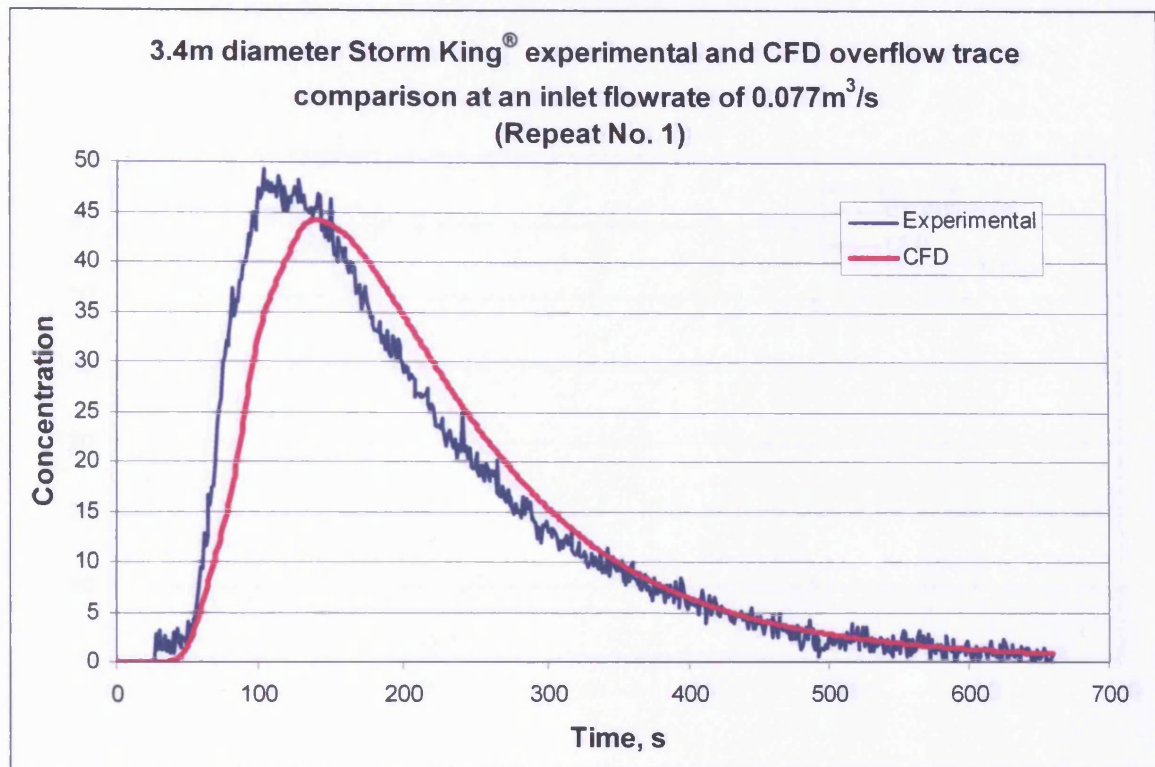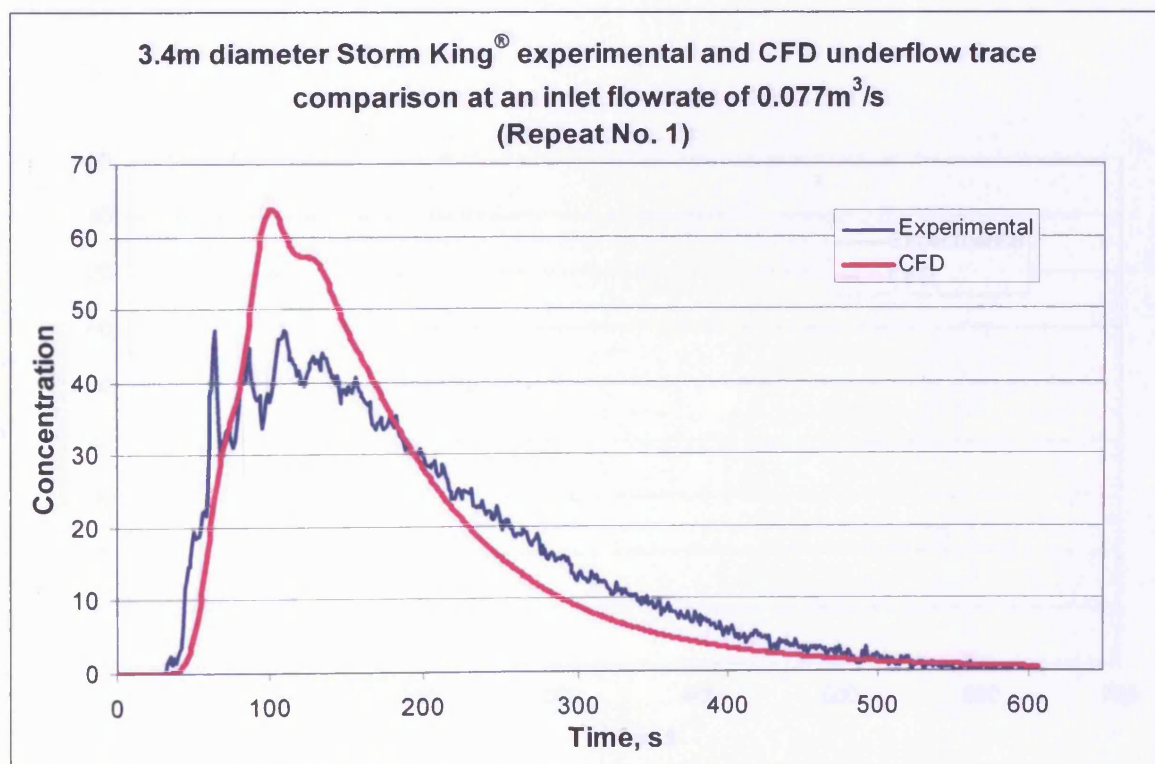

3.4m diameter Storm King® experimental and CFD underflow trace comparison at an inlet flowrate of 0.077m³/s (Repeat No. 3)
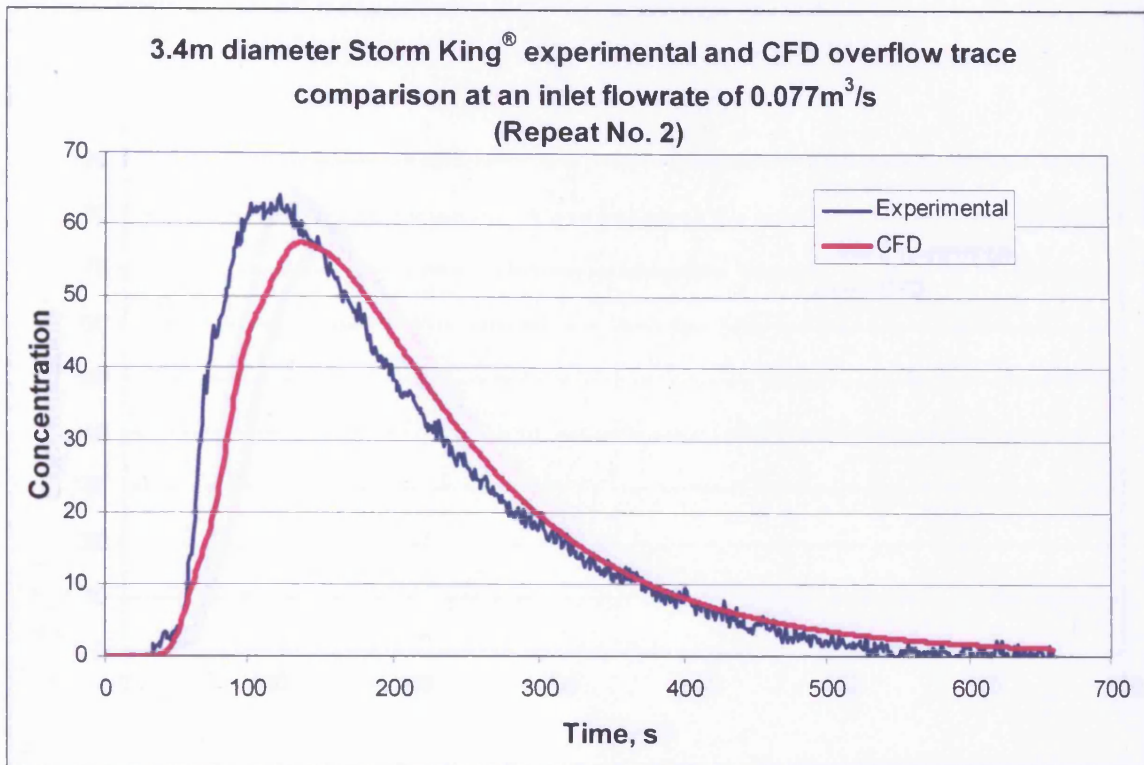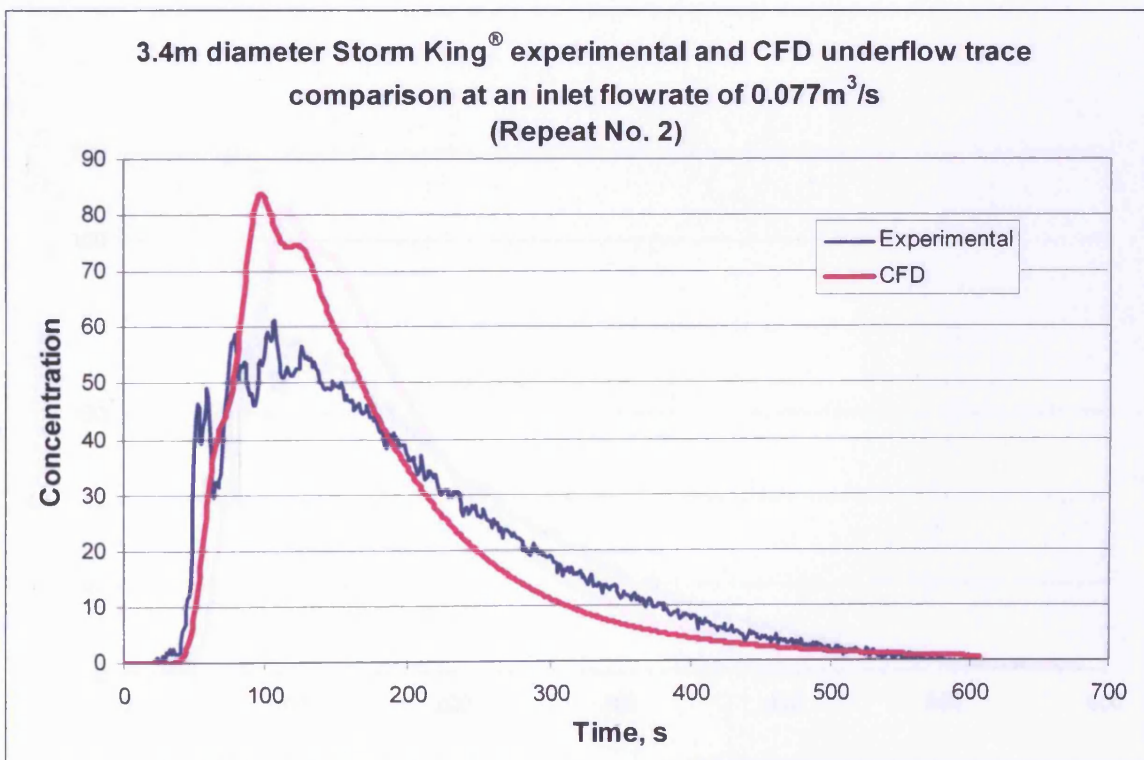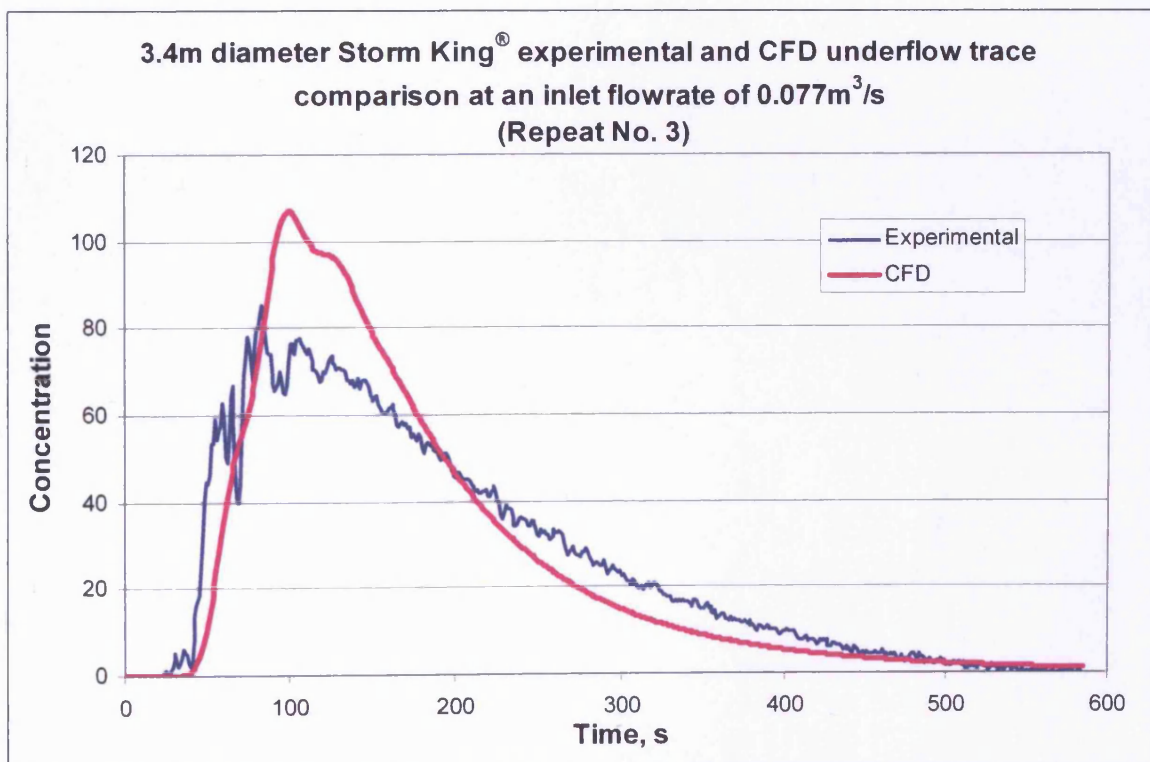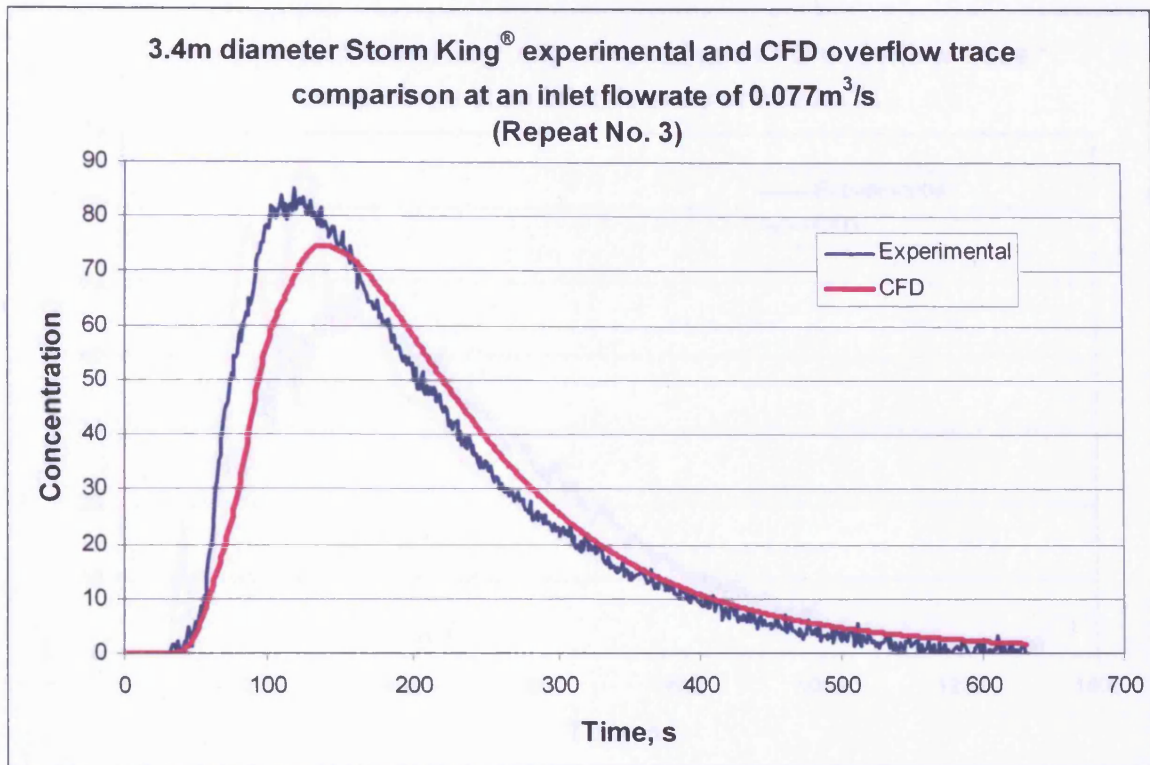
Figure M24. 3.4m diameter Storm King® CFD and experimental RTD comparison at the underflow with an inlet flowrate of 0.077m³/s (Repeat No. 3, R_t^2 =0.907).
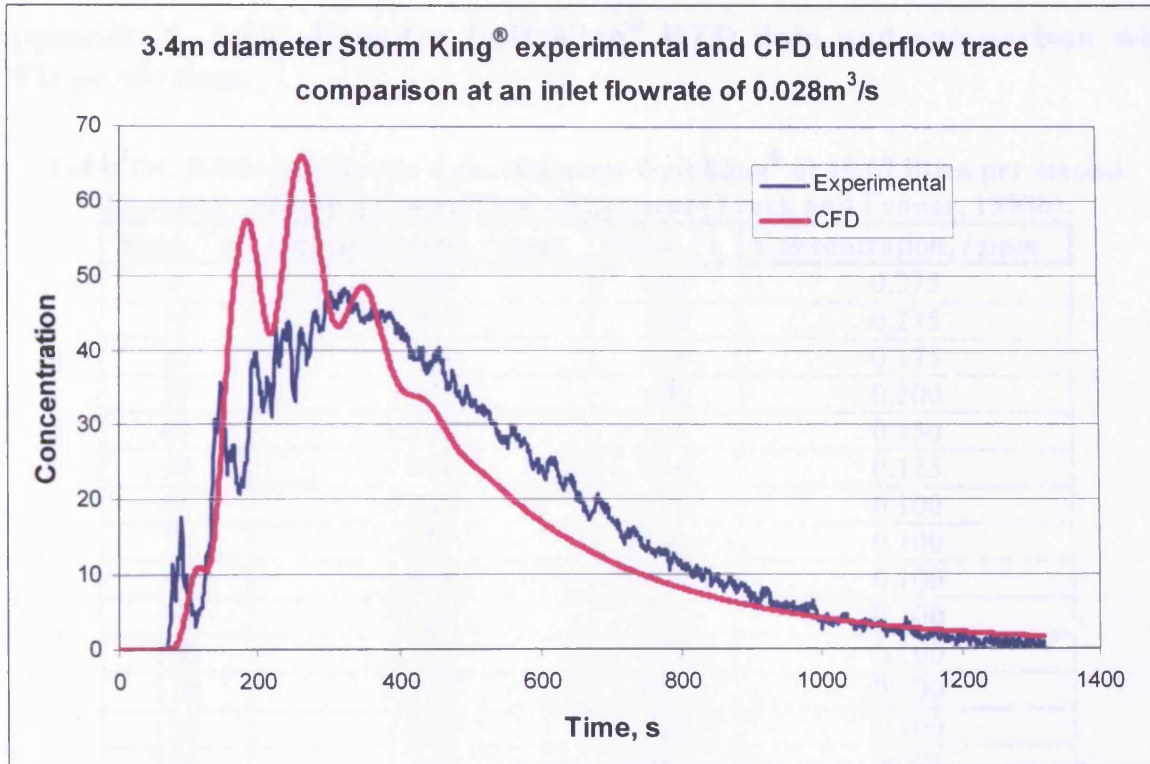
Figure M25. 3.4m diameter Storm King $^{®}$ *CFD and experimental RTD comparison at the underflow with an inlet flowrate of 0.028m* ^{3}*/s* (R_t^2 =0.774).

Appendix N. 1.6m diameter Grit King® RTD data and comparison with CFD predictions

Table N1. RTD data for the 1.6m diameter Grit King® at 10.67 litres per second operating without an underflow component (Tyack and Fenner, 1998b).

Time, / s	Concentration, / ppm	Time, / s	Concentration, / ppm
0	0.000	390	0.275
10	0.000	420	0.275
20	0.000	450	0.175
30	0.025	480	0.200
40	0.100	510	0.150
50	1.950	540	0.125
60	0.900	570	0.100
70	1.825	600	0.100
80	1.625	630	0.100
90	1.950	660	0.100
100	2.325	690	0.100
110	1.575	720	0.100
120	1.800	750	0.100
130	1.500	780	0.075
140	1.425	810	0.075
150	1.325	840	0.050
160	1.275	870	0.075
170	1.250	900	0.075
180	1.125	930*	0.075*
210	0.850	960*	0.100*
240	0.675	990*	0.075*
270	0.550	1020*	0.075*
300	0.475	1050*	0.075*
330	0.400	1080*	0.150*
360	0.300		

1.6m diameter Grit King® residence time distribution at 10.67 litres per second

Figure N1. CFD and experimental RTD comparison of the 1.6m diameter Grit King® at 10.67 litres per second operating without an underflow component.

Table N2. RTD data for the 1.6m diameter Grit King® at 15.51 litres per second operating without an underflow component (Tyack and Fenner, 1998b).

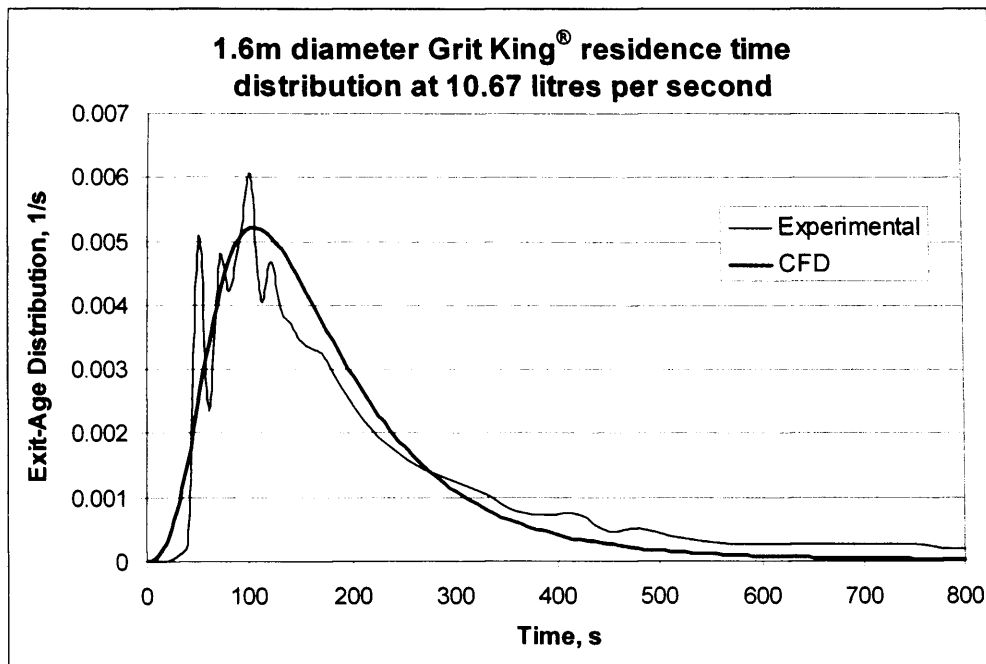| Time, / s	Concentration, / ppm	Time, / s	Concentration, / ppm
0	0.000	390	0.125
10	0.025	420	0.075
20	0.025	450	0.050
30	0.725	480	0.050
40	1.000	510	0.050
50	2.125	540	0.025
60	2.150	570	0.050
70	1.925	600	0.050
80	1.900	630	0.050
90	1.700	660	0.050
100	1.400	690	0.050
110	1.250	720*	0.050*
120	1.100	750*	0.050*
130	1.000	780*	0.050*
140	0.925	810*	0.050*
150	0.800	840*	0.050*
160	0.725	870*	0.050*
170	0.675	900*	0.050*
180	0.600	930*	0.050*
210	0.400	960*	0.050*
240	0.325	990*	0.050*
270	0.225	1020*	0.050*
300	0.225	1050*	0.050*
330	0.150	1080*	0.050*
360	0.125		

Figure N2. CFD and experimental RTD comparison of the 1.6m diameter Grit King® at 15.51 litres per second operating without an underflow component.

Table N3. RTD data for the 1.6m diameter Grit King® at 20.22 litres per second operating without an underflow component (Tyack and Fenner, 1998b).

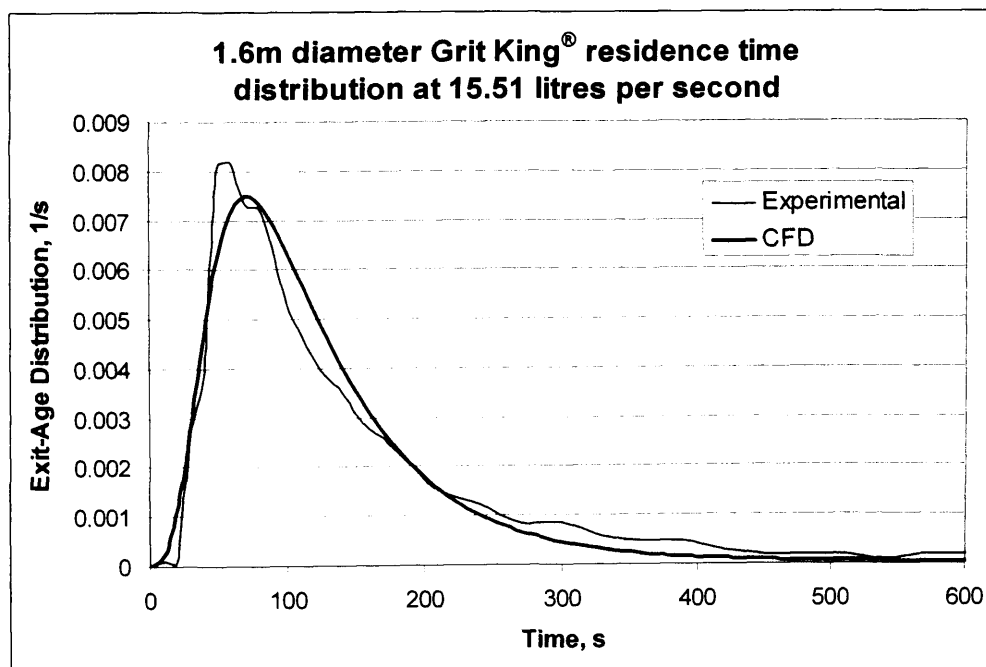| Time, / s	Concentration, / ppm	Time, / s	Concentration, / ppm
0	0.000	180	0.200
10	0.000	210*	0.075*
20	0.025	240*	0.025*
30	1.050	270*	0.025*
40	2.450	300*	-0.100*
50	2.325	330*	-0.075*
60	1.825	360*	-0.075*
70	1.425	390*	-0.125*
80	1.250	420*	-0.125*
90	1.100	450*	-0.150*
100	0.925	480*	-0.150*
110	0.800	510*	-0.150*
120	0.650	540*	-0.150*
130	0.525	570*	-0.150*
140	0.425	600*	-0.150*
150	0.400	630*	-0.150*
160	0.350	660*	-0.125*
170	0.300	690*	-0.150*

Figure N3. CFD and experimental RTD comparison of the 1.6m diameter Grit King® at 20.22 litres per second operating without an underflow component.

Table N4. RTD data for the 1.6m diameter Grit King® at 24.85 litres per second operating without an underflow component (Tyack and Fenner, 1998b).

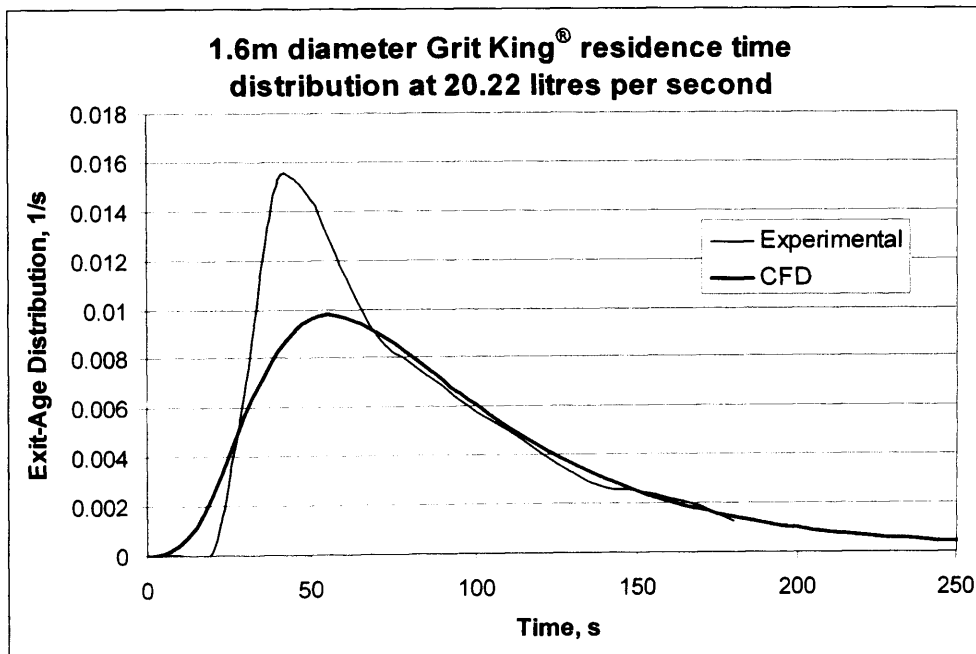| Time, / s	Concentration, / ppm	Time, / s	Concentration, / ppm
0	0.000	180	0.200
10	0.050	210	0.175
20	1.375	240	0.225
30	2.550	270	0.125
40	2.500	300*	0.100*
50	2.050	330*	0.075*
60	1.725	360*	0.050*
70	1.400	390*	0.150*
80	1.175	420*	0.050*
90	0.950	450*	0.050*
100	0.800	480*	0.050*
110	0.650	510*	0.050*
120	0.600	540*	0.050*
130	0.500	570*	0.050*
140	0.400	600*	0.050*
150	0.350	630*	0.050*
160	0.450	660*	0.100*
170	0.250		

Figure N4. CFD and experimental RTD comparison of the 1.6m diameter Grit King® at 24.85 litres per second operating without an underflow component.

Table N5. RTD data for the 1.6m diameter Grit King® at 29.76 litres per second operating without an underflow component (Tyack and Fenner, 1998b).

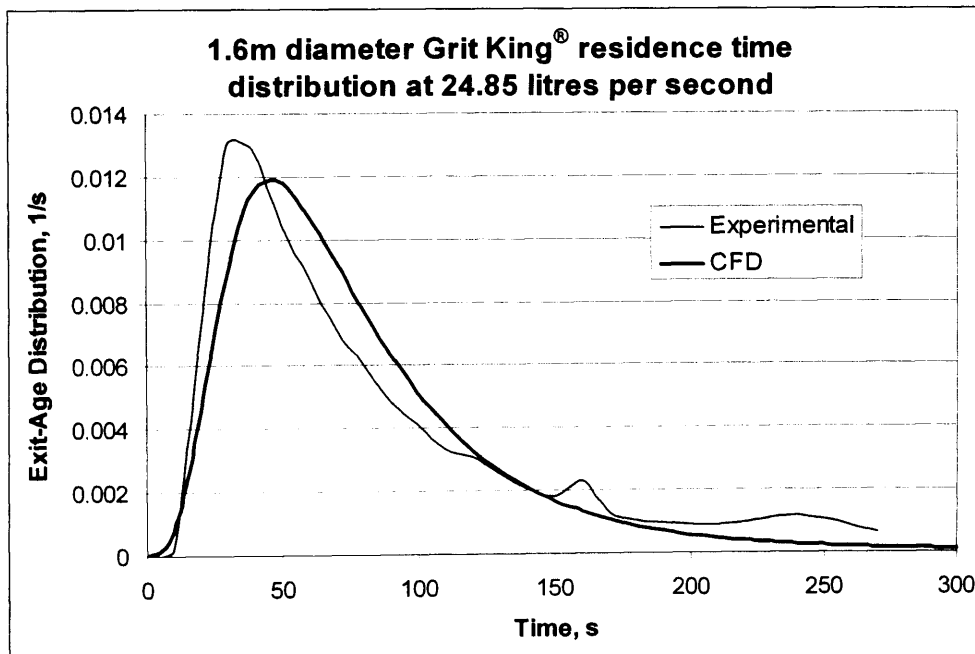| Time, / s	Concentration, / ppm	Time, / s	Concentration, / ppm
0	0.00	210	0.20
10	0.10	240*	0.10*
20	0.90	270*	0.10*
30	2.30	300*	0.10*
40	2.20	330*	0.10*
50	1.70	360*	0.10*
60	1.30	390*	0.10*
70	1.10	420*	0.10*
80	0.90	450*	0.10*
90	0.70	480*	0.10*
100	0.50	510*	0.10*
110	0.40	540*	0.10*
120	0.30	570*	0.10*
130	0.30	600*	0.10*
140	0.30	630*	0.10*
150	0.30	660*	0.10*
160	0.20	690*	0.10*
170	0.20	720*	0.10*
180	0.20		

Figure N5. CFD and experimental RTD comparison of the 1.6m diameter Grit King® at 29.76 litres per second operating without an underflow component.

Table N6. RTD data for the 1.6m diameter Grit King® at 35.33 litres per second operating without an underflow component (Tyack and Fenner, 1998b).

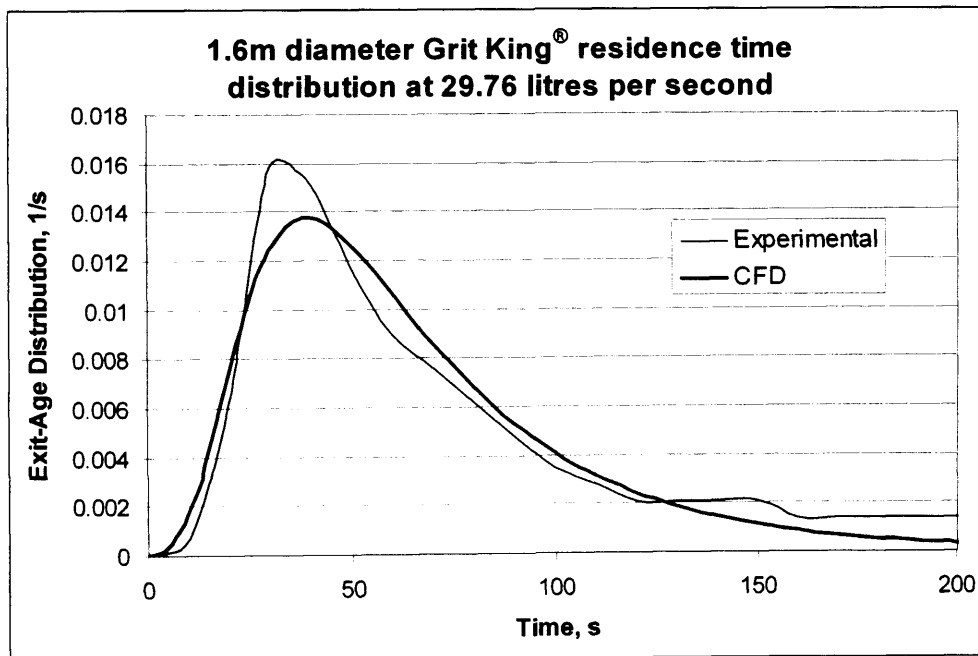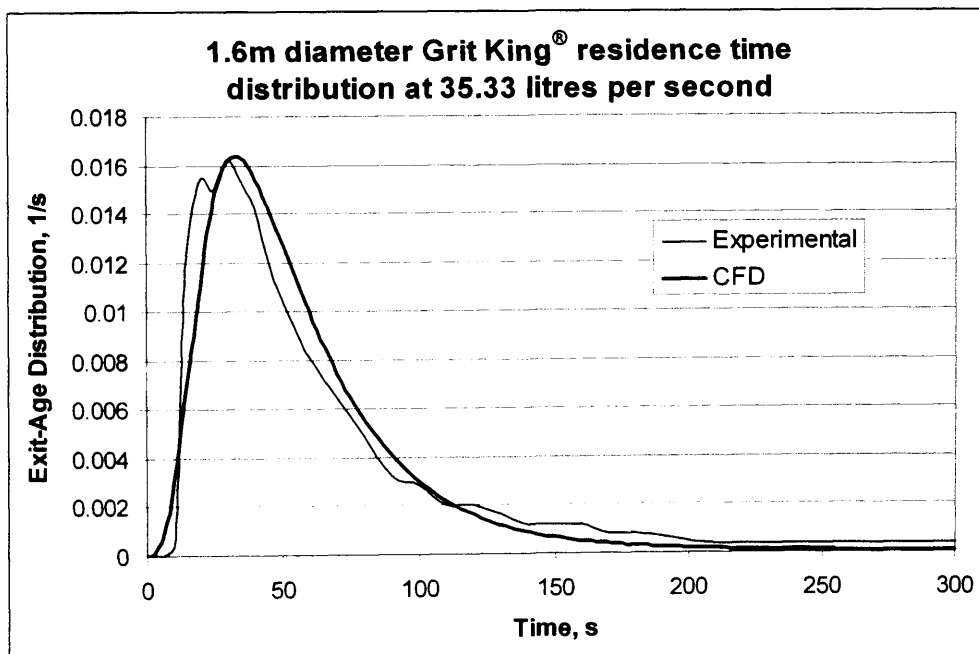| Time, / s	Concentration, / ppm	Time, / s	Concentration, / ppm
0	0.00	130	0.40
5	0.00	140	0.30
10	0.10	150	0.30
15	3.00	160	0.30
20	3.80	170	0.20
25	3.70	180	0.20
30	4.00	210	0.10
35	3.80	240	0.10
40	3.50	270	0.10
45	3.00	300	0.10
50	2.60	330	0.10
55	2.30	360	0.10
60	2.00	390*	0.10*
70	1.60	420*	0.10*
80	1.20	450*	0.10*
90	0.80	480*	0.10*
100	0.70	510*	0.10*
110	0.50	540*	0.20*
120	0.50		

Figure N6. CFD and experimental RTD comparison of the 1.6m diameter Grit King® at 35.33 litres per second operating without an underflow component.

Table N7. RTD data for the 1.6m diameter Grit King® at 39.93 litres per second operating without an underflow component (Tyack and Fenner, 1998b).

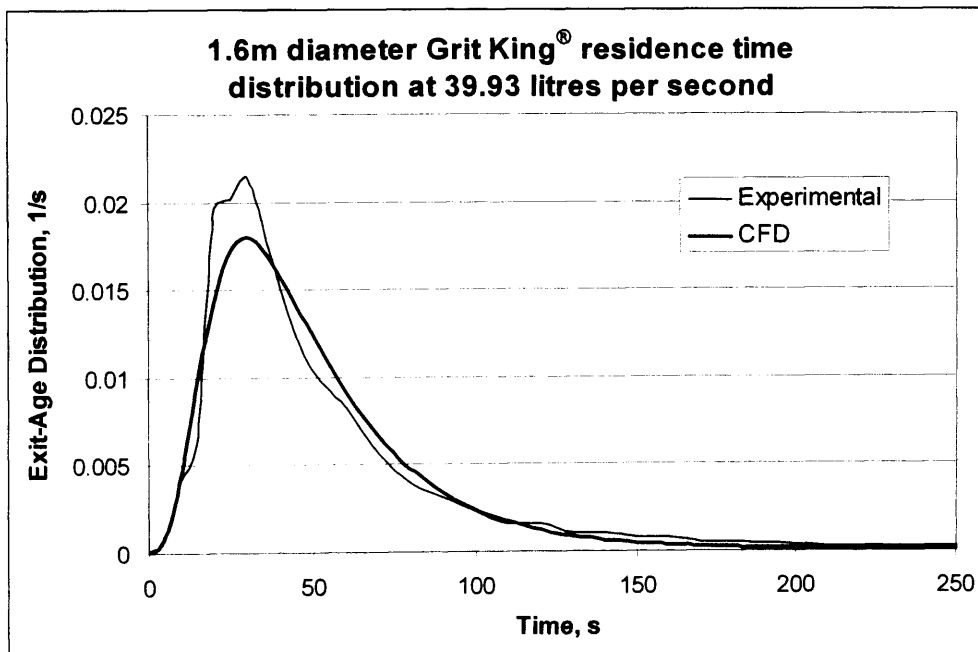| Time, / s	Concentration, / ppm	Time, / s	Concentration, / ppm
0	0.00	130	0.20
5	0.15	140	0.20
10	0.80	150	0.15
15	1.20	160	0.15
20	3.80	170	0.10
25	3.90	180	0.10
30	4.15	210	0.05
35	3.60	240	0.05
40	2.95	270	0.05
45	2.40	300	0.05
50	2.00	330	0.05
55	1.80	360*	0.05*
60	1.60	390*	0.05*
70	1.10	420*	0.05*
80	0.75	450*	0.05*
90	0.60	480*	0.05*
100	0.45	510*	0.10*
110	0.30	540*	0.10*
120	0.30		

Figure N7. CFD and experimental RTD comparison of the 1.6m diameter Grit King® at 39.93 litres per second operating without an underflow component.

Table N8. RTD data for the 1.6m diameter Grit King® at 45.65 litres per second operating without an underflow component (Tyack and Fenner, 1998b).

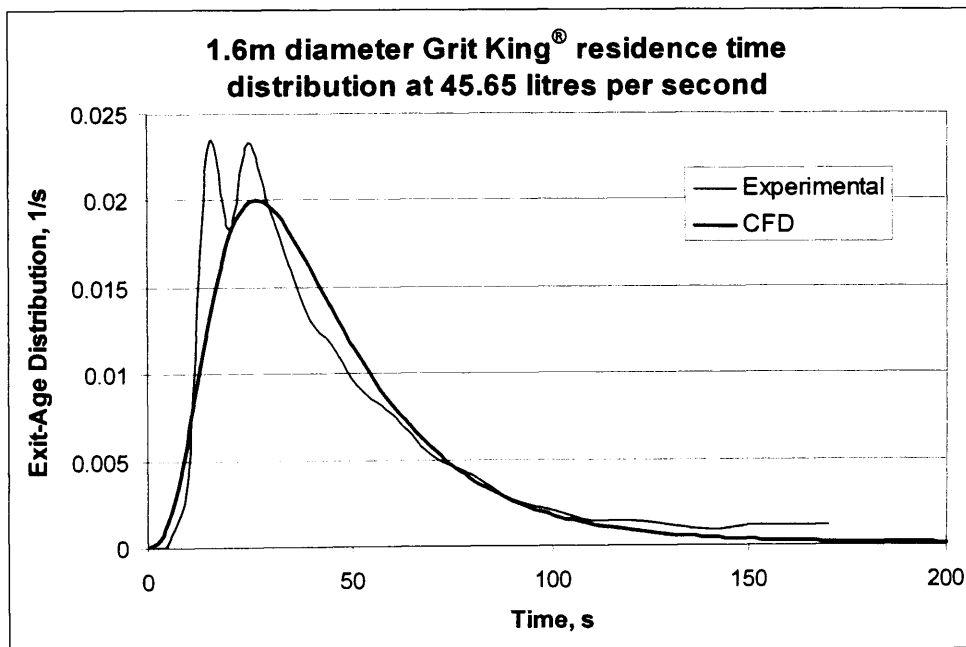| Time, / s	Concentration, / ppm	Time, / s	Concentration, / ppm
0	0.00	120	0.25
5	0.05	130	0.20
10	0.65	140	0.15
15	3.95	150	0.20
20	3.15	160	0.20
25	4.00	170	0.20
30	3.35	180*	0.15*
35	2.75	210*	0.15*
40	2.25	240*	0.10*
45	2.00	270*	0.10*
50	1.65	300*	0.15*
55	1.45	330*	0.15*
60	1.3.0	360*	0.15*
70	0.90	390*	0.15*
80	0.70	420*	0.20*
90	0.45	450*	0.25*
100	0.35	480*	0.25*
110	0.25	510*	0.25*

Figure N8. CFD and experimental RTD comparison of the 1.6m diameter Grit King® at 45.65 litres per second operating without an underflow component.

Table N9. RTD data for the 1.6m diameter Grit King® at 51.81 litres per second operating without an underflow component (Tyack and Fenner, 1998b).

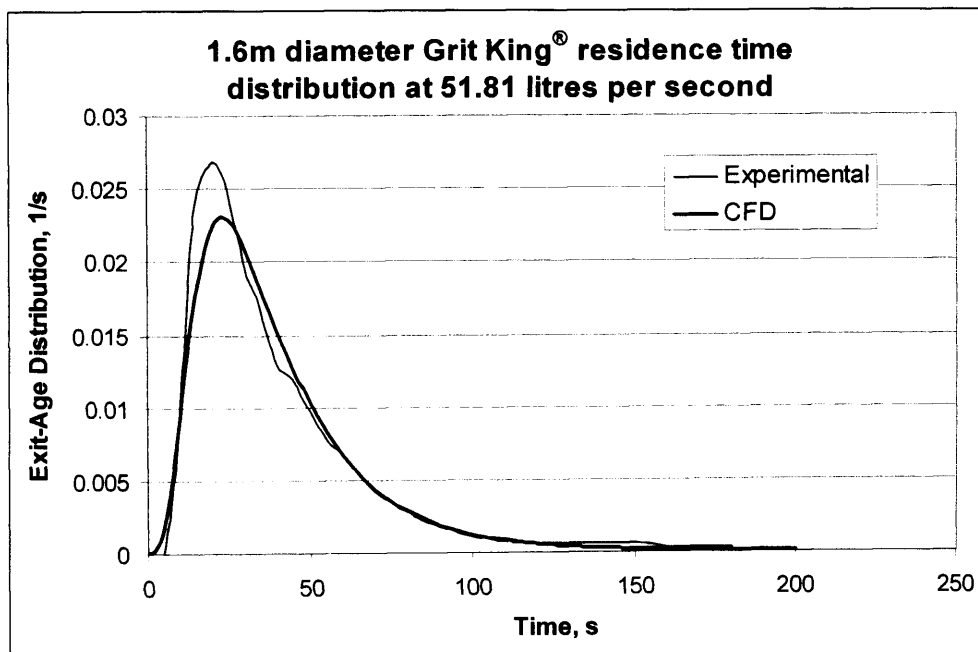| Time, / s	Concentration, / ppm	Time, / s	Concentration, / ppm
0	0.00	130	0.10
5	0.00	140	0.10
10	1.35	150	0.10
15	3.65	160	0.05
20	4.13	170	0.05
25	3.80	180	0.05
30	3.05	210*	0.10*
35	2.60	240*	0.10*
40	2.00	270*	0.15*
45	1.85	300*	0.10*
50	1.50	330*	0.10*
55	1.20	360*	0.10*
60	1.05	390*	0.10*
70	0.65	420*	0.15*
80	0.45	450*	0.15*
90	0.30	480*	0.10*
100	0.20	510*	0.10*
110	0.15	540*	0.15*
120	0.10		

Figure N9. CFD and experimental RTD comparison of the 1.6m diameter Grit King® at 51.81 litres per second operating without an underflow component.

Table N10. RTD data for the 1.6m diameter Grit King® at 55.20 litres per second operating without an underflow component (Tyack and Fenner, 1998b).

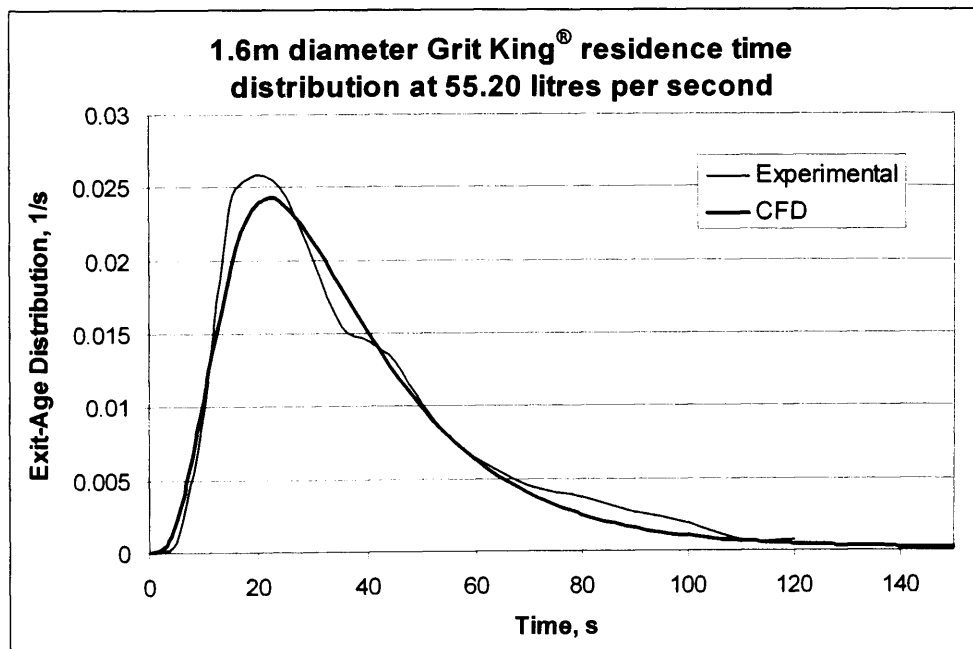| Time, / s	Concentration, / ppm	Time, / s	Concentration, / ppm
0	0.00	130*	0.15*
5	0.10	140*	0.10*
10	1.30	150*	0.10*
15	3.25	160*	0.10*
20	3.50	170*	0.10*
25	3.30	180*	0.10*
30	2.70	210*	0.10*
35	2.10	240*	0.05*
40	1.95	270*	0.10*
45	1.75	300*	0.10*
50	1.35	330*	0.10*
55	1.05	360*	0.15*
60	0.85	390*	0.15*
70	0.60	420*	0.15*
80	0.50	450*	0.10*
90	0.35	480*	0.10*
100	0.25	510*	0.10*
110	0.10	540*	0.10*
120	0.10		

Figure N10. CFD and experimental RTD comparison of the 1.6m diameter Grit King® at 55.20 litres per second operating without an underflow component.

Table N11. RTD data for the 1.6m diameter Grit King® at 60.20 litres per second operating without an underflow component (Tyack and Fenner, 1998b).

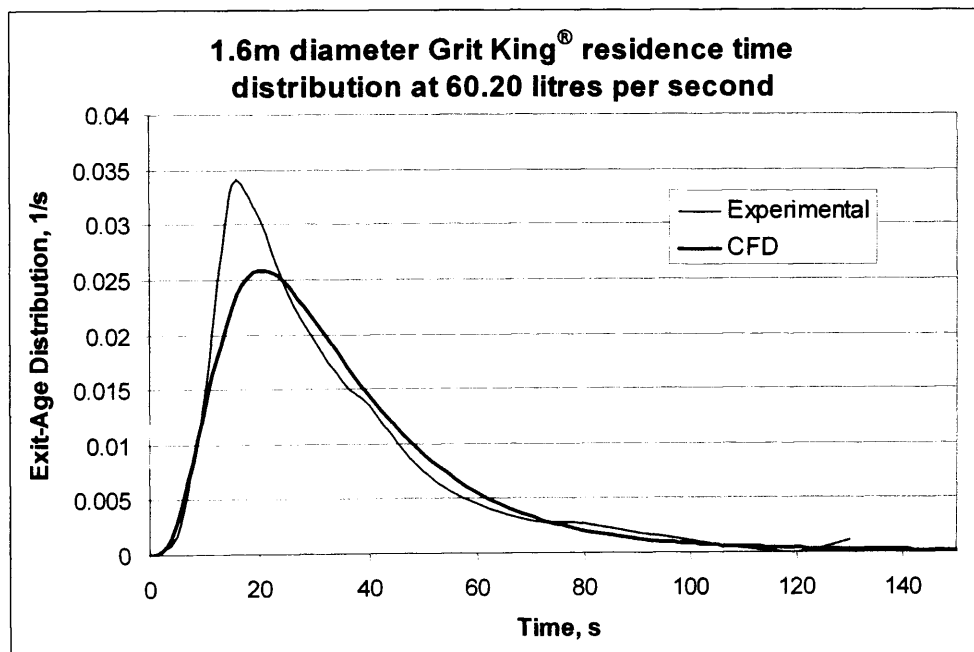| Time, / s	Concentration, / ppm	Time, / s	Concentration, / ppm
0	0.00	120	0.00
5	0.22	130	0.15
10	1.90	140*	0.15*
15	4.50	150*	0.05*
20	4.10	160*	0.05*
25	3.20	170*	0.05*
30	2.60	180*	0.05*
35	2.10	210*	0.05*
40	1.80	240*	0.10*
45	1.35	270*	0.05*
50	1.00	300*	0.15*
55	0.75	330*	0.10*
60	0.60	360*	0.10*
70	0.40	390*	0.05*
80	0.35	420*	0.10*
90	0.25	450*	0.10*
100	0.15	480*	0.10*
110	0.05	510*	0.15*

Figure N11. CFD and experimental RTD comparison of the 1.6m diameter Grit King® at 60.20 litres per second operating without an underflow component.